DOE/ER-0313/20
Distribution
Categories
UC-423, -424

FUSION MATERIALS
SEMIANNUAL PROGRESS REPORT
FOR THE PERIOD ENDING
JUNE 30, 1996

Prepared for
DOE Office of Fusion Energy
(AT 60 20 00 0)

DATE PUBLISHED: OCTOBER 1996

Prepared for
OAK RIDGE NATIONAL LABORATORY
Oak Ridge, Tennessee 37831
Managed by
Lockheed Martin Energy Research Corp.
for the
U.S. DEPARTMENT OF ENERGY
under Contract DE-AC05-96OR22464

DISCLAIMER

FOREWORD

This is the nineteenth in a series of semiannual technical progress reports on fusion materials. This report combines the full spectrum of research and development activities on both metallic and non-metallic materials with primary emphasis on the effects of the neutronic and chemical environment on the properties and performance of materials for in-vessel components. This effort forms one element of the materials program being conducted in support of the Magnetic Fusion Energy Program of the U.S. Department of Energy. The other major element of the program is concerned with the interactions between reactor materials and the plasma and is reported separately.

The Fusion Materials Program is a national effort involving several national laboratories, universities, and industries. A large fraction of this work, particularly in relation to fission reactor experiments, is carried out collaboratively with our partners in Japan, Russia, and the European Union. The purpose of this series of reports is to provide a working technical record for the use of the program participants, and to provide a means of communicating the efforts of materials scientists to the rest of the fusion community, both nationally and worldwide.

This report has been compiled and edited under the guidance of A. F. Rowcliffe by Gabrielle Burn, Oak Ridge National Laboratory. Their efforts, and the efforts of the many persons who made technical contributions, are gratefully acknowledged.

F. W. Wiffen
Division of Advanced Physics
and Technology

Reports previously listed in this series are as follows:

DOE/ER-0313/1	Period ending September 30, 1986
DOE/ER-0313/2	Period ending March 31, 1987
DOE/ER-0313/3	Period ending September 30, 1987
DOE/ER-0313/4	Period ending March 31, 1988
DOE/ER-0313/5	Period ending September 30, 1988
DOE/ER-0313/6	Period ending March 31, 1989
DOE/ER-0313/7	Period ending September 30, 1989
DOE/ER-0313/8	Period ending March 31, 1990
DOE/ER-0313/9	Period ending September 30, 1990
DOE/ER-0313/10	Period ending March 31, 1991
DOE/ER-0313/11	Period ending September 30, 1991
DOE/ER-0313/12	Period ending March 31, 1992
DOE/ER-0313/13	Period ending September 30, 1992
DOE/ER-0313/14	Period ending March 31, 1993
DOE/ER-0313/15	Period ending September 30, 1993
DOE/ER-0313/16	Period ending March 31, 1994
DOE/ER-0313/17	Period ending September 30, 1994
DOE/ER-0313/18	Period ending March 31, 1995
DOE/ER-0313/19	Period ending December 31, 1996
DOE/ER-0313/100	Technical Evaluation of the Technology of Vanadium Alloys for Use as Blanket Structural Materials in Fusion Power Systems

CONTENTS

(HT1) or 1050°C for two hours (HT2). Specimens given the HT1 treatment were annealed after final machining, whereas the HT2 specimens received the 1050°C anneal at Teledyne Wah Chang prior to final machining. Following machining HT2 specimens were than vacuum annealed at 180°C for two hours to remove hydrogen. Specimens treated using HT1 had a partially recrystallized microstructure and those treated using HT2 had a fully recrystallized microstructure. The fracture toughness as 25°C was determined by J-integral tests and at -196°C by ASTM 399 type tests. Toughness values obtained at -196°C were converted to J-integral values for comparison to the 25°C data. The 25°C fracture toughness was very high with none of the specimens giving valid results per ASTM criteria. Specimens fractured by microvoid coalescence. The fracture toughness at -196°C was much lower than that at 25°C and the fracture surface showed predominantly cleavage features. The present results show a transition from ductile to brittle behavior with decreasing test temperature which is not observed from one-third scale Charpy impact tests. The fracture toughness at -196°C was still quite high, however, at about 75 kK/m^2.

Delaminations in planes normal to the thickness direction wee seen at both test temperatures. Fracture surfaces inside the delaminations exhibited nearly 100% cleavage facets. The cause of the brittle delaminations was not determined, but will be a subject for further investigation.

Grain growth studies were conducted to evaluate the effect of time and temperature on the grain size of pure V,V-4 wt.%Cr-4 wt.%Ti, and V-5 wt.%Cr-5 wt.%Ti alloys. The temperatures used in the study were 500, 650, 800, and 1000°C, and exposure times ranged between 100 and ≈5000 h. All three materials exhibited negligible grain growth at 500, 650, and 800°C, even after ≈5000 h. At 1000°C, pure V showed substantial grain growth after only 100 h, and V-4Cr-4Ti showed growth after 2000 h, while V-5Cr-5Ti showed no grain growth after exposure for up to 2000 h.

Tensile testing was carried out on SS-3 tensile specimens punched from 0.762-mm-thick sheets of the large heat of V-4Cr-4Ti and small heats of V-3Cr-3Ti and V-6Cr-6Ti. The tensile specimens were annealed at 1000° for 2 h to obtain a fully recrystallized, fine grain microstructure with a grain size in the range of 10-19 μm. Room temperature tests at strain rates ranging from 10^{-3} to 5×10^{-1}/s were carried out in air; elevated temperature testing up to 700°C was conducted in a vacuum better than 1×10^{-5} torr (<10^{-3} Pa). To study the effect of atomic hydrogen on ductility, tensile tests were conducted at room temperature in an ultra high vacuum chamber (UHV) with a hydrogen leak system.

Tensile properties of V-3Cr-3Ti, V-4Cr-4Ti, and V-6Cr-6Ti were measured at room temperature and 100–700°C at a strain rate of 1.1×10^{-3}/s. The ultimate tensile strength of all the alloys exhibited a minima at 300°C, whereas the 0.2% yield strength was relatively independent of temperature between 400° and 700°C. The total and uniform elongations were relatively insensitive to variation in test temperature above 400°C. All the alloys exhibited good ductility (e.g., uniform elongation >15%) and a large amount of work hardening ability. A yield point

1.0 VANADIUM ALLOYS

PRODUCTION AND FABRICATION OF VANADIUM ALLOYS FOR THE RADIATIVE DIVERTOR PROGRAM OF DIII–D — ANNUAL REPORT INPUT FOR 1996 —

W.R. Johnson, J.P. Smith, and R.D. Stambaugh (General Atomics)

SUMMARY

V-4Cr-4Ti alloy has been selected for use in the manufacture of a portion of the DIII–D Radiative Divertor (RD) upgrade. The production of a 1200-kg ingot of V-4Cr-4Ti alloy has been completed at Teledyne Wah Chang of Albany, Oregon (TWCA) to provide ~800-kg of applicable product forms, and two billets have been extruded from the ingot. Chemical compositions of the ingot and both extruded billets were acceptable. Material from these billets will be converted into product forms suitable for components of the DIII–D Radiative Divertor structure. Joining of V-4Cr-4Ti alloy has been identified as the most critical fabrication issue for its use in the RD Program, and research into several joining methods for fabrication of the RD components, including resistance seam, friction, and electron beam welding, is continuing. Preliminary trials have been successful in the joining of V-alloy to itself by electron beam, resistance, and friction welding processes and to Inconel 625 by friction welding.

PROGRESS AND STATUS

1. Introduction

General Atomics (GA), along with the Argonne National Laboratory (ANL) and Oak Ridge National Laboratory (ORNL), has developed and is implementing a plan for the utilization of vanadium alloys in the DIII–D tokamak. This plan will culminate in the fabrication, installation, and operation of a water-cooled vanadium alloy structure in the DIII–D RD upgrade.[1,2] The use of a vanadium alloy will provide a meaningful step towards developing advanced materials for fusion power applications by 1) demonstrating the in-service behavior of a vanadium alloy (V-4Cr-4Ti) in a typical tokamak environment, and 2) developing knowledge and experience on the design, processing, and fabrication of full-scale vanadium alloy components.

The program consists of three phases: first, small vanadium alloy specimens and coupons will be exposed in DIII–D; second, a small vanadium alloy component will be designed, manufactured, and operated in conjunction with the existing DIII–D divertor; and third, the upper private flux baffle of the new double-null, slotted divertor will be designed, fabricated from vanadium alloy product forms, and installed in DIII–D. A major portion of the program is research and development to support fabrication and resolve key issues related to environmental effects. The plan is being carried out in conjunction with GA and the Materials Program of the Department of Energy's Office of Fusion Energy (DOE/OFE). The execution of the plan is a joint effort by GA, the DIII–D Program, and DOE Material Program participants, primarily ANL, ORNL, and Pacific Northwest National Laboratory (PNNL).

2. PHASE 1: Specimen and Coupon Exposures and Analysis

Miniature Charpy V-notch (CVN) impact and tensile specimens of V-4Cr-4Ti alloy were exposed/monitored in DIII–D in positions behind the divertor baffle for ~9 months.[4] GA has collated the environmental data, and ANL has developed and is now implementing an analysis plan for the evaluation of the specimens. A new set of samples, installed during the January 1996 vent, is currently undergoing exposure.

In parallel to these exposures, other V-4Cr-4Ti alloy samples underwent short-term exposures utilizing the DIII–D Divertor Material Exposure System (DiMES). A V-4Cr-4Ti alloy disc, and subsequently CVN specimens, were exposed/monitored during baking and cleaning of DIII–D.[4] GA has collated the environmental data, and ANL has developed and is now implementing an analysis plan to determine the pickup of any impurities in these specimens. Other DiMES exposures are being considered to evaluate the effects of other DIII–D environmental conditions (e.g., discharge cleaning, boronization, etc.).

3. PHASE 2: Small Component Exposure

A second step in the DIII–D Vanadium Plan is to install a small V-4Cr-4Ti alloy component in DIII–D. This component will be manufactured utilizing many of the methods proposed for the Phase 3 water-cooled private flux baffle. The component will be installed, exposed for some period of tokamak operations, and then removed. Samples from the component will be excised, and metallurgical analyses and property measurements will be made on the excised materials. Specific plans have not yet been defined.

4. PHASE 3: Radiative Divertor Program

The design, manufacture, and installation of a V-4Cr-4Ti alloy private flux baffle structure for the upper divertor of the RD program will be performed as the third phase of the vanadium alloy program (Fig. 1). The V-4Cr-4Ti alloy structure will contain two, toroidally-continuous, water-cooled structural panels with inertially-cooled graphite tiles mechanically attached to their surfaces by welded studs. The panels will be water cooled during machine operation, experiencing a maximum temperature of ~60°C. During post-vent clean-up, hot air will replace the water in the coolant channels of the structure, and the structure (along with the DIII–D vessel) will be baked to ~400°C. The panels will be supported from the vacuum vessel by Inconel 718 supports which will provide the required strength for reacting disruption loads and the flexibility for withstanding differential thermal growth during baking. Due to the lower electrical resistivity of the V-4Cr-4Ti alloy as compared to Inconel 625, the toroidal current flow during disruption will be approximately four times larger. The design of the panels and supports will be modified to react the larger loads.[1]

The panels will be made in six segments and fabricated of sandwich construction from two 4.8 mm sheets, each containing a 1.5 mm deep coolant channel milled into its side to provide an internal coolant channel. Resistance seam welding is the primary candidate process being considered for structurally joining the panels edges, with electron beam welding utilized for making a perimeter leak tight seal. Other methods of joining are proposed for different areas of the design. To facilitate installation, bi-metallic V-4Cr-4Ti alloy to Inconel 625 tube-to-tube joints are planned for effecting in-vessel gas-tungsten arc field welds to Inconel 625 water supply tubes.

A. Fabrication of Product Forms for the Radiative Divertor

Processing of the V-4Cr-4Ti alloy by TWCA was initiated in September 1995. Details of this processing up to the vacuum-arc melting of a 1200-kg V-4Cr-4Ti alloy ingot, including processing of the raw vanadium from high purity vanadium oxide, selection of raw vanadium lots, and electron beam melting of two (2) high purity vanadium ingots (a ~900-kg ingot and ~400-kg of another ingot) for the alloy, were presented in a previous report.[4] During February 1996, the two vanadium ingots were

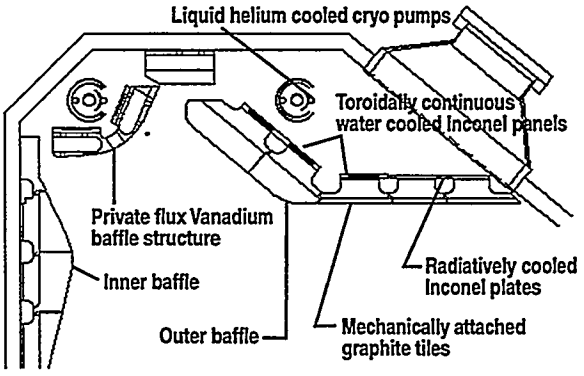

Fig. 1. Location of vanadium structure in radiative divertor.

machined into large chips and consolidated with high purity Cr and Ti (double vacuum-melted Ti), and a 1200-kg V-4Cr-4Ti alloy ingot was produced by double vacuum-arc melting (Fig. 2). The resulting ingot was 34.9 cm in diameter × 210.8 cm in length. Chemical analysis of the ingot (Table 1) at three separate locations (top, middle, and bottom) indicated that the ingot was generally within specification limits for all elements except primarily for Nb, as was expected based on the Nb levels measured on the high purity vanadium ingots used for its production.[4] Based on this analysis, the ingot was accepted for continued processing.

The diameter of the ingot was machined to 32.1 cm and the ingot was sectioned into two (2) ~85 cm pieces. Each section was encapsulated in a stainless steel can fabricated from rolled and seam-welded ~4.8 mm thick sheet. Each can was evacuated (to ~2×10^{-4} Torr), and seal welded. The canned ingot sections were shipped to CSM Inc. in Coldwater, Michigan for extrusion into billets (sheet bar). On 1 May, the canned sections were extruded into rectangular billets, ~11.4 cm × ~24.1 cm in cross-section, after heating for several hours in a slightly reducing, gas-fired furnace to a temperature of ~1140°C. Extrusion of the first ingot section (Section A) went as planned, resulting in a ~274 cm long billet which appeared to have an intact can and no observable cracks, tears, etc. During the extrusion of the second ingot section (Section B), however, the extrusion stalled about halfway through the die, yielding only a partial rectangular billet, ~126 cm long, which appeared to have a ~19 cm long crack near the nose end of the billet. This cracked material was later removed by sectioning from the remainder of the billet. Subsequent to the extrusion, the two billets were shipped back to TWCA and sampled for chemical analysis at each end. The stainless steel cans were removed from the billets by rough grinding, the ends of the billets were sectioned to remove any cracks, and the billets were then finely ground/pickled to final sheet bar dimensions (10.4 cm × 23.4 cm × 245.1 cm and 107.4 cm, respectively). The sheet bar materials were then vacuum annealed in preparation for longitudinal rolling into 4.7 cm thick plate. Further processing is currently on hold until the chemical analysis of the two extruded billet materials is completed and accepted.

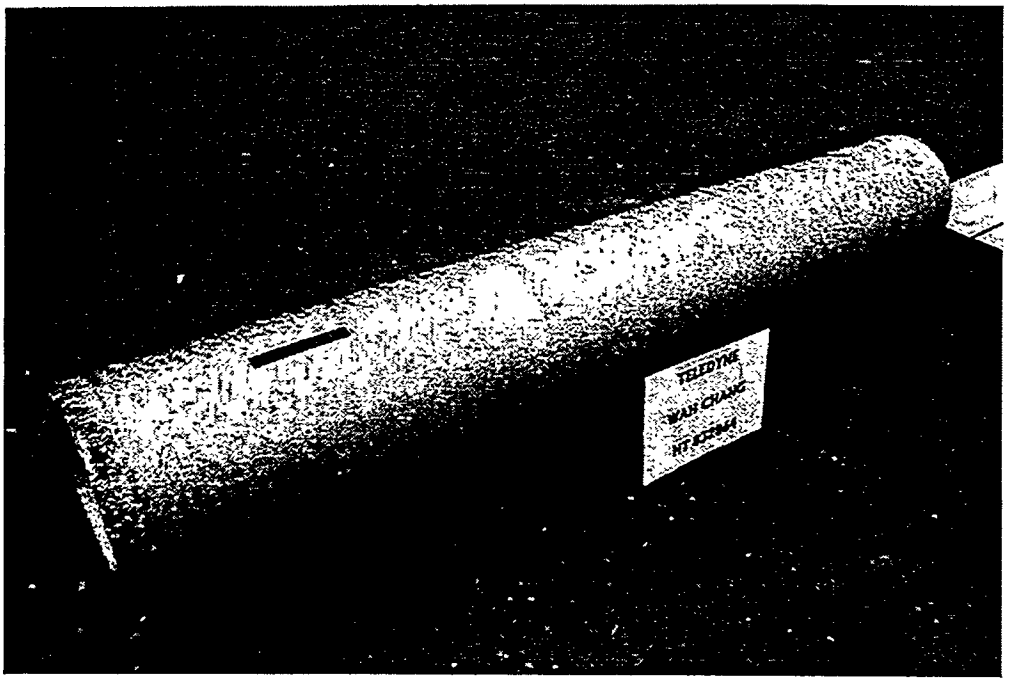

Fig. 2. This V-4Cr-4Ti ingot (the largest of its type ever made) will be formed into plate and rod for use in GA's DIII–D divertor modification.

TABLE 1
CHEMICAL COMPOSITION GOALS AND CHEMISTRY FOR V-4Cr-4Ti ALLOY
(Heat ID #832864)

	Content, parts/million by weight (ppm)[a]			
Element	Specification for Alloyed Vanadium Ingot	Alloyed Vanadium Ingot (Top of Ingot)	Alloyed Vanadium Ingot (Middle of Ingot)	Alloyed Vanadium Ingot (Bottom of Ingot)
Cr	4 ± 0.5 wt. %	3.9	3.8	3.6
Ti	4 ± 0.5 wt. %	3.9	3.6	3.8
Si	400–1000	270	270	280
H	<10	<3	<3	<3
O	<400	380	370	440
N	<200	150	120	120
C	<200	35	29	46
Al	<200	190	200	190
Fe	<300	220	260	205
Cu	<50	<50	<50	<50
Mo	<50[b]	<50	<50	<50
Nb	<20[b]	140	91	87
Cl	<3	<3	<3	<3
Ga	<10	<1	<1	<1
Ca	<1[b]	4	3	4
Na	<1[b]	<2	<2	<2
K	<1[b]	2	2	2
Mg	<1[b]	1	<1	1
P	<30	<30	<30	<30
S	<30	<10	<10	<10
B	<5	<5	<5	<5
Ag	<1	<1	<1	<1
V	balance	balance	balance	balance

[a]Unless otherwise specified in weight %
[b]Desired values – <5 ppm Mo, <1 ppm Nb, <1 ppm total Ca+Na+K+Mg.

B. Manufacturing Technology Development

As manufacturing development is a major focus of this project a significant amount of research and development is being performed in this area. The RD structure will require many metal/metal joints, and joining development is therefore a key area of study. GA is using corporate IR&D funds to complement welding efforts at ANL and ORNL, investigating several different joining processes which are attractive for

fabrication of RD components including resistance seam, friction, and electron beam welding. The scope of the GA joining development efforts has been limited by the availability of material, some of which has been purchased from TWCA (V-5Cr-5Ti; Heat ID #932394) and some of which has been supplied by ANL (V-5Cr-5Ti alloy; Heat ID #832394 and V-4Cr-4Ti alloy; Heat ID #832665[3]).

Resistance Welding Studies

Resistance seam welding is planned for structurally joining two sheets of vanadium alloy together to make the water-cooled panels for the RD program. However, based on experience with Inconel 625, it is not expected to provide a vacuum-tight weld, and therefore, another process will be used to make the seal weld.

As reported previously,[4] 3.8 mm thick sheet material of V-4Cr-4Ti alloy was obtained from ANL and initial resistance spot weld trials were performed in air. No weld nuggets were achieved on 3.8 mm sheet, although some diffusion bonding was obtained, indicating that the material had reached 80% to 90% of its melting point. These diffusion-bonded samples demonstrated considerable strength (up to 135 MPa) in crude shear tests. Additional trials were performed with similar V-4Cr-4Ti alloy sheet material using weld parameters adjusted upward by an amount estimated to produce melting between the facing surfaces of the sheet samples based on the observed diffusion bonding in previous trials. These trials were successful, yielding weld nuggets ~7 mm in diameter, and microhardness values in the weld and heat-affected zoneds (HAZs) only ~10% greater than that of the parent metal (Fig. 3).

Additional spot weld trials have recently been performed using material similar in thickness to that to be used for the RD water-cooled panels (4.8 mm). For these trials, 6.35 mm thick V-5Cr-5Ti alloy sheet material was supplied by ANL, and this material was cold rolled by ORNL to the required thickness and annealed. Power settings for this thickness were increased (and varied) over that used for the thinner material, using as a starting point, current versus thickness data obtained from the literature for carbon steel, which was found to have similar strength and resistivity to V-4Cr-4Ti and V-5Cr-5Ti alloys. These weld trials were also successful, producing weld nuggets with diameters which correlated with the average power per unit time in the welding cycle, varying from ~3.8 to ~12 mm in diameter. Although all of the weld nuggets generally contained single, small, centrally-located pores, welds ~10 mm in diameter demonstrated considerable strength (~685 MPa based on the nugget diameter measured on a companion sample welded using the same weld parameters) in simple single spot lap shear tests. Although the central pores in these welds do not appear to substantially degrade the strength of the weld joints, several additional spot weld trials using increased electrode (forge) pressures at the end of the weld cycle are

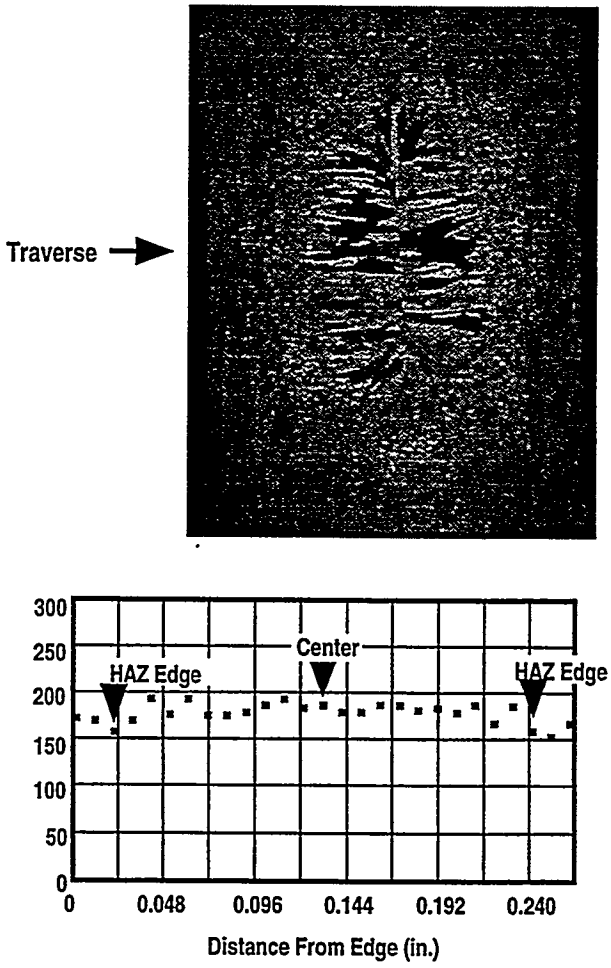

Fig. 3. Resistance spot weld of 3.8 mm thick V-Cr-4Ti alloy sheets with microhardness profile across the weld nugget.

being planned in an attempt to eliminate or minimize them. These trials will then be followed by seam welding trials.

Friction Welding Studies

Two types of friction welding trials are in progress. Inertia (shop) and portable friction welding have been selected as candidate processes for joining vanadium alloy to itself, and inertia welding has been selected for creating a bi-metallic joint between vanadium alloy and Inconel 625. The first inertia weld trials of vanadium alloy (V-5Cr-5Ti alloy) to itself were successful in air. Metallography showed complete bonding with no indications of porosity or cracking, and microhardness measurements showed only slight increases in hardness in the weld and HAZs (Fig. 4). In the photomicrograph shown in Fig. 4, the weld interface maintained a fine grain structure, with little or no grain growth, and a very minimal HAZ. Tensile and torsion tests at room temperature resulted in failures in the parent metal away from the joint and HAZs.

As reported previously,[4] inertia welding trials in air continued with the successful joining of Inconel 625 rod to V-5Cr-5Ti alloy rod. Metallography showed complete bonding with no porosity or cracking, and tensile pull tests performed at room temperature yielded joint strengths greater than ~760 MPa, i.e., near that of the Inconel 625. Inertia weld trials were then performed to fabricate bi-metallic joints using a tube-to-tube configuration. These trials, although encouraging, were not completely successful, producing joints which were not leak tight during helium leak checking and with variable strengths in room-temperature tensile tests (~70–380 MPa). Metallography of a sample showed substantial bonding at the joint interface, but with noticeable porosity. Plastic deformation (buckling) of the tubular portion of the Inconel 625 part in a radially-inward direction (Fig. 5), caused by 1) an inadequate wall thickness (for the applied ram load), and 2) a lack of lateral support from the mating V-5Cr-5Ti alloy part near the inner surface of the Inconel 625 part, which reduced the loading (and also frictional heating) at the joint interface, are postulated as the reasons for the observed results. Additional trials, using a new configuration to alleviate this problem, are currently in progress.

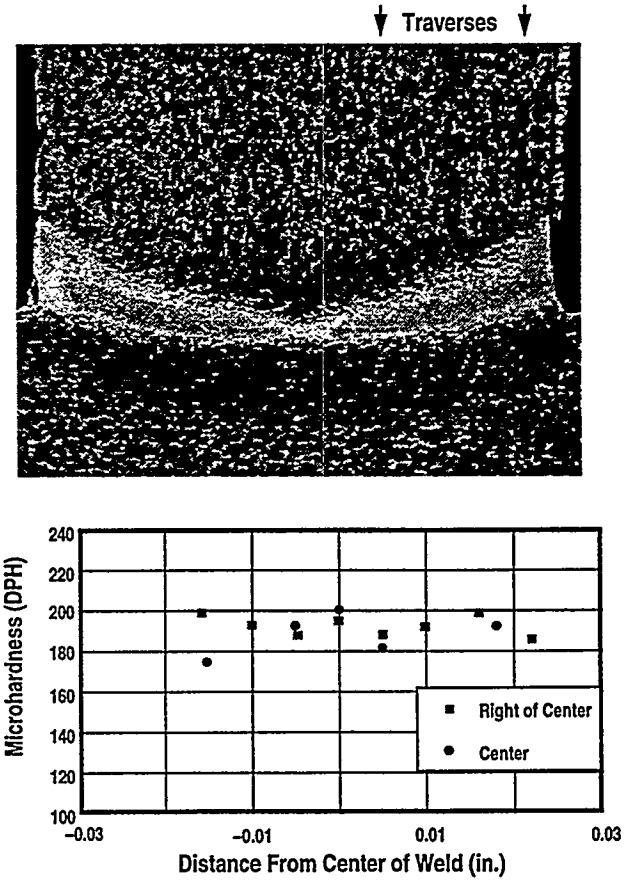

Fig. 4. Etched cross-section of V-5Cr-5Ti alloy inertia weld trial sample showing location of weld joint and microhardness measurements.

Preliminary portable friction welding trials of vanadium alloy rod to plate have been performed, GA to develop methods of *in-situ* replace-ment of studs on water-cooled panels. Initial trials achieved substantial bonding, but the hardness of the weld interface increased significantly over that of the parent metal. In addition, a large amount of grain growth occurred at the interface and substantial HAZs were developed (Fig. 6). It was noted during the trials that the temperature of the weld interface was significantly higher than that observed in the inertia weld process, and the time to create the weld was considerably onger. It is believed that both of these factors resulted in the observed grain growth, large HAZs, and increase in weld interface hardness. Additional trials are in progress using weld parameters to minimize these effects.

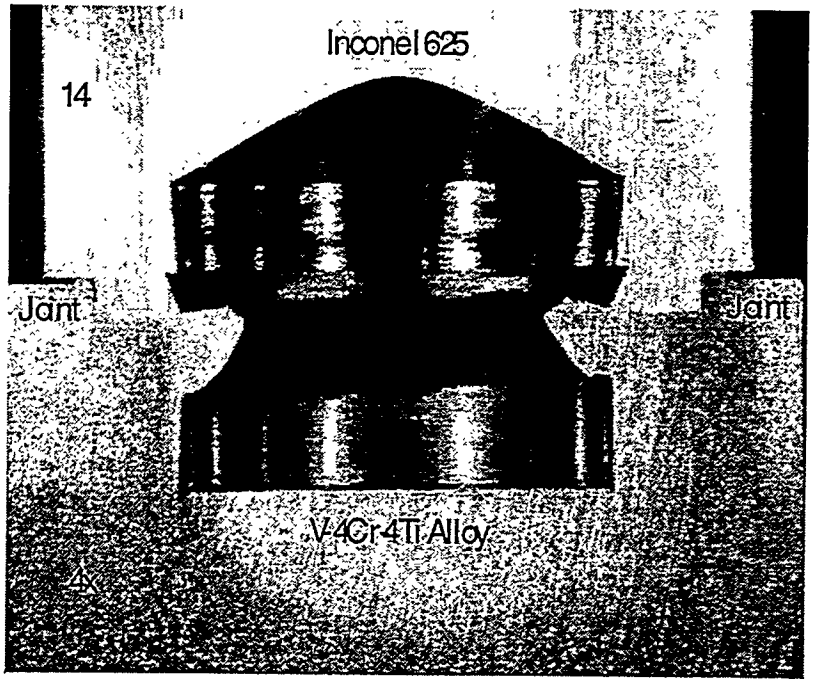

Fig. 5. Ground cross section of inertia-welded V-4Cr-4Ti alloy (bottom)/Inconel 625 (top) joint in simulated tube-tube configuration. Note: indentation and inward plastic flow of original V-alloy surface and inward flow (buckling) of tubular Inconel 625 lip.

Electron Beam Welding Studies

Preliminary electron beam welding trials have also been performed at GA to complement the work being performed at ORNL. Initial weld parameters were obtained from ORNL personnel and weld penetration tests were performed using 6.35 mm thick V-5Cr-5Ti alloy plate acquired from ANL to establish specific weld parameters for creating a lap weld of two 3.85 mm thick vanadium alloy sheet materials (V-5Cr-5Ti alloy to V-4Cr-4Ti alloy). A lap weld of the materials was created and verified by metallography to be free of cracks. Microhardness measurements showed less than ~10% increase in hardness across the weld and HAZs, and room-temperature tensile tests performed on flat reduced-section specimens failed in the parent metal well away from the weld joints and HAZs at values greater than the parent metal strength.

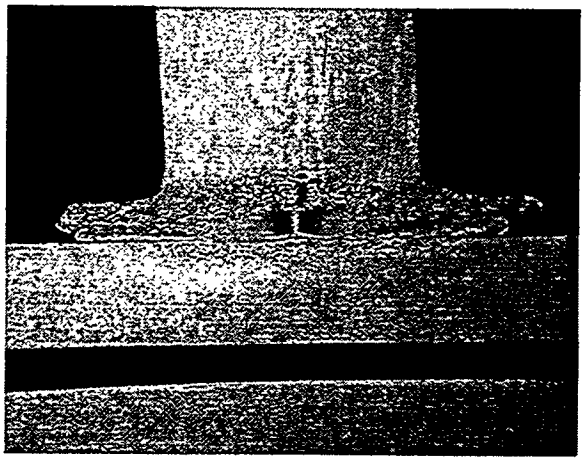

Fig. 6. Etched cross-section of V-5Cr-5Ti alloy portable friction weld trial sample showing location of weld joint.

CONCLUSIONS

A program for utilizing vanadium alloys in DIII–D has been developed to progress the development of low activation alloys for fusion, and production of material for this program has started. Two vanadium ingots have been electron beam melted, consolidated with high purity Cr and Ti, and double vacuum-arc melted to produce a 1200-kg V-4Cr-4Ti alloy ingot of acceptable chemical

composition. The alloy ingot has been extruded into rectangular billets and machined into sheet bar for further processing into sheet and rod product forms. Preliminary successes have been achieved in developing similar and dissimilar metal welds in vanadium alloy by resistance, inertia, portable friction, and electron beam welding methods.

ACKNOWLEDGMENTS

This is a report of work supported by the U.S. Department of Energy under Contract No. DE-AC03-89ER51114, and General Atomics under internal R & D funding.

REFERENCES

[1]J.P. Smith, W.R. Johnson, R.D. Stambaugh, P.W. Trester, D. Smith, and E. Bloom, "Vanadium Alloys For The Radiative Divertor Program of DIII–D," to be published in *Proc. of the 16th IEEE/NPSS Symposium on Fusion Engineering*, Champaign, Illinois, September 30 through October 5, 1995.

[2]J.P. Smith, W.R. Johnson, R.D. Stambaugh, P.W. Trester, D. Smith, and E. Bloom, "Utilization of Vanadium Alloys in the DIII–D Radiative Divertor Program," to be published in Proc. of the 7th International Conf. *on Fusion Reactor Materials (ICFRM-7)*, Obninsk, Russia, September 25–29, 1995.

[3]H.M. Chung, H.--C. Tsai, D.L. Smith, R. Peterson, C. Curtis, C. Wojcik, and R. Kinney, "Fabrication of 500-kg Heat of V-4Cr-4Ti," *Fusion Reactor Materials Semiannual Progress Report,* DOE/ER-0313/17, Oak Ridge National Laboratory, Oak Ridge, Tennessee (1994), p. 178.

[4]W.R. Johnson, J.P. Smith, and R.D. Stambaugh, "Production and Fabrication of Vanadium Alloys for the Radiative Divertor Program of DIII–D," *Fusion Reactor Materials Semiannual Progress Report,* DOE/ER-0313/19, Oak Ridge National Laboratory, Oak Ridge, Tennessee (1995), p. 5.

A MASTER CURVE-MECHANISM BASED APPROACH TO MODELING THE EFFECTS OF CONSTRAINT, LOADING RATE AND IRRADIATION ON THE TOUGHNESS-TEMPERATURE BEHAVIOR OF A V-4Cr-4Ti ALLOY

G. R. Odette, E. Donahue, G. E. Lucas, and J. W. Sheckherd (University of California, Santa Barbara)

OBJECTIVE

The objective of this work is to develop an understanding of fracture in the vanadium alloy system in support of quantitative methods for predicting failure of flawed fusion structures.

SUMMARY

The influence of loading rate and constraint on the effective fracture toughness as a function of temperature [$K_e(T)$] of the fusion program heat of V-4Cr-4Ti was measured using subsized, three point bend specimens. The constitutive behavior was characterized as a function of temperature and strain rate using small tensile specimens. Data in the literature on this alloy was also analysed to determine the effect of irradiation on $K_e(T)$ and the energy temperature (E-T) curves measured in subsized Charpy V-notch tests. It was found that V-4Cr-4Ti undergoes "normal" stress-controlled cleavage fracture below a temperature marking a sharp ductile-to-brittle transition. The transition temperature is increased by higher loading rates, irradiation hardening and triaxial constraint. Shifts in a reference transition temperature due to higher loading rates and irradiation can be reasonably predicted by a simple equivalent yield stress model. These results also suggest that size and geometry effects, which mediate constraint, can be modeled by combining local critical stressed area σ^*/A^* fracture criteria with finite element method simulations of crack tip stress fields. The fundamental understanding reflected in these models will be needed to develop $K_e(T)$ curves for a range of loading rates, irradiation conditions, structural size scales and geometries relying (in large part) on small specimen tests. Indeed, it may be possible to develop a master $K_e(T)$ curve-shift method to account for these variables. Such reliable and flexible failure assessment methods are critical to the design and safe operation of defect tolerant vanadium structures.

INTRODUCTION

Vanadium alloys are attractive candidates for structural applications in fusion reactors because of their low neutron activation, favorable thermal properties and potential for radiation stability. However, a potential problem that these alloys share with other body centered cubic (bcc) metals is a so-called ductile-to-brittle transition below a temperature (T_t) which may be significantly elevated as a consequence of irradiation. Preliminary studies using nonstandard tests -- including one-third-size, Charpy V-notch and disc bend specimens -- have suggested that alloy compositions in the range V-4Cr-4Ti are highly resistant to embrittlement, with T_t in the vicinity of or below -196°C (liquid nitrogen temperatures) even following high fluence irradiations and exposure to hydrogen [1-5].

However, T_t depends on the details of the test procedure[6], and it cannot be used to quantify structural stress and strain limits; hence, it is neither a fundamental material property nor a useful engineering parameter. Indeed, while $K_e(T)$ is a useful quantitative measure of fracture resistance, it also depends on variables such as size scales and flaw geometry (mediating the stress intensity factor, crack tip energy release rate and constraint), loading(strain) rate, irradiation and other sources of embrittlement (e.g., hydrogen). As discussed in detail elsewhere[7], it may be possible to develop a method to predict the stress and strain limits of flawed fusion structures using a master $K_e(T)$ curve adjusted on an absolute temperature scale using measured shifts (ΔT) to account for variables such as constraint (ΔT_c), irradiation (ΔT_i) and strain rate ($\Delta T_{\dot{\varepsilon}}$): that is,

$$K_e(T) = K_{mc}(T - [T_o + \Delta T_c + \Delta T_i + \Delta T_{\dot{\varepsilon}} + \Delta T_m]) \quad (1)$$

where T_o is a reference temperature at a valid reference K_{Jc} level (e.g., 60 MPa$\sqrt{m}$) and ΔT_m is a specified safety margin.

In addition to developing the master curve-shift method for vanadium structures, the broader objective of this research is to integrate measurements of $K_e(T)$ with observations of fracture processes and modeling to: 1) determine the basic fracture mechanisms and obtain a fully quantitative micromechanically-based local fracture model; 2) develop methods to use small specimens to measure the intrinsic fracture resistance of these alloys; 3) determine methods to use the intrinsic properties of these alloys (note, $K_e(T)$ is not an intrinsic property) to predict load-displacement limits of flawed fusion structures; and 4) develop microstructure-property-property models of the effects of metallurgical variables and irradiation on fracture toughness.

EXPERIMENT

The study was carried out on the program heat of V-4Cr-4Ti (#832665) procured from Teledyne Wah Chang by Argonne National Laboratory[8]. Three-point bend tests were carried out on 1/3-sized Charpy V-notch specimens (3.33 x 3.33 x 25.4 mm) provided by Oak Ridge National Laboratory. The subsized Charpy specimen blanks were electro-discharge machined from 3.8 mm thick plate in the 40% warm-rolled (400°C) as-received condition with a T-L orientation (crack propagation parallel to the rolling direction). The machined specimens were annealed for 2h at 1000°C in a vacuum of better than 10^{-4} Pa to produce a recrystallized microstructure and remove residual hydrogen. This series of heat treatments produces an average grain size of about 25 μm and a Vickers microhardness of about 150 ± 5[9,10].

Fatigue pre-cracking was carried out at a final $\Delta K \leq 15$ MPa$\sqrt{m}$ to a nominal crack length (a) to specimen width (W) ratio of $a/W \approx 0.5$. Considerable care was taken to insure that the pre-cracked miniature Charpy specimens (PMC) were kept well below their yield load. Side grooves were machined into subset of the PMC specimens with a dry abrasive cutting wheel; the side grooves had root radii of about 0.25 mm and a depth of about 0.1W on each side. A third set of PMC specimens was fatigue pre-cracked on each side from shallow notches to a depth of about 0.1W. Side notched specimens (PNC) and side pre-cracked specimens (PPC) had increased lateral (plane strain) constraint following general yielding compared to the smooth sided (PMC) specimens. The specimens were tested in three point bending over a temperature range from -196 to 21°C at approximate loading rates of 8.8×10^{-6} m/s (static, S), 0.3 m/s (low dynamic, LD) and 3 m/s (intermediate dynamic, ID).

Due to the very small size of the specimens combined with the relatively low strength of the V-4Cr-4Ti alloy (e.g., a room temperature yield stress (σ_y) of about 350 MPa) the only true fracture events that were observed were cleavage pop-ins that occurred at low temperatures below a (varying) sharp transition. Roughly semicircular pop-in cleavage cracks were pinned and arrested at various distances towards the sides and back of the specimen. At only slightly higher temperatures, fracture was generally not observed. In this case, the specimen responded to the applied load by massive crack blunting and bending until it simply bottomed out in the test fixture. A limited amount of stable crack tearing was observed in at least one case at a K_e greater than about 300 MPa$\sqrt{m}$.

In a few cases (e.g., low-dynamic loading rates at very low temperature and the static test at -196°C) a standard K_e could be determined from $K_e = \sqrt{J_{Ie} E'}$, where E' is the plane strain elastic modulus and J_{Ie} is the critical effective energy release rate given by the area under the stress-displacement (time) curve up to the load drop at cleavage pop-in. However, determining J_{Ie} from load-displacement/time data was not generally possible. In these cases, K_e was evaluated from $K_e = \sqrt{\delta^* \sigma_y E'}$ where δ^* is the critical crack tip opening displacement at the point of initiation of crack extension[11,12]. A confocal microscopy (CF)-

fracture reconstruction (FR) technique was used to measure δ^*. The FR algorithms use conjugate fracture surface topographs measured with CM to resolutions around 1 μm to tomographically determine the sequence of deformation and microfracture events in the process zone in front of the crack tip ultimately leading to macroscopic fracture (e.g., a macroscopic pop-in). The CM-FR method is described elsewhere[11,12]. In cases where both could be compared, the two methods of estimating K_e were in good agreement. In addition to CM-FR, the fracture surfaces of all of the specimens were characterized by optical and scanning electron microscopy (SEM).

As-received, 1.07mm-thick sheets from the same heat of V-4Cr-4Ti were cold rolled (less than 5% per pass) to a thickness of 0.5mm with an intermediate heat treatment (at 0.86 mm) at 1000°C for 2h in vacuum. Miniature tensile specimens (25mm long) were punched from the 40% cold worked sheet with their axis perpendicular to the plate rolling direction. They were then given a final heat treatment at 1000°C for 2h in vacuum. The grain sizes and diamond pyramid hardness of the tensile specimens in this condition were roughly the same as the fracture specimens. A nearly complete matrix of tensile tests was conducted at temperatures from -196° C to 100°C in roughly 100°C intervals at estimated strain rates of about $4x10^{-4}$, $2x10^{-2}$ and $2s^{-1}$. Load-cross head displacement data were analyzed to determine the engineering stress-strain [$\sigma(\varepsilon)$] curves. Previous measurements have shown that this expedient provides values of yield stress (σ_y) and ultimate tensile strength (σ_u) that are similar to those measured with methods using direct extensometry (of course, the apparent moduli and yield strains are greatly decreased and increased, respectively, by the load train compliance in the tests without direct extensometry). In most cases, a sharp well-defined σ_y was observed, and σ_y was defined at the Luders plateau if one was present. When a Luders plateau was not present, σ_y was defined at the 0.2% offset strain. The accuracy of was estimated to be about ±15 MPa for the static tests and about ±30 MPa at the intermediate and high strain rates.

EXPERIMENTAL RESULTS

Tensile Properties

Figure 1 shows representative $\sigma(\varepsilon)$ curves obtained as a function of strain rate and test temperature. In general, the $\sigma(\varepsilon)$ behavior is complex and variously includes yield drops, Luders plateaus, regions of strain hardening and necking; and the overall $\sigma(\varepsilon)$ curve is influenced by factors such as the specimen geometry, adiabatic heating and stress state. Hence, the simpler property, σ_y, is primarily used in this study. Nonetheless, some general observations about $\sigma(\varepsilon)$ are pertinent. First, both σ_y and σ_u increase with decreasing temperature and increasing strain rate (see below). The strain hardening rate overall is very low, with strain hardening exponents estimated to be less than 0.1. However, the macroscopic ductilities, including uniform (UE) and total elongation (TE), are typical of structural alloys and do not appear to vary significantly over much of the test parameter range. Both TE and UE, however, do decrease at the lowest temperatures and highest strain rates, where the latter drops essentially to zero. Closer examination shows that, with the exception of several data points, there is a trend towards decreased UE with increased σ_y. This trend, associated with a corresponding decrease in the strain hardening rate, is clearly seen in Figure 2 which shows that the ratio σ_y/σ_u increases with increasing σ_y. The data for the intermediate and high rates overlap and fall only slightly above the low rate, static data at high σ_y. If the σ_y/σ_u ratio is taken as a rough measure of the post yield constitutive behavior, these results suggest that conditions that produce the same σ_y also result in similar overall $\sigma(\varepsilon)$ behavior. The validity of this hypothesis, including the effects of irradiation hardening, will be examined in future research.

However, in the current work emphasis is on deriving a $\sigma_y(\dot{\varepsilon},T)$ correlation. As shown in Figure 3, similar to the behavior of bcc steels[13], the σ_y data can be collapsed onto a common strain rate ($\dot{\varepsilon}$) compensated temperature (T') scale defined by

$$T'(K) = T(K)[1 + C \ln (\dot{\varepsilon}_O/\dot{\varepsilon})]. \qquad (2)$$

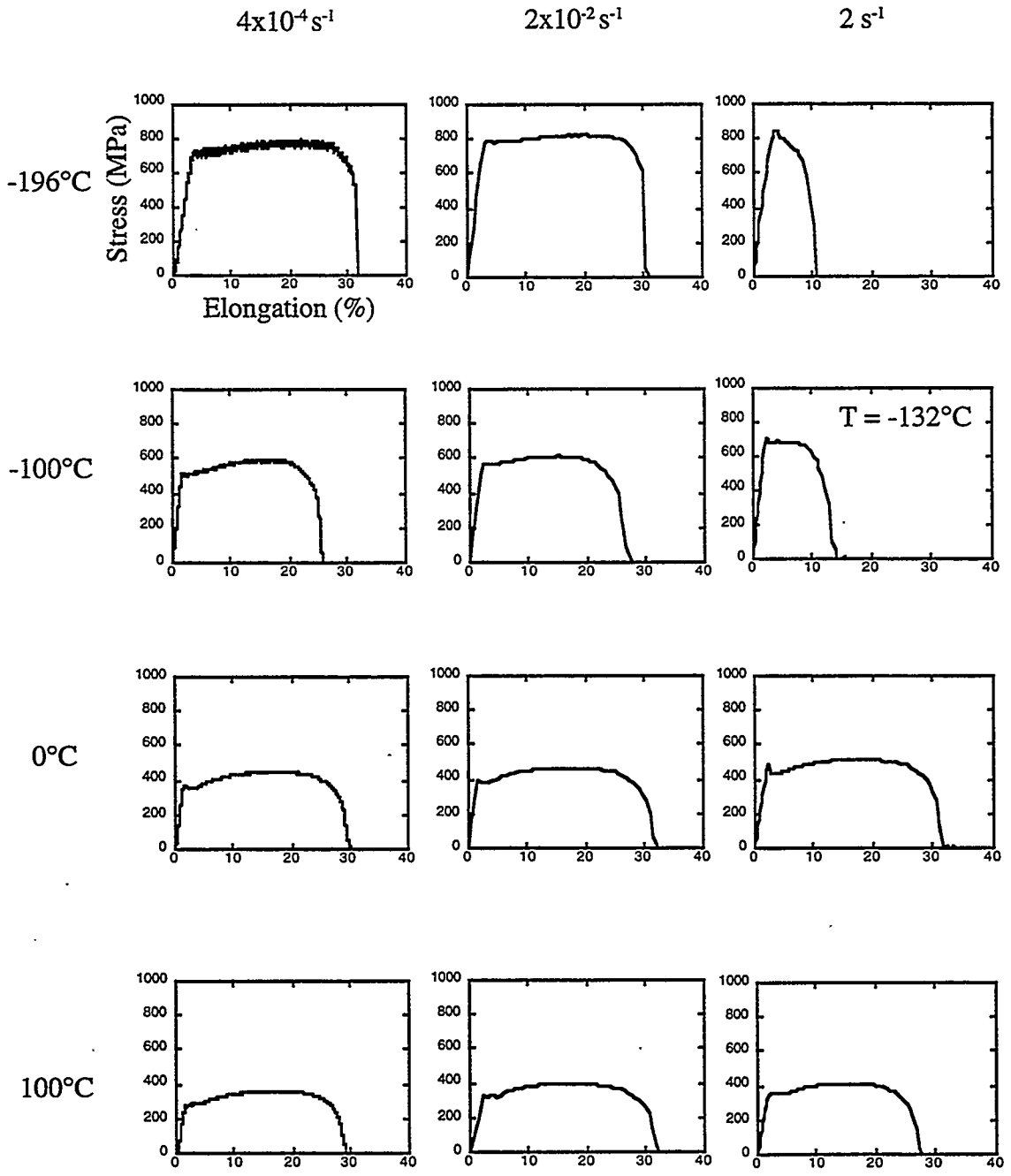

Figure 1. Examples of variation of stress-strain behavior with test temperature and strain rate.

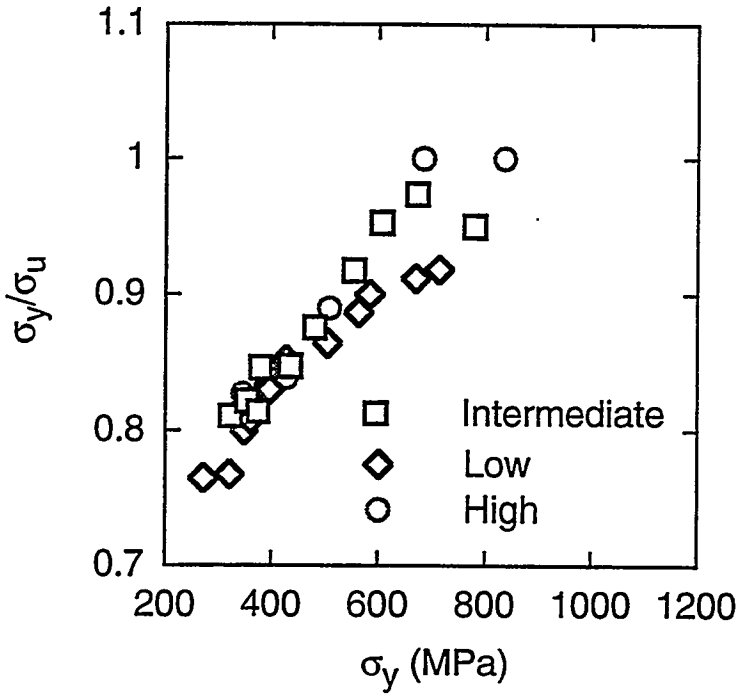

Figure 2 Variation of the ratio of yield stress to ultimate tensile strength with yield stress

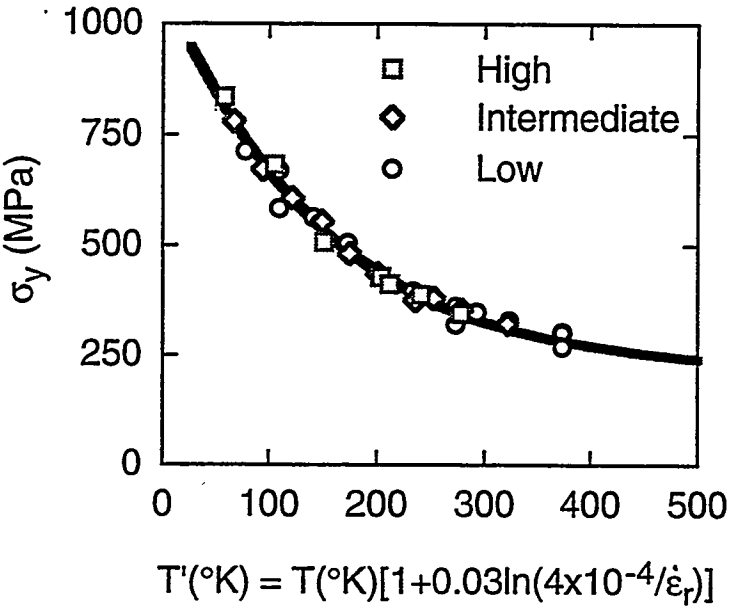

Figure 3 Variation of yield stress with strain-rate compensated temperature

When this is referenced at the lowest static rate, $\dot{\varepsilon}_0 = 4x10^{-4}s^{-1}$ and C = 0.03. Thus, σ_y's at high rates are equivalent to σ_y's at static rates at a lower temperatures; e.g., σ_y (2 s^{-1}, 20°C) ≈ σ_y ($4x10^{-4}$ s^{-1}, -27°C). The yield stress versus strain-rate-compensated temperature data in Figure 3 can be fit by an empirical polynomial as

$$\sigma_y(MPa) = 6.65x10^{-9}T'^4 - 1.53x10^{-5}T'^3 + 1.31x10^{-2}T'^2 - 5.22T' + 1070 \quad (3)$$

As discussed below, it will be critical to evaluate the effect of irradiation on the temperature and strain rate dependence, as well as the magnitude, of σ_y .

$K_e(T)$ Curves

Figure 4 summarizes the $K_e(T)$ data for the various specimen geometries (PMC, PNC, and PPC) and loading rates (S, LD, and ID). All fracture events that could be reliably measured occurred by cleavage with $50 \leq K_e \leq 200$ MPa√m. The higher values of K_e, plotted at a "nominal" 300 MPa√m, denote the absence of cleavage and represent crude estimates of ductile fracture initiation toughness, which could not be measured in the small specimens used in this work. Figure 5 shows a SEM micrograph of the large cleavage pop-in for the S-PMC test at -196°C. The higher magnification views in Figure 6 show the predominance of cleavage in the pop-in region with some indications of a minor amount of intergranular fracture and subsurface cracking resulting in a plug-and-socket type of feature. A S-PMC test at -150°C produced only massive deformation and crack blunting as shown in Figure 7. However, as shown in Figure 8a the increased loading rate for the LD-PMC test resulted in a much higher brittle-to-ductile transition temperature (T_t) around -140°C . Increased lateral constraint provided by the side notching in the LD-PNC tests increased T_t to even an higher value of around -120°C, as shown in comparisons of Figures 8b and 8c. The additional lateral constraint from the sharp side pre-crack in the LD-PPC tests increased T_t slightly to about -110°C, as shown in comparisons of Figures 8d and 8e. Further increases in loading rate in the ID-PNC and ID-PPC specimen increased T_t to -110°C and -105°C, respectively. Again, the additional lateral constraint from the sharp side pre-crack in the ID-PPC tests increased T_t over that in the ID-PNC test, as seen by comparison of Figures 8f and 8g. The estimated values of T_t at of 60 MPa√m are summarized in Table 1.

Table 1 - Variation of T_t with Constraint and Strain Rate

Loading Rate	Specimen (Constraint)	T_t (°C)
S	PMC	-198 ±5
LD	PMC	-140 ±5
LD	PNC	-120 ±5
LD	PPC	-110 ±5
ID	PNC	-110 ±5
ID	PPC	-105 ±5

DISCUSSION OF LOADING RATE AND LATERAL CONSTRAINT EFFECTS

The variation of transition temperature with lateral constraint and strain rate and the very sharp transitions observed in these tests can be understood in terms of the (simplified) micromechanics of cleavage fracture[7]. For deep cracks in large specimens where plane strain, small scale yielding (SSY) conditions prevail, the

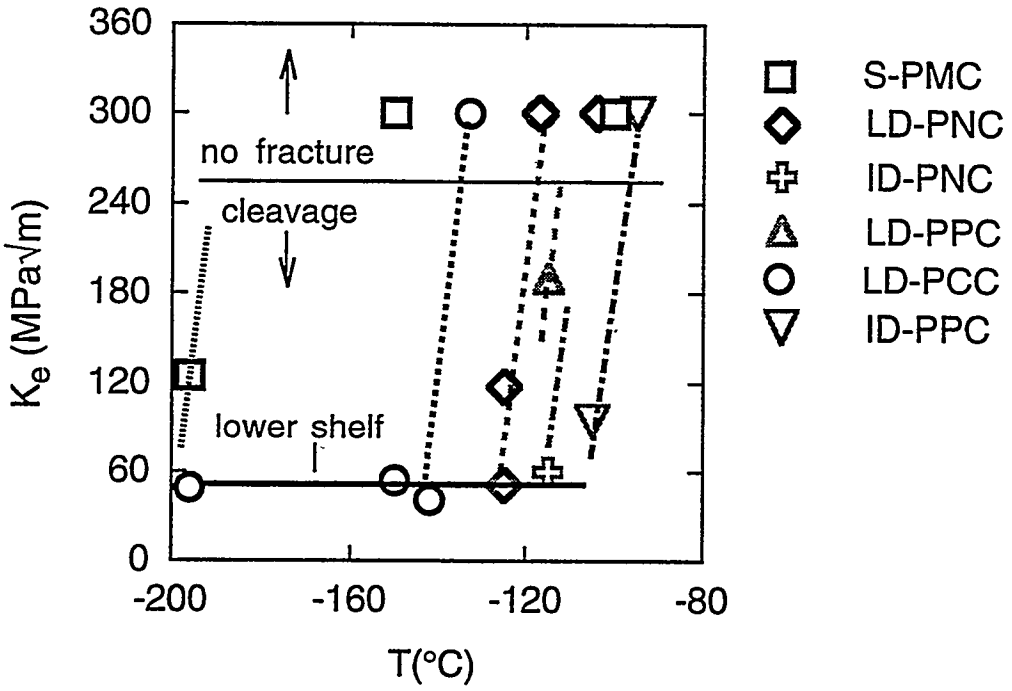

Figure 4 Variation of effective toughness with test temperature for various specimen types (PMC, PNC, and PPC) and loading rates (S, LD, and ID).

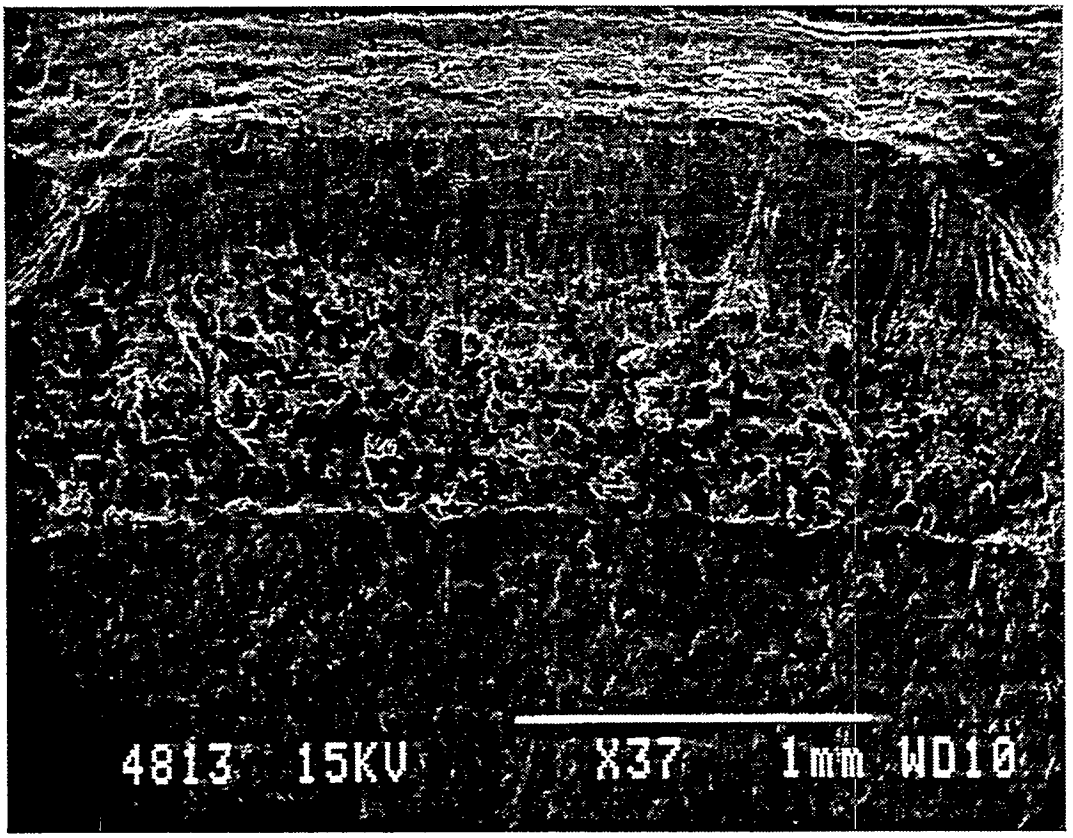

Figure 5. Low magnification SEM micrograph of the fracture surface of a PMC specimen tested statically at -196°C.

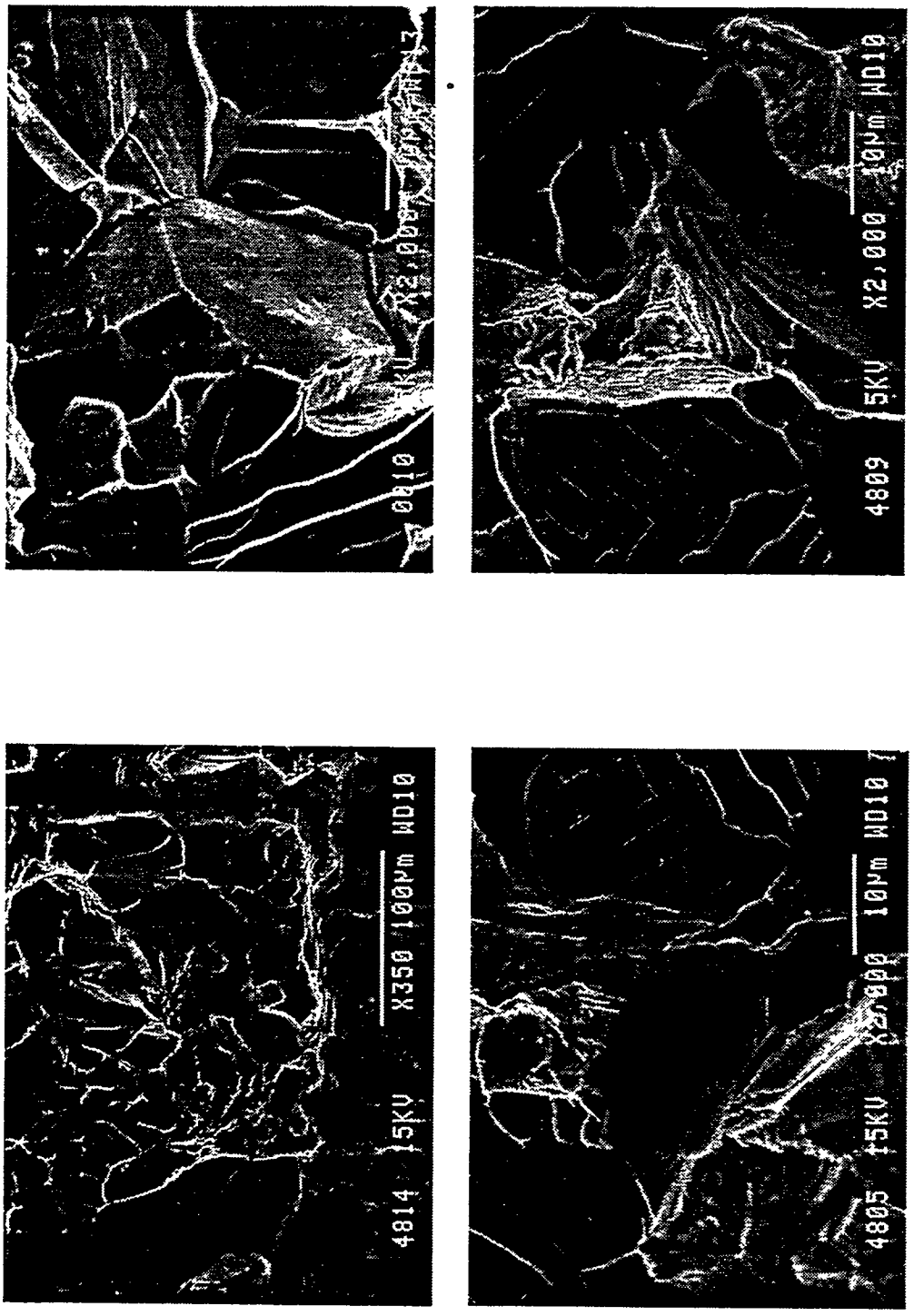

Figure 6. High magnification SEM micrographs of the cleavage fracture surface of a PMC specimen tested statically at -196°C.

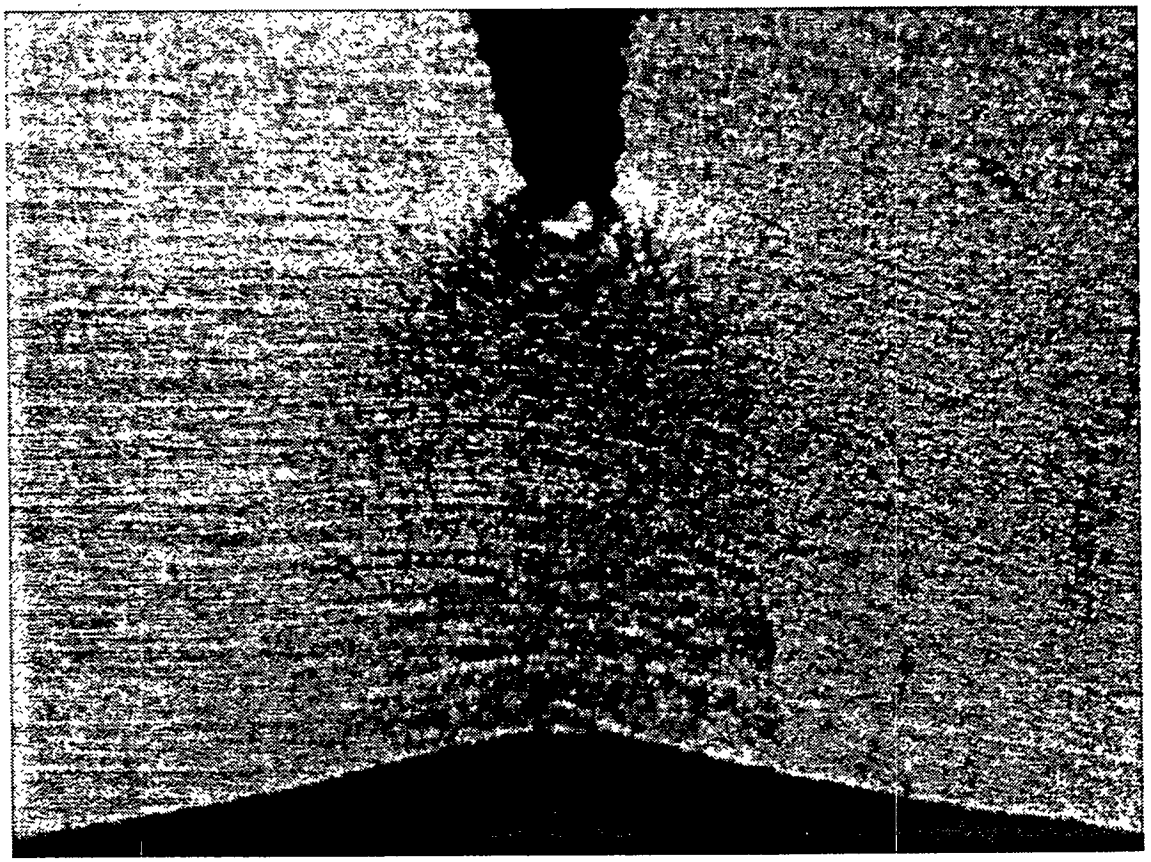

Figure 7. Side view of large deformation bending of PMC speciment tested statically at -150°C.

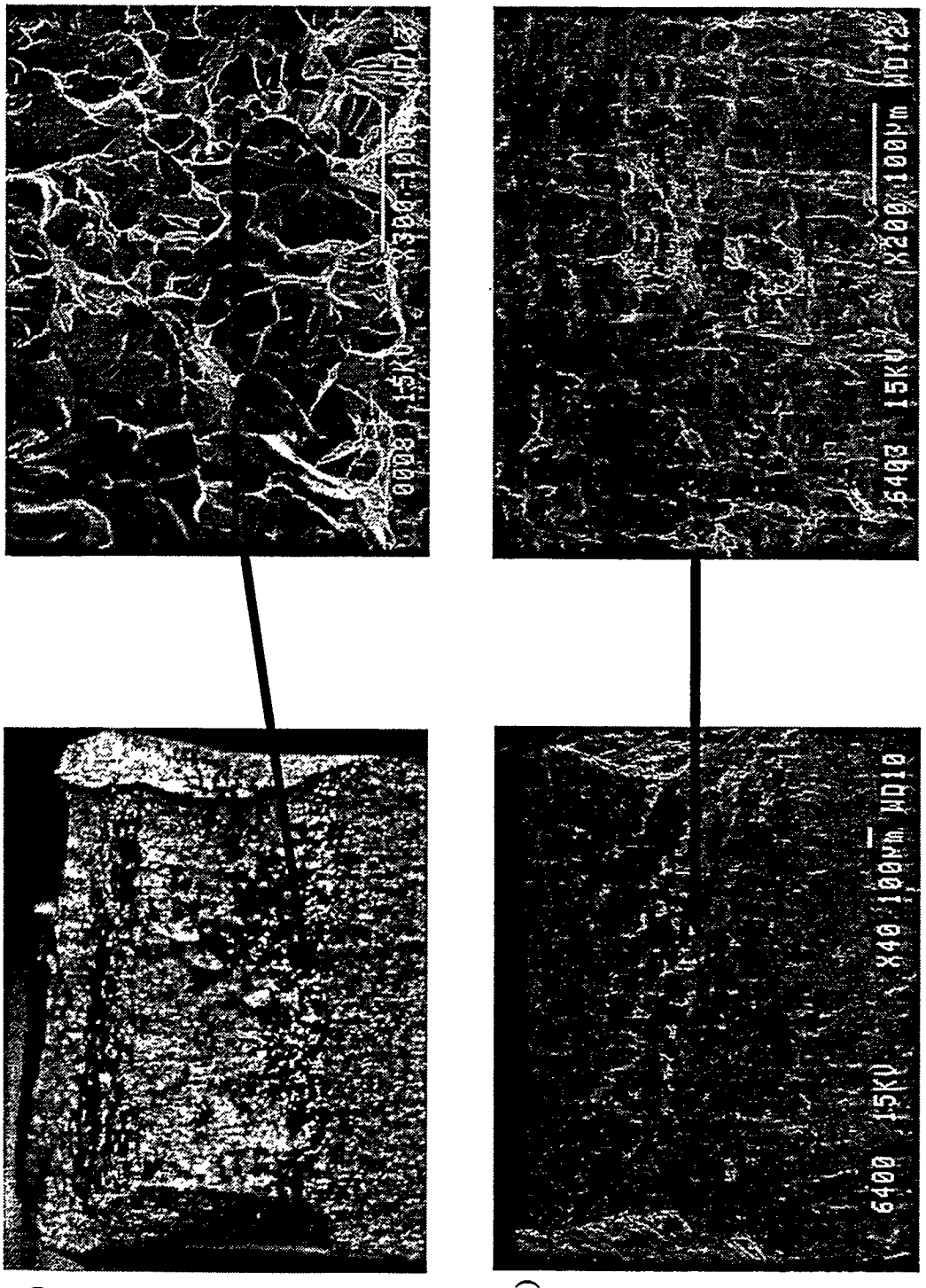

Figure 8. a) Low magnification optical and higher magnification SEM micrographs of LD-PMC specimen tested at -142°C; b) Low and high magnification SEM micrographs of LD-PMC specimen tested at -133°C.

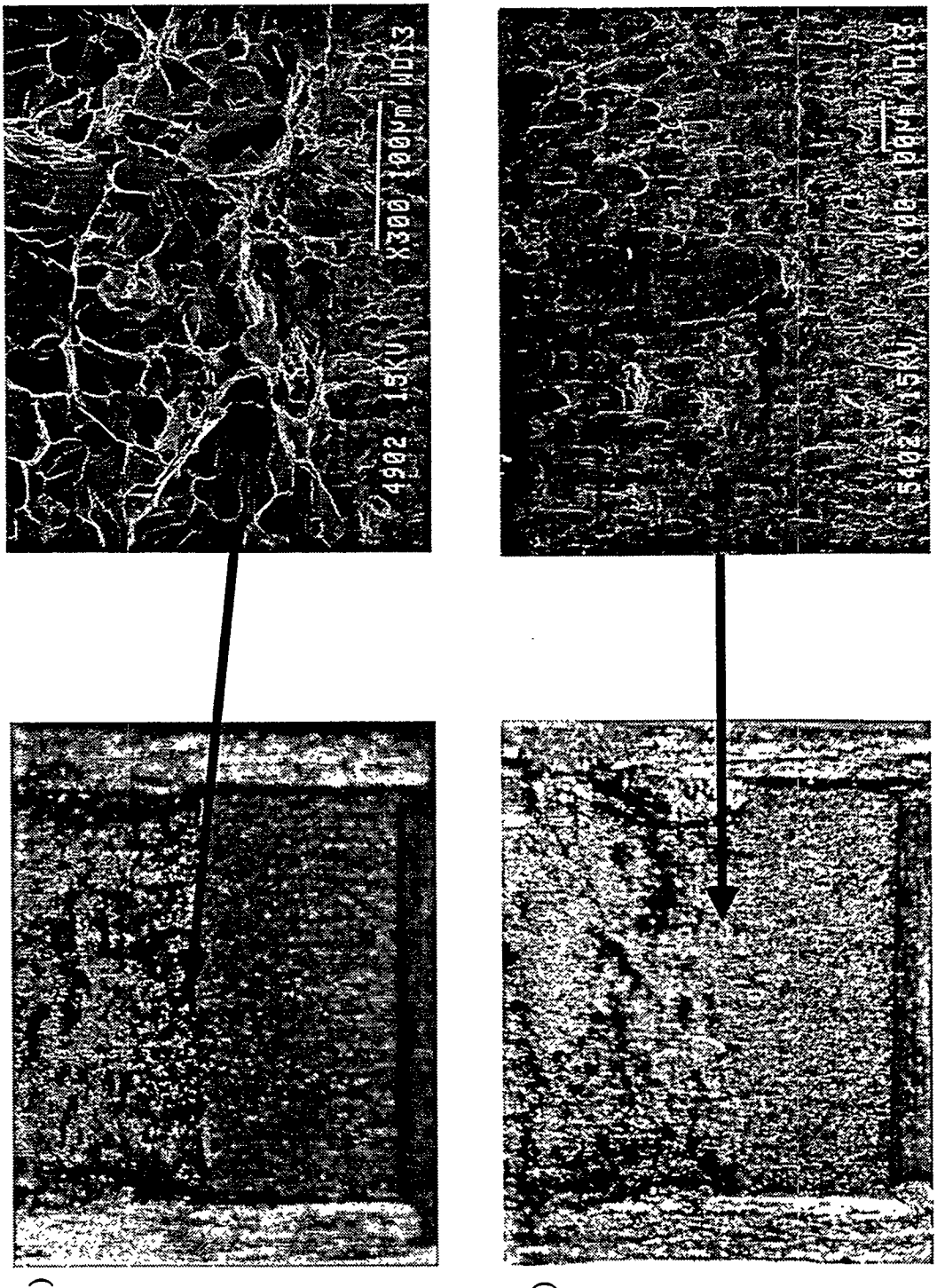

Figure 8. (cont.) Low magnification optical micrographs and higher magnification SEM micrographs of: c) LD-PNC specimen tested at -125°C; d) LD-PNC specimen tested at -117°C.

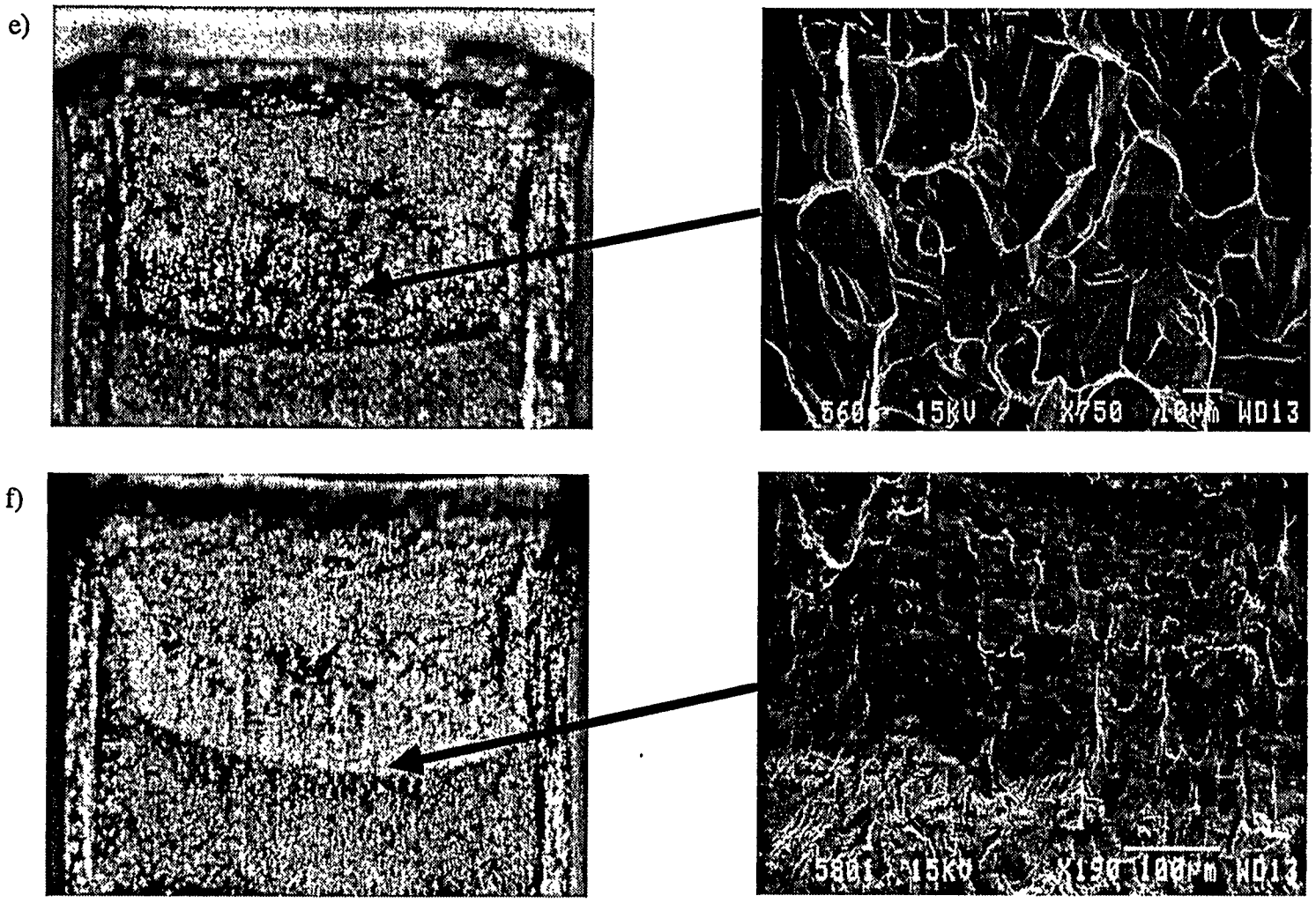

Figure 8. (cont.) Low magnification optical micrographs and higher magnification SEM micrographs of: e) LD-PPC specimen tested at -115°C; f) LD-PPC specimen tested at -105°C.

g)

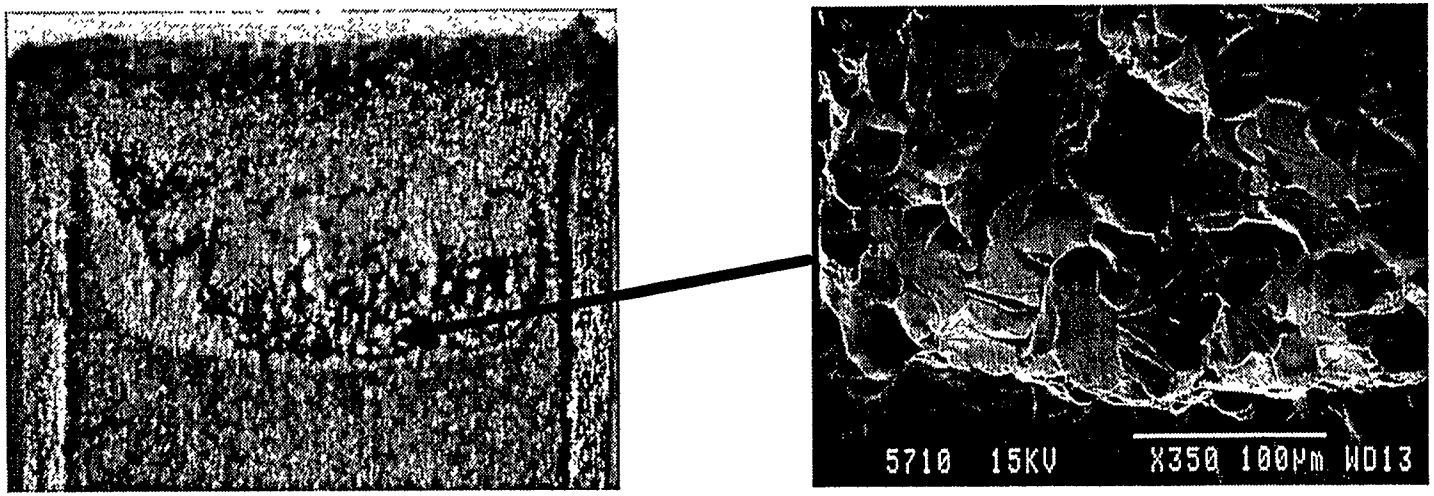

Figure 8. (cont.) g) Low magnification optical micrograph and higher magnification SEM micrograph of the ID-PNC specimen tested at -105°C.

peak tensile stress near the crack tip σ_t is a small multiple of the yield stress σ_y, with constraint factors $M_{SSY} = \sigma_t/\sigma_y$ of about 3 to 3.2 (note these constraint factors pertain to V alloys which have low strain hardening rates). In contrast, the maximum stress in specimens without a crack is approximately 1 to 1.2 σ_y. Cleavage and quasi-cleavage fracture are now believed to occur when the tensile stresses ahead of a crack tip exceed some critical value (σ^*) over a sufficiently large area (A^*)[11,12,14]. Hence, σ^*/A^* are local measures of toughness that are intrinsic to the material and its microstructure. The onset of cleavage requires sufficiently low temperatures for $\sigma_t = M\sigma_y$ to exceed σ^*. Under SSY the area within a stress contour varies with the crack tip opening (δ) as δ^2 (or either K^4 or J^2, where K is the linear elastic stress intensity factor and J is the elastic plastic crack tip energy release rate). Thus the crack must also blunt to a critical opening (δ^*) so that the $\sigma_t = M\sigma_y \geq \sigma^*$ occurs at $A \geq A^*$. Increasing strain rate (or irradiation hardening) increases σ_y, so the onset of cleavage occurs at higher temperatures.

For small pre-cracked specimens $M < M_{SSY}$. Thus a higher applied K is needed to reach the σ^*/A^* condition. Alternately, cleavage occurs at lower temperatures and/or higher strain rates where σ_y is higher. Thus the $K_e(T)$ curves for subsized specimens are shifted down in temperature compared to the intrinsic $K_{Ic}/J_{Ic}(T)$ curves for deep crack, plane strain, SSY conditions. Loss of constraint under plane strain conditions occurs when plastic deformation reaches free surfaces in specimens with a small width (W) or short crack lengths (a), viz., when a or W-a is less than about $100\delta^*$. However, constraint loss is also associated with lateral deformation in the direction of the specimen thickness (B) that occurs during crack blunting. Both sources of constraint loss reduce M and, hence, retard cleavage. Since the specimen W was fixed in this study, only the lateral plane strain constraint contribution could be increased by side notching or side pre-cracking. However, even these modest constraint enhancements resulted in T_t increases by 20 to 30°C.

The very sharp transition in the small pre-cracked specimens can also be understood based on these concepts, since: a) $d\sigma_y/dT$ is higher at lower temperature; b) $\delta(A^*/\sigma^*)$ increases with δ; thus, an initial loss of constraint leads to even more loss of constraint before fracture; c) there is a loss of lateral plane strain conditions at larger deformation; and d) at high loading rates adiabatic heating after general yielding reduces the local yield stress and hence tensile stresses.

Similar concepts apply to impact tests on blunt Charpy V-notched specimens, with some modifications. First, the intrinsic constraint factor for notches (M_{CVN}) is smaller than for cracks: viz., $M_{CVN} \approx 2.2$. Further, beyond general yielding, the area within a stress contour scales roughly with the load (P)-deflection (Δ) energy and the root radius of the notch. For specimens with all dimensions (L) fully scaled, these vary as L^3 and L, respectively. Thus, the normalized energy (E_n, the P-Δ energy up to cleavage initiation divided by L^3)-temperature curve (E_n-T) required for cleavage (σ^*/A^*) is shifted down in temperature in small specimens even without large scale deformation. Further, cleavage is strongly retarded after general yielding by low strain hardening rates. Finally, the total energy measured in Charpy-type tests contains many contributions that have nothing to due with the fracture initiation process.

The inescapable conclusion from these results is that the low transition temperatures reported to date for V-4Cr-4Ti are largely a consequence of the relatively low yield stress and strain hardening of the alloy and the low constraint imposed by small, shallow blunt-notched Charpy specimens. Note that since the same material configured and tested in different ways showed a enormous range of T_t, the observation of brittle fracture in vanadium alloys cannot be attributed to impurity contamination. Indeed, it is estimated that for pre-cracked specimens sufficiently large to maintain plane strain SSY at cleavage fracture, the T_t for dynamic loading would be about -50°C or more. This is not much lower than T_t for the low activation, tempered martensitic steels that are also being considered for fusion structures.

More generally, these results demonstrate that great caution must be used in interpreting small specimen test data. Specifically, such tests may not only fail to provide "valid" data, but they may also not even "detect" important processes, such as cleavage, or even any type of fracture.

MODELING THE EFFECTS OF LOADING RATE AND IRRADIATION

In the case of bcc steel alloys, σ^* and A^* are known to be relatively insensitive to temperature, strain rate and the fine scale damage imposed by irradiation[11,15]. If this is also the case for vanadium alloys, a simple way to model shifts in a reference transition temperature (ΔT_r) due to loading rate and irradiation hardening is to define transition temperatures at an *equivalent* reference σ_y. The appropriate reference condition is near the highest temperature of elastic cleavage fracture; this is at about $K_e = 60$ MPa$\sqrt{m}$ in a pre-cracked specimen toughness test. Hence, ΔT_r can be modeled from a knowledge of the dependence of σ_y on temperature, strain rate and irradiation. In applying this model it is further assumed that: a) the overall $\sigma(\varepsilon)$ for different temperatures, strain rates and levels of irradiation hardening ($\Delta\sigma_i$) are similar if the σ_y are the same; b) $\Delta\sigma_i$ is independent of temperature and strain rate; and c) Equations 2 and 3 provide an adequate description of $\sigma_y(\dot{\varepsilon},T)$ for the V-4Cr-4Ti alloy.

First, consider the effect of dynamic versus static loading rate on the PMC T_t ($= T_r$) data given in Table 1. For the S-PMC test, $T_{rs} = 198\pm4$°C; and for the ID-PMC test, $T_{rd} = -140\pm4$°C; thus, $\Delta T_r \sim 58\pm6$°C. For this case, the equivalent yield stress model (EYSM) gives $\Delta T_r = T_{rd} - T_{rs}$ where T_{rd} is related to T_{rs} by requiring

$$\sigma_y(\dot{\varepsilon}_s, T_{rs}) = \sigma_y(\dot{\varepsilon}_d, T_{rd}) \tag{4a}$$

Since the strain-rate-compensated temperatures are the same at the same yield stress, T_{rd} and T_{rs} are also related by

$$T'(\sigma_{y,ref}) = T_{rs}[1 + C \ln (\dot{\varepsilon}_0/\dot{\varepsilon}_s)] = T_{rd}[1 + C \ln (\dot{\varepsilon}_0/\dot{\varepsilon}_d)] \tag{4b}$$

The effective strain rates for the PMC tests can be estimated by dividing the local strain at the peak stress location ahead of the crack (≈ 0.1) by the time to fracture (≈ 60 s for the S tests and 1 ms for the LD tests); this gives $1.7\text{x}10^{-3}$ and 96s^{-1}, respectively. Using Equation 2, T' at T_{rs} (75K) for the S tests is 71.8°K and from Equation 3 the corresponding $\sigma_{y,ref}$ is 757 MPa. Solving Equation 4b, the value of T_{rd} at the same σ_y (and T') for the LD test is 115°K. Thus compared to the measured value of 58±6°C, the EYSM predicts a shift of about 40°C, a little smaller but of the right order.

The effects of irradiation on shift can also be predicted from $\Delta\sigma_i$ in a similar way: namely, $\Delta T_r = T_{ri} - T_{ru}$ when

$$\sigma_{yi}(T_{ri}) = \sigma_{yu}(T_{ru}) + \Delta\sigma_i \tag{5}$$

where the evaluation is at the pertinent strain rate.

Alexander and Snead[16] have recently reported values of $\Delta\sigma_i$ and ΔT_r for the same heat of V-4Cr-4Ti for blunt notched (MCVN) and pre-cracked miniaturized Charpy specimens (1/3 cross section and 1/2 length) irradiated in HFBR to 0.5 dpa at about 110 to 235°C. The T_r for these MCVN tests is nominally at about 0.5 J (10J times the MCVN/CVN volume ratio). However, for a variety of reasons it is very difficult to establish T_r experimentally. Thus it was simply estimated by extrapolating the MCVN E-T curve in the transition region to zero energy, giving an estimated T_{ru} of -205°C. The predicted ΔT_r versus $\Delta\sigma_i$ curve from Equations 2, 3 and 5 for a nominal strain rate of 100 s^{-1} is shown as the solid line in Figure 9a along with the experimentally observed shifts for the blunt notched MCVN specimens. Figure 9b shows a similar

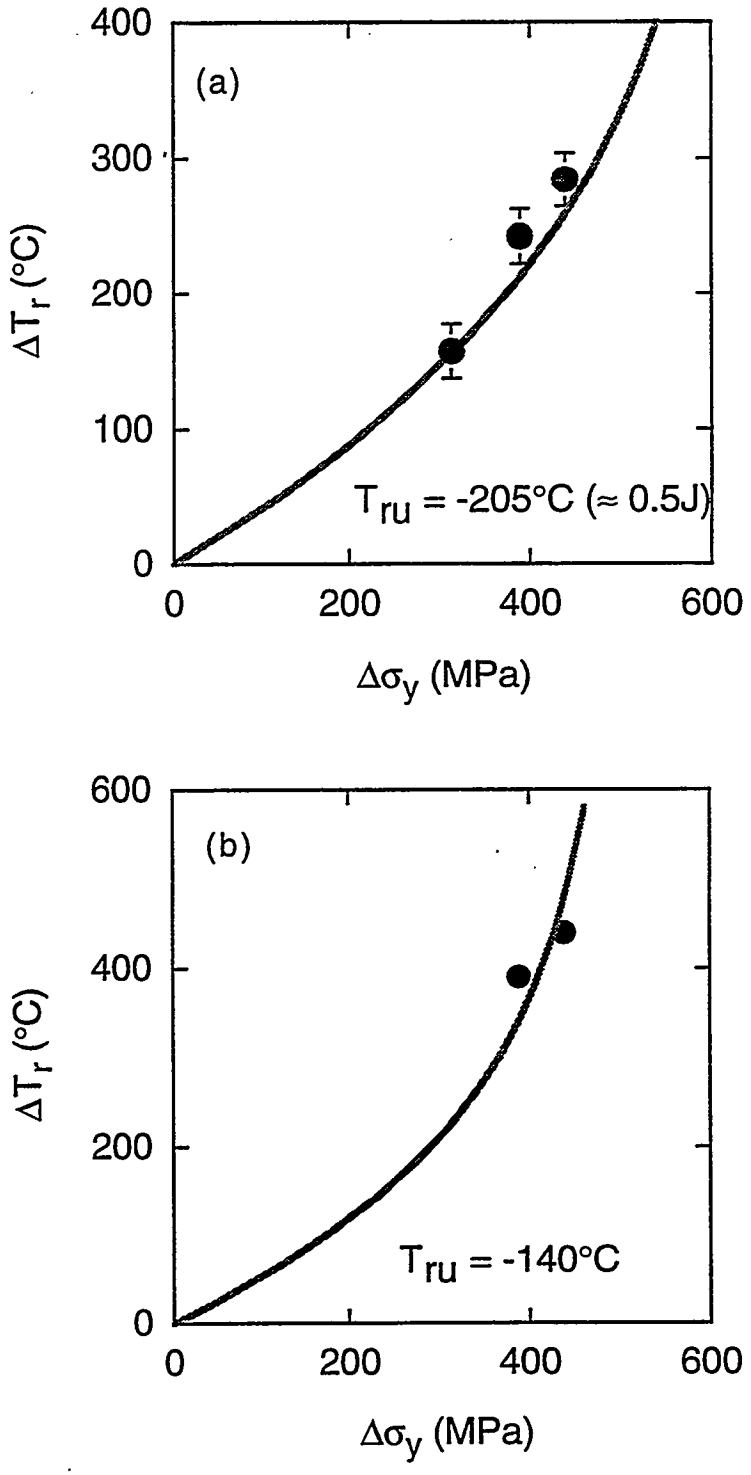

Figure 9 Shift versus hardening for a) blunt notched and b) pre-cracked MCVN specimens. The data points are taken from Alexander and Snead and the line is predicted from the equivalent yield stress model.

comparison for pre-cracked specimens. In both cases the predictions of the EYSM are in remarkably good agreement with the measurements. Notably, the ΔT_r for the pre-cracked MCVN tests are larger than the blunt-notched MCVN tests for the same $\Delta\sigma_i$; this is simply a consequence of the higher T_{ru} ($\approx$ -140°C) for the sharp crack versus the blunt notch specimens.

CONCLUSIONS

In summary, the data and analysis presented here demonstrate that the program heat of V-4Cr-4Ti undergoes a "normal" stress-controlled ductile-to-cleavage transition, typical of bcc alloys. The temperature marking this transition is strongly affected by constraint (experimentally demonstrated only for loss of plane strain constraint), loading rate and irradiation. Hence, the observations to date of the low transition temperature and embrittlement resistance of this alloy are primarily the result of the low yield stress of this alloy coupled with the relatively small constraint associated with small specimen sizes and blunt notches. This emphasizes that caution must be exercised in interpreting small specimen data. Not only may such small specimens lack the capacity to provide "valid" intrinsic properties, but they may even fail to detect real physical phenomena, such as cleavage.

The preliminary results also show that temperature shifts due to high loading rates and irradiation can be predicted using a very simple EYSM. The excellent quantitative agreement between the EYSM predictions and experiment also demonstrate the primary role of irradiation hardening in embrittlement of these alloys, and strongly contradicts alternate ad hoc explanations (e.g., impurity pickup). While not explicitly treated in this work, this research also suggests that the effect of specimen/structure size and geometry, that mediate constraint effects even under plane strain conditions, can be modeled by combining finite element method simulations of crack tip stress (and strain fields) with local fracture properties (e.g., σ^*/A^*). While additional research is needed, the present results are also very encouraging about the possibility of developing a powerful and practical master curve-shift method that is founded on physical understanding and complemented by basic measurements and models to reliably predict the stress and strain limits of flawed fusion structures .

ACKNOWLEDGMENTS

This work was supported in part by the Office of Fusion Energy, DOE, Grant No. DE-FG03-87ER-52143. The assistance of A. Rowcliffe and A. N. Gubbi of ORNL in specimen acquisition and preparation is gratefully acknowledged.

REFERENCES

1. B.A. Loomis, D. L. Smith, J. Nucl. Mater. 179-181 (1991) 783.

2. B. A. Loomis, D. L. Smith, F. A. Garner, ibid., 771.

3. H. Chung, and D. L. Smith, J. Nucl. Mater., 191-194 (1992) 942.

4. B. A. Loomis, L. J. Nowicki, J. Gazda, D. L. Smith, Fusion Reactor Materials Semiannual Progress Report, DOE/ER-0313/15, March 31 (1993) 318.

5. B. A. Loomis, H. M. Chung, L. J. Nowicki, D. L. Smith, J. Nucl. Mater., 212-215 (1994) 799.

6. K. Edsinger, G. R. Odette, G. E. Lucas, J. W. Sheckherd, Proceedings of the 7th Int'l Conference on Fusion Reactor Materials, *J. Nucl. Mater.* (in press)

7. G. R. Odette, Proceedings of the IEA/JUPITER Symposium on Small Specimen Test Technologies for Fusion Materials, Sendai, Japan, March 1996.

8. H. M. Chung, H.-C. Tsai, D. L. Smith, R. Peterson, C.Curtis, C. Wojcik, and R. Kinney, Fusion Reactor Materials Semiannual Progress Report, DOE/ER-0313/17, March (1994).

9. M. L. Grossbeck, D. J. Alexander, J. J. Henry, W. S. Eatherly, L. T. Gibson, Fusion Reactor Materials Semiannual Progress Report, DOE/ER-0313/18, March (1995).

10. A. N. Gubbi, A. F. Rowcliffe, W. S. Eatherly, ibid.

11. K. Edsinger, G. R. Odette, G. E. Lucas, B.Wirth, ASTM-STP-1270, American Society for Testing and Materials, Philadelphia, PA (in press)

12. K. Edsinger, G. R. Odette, G. E. Lucas, Proceedings of the IEA International Symposium on Miniaturized Specimens for Testing Irradiated Materials, KFA Julich, September 22-23, 1994 (1995) 150-159.

13. J. M. Steichen and J. A. Williams, J. Nucl. Mater., 57 (1975) 303.

14. G. R. Odette, J. Nucl. Mater., 212-215 (1994) 45.

15. K. Edsinger, PhD Thesis, Department of Chemical Engineering, UCSB (1996).

16. D. J. Alexander and L. Snead, presented at the 18th International Symposium on Effects of Radiation on Materials, ASTM, Hyannis, Massachusetts, June, 1996.

FRACTURE TOUGHNESS TESTING OF V-4Cr-4Ti AT 25 °C AND -196 °C - H-X (Huaxin) Li, and R. J. Kurtz (Pacific Northwest National Laboratory)[1]

OBJECTIVE

To determine the effect of temperature on the fracture toughness of the production-scale heat (#832665) of V-4Cr-4Ti using compact tension specimens and to compare the results with data obtained from one-third scale Charpy impact specimens.

SUMMARY

Measurements of the fracture toughness of the production-scale heat (#832665) of V-4Cr-4Ti have been performed at 25°C and -196°C using compact tension (CT) specimens. Test specimens were vacuum annealed at either 1000°C for 1 hour (HT1) or 1050°C for two hours (HT2). Specimens given the HT1 treatment were annealed after final machining, whereas the HT2 specimens received the 1050°C anneal at Teledyne Wah Chang prior to final machining. Following machining HT2 specimens were then vacuum annealed at 180°C for two hours to remove hydrogen. Specimens treated using HT1 had a partially recrystallized microstructure and those treated using HT2 had a fully recrystallized microstructure. The fracture toughness at 25°C was determined by J-integral tests and at -196°C by ASTM E 399 type tests. Toughness values obtained at -196°C were converted to J-integral values for comparison to the 25°C data. The 25°C fracture toughness was very high with none of the specimens giving valid results per ASTM criteria. Specimens fractured by microvoid coalescence. The fracture toughness at -196°C was much lower than that at 25°C and the fracture surface showed predominantly cleavage features. The present results show a transition from ductile to brittle behavior with decreasing test temperature which is not observed from one-third scale Charpy impact tests. The fracture toughness at -196°C was still quite high, however, at about 75 kJ/m^2.

Delaminations in planes normal to the thickness direction were seen at both test temperatures. Fracture surfaces inside the delaminations exhibited nearly 100% cleavage facets. The cause of the brittle delaminations was not determined, but will be a subject for further investigation.

PROGRESS AND STATUS

1. Material and Experimental Method

The production-scale heat (#832665) of V-4Cr-4Ti was used for this study. CT specimens were machined from 6.35 mm (0.25 in.) thick plates. One plate was received in the warm-rolled condition and was heat treated at 1000°C for 1 hour in a vacuum of 10^{-7} torr (HT1) at PNNL following machining of specimens. The other plate had been warm-rolled and heat treated at 1050°C for two hours (HT2) by Teledyne Wah Chang, Albany, OR. After machining HT2 specimens were vacuum annealed at 180°C for two hours to remove hydrogen.

CT specimens were used for all tests and all specimens had the T-L orientation. Two specimen

[1]Operated for the U.S. Department of Energy by Battelle Memorial Institute under Contract DE-AC06-76RLO 1830.

widths, 30.5 mm (1.2 in.) and 50.8 mm (2 in.) were used for the HT2 material. HT2 specimens were tested only at 25°C. All HT1 specimens were 30.5 mm (1.2 in.) wide. Fracture toughness values at 25°C were determined using the J-integral test procedure given in ASTM E 813 and those at -196°C were determined using the ASTM E 399 procedure. For the purpose of comparison, K-values determined from the -196°C tests were converted to J-values using Equation 1:

$$J = \frac{K^2}{E}(1-\nu^2) \qquad (1)$$

where E is Young's modulus and ν is Poison's ratio. Values for E and ν at -196°C for V-4Cr-4Ti were not available so estimates were obtained from data on pure vanadium. E and G (shear modulus) for pure vanadium at -196 °C can be determined from Equations 2 and 3 [1]:

$$E\ (GPa) = 0.1*(1.28 - 9.61x10^{-5}*T) \qquad (2)$$

$$G\ (GPa) = 0.1*(0.488 - 8.43x10^{-5}*T) \qquad (3)$$

where T is temperature in Kelvin. At -196 °C the estimated value of E is 127.3 GPa and G is 48.2 GPa. Assuming isotropic behavior, ν value can be determined from Equation 4.

$$G = \frac{E}{2(1+\upsilon)} \qquad (4)$$

Substituting the E and G values into Equation 4 gives a value of 0.32 for ν at -196 °C.

Fracture surfaces were examined in a scanning electron microscope (SEM) to determine the effect of temperature on the failure mode and to determine the failure mechanism inside the delaminations.

2. Results And Discussion

The fracture toughness test results for both temperatures are plotted in Figure 1. The toughness of specimens tested at 25°C was very high such that ASTM E 813 validity criteria were not satisfied for the specimen dimensions utilized. The 6.35 mm specimen thickness gives a valid toughness up to about 250 kJ/m^2 which suggests a minimum value for the toughness of V-4Cr-4Ti at 25°C. Toughness values determined from 30.5 mm and 50.8 mm wide specimens were nearly same, indicating little effect of specimen width within this range. Similar high fracture toughness values have also been measured on samples prepared from heat BL-63 heat treated at 1100°C for one hour plus an additional anneal at 890°C for 24 hours. J-integral tests for specimens given the HT1 anneal are in progress. It is anticipated that the 25°C fracture toughness behavior of HT1 specimens will be similar to HT2 specimens since Charpy impact data shows HT1 material exhibits upper shelf properties at 25°C similar to HT2 material. Thus, 25°C fracture toughness values from HT2 specimens are compared to -196°C fracture toughness values from HT1 specimens.

The results plotted in Figure 1 show that temperature has a significant effect on the fracture toughness of V-4Cr-4Ti. Specimens tested at -196°C yielded fracture toughness values of about 103 MPa$\sqrt{m}$. This is equal to about 75 kJ/m^2, which is significantly lower than the 25°C fracture toughness. The present results are in contrast to recent data obtained from one-third scale pre-cracked Charpy tests [3]. The Charpy data does not display a transition in absorbed energy with decreasing temperature. The absorbed energy was found to increase gradually with decreasing test temperature, reaching a peak at

around -150°C. Below -150°C the absorbed energy decreased with temperature, but even at -196°C it was still larger than that at room temperature [3]. In addition, Charpy specimens failed by microvoid coalescence at all temperatures.

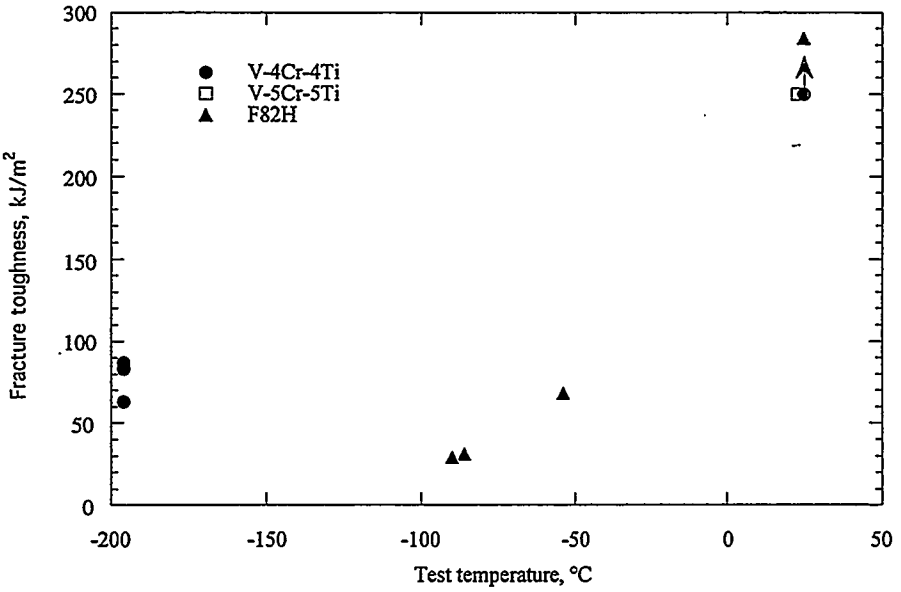

Figure 1. Effect of temperature on the fracture toughness of a production scale heat of V-4Cr-4Ti. Data from a V-5Cr-5Ti alloy and F-82H steel are included for comparison.

SEM examination of fracture surfaces showed that the 25°C specimens failed by microvoid coalescence, as depicted in Figure 2. At -196°C the fracture surface was predominantly cleavage with some microvoid coalescence, as displayed in Figure 3. Taken together, the fractographic results and fracture toughness data clearly shows that V-4Cr-4Ti undergoes a ductile-to-brittle transition at a temperature higher than -196°C. This result differs from Charpy impact data, where no ductile-to-brittle transition was found at temperatures above -196°C [3]. The reason for this difference may be due to differences in constraint between the two types of specimens. The state of stress at the crack tip for the larger CT specimen will be more triaxial than for the small Charpy specimen. This favors crack extension in the CT specimen more than for the Charpy specimen.

It was also found that V-4Cr-4Ti was prone to delaminate in planes normal to the thickness direction, regardless of test temperature, as shown in Figure 4. More significantly, the fracture surfaces inside the delaminations were largely cleavage (see Figure 5). The delaminations were caused, in part, by development of tensile stresses in the thickness direction due to the constraining effect of the material surrounding the crack tip plastic zone, which limits through thickness deformation. Brittle delaminations are significant, from an operational viewpoint, because local triaxial states of stress will likely exist in actual power systems. The cause of the delaminations in this material is not known yet. Inclusions could act as stress concentrators to promote cleavage fracture, but examination by optical metallography did not reveal inclusions that could produce such an effect. Weakening of grain boundaries by impurity segregation might cause intergranular separations which could trigger cleavage fracture, but no evidence for this mechanism has been obtained at the present time.

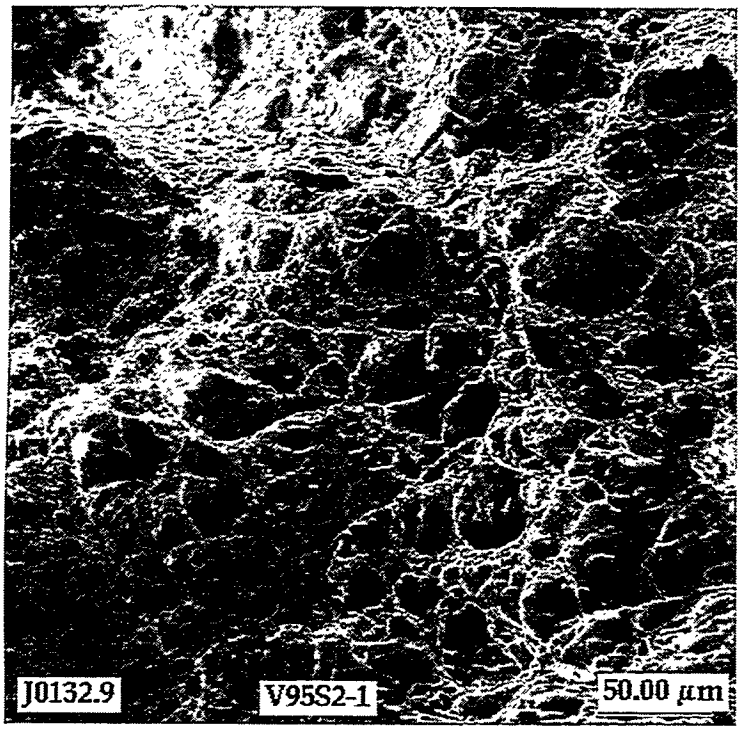

Figure 2. SEM photograph showing microvoid coalescence fracture of V-4Cr-4Ti alloy at 25°C.

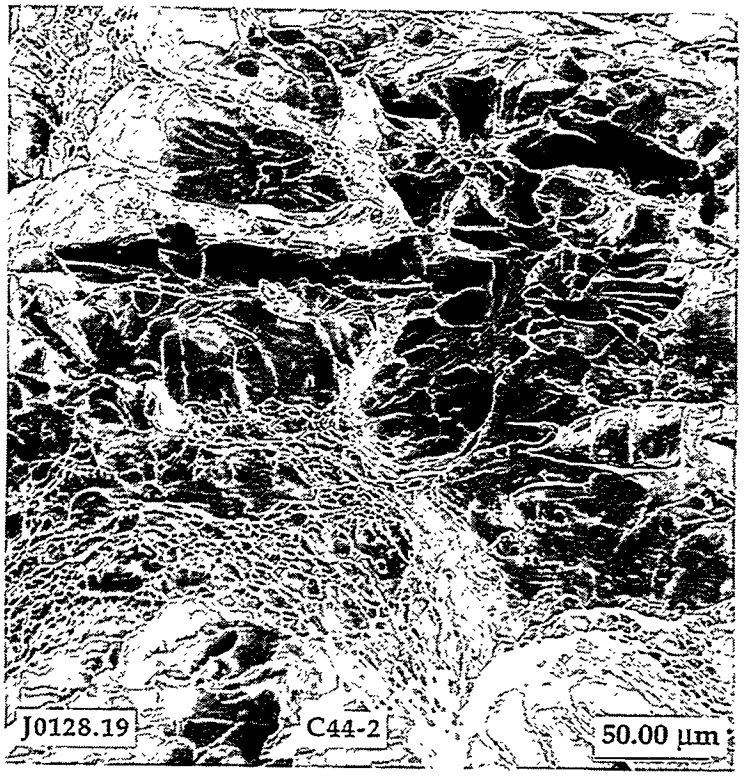

Figure 3. SEM photograph shows predominantly cleavage fracture of V-4Cr-4Ti alloy at -196°C.

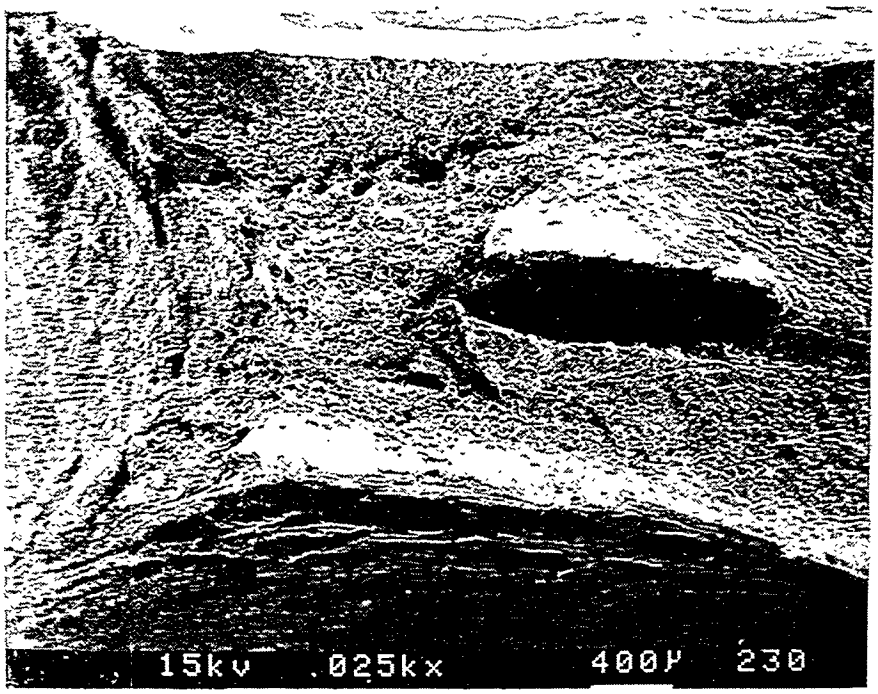

Figure 4. SEM photograph of delaminations in V-4Cr-4Ti specimen tested at 25°C.

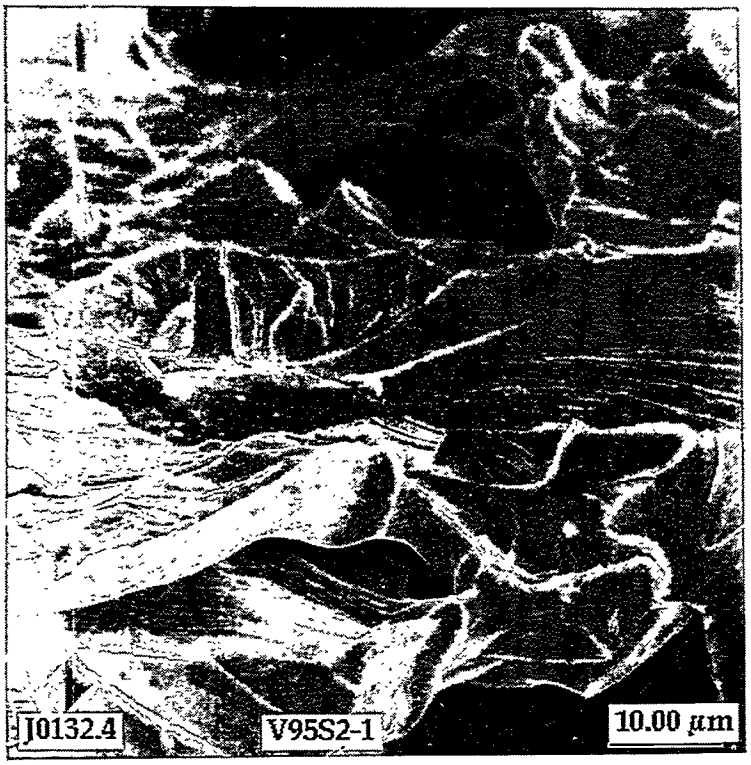

Figure 5. SEM photograph of cleavage facets inside delamination in V-4Cr-4Ti tested at 25°C.

FUTURE WORK

Detailed examination by electron microprobe will be performed to search for micro-chemical segregation effects which may be responsible for the delaminations. The effect of mixed-mode I/III loading on the fracture toughness of V-4Cr-4Ti alloy heat treated at 1000°C for 1 hour is being studied. Preliminary results indicate that mixed-mode loading enhances crack initiation and propagation.

REFERENCES

1. R. J. Farraro and R. B. McLellan, "High Temperature Elastic Properties of Polycrystalline Niobium, Tantalum, and Vanadium", Met. Trans. A, 10A (1979), p 1699.

2. Huaxin Li, M. L. Hamilton and R. H. Jones, "Effect of Heat Treatment and Test Method on DBTT of a V-5Cr-5Ti Alloy", Fusion Reactor Materials Semiannual Progress Report. DOE/ER-0313/18, Oak Ridge National Lab., Oak Ridge, TN (March 1995), p. 215.

3. H. M. Chung, L. Nowicki and D. L. Smith, "Impact Properties of Precracked V-4Cr-4Ti Charpy Specimens", Fusion Reactor Materials Semiannual Progress Report. DOE/ER-0313/18, Oak Ridge National Lab., Oak Ridge, TN (March 1995), p. 253.

EFFECT OF TIME AND TEMPERATURE ON GRAIN SIZE OF V AND V-Cr-Ti ALLOYS*

K. Natesan and D. L. Rink (Argonne National Laboratory)

OBJECTIVE

The objectives of this task are to evaluate the effect of temperature and exposure time on grain growth kinetics and associated microstructural changes in V, V-4 wt.%Cr-4 wt.%Ti, and V-5 wt.%Cr-5 wt.%Ti alloys and to correlate the information with the long-term mechanical properties of the materials.

SUMMARY

Grain growth studies were conducted to evaluate the effect of time and temperature on the grain size of pure V, V-4 wt.%Cr-4 wt.%Ti, and V-5 wt.%Cr-5 wt.%Ti alloys. The temperatures used in the study were 500, 650, 800, and 1000°C, and exposure times ranged between 100 and ≈5000 h. All three materials exhibited negligible grain growth at 500, 650, and 800°C, even after ≈5000 h. At 1000°C, pure V showed substantial grain growth after only 100 h, and V-4Cr-4Ti showed growth after 2000 h, while V-5Cr-5Ti showed no grain growth after exposure for up to 2000 h.

EXPERIMENTAL PROGRAM

The materials selected for the evaluation included pure V, V-5 wt.%Cr -5 wt.%Ti (designated as BL-63), and V-4 wt.%Cr-4 wt.%Ti (designated as BL-71). Sheet samples of the materials were annealed for 1 h at 1050°C prior to their use in grain growth studies. Coupon specimens measuring ≈15 x 7.5 x 1 mm were enclosed in Vycor capsules in vacuum and exposed at temperatures of 500, 650, 800, and 1000°C for several time periods in the range of 100-5000 h. After exposure, specimen surfaces and cross sections were examined by scanning electron microscopy. The aged specimens were analyzed for grain size with the ASTM/E-112 Intercept procedure.

RESULTS AND DISCUSSION

The grain size of a material and the grain growth rate for the material as a function of temperature and exposure time can influence the mechanical properties of the material, as well as the transport of interstitial elements such as O, C, N, and H. A finer grain size can lead to increased diffusion of interstitials via grain boundaries, with a resultant increase in total concentration of the interstitial elements. On the other hand, grain boundary diffusion of these elements can also result in a fine precipitates of second-phase particles that can pin the grain boundaries and thereby stabilize the microstructure over extended periods of time at temperature.

Figures 1-3 show measured grain size values as a function of exposure time for V, V-4 wt.%Cr-4 wt.%Ti, and V-5 wt.%Cr-5 wt.%Ti alloys after exposure at 500, 650, 800, and 1000°C. The results in Fig. 1 indicate that the initial grain size of the V specimens was ≈120-140 μm and that the grain growth in pure V is negligible at 500, 650, and 800°C for times up to ≈5000 h. The specimen exhibits a substantial grain growth at 1000°C even after 100 h exposure. Even though many grains were examined by the line-intercept method, a significant variation in grain size was noted in the specimens exposed at 1000°C. This is indicative that at some locations, the larger grains gave very few intercepts while in other locations with smaller grains a large number of intercepts was noted. This also reveals the dynamic nature of grain growth at 1000°C, which involves time-dependent dissolution of smaller grains and growth of a few larger grains.

Grain size measurements on the V-4 wt.%Cr-4 wt.%Ti alloy (see Fig. 2) showed virtual absence of grain growth at 500, 650, and 800°C after ≈5000 h. The initial grain size of the alloy was in the range of 18-20 μm and changed little with exposure. At 1000°C, the alloy showed no grain growth after 100 and 600 h but showed an increase to 62-84 μm after 2000 h. Similar measurements made on V-5 wt.%Cr -5 wt.%Ti alloy showed virtually no grain growth under all conditions tested. The specimens are presently being examined by several electron-optical techniques to examine the grain boundary precipitate phases.

---

*This work has been supported by the U.S. Department of Energy, Office of Fusion Energy Research, under Contract W-31-109-Eng-38.

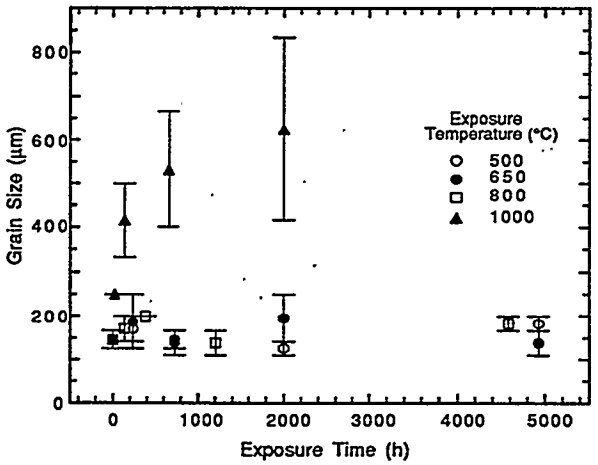

Fig. 1. Grain size variation in pure V as a function of time and temperature

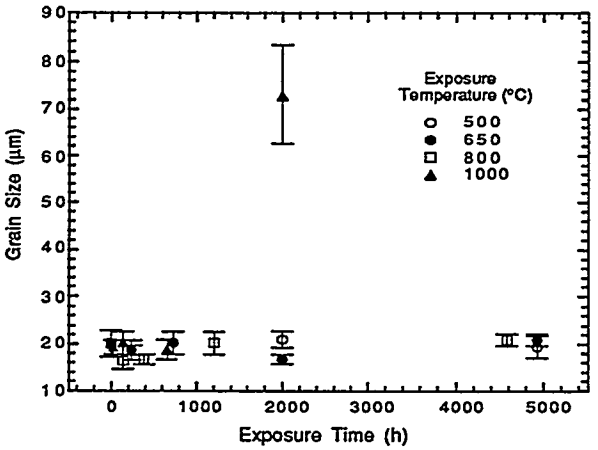

Fig. 2. Grain size variation in V-4 wt.%Cr-4 wt.%Ti alloy as a function of time and temperature

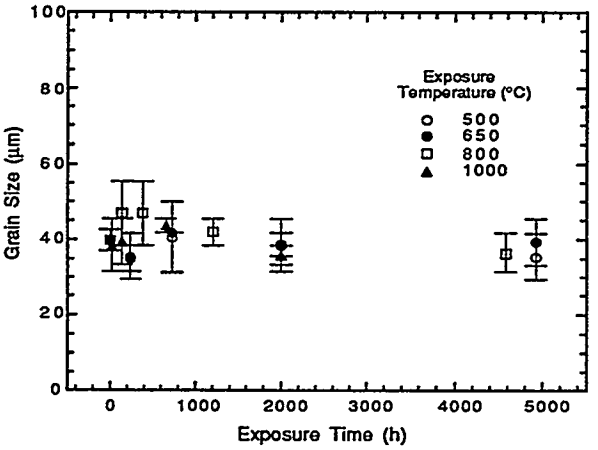

Fig. 3. Grain size variation in V-5 wt.%Cr-5 wt.%Ti alloy as a function of time and temperature

EFFECTS OF STRAIN RATE, TEST TEMPERATURE AND TEST ENVIRONMENT ON TENSILE PROPERTIES OF VANADIUM ALLOYS — A. N. Gubbi, A. F. Rowcliffe, W. S. Eatherly, and L. T. Gibson (Oak Ridge National Laboratory)

OBJECTIVE

The aim of this work is to examine the effects of test temperature, strain rate, and test environment on the tensile properties of the large heat of V-4Cr-4Ti and the small heats of compositional variants.

SUMMARY

Tensile testing was carried out on SS-3 tensile specimens punched from 0.762-mm-thick sheets of the large heat of V-4Cr-4Ti and small heats of V-3Cr-3Ti and V-6Cr-6Ti. The tensile specimens were annealed at 1000° for 2 h to obtain a fully recrystallized, fine grain microstructure with a grain size in the range of 10-19 μm . Room temperature tests at strain rates ranging from 10^{-3} to 5×10^{-1}/s were carried out in air; elevated temperature testing up to 700°C was conducted in a vacuum better than 1×10^{-5} torr ($<10^{-3}$ Pa). To study the effect of atomic hydrogen on ductility, tensile tests were conducted at room temperature in an ultra high vacuum chamber (UHV) with a hydrogen leak system.

Tensile properties of V-3Cr-3Ti, V-4Cr-4Ti, and V-6Cr-6Ti were measured at room temperature and 100–700°C at a strain rate of 1.1×10^{-3}/s. The ultimate tensile strength of all the alloys exhibited a minima at 300°C, whereas the 0.2% yield strength was relatively independent of temperature between 400° and 700°C. The total and uniform elongations were relatively insensitive to variation in test temperature above 400°C. All the alloys exhibited good ductility (e.g., uniform elongation >15%) and a large amount of work hardening ability. A yield point was typically obtained at all test temperatures. Serrations, indicative of dynamic strain aging, were observed in the stress-strain curves of all the alloys at test temperatures above 300°C.

V-6Cr-6Ti is the strongest of the three alloys with the highest values of 0.2% yield strength (YS) and the ultimate tensile strength (UTS), and V-3Cr-3Ti is the weakest showing the lowest values at all strain rates; V-4Cr-4Ti possesses intermediate strength. Both YS and UTS showed a similar trend of incremental increase with strain rate for the three alloys. All three alloys exhibited almost no change in uniform and total elongations up to a strain rate of 10^{-1}/s followed by a decrease with further increase in strain rate. The room temperature tensile behavior of V-4Cr-4Ti was unaffected by the introduction of a significant partial pressure of atomic hydrogen into the testing environment.

INTRODUCTION

In the early stages of the program on the development of alloys for fusion reactor applications, vanadium alloys with 3 to 6 wt.% Cr and Ti were investigated.[1-4] This composition range was subsequently narrowed down to vanadium alloys with 4 wt.% each of Cr and Ti based on the thermal creep properties, low DBTT under Charpy impact testing, resistance to swelling, and also resistance to helium– and irradiation-induced embrittlement exhibited by a laboratory-scale heat of this alloy.[5] A production-scale heat (~500–kg, heat 832665) of V-4Cr-4Ti alloy was fabricated by Teledyne Wah Chang, Albany, Oregon (TWCA). Impact data have been reported from the testing conducted on the samples machined from a warm-worked plate[6] as well as from an annealed plate.[7] Also, recovery and recrystallization behavior of this heat has been documented.[8] Impact data for compositional variants with Ti and Cr contents ranging from 3 to 6 wt.% have been presented earlier[7] as well as their recovery and recrystallization behavior.[8] The present study reports the results from the tensile testing of the large heat of V-4Cr-4Ti and the small heats of compositional variants with Ti and Cr contents ranging from 3 to 6 wt.%. These alloys will help to define a window for permissible ranges of Cr and Ti concentrations for consistent properties. Any candidate material for first wall of fusion reactor is exposed to both molecular and atomic hydrogen in service; tensile tests were carried out in a controlled atmosphere of hydrogen to examine the effect of hydrogen on the tensile behavior of the V-4Cr-4Ti alloy.

EXPERIMENTAL PROCEDURE

Two small heats (~15-kg melt), V-3Cr-3Ti (heat T91) and V-6Cr-6Ti (heat T90), were fabricated by TWCA according to the specifications set by Oak Ridge National Laboratory. The chemical compositions of the small heats of compositional variants have been presented elsewhere.[8] Tensile specimens (SS-3s) of these two alloys, with gage dimensions of $0.76 \times 1.52 \times 7.6$ mm, were punched from the as-received sheets of ~0.76 mm thickness from TWCA. Tensile specimens of the large heat of V-4Cr-4Ti (heat 832665), the chemical composition for which is given elsewhere[8], were punched from a 0.76 mm sheet of which was cold rolled from 1.05-mm-thick sheet received from TWCA. The punched specimens from the three alloys were recrystallized by annealing for 2 h at 1000°and 1100°C in a vacuum better than 1×10^{-6} torr ($<10^{-4}$ Pa). In order to study the effect of strain rate, tensile testing was carried out in air at room temperature on 1000°C–annealed specimens of all three alloys at strain rates ranging from 1.1×10^{-3} to 5×10^{-1}/s. The effects of test temperature and grain size on tensile properties were investigated on the 1000°C– and 1100°C–annealed specimens of the three alloys by testing them at room temperature in air, and 100–700°C in a vacuum better than 1×10^{-5} torr ($<10^{-3}$ Pa), and at a strain rate of 1.1×10^{-3}/s.

To analyze the effect of hydrogen on tensile behavior, tensile tests were conducted on SS-3 specimens of V-4Cr-4Ti (annealed at 1000°C for 2 h) in an UHV chamber which had a provision for bleeding in hydrogen so that a desired partial pressure of hydrogen could be maintained in the test chamber. The details of the testing setup are given elsewhere.[9] The pumping system of the UHV test chamber consisted of two liquid-nitrogen-cooled sorption pumps and an ion pump, wherein the sorption pumps were used for roughing, and the ion pump was used for bake out and maintaining subsequent UHV in the chamber. High purity (99.9999%) hydrogen was supplied to the chamber through a leak valve. For each test, after loading the specimen, the chamber was baked out for ~18 h at ~200°C in dynamic vacuum. The vacuum in the chamber was better than 5×10^{-10} torr (5×10^{-8} Pa) after baking out and cooling to room temperature. The chamber was then backfilled with pure, dry hydrogen (dried by flowing it through a liquid nitrogen trap) to a partial pressure of 30 to 50 torr (3 to 5 KPa). Hydrogen pressures were measured with a bare ionization gage located in the UHV chamber. The tensile tests were conducted at room temperature, 30 minute after back-filling with hydrogen, at a strain rate of ~10^{-3}/s. By assuming that the specimen strain occurred completely in the gage length, the total elongations were determined by measuring the specimen lengths before and after fracture.

RESULTS AND DISCUSSION

Effect of Strain Rate

Figure 1 shows the variation of 0.2% yield strength with strain rate and Figure 2 shows the ultimate tensile strength (UTS) as a function of strain rate for the V-3Cr-3Ti, V-4Cr-4Ti and V-6Cr-6Ti alloys. There is a general tendency for yield strength and UTS to increase incrementally with strain rate for all three alloys. This strain rate sensitivity for vanadium alloys is similar to the observed results for many other bcc metals e.g., niobium and high–purity iron.[10] At all strain rates, V-3Cr-3Ti showed the lowest strength properties for all strain rates with V-6Cr-6Ti being the strongest of the three alloys. V-6Cr-6Ti is stronger than V-4Cr-4Ti both at 0.2% strain and in UTS at all strain rates except between 1.1×10^{-3} and 1.1×10^{-2}/s where it appears that the two alloys have similar yield strength. It is useful to recall here the results of the microhardness testing from an earlier study[8] which showed that in both the recovered and fully recrystallized states, V-6Cr-6Ti was the hardest alloy (160-185 DPH) and V-3Cr-3Ti was the weakest alloy (130-140 DPH), with V-4Cr-4Ti being in the intermediate range (140-160 DPH). Hence, the results of tensile testing for strain rate sensitivity in the present study in conjunction with the previous results from microhardness testing reveal that the V-6Cr-6Ti alloy is an intrinsically stronger alloy (possibly due mainly to solid solution strengthening from higher Cr and Ti contents) compared to both V-3Cr-3Ti and

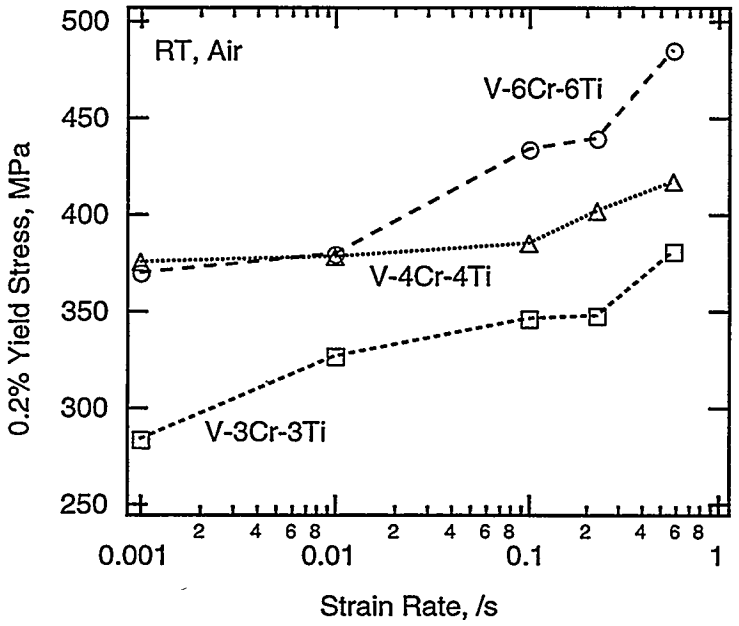

Figure 1. Variation of 0.2% yield strength with strain rate for the V-3Cr-3Ti, V-4Cr-4Ti and V-6Cr-6Ti alloys.

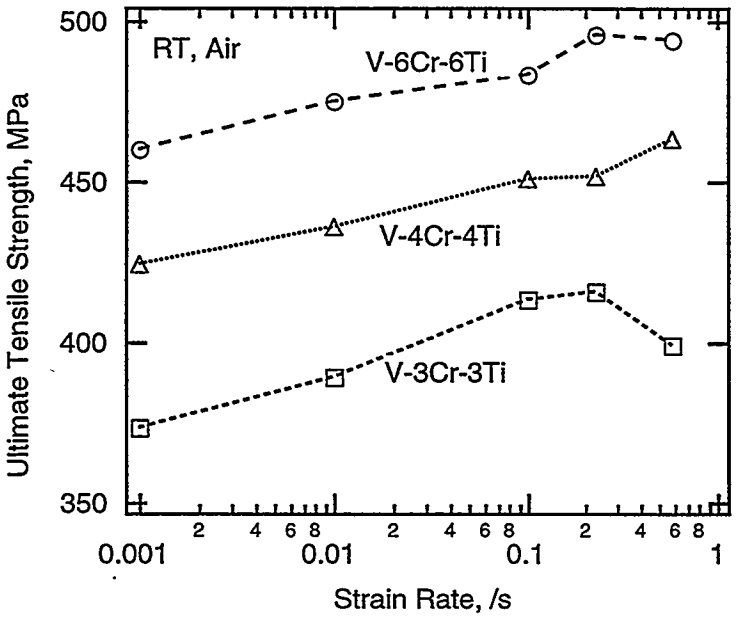

Figure 2. The ultimate tensile strength as a function of strain rate for the V-3Cr-3Ti, V-4Cr-4Ti and V-6Cr-6Ti alloys.

V-4Cr-4Ti alloys.

The effect of strain rate on the uniform and total elongations of the V-3Cr-3Ti, V-4Cr-4Ti and V-6Cr-6Ti alloys is shown in Figure 3 and Figure 4, respectively. For all the three alloys, both uniform and total elongations were nearly independent of strain rate up to 0.1/s, but showed a significant decrease at strain rates above 0.1/s.

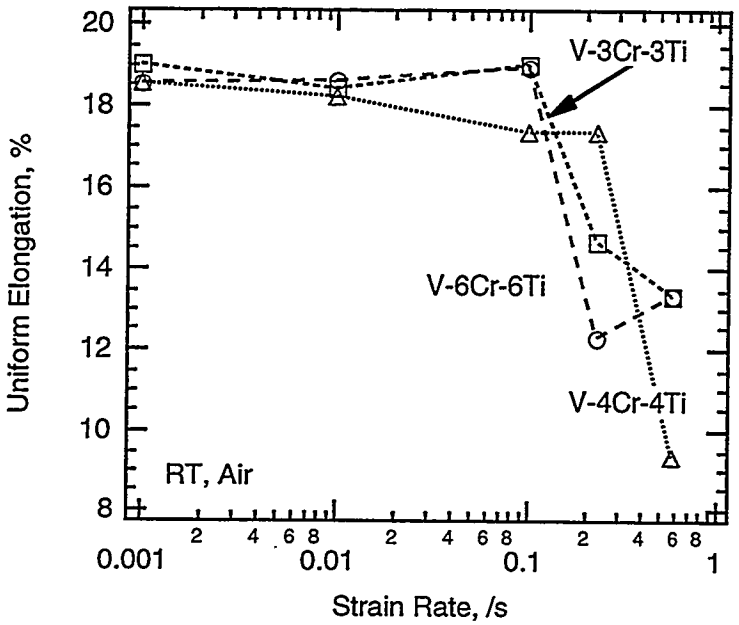

Figure 3. The uniform elongation as a function of strain rate for the V-3Cr-3Ti, V-4Cr-4Ti and V-6Cr-6Ti alloys.

The general relationship between flow stress σ and strain rate Φ (at constant temperature T and strain ε) is given as[11]

$$\sigma = C(\Phi)^m\Big|_{\varepsilon,T} \qquad (1)$$

where C is a constant and m is the strain–rate sensitivity parameter. If one plots logarithm of stress as a function of logarithm of strain rate (at a constant temperature and strain), the slope of the line of fit gives the value of exponent m. In general, for most metals, the value of m is less than 0.1.[11] Figure 5 shows a plot of logarithm of stress as a function of logarithm of strain rate which contains data for the three alloys, V-3Cr-3Ti, V-4Cr-4Ti and V-6Cr-6Ti, at a nominal strain of 8% and tested at room temperature. It is interesting to note that, for all the three alloys, the exponent m is almost identical and falls in the range of 0.022 to 0.024. Thus the strain–rate sensitivity of the three alloys is similar at room temperature for strain rates ranging from 1.1×10^{-3} to 5×10^{-1}/s. The range of values for strain–rate sensitivity for the alloys studied in the present work compares favorably with the value of 0.024 for unalloyed vanadium (containing 265 wppm oxygen) determined by Bradford and Carlson.[12] Hence, it can be inferred here that vanadium has similar strain–rate sensitivity in both unalloyed and alloyed (with Ti and Cr) states.

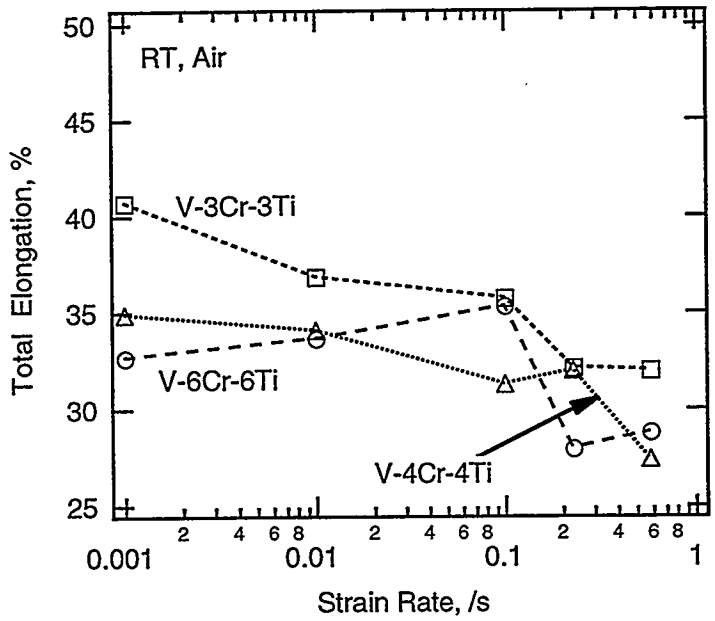

Figure 4. The total elongation as a function of strain rate for the V-3Cr-3Ti, V-4Cr-4Ti and V-6Cr-6Ti alloys.

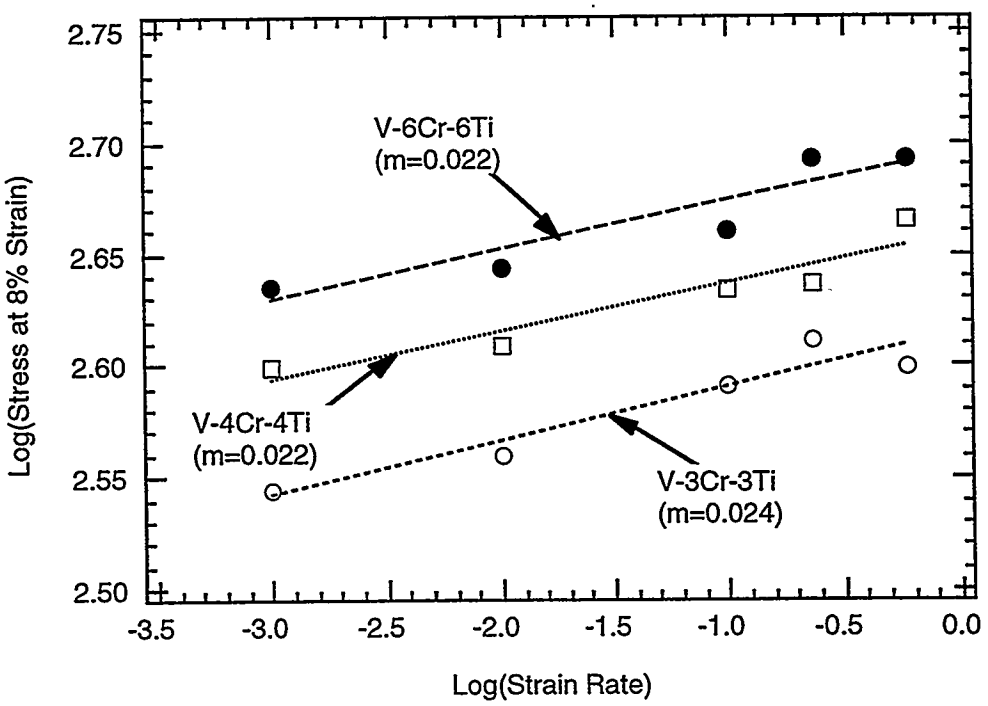

Figure 5. Logarithm of stress as a function of logarithm of strain rate at a nominal strain of 8%, and at room temperature for the V-3Cr-3Ti, V-4Cr-4Ti and V-6Cr-6Ti alloys.

Effect of Test Temperature

Figures 6, 7, and 8 show, respectively, for the V-3Cr-3Ti, V-4Cr-4Ti and V-6Cr-6Ti alloys, the variation of 0.2% yield strength and ultimate tensile strength with test temperature. The ultimate tensile strength of all the alloys decreases with increase in temperature from room temperature and passes through a minimum at 300°C, before increasing with further increase in temperature up to 700°C. For all the three alloys, the yield strength also decreases with increase in temperature up to 300–400°C and then becomes relatively independent of temperature up to 700°C.

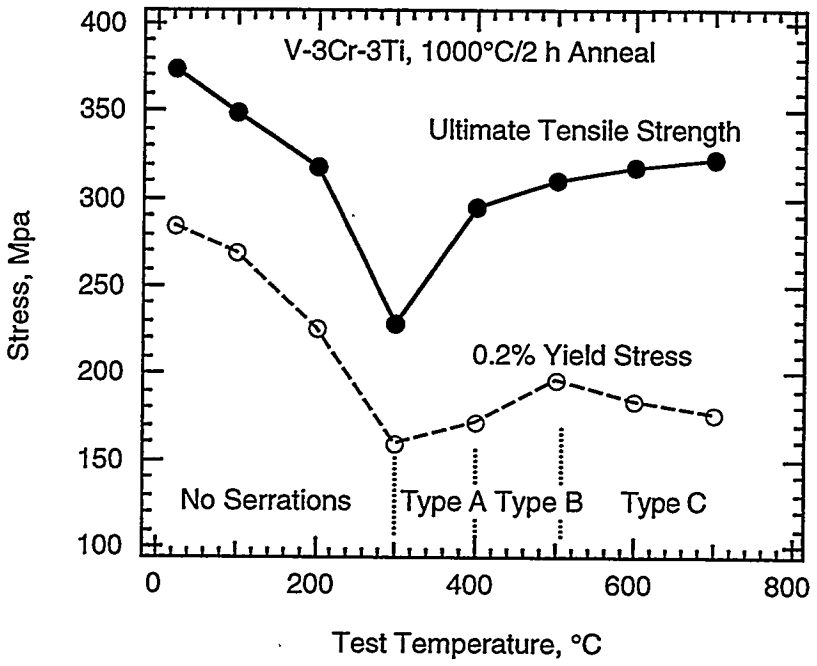

Figure 6. Variation of 0.2% yield strength and ultimate tensile strength with test temperature for the V-3Cr-3Ti alloy.

The effect of test temperature on the uniform and total elongations of the V-3Cr-3Ti, V-4Cr-4Ti and V-6Cr-6Ti alloys is shown in Figures 9, 10 and 11, respectively. Both uniform and total elongations are relatively unaffected by the temperature for all the alloys except V-3Cr-3Ti which shows much higher ductility at room temperature than the other two alloys.

***Discontinuous Yielding*:**

The phenomenon of discontinuous yielding (also called jerky flow or Portevin–Le Chatelier effect),[13] has been seen in solid solution alloys by many researchers. To cite a few, Russel[14] on his work on tin bronze alloys, Soler–Gomez and McG.Tegart[15] on their work on gold–indium, Brindley and Worthington[16] on their work on aluminum–3% magnesium, Keh et al[17] on their study on iron and steel, and Bradford and Carlson[12] on vanadium, observed serrations in the flow curves during tensile testing. In general, there are three types of serrations,[13-15] *Type A, Type B,* and *Type C*. The serrations which are periodic in nature and rise above the general level of stress–strain curve are termed as *Type A*. The serrations which occur in rapid succession and oscillate about the general level of stress–strain curve are termed as *Type B*, and serrations which fall always below the general level of the stress–strain curve are *Type C*.

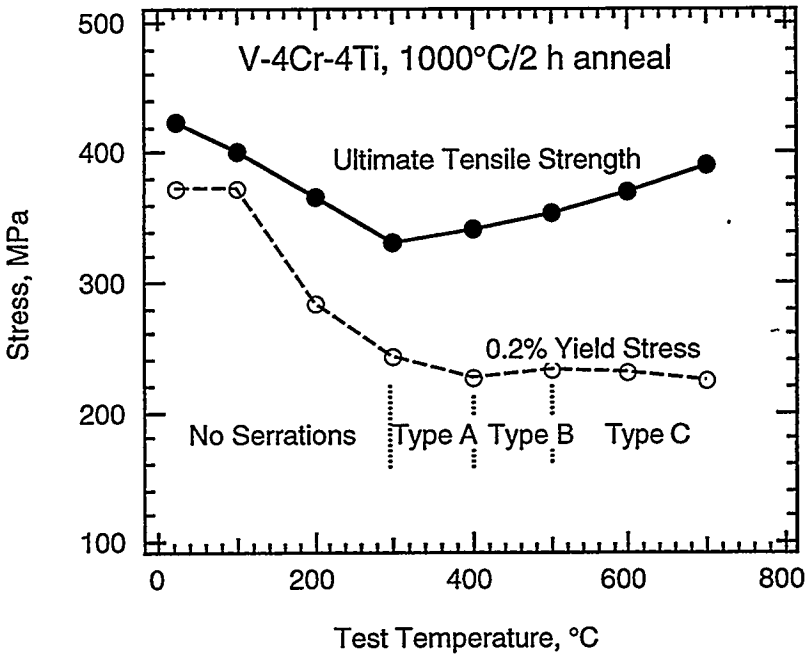

Figure 7. Variation of 0.2% yield strength and ultimate tensile strength with test temperature for the V-4Cr-4Ti alloy.

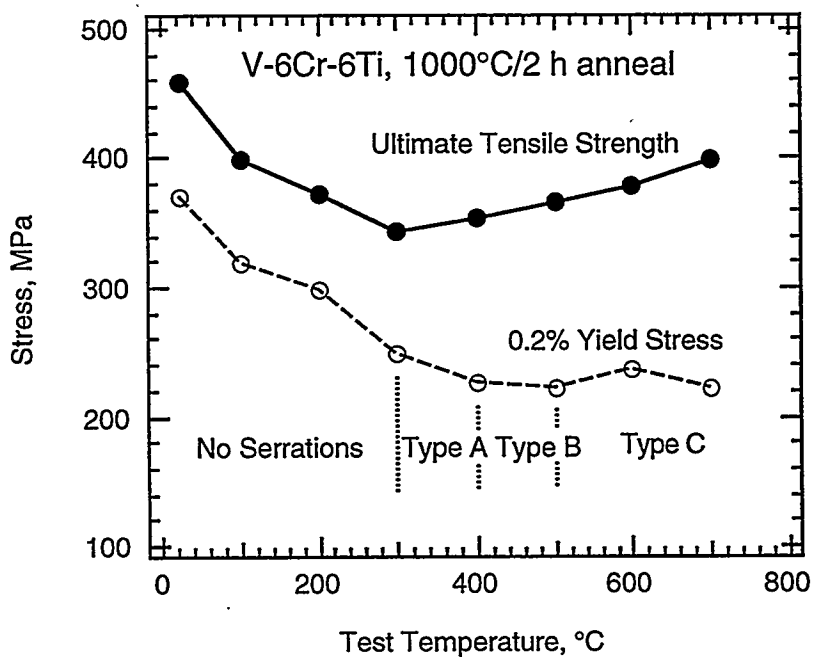

Figure 8. Variation of 0.2% yield strength and ultimate tensile strength with test temperature for the V-6Cr-6Ti alloy.

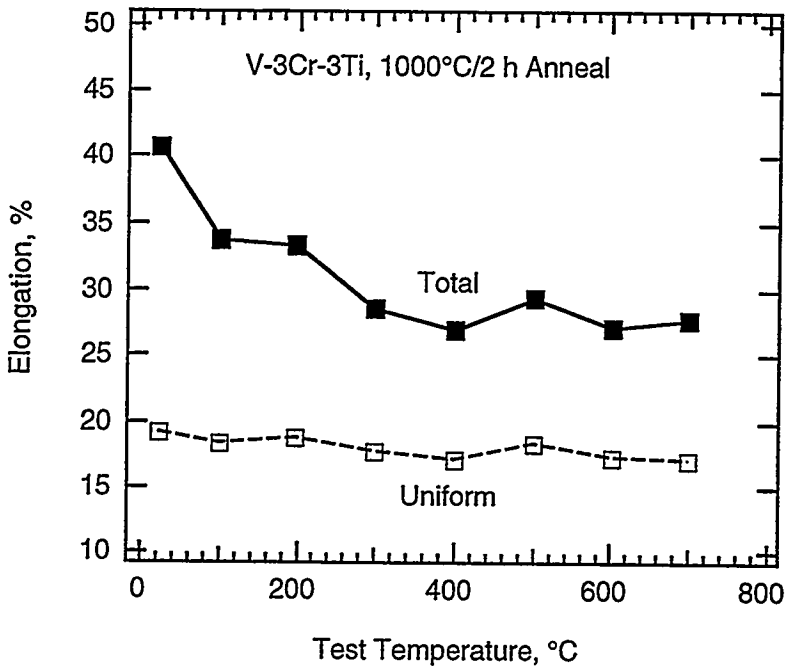

Figure 9. Variation of uniform and total elongations with test temperature for the V-3Cr-3Ti alloy.

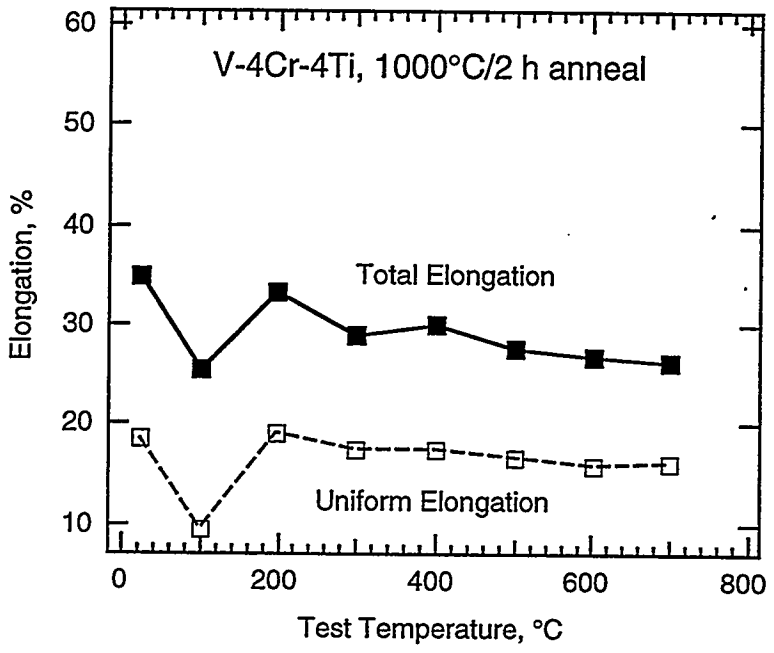

Figure 10. Variation of uniform and total elongations with test temperature for the V-4Cr-4Ti alloy.

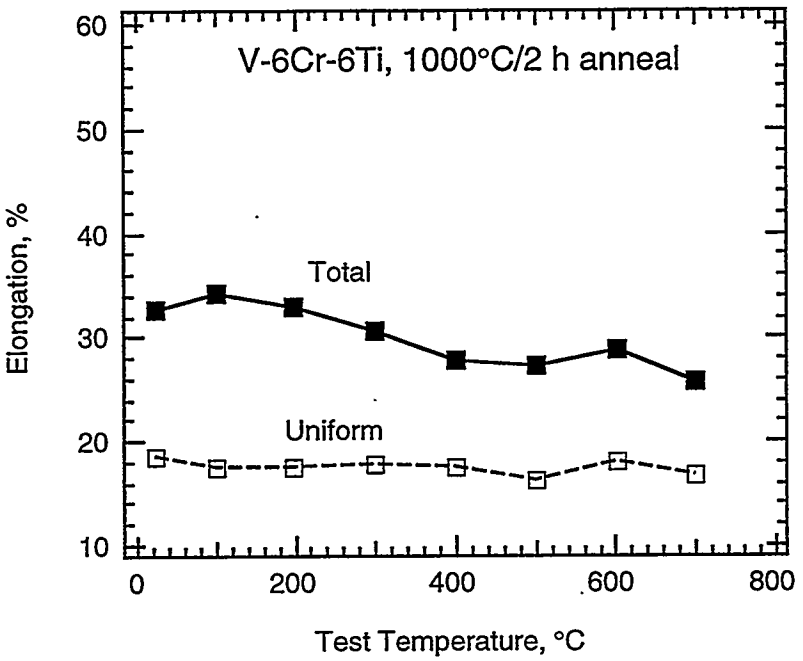

Figure 11. Variation of uniform and total elongations with test temperature for the V-6Cr-6Ti alloy.

The stress–strain curves for the V-3Cr-3Ti, V-4Cr-4Ti and V-6Cr-6Ti alloys are smooth with no serrations in the temperatures ranging from room temperature to 300°C. For temperatures above 300°C, discontinuous yielding is observed in all three alloys. Figures 12, 13, and 14 show flow curves (partial curves are shown for temperatures from 300 to 700°C for the V-4Cr-4Ti and V-6Cr-6Ti alloys due to the failure of a computer used in data acquisition during testing) at various test temperatures. At 400°C, *Type A* (periodic in nature) appear after a small strain beyond the lower yield point in all the three alloys. In addition to *Type A* serrations in the beginning of the stress–strain curve, V-6Cr-6Ti showed *Type B* (oscillating) after some strain. Figure 15 shows the variation of serration magnitude with test temperature for the three alloys. The magnitude of the *Type A* serrations is similar in these alloys in the range of 8–10 MPa. With an increase in temperature to 500°C, *Type B* serrations appear immediately following the lower yield point for all the three alloys. At this temperature, the magnitude of *Type B* serrations is around 10 MPa in V-3Cr-3Ti and much higher in the range of 16–18 MPa in V-4Cr-4Ti and V-6Cr-6Ti, see Figure 15. A further increase in temperature to 600°C causes the mode of serrations to change to *Type C* (always below the general stress–strain level) in all the three alloys. These serrations appear generally after some strain and their magnitude is similar for all three alloys around 22–25 MPa, see Figure 15. At 700°C, *Type C* serrations appear in the three alloys after an appreciable amount of strain. The frequency of the serrations decreases whereas their magnitude increases (except in V-3Cr-3Ti where it remains the same as at 600°C) to around 28–33 MPa, see Fig. 15. In addition to the discontinuous yielding or serrations in the flow curves, the V-3Cr-3Ti, V-4Cr-4Ti and V-6Cr-6Ti alloys exhibit a general trend of increasing work hardening ability with increase in temperature which is quite evident from the stress–strain curves in Figures 12, 13 and 14. Another observation is that all the three alloys showed minima in both yield and ultimate tensile strengths at 300°C, the highest temperature at which no serrations were seen in the stress–strain curves. With the increase in temperature above 300°C, the serrations start appearing, and the ultimate tensile strength increases monotonically with increase in the height of serrations with temperature, compare Figures 6, 7, 8, with Figure 15.

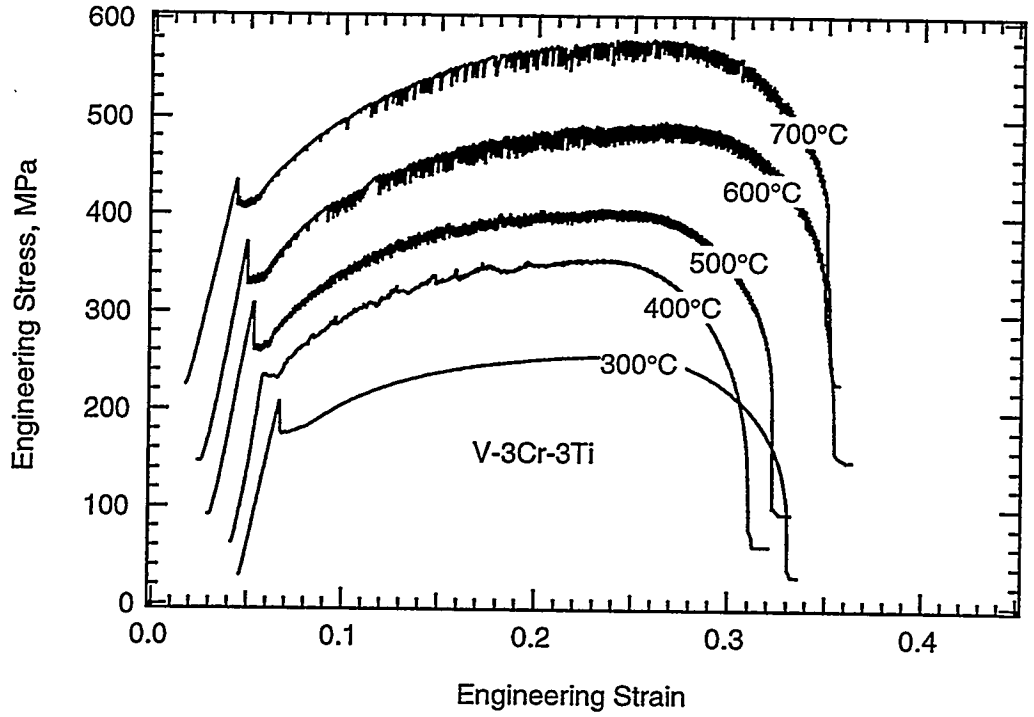

Figure 12. The stress–strain curves as a function of test temperature for the V-3Cr-3Ti alloy.

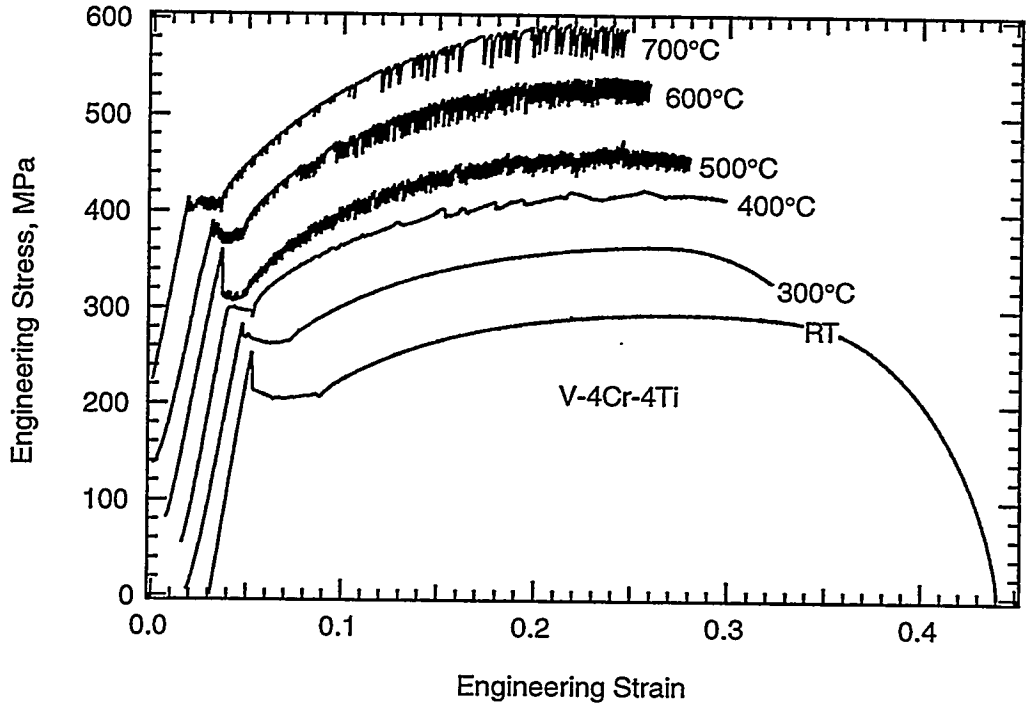

Figure 13. The stress–strain curves as a function of test temperature for the V-4Cr-4Ti alloy.

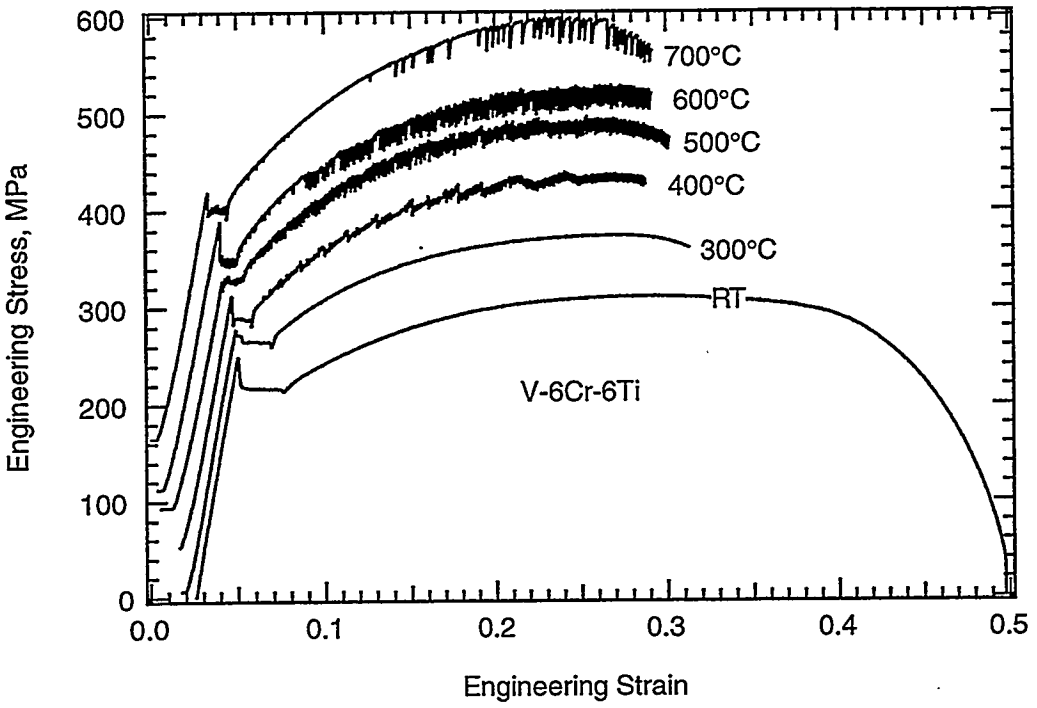

Figure 14. The stress–strain curves as a function of test temperature for the V-6Cr-6Ti alloy.

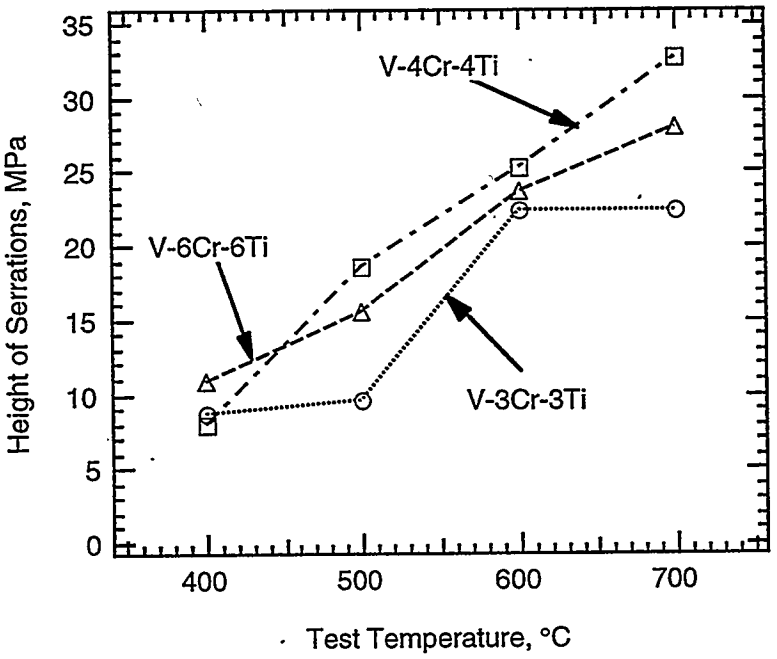

Figure 15. Plot of the variation in height of serrations with test temperature for the V-3Cr-3Ti, V-4Cr-4Ti and V-6Cr-6Ti alloys.

Dynamic strain aging due to solute atoms has been identified as the probable cause for the appearance of serrations in the stress–strain curves of many alloys.[12-18] The vanadium alloys examined in the present study contain the interstitial impurities, oxygen (around 250 wppm), carbon (around 100 wppm), and nitrogen (around 100 wppm). At low temperatures, these interstitials are relatively immobile compared to dislocations, and hence, no serrations are observed for test temperatures up to 300°C. At temperatures of 400°C and above, the interstitials atoms become sufficiently mobile so that they can diffuse fast enough to form a solute atmosphere around the freely moving dislocations after the initial yielding, reducing their velocity and eventually pinning them. Rapid dislocation multiplication takes place with further increase in load, the overall effect of which is to cause serrations in the flow curves and an increase in yield and tensile strengths. This enhanced multiplication of dislocations, rather than unlocking of existing ones, is quite evident from the increased work hardening ability (which indicates continuous creation of new dislocations). Cottrell,[19] in his work on interstitial strain-aging in iron, established a relationship between strain rate Φ and diffusivity of nitrogen atoms D as

$$\Phi = 10^9 D \qquad (2)$$

for calculating the minimum temperature for serrated yielding. In equation (2), D is given by

$$D = D_o \exp\left[\frac{-Q}{RT}\right] \qquad (3)$$

where D_o is the diffusion coefficient, Q is the activation energy, with R and T having the usual meaning. Equation (2) can be used to estimate the minimum temperatures for serrated yielding for the three interstitials, oxygen, carbon, and nitrogen in the present study. By using the values for diffusion coefficient and activation energy for oxygen, carbon, and nitrogen in vanadium[18] in Table 1, one can estimate the temperatures for each interstitial element.

By using the strain rate value of 1.1×10^{-3}/s used in the tensile testing in this study in equation (2), the temperatures so determined for oxygen, carbon, and nitrogen are 370°C, 350°C, and 480°C, respectively. These calculations suggest that the serrations in the stress–strain curves of the V-3Cr-3Ti, V-4Cr-4Ti and V-6Cr-6Ti alloys at ~400°C are most probably related to the mobility of either oxygen or carbon, or both.

Table 1. Diffusion coefficient and activation energy for various interstitial elements

Diffusing Element	D_o cm^2/s	Q kJ/mole
Oxygen	0.0025	115
Carbon	0.0047	114
Nitrogen	0.0018	147

For temperatures of 500°C and above, the strain-aging phenomenon is probably controlled by the diffusion of nitrogen.

Effect of Hydrogen

Cohron et al[9] found in their study on the effect of hydrogen on the intermetallic Ni_3Al alloy that the tensile elongation was affected by whether the ionization gage, which is used to measure the hydrogen pressure, was on or off. There was a significant reduction in the elongation of Ni_3Al when the ion gage was on as opposed to the much higher elongations obtained with the gage off. They proposed that when the gage is on, molecular hydrogen is converted into atomic hydrogen by the tungsten filament, and this atomic hydrogen embrittles the Ni_3Al specimens. The present work was limited to determining whether or not the V-4Cr-4Ti alloy would be similarly embrittled by exposure to an atmosphere containing atomic hydrogen. Exposure and tensile testing were carried out under hydrogen partial pressures of 30 and 50 torr

(3 and 5 KPa). Cohron et al[9] have determined the true temperature of the ion gage filament, with corrections made for emissivity of tungsten and absorption by the Pyrex viewport, to be around 1677°C (with the temperature measured with an optical pyrometer being ~1552°C). They estimated that at this temperature and 1 torr (1.3×10^2 Pa) pressure of hydrogen, approximately 10% of the hydrogen gas is in the form of atomic hydrogen, with the degree of hydrogen dissociation decreasing with increase in pressure. As shown in Figure 16, the ductility of the V-4Cr-4Ti alloy remains the same under high vacuum (~5×10^{-10} torr or 5×10^{-8} Pa) conditions and under the conditions which create atomic hydrogen. The proposed mechanism[9] for embrittlement of Ni_3Al involves the diffusion of hydrogen to the crack tip. In the case of V-4Cr-4Ti studied in the present work, this type of hydrogen embrittlement was not observed and the alloy remained ductile for hydrogen partial pressures up to 50 torr (5 KPa).

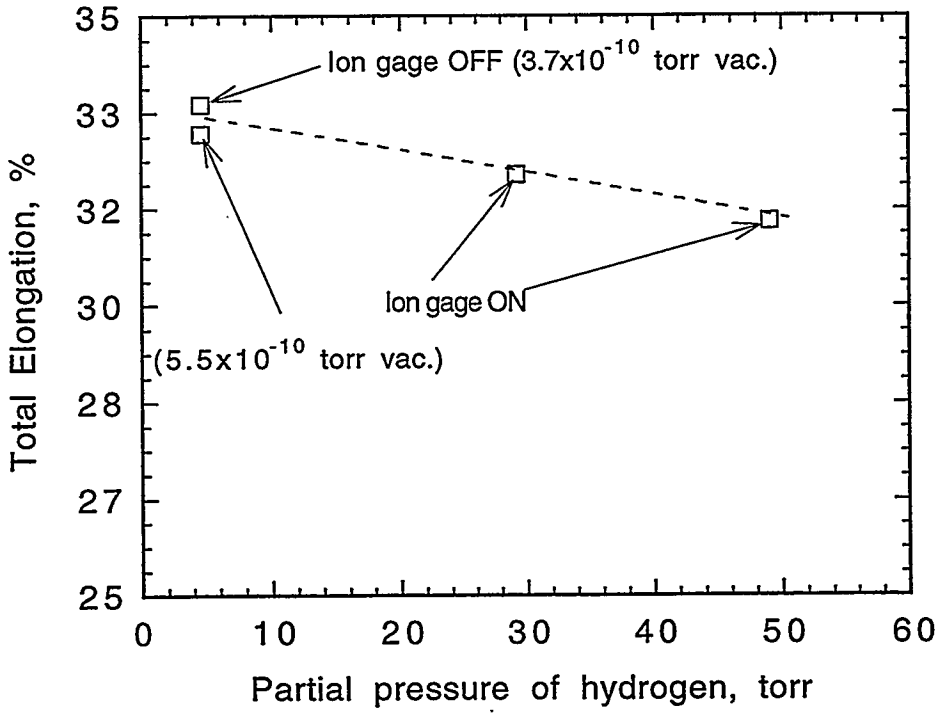

Figure 16. The total elongation as a function of the partial pressure of hydrogen for the V-4Cr-4Ti alloy.

SUMMARY AND CONCLUSIONS

The results from this investigation reveal that:

(1) Of the three vanadium alloys tested, V-6Cr-6Ti was the strongest and V-3Cr-3Ti was the weakest with V-4Cr-4Ti showing intermediate yield and ultimate tensile strengths at all strain rates. The strain–rate sensitivity of the vanadium alloys was found to be similar to that of unalloyed vanadium.

(2) All the three alloys exhibited almost no change in uniform and total elongations up to a strain rate of 10^{-1}/s, followed by a decrease with a further increase in strain rate.

(3) The ultimate tensile strengths of all the alloys exhibited minima at 300°C, whereas the yield strength, total, and uniform elongations were relatively insensitive to temperatures between 400 and 700°C.

(4) Serrated yielding (indicative of dynamic strain aging) was observed in the stress-strain curves of all the alloys at test temperatures above 300°C.

(5) At room temperature, the test environment (vacuum, air and atomic hydrogen) showed no significant influence on the tensile behavior of the V-4Cr-4Ti alloy.

ACKNOWLEDGMENTS

This research is sponsored by the Office of Fusion Energy Sciences, U. S. Department of Energy, under contract DE-AC05-96OR22464 with Lockheed Martin Energy Research Corp. This research was supported in part by an appointment (ANG) to the Oak Ridge National Laboratory Postdoctoral Research Associates Program administered jointly by the Oak Ridge National Laboratory and the Oak Ridge Institute for Science and Education. We are thankful to Dr. E. E. Bloom for useful suggestions and Dr. E. P. George for his help in conducting hydrogen tensile tests.

REFERENCES

[1] B. A. Loomis and D. L. Smith, J. Nucl. Matls., 179-181 (1991), pp 783-786.

[2] B. A. Loomis, D. L. Smith, and F. A Garner, J. Nucl. Matls., 179-181 (1991), pp 771-776.

[3] H. M. Chung and D. L. Smith, J. Nucl. Matls., 191-194 (1992), pp 942-947.

[4] B. A. Loomis, L. J. Nowicki, J. Gazda, and D. L. Smith, Fusion Reactor Materials Semiannual Progress Report, DOE/ER-0313/14, March 31, 1993, pp 318-325.

[5] B. A. Loomis, H. M. Chung, L. J. Nowicki, and D. L. Smith, J. Nucl. Matls., 212-215 (1994), pp 799-803.

[6] H. M. Chung, L. Nowicki, J. Gazda, and D. L. Smith, Fusion Reactor Materials Semiannual Progress Report, DOE/ER-0313/17, September 30, 1994.

[7] A. N. Gubbi, A. F. Rowcliffe, D. J. Alexander, M. L. Grossbeck, and W. S. Eatherly, Fusion Reactor Materials Semiannual Progress Report, DOE/ER-0313/18, March 31, 1995, pp 203-213.

[8] A. N. Gubbi, A. F. Rowcliffe, and W. S. Eatherly, Fusion Reactor Materials Semiannual Progress Report, DOE/ER-0313/18, March 31, 1995, pp 187-201.

[9] J. W. Cohron, E. P. George, L. Heatherly, C. T. Liu and R. H. Zee, In press, Scripta Metall., 1996.

[10] J. Harding, in *Materials at High Strain Rates*, T. Z. Blazynski, Ed., Elsevier Applied Science, 1987.

[11] G. E. Dieter, in *Mechanical Metallurgy* , 3rd ed.(1986), McGraw Hill Book Co., NY, pp 295-300.

[12] S. A. Bradford and O. N. Carlson, Trans. AIME, 224 (1962), pp 738-742.

[13] B. J. Brindley and P. J. Worthington, Metall. Rev., 4 (1970), pp 101-114.

[14] B. Russell, Phil. Mag., 8 (1963), pp 615-630.

[15] A. J. R. Soler-Gomez and W. J. McG. Tegart, Phil Mag., 20 (1969), pp 495-509.

[16] B. J. Brindley and P. J. Worthington, Acta Metall., 17 (1969), pp 1357-1361.

[17] A. S. Keh, Y. Nakada and W. C. Leslie, in *Dislocation Dynamics* (1968), McGraw Hill Book Co., NY, pp 381-408.

[18] J. W. Edington, T. C. Lindley and R. E. Smallman, Acta Metall., 12 (1964), pp 1025-1031.

[19] A. H. Cottrell, Phil. Mag., 44, No. 355 (1953), pp 829-832.

DEVELOPMENT OF LASER WELDING TECHNIQUES FOR VANADIUM ALLOYS*

R. V. Strain, K. H. Leong, and D. L. Smith (Argonne National Laboratory)

OBJECTIVE

The development of techniques for joining vanadium alloys, and possibly vanadium, to steel will be required for the construction of fusion devices. The primary objective of this program is to develop laser welding techniques for vanadium alloys, and to evaluate the performance of weldments.

BACKGROUND

Laser welding is potentially advantageous because of its flexibility and the reduced amount of material affected by the weld. Bead-on-plate and butt welds were previously performed to depths of about 4 mm with a 6-kW CO_2 laser on V-4%Cr-4%Ti and V-5%Cr-5%Ti alloys. These welds were made at a speed of 0.042 m/s using argon purging at a flow rate of 2.8 m^3/s. The purge was distributed with a diffuser nozzle aimed just behind the laser beam during the welding operation. The fusion zones of welds made under these conditions consisted of very fine, needle-shaped grains and were also harder than the bulk metal (230-270 dph, compared to ≈180 dph for the bulk metal). A limited number of impact tests showed that the as-welded ductile–brittle transition temperatures (DBTT) was above room temperature, but heat treatment at 1000°C for 1 h in vacuum reduced the DBTT to <-25°C.

Activities during this reporting period focused on improvements in the purging system and determination of the effect of welding speed on welds. A 2-kW continuous YAG laser at Lumonics Corp. in Livonia, MI, was used to make 34 test welds for this study.

EXPERIMENTAL PROGRAM

A YAG laser was chosen for this series of weld tests because its shorter wavelength (compared to that of the CO_2 laser) is expected to provide higher irradiance and thus may improve coupling of the beam with the specimen during the welding operation. Welding speeds of 0.007 to 0.034 m/s were used in making the sample welds. Most of the welds were made with a continuous beam, but a few tests were made while oscillating the beam power as a sine wave function to increase the weld penetration. The amplitude of the oscillations equaled 68 or 90% of full power at repetition rates of 300 and 150 cycles/s, respectively. To reduce oxygen entrainment in the argon purge, the top of the specimen was flooded with argon from two diffusers facing each other, as shown in Fig. 1. The bottom of the specimen was flooded with argon confined in a box, with the exit around the edges of the specimen.

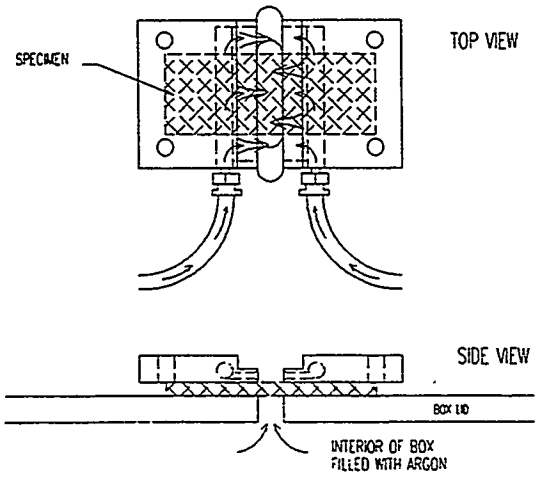

Fig. 1. Schematic Drawing of Argon Purging System

*Work supported by U.S. Department of Energy, Office of Fusion Energy Research, under Contract W-31-109-Eng-38.

RESULTS

Metallographic examination and testing of all of the specimens from this series of welds has been initiated. Initial results indicate that the depth of weld penetration and the microhardness of the welds increases as the welding speed is decreased. Use of oscillating beam power also increased weld penetration and weld hardness. The microstructure and grain size of the welds were not changed by the welding speed. The characteristics of the YAG laser weld at 0.034 m/s were essentially the same as those of the CO_2 laser welds at 0.042 m/s.

These results are interpreted as indicating that the "improved" argon purge did not completely prevent the pickup of oxygen during the welding operation. The slower welding speeds resulted in the metal remaining molten longer, which caused greater oxygen contamination than at the higher speeds. Conversely, the weld microstructure is controlled by the solidification rate, which is probably controlled by the thermal conductivity of the alloy and by the purging rate, rather than by the speed of the weld.

FUTURE ACTIVITIES

An enclosure is being fabricated to allow welding in a vacuum or pure inert atmosphere by passing the laser beam through a window. The effectiveness of variations in the gas environment, as well as changes in welding speed, will be assessed by impact testing and by microstructural and microhardness measurements. Postweld heat treating will be studied, if it is needed to obtain material properties in the weld that are comparable to those in the bulk material.

IMPACT PROPERTIES AND HARDENING BEHAVIOR OF LASER AND ELECTRON-BEAM WELDS OF V-4Cr-4Ti*

H. M. Chung, R. V. Strain, H.-C. Tsai, J.-H. Park, and D. L. Smith
(Argonne National Laboratory)

SUMMARY

We are conducting a program to develop an optimal laser welding procedure that can be applied to large-scale fusion-reactor structural components to be fabricated from vanadium-base alloys. Results of initial investigation of mechanical properties and hardening behavior of laser and electron-beam (EB) welds of the production-scale heat of V-4Cr-4Ti (500-kg Heat #832665) in as-welded and postwelding heat-treated (PWHT) conditions are presented in this paper. The laser weld was produced in air using a 6-kW continuous CO_2 laser at a welding speed of ≈45 mm/s. Microhardness of the laser welds was somewhat higher than that of the base metal, which was annealed at a nominal temperature of ≈1050°C for 2 h in the factory. In spite of the moderate hardening, ductile-brittle transition temperatures (DBTTs) of the initial laser (≈80°C) and EB (≈30°C) welds were significantly higher than that of the base metal (≈-170°C). However, excellent impact properties, with DBTT < -80°C and similar to those of the base metal, could be restored in both the laser and EB welds by postwelding annealing at 1000°C for 1 h in vacuum.

INTRODUCTION

Recent research in vanadium alloys has focused on development of welding procedures and investigation of the weld properties of the reference alloy V-4Cr-4Ti. A program is being conducted in this laboratory to develop an optimal laser welding procedure that can be applied to welding of large-scale fusion-reactor structural components. An initial bead-on-plate laser weld was produced on 3.8-mm-thick plates of the production-scale heat of V-4Cr-4Ti (500-kg Heat #832665).[1] The base plates were annealed in the factory at a nominal temperature of ≈1050°C for 2 h. To complement the investigation on the structure and properties of the laser weld, EB welds were also obtained from a separate program. In the program, a large-scale MHD test loop was fabricated from the same heat of V-4Cr-4Ti, and a few EB welds were produced as part of the fabrication effort. In this paper, we report results of initial investigation of mechanical properties and hardening behavior of the laser and EB welds of the production-scale heat of V--4Cr-4Ti in as-welded condition and after postwelding heat-treatment (PWHT) at ≈1000°C for 1 h in high vacuum.

MATERIALS AND PROCEDURES

The bead-on-plate laser weld was produced in air with an argon gas purge using a 6-kW continuous CO_2 laser at a welding speed of ≈45 mm/s. Details of the welding procedure are reported in Ref. 1. One-third-size Charpy impact specimens (3.3 x 3.3 x 25.4 mm, 30° notch angle, and 0.61-mm notch depth) were machined from the welded plate. The orientation of the Charpy specimens (L-S orientation) is shown schematically in Fig. 1. Direction of crack propagation was perpendicular to the rolling direction and the flat surface of the plate. As shown, a V-notch was located in the center of the weld zone so that the crack would propagate entirely within the weld zone.

The machined Charpy specimens were subjected to the customary degassing treatment at 400°C for 1 h in ion-pumped vacuum to expel hydrogen. This state of the material is referred to as the "as-welded" condition. Some of the machined specimens were annealed instead at 1000°C for 1 h in ion-pumped vacuum, resulting in the "postwelding heat-treated" (PWHT) condition. Following impact testing at -100 to +300°C, fractographic analysis and microhardness measurement were conducted on broken or bent pieces of the Charpy specimen. Vickers microhardness was measured with a 25-g load near the fracture region on one side of the Charpy specimen. Results of microstructural and microchemical analyses aimed at mechanistic understanding of the fracture behavior are given Ref. 2.

*Work supported by the U.S. Department of Energy, Office of Fusion Energy Research, under Contract W-31-109-Eng-38.

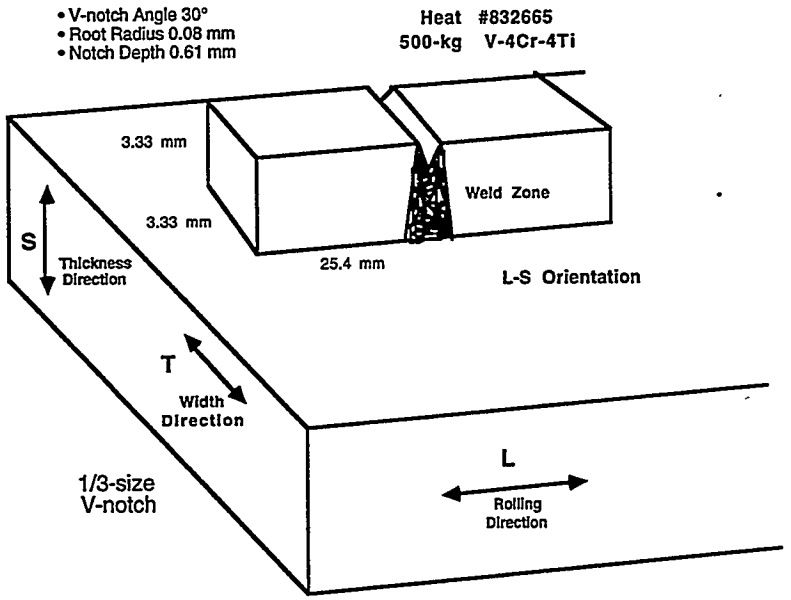

Fig. 1.
Orientation of Charpy-impact specimens of laser and EB welds of V-4Cr–4Ti

RESULTS AND DISCUSSION

Impact properties of the laser and EB welds measured at –100 to 300°C are shown in Figs. 2 and 3, respectively. In the figures, weld impact energies measured after degassing the machined Charpy specimens at 400°C (as–welded condition) and at 1000°C (PWHT condition) are shown for comparison. Impact energy of the base metal is also plotted in Fig. 2 as a function of temperature. The DBTTs of the laser and EB welds were ≈80°C and ≈30°C, respectively. These are significantly higher than the DBTT of the base metal (≈–170°C). However, excellent impact properties with DBTTs <–80°C could be restored in both the laser and EB welds by postwelding annealing at 1000°C for 1 h. Impact energies at <–80°C could not be measured because a sufficient number of specimens were not available. True DBTTs of the postwelding annealed laser and EB welds are probably as low as, or lower than, the DBTT of the base metal. However, this must be verified by further testing at <–80°C.

Consistent with the effects of PWHT on impact properties, the microhardnesses of the laser and EB welds decreased significantly after postwelding annealing. This is shown in Figs. 4 and 5, respectively. Vickers hardnesses of the fusion zones of the laser and EB welds were ≈200 and ≈170, respectively, in as–welded condition. After the postwelding annealing, hardness decreased to ≈130. Hardness of the base metal decreased from ≈160 to ≈130 after the postwelding annealing.

As expected, impact properties of the laser and EB welds seems to be more sensitive to postwelding annealing at 1000°C than hardening behavior. Apparently, a similar type of metallurgical process seems to occur during the postwelding annealing of laser and EB welds. Identifying this process is therefore important in gaining an understanding of the mechanism causing the drastic improvement in impact toughness that is associated with the postwelding annealing.

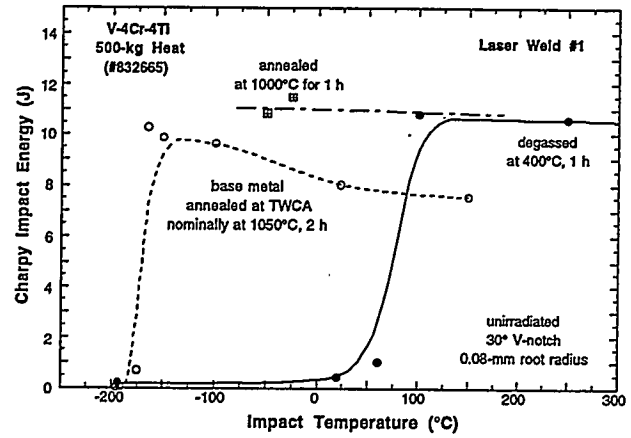

Fig. 2.

Impact properties of base metal and laser weld of V–4Cr–4Ti after annealing under various conditions.

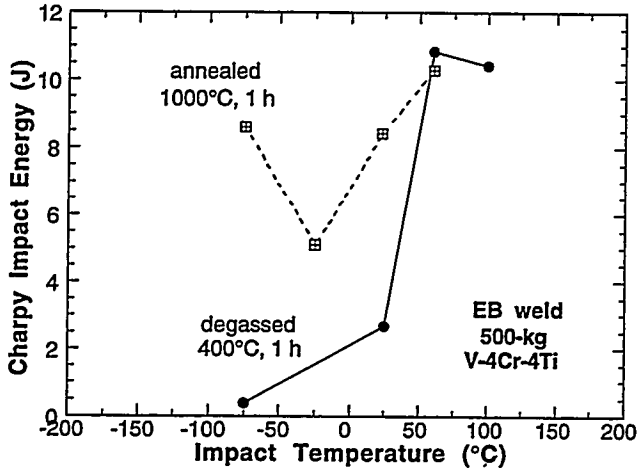

Fig. 3.

Impact properties of electron–beam weld of V–4Cr–4Ti after annealing at 400 and 1000°C.

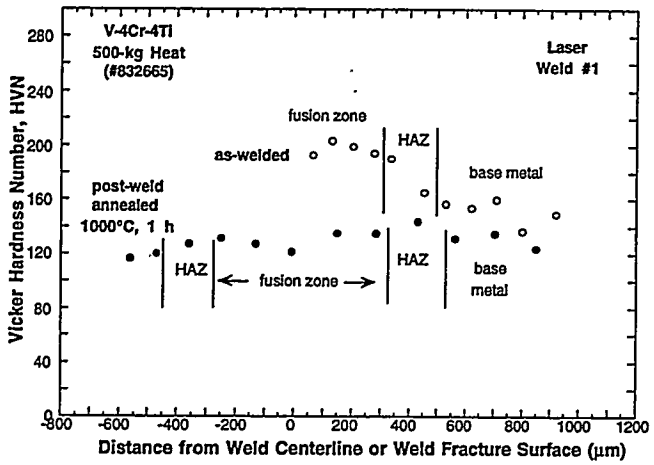

Fig. 4.

Hardness of laser weld of V-4Cr-4Ti before and after annealing at 400 and 1000°C.

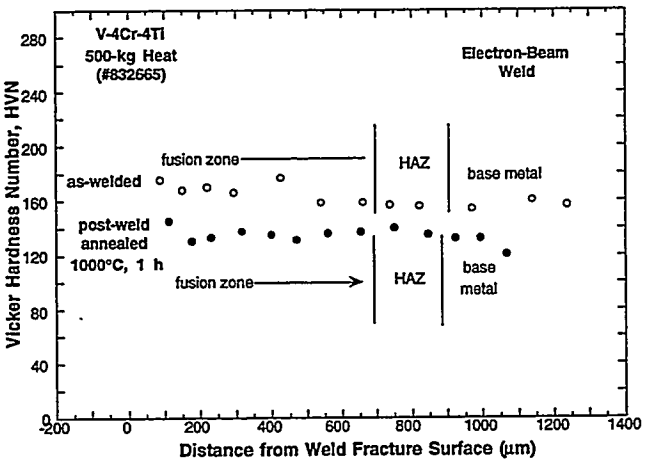

Fig. 5.
Hardness of electron–beam weld of V-4Cr–4Ti after annealing at 400 and 1000°C.

CONCLUSIONS

1. Hardening behavior and impact properties of laser and electron–beam (EB) welds of V–4Cr–4Ti were investigated with and without postwelding annealing at 1000°C for 1 h in high vacuum. Ductile–brittle transition temperatures (DBTTs) of the laser and EB welds were ≈80°C and EB ≈30°C, respectively, significantly higher than the DBTT of the base metal. However, excellent impact properties could be restored in both the laser and EB welds by postwelding annealing at 1000°C for 1 h in vacuum.

2. Consistent with the effect on impact properties, microhardness of the laser and EB welds decreased significantly following postwelding annealing.

3. Impact properties seem to be more sensitive than hardening behavior to postwelding annealing at 1000°C. Apparently, a similar type of metallurgical process seems to occur during the postwelding annealing of laser and EB welds. Identifying this process is therefore important in gaining an understanding of the mechanism that drastically improves impact toughness, as well as in developing an innovative procedure to produce high–quality welds.

REFERENCES

1. R. V. Strain, K. H. Leong, and D. L. Smith, "Development of Laser Welding Techniques of Vanadium Alloys," in Fusion Reactor Materials, Semiannual Prog. Rep. DOE/ER-0313/19, Oak Ridge National Laboratory, Oak Ridge, TN (1995), pp. 3–4.
2. H. M. Chung, J.–H. Park, J. Gazda, and D. L. Smith, "Microstructural Characteristics and Mechanism of Toughness Improvement of Laser and Electron–Beam Welds of V–4Cr–4Ti Following Post–Weld Heat–Treatment," in this report.

MICROSTRUCTURAL CHARACTERISTICS AND MECHANISM OF TOUGHNESS IMPROVEMENT OF LASER AND ELECTRON-BEAM WELDS OF V–4Cr–4Ti FOLLOWING POSTWELDING HEAT–TREATMENT*

H. M. Chung, J.–H. Park, J. Gazda, and D. L. Smith
(Argonne National Laboratory)

SUMMARY

We are conducting a program to develop an optimal laser welding procedure for large–scale fusion–reactor structural components to be fabricated from vanadium–base alloys. Microstructural characteristics were investigated by optical microscopy, X–ray diffraction, transmission electron microscopy, and chemical analysis to provide an understanding of the mechanism of the drastic improvement of impact toughness of laser and electron-beam (EB) welds of V–4Cr–4Ti following postwelding annealing at 1000°C. Transmision electron microscopy (TEM) revealed that annealed weld zones were characterized by extensive networks of fine V(C,O,N) precipitates, which appear to clean away O, C, and N from grain matrices. This process is accompanied by simultaneous annealing-out of the dense dislocations present in the weld fusion zone. It seems possible to produce high–quality welds under practical conditions by controlling and adjusting the cooling rate of the weld zone by some innovative method to maximize the precipitation of V(C,O,N).

INTRODUCTION

For the vanadium alloys, recent attention has focused on development of welding procedures and investigation of the weld properties of the reference alloy V–4Cr–4Ti. The objective of this task is to develop an optimal laser welding procedure that can be applied to welding of large–scale fusion–reactor structural components. Initial investigation of mechanical properties of laser and EB welds of the production–scale heat of V–4Cr–4Ti (500–kg Heat #832665) has demonstrated that impact toughness of the welds is improved drastically by postwelding heat–treatment (PWHT) at ≈1000°C for 1 h.[1]

Although postwelding annealing at 1000°C for as long as 1 h is obviously impractical for field application, it was thought to be important to understand the mechanism of the drastic improvement of the impact toughness, because once the mechanism is understood, it would be possible to develop an innovative method to apply the underlying principle to produce a good weld under practical conditions. Therefore, a microstructural investigation by optical microscopy, X–ray diffraction, TEM, and chemical analysis has been conducted on as-welded and postwelding-annealed specimens of V-4Cr-4Ti to provide an understanding of the mechanism of the toughness improvement.

MICROSTRUCTURAL ANALYSES

Optical Microscopy

Optical micrographs of the as-welded and postwelding-annealed specimens of the laser weld are shown in Fig. 1. The low- and high-magnification photomicrographs in the figures were obtained from the side of the broken or bent Charpy specimens that were impact-tested after the heat treatment. Elongated grains and fracture line in the weld fusion zone are visible in Fig. 1(A), the low-magnification phototmicrograph.

In the high-magnification photomicrograph of the postwelding-annealed material, Fig. 1(C), a characteristic fine substructure is visible within the elongated grains of the fusion zone. This substructure is absent in the

*Work supported by U.S. Department of Energy, Office of Fusion Energy Research, under Contract W-31-109-Eng-38.

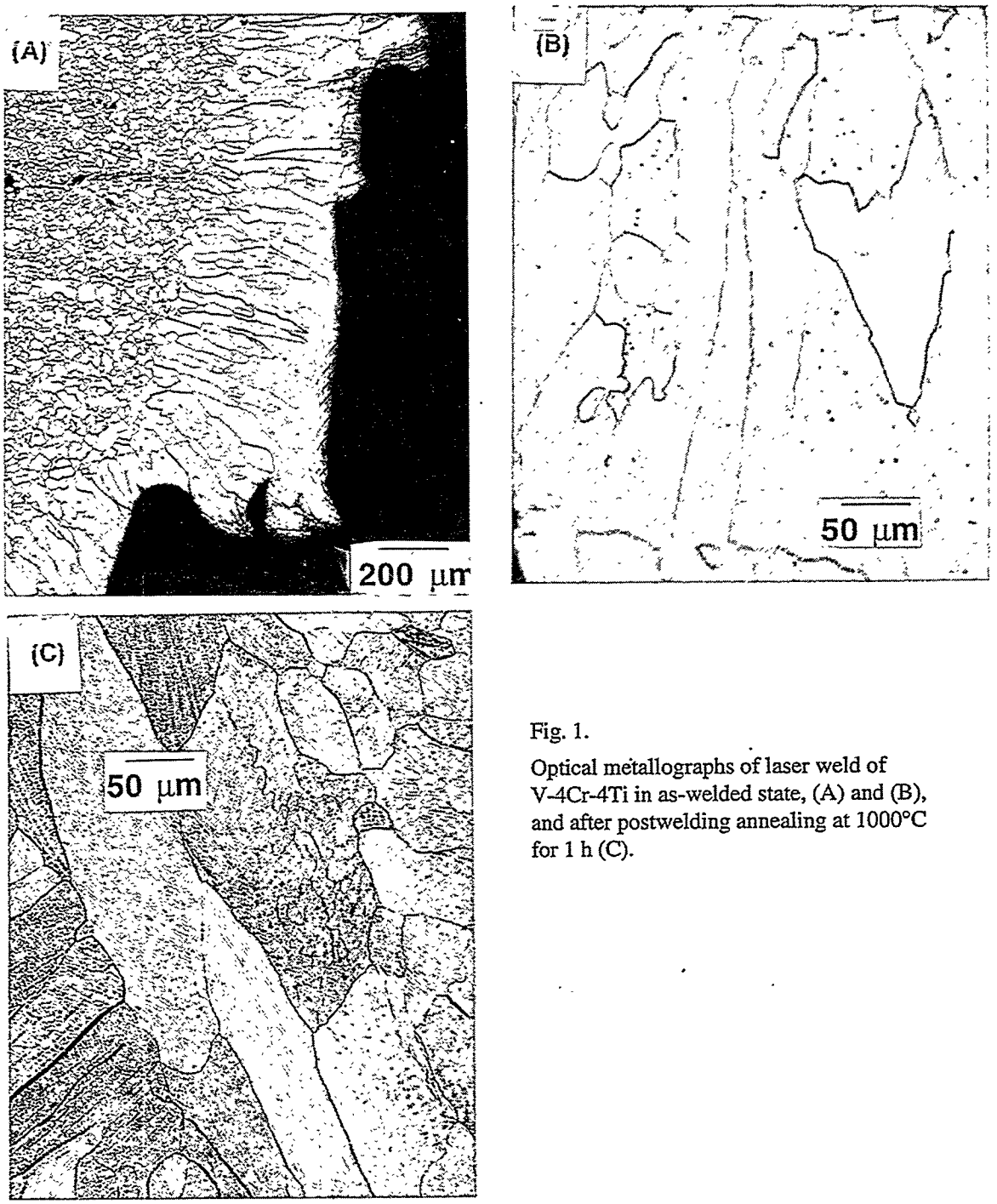

Fig. 1.
Optical metallographs of laser weld of V-4Cr-4Ti in as-welded state, (A) and (B), and after postwelding annealing at 1000°C for 1 h (C).

as-welded material, Fig. 1(B). In EB welds, early-stage development of the similar fine substructure was observed even in as-welded material, Fig. 2(B). In the postwelding-annealed material, the substructure appears to have developed into an advanced stage, Fig. 2(C). Thus, identification of this fine substructure seems to be the key to understanding the mechanism of toughness improvement following the PWHT.

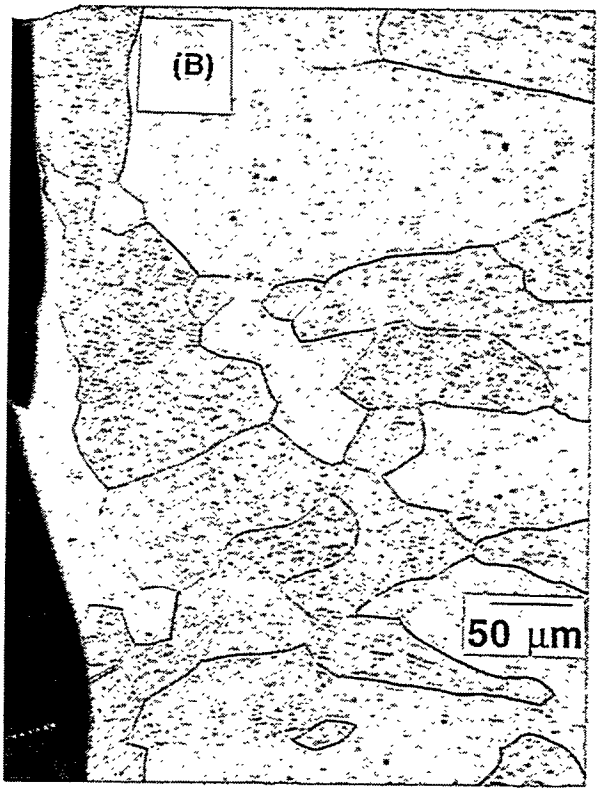

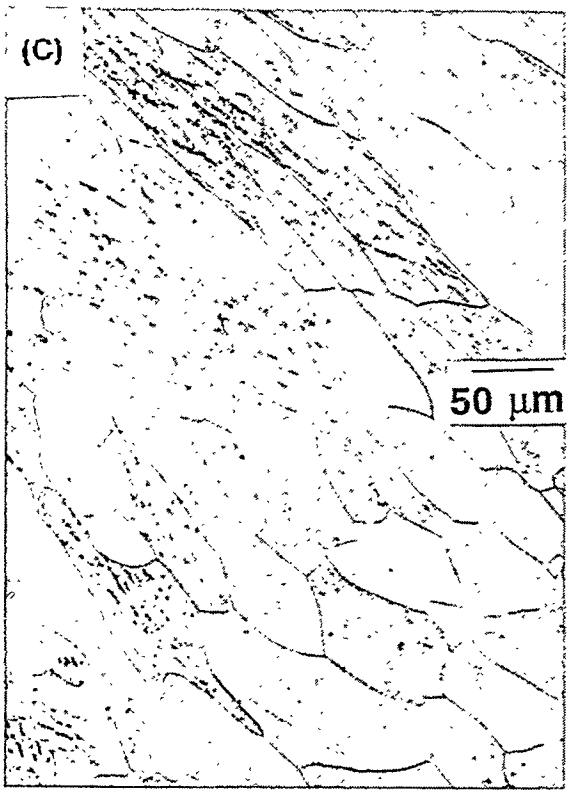

Fig. 2.

Optical metallographs of EB weld of V-4Cr-4Ti in as-welded state, (A) and (B), and after postwelding annealing at 1000°C for 1 h (C).

Chemical Analysis

Concentrations of O, C, and N were analyzed in EB welds. Three specimens of base metal and three specimens of EB weld were analyzed. These concentrations were compared in Table 1 with those measured on an extruded plate (64 mm thick) and a rolled base-metal plate (3.8 mm thick). The base-metal plate was annealed in the factory at ≈1050°C for 2 h and subsequently used in the present welding. Compared to the composition of the rolled and annealed base–metal plate, increase in O, N, and C in the EB welds was insignificant. Therefore, contamination by O, N, and C in the EB and laser welds appears to be at best a secondary factor in the large shifts in the ductile-brittle transition temperature (DBTT) before and after welding.[1]

Table 1. Impurity concentration (in wppm) in 500-kg V-4Cr-4Ti Heat #832665 after extrusion, rolling and annealing, and electron-beam welding

	O		N		C	
Material	reading	average	reading	average	reading	average
Extruded plate	310	310	85	85	80	80
Rolled Plate	450, 480, 467	466	25, 28, 30	27	300, 230, 240	257
EB weld	510, 520, 520	517	30, 25, 29	28	240, 270, 240	250

X-Ray Diffraction Analysis

Tetragonal distortion was suspected initially in the crystallographic structure of the elongated grains in the fast-cooled weld fusion zone, which was thought to be associated with the high DBTT. However, X-ray diffraction analysis showed no evidence of tetragonal distortion; only the diffraction peaks that correspond to the bcc structure of vanadium were present, i.e., (110), (200), (211), (220), and (310). However, the lattice constant of the weld fusion zone was found to be ≈0.13% larger than that of the base metal, i.e., 0.30315 vs. 0.30275 nm, respectively. These lattice constants were used to index the TEM diffraction patterns (see below).

TEM Analysis

As-welded microstructures of laser and EB welds were characterized by dense dislocations as shown in Fig. 3. Ti(O,N,C) precipitates normally present in extruded, rolled, and annealed plates were conspicuously absent, showing that they had dissolved in the grain matrices during welding. Reprecipitation of Ti(O,N,C) during cool-down of the weld fusion zone was negligible.

Postwelding-annealed laser and EB welds were characterized by an extensive network of precipitates that were not observed in the base metals of any vanadium alloys investigated in this program. Examples of the network precipitate structures are shown in Figs. 4 and 5, for laser and EB welds, respectively. Individual precipitates were typically rodlike in shape, 200-500 nm in length, and ≈50-100 nm in diameter. The rodlike morphology indicates immediately that the precipitates are not Ti(O,N,C), which is usually spherical or ellipsoidal and 300-500 nm in diameter. Dark-field morphologies shown in Figs. 3(B) and 4(B) indicate that the precipitates in the laser and EB welds are of the same type.

To obtain a clue as to the nature of the precipitates, selected precipitates were analyzed by energy-dispersive spectroscopy (EDS). A few precipitates located at the edge of the of the hole of the perforated TEM foil were analyzed. The measured EDS spectrum, therefore, consisted of X-rays that originated predominantly from the precipitate, while X-rays from the alloy matrix were negligible. Results of the EDS analysis of the precipitate and alloy matrix, given in Table 2, show that the precipitate is a vanadium-base phase rich in C and O.

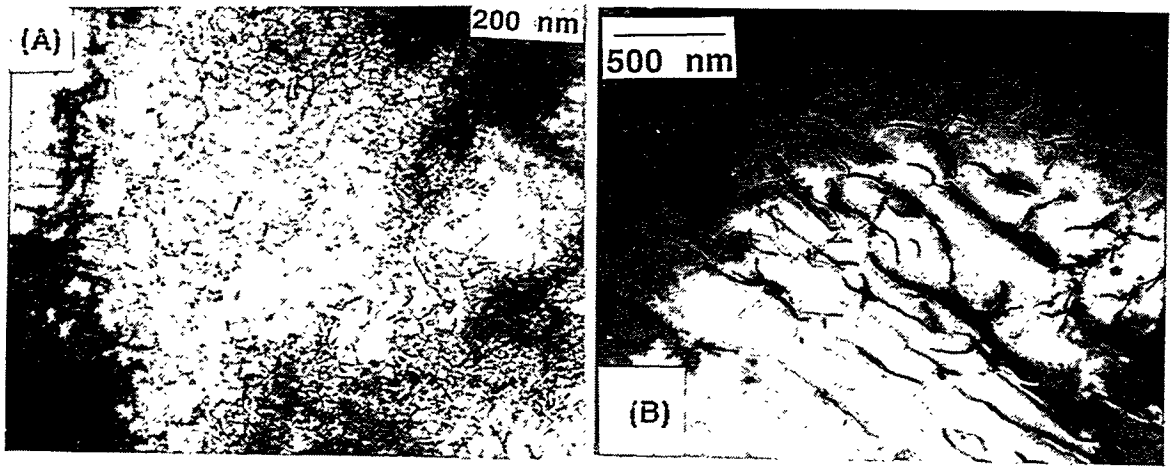

Fig. 3 TEM bright-field micrographs of laser (A) and EB (B) welds of V-4Cr-4Ti before post-weld anneling. Note dense dislocations and absence of the normal Ti (O, N, C) precipitates.

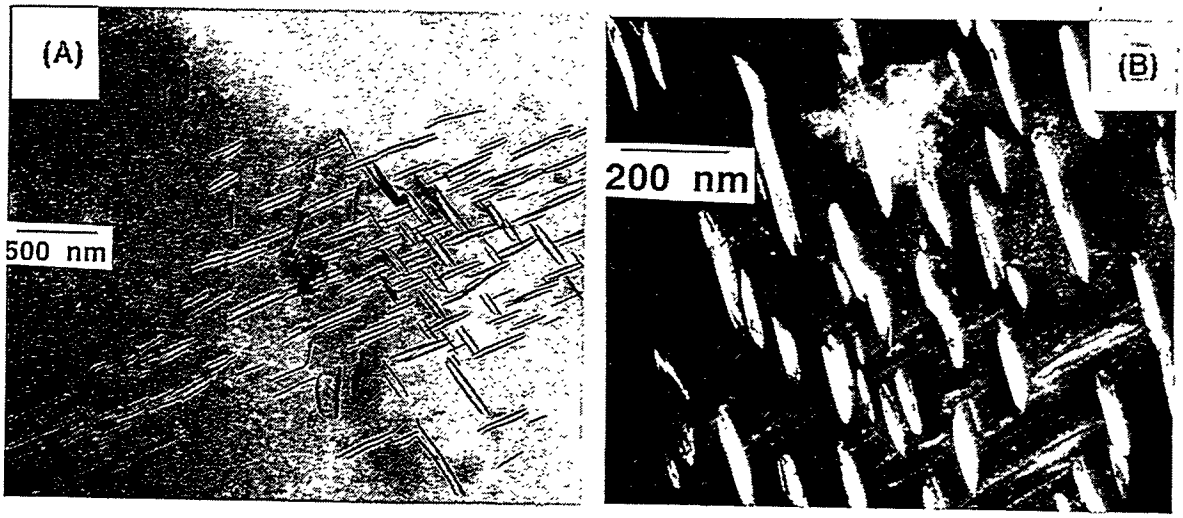

Fig. 4. Bright- (A) and dark-field (B) photomicrographs of laser weld fusion zone of V–4Cr–4Ti after postwelding annealing at 1000°C for 1 h. Note dense precipitate substructure and absence of dislocations and Ti(O,N,C).

Table 2. Summary of EDS analysis of the composition (at.%) of the characteristic precipitates in the laser weld fusion zone after postwelding annealing at 1000°C for 1 h in vacuum

	V	Ti	Cr	C	O
Matrix	92.55	3.68	3.77	-	-
Precipitate	16.72	5.94	0.76	66.99	9.59

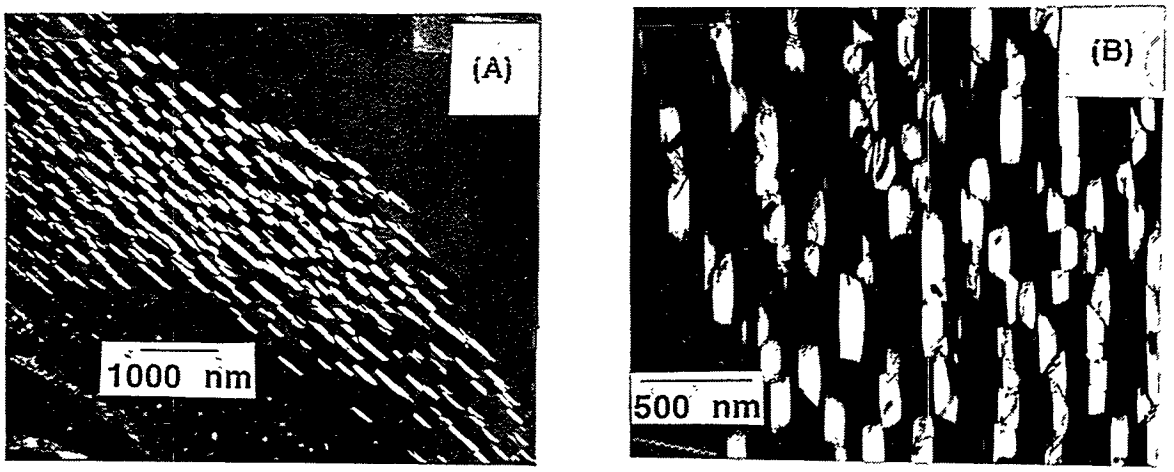

Fig. 5. Dark-field (B) micrographs of precipitates in EB weld fusion zone of V-4Cr-4Ti after postwelding annealing at 1000°C for 1 h.

However, exact compositions of C and O in this type of analysis must be considered as only qualitative, because contamination of C from the TEM vacuum chamber and hydrocarbon thinning solution is possible. Furthermore, accurate determination of C and O by EDS is complicated because the weak K lines of C and O nearly overlap the L lines of V and Ti. Therefore, exact identification of the precipitate phase must be verified by a more precise analysis through dark–field imaging and indexing selected-area diffraction patterns.

Systematic analysis by dark-field imaging and selected-area-diffraction (SAD) showed that the characteristic precipitates are V(C, O, N), which is an fcc phase with a lattice constant of 0.419 nm. An example of the indexed diffraction patterns is shown in Fig. 6. In this pattern, one zone axis of vanadium and two zone axes of V(C, O, N) phase are operating. Indexed diffraction patterns obtained from the laser and EB welds showed that the precipitates formed in the two types of welds are the same V(C,O,N) phase.

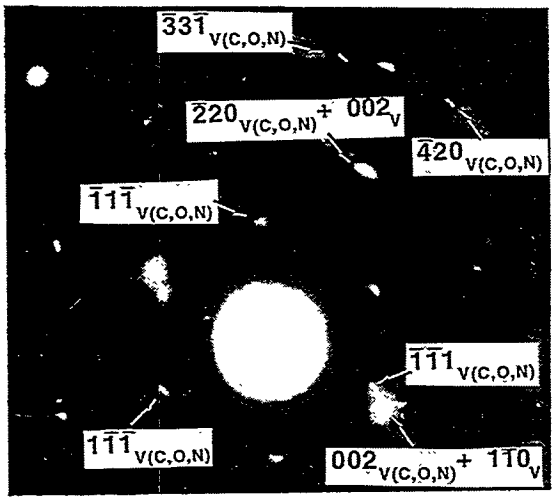

Fig. 6.

Indexed selected area diffraction pattern of laser weld fusion zone of V~4Cr–4Ti postwelding-annealed at 1000°C for 1 h.

DISCUSSION

VC (lattice constant 0.417 nm), VO (0.409 nm), and VN (0.413 nm) phases are isostructural (fcc, Na–Cl type) and have similar lattice constants[2] and high miscibility with one another.[3] This is similar to the

characteristics of TiC, TiO, and TiN, which are also isostructural fcc with similar lattice constants and high miscibility. Therefore, as for Ti(C,O,N), the vanadium-base precipitates characteristically contained in the postwelding-annealed welds are believed to be in the chemical form of V(C,O,N), with variable proportions of C, O, and N in the precipitate. For the precipitate analyzed in Table 2, N content was negligible. The substructures observed in the low-magnification optical photomicrographs of Figs. 1 and 2 are indeed the same as the precipitate network shown in the high-magnification TEM photomicrographs of Figs. 4 and 5.

Vanadium-base precipitates have been observed only rarely in V-Ti or V-Cr-Ti alloys.[4–6] In the Ti-containing binary or ternary alloys, observed precipitates are usually Ti-based phases, such as titanium oxycarbonitrides, titanium sulfides, or titanium phosphides.[4] Vanadium–base precipitates were observed only in alloys containing high levels of unusual impurities such as Cl, Ca, and Li, i.e., vanadium oxychlorides in V-5Cr-5Ti, which was melted with low-quality sponge Ti[5] and Ca-vanadate in unalloyed vanadium produced by the calcia-reduction process.[5] In an irradiated V-20Ti alloy rich in boron, Li-vanadate was also observed.[6]

As pointed out previously, from the thermodynamic standpoint, the precipitation of vanmadium oxychlorides or Ca-vanadates seems to be preferred over precipitation of Ti-based precipitates in Cl- or Ca-rich alloys containing a certain level of oxygen. Precipitation of V(C,O,N) seems to be preferred over precipitation of Ti(C,O,N) in a metastable structure such as the weld fusion zone. A laser or EB weld fusion zone contains dense dislocations and higher levels of O, N, and C as interstitial solutes in the grain matrices following dissolution of Ti(O,N,C) during melting. It appears that a dense dislocation structure plays an essential role in the precipitation of V(C,O,N) in the welds. The network-like distribution of clusters of the V(C,O,N) precipitates shown in Figs. 4 and 5 seems to support this premise.

Under the same annealing condition at 1000°C for 1 h in high vacuum, V(C,O,N) precipitates were not observed in the factory-annealed base metal, which is relatively free of dislocations and contains the normal Ti(O,N,C) precipitates. This seems to be additional evidence that high-density dislocations play an important role in the precipitation of (V(C,N,O) in the welds during postwelding-annealing.

It seems evident that the drastic improvement in impact toughness is a result of the simultaneous process of profuse formation of V(C,O,N) precipitates and annealing-out of the dense dislocations that occurs in the weld zone during the postwelding annealing. The combined process seems to make grain matrices that are very low in O, C, and N and virtually free of dislocations and residual stress. Crack propagation through this type of microstructure would then be very difficult, which leads to excellent impact toughness.

The precipitation kinetics of V(C,O,N) in the metastable structure of laser welds are believed to be strongly influenced by annealing temperature. Therefore, identification of the temperature of fastest precipitation kinetics in the time-temperature-transformation (TTT) curve will be important. This temperature is probably significantly higher than 1000°C, and the kinetics at that temperature seem to be fast. This can be deduced from the observation of the early-stage development of the precipitate network in EB welds even without postwelding annealing, Fig. 2(B). A controlled cooling of a laser weld would then be an attractive idea, in which the weld structure remains at the temperature of maximum precipitation kinetics for a reasonable period of time under reasonably practical conditions.

CONCLUSIONS

1. Postwelding–annealed welds were characterized by extensive formation of networks of fine V(C,O,N) precipitates. This process occurs with simultaneous annealing-out of the dense dislocations present in the metastable weld fusion.

2. The drastic improvement in impact toughness is a result of this simultaneous process, which occurs in the weld fusion zone during the postwelding annealing at 1000°C for 1 h. The combined process seems to make grain matrices that are very low in O, C, and N and virtutally free of dislocations and residual stress. Resistance to crack propagation through the grains of this type of microstructure seems to be high, and as a result, excellent impact toughness is produced.

3. The precipitation kinetics of V(C,O,N) in the metastable structure of laser welds are predicted to be strongly influenced by annealing temperature, and hence by cooling history. Therefore, it seems possible to produce high–quality welds under practical conditions by controlling and adjusting the cooling rate of the weld fusion zone through some innovative method to maximize the precipitation of V(C,O,N).

ACKNOWLEDGMENT

The authors thank R. V. Strain and H.–C. Tsai for suppy of a laser weld specimen and K. Fukumoto for preparation and initial examination of TEM specimens from the laser weld.

REFERENCES

1. H. M. Chung, R. V. Strain, H.–C. Tsai, J.–H. Park, and D. L. Smith, "Impact Properties and Hardening Behavior of Laser and Electron–Beam Welds of V–4Cr–4Ti," in this report.

2. M. Hansen, Constitution of Binary Alloys, 2nd Ed., McGraw–Hill, New York, 1958.

3. C. K. Gupta and N. Krishnamurthy, Extractive Metallurgy of Vanadium, Elsevier, Amsterdam, 1992.

4. H. M. Chung, B. A. Loomis, and D. L. Smith, in Effects of Radiation in Metals: 16th Intl. Symp., ASTM STP 1175, D. S. Gelles, R. K. Nanstad, and T. A. Little, eds., American Society for Testing and Materials, Philadelphia, 1993, pp. 1185–1120.

5. H. M. Chung, J. Gazda, L. J. Nowicki, J. E. Sanecki, and D. L. Smith, in USDOE Fusion Reactor Materials Semiannual Report, DOE/ER–0313/15, 1994, pp. 207–218.

6. H. M. Chung, B. A. Loomis, D. L. Smith, J. Nucl. Mater. 212–215 1994), pp. 804–812.

EVALUATION OF FLOW PROPERTIES IN THE WELDMENTS OF VANADIUM ALLOYS USING A NOVEL INDENTATION TECHNIQUE — A. N. Gubbi, A. F. Rowcliffe, E. H. Lee, J. F. King, and G. M. Goodwin (Oak Ridge National Laboratory)

OBJECTIVE

The aim of this work is to evaluate the flow properties of the fusion zone, heat affected zone, and base metal of gas tungsten arc and electron beam welds on V-Cr-Ti alloys

SUMMARY

Automated Ball Indentation (ABI) testing, was successfully employed to determine the flow properties of the fusion zone, heat affected zone (HAZ), and base metal of the gas tungsten arc (GTA) and electron beam (EB) welds of the V-4Cr-4Ti (large heat no. 832665) and the V-5Cr-5Ti (heat 832394) alloys. ABI test results showed a clear distinction among the properties of the fusion zone, HAZ, and base metal in both GTA and EB welds of the two alloys. GTA and EB welds of both V-4Cr-4Ti and V-5Cr-5Ti alloys show strengthening of both the fusion zone and the HAZ (compared to base metal) with the fusion zone having higher strength than the HAZ. These data correlate well with the Brinell hardness. On the other hand, GTA welds of both alloys, after a post–weld heat treatment of 950°C for 2 h, show a recovery of the properties to base metal values with V-5Cr-5Ti showing a higher degree of recovery compared to V-4Cr-4Ti. These measurements correlate with the reported recovery of the Charpy impact properties.[1,2]

INTRODUCTION

In ABI tests, a spherical indenter makes sequential indentation cycles with increasing loads at the same penetration spot on a polished horizontal metallic surface under suitable strain-controlled conditions, the details of which are given elsewhere.[3] The depth-penetration measurements with successively increasing loads are converted to the load-displacement data for each unloading sequence, which in turn, are analyzed by the data processing software program in the computerized ABI test system to determine the values of mechanical properties such as yield strength, true–stress/true–plastic strain curve, and Brinell hardness number (BHN), with proper input values of materials constants. The mechanical properties of the base metal, HAZ, and fusion zone have been measured by Haggag and Bell[4] from the resistance spot welds of 1020 ferritic steel and 2219 aluminum sheets using the ABI technique. In 1020 steel, there was an increase in strength of the weld zone and HAZ relative to the base metal due to martensite or bainite formation. On the other hand, in 2219 aluminum, the strength of the weld zone and HAZ relative to the base metal dropped due to dissolution of precipitates. In another study by Byun et al[5], the ABI test was sensitive enough to identify the local variation in material property in determining the mechanical properties of SA508C1.3 Reactor Pressure Vessel (RPV) steels. Farrell and co-workers[6] have tried to correlate the tensile properties obtained from the uniaxial tensile tests with those determined by the ABI tests on ferritic alloys and found that the two results agree reasonably well; one could evaluate the tensile properties from the ABI technique with a proper selection of material parameters used in the analysis of the results. A comparison of the tensile data derived from instrumented hardness testing with those from conventional tensile tests has been made for various alloys including aluminum, brass and stainless steel.[7]

Vanadium alloys with Cr and Ti contents ranging from 3 to 6 wt.% have been proposed as possible candidate materials for the first wall/blanket structure in a demonstration reactor.[8-11] Welding research, being carried out on vanadium alloys at Oak Ridge National Laboratory, has concentrated primarily on optimizing the parameters for obtaining GTA and EB welds with suitable mechanical properties. To supplement the welding research, an attempt has been made in the present work to characterize the variation in the mechanical properties of the fusion zone, HAZ and base metal of both GTA and EB welds in a non-

destructive manner using an indentation technique. These data are extremely difficult to obtain using conventional tensile tests. A microprobe system, which is based on an automated ball indentation (ABI) technique, has been used to determine mechanical properties such as true stress–true plastic strain curve, yield strength, and Brinell hardness number.

EXPERIMENTAL PROCEDURE

Both GTA and EB welds were made on ~7mm–thick plates of the vanadium alloy with a nominal composition of 4 wt.% each of Cr and Ti and the rest vanadium, designated V-4Cr-4Ti (heat 832665) and the vanadium alloy with a nominal composition of 5 wt.% each of Cr and Ti and the rest vanadium (heat 832394, ANL designation BL63). The plates of both V-4Cr-4Ti and V-5Cr-5Ti used for GTA welding were in an annealed state with a fully recrystallized microstructure after a heat treatment of 1050°C for 2 h by the supplier (Teledyne Wah Chang, Albany, Oregon) whereas the plate of V-4Cr-4Ti used for EB welding was in warm–worked state. The details regarding the welding conditions used in both GTA and EB welds are given elsewhere.[1] Metallography samples from the GTA welds in as–welded and post–weld heat treated (vacuum-anneal of 950°C for 2 h) conditions, and EB welds in as–welded condition were mounted in bakelite (a hard material which eliminates the contribution from the compliance of the sample mounting material to ABI test results). The mounted specimens were polished and etched to reveal weld microstructure so that one could clearly distinguish the fusion zone, HAZ, and base metal.

Automated Ball Indentation Test:

The automated ball indentation tests were conducted on the fusion zone, HAZ, and base metal of each specimen by employing a fully computerized ABI system[12] using a tungsten carbide spherical indenter of 0.254 mm dia at a strain rate of ~8 x 10^{-3}/s. The indentation load and depth were monitored by a sensitive load cell and a linear variable displacement transducer (LVDT), respectively, which were fedback to the computer. Figure 1 shows a typical load vs. indentation depth curve from the base metal region of the post-weld heat treated GTA weld of V-4Cr-4Ti. Each ABI test consists of seven load-unload sequences, and the computer software carries out a regression analysis of the partial elastic unloading of each sequence. The plastic indentation depth for each load–unload cycle is determined by extrapolating the calculated line to the zero load. This plastic depth for each load–unload cycle is used in obtaining the true stress and true plastic strain. Values of yield strength and BHN were also estimated and included by the computer in the results.

The detailed procedure followed in the analysis of ABI test data is given elsewhere.[3] A brief description of the various equations and steps involved are given here. In an ABI test both inhomogeneous (Lüders) and homogeneous (work hardening) material behavior occur simultaneously during the test. Using the values of indentation load and indentation depth obtained from the ABI test, flow stress and strain are determined by the computer program based on elastic and plastic theories. For each loading cycle in the ABI test, the total indentation diameter d_t is calculated from the total indentation depth h_t using the relationship

$$d_t = 2\sqrt{h_t D - h_t^2} \qquad (1)$$

The true plastic strain ε_p and true stress σ_t are given by

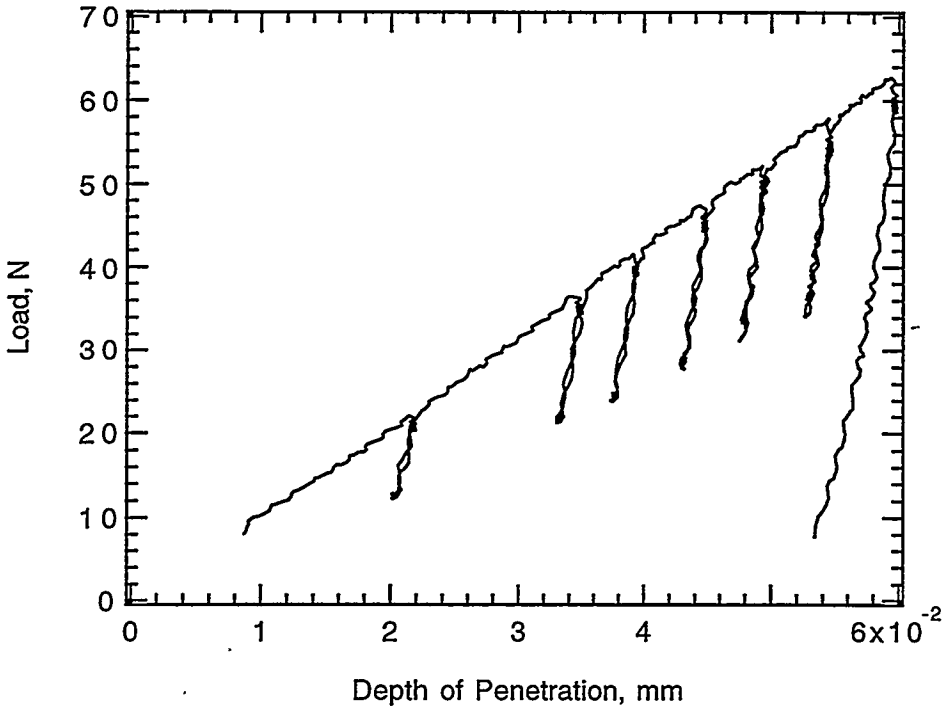

Figure 1. A typical plot of load as a function of depth of penetration of indenter from the base metal region of the post–weld heat treated V-4Cr-4Ti GTA weld.

$$\varepsilon_p = 0.2\frac{d_p}{D} \tag{2}$$

and

$$\sigma_t = \frac{4P}{\pi d_p^2 \delta} \tag{3}$$

where d_p is the plastic chordal indentation diameter, D is the indenter diameter, P is the indentation load, and δ is a function of the plastic zone development beneath the indenter and is given by 2.87α. Here α is known as constraint factor whose value is proportional to the strain rate sensitivity of the test material. For vanadium, it was assumed as 1.15. The plastic indentation diameter d_p is obtained iteratively by a complex equation[3], and the derived true stress–true plastic strain data are fitted to the well–known power law equation

$$\sigma_t = K\varepsilon_p^n \tag{4}$$

where n is the strain hardening exponent, and the K is the strength coefficient. The values of n and K determined from the fit are a part of ABI test results.

Determination of 0.2% yield strength is not straight forward as one cannot simply extrapolate the true stress–true plastic strain data due to the fact that strain hardening exponent could be different at strain as low as 0.2% compared to higher strains. The computer program of the ABI test system performs a linear regression analysis to ABI data points from all loading cycles to fit Meyer's law and obtains material yield parameter A . Meyer's law is given by

$$\frac{P}{d_t^2} = A\left[\frac{d_t}{D}\right]^{m-2} \qquad (5)$$

where m is Meyer's coefficient and A is the stress at $[d_t/D]$ equals unity. Figure 2 shows a representative plot where $[P/d_t^2]$ is plotted as a function of $[d_t/D]$ and the material yield parameter A determined from the extrapolated linear regression fit. The yield strength σ_y is then calculated by using the relationship

$$\sigma_y = \Omega A \qquad (6)$$

where Ω is another material constant (for vanadium alloys it was taken as 0.25).

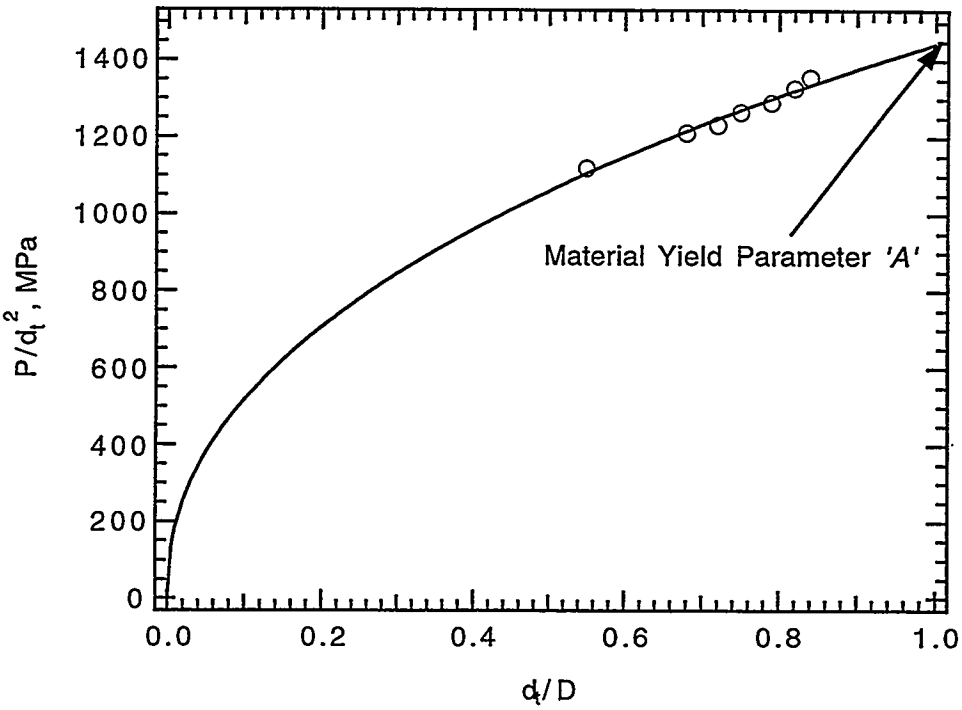

Figure 2. A typical plot of $[P/d_t^2]$ as a function of $[d_t/D]$ from the base metal region of the post–weld heat treated V-4Cr-4Ti GTA weld showing the calulation of material yield parameter A..

RESULTS AND DISCUSSION

GAS TUNGSTEN ARC WELDS

Table 1 lists the mechanical property parameters obtained from the ABI test results on the GTA and EB welds of V-4Cr-4Ti (Heat 832665). ABI tests were done at two different locations in each region of the post–weld heat treated GTA weld to examine the repetitiveness of the test and the results are included in

Table 1. Parameters of Mechanical Properties obtained from ABI test results on Welds of V-4Cr-4Ti (Heat 832665)

WELD MATERIAL	YIELD STRENGTH (MPa)	Strength Coeff. K (MPa)	BHN (kg/sq.mm)	Strain Hardening Exponent (n)
GTA As-Welded				
Base Metal	360	604	132	0.083
Heat Affected Zone	424	719	159	0.084
Fusion Zone	445	761	167	0.086
PWHT 2h/950°C				
Base Metal 1	383	636	143	0.082
Base Metal 2	365	642	139	0.090
Heat Affected Zone 1	373	665	140	0.091
Heat Affected Zone 2	402	649	146	0.077
Fusion Zone 1	407	686	150	0.083
Fusion Zone 2	410	686	152	0.082
EB As-Welded				
Base Metal	489.5	842	183	0.087
Heat Affected Zone	418.5	684	151	0.079
Fusion Zone	430.9	719	158	0.082

Table 1. It can be seen that the mechanical properties evaluated from different locations in the same region are similar (except for HAZ, may be due to some microstructural change), which shows the consistency in results of ABI testing for the same region. Figure 3 shows typical true stress–true plastic strain curves, derived from ABI test analyses, from the fusion zone, HAZ and base metal of the as–welded GTA weld on V-4Cr-4Ti. The numbers in parentheses in Fig. 3 are the Brinell hardness values and it can be seen that the HAZ and fusion zone are at least 20% harder than the base metal, with the fusion zone being the hardest. Also, the calculated yield strengths for the HAZ and fusion zone are ~18 and 24% higher, respectively, than that for the base metal.

Similarly, Figure 4 exhibits typical true stress–true plastic strain curves from the fusion zone, HAZ, and base metal of the GTA weld on V-4Cr-4Ti after a post–weld anneal of 950°C for 2 h. The dashed line in Fig. 4 shows the flow curve obtained from a second location of the base metal which is very similar to that obtained from the first location. This shows consistency in ABI test results for the same region. The GTA weld after 950°C–anneal shows a recovery in the hardness of the fusion zone and HAZ but still 10%

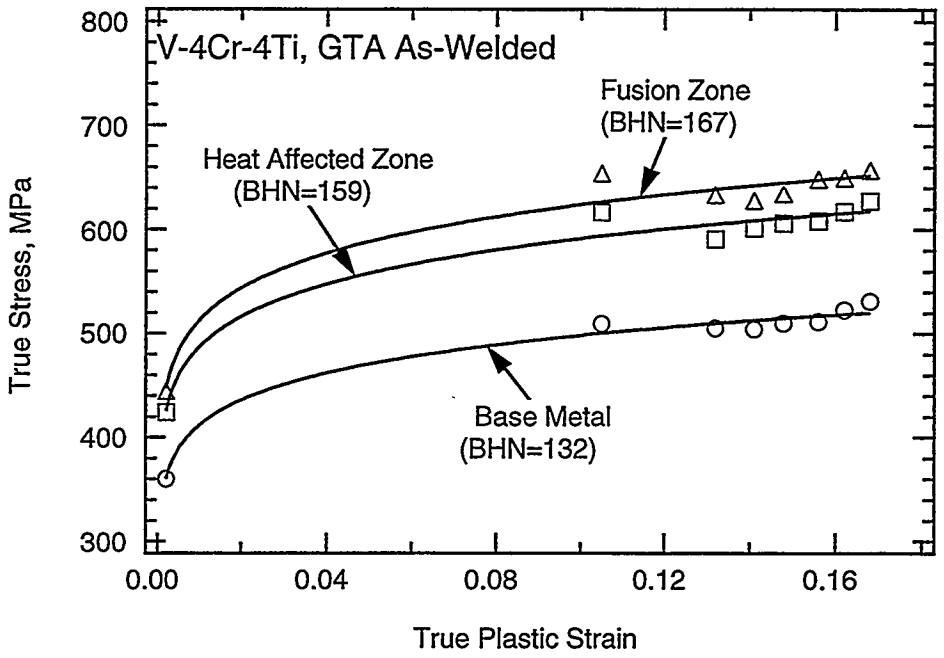

Figure 3. True stress–true plastic strain curves from the fusion zone, HAZ, and base metal of the as–welded V-4Cr-4Ti GTA weld.

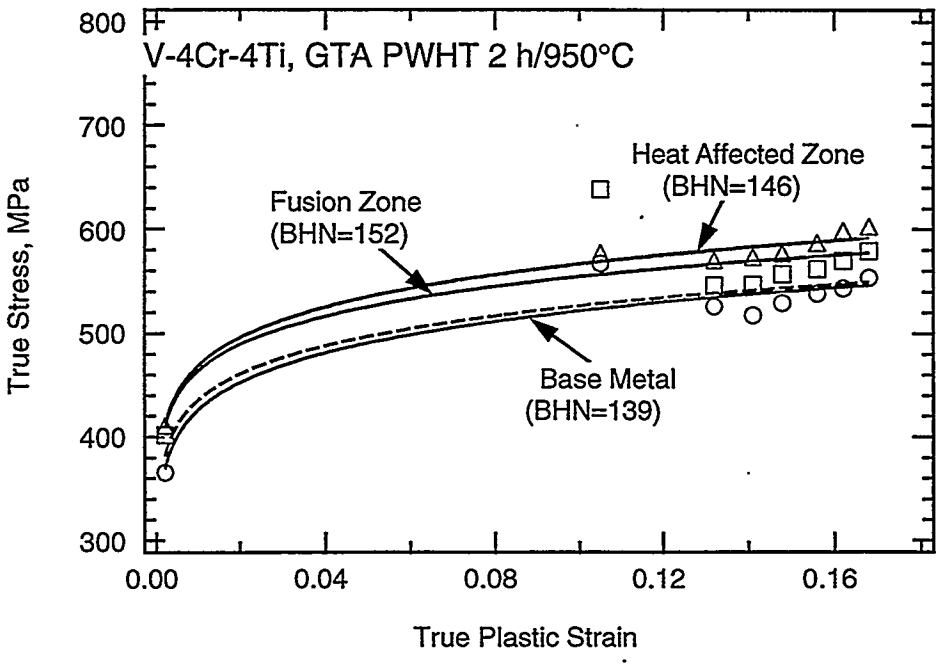

Figure 4. True stress–true plastic strain curves from the fusion zone, HAZ, and base metal of the post–weld heat treated (at 950°C for 2 h) V-4Cr-4Ti GTA weld.

or more higher than that of the base metal. The yield strength also drops for the two zones but both zones are still stronger than the base metal by as much as 10%. This recovery of mechanical properties observed in ABI tests correlates well with the results from impact properties[2] obtained by the testing of sub–size Charpy specimens of the GTA welds and the base metal. The base metal of V-4Cr-4Ti exhibited a DBTT of around –190°C whereas the as–welded GTA weld showed a much higher DBTT of ~+250°C. But, after a post–weld heat treatment of 950°C for 2 h, the DBTT dropped to +75°C, which is still higher than that for the base metal.

The key parameters of the mechanical properties delivered by the ABI test results on the GTA and EB welds of V-5Cr-5Ti (Heat 832394) are tabulated in Table 2. The true stress–true plastic strain curves, obtained from the ABI analyses, from the fusion zone, HAZ, and base metal of the GTA weld on V-5Cr-5Ti in as–welded condition are plotted in Figure 5. Similar to the observations made for the as–welded GTA weld of V-4Cr-4Ti, here also it is clear that the curves for the HAZ and fusion zone are higher than that for the base metal of V-5Cr-5Ti. From the Brinell hardness numbers given in parentheses, the HAZ and fusion zone are harder by 7% and 16%, respectively, than the base metal. In the same token, the calculated yield strengths for the HAZ and fusion zone are higher than that for the base metal by 8 and 16%, respectively.

Table 2. Parameters of Mechanical Properties obtained from ABI test results on Welds of V-5Cr-5Ti (Heat 832394)

WELD MATERIAL	YIELD STRENGTH (MPa)	Strength Coeff. K (MPa)	BHN (kg/sq.mm)	Strain Hardening Exponent (n)
GTA As-Welded				
Base Metal	430	746	159	0.089
Heat Affected Zone	465	783	170	0.084
Fusion Zone	499	835	185	0.083
PWHT 2h/950°C				
Base Metal	381	674	143	0.092
Heat Affected Zone	387	666	147	0.087
Fusion Zone	403	693	151	0.088
EB As-Welded				
Base Metal	405	690	153	0.086
Heat Affected Zone	472	794	177	0.084
Fusion Zone	470	778	175	0.082

Figure 6 is a composite plot comprising the true stress–true plastic strain curves from the fusion zone, HAZ and base metal of the GTA weld on V-5Cr-5Ti after a post–weld heat treatment of 950°C for 2 h. A nearly complete recovery in the hardness values and yield strengths of the HAZ and fusion zone to the base metal values is observed. Also, the stress–strain curves of the HAZ and base metal overlap each other and the curve for the fusion zone approaches that of the other two regions. This recovery of mechanical

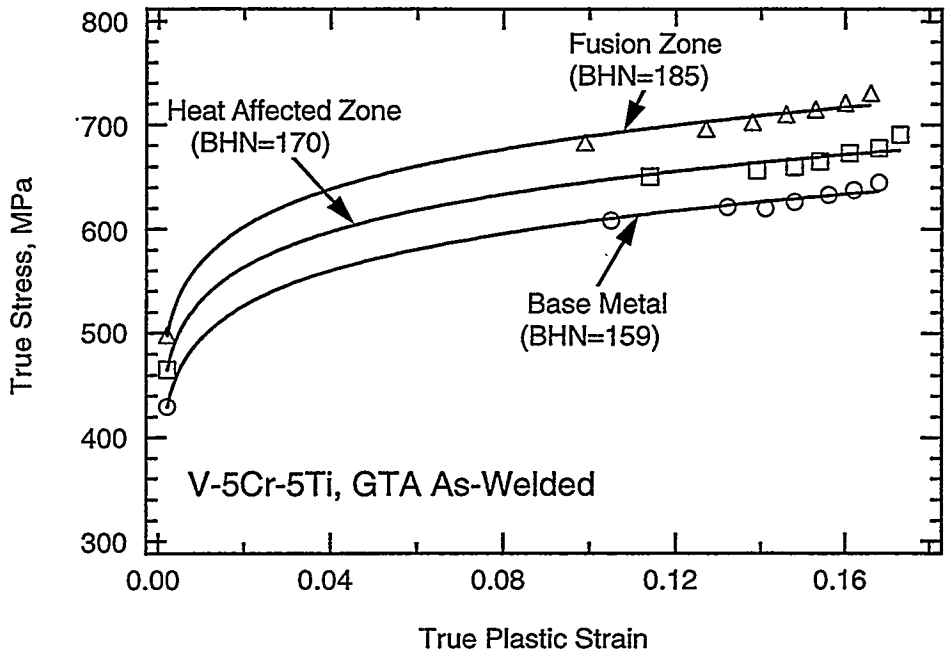

Figure 5. True stress–true plastic strain curves from the fusion zone, HAZ, and base metal of the as–welded V-5Cr-5Ti GTA weld.

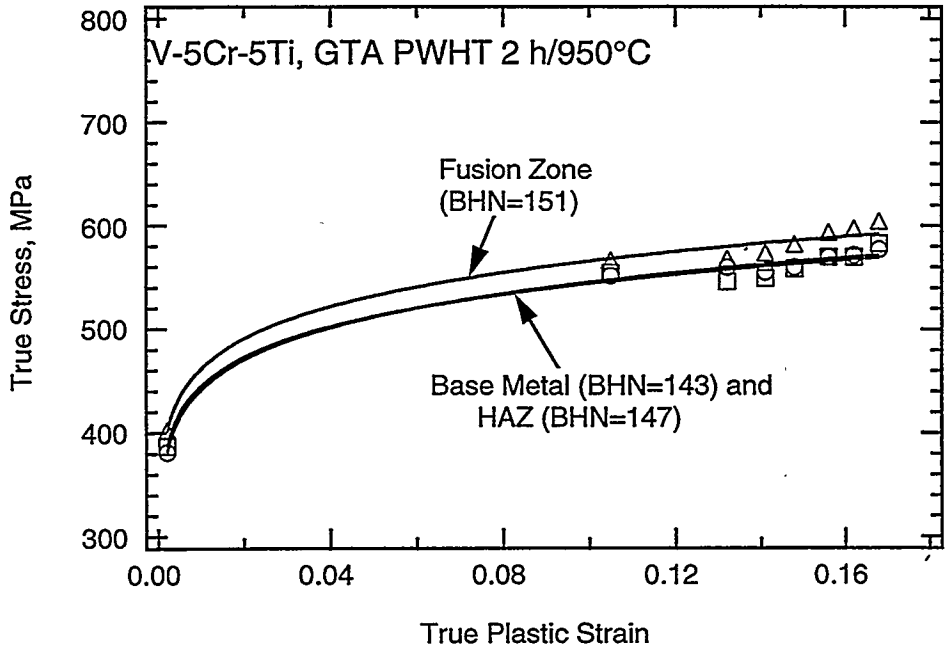

Figure 6. True stress–true plastic strain curves from the fusion zone, HAZ, and base metal of the post–weld heat treated (at 950°C for 2 h) V-5Cr-5Ti GTA weld.

properties observed in ABI analyses agrees very well with the impact properties[1] obtained by the testing of sub–size Charpy specimens of the GTA welds and the base metal of V-5Cr-5Ti. The DBTT for the as–welded GTA weld was determined to be around 250°C and a post–weld heat treatment of 950°C for 2 h reduced the DBTT to 0°C, which was below that (+75°C) for the base metal.

The much higher DBTT (compared to the base metal) obtained from the Charpy impact testing of the GTA welds in both V-4Cr-4Ti and V-5Cr-5Ti in as–welded condition is thought of primarily due to the oxygen in solution which was picked up during welding[2] in a dynamically evacuated glove box environment, and also from the dissolution of Ti (O, N, C) precipitates . An increase in strength (as well as the hardness) can be attributed to the combined effects of dissolved oxygen (resulting in solution–strengthening) and thermal stresses developed during weld solidification. The recovery in DBTT after 950°C–anneal in the two alloys is attributed to the precipitation of oxygen in the form of oxides.[2] This precipitation combined with the thermal stress relief due to annealing results in the softening of the fusion zone as well as the HAZ.

ELECTRON BEAM WELDS

Figure 7 depicts typical true stress–true plastic strain curves derived from ABI test analyses from the base metal, HAZ, and fusion zone of the EB weld on V-4Cr-4Ti. Here, the flow curve for the base metal region lies above the flow curves for the HAZ and fusion zone; in contrast, results from the GTA weld (which was done on a plate annealed at 1050°C for 2 h with a fully recrystallized microstructure) showed that the curve for the base metal was always lower than that for the HAZ and fusion zone, see Figs 3 and 4. This is not surprising as the plate used for EB welding was a warm–worked plate which had a deformed, elongated grain structure with the hardness higher than that for both HAZ and fusion zone, see numbers given in parentheses in Fig. 5. For comparison, the true stress–true plastic strain curve from the recrystallized base metal region of GTA weld has been shown in dashed lines in Fig. 5. Both HAZ and fusion zone exhibit similar yield strengths (see Table 1) with a slight difference in the flow curves.

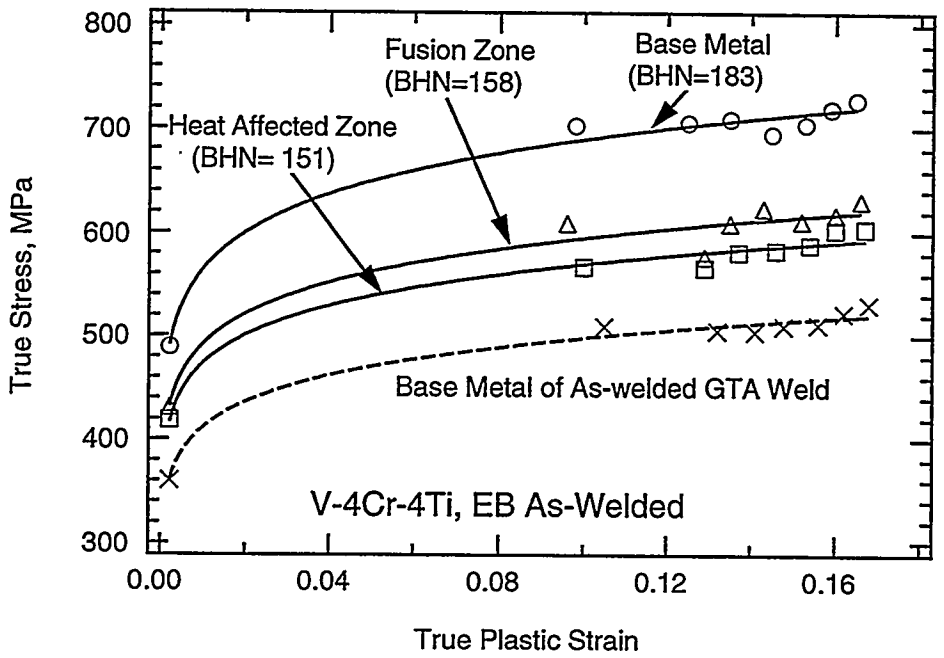

Figure 7. True stress–true plastic strain curves from the fusion zone, HAZ, and base metal of the EB weld of V-4Cr-4Ti.

A similar family of stress–strain curves for the EB weld on V-5Cr-5Ti is presented in Fig. 8. The HAZ and fusion zone show almost identical flow curves with their yield strengths being similar (see Table 2). Both regions are much stronger and harder (refer to Brinell hardness numbers in parentheses in Fig. 6) than the base metal region.

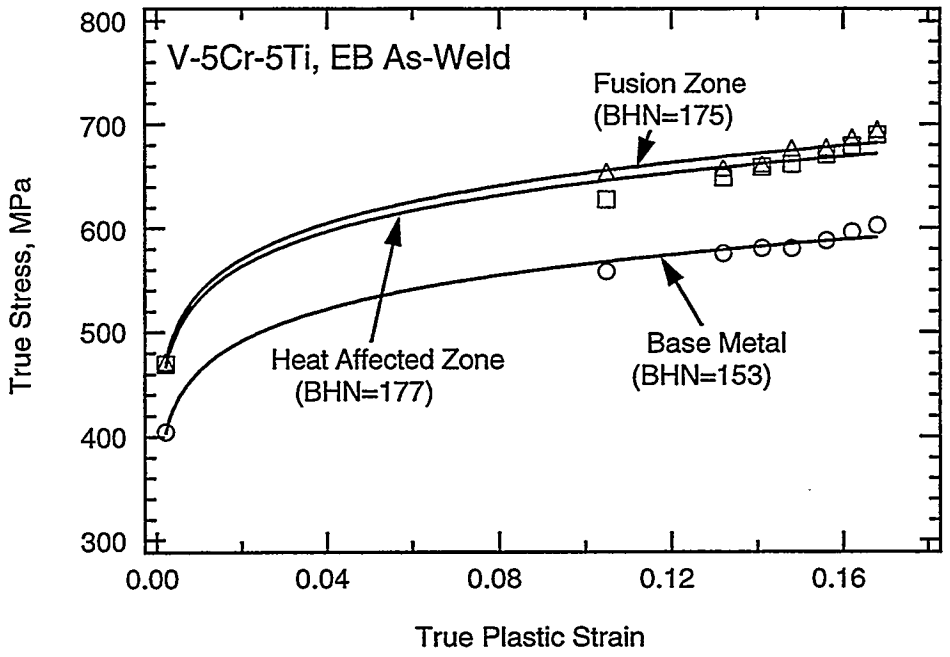

Figure 8. True stress–true plastic strain curves from the fusion zone, HAZ, and base metal of the EB weld of V-5Cr-5Ti.

Charpy impact testing of the sub–size specimens of EB weld on V-4Cr-4Ti showed a DBTT of –100°C (with DBTT for base metal being around –190°C)[2] and similar tests on EB weld of V-5Cr-5Ti showed no transition with predominantly ductile fracture mode and high values of absorbed energy (with DBTT for base metal being around +75°C)[1]. The lower DBTTs obtained for the EB welds compared to that for the as–welded GTA welds of the two alloys (inspite of the ABI results showing similar strengthening and hardening of the HAZ and fusion zone for the two weld processes) is probably due to much finer grain size[2] in the case of EB welds compared to that of GTA welds.

SUMMARY AND CONCLUSIONS

Automated ball indentation tests were successfully used to evaluate the gradients in the mechanical properties of the fusion zone, heat affected zone, and base metal from the GTA and EB welds on the large heats of the V-4Cr-4Ti (Heat 832665) and V-5Cr-5Ti (Heat 832394) alloys. The following observations were made from the investigation.

(1) Automated ball indentation tests were sensitive enough to distinguish the variations in the properties of the fusion zone, heat affected zone, and base metal in both GTA and EB welds of V-Cr-Ti alloys.

(2) The gas tungsten arc welds from the V-4Cr-4Ti and V-5Cr-5Ti alloys showed much stronger and harder heat affected zone and fusion zone compared to the base metal. A recovery in the mechanical properties of the two zones after a post–weld heat treatment at 950°C for 2 h agrees quite satisfactorily with the recovery observed in the Charpy impact properties in other studies.[1,2]

(3) The electron beam welds from the V-4Cr-4Ti and V-5Cr-5Ti alloys showed the mechanical properties of the heat affected zone and fusion zone to be significantly different from the base metal properties. The V-4Cr-4Ti alloy showed a higher stress–strain curve for the base metal due to it being a warm–worked plate whereas the V-5Cr-5Ti alloy exhibited much stronger and harder heat affected zone and fusion zone with both zones being almost similar in properties.

ACKNOWLEDGMENTS

This research is sponsored by the Office of Fusion Energy, U. S. Department of Energy, under contract DE-AC05-96OR22464 with Lockheed Martin Energy Research Corp. We thank Fahmy M. Haggag of Advanced Technology Corporation, Oak Ridge for his assistance in carrying out ABI tests. This research was supported in part by an appointment (ANG) to the Oak Ridge National Laboratory Postdoctoral Research Associates Program administered jointly by the Oak Ridge National Laboratory and the Oak Ridge Institute for Science and Education.

REFERENCES

[1] J. F. King, G. M. Goodwin, and D. J. Alexander, Fusion Reactor Materials Semiannual Progress Report, DOE/ER-0313/17, September 30, 1994, pp 152-155.

[2] J. F. King, G. M. Goodwin, D. J. Alexander, and M. L. Grossbeck, Unpublished research, Oak Ridge National Laboratory, 1996.

[3] F. M. Haggag, in *Small Specimen Test Techniques Applied to Nuclear Reactor Vessel Thermal Annealing and Plant Life Extension,* ASTM STP 1204, W. R. Corwin, F. M. Haggag, and W. L. Server, Eds., ASTM, Philadelphia, 1993, pp 27-44.

[4] F. M. Haggag and G. E. C. Bell, in *International Trends in Welding Sciences and Technology,* S. A. David and J. M Vitek, Eds., ASM, Metals Park, OH, 1993, pp 637-642.

[5] Thak–Sang Byun, F. M. Haggag, K. Farrell, and E. H. Lee, unpublished research, Oak Ridge National Laboratory, 1996.

[6] K. Farrell, S. T. Mahmood, H. Kurishita, K. L. Murty, and F. M. Haggag, unpublished research, Oak Ridge National Laboratory, 1996.

[7] P. Au, G. E. Lucas, J. W. Sheckherd, and G. R. Odette, in *Proc. of the Third Intl. Conf. on Nondestructive Evaluation in Nuclear Industry,* ASM, Metals Park, OH, (1980), pp 597-610.

[8] B. A. Loomis and D. L. Smith, J. Nucl. Matls., 179-181 (1991), pp 783-786.

[9] B. A. Loomis, D. L. Smith, and F. A Garner, J. Nucl. Matls., 179-181 (1991), pp 771-776.

[10] H. M. Chung and D. L. Smith, J. Nucl. Matls., 191-194 (1992), pp 942-947.

[11] B. A. Loomis, L. J. Nowicki, J. Gazda, and D. L. Smith, Fusion Reactor Materials Semiannual Progress Report, DOE/ER-0313/14, March 31, 1993, pp 318-325.

[12] F. M. Haggag, Advanced Technology Corp., Oak Ridge, TN.

PROPERTIES OF V–(8–9)Cr–(5–6)Ti ALLOYS IRRADIATED IN THE DYNAMIC HELIUM CHARGING EXPERIMENT*

H. M. Chung, L. Nowicki, and D. L. Smith
(Argonne National Laboratory)

SUMMARY

In the Dynamic Helium Charging Experiment (DHCE), helium was produced uniformly in vanadium alloy specimens by the decay of tritium during irradiation to 18–31 dpa at 425–600°C in lithium-filled capsules in the Fast Flux Test Facility. This report presents results of postirradiation tests of tensile properties and density change in V-8Cr-6Ti and V–9Cr–5Ti. Compared to tensile properties of the alloys irradiated in the non–DHCE (helium generation negligible), the effect of helium on tensile strength and ductility of V-8Cr-6Ti and V–9Cr–5Ti was insignificant after irradiation and testing at 420, 500, and 600°C. Both alloys retained a total elongation of >11% at these temperatures. Density change was <0.48% for both alloys.

INTRODUCTION

For the vanadium alloys, recent attention has focused on V-4Cr-4Ti for fusion reactor structural components because of its excellent mechanical and physical properties before and after neutron irradiation with and without helium generation. Compared to V–4Cr–4Ti, V–(8–9)Cr–(5–6)Ti alloys are known to exhibit better tensile and creep strengths (Fig. 1). However, impact properties of V–(8–9)Cr–(5–6)Ti alloys are less attractive than those of V–4Cr–4Ti. Ductile–brittle transition temperatures (DBTTs) of the alloys are significantly higher than that of V–4Cr–4Ti , i.e., ≈–70 to –85°C vs. <–196°C (Fig.2). DBTTs of V-(8-9)Cr–(5–6)Ti alloys shown in the figure were obtained on specimens annealed at a nominal temperature of ≈1125°C when the strong effect of annealing temperature on impact properties was not known. Preliminary data obtained recently on V–8Cr–6Ti annealed at ≈1000°C (for 1 h in high vacuum) indicated, however, a significantly improved DBTT, i.e., ≈–125°C vs. ≈–85°C. Therefore, there is some interest in improving the properties of V–(6–9)Cr–(5–6) Ti alloys by optimizing impurity composition and thermomechanical treatment, i.e.,obtaining both higher strength than V–(4–5)Cr–(4–5)Ti and acceptable impact properties.

With this background, we present in this report results of postirradiation tensile testing and density measurements on V–8Cr–6Ti and V–9Cr–5Ti specimens irradiated in the DHCE. Details of the experiment are described in Ref. 1. Tensile specimens (subsize SS–3 geometry) were annealed at a nominal temperature of ≈1125°C before insertion in the DHCE capsules. In the DHCE, fusion–relevant helium-to-dpa damage ratio (≈4–5 appm He/dpa) is simulated by utilizing slow transmutation of controlled amounts of ^{6}Li and a tritium–doped mother alloy immersed in $^{6}Li + {}^{7}Li$.

MATERIALS AND PROCEDURES

The elemental composition of the V–8Cr–6Ti, and V–9Cr–5Ti alloys, determined prior to irradiation, is given in Table 1. Tensile specimens with a gauge length of 7.62 mm and a gauge width of 1.52 mm were machined from 1.0–mm–thick sheets that had been annealed at a nominal temperature of ≈1125°C. Following irradiation in the DHCE, tensile properties were measured at 23, 100, and 200°C and at irradiation temperatures (425, 500, and 600°C) in flowing argon at a strain rate of 0.0011 s^{-1}. The thickness and gauge width of each specimen were measured individually before each tensile test.

*Works supported by the U.S. Department of Energy, Office of Fusion Energy Research, under Contract W-31-109-Eng-38.

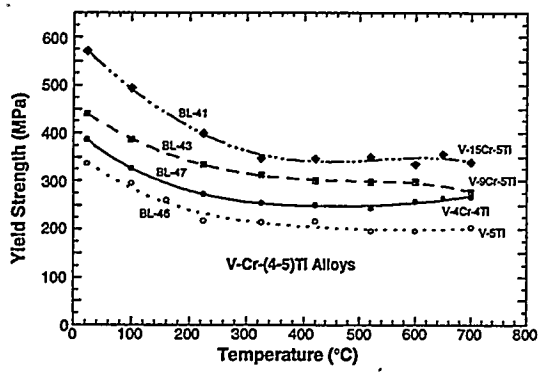

Fig. 1.

Yield strength vs. temperature of V-Cr-(4-5)Ti alloys as function of increased Cr content.

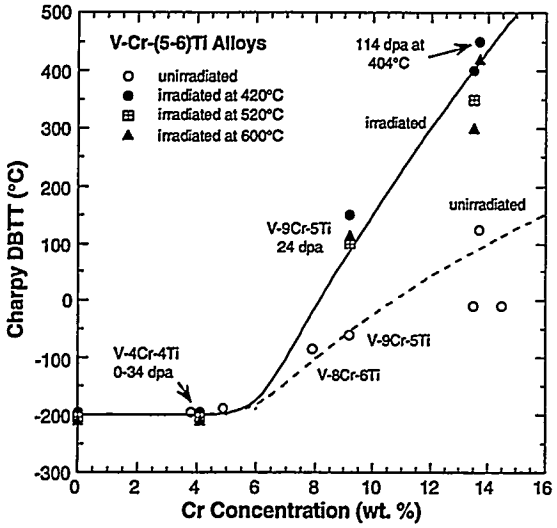

Fig. 2.

Comparison of ductile-brittle transition temperatures of V-4Cr-4Ti and V-(8-9)Cr-(5-6)Ti alloys.

The alloy specimens were irradiated in the Fast Flux Test Facility (FFTF) at 420, 520, and 600°C to neutron fluences (E > 0.1 MeV) ranging from 3.7 x 10^{22} n/cm^2 (≈18 displacements per atom, or dpa) to 6.4 x 10^{22} n/cm^2 (≈31 dpa). Helium in the alloy specimens has not yet been analyzed, but based on the helium contents measured previously on V–4Cr–4Ti, V–5Ti, and V–3Ti–1Si specimens that were irradiated in the same DHCE capsules,[1] helium contents in V–8Cr–6Ti and V–9Cr–5Ti are estimated to be in the range of 10–70 appm (see Table 2). Table 2 summarizes the irradiation parameters of the seven DHCE capsules in which V–8Cr–6Ti and V–9Cr–5Ti specimens were irradiated with V–4Cr–4Ti, V–5Ti, and V-3Ti–1Si alloys.

Table 1. Elemental Composition of V–8Cr–6Ti and V-9Cr-5Ti Alloys (wppm, unless otherwise noted)

Heat ID	Material	Cr, wt.%	Ti, wt.%	Si	O	N	C
BL-49	V-8Cr-6Ti	7.9	5.7	360	400	150	127
BL-43	V-9Cr-5Ti	9.2	4.9	340	230	31	100

Table 2. Summary of Irradiation Parameters of the Dynamic Helium Charging Experiment

Capsule ID NO.	Irradiation Temperature (°C)	Fluence (E > 0.1 MeV) (10^{22}n cm^{-2})	Total Damage[c] (dpa)	Helium Content Measured in V-4Cr-4Ti (appm)
4D1	425	6.4	31	112-13.3
4D2	425	6.4	31	22.4-22.7
5E2	425	3.7	18	3.3-3.7
5D1	500	3.7	18	14.8-15.0
5E1	500	3.7	18	6.4-6.5
5C1	600	3.7	18	8.4-11.0
5C2	500	3.7	18	74.9-75.3

TENSILE PROPERTIES

Yield strength, ultimate tensile strength, uniform elongation, and total elongation, measured on tensile specimens of V–8Cr–6Ti (Heat ID BL-49) and V–9Cr–5Ti (Heat ID BL-43) irradiated at 425°C–600°C to 18–34 dpa in the DHCE, are summarized in Figs. 3 and 4, respectively. For comparison, similar properties measured on non-DHCE-irradiated counterpart specimens (helium generation negligible) are also plotted as a function of irradiation temperature. In the figures, two groups of postirradiation tensile properties are shown, those measured at the irradiation temperatures and those measured at 23–200°C after irradiation at 420-600°C.

As shown in Figs. 3 and 4, after irradiation to ≈30 dpa in either a DHCE or other experiment, the two alloys retained high ductilities, i.e., >7% uniform elongation and >11% total elongation. Tensile properties of DHCE specimens, measured at 600°C (the same as the irradiation temperature), were essentially the same as those measured on non–DHCE specimens. This shows that the effect of helium was insignificant.

For both alloys, ductilities of the DHCE specimens irradiated at 425° were higher at 23°C than at 425°C. This behavior, similar to those observed for V-4Cr-4Ti, V-5Ti, and V-3Ti-1Si, is in contrast to the behavior of non–DHCE specimens in which ductility of specimens irradiated at 425° and measured at 23°C were similar to or slightly lower than the ductility measured at 425°C.[1] A similar comparison for DHCE and non–DHCE specimens irradiated at 500 and 600°C could not be made because no extra specimens of the latter type were available.

In contrast to results obtained from specimens in which helium atoms were produced by the tritium–trick method, low plastic deformation associated with intergranular cracking was not observed in either V-8Cr-6Ti or V-9Cr-5Ti. In the tritium-trick experiments, total elongation measured at room temperature is usually significantly lower than that measured at 500–600°C. This has been attributed to strong susceptibility to intergranular cracking in association with extensive formation of grain–boundary helium bubbles. No such grain-boundary coalescence of helium bubbles was observed in either the V-8Cr-6Ti or V-9Cr-5Ti specimens irradiated in the DHCE.

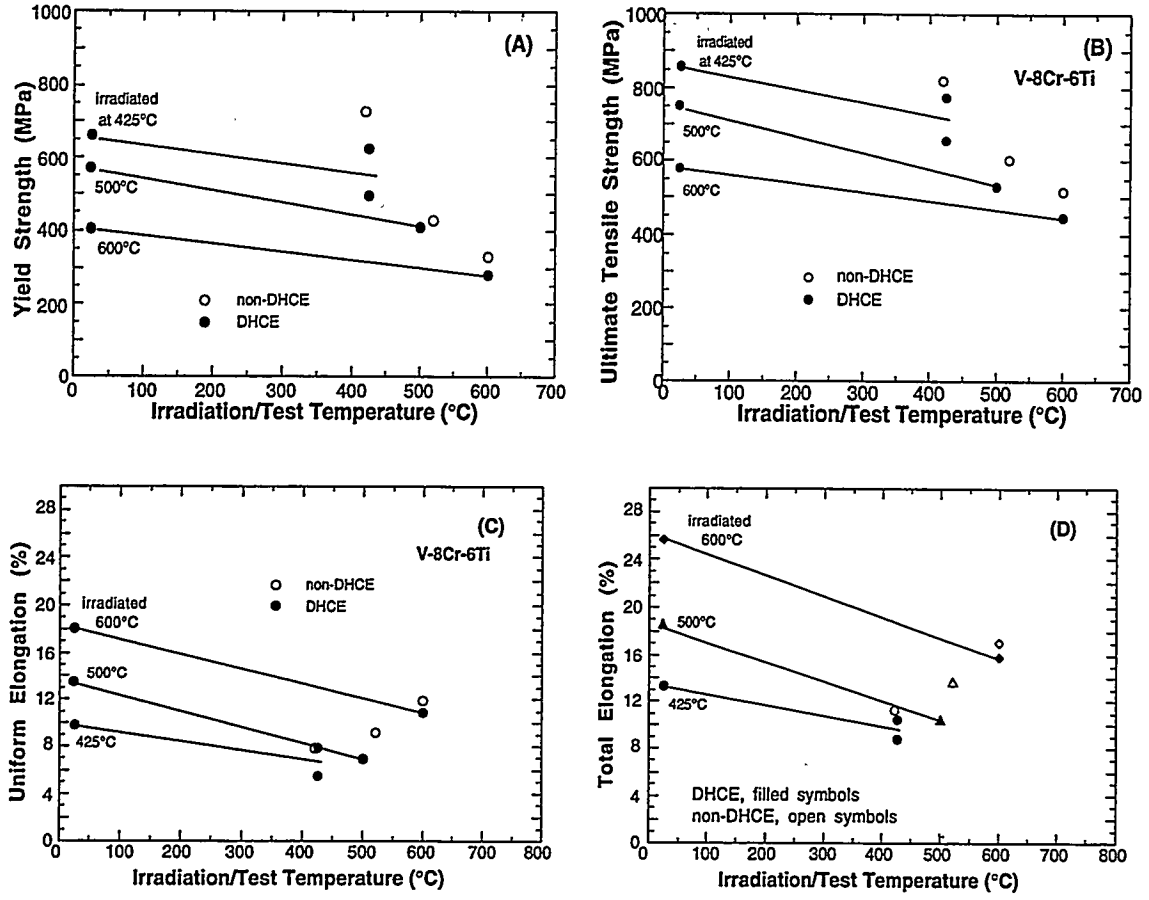

Fig. 3. Yield Strength (A), Ultimate Tensile Strength (B), Uniform Elongation (C), and total elongation (D) of V–8Cr–6Ti after irradiation at 420–600°C to 18–34 dpa in DHCE and other experiments (non-DHCE).

DENSITY CHANGE

Density decreases of V-8Cr-6Ti and V-9Cr-5Ti irradiated in the DHCE are shown in Figs. 5 and 6, respectively. Density was measured on pieces broken from the shoulder region of the tensile specimens. The density change in the figures represents the average of three measurements and was small, i.e., <0.48% after ≈18–31 dpa. However, density change in V–8Cr–6Ti was larger under DHCE conditions than under the non–DHCE conditions.

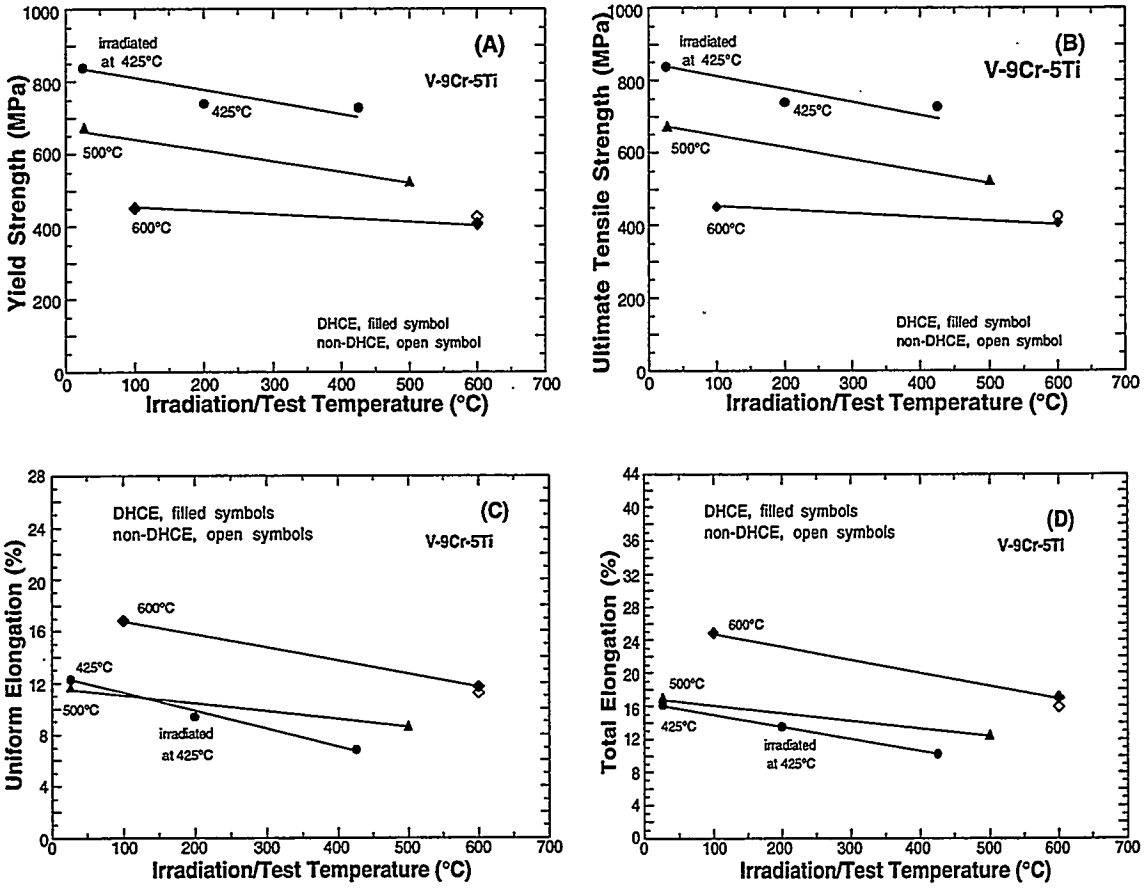

Fig. 4. Yield strength (A), ultimate tensile strength (B), uniform plastic elongation (C), and total elongation (D) of V–9Cr–5Ti after irradiation at 420–600°C to 18–34 dpa in DHCE and other experiments (non-DHCE).

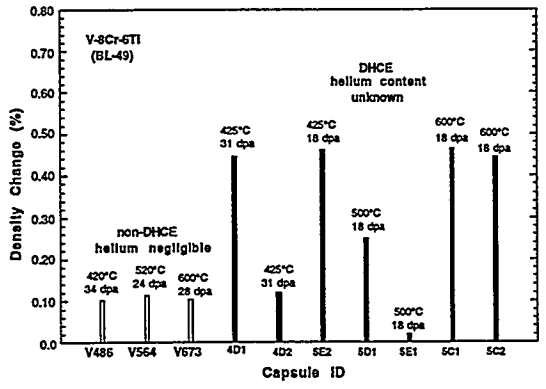

Fig. 5.

Density decrease of V–8Cr–6Ti after irradiation to 18–34 dpa at 420–600°C with (DHCE) and without helium generation (non-DHCE).

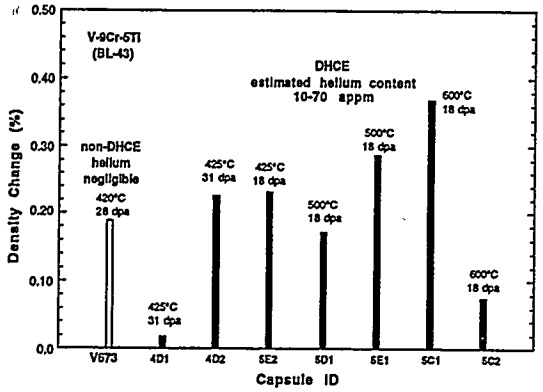

Fig. 6.

Density decrease of V–9Cr–5Ti after irradiation to 18–34 dpa at 420–600°C with (DHCE) and without helium generation (non–DHCE).

CONCLUSIONS

1. Tensile ductilities of V–8Cr–6Ti and V–9Cr–6Ti, irradiated to 18–31 dpa at 425°C to 600°C in the Dynamic Helium Charging Experiment (DHCE) at estimated helium generation rates of 0.4–4 appm He/dpa, remained significantly high at 25–600°C, i.e., >7% uniform elongation and >11% total elongation.

2. Tensile properties of the alloys irradiated and measured at 600°C were essentially the same as those measured on the counterpart non–DHCE specimens (negligible helium generation). No intergranular fracture was observed in tensile specimens irradiated in the DHCE and tested at 20–600°C. This shows that effects of helium were insignificant.

3. Ductilities of the DHCE specimens irradiated at 425° were higher at 23°C than at 425°C. This behavior, similar to those observed for V-4Cr-4Ti, V-5Ti, and V-3Ti-1Si, is in contrast to the behavior under non–DHCE conditions (helium generation negligible) in which ductility of the specimens irradiated at 425° and measured at 23°C were similar to or slightly lower than that measured at 425°C. These observations indicate that different types of hardening centers are produced at ≈425°C in the DHCE condition (probably a helium–vacancy–impurities complex, impurities being O, N, and C) and in non–DHCE condition (defects and defect clusters, impurities in interstitial sites).

4. Density decrease of V-8Cr-6Ti and V-9Cr-5Ti irradiated in the DHCE was small, i.e., <0.48% after ≈18–31 dpa.

REFERENCES

1. H. M. Chung, B. L. Loomis, L. Nowicki, and D. L. Smith, "Effect of Dynamically Charged Helium on V–5Ti, V–4Cr–4Ti, and V–3Ti–1Si," in Fusion Reactor Materials, Semiannual Prog. Rep. DOE/ER-0313/19, Oak Ridge National Laboratory, Oak Ridge, TN (1995), pp. 77–82.

TENSILE PROPERTIES OF V–(4–15)Cr–5Ti ALLOYS IRRADIATED AT 400°C IN THE HFIR*

H. M. Chung, L. Nowicki, and D. L. Smith (Argonne National Laboratory)

SUMMARY

V–(4–15)Cr–5Ti alloys were irradiated in a helium environment to ≈10 dpa at ≈400°C in the High Flux Isotope Reactor (HFIR). This report presents results of postirradiation tests of tensile properties of V-4Cr-4Ti, V–8Cr–6Ti, V–10Cr–5Ti, and V–15Cr–5Ti. Despite concerns on the effects of transmutation of vanadium to Cr and impurity pickup from the helium environment, all of the alloys exhibited ductile tensile behavior. However, the alloys exhibited ductilities somewhat lower than those of the specimens irradiated to a similar dose and at a similar temperature in an Li environment in fast reactors. Uniform plastic strain in the V–Cr–(4–5)Ti alloys decreased monotonically with increasing Cr content.

INTRODUCTION

Recently, attention to the vanadium alloys has focused on V-Cr-Ti ternary alloys containing ≈5 wt.% Ti. Most of the data base information on the irradiation performance of these alloy class was obtained from specimens irradiated in an Li environment in fast reactors such as the Fast Flux Text Reactor (FFTF) and EBR–II. In the present irradiation experiment in the HFIR, a large number of vanadium–base alloys were irradiated to investigate their performance at 200 and 400°C in a helium environment. A primary concern on the irradiation performance at 400°C in the HFIR has been the effects of corrosion of the alloys by uptake of impurities (such as O, C, and N) from the helium environment.

A higher Cr content in V–Cr–5Ti ternary alloys is known to provide better resistance to corrosion, as well as higher strength, whereas more pronounced irradiation–induced embrittlement is a major drawback of the high–Cr alloys. Therefore, several alloys of the V–(4–15)Cr–5Ti family, i.e., V–4Cr–4Ti, V–8Cr–6Ti, V-10Cr–5Ti, and V–15Cr–5Ti, were irradiated at ≈400°C to determine the effects of Cr on mechanical properties and density change. This report presents results of postirradiation tests of tensile properties of these alloys irradiated at 400°C. Tensile tests on alloys irradiated at 200°C are in progress, and initial results indicate very different brittle–type behavior for most of these alloys. Therefore, the irradiation performance at 200°C will be reported in separate.

MATERIALS AND PROCEDURES

The elemental composition of the alloys, determined prior to irradiation, is given in Table 1. Tensile specimens with a gauge length of 7.62 mm and a gauge width of 1.52 mm were machined from 1.0-mm-thick sheets that had been annealed at a nominal temperature of ≈1125°C. Following irradiation and specimen retrieval, the tensile specimens were cleaned ultrasonically in alcohol and tested without the customary degassing treatment at 400°C (used to expel hydrogen). Tensile properties were measured at 400°C in flowing argon at a strain rate of 0.0011 s^{-1}. The thickness and gauge width of each specimen were measured individually before each tensile test.

The tensile specimens were irradiated in the MFE–RB* 400J–1 capsule in the removable beryllium (RB*) position in the HFIR. The specimens were irradiated at ≈400°C to ≈10 dpa in circulating helium. Details of the capsule design and irradiation conditions are reported in Ref. 1. Helium in the line was purified continuously by a Ti–sponge getter located outside the core region.

The specimens were shielded from thermal neutrons by an Hf sleeve located outside the capsule. The Hf shield was designed to tailor the neutron spectrum to closely simulate the fusion–relevant helium–to–dpa

* Work supported by the U.S. Department of Energy, Office of Fusion Energy Research, under Contract W-31-109-Eng-38.

ratio in stainless steels (i.e., ≈14 appm/dpa) rather than in vanadium. Under these irradiation conditions, appreciable transmutation of vanadium to Cr is expected. According to the calculation reported by Gomes and Smith, Cr content in V–4Cr–4Ti is predicted to increase to ≈5.6 wt.% after irradiation to ≈10 dpa in the Hf–shielded capsules in HFIR.[2] At this time, however, results of chemical analysis of Cr in the vanadium alloys are not available.

Table 1. Chemical composition of vanadium alloys irradiated at 400°C in HFIR

	Nominal Comp.	Impurity Concentrations (wt.ppm)			
Heat ID	(wt.%)	O	N	C	Si
BL-41	14.5Cr-5.0Ti	450	120	93	390
BL-43	9.2Cr-4.9Ti	230	31	100	340
BL-49	7.9Cr-5.7Ti	400	150	127	360
BL-47	4.1Cr-4.3Ti	350	220	200	870

RESULTS AND DISCUSSION

Tensile properties of the alloys irradiated at 400°C in a helium environment in HFIR were similar to the tensile properties measured after irradiation in a lithium environment in the sodium–cooled fast reactor FFTF. Ductile behavior of V–4Cr–4Ti, V–8Cr–6Ti, V–10Cr–5Ti, and V–15Cr–5Ti alloys was manifested by significant levels of uniform plastic elongation, total elongation, and work-hardening capability. This is shown, as an example, in the stress–strain curve of V–8Cr–6Ti (Heat ID BL–49) in Fig. 1. Similar stress–strain curves of the same heat, determined after irradiation in Li–bonded capsules in the FFTF, are also shown in the figure for comparison.

In the latter types of irradiation in an Li environment, tensile properties of V–8Cr–6Ti were determined after irradiation at the comparable temperature of ≈420°C under the condition of significant helium generation in the Dynamic Helium Charging Experiment[3] (DHCE) and under a non–DHCE condition (with negligible helium generation). In spite of the lower damage level of ≈10 dpa in the HFIR, total elongation was somewhat lower than the elongation measured after irradiation to ≈31–34 dpa in Li environment under both DHCE and non–DHCE conditions. Although the relative effect of increased Cr (from transmutation) and impurities (from the helium environment) must be determined quantitatively from postirradiation chemical analysis, the lower elongation in the HFIR specimen is believed to be associated primarily with vanadium–to–Cr transmutation and higher impurity contamination such as oxygen from the circulating helium. The slightly lower irradiation temperature is also conducive to somewhat lower tensile ductility.

In Figs. 2 and 3, effects of Cr (concentration measured before irradiation) on tensile strength and ductility are shown for the present family of V-(4-15)Cr–5Ti alloys. Uniform plastic elongation decreased significantly (to <2%) for Cr > 7 wt.%. However, V–4Cr–4Ti retained good ductility and high strength.

CONCLUSIONS

1. Despite concerns about the effects of vanadium–to–Cr transmutation and impurity pickup from the helium environment, V–4Cr–4Ti, V-8Cr–6Ti, V–10Cr–5Ti, and V–15Cr–5Ti alloys exhibited ductile tensile behavior after irradiation at 400°C to ≈10 dpa in the HFIR.

2. The alloys exhibited ductilities somewhat lower than those of the specimens irradiated to a similar dose at similar temperature in an Li environment in fast reactor. Vanadium–to–Cr transmutation by thermal neutrons and impurity uptake from helium such as oxygen are believed to be the primary factors.

3. Uniform plastic elongation in V–(4–15)Cr–5Ti alloys decreased significantly (to <2%) for Cr > 7 wt.%. However, the V–4Cr–4Ti alloy specimens, predicted to have a composition close to V-5.6Cr-5Ti after the irradiation to ≈10 dpa, retained good ductility and high strength.

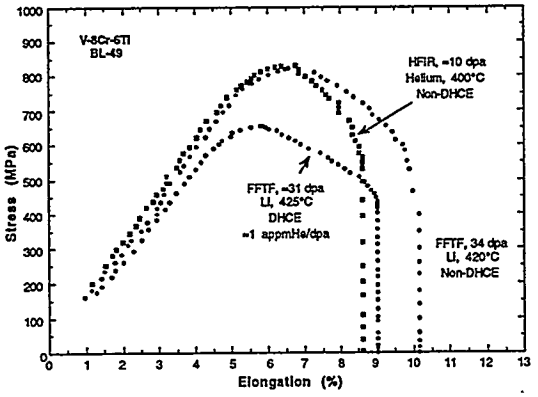

Fig. 1.

Comparison of stress vs. strain curves of V-8Cr–6Ti irradiated at 400–420°C in helium in HFIR and in lithium in FFTF in non-DHCE and DHCE.

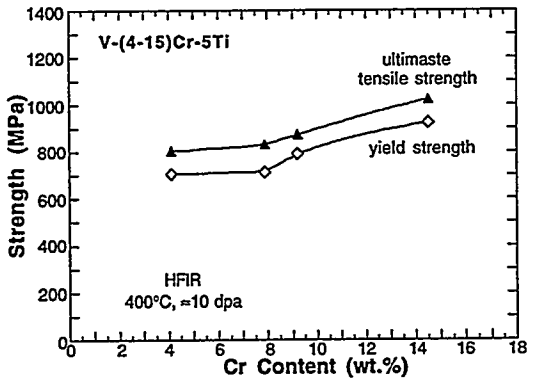

Fig. 2.

Effects of Cr content on yield and ultimate tensile strength of V–(4–15)Cr–5Ti alloys irradiated at ≈400°C to ≈10 dpa in helium in the HFIR.

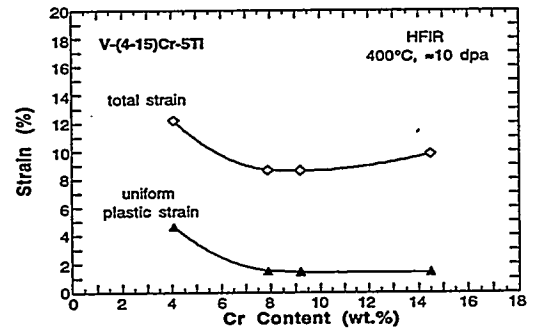

Fig. 3.

Effects of Cr content on total strain and uniform plastic strain of V–(4–15)Cr–5Ti alloys irradiated at ≈400°C to ≈10 dpa in helium in the HFIR.

ACKNOWLEDGMENT

Authors thank J. Pawel and H.–C. Tsai for the irradiation in HFIR and retrieval of the specimens, respectively.

REFERENCES

1. A. W. Longest, J. E. Pawel, D. W. Heatherly, R. G. Sitterson, and R. L. Wallace, "Fabrication and Operation of HFIR–MFE RB* Spectrally Tailored Irradiation Capsules," in Fusion Reactor Materials, Semiannual Prog. Rep. DOE/ER-0313/14, Oak Ridge National Laboratory, Oak Ridge, TN (1993), pp. 14–40.

2. I. C. Gomes and D. L. Smith, "Vanadium Irradiation at ATR – Neutronics Aspects," in Fusion Reactor Materials, Semiannual Prog. Rep. DOE/ER-0313/17, Oak Ridge National Laboratory, Oak Ridge, TN (1995), pp. 17–20.

3. H. M. Chung, L. J. Nowicki, and D. L. Smith, "Properties of V–(8–9)Cr–(5–6)Ti Alloys Irradiated in The Dynamic Helium Charging Experiment," in this report.

EFFECTS OF IRRADIATION AT LOW TEMPERATURE ON V-4Cr-4Ti -

D. J. Alexander, L. L. Snead, S. J. Zinkle, A. N. Gubbi, A. F. Rowcliffe, and E. E. Bloom
(Oak Ridge National Laboratory)

OBJECTIVE

The effects of irradiation at low temperatures (nominally 100 to 275°C) on the properties of V-4Cr-4Ti have been examined to define the lower operating temperature limits for this alloy.

SUMMARY

Irradiation at low temperatures (100 to 275°C) to 0.5 dpa causes significant embrittlement and changes in the subsequent room temperature tensile properties of V-4Cr-4Ti. The yield strength and microhardness at room temperature increase with increasing irradiation temperature. The tensile flow properties at room temperature show large increases in strength and a complete loss of work hardening capacity with no uniform ductility. Embrittlement, as measured by an increase in the ductile-to-brittle transition temperature, increases with increasing irradiation temperature, at least up to 275°C. This embrittlement is not due to pickup of O or other interstitial solutes during the irradiation.

INTRODUCTION

Vanadium alloys are candidate materials for structural applications in fusion reactors, due to their low activation, high thermal stress figure of merit (high thermal conductivity, moderate strength, and low coefficient of thermal expansion), and compatibility with liquid lithium. Successful application of these alloys will require understanding of the effects of irradiation on the mechanical properties, such as strength, ductility, and toughness.

The U.S. program has identified V-4Cr-4Ti (wt%) as a leading candidate material. Fast reactor experiments at temperatures in the range 425-600°C have demonstrated promising resistance to radiation damage.[1] The present work examines irradiation behavior in the low temperature regime (100-275°C) to define the lower operating temperature limit for this alloy.

EXPERIMENTAL PROCEDURE

The material used for this experiment was taken from the 500 kg heat produced by Teledyne Wah Chang Albany (TWCA) for the U. S. Fusion Program (heat 832665). This material contains approximately 300 ppm O, 85 ppm N, and 80 ppm C (by weight) [2]. This plate was processed by TWCA and supplied in the form of 6.4-mm thick plate that had been annealed for 2 h at 1050°C, in a vacuum better than 10^{-5} torr. Additional material was supplied as ~40% CW sheet, 1 mm thick.

Subsize Charpy specimens were machined from the annealed plate. These specimens were 3.3 × 3.3 × 25.4 mm with a 30° notch, 0.67 mm deep with a 0.08 mm root radius. The notch was oriented for crack growth perpendicular to the rolling direction (L-T orientation).[1] The specimens were annealed for 2 h at 1000°C in vacuum (better than 10^{-7} torr) after machining. The resultant grain size was 16 μm. Some specimens were fatigue precracked by cyclic loading in 3-point bending in stroke control, so the load would shed automatically as the crack extended. The final load was approximately 130 N, and the final crack length to specimen width ratio (a/W) was nominally 0.5.

---

[1] Note that these specimens were incorrectly described as having a notch 0.51 mm deep and being oriented for crack growth parallel to the rolling direction in a previous report "Effect of Cr and Ti Contents on the Recovery, Recrystallization, and Mechanical Properties of Vanadium Alloys" by A. N. Gubbi, A. F. Rowcliffe, D. J. Alexander, M. L. Grossbeck, W. S. Eatherly, and L. T. Gibson, Fusion Materials Semiannual Progress Report for Period Ending December 31, 1995, DOE/ER-0313/19, pp. 37-43, Oak Ridge National Laboratory, Oak Ridge, TN 37831.

Small SS-3 sheet tensiles (0.76 × 1.52 × 7.6 mm gage section) were machined from the cold-rolled sheet. These specimens were oriented in the longitudinal orientation (parallel to the rolling direction) and were annealed for 2 h at 1000°C in vacuum (better than 10^{-7} torr) after machining. The final grain size of both the Charpy and SS-3 specimens was around 16 μm.

The irradiation capsules were designed for insertion into the core thimble position in the High Flux Beam Reactor at Brookhaven National Laboratory. The experiment consisted of two separate capsules each containing 5 subcapsules (Fig. 1). The irradiation temperatures were varied from 100 to 275°C by varying the width of the gas gap for each subcapsule. The capsules were purged with ultra high-purity He, evacuated with a turbopump (three cycles), and finally filled to 10^5 Pa. Each subcapsule contained 8 Charpy specimens and 4 tensile specimens held against the holder with a roll pin to provide intimate contact between the holder and the specimens to improve the heat transfer. Vanadium alloy tensile specimens were not included in the 275°C capsule. Each subcapsule had one thermocouple that was attached to a Charpy specimen to monitor temperature throughout the irradiation. One subcapsule in each capsule had 2 thermocouples (cf Fig. 1) for continuous temperature measurement and to detect any asymmetry in heat flow distribution.

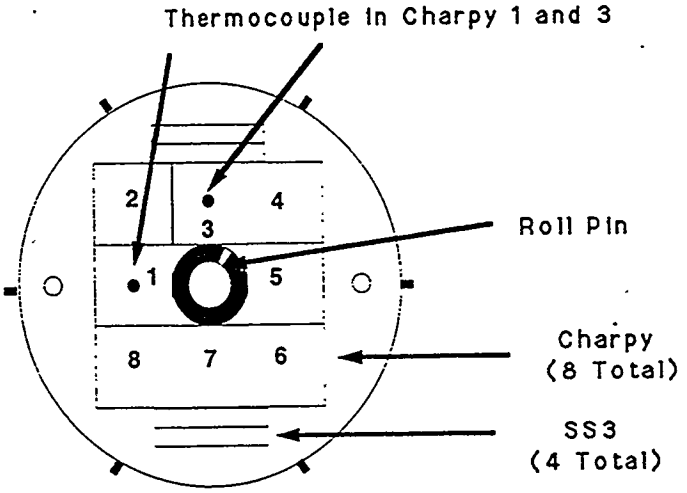

Fig. 1. Schematic illustration of a cross-section of the irradiation capsule, showing location of the subsize Charpy and tensile specimens in a subcapsule.

Each of the two capsules was irradiated for 545 h (23 days) for estimated fast (E > 0.1 MeV) and thermal fluences of 8×10^{24} and 3×10^{24} n/m^2 respectively. This dose was calculated to produce about 0.1% Cr and a damage level of 0.4 dpa. Flux monitors in the capsule will be analyzed in the future to provide a more accurate determination of the fluence. It was noticed that the temperature typically increased about 10°C during the course of the irradiation, although the reason for this increase is not clear. The temperatures recorded by the two thermocouples in each subcapsule differed by <10°C for each irradiation temperature.

The subsize Charpy specimens (both blunt notch and precracked) were tested in air on a pendulum machine modified for small specimens. The tensile specimens were all tested in air at room temperature, with a single test for each irradiation temperature. The tensile tests were conducted on a servohydraulic machine at an initial strain rate of 10^{-3} s^{-1}. The load vs crosshead displacement test record was used to determine the tensile properties.

Vickers hardness measurements were made at room temperature with a 500 g load using the grip-section of SS-3 specimens prior to tensile testing; 2 specimens were tested in each condition, with at least 20 VHN measurements on each specimen.

The room temperature resistivity of the unirradiated control and irradiated tensile specimens was measured prior to tensile testing, using standard 4-point probe techniques (ASTM B 193-87, Standard Test Method for Resistivity of Electrical Conductor Materials, reapproved 1992). An electrical current of 100 mA was supplied by a Keithley model 237 Source Measure Unit through spring-loaded electrical contacts located in the end tab regions of the specimens. The potential drop in the gage region of the specimen was measured between two spring-load electrical contacts that were separated by a distance of 7.1 mm with a Keithley model 182 Sensitive Digital Voltmeter with a low thermal connector (resolution limit of 1 nV). Potentials associated with thermal emfs in the electrical leads were subtracted by using the "relative reading" function of the model 182 voltmeter. Three different tensile specimens were measured for each irradiation temperature. The typical measured resistances were ~1.5-1.8 mΩ. The gage dimensions were measured to an accuracy of ±2 μm in two different locations using a Mitutoyo digital micrometer in order to convert the resistance measurement to resistivity values. The experimental error in the resistivity measurements was mainly due to uncertainties in the gate cross-sectional area; the typical measured standard error was ±0.7 nΩ-m. The temperature was recorded for each measurement (24.5-26°C), and the data were corrected to a reference temperature of 20°C using the V-Ti-Cr alloy resistivity temperature coefficient [3, 4, 5] of 0.75 nΩ-m/K.

RESULTS AND DISCUSSION

The room temperature yield strength and hardness are increased significantly by irradiation from 100 to 275°C (Fig. 2). The increase in yield strength and hardness increases with increasing irradiation temperature, and the yield strength and hardness show similar responses to irradiation. In addition, the tensile flow properties at room temperature change significantly. For each irradiation temperature there is a complete loss of work hardening capability (Fig. 3). Following yielding, the material fails rapidly through plastic instability.

Irradiation at these temperatures (100 to 275°C) produces a very large increase in the ductile-to-brittle transition temperature (DBTT) and a large decrease in the upper-shelf energy (USE) (see Fig. 4). The shift in the DBTT increases with increasing irradiation temperature.

The precracked specimens have higher DBTTs than the blunt notch specimens irradiated at the same temperature. The USE is much lower, primarily due to the greatly reduced cross-sectional area for the precracked specimens.

The existence of a radiation-damage regime associated with rapid hardening and susceptibility to brittle cleavage failure is a common characteristic of BCC metals and alloys. However, the magnitude of the property changes in the V-4Cr-4Ti alloys were larger than those observed, for example, in many reduced activation ferritic-martensitic steels irradiated at ~250°C [6]. Other factors which could contribute to the observed embrittlement are (a) the inadvertent introduction of hydrogen during pre or postirradiation handling and (b) the pick-up of oxygen and nitrogen from the capsule atmosphere during irradiation. These are considered remote possibilities; hydrogen-induced embrittlement has never been observed as a result of the handling procedures used for unirradiated specimens at ORNL and the irradiation temperatures are too low for significant transfer of interstitials into the specimen interior to occur. Nevertheless, two experiments were carried out to test these possibilities.

Several irradiated Charpy specimens were annealed at 400°C for 1 hr in a vacuum of 10^{-7} torr. These conditions were chosen to remove hydrogen while minimizing recovery of radiation damage. The results of subsequent Charpy testing of these specimens are indicated by the solid symbols in Fig. 5. It can be seen that vacuum annealing did not result in significant recovery of impact properties, and it is concluded that hydrogen pick-up is not a significant factor in the observed embrittlement.

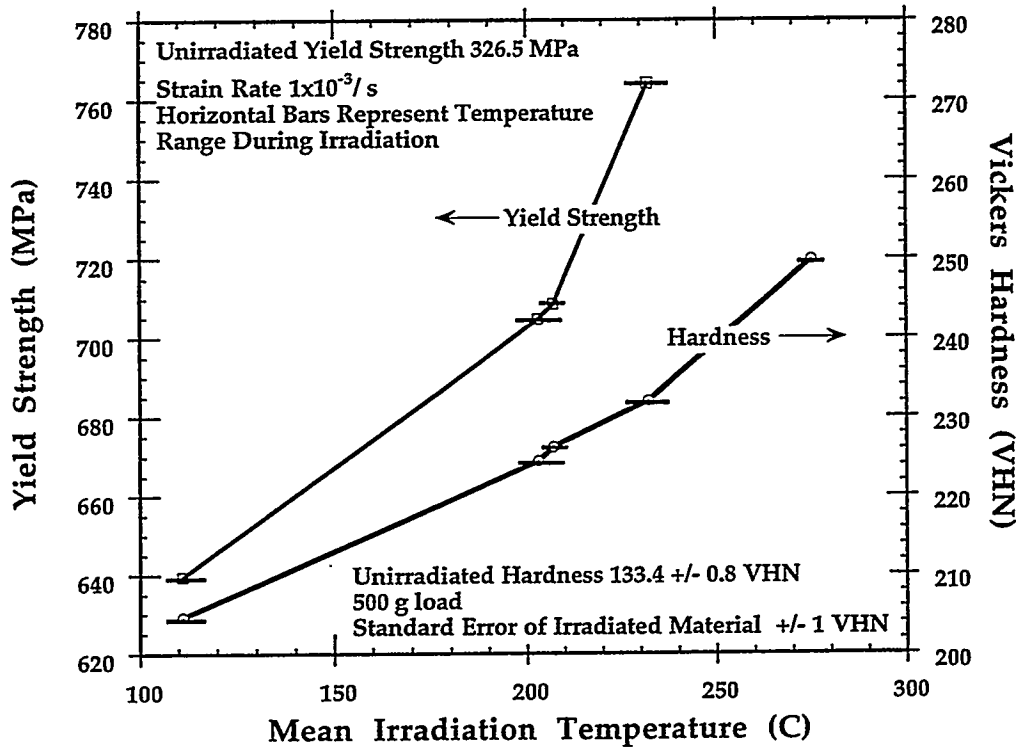

Fig. 2. Effect of irradiation on yield strength and microhardness, measured at room temperature.

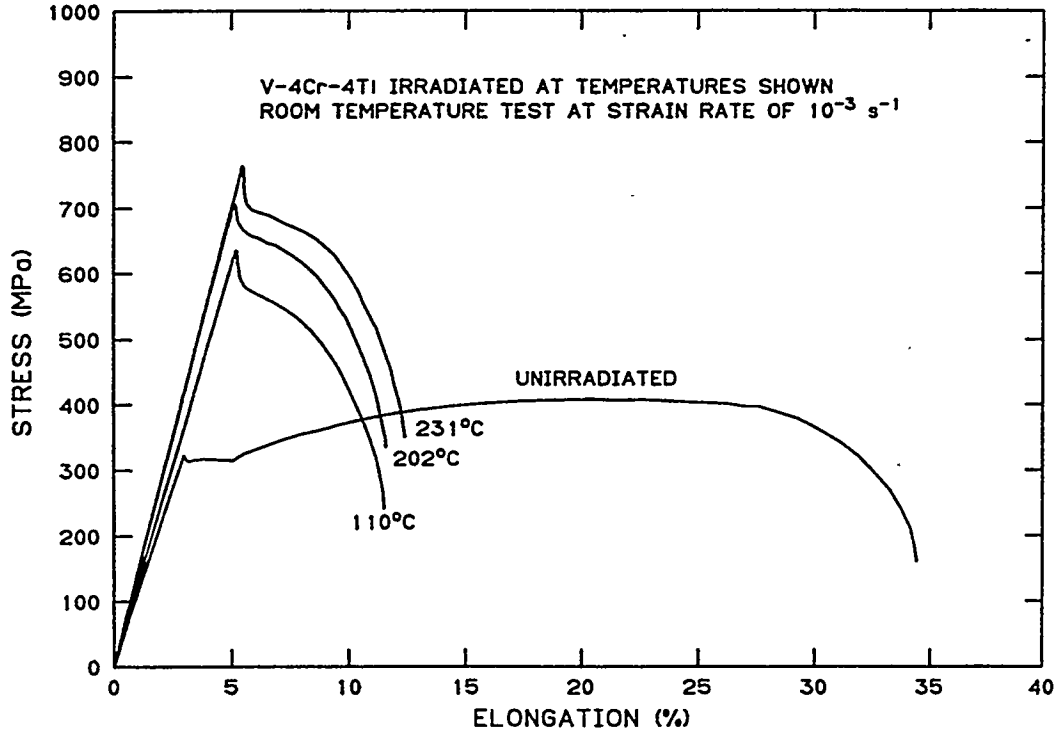

Fig. 3. Stress-elongation curves measured at room temperature, showing the significant decrease in total elongation and the complete loss of work hardening capacity following irradiation.

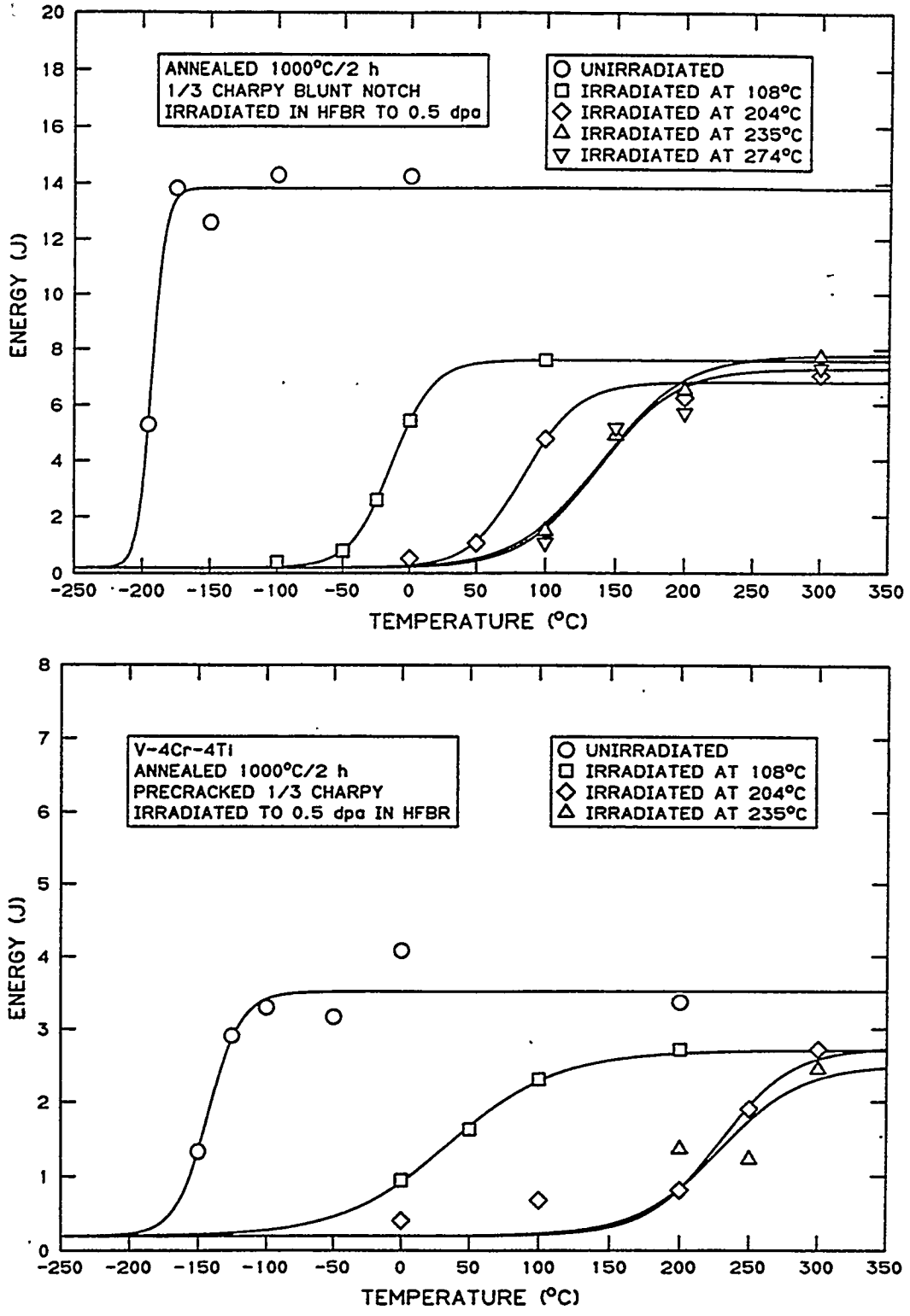

Fig. 4. Impact properties of V-4Cr-4Ti, showing significant embrittlement due to irradiation. Top: blunt notched specimens; bottom: fatigue precracked specimens.

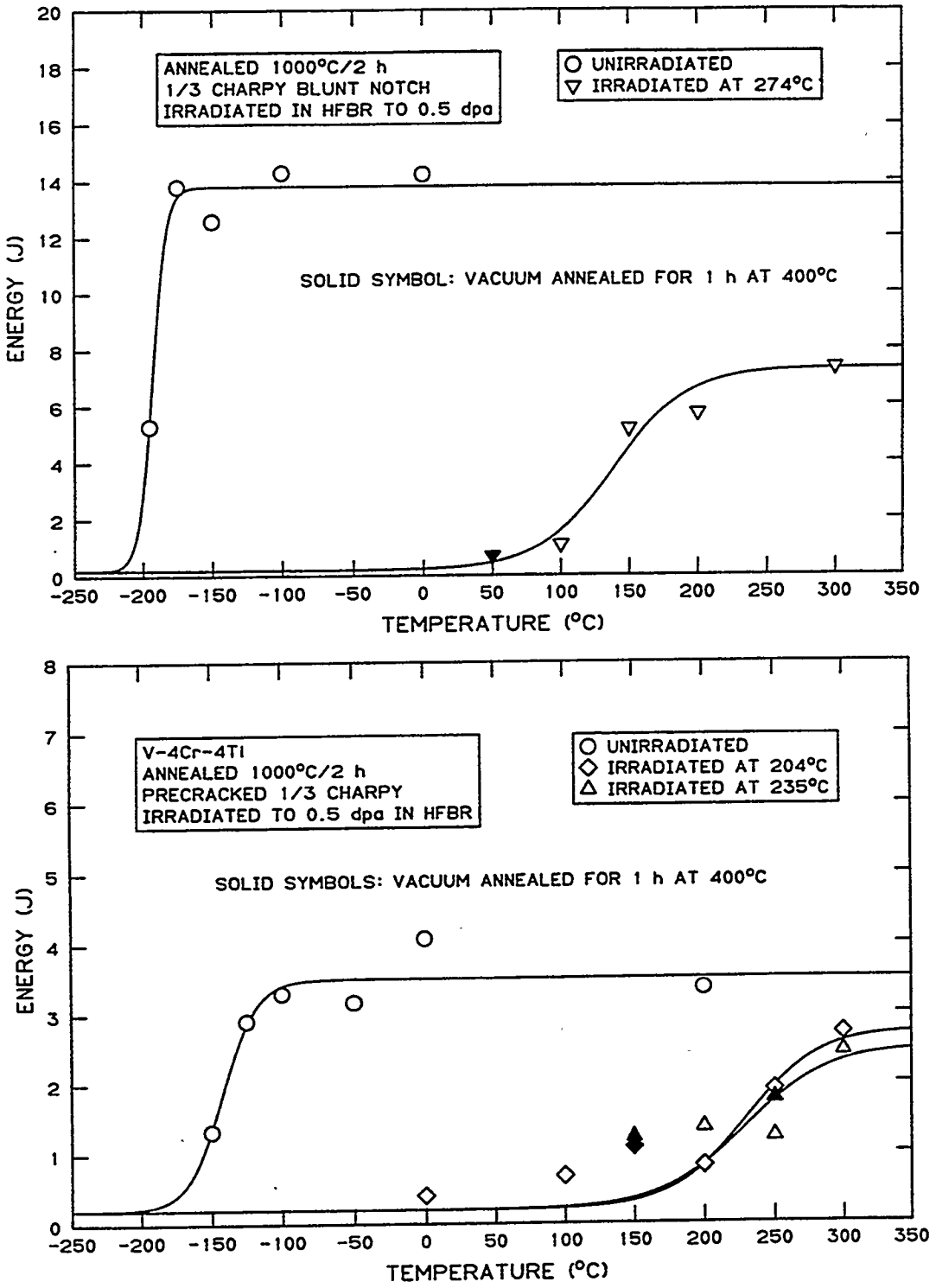

Fig. 5. A comparison of impact properties of specimens after annealing 1 h at 400°C in vacuum with as-irradiated specimens. Annealing had little effect on the impact properties. Top: blunt notched specimens; bottom: precracked specimens.

In a second experiment, one set of unirradiated pre-cracked specimens was placed in aluminum capsules and helium back-filled using procedures identical to those used for the sub-capsules for the irradiation experiment. These capsules were then held at 275°C or 400°C for 21 days. This exposure was sufficient to produce surface oxide films on both sets of specimens. The results of impact tests on these specimens are shown in Fig. 6. At the lower temperatures, impact energies were somewhat above those for the as-annealed specimens, whereas at the higher temperatures, impact energies were slightly lower. However, it is quite clear that the helium-exposed control specimens do not exhibit the completely brittle behavior of the irradiated specimens tested over the same temperature range.

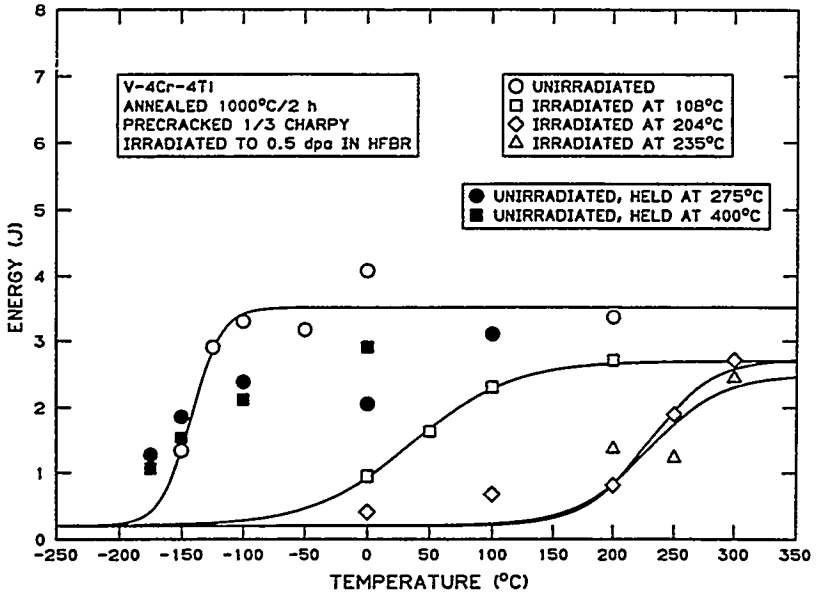

Fig. 6. Impact properties of precracked unirradiated specimens after holding for 21 days at 275 or 400°C in He atmosphere, as compared to unirradiated specimens. Holding at 275 or 400°C had little effect on the impact properties, indicating that no embrittling interstitials were picked up from the He atmosphere.

The room temperature resistivity measurements provide further evidence that interstitial elements are not creating the embrittlement. The room-temperature resistivity increased for irradiation at 108°C as compared to the unirradiated materials (see Fig. 7). This increase in resistivity is solely due to generation of point defect clusters in the lattice, since this temperature is too low for O, C, or N migration in vanadium. The measured migration temperatures and migration enthalpies of C, O, and N in vanadium for 1 h isochronal anneals are ~185°C (1.18 eV), ~185°C (1.26 eV) and ~275°C (1.48 eV) [7]. Similar activation energies have been obtained for oxygen diffusion in V-4Cr-4Ti alloys [8]. After irradiation to 0.4 dpa at ~200°C, the resistivity was similar to the unirradiated value. Electron microscopy studies performed on vanadium irradiated to ~0.1 dpa have found that the defect cluster density decreased by about an order of magnitude as the irradiation temperature increased from 70 to 200°C [9]. Therefore, the lower resistivity of the HFBR specimens irradiated at ~200°C compared to 108°C is likely mainly due to a reduced defect cluster density. In addition, C and O interstitial solutes have moderate mobility at these temperatures [7]. These solutes could migrate to the remaining defect clusters and increase the dislocation barrier strength of the clusters, in a manner analogous to radiation anneal hardening. This proposed interstitial solute strengthening of defect clusters is a possible explanation for the observed increase in microhardness and tensile strength of vanadium irradiated at 200°C compared to 108°C. The observation that the resistivity did not increase dramatically at an irradiation temperature of ~200°C indicates that the observed increase in radiation hardening was not due to solution hardening from pickup of O or C interstitial solutes from the surrounding environment. The specific resistivities for O, C, and N solutes in vanadium are ~54 to 87 nΩ-m/at.% solute [7]. Therefore, the incorporation of significant (>1000 appm) concentrations of O or C in the matrix as solid solution impurities would have caused an easily detected (>5 nΩ-m) increase in the resistivity. The resistivity measured for an irradiation temperature of 240°C was less than that measured in unirradiated

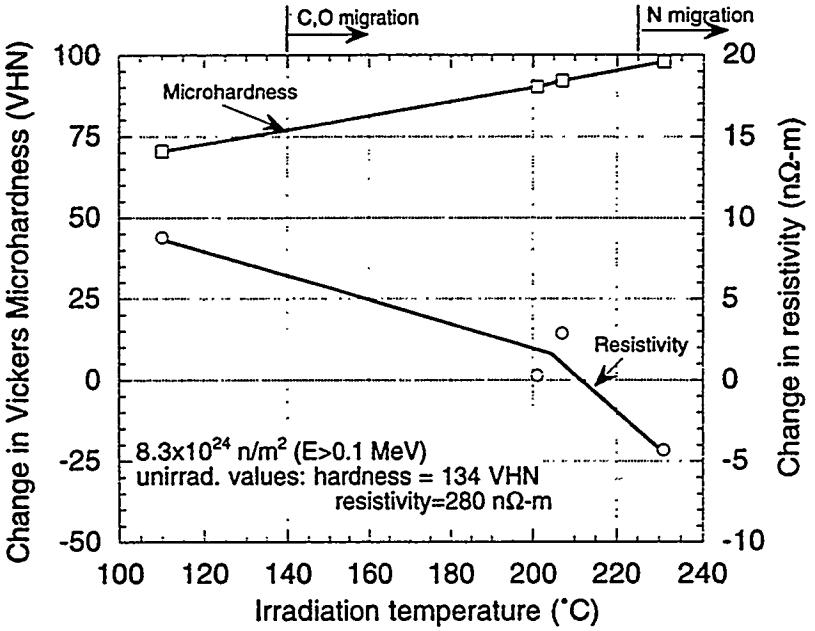

Fig. 7. Resistivity and microhardness after irradiation, as measured at room temperature.

controls. One possible explanation for this result is that ballistic dissolution of the submicroscopic precipitates containing Ti-(O,C,N) has occurred, and that many of the O, C, and N interstitials have migrated to defect clusters. This process would cause a reduction in the measured resistivity compared to the unirradiated alloy if the defect cluster density was much lower than the initial submicroscopic precipitate density, since the resistivity per solute atom should decrease with increasing size. This process would also explain the observed increase in radiation hardening at 240°C compared to the 200°C irradiation (increased barrier strength of defect clusters containing interstitial solute atoms). Additional work, including transmission electron microscopy, is needed to verify this proposed explanation for the temperature-dependent radiation hardening behavior of V-4Cr-4Ti alloys.

SUMMARY AND CONCLUSIONS

It is clear from this experiment that irradiation to 0.5 dpa at low temperatures (100 to 275°C) causes significant embrittlement of V-4Cr-4Ti. This embrittlement is not due to pickup of interstitial solutes during the irradiation, but is directly related to radiation hardening. The degree of embrittlement increases with increasing irradiation temperature, at least up to 275°C. The resistivity results suggest that the effectiveness of defect clusters as barriers to dislocation motion is enhanced by the migration of oxygen and carbon to defect clusters at temperatures above ~200°C.

Irradiation at these low temperatures causes significant changes in the subsequent tensile flow properties at room temperature, with large increases in strength and a complete loss of work hardening capacity with no uniform ductility. The loss of work hardening may be related to dislocation channeling; further work is needed to characterize the defect microstructure produced during irradiation to identify the mechanism of hardening. The range of temperatures over which embrittlement occurs needs to be determined, and further irradiation experiments at 330 and 400°C are in preparation.

REFERENCES

1. B. A. Loomis et al., J. Nucl. Mat. 212-215 (1994) 799.

2. M. L. Grossbeck et al., "Characterization of V-4Cr-4Ti Heat 832665," Fusion Materials Semiannual Progress Report for Period Ending March 31, 1995, DOE/ER--0313/18, p. 183, 1995.

3. E. W. Collings, Phys. Rev. B 9 (1974) 3989.

4 A. Giannuzzi et al., Phil. Mag. 21 (1970) 479.

5. K. Hirata et al., J. Phys, F7 (1977) 419.

6. "Charpy Impact Properties of Low Activation Alloys for Fusion Applications after Neutron Irradiation," to be published, Proc. ICFRM-8, Obninsk, RF, 1995.

7. J. T. Stanley et al., Acta Met. 20 (1972) 191.

8. K. Natesan, W. K. Soppet, and M. Uz, viewgraphs presented at Vanadium Alloy Task Group Meeting, Argonne National Lab, April 8-9, 1996.

9. K. Shiraishi et al., in Tritium Technology and Radiation Effects for Fusion Technology, Eds. J. S. Watson and F. W. Wiffen, CONF-750989, Vol. II, p. 122.

10. G. Hörz et al., Z. Metallk. 56 (1965) 554.

GRAIN BOUNDARY MIGRATION INDUCED SEGREGATION IN V-Cr-Ti ALLOYS

D. S. Gelles (Pacific Northwest National Laboratory)[a] and S. Ohnuki and H. Takahashi (University of Hokkaido, Japan)

OBJECTIVE

The objective of this research is to assess effects of irradiation on microchemical stability in vanadium alloys for first wall applications in a fusion energy system.

SUMMARY

Analytical electron microscopy results are reported for a series of vanadium alloys irradiated in the HFIR JP23 experiment at 500°C. Alloys were V-5Cr-5Ti and pure vanadium which are expected to have transmuted to V-15Cr-5Ti and V-10Cr following irradiation. Analytical microscopy confirmed the expected transmutation occurred and showed redistribution of Cr and Ti resulting from grain boundary migration in V-5Cr-5Ti, but in pure V, segregation was reduced and no clear trends as a function of position near a boundary were identified.

PROGRESS AND STATUS

Introduction

The present work is part of an ongoing collaboration effort in the area of irradiation effects in vanadium alloys[1-4] and arose because of interest in using the JEOL 2010F analytical electron microscope at PNNL for high resolution microchemical segregation studies. Specimens of pure vanadium and V-5Cr-5Ti were included in the HFIR-JP23 experiment in order to study transmutation effects in vanadium alloys. It is of interest to note that the V-5Cr-5Ti alloy effectively transmuted to V-15Cr-5Ti, an early candidate composition previously studied.[1] Examination demonstrated that irradiation not only resulted in precipitation similar to that found in fast reactor irradiated V-15Cr-5Ti, but also led to radiation induced grain boundary migration. This report is intended to describe the segregation observed at these boundaries.

Experimental Procedure

Specimens UB06 of V-5Cr-5Ti and U006 of pure vanadium were examined following irradiation in the HFIR MFE-JP23 500°C Monbusho specimen holder.[5] The fluence accumulated was 4.23×10^{22} n/cm^2 (E total) corresponding to 10.02 dpa in pure vanadium.[6] It may be noted that irradiation of V-4Cr-4Ti in the HFIR core to 10 dpa will produce approximately 10% additional chromium.[7] Specimen preparation and examination followed standard procedures. Examinations were performed on a JEOL 2010F transmission electron microscope operating at 200 KeV with a field emission gun and compositional analysis used an Oxford Instruments ISIS system with a thin window detector.

Results

---

[a]Operated for the U.S. Department of Energy by Battelle Memorial Institute under Contract DE-AC06-76RLO 1830.

Results

Specimen UB06 of V-5Cr-5Ti was found to be remarkably similar to specimens of V-15Cr-5Ti irradiated in FFTF.[1] Chromium levels had been increased to about 13% by transmutation and extensive precipitation consisting of both large and small rod shaped particles was found. Compositional analysis of precipitates contained in the foil only indicated enrichment of Ti.

However, in the course of observation, it became apparent that significant grain boundary migration had occurred, providing the possibility for grain boundary segregation measurements. Figure 1 gives examples of two areas along the same grain boundary in specimen UB06 chosen for chemical analysis. Figure 1a contains a section of boundary which did not appear to have moved due to irradiation whereas Figure 1b contains a very convoluted grain boundary which has moved from its original position. In each figure, fiducial numbers have been added to define areas used for compositional analysis. Figures 1c, d and e give those composition measurements as a function of distance from the position of the grain boundary prior to irradiation, so that Figure 1c represents the case for the grain boundary that did not migrate shown in Figure 1a and Figures 1d and 1e show behavior in Figure 1b for grain boundary migration of several hundred nm. Each composition plot is labelled to show the starting position, and where different, the final position of the grain boundary. From these figures, it can be concluded that compositional changes are small but there appears to be enrichment of Cr and depletion of Ti in the vicinity of the grain boundary path, with changes as large as 2%. It can also be noted that Si was measured in the specimen at levels between 0.3 and 1.3%, but no consistent trends for Si could be identified.

Specimen U006 of pure vanadium was similar except that titanium was not present. Chromium levels had been increased to about 8.5% by transmutation, and silicon levels ranged from 0.3 to 1.5%. However, rod shaped precipitates were not found, corroborating conclusions that such precipitates are titanium rich. Specimen U006 also contained examples of large scale grain boundary migration. Figure 2a and b show two grain boundaries where sections of the boundary had moved. These figures are also marked with fiducial numbers corresponding to areas for which compositional analysis was performed so that in each case one boundary section had not moved and a second section had moved 400 or 500 nm. The analyses as a function of distance from the original grain boundary position are given in Figures 2c, and d for Figure 2a and Figures 2e and f for Figure 2b. Figures 2e and f include duplicate measurements, for a second series of measurements performed after the first was completed. From these figures, it can be concluded that segregation following irradiation was small, that scatter in the data was as large as any segregation measured, and there were no clear trends as a function of position relative to a grain boundary.

Discussion

Definition of a candidate vanadium alloy for fusion applications appears to require fairly precise control of the levels of alloying elements used.[8] The present work appears to indicate that solute segregation accompanying irradiation induced grain boundary migration does not significantly alter local chemistries. For example, local chromium and titanium levels are altered only by about 2% following irradiation to 10 dpa at 500°C. Therefore, it can be anticipated that precise control of composition is not unreasonable in light of the level of segregation that can result during irradiation. However, this work does demonstrate the importance of radiation induced grain boundary migration and the consequent instability of the microstructure for grain growth during irradiation.

CONCLUSIONS

Radiation induced solute segregation in association with extensive grain boundary migration has been

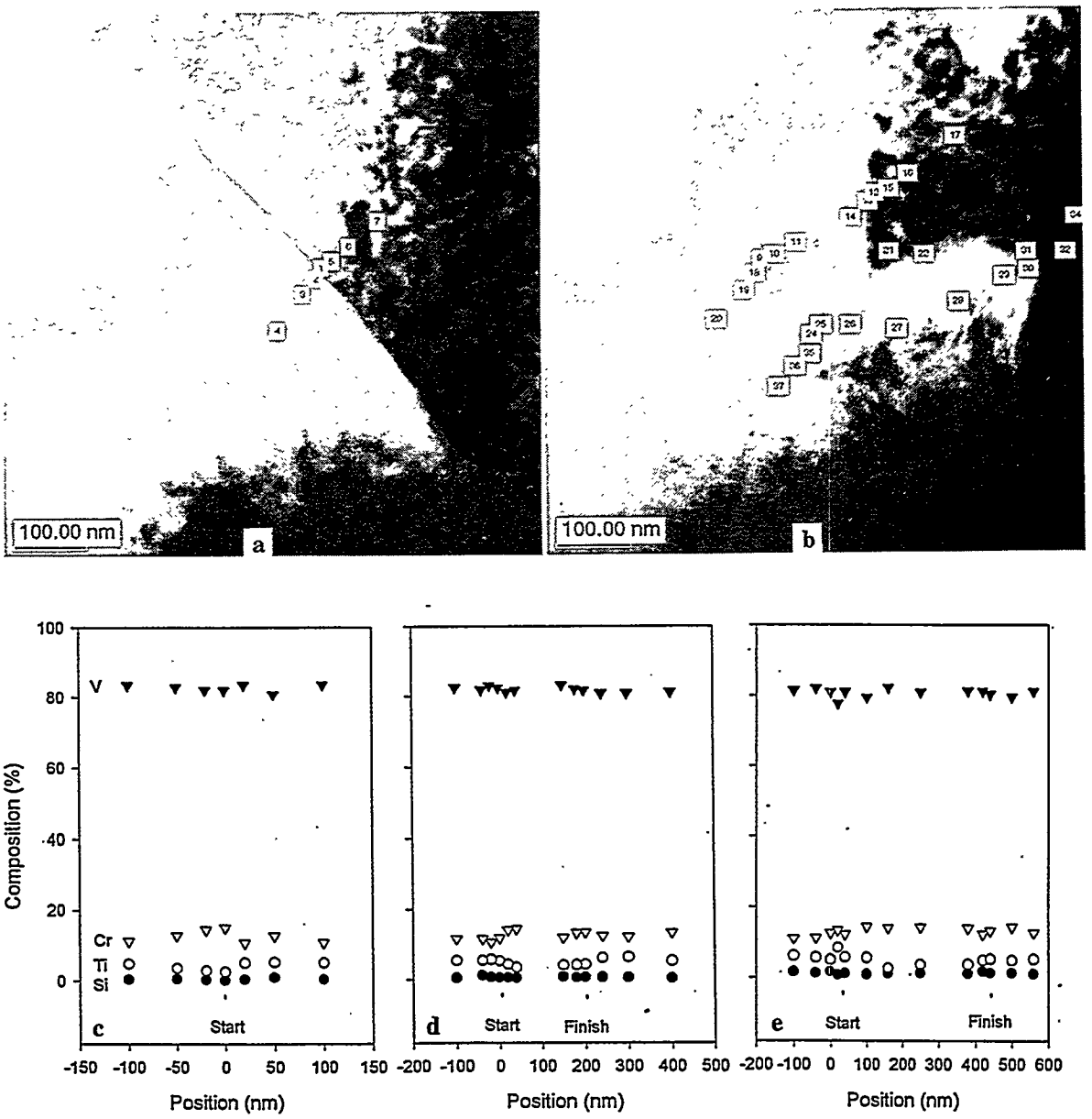

Figure 1 Two sections of a grain boundary in specimen UB06 of V-5Cr-5Ti following irradiation at 500°C to 10 dpa, a), and b), and compositional analysis for locations indicated c), d), and e).

measured in two experimental alloys, V-5Cr-5Ti and pure vanadium following irradiation at 500°C to 10 dpa in the HFIR JP23 experiment. Results indicate that Cr levels are increased by about 8% due to transmutation, and up to 2% enrichment in Cr and 2% depletion in Ti occurs at grain boundaries in V-5Cr-5Ti whereas in pure vanadium, segregation was reduced and no clear trends as a function of position near a boundary were identified.

Future work

This work will be resumed when suitable specimens are available.

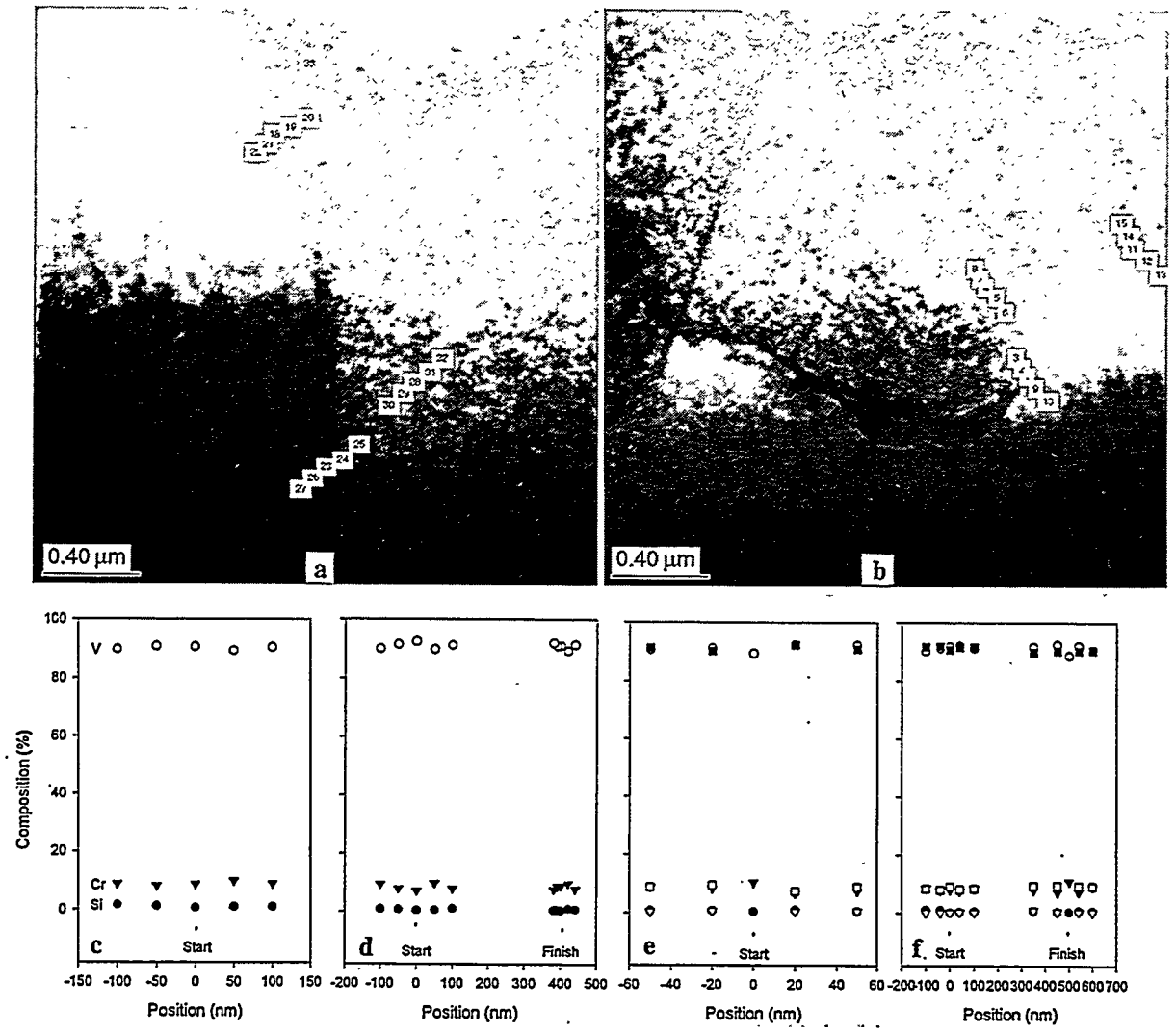

Figure 2 Two grain boundaries in specimen U006 of pure vanadium following irradiation at 500°C to 10 dpa, a), and b), and compositional analysis for locations indicated c), d), e), and f).

REFERENCES

1 D. S. Gelles, S. Ohnuki, B. A. Loomis, H. Takahashi, and F. A. Garner, in DOE/ER-0313/7 (1989) 193.

2 S. Ohnuki, D. S. Gelles, B. A. Loomis, H. Takahashi, and F. A. Garner, in DOE/ER-0313/7 (1989) 177.

3 S. Ohnuki, H. Kinoshita, F. A. Garner, and H. Takahashi, in DOE/ER-0313/19 (1996) 92.

4 S. Ohnuki, H. Takahashi, F. A. Garner, J. E. Pawel, K. Shiba and A. Hishinuma in DOE/ER-0313/19 (1996) 93.

5 A. M. Ermi and D. S. Gelles, in DOE/ER-0313/17 (1994) 35.

6 L. R. Greenwood and R. T. Ratner, to be published in Fusion Materials Semiannual Progress Report for the Period Ending June 30, 1996, DOE/ER-0313/20.

7 I. C. Gomes and D. L. Smith, in DOE/ER-0313/16 (1994) 33.

8 B. A. Loomis, H. M. Chang, L. J. Nowicki and D. L. Smith, J. Nucl. Mater., 212-215 (1994) 799.

HELIUM EFFECTS ON IRRADIATION DAMAGE IN V ALLOYS

N. Doraiswamy and D. Alexander (Argonne National Laboratories)

OBJECTIVE

The objective of this study is to determine the role of He in the microstructural evolution of V-4Cr-4Ti subjected to a fusion radiation environment by insitu monitored 200keV He ion irradiations using the ion accelerator/intermediate voltage electron microscopy facility at Argonne National laboratories.

SUMMARY

Preliminary investigations were performed on V-4Cr-4Ti samples to observe the effects of He on the irradiation induced microstructural changes by subjecting 3mm electropolished V-4Cr-4Ti TEM disks, with and without prior He implantation, to 200kev He irradiation at room temperature and monitoring, insitu, the microstructural evolution as a function of total dose with an intermediate voltage electron microscope directly connected to an ion implanter. A high density of black dot defects were formed at very low doses in both He pre-implanted and unimplanted samples.

INTRODUCTION

Vanadium alloys have been shown to have substantial advantages for use as structural materials in fusion devices. Among these alloys, V-4Cr-4Ti has been shown to exhibit excellent physical and mechanical properties, both, before and after irradiation. However, the effect of helium on this alloy has still not been fully understood. Recent simulations of the fusion environment using the DHCE experiment[1] have indicated that the mechanical properties of vanadium alloys are altered by the presence of helium in post-irradiation tests performed at room temperature. While the strengths were lower, room temperature ductilities of the DHCE specimens were higher than those of non-DHCE specimens. The changes have been attributed to the formation of different types of hardening centers in these alloys. Independent thermal desorption experiments[2-4] suggest that these hardening centers may be associated with helium-vacancy-impurity (for example O, N, and C) complexes. These complexes are stable below 290°C and persist at room temperature. However, there has been no direct evidence correlating the complexes with the irradiation induced microstructure.

This work is a report of our efforts to determine the role of helium on the microstructural evolution of irradiated vanadium alloys by in-situ Transmission Electron Microscopy (TEM) observations of ion irradiated V-4Cr-4Ti

MATERIALS AND PROCEDURES

3mm disks were punched from a 10 mil sheet of V-4Cr-4Ti (Heat ID 832665) which had been subjected to a series of extrusion and rolling processes as described in reference[5]. The disks were then annealed in an inert Ar atmosphere for 1 hour at 1000°C and electropolished to electron transparency. He was implanted into the foils at an energy of 40keV to a total of 500appm at room temperature. The energy of 40keV was chosen as computer simulations using TRIM code[6] showed that it produced the He concentration with damage to the foil. Both the as-prepared and He-implanted samples were ion irradiated with 200keV He ions at room temperature. All the ion irradiation and experimental observations were conducted at the ion accelerator/intermediate voltage electron microscopy facility operated by the Materials Science Division at Argonne National Laboratory.

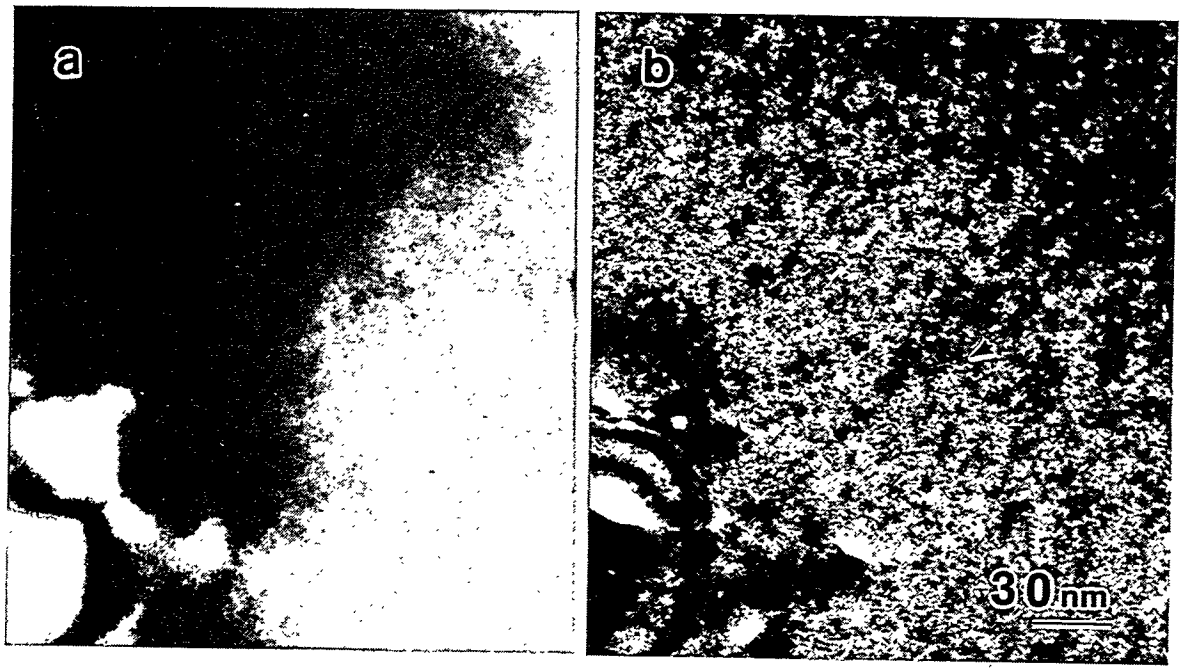

Figure 1: (a) A typical two beam dark field TEM micrograph using the (200) reflection of an unirradiated V-4Cr-4Ti crystal. (b) The same region after 200keV He irradiation imaged using the same two beam conditions. The arrow indicates a black dot defect.

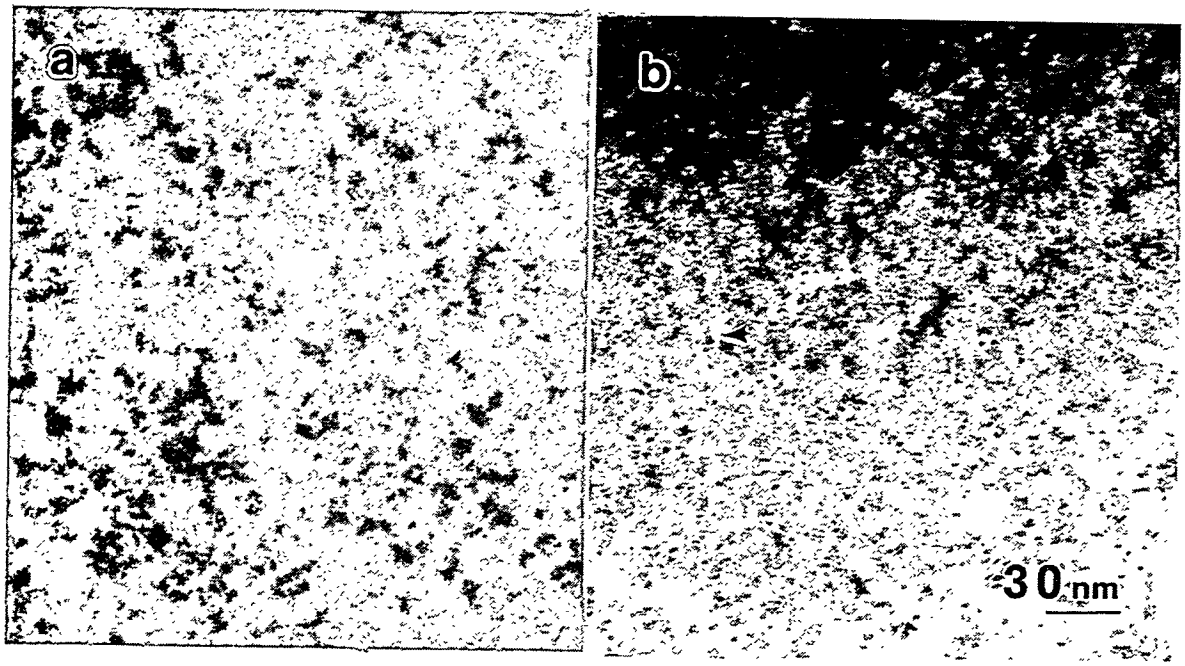

Figure 2: (a) A characteristic two beam dark field TEM micrograph using the (200) reflection of an unirradiated V-4Cr-4Ti crystal pre-implanted with 500 appm He. (b) The same region after 200keV He irradiation imaged using the same two beam conditions. The arrow indicates a black dot defect.

EXPERIMENTAL RESULTS

Fig 1(a) is a typical two beam dark field TEM micrograph using the 200 reflection of an unirradiated V-4Cr-4Ti sample and Fig1(b) that of the same region after irradiation, using the same two beam conditions. The images show the formation of black dot defects with no clear black white lobe contrast. There was no indication of a ring or additional spots in the diffraction pattern which is suggestive of the lack of formation of precipitates. The black dot defects formed at very low doses(6.9×10^{-3} dpa). Similar results were obtained for the He implanted samples. These are shown in fig2. Further analysis is being carried out to determine the number density and size of the defects as functions of the total dose.

FUTURE WORK:

A series of higher dose of He irradiation are planned to be conducted on both the unimplanted and implanted V-4Cr-4Ti samples at room temperature and temperatures greater than 290°C. The study will allow for the determination of the effect of He and the role of He-vacancy-interstitial complexes by the microstructural change in size and density of defects generated in V-4Cr-4Ti.

REFERENCES

1. Chung, H.M., *et al. Effect of dynamically charged helium on tensile properties of V-5Ti, V-4Cr-4Ti, and V-3Ti-1Si.* in *Fusion Reactor Materials, Semiannual. Progress Report.* 1995. **DOE/ER-0313/18.** Oak Ridge National Laboratories, Oak Ridge, TN.
2. Van Veen, A., H. Eleveld, and M. Clement, *Helium impurity interactions in vanadium and niobium.* Journal of Nuclear materials, 1994. **212-215**: p. 287-292.
3. Ryazanov, A.I., V.M. Manichev, and W. Van Witzenburg, *Influence of helium and impurities on the tensile properties of irradiated vanadium alloys.* Journal of Nuclear materials, 1996. **227**: p. 304-311.
4. Fedorov, A.V., *et al., Helium desorption studies on vanadium and V-5Ti and V-3Ti-1Si alloys and their relevance to helium embrittlement.* Journal of Nuclear materials, 1996. **227**: p. 312-321.
5. Chung, H.M., *et al., Fabrication of 500kg heat of V-4Cr-4Ti.* Fusion Reactor Materials, Semiannual Progress Reports, 1994. **DOE/ER-0313/17.** Oak Ridge National Laboratories, Oak Ridge, TN
6. Ziegler, J.F., *TRIM-The Transport of Ions in Matter.* Vol. Version 92, Yorktown, NY: IBM Research.

STUDY OF IN-REACTOR CREEP OF VANADIUM ALLOY IN THE HFIR RB-12J EXPERIMENT*

R. V. Strain, C. F. Konicek, and H. Tsai (Argonne National Laboratory)

SUMMARY

Biaxial creep specimens will be included in the HFIR RB-12J experiment to study in-reactor creep of the V-4Cr-4Ti alloy at ≈500°C and 5 dpa. These specimens were fabricated with the 500-kg heat (832665) material and pressurized to attain 0, 50, 100, 150, and 200 MPa mid-wall hoop stresses during the irradiation.

OBJECTIVE

The objective of this task was to investigate the in-reactor creep of the 832665 heat of V-4Cr-4Ti alloy at ≈500°C and 5 dpa. Comparable creep specimens were included in the ATR-A1 experiment at ≈200 and 300°C.

SPECIMEN DESIGN AND TEST MATRIX

The creep specimens are 0.180 in. OD x 0.160 in. ID x 1.0 in. long drawn tubes with welded end plugs. The construction of these creep specimens is identical to that used in the ATR-A1 experiment.

The design mid-wall hoop stresses are 0, 50, 100, 150, and 200 MPa at the target irradiation temperature of 500°C. These stresses will allow the determination of creep rates over a wide range with no undue risk of specimen failure. Furthermore, they permit a direct comparison with the lower-temperature ATR-A1 test data at 0, 100, 150, and 200 MPa.

FABRICATION OF CREEP SPECIMENS

The procedure used for fabricating the HFIR RB-12J creep specimens is essentially the same as that used for the ATR-A1 experiment.

- Perform X-ray radiography with machined defect standards to determine the condition of the as-drawn tubing.
- Produce 1-in.-long tube blanks from defect-free regions of the tubing.
- Measure the ID, OD, thickness, concentricity, and roundness of the tube blanks.
- Produce end plugs from 832665-heat plate stock with electrode discharging machining (EDM).
- Clean the machined end plugs with nitric acid to remove residual copper from the EDM brass wire. (Residual copper caused intergranular cracking in some qualification welds.)
- Clean all tube blanks and end plugs with a pickling solution (HF/HNO_3/lactic acid) and alcohol.
- Weld the top and bottom end plugs to the tube blanks with an electron-beam welder.
- Perform visual and radiographic inspections of the girth welds.
- Measure the diameters of the specimens with a laser profilometer at five axial locations (0.1, 0.3, 0.5, 0.7, 0.9 in.) and every 10° azimuthal.
- Anneal the specimens at 1000°C for 1.0 h in vacuum, with each specimen wrapped in a Ti getter foil.
- Pressurize the specimens with high-purity helium and seal the vent hole in the top end plug with a laser.
- Perform helium leak check, weighing, and length measurement of each specimen.
- Repeat the diameter measurements with the laser profilometer.
- Package the specimens for shipment.

*Work supported by U.S. Department of Energy, Office of Fusion Energy Research, under Contract W-31-109-Eng-38.

The required room-temperature pressurization of the specimens was determined with a PNNL-supplied computer program, "FILPRESS.BAS," which takes into account thermal expansion of the vanadium tube and helium compressibility. The design values and the actual pressure loading in the specimens are compared in Table 1. Dimensions of the pressurized specimens are shown in Table 2.

Six archival creep specimens (identical to the test specimens in every way except without pressurization) were produced and are in protective storage along with the qualification welds.

Table 1. Design and Actual Pressure Loading in Vanadium Alloy Creep Specimens for HFIR RB-12J Experiment

Specimen No.	Design Mid-Wall Hoop Stress (MPa)	Design Pressure Loading (psi)	Actual Pressure Loading (psi)
B1	0	3	8
B12	50	360	363
B11	100	720	727
B3	150	1082	1083
B9	150	1082	1086
B5	200	1448	1446

Table 2. Dimensions of Vanadium Alloy Creep Specimens for the HFIRRB-12J Experiment

	Azimuthally-Averaged Diameter (in.) at Axial Locations of					
Specimen No.	0.1 in.	0.3 in.	0.5 in.	0.7 in.	0.9 in.	Specimen Length (in.)
B1 (0 MPa)	0.18002	0.17997	0.18000	0.18000	0.18002	1.002
B12 (50 MPa)	0.17980	0.17979	0.17978	0.17979	0.17976	1.013
B11 (100 MPa)	0.17984	0.17982	0.17982	0.17981	0.17985	1.017
B3 (150 MPa)	0.17997	0.18000	0.18001	0.18001	0.18001	1.007
B9 (150 MPa)	0.17991	0.17989	0.17988	0.17987	0.17994	1.012
B5 (200 MPa)	0.17999	0.17995	0.17997	0.17997	0.17994	1.000

FUTURE ACTIVITIES

At ORNL, the specimens will be loaded in semisealed Zr getter enclosures before being placed in the RB-12J vehicle. The purpose of the getter enclosures is to prevent excessive impurity pickup from the flowing helium environment during irradiation. The locations in the vehicle selected for the specimens are such that all six specimens will receive approximately the same neutron and thermal exposure during irradiation.

The RB-12J irradiation is expected to produce ≈5 dpa neutron damage in the specimens. After irradiation, the specimens will be retrieved and the diameters will be measured again with the same profilometer and the same procedure. The creep rates will be determined from the measurements and compared with those of the ATR-A1 specimens irradiated at lower temperatures. Microstructural characterization will be performed to elucidate the observed creep behavior.

OXIDATION KINETICS AND MICROSTRUCTURE OF V-(4-5) WT.%Cr-(4-5) WT.%Ti ALLOYS EXPOSED TO AIR AT 300-650°C*

K. Natesan (Argonne National Laboratory) and M. Uz (Lafayette College, Easton, PA)

OBJECTIVE

The objectives of this task are to (a) evaluate the oxygen uptake of V-Cr-Ti alloys as a function of temperature and oxygen partial pressure in the exposure environment, (b) examine the microstructural characteristics of oxide scales and oxygen trapped at the grain boundaries in the substrate alloys, and (c) evaluate the influence of oxygen uptake on the tensile properties of the alloys at room and elevated temperatures.

SUMMARY

A systematic study was conducted to determine the effects of time and temperature of air exposure on the oxidation behavior and microstructure of V-4Cr-4Ti (44) and V-5Cr-5Ti (55) alloys. All samples were from 1-mm-thick cold-rolled sheets, and each was annealed in vacuum at 1050°C for 1 h prior to high-temperature exposure. Different samples from each alloy were heated in ambient air at 500°C for times ranging from 24 to ≈2000 h, and in a thermogravimetric analysis (TGA) apparatus at 300 to 650°C. Models describing the oxidation kinetics, the oxide type and its thickness, alloy grain size, and the depth of oxygen diffusion in the substrate alloy were determined for the two alloys and compared. The results showed that the oxide layers that formed on the surfaces of both alloys in air in the temperature range of 300-650°C are protective, and that the 55 alloy is slightly more oxidation-resistant than the 44 alloy.

EXPERIMENTAL PROGRAM

The 44 and 55 alloys were obtained as 1-mm-thick cold-rolled sheets. Samples with dimensions of about 1 x 10 x 20 mm were cut from each alloy. Before any further treatment or testing, all samples were annealed for 1 h at 1050°C under a pressure of $\approx 10^{-6}$ torr. The samples were wrapped in tantalum foil to protect them from contamination during this heat treatment process. Samples from each alloy were analyzed for chemical composition before and after annealing, and the results can be seen in Table 1. As shown, the total amount of other impurities in either alloy was less than 0.3%, with silicon (Si) as the major impurity at ≈0.08%.

Samples from the 44 and 55 alloys were heated in air at 500°C for about 24, 250, 600, 1050, and 2100 h to study the effects of time on their oxidation behavior. Samples from each alloy were also heated in a TGA apparatus in air at different temperatures to determine oxidation kinetics as a function of temperature. The TGA experiments were carried out at 320, 400, 500, 575, and 620°C for the 44 samples, and at 300, 400, 500, 575, and 650°C for the 55 samples. Weight gain was recorded continuously on a strip chart throughout each experiment.[1,2] All samples were also weighed separately before and after any high-temperature exposure to determine the resulting total weight change.

The oxide scales on the samples were identified by X-ray diffraction (XRD) analysis on the surfaces of several samples, as well as on the oxides scraped from their surfaces. Oxide residues obtained from the 44 and 55 alloys exposed to air at 500°C for 2100 h by dissolving away the matrix were analyzed for the V, Cr, and Ti using the inductively coupled plasma (ICP) technique. A 900 mL methanol-100 mL bromine-10 g tartaric acid was used for phase extraction with platinum wire as the catalyst. Metallographic examination of the longitudinal and transverse cross-sections of the cold-rolled and thermally treated samples used both an optical microscope and a scanning electron microscope (SEM).

The metallographic specimens were chemically etched with a solution of lactic-nitric-hydrofluoric acids at a volume ratio of 30-15-5. The grain size of each sample exposed to high temperature (annealed or air-oxidized) was determined by both lineal and areal analysis methods according to ASTM Standard E112, and

*This work has been supported by the U.S. Department of Energy, Office of Fusion Energy Research, under Contract W-31-109-Eng-38.

the average of the two was reported as the grain size of each sample. Oxygen diffusion depth (or the depth of the hardened layer) of each oxidized sample was estimated from the microhardness profile along its thickness, which was obtained with a Vickers microhardness tester and a load of 25-50 g. Furthermore, the oxygen profiles of several samples were determined by secondary ion mass spectroscopy (SIMS) line profiles along the thickness to verify the results obtained by the microhardness measurements.

All data in this study were processed and analyzed with a spreadsheet program capable of graphical, statistical, and regression analyses.

RESULTS AND DISCUSSION

The results of the TGA experiments (carried out to determine the oxidation behavior of the 44 and 55 alloys in the temperature range of 300-650°C) are tabulated in Table 1, with the sample and the oxidation temperature given in columns 1 and 2, respectively. In column 3, the first equation at each temperature represents the oxidation model that best fit the experimental data. The second equation represents the parabolic model and provides a more conservative rate constant (coefficient of time) at that temperature. In the first two equations, w_f and w_p have the units of $mg \cdot mm^{-2}$, and time t is in hours (h). The third equation in column 3 at each temperature, x with units of $mm^2 \cdot h^{-1}$, was obtained by dividing the first equation by the square of density which is 3.357 $g \cdot cm^{-3}$ (or $mg \cdot mm^{-3}$), and is provided to allow ready estimation of the scale thickness, x, for any desired time at each temperature. The coefficient of time (t) in each equation is the rate constant (denoted by k in general, and by k_f, k_p or k_x depending on the models described in Table 1) at the corresponding temperature with the units as indicated.

No measurable weight gain was observed in the 55 alloy oxidized at 300°C. The TGA data for the 44 and 55 alloys are presented in Fig. 1 as plots of weight gain versus time. In these plots, the lines represent the oxidation models that best fit the experimental data, which are shown as circles for the 44 samples and as squares for the 55 samples. The results show that in both alloys, oxidation (scale growth) occurs according to a nonlinear growth rate law, and the rate of oxidation decreases with time, indicating a protective oxide scale. Together with the lack of spalling of the scale, these results provide evidence that V_2O_5 forms as a nonporous and tenacious oxide on the surface of 44 and 55 alloys in the temperature range of 350-650°C. As can be seen from the plots in Fig. 1, oxidation rate increased with increasing temperature. As expected, the temperature-dependence of the rate constant was in Arrhenius form, and the data for both alloys fit well an equation of the form

$$k = k_0 \exp[Q_{ox}/(RT)], \quad (1)$$

where k is the rate constant, (k_f, k_p or k_x), k_0 is the pre-exponential constant, Q_{ox} is the activation energy for the oxidation process, and R and T are the gas constant and absolute temperature, respectively. The Arrhenius plots for the 44 and 55 alloys are shown in Fig. 2, which indicates little difference between the rate constants at a given temperature and the slope of the line for the two alloys, with those for the 44 slightly higher. While the oxide that forms on both alloys is predominantly V_2O_5, the slightly higher oxidation resistance of the 55 alloy is attributable to its slightly higher substitutional alloying content, especially Ti, which is known to trap oxygen and slow its diffusion in the matrix. This may also be due to the larger average grain size of the 55 alloy, which means less grain boundary area and thus allowing a fast transport path for oxygen. The activation energies for the air-oxidation process as determined from Fig. 2 were about 135 kJ/mol for the 44 alloy and 130 kJ/mol for the 55 alloy.

Oxidation rate constants, and data for diffusion of O in V and its alloys with Cr and/or Ti and in V_2O_5, are tabulated in Table 2, data sources are identified. The rate constants for the 44 and 55 alloys in column 2 were obtained from the variation of the measured oxide scale thickness with time, and those in column 3 are from the oxidation models developed from the TGA results. Data for oxygen diffusion in V and its alloys, as well as in the oxides that form on them, are given in columns 4-7 of the table; values for the 44 and 55 alloys are from this work, and those for others are from the literature as indicated. The diffusion coefficients, D, of O in the 44 and 55 alloys were determined from the oxygen diffusion distance-time data assuming one-dimensional diffusion, which should be valid on the basis of the geometry of the samples

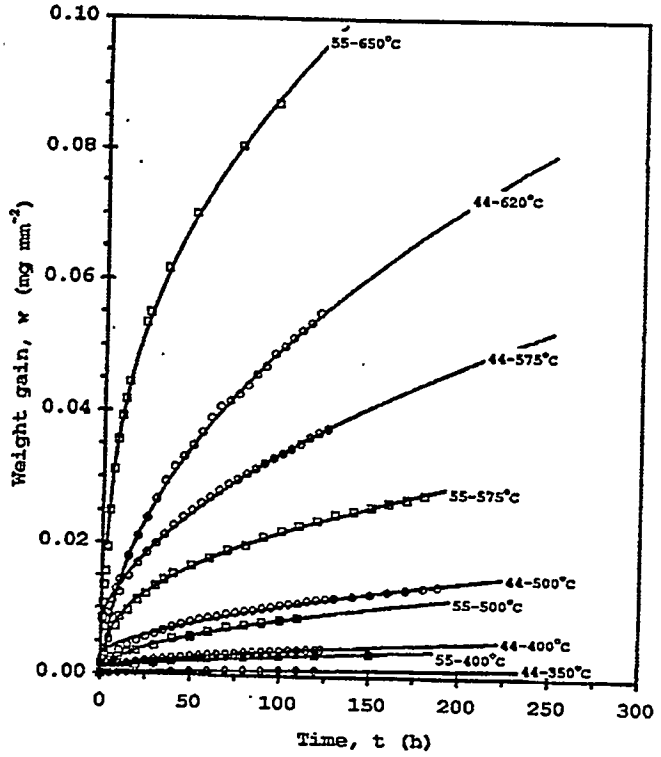

Fig. 1 Variation of weight gain with time in air for 44 and 55 alloys. At each temperature, data points are from TGA experiments, and solid lines represent model that best describes the oxidation behavior of the alloy

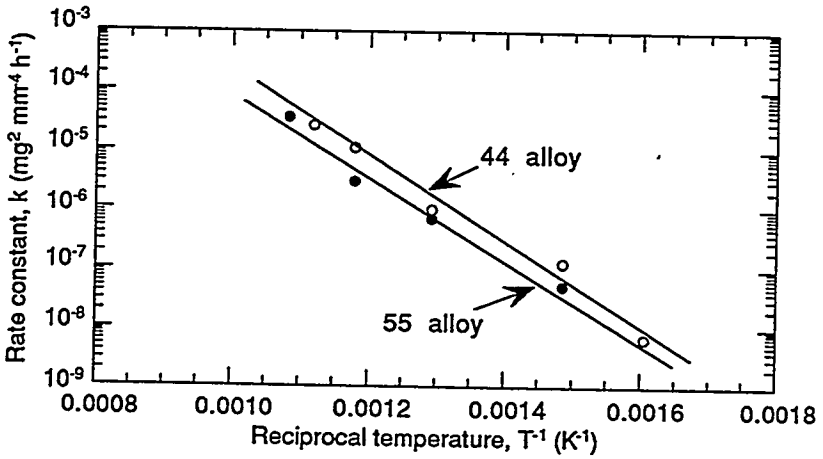

Fig. 2 Arrhenius plots of oxidation rate constants for 44 and 55 alloys exposed to air at temperatures up to 650°C

Table 1. Mathematical models describing oxidation behavior of V-4 wt.%Cr-4 wt.%Ti (44) and V- 5 wt.%Cr-5 wt.%Ti (55) alloys as obtained using data from TGA experiments.[a]

Alloy	T (°C)	Oxidation model	R^2
44	350	$w_f^2 = -1.77 \times 10^{-8} + 6.76 \times 10^{-9}\ t$	0.999
		$w_p^2 = 6.54 \times 10^{-9}\ t$	0.997
		$x^2 = -1.57 \times 10^{-9} + 6.00 \times 10^{-10}\ t$	
44	400	$w_f^2 = 1.31 \times 10^{-6} + 1.28 \times 10^{-7}\ t$	0.999
		$w_p^2 = 1.43 \times 10^{-7}\ t$	0.984
		$x^2 = 1.16 \times 10^{-7} + 1.14 \times 10^{-8}\ t$	
44	500	$w_f^2 = 1.17 \times 10^{-5} + 9.82 \times 10^{-7}\ t$	1.0
		$w_p^2 = 1.08 \times 10^{-6}\ t$	0.992
		$x^2 = 1.04 \times 10^{-6} + 8.71 \times 10^{-8} t$	
44	575	$w_f^2 = 7.81 \times 10^{-5} + 1.07 \times 10^{-5}\ t$	1.0
		$w_p^2 = 1.16 \times 10^{-5}\ t$	0.998
		$x^2 = 6.93 \times 10^{-6} + 9.50 \times 10^{-7}\ t$	
44	620	$w_f^2 = -5.40 \times 10^{-5} + 2.54 \times 10^{-5}\ t$	1.0
		$w_p^2 = 2.48 \times 10^{-5}\ t$	0.998
		$x^2 = -4.79 \times 10^{-6} + 2.25 \times 10^{-6}\ t$	
55	†300		
55	400	$w_f^2 = -3.88 \times 10^{-7} + 4.13 \times 10^{-7}\ t^{1/2} + 5.23 \times 10^{-8}\ t$	0.999
		$w_p^2 = 8.90 \times 10^{-8}\ t$	0.997
		$x^2 = -3.44 \times 10^{-8} + 3.67 \times 10^{-8}\ t^{1/2} + 4.64 \times 10^{-9}\ t$	
55	500	$w_f^2 = 1.16 \times 10^{-8} + 7.02 \times 10^{-7}\ t$	0.999
		$w_p^2 = 7.07 \times 10^{-7}\ t$	0.977
		$x^2 = 1.03 \times 10^{-9} + 6.23 \times 10^{-8}\ t$	
55	575	$w_f^2 = -1.78 \times 10^{-5} + 2.02 \times 10^{-5} t^{1/2} + 2.94 \times 10^{-6}\ t$	1.0
		$w_p^2 = 4.59 \times 10^{-6}\ t$	0.986
		$x^2 = -1.58 \times 10^{-6} + 1.79 \times 10^{-6}\ t^{1/2} + 2.61 \times 10^{-7}\ t$	
55	650	$w_f^2 = -3.77 \times 10^{-4} + 4.88 \times 10^{-4}\ t^{1/2} + 3.48 \times 10^{-5}\ t$	0.998
		$w_p^2 = 8.99 \times 10^{-5}\ t$	0.946
		$x^2 = -3.35 \times 10^{-5} + 4.33 \times 10^{-5}\ t^{1/2} + 3.09 \times 10^{-6}\ t$	

[a]The three equations at each temperature correspond to best fit of the experimental data, parabolic model, and scale thickness.

†No measurable weight gain was observed for this specimen.

The last column indicates the degree of fit obtained from the regression analysis of data.

Table 2. Rate constants for oxidation of V and V-4 wt.%Cr-4 wt.%Ti (44) and V-5 wt.%Cr-5wt.%Ti (55) alloys, and calculated values of diffusion coefficients at 500°C, and activation energies of diffusion of oxygen in V_2O_5 under conditions indicated.

Alloy[a]	T (°C)	pO_2 (torr)	Oxide	Rate constant[b] ($mg^2 \cdot mm^{-4} \cdot h^{-1}$) ($k \times 10^9$)	D[c] ($m^2 \cdot h^{-1}$) ($D \times 10^{15}$)	Q_D[d] ($kJ \cdot mol^{-1}$)
V	450	760	V_2O_5	201	497	174.4
V	500	7.6	VO_2	367	56.9	193.6
V	500	760	V_2O_5	2740	630	164.7
V	550	3	VO_2	918	142	202.7
V	550	9	VO_2	1920	297	194.3
V	550	36	VO_2	2100	338	192.8
V	550	760	V_2O_5	8530	1980	172.0
V	600	1	VO_2	2880	446	209.7
V	600	4	VO_2	6160	954	200.1
V	600	7.6	VO_2	7420	1150	197.8
V	600	760	V_2O_5	19600	4500	179.9
V	650	0.76	VO_2	4790	742	224.5
V	650	7.6	VO_2	10800	1680	213.1
44	350	160	V_2O_5	6.76	1.6	165.6
44	400	160	V_2O_5	128	29.3	161.0
44	500	160	V_2O_5	982	225	178.0
44	575	160	V_2O_5	10700	2460	179.0
44	620	160	V_2O_5	25400	5830	184.0
55	400	160	V_2O_5	52.3	12	168.4
55	500	160	V_2O_5	702	161	181.7
55	575	160	V_2O_5	2940	673	194.0
55	650	160	V_2O_5	34780	7980	191.0

[a]Data on V are from Ref. 3, and those on 44 and 55 are from this study.

[b]Rate coefficients for V are coefficients of time in a parabolic oxide growth rate model, and those for 44 and 55 alloys are coefficients of time in oxidation models that best fit the data in Table 1.

[c]Calculated at 500°C with rate constants in Table 2.

[d]Calculated with D values in Table 2.

used in this study. Using these diffusion coefficients, we calculated the activation energies of diffusion of oxygen in these alloys. The good agreement between the rate constant calculated from the measured data and that from the model for both the 44 and 55 alloys indicates once again that the models developed in this study describe the oxidation behavior of these alloys rather well. The diffusion coefficients were greater for oxygen diffusion in the 44 alloy than in the 55 alloy, and their magnitudes were between those of the V-5Cr and V-5Ti alloys. The activation energy of oxygen diffusion was, as expected, greater for the 55 alloy than for the 44 alloy. However, the activation energies of oxygen diffusion in both alloys were greater than those in unalloyed V and V-5Cr alloy, but considerably lower than that in V-5Ti alloy. These trends may be attributed to the binding or trapping of O by the Ti atoms that are in solid solution. On the other hand, the activation energies for the diffusion of oxygen in the oxides that formed on V and on the 44 and 55 alloys were within 10% of one another. This strongly indicates that the oxides that formed on these

materials were similar in nature, namely V_2O_5.

REFERENCES

[1] K. Natesan and W. K. Soppet, "Effect of Oxidation on Tensile Properties of a V-5Cr-5Ti Alloy," Proc. 2nd Intl. Conf. Heat-Resistant Materials, eds. K. Natesan, P. Ganesan, and G. Lai, ASM International, September 11-14, 1995, Gatlinburg, TN, 375.

[2] K. Natesan and W. K. Soppet, "Effect of Oxygen and Oxidation on Tensile Properties of V-5Cr-5TiAlloy," J. Nucl. Mater. in press.

[3] A. Mukherjee and S. P. Wach, J. Less-Common Metals, 92 (1983) 289.

CaO INSULATOR COATINGS ON A VANADIUM–BASE ALLOY IN LIQUID 2 at.% CALCIUM-LITHIUM*

J.–H. Park and T. F. Kassner (Argonne National Laboratory)

OBJECTIVE

In the design of liquid–metal blankets for magnetic fusion reactors, corrosion resistance of structural materials and magnetohydrodynamic (MHD) forces and their influence on thermal hydraulics and corrosion are major concerns. The objective of this study is to develop stable in–situ coatings at the liquid–metal/structural–material interface, with emphasis on coatings that can be converted to an electrically insulating film to prevent adverse currents that are generated by MHD forces from passing through the structural walls.

SUMMARY

The electrical resistance of CaO coatings produced on V-4%Cr-4%Ti and V-15%Cr-5%Ti by exposure of the alloy (round bottom samples 6–in. long by 0.25–in. dia.) to liquid lithium that contained 2 at.% dissolved calcium was measured as a function of time at temperatures between 300–464°C. The solute element, calcium in liquid lithium, reacted with the alloy substrate at these temperatures for 17 h to produce a calcium coating ≈7-8 μm thick. The calcium–coated vanadium alloy was oxidized to form a CaO coating. Resistance of the coating layer on V-15Cr-5Ti, measured in-situ in liquid lithium that contained 2 at.% calcium, was 1.0×10^{10} Ω-cm^2 at 300°C and 400 h, and 0.9×10^{10} Ω-cm^2 at 464°C and 300 h. Thermal cycling between 300 and 464°C changed the resistance of the coating layer, which followed insulator behavior. Examination of the specimen after cooling to room temperature revealed no cracks in the CaO coating. The coatings were evaluated by optical microscopy, scanning electron microscopy (SEM), electron dispersive spectroscopy (EDS), and X-ray analysis. Adhesion between CaO and vanadium alloys was enhanced as exposure time increased.

INTRODUCTION

Electrically insulating and corrosion–resistant coatings are required at the liquid–metal/structural interface in a fusion reactor to minimize magnetohydrodynamic forces and their influence on the thermal hydraulics of liquid–metal cooling systems.[1] Vanadium and vanadium–base alloys (V–Ti or V–Ti–Cr) are leading candidate materials for structural applications in fusion reactors.[2] In–situ formation of CaO on V–5Cr–5Ti in liquid lithium was investigated because the electrical resistivity of CaO is very high and also because CaO exhibits a higher thermodynamic stability in liquid lithium than do other potential insulator candidates (Y_2O_3, BeO, MgO, $MgAl_2O_4$, $Y_3Al_2O_{12}$, etc.).[3] In–situ self–healing behavior of defects (such as cracks in the coating) in liquid–lithium environments[4] is also an important consideration. These coatings should be formable on various shapes such as the inside of tubes or irregular configurations. The coatings could also improve general corrosion resistance and act as a diffusion barrier for hydrogen isotopes, i.e., deuterium and tritium.

EXPERIMENTAL PROCEDURE

V-Ti-Cr alloys in the form of round–bottom pencil–shaped samples (6.35 mm dia x 150 mm long) and flat–tab samples (12.7 x 25.4 x 1.0 mm) were used in this study. Various steps and experimental methods have been explored to fabricate and characterize insulator coatings for use in liquid–lithium environments: as a first step, the near–surface regions of vanadium–base alloys were charged with oxygen by exposure to flowing argon that contained either 10-20 ppm oxygen (i.e., impurity level of commercial 99.999% Ar) or 200 ppm oxygen in argon at 610-658°C for 17–19.5 h. As a second step, the oxygen–

*Work supported by U.S. Department of Energy, Office of Fusion Energy Research, under Contract W-31-109-Eng-38.

enriched vanadium–base alloy reacted with dissolved calcium (2 at.%) in lithium for 16-17 h at 300-550°C to form a CaO. During this process in–situ electrical resistance was monitored as a function of time. Subsequently, the samples were raised 10–30 mm above the liquid metal, where they remained for 16–72 h to allow excess molten alloy to drip from the samples. As a third step, the CaO/Ca layer was oxidized in a flowing gas mixture that contained 10–5000 ppm oxygen in argon for 17 h at 450-650°C.

Finally, the samples were examined for coating uniformity, two–point ohmic resistance measurements were made at numerous locations around the CaO–coated rod, and only the samples that showed an infinite ohmic resistance were selected for in-situ resistance measurements during exposure to the same liquid metal at temperatures between 250–500°C for up to 700 h. Samples were evaluated after each step by weighing, optical microscopy, SEM, EDS, and microhardness testing.

RESULTS AND DISCUSSION

Oxygen charging of the surface of V–Cr–Ti. It is well known that oxygen can be incorporated into the interstitial sublattice of body–centered–cubic (bcc) vanadium and its alloys.[5] Detailed information pertaining to oxygen incorporation in the alloys has been reported in Ref. 6. Figure 1 shows thermogravimetric results for the oxygen–charging experiment, and Fig. 2 shows the weight gain for various samples at 650°C after 17 h in argon that contained 10 ppm oxygen. Oxygen concentration in the near–surface layer was calculated from the weight gain, surface area, and thickness of the hardened region; it ranged from 250 ppm (as–received) to ≈1%, within 25 μm of the surface layer.

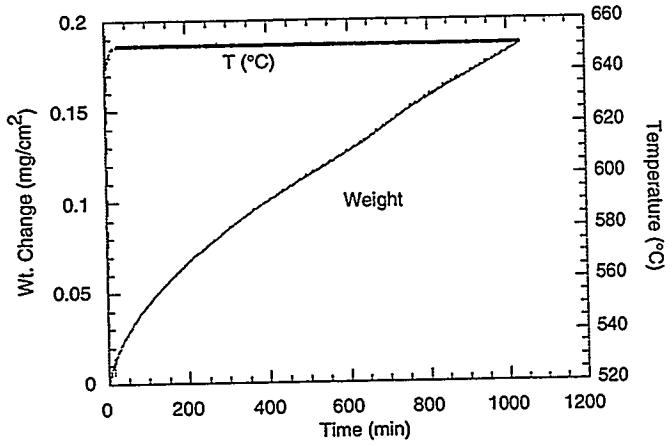

Figure 1.
Thermogravimetric results for V–4Cr–4Ti specimens during oxygen charging

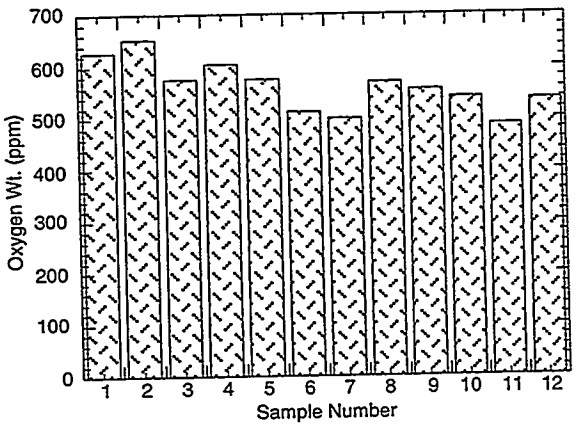

Figure 2.
Weight gain of V–4Cr–4Ti tab–shaped specimens after exposure in argon with 10 ppm oxygen for 17 h at 650°C

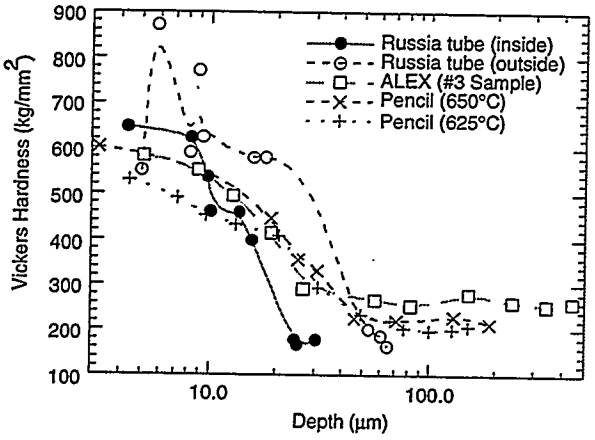

Figure 3.
Vickers hardness profiles from cross sections of various V-4Cr-4Ti specimens exposed to argon with 10 ppm oxygen for 17 h at 650°C

Figure 3 shows Vickers hardness profiles from cross sections near the surface area of various V-4Cr-4Ti specimens exposed to argon that contained 10 ppm oxygen for 17 h at 650°C. Long pencil–shaped samples placed in a temperature gradient exhibited somewhat lower oxygen uptake in the lower temperature zone. However, a Russian–supplied tube sample showed a higher surface hardness than other samples in this experiment. Oxygen charging was also performed in argon that contained 200 ppm oxygen. However, in this environment, the vanadium alloy surface developed a blue oxide layer over the thin black surface. The ohmic values of specimens before and after oxygen charging were the same. The blue oxide is not stable in liquid lithium.

Exposure of oxygen–charged V–Cr–Ti samples in 2 at.% Ca-Li. Figure 4 shows the product of the in-situ ohmic resistance times the liquid–metal contact area of the oxygen–charged samples in 2 at.% Ca-Li at 500°C for 17 h. The R*A (resistance x area) values for various samples were 20–50 Ω-cm^2. Before exposure to the liquid metal, the temperature difference between the samples and the liquid metal was minimized. Typically, at the beginning of the exposure, the resistance is high (~0.2-0.3 Ω), but it drops to almost zero within a few seconds, and then the resistance increases to 0.8-2.0 Ω within 10 min and remains constant for 17 h.

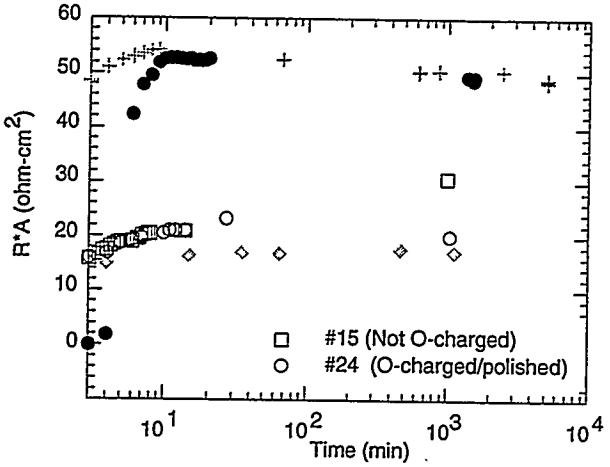

Figure 4.
R*A vs. time at 500°C for oxygen-charged V–4Cr–4Ti specimens after exposure in 2 at.% Ca-Li. Cross and diamond symbols denote specimens charged in argon with 10 ppm oxygen, and closed circle denotes specimen charged in argon with 200 ppm oxygen

According to our previous work, we produced in–situ CaO coatings on vanadium–base alloys that contained 250 ppm oxygen during a 7–day exposure in liquid lithium that contained 4 at.% calcium at 700°C.[3] We believe the reaction that forms CaO takes place at the interface between oxygen at the alloy surface and calcium in the liquid metal. The coating did not completely cover the vanadium alloy surface, but a high ohmic resistance, typical of CaO (two–point contact > 20 MΩ at room temperature), was

obtained. To improve formation of CaO on alloy substrates, oxygen–charged specimens were immersed in calcium–bearing (0.1–50 at.% Ca) liquid lithium for various times at various temperatures. This approach was adopted because oxygen in the alloy (as a reactant) may have a higher affinity for a solute such as calcium dissolved in lithium than for the alloy elements (V, Cr, and Ti). A lower calcium concentration in liquid metal lowers its viscosity.

To confirm the optimal time for calcium deposition at the surface of the oxygen–charged V-4Cr-4Ti specimens in 2 at.%Ca-Li, two samples, i.e., strip samples (140 x 12.7 x 1.0 mm), with and without oxygen–charging, were exposed for 2, 4, 8, and 16 h at 464°C. The sample not charged with oxygen did not form a clear black coating as did the oxygen–charged sample. In the oxygen–charged sample, the black coating layer looked identical for exposures >4 h. This black layer was identified by X-ray diffraction as CaO. In the X-ray spectrum, peaks were mainly attributed to V-4Cr-4Ti, but CaO peaks were also present. In a normal X-ray, beam penetration for CaO and vanadium alloys is ≈40 and ≈8 μm, respectively. However, according to the in-situ ohmic resistance (Fig. 4), the thin CaO coating may not be entirely uniform. To conduct gas–phase oxidation, the samples were withdrawn from the liquid and the excess liquid metal was allowed to drip from the samples for 17-72 h.

CaO coating via gas–phase oxidation. Liquid–metal exposed samples were oxidized in flowing 200– and 5000–ppm oxygen/argon gas mixtures. To avoid abrupt oxidation during exposure to a high oxygen pressure, high–purity argon gas flowed during heating, and gradually the higher oxygen–bearing argon gas mixture was admitted. Oxidation was conducted at 400 and 650°C for 17 h. A good CaO coating was gray and without cracking or spallation. At room temperature, most samples had infinite ohmic values. X-ray and chemical analyses indicated that the coatings were CaO or Ca-V-O. Currently, we do not have quantitative analytical data for lithium in the CaO layer because of the difficulty in obtaining this information.

In-situ resistance measurement for CaO coating. Figure 5 shows in-situ R*A vs time for CaO coatings on V-15Cr-5Ti prepared by the present method in lithium that contained 2 at.% calcium, for 700 h at 300-464°C. During in-situ ohmic resistance measurements, we used a DC current of 1-10 nA and observed polarization behavior. When we switch the polarity, the potential drop stabilized within several min at 1 nA, but the response was much faster at 10 nA. The ohmic values were monitored by applying Ohm's law; R = V/i. When the temperature was increased from 300 to 464°C, the ohmic values decreased only slightly, as shown in Fig. 5. When the sample was removed from the melt after 700 h, we observed a shiny liquid metal coating at the bottom end of the rods, which is indicative of good wetting by the liquid metal. Normally, wetting occurred within ≈2 min at 250°C.

Six months later, we conducted a similar experiment in the same apparatus. The calcium–lithium alloy was heated above its melting point and then cooled to ambient temperature. The cooling curve had two arrests at 176 and 146°C, which indicate that the dissolved calcium concentration in lithium decreased from 2.0 to 1.4 at.%, based on our previous study.[7] This decrease is caused by oxidation of calcium by impurity oxygen in the argon cover gas and by interaction of calcium with the vanadium–base alloy to form CaO in the previous experiment. Figure 6 shows R*A vs. time at 300°C for an oxygen–charged V–4Cr–4Ti specimen and a specimen that was coated previously at 500°C in the liquid metal that contained 2 at.% calcium. After ≈3 h, the previously coated specimen that exhibited a high ohmic value became conductive because either the concentration of calcium in the liquid metal was too low or the initial CaO layer was too thin (≈3 μm).

Microstructural analysis. The specimens were removed from the melt, cleaned in absolute ethanol, and examined by X-ray diffraction and SEM/EDS. Figure 7 shows the concentration of calcium, vanadium,

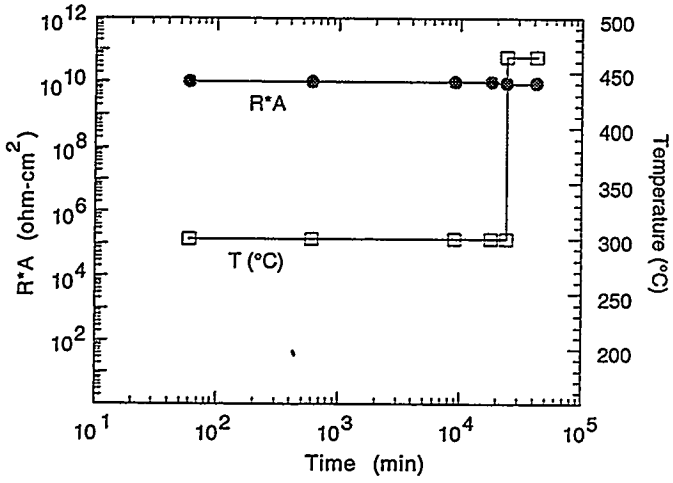

Figure 5.
In-situ R*A (solid symbol) and temperature (open symbol) vs. time for CaO coating on V-15Cr-5Ti

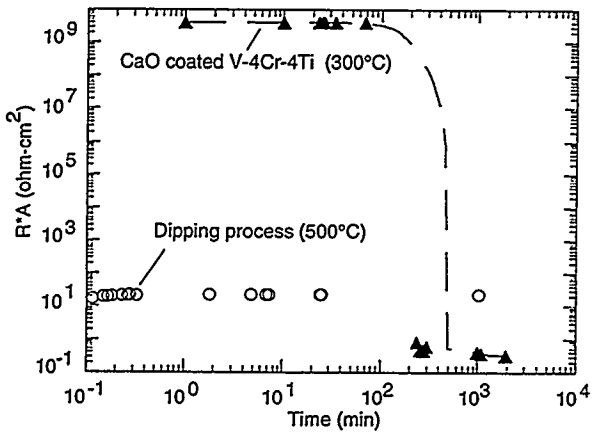

Figure 6.
In-situ R*A vs. time for oxygen–charged (open symbol) and previously coated (closed symbol) V-4Cr-4Ti specimens in lithium with 2 at.% calcium at 300°C

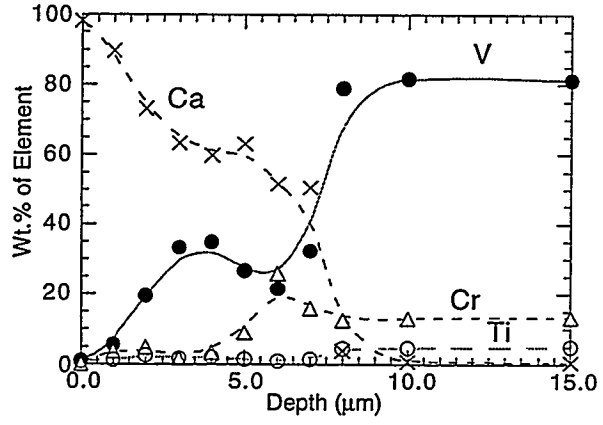

Figure 7.
Chemical composition from EDS analysis vs. depth for CaO/V-15Cr-5Ti specimen after exposure to lithium with 2 at.% calcium for 700 h at 300-464°C

titanium, and chromium as a function of depth from the liquid/alloy interface obtained by EDS analysis of the cross section of a CaO–coated V-15Cr-5Ti specimen after exposure to lithium that contained 2 at.% calcium, for 700 h at 300-464°C. SEM photomicrographs of the cross section revealed a crack–free layer 7-8 μm thick. Table 1 shows the characteristics of this coating and a coating produced in lithium that contained 50 at.% calcium.

Table 1. Characteristics of CaO coatings produced on V–(4, 5, and 15)Cr–(4 and 5)Ti in liquid lithium that contained 2 and 50 at.% calcium

Liquid metal composition	2 at.% Ca-Li	50 at.% Ca-Li[a]
Microcracks in CaO layer	None	Crazing cracks
V concentration in CaO layer	≈35 at.% (center)	<2 at. %
Thickness of CaO layer	7-8 μm (2 at.% Ca); 3 μm (1.4 at.% Ca)	10-14 μm
Stability of CaO layer in liquid Li	Good, ≈8 μm Poor, ≈4 μm	Good

[a]Data from Ref. 6.

Figure 8 shows the Vickers hardness as a function of depth for a CaO/V-15Cr-5Ti specimen. The CaO layer on the oxygen–charged specimen is much harder (~780 kg/mm^2) than the surface region of several V-4Cr-4Ti specimens that were exposed to argon containing 10 ppm oxygen for 17 h at 650°C (Fig. 3). Visual examination of the surface of the CaO coating indicated no microcracks or spallation of the layer.

The coefficient of thermal expansion of CaO is higher than that of V–Cr–Ti alloys (12 x 10^{-6} vs. 9.2 x 10^{-6}/K). Therefore, a CaO layer that forms in–situ on a vanadium alloy will be subjected to a tensile stress during cooling. Photomicrographs of CaO coatings on V–15Cr–5Ti did not show any cracks. However, CaO coatings that were produced in lithium containing higher calcium concentrations revealed a network of microcracks that consisted of regions ≈30–40 μm in diameter separated by narrow cracks, ≈2000 Å in width, over most of the CaO surface. This suggests that the cracks originate from a mismatch of the thermal expansion coefficients during cooling, i.e., they are "crazing cracks." One way to minimize microcracking would be to decrease the thickness of the CaO film so that its mechanical strength better matches that of the V–Cr–Ti alloy substrates. However, if the coating is too thin, it may not be stable in liquid lithium containing 2 at.% calcium. In this study, the incorporation of vanadium in the CaO layer produces a somewhat thicker but adherent coating.

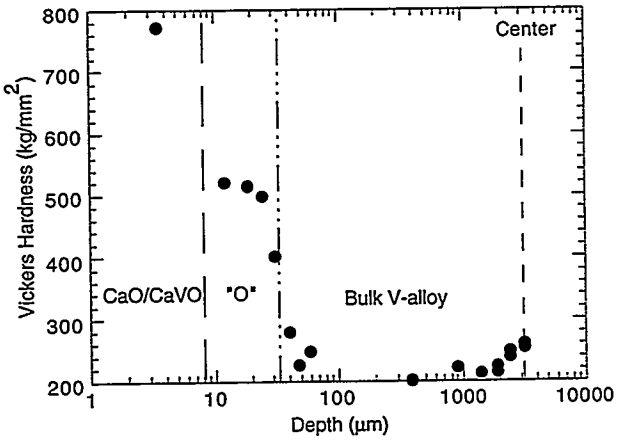

Figure 8.
Vickers hardness vs. depth for CaO/V-15Cr-5Ti specimen after exposure to lithium with 2 at.% calcium for 700 h at 300-464°C

FUTURE WORK

The performance of a CaO coating on the inner surface of a vanadium alloy tube will be evaluated after an MHD pressure–drop test on the tube.

ACKNOWLEDGMENTS

P. Johnson of Argonne's Analytical Laboratory performed the X–ray diffraction studies.

REFERENCES

[1] C. C. Baker et al., Tokamak Power System Studies FY 1985, Argonne National Laboratory Report ANL/FPP–85–2 (Dec. 1985).

[2] R. F. Mattas, B. A. Loomis, and D. L. Smith, Vanadium Alloys for Fusion Reactor Applications, JOM, 44(8), 26 (1992).

[3] J.–H. Park, T. Domenico, G. Dragel, and R. W. Clark, Development of Electrical Insulator Coatings for Fusion Power Applications, Fusion Engineering and Design 27 (1995) 682-695.

[4] J.–H. Park and T. F. Kassner, CaO Insulator Coating and Self-Healing of Defects on a V-Cr-Ti Alloys in Liquid Lithium System, J. Nucl Mater., to be published (1996).

[5] A. U. Seybolt and H. T. Sumsion, Vanadium–Oxygen Solid Solutions, Met. Trans. AIME, 292–299 (1953).

[6] J.–H. Park, D. Kupperman, and E. T. Park, Mechanical Properties of V-Cr-Ti-(O and N) Solid Solutions, Submitted to Acta Materialia (1996).

[7] J.–H. Park and T. F. Kassner, Selection of a Liquid Calcium-Lithium Alloy for Fabricating CaO Insulator Coatings on V-5%Cr-5%Ti, Fusion Reactor Materials Semiannual Progress Report for the Period Ending March 31, 1995, DOE/ER-0313/18, pp. 347-351 (July 1995).

2.0 SILICON CARBIDE COMPOSITE MATERIALS

REVISED ACTIVATION ESTIMATES FOR SILICON CARBIDE- H. L. Heinisch (Pacific Northwest National Laboratory[1]), E. T. Cheng (TSI Research) and F. M. Mann (Westinghouse Hanford Company)

OBJECTIVE

The objective of this work is to review the information on activation of silicon carbide with respect to use as a low activation material in fusion energy systems.

SUMMARY

Recent progress in nuclear data development for fusion energy systems includes a reevaluation of neutron activation cross sections for silicon and aluminum. Activation calculations using the newly compiled Fusion Evaluated Nuclear Data Library result in calculated levels of ^{26}Al in irradiated silicon that are about an order of magnitude lower than the earlier calculated values. Thus, according to the latest internationally accepted nuclear data, SiC is much more attractive as a low activation material, even in first wall applications.

PROGRESS AND STATUS

The International Atomic Energy Agency/ Nuclear Data Section has long promoted the international compilation and evaluation of nuclear data. Under IAEA/NDS, international nuclear data developers and users exchange information and reach consensus, not only on the reliability of the data, but also on the priorities in addressing deficiencies in the data base. Recently there has been significant progress toward the completion of a high quality, non-restricted nuclear data library, the Fusion Evaluated Nuclear Data Library (FENDL), specifically developed to support the design analysis of ITER and other fusion energy systems[1]. One of the consequences of the FENDL development is the inclusion in it of some neutron activation cross sections that are significantly smaller than the values used in earlier evaluations of activation of potential fusion materials[1].

The recently completed FENDL/A-2.0 activation library was made from existing international nuclear data files developed in the European Community, the Russian Federation, Japan, the Peoples Republic of China, and the United States. It was compiled using a comprehensive selection procedure adopted by an IAEA/NDS Selection Panel[2]. No additional evaluation work was performed on information in these files, and many cross sections, including the subject Al and Si cross sections, are theoretical estimates. Verification of these cross sections by experimental measurement is highly desirable and remains a top priority in nuclear data development.

Long term environmental limitations on SiC due to the production of ^{26}Al have been noted in evaluations of neutron activation of SiC in a fusion device first wall environment since at least 1988[3-6]. Production of ^{26}Al from Si proceeds by the two step reaction with neutrons: ^{28}Si(n,x)^{27}Al(n,2n)^{26}Al. Thus, two neutron activation cross sections govern its production. In FENDL/A-2.0 both cross sections are smaller than the cross sections used earlier, such as those in the REAC*3 activation code[7]. The ^{28}Si(n,x)^{27}Al cross section is smaller by an average factor of about 4.5 in the energy range 13.5 MeV<E<15 MeV, while the ^{27}Al(n,2n)^{26}Al cross section is smaller by about a factor of 2 in that range. (The threshold energies for the ^{28}Si and ^{27}Al reactions are E=10 MeV and E=12 MeV, respectively). Thus, the effect of using the

---

[1]*Pacific Northwest National Laboratory is operated for the U.S. Department of Energy by Battelle Memorial Institute under Contract DE-AC06-76RLO 1830.*

FENDL/A-2.0 cross sections is that ^{26}Al production is predicted to be about an order of magnitude less than that predicted using REAC*3 cross sections.

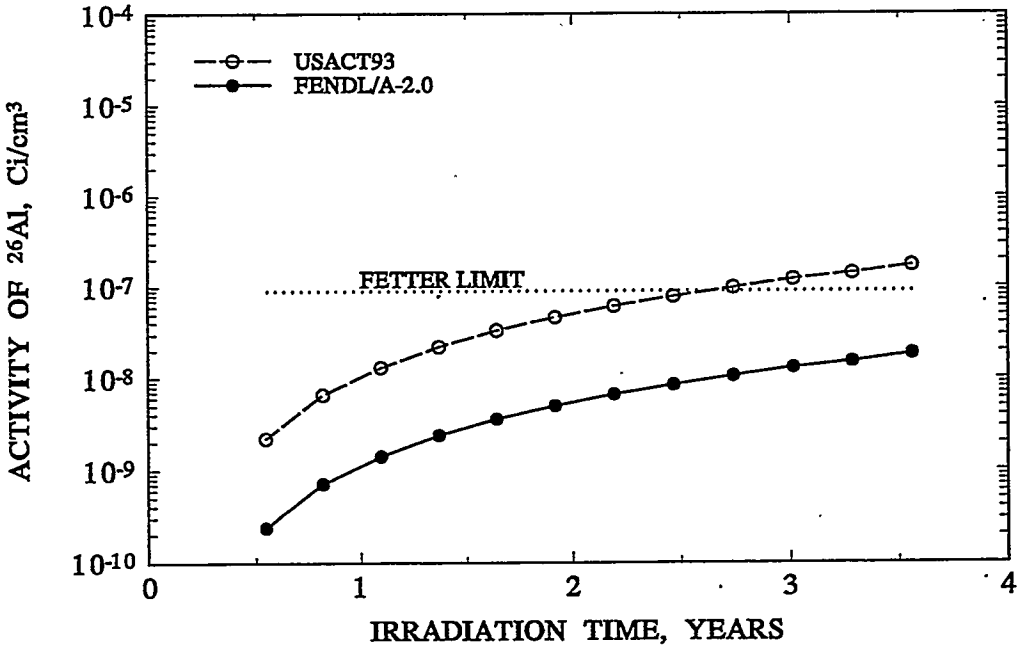

Figure 1. The buildup of ^{26}Al in SiC irradiated in STARFIRE for 3.5 years (12.5 MWY/m^2) in the first wall using the original REAC cross sections (USACT93) and FENDL/A-2.0. The limit for ^{26}Al activity calculated by Fetter et al.[3] is indicated.

The effects of this smaller level of ^{26}Al production on the potential use of SiC in fusion energy devices can be seen by estimating the changes that would occur if the new cross sections were used in activation calculations such as those in Ref.[6]. Figure 1 shows the activity of ^{26}Al for SiC irradiated in the first wall of STARFIRE to a loading of 12.5 MWY/m^2 as calculated with REAC*2 (an earlier version of REAC*3)in [6]. Also plotted is the same curve scaled by the ratio of the FENDL/A-2.0 cross sections to those used in REAC*2. The activity calculated using FENDL/A-2.0 cross sections is estimated to be about an order of magnitude less than the REAC*2 values, which means the Fetter limit on ^{26}Al[3], based on 10 CFR 61 methodology, will be reached in about 7 years, or at a wall loading of about 25 MWY/m^2 in STARFIRE. Butterworth[4] compared the activity of SiC irradiated in the DEMO first wall as a function of decay time to the "hands on limit" of 25 μSv, finding it to be about 40 times higher than the limit. Using FENDL/A-2.0 cross sections in Butterworth's calculations would bring the activity to within a factor of 4 of the hands on limit, which makes SiC significantly more attractive. Both of these comparisons have been done in neutron spectra that are not representative of a fusion energy device designed to be constructed of ceramic materials, where the actual values of ^{26}Al production may be somewhat different. Thus, comparisons to absolute limits will depend on the neutron spectrum considered. However, the relative changes in ^{26}Al production due to the smaller cross sections will be the same in any neutron spectrum.

FUTURE WORK

Activation calculations will be performed for SiC in ARIES, a conceptual fusion energy device specifically designed for ceramic structural materials, using the FENDL/A-2.0 cross sections. Experimental measurements of neutron activation cross sections for Si are being pursued.

REFERENCES

1. E.T. Cheng, A.B. Pashchenko and J. Kopecky, "Overview on Recent Nuclear Data Development for Fusion Reactor Technology," Proceedings of 12th ANS Topical Meeting on the Technology for Fusion Energy, 16-20 June 1996, Reno, Nevada, to be published in Fusion Technology.

2. A.B. Pashchenko, Summary Report of the IAEA Consultants' Meeting on Selection of Evaluations for the FENDL/A-2 Activation Cross Section Library, St. Petersburg, Russia, 1995, IAEA/INDC(NDS)-341 (1996).

3. S. Fetter, E.T. Cheng and F.M. Mann, "Long Term Radioactivity in Fusion Reactors," Fusion Eng. Des. 6 (1988) 123.

4. G.J. Butterworth, "Low Activation Structural Materials for Fusion," Fusion Eng. Des. 11 (1989) 231.

5. E.T. Cheng, "Assessment of Low Activation Materials," Proc. 14th IEEE Symp. Fusion Engineering, Sept. 30-Oct. 1, 1991, San Diego CA.

6. H.L. Heinisch, "Activation of Silicon Carbide in Fusion Energy Systems," Fusion Materials Semiannual Progress Report, DOE/ER-0313/18 (1995) 91.

7. F.M. Mann, "REAC*3 Nuclear Data Library," Proc. Intl. Conf. Nuclear Data for Science and Technology, Julich, Germany, 13-17 May, 1991, 936.

TIME-DEPENDENT BRIDGING AND LIFE PREDICTION OF SiC/SiC IN A HYPOTHETICAL FUSION ENVIRONMENT -- C. H. Henager, Jr., C. A. Lewinsohn, C. F. Windisch, Jr., and R. H. Jones (Pacific Northwest National Laboratories)*

OBJECTIVE

The objective of this work is to discuss a methodology for component life prediction based on subcritical crack growth in typical fusion environments. Data are supplied for effects of C-interphase oxidation rates on crack growth rates in SiC/SiC composites. A simple crack growth model is presented based on time-dependent bridging concepts and used to predict the time for an initially bridged crack to grow 5 x 10^{-4} m as an estimate of component useable life. These calculations are useful in determining the relative merits of pursuing material modifications for the fusion environment, which can be a very expensive proposition. A useful outcome of this effort is to define the performance limitations for these materials as a function of temperature and oxygen.

SUMMARY

Growth of subcritical cracks in SiC/SiC composites of CG-Nicalon fibers with a ~1 μm C-interphase has been measured on a related Basic Energy Sciences program using environments of purified argon and mixtures of argon and oxygen at 1073K to 1373K. Companion thermo-gravimetric (TGA) testing measured mass loss in identical environments. The TGA mass loss was from C-interphase oxidation to CO and CO_2, which was undetectable in argon and linear with oxygen concentration in argon-oxygen mixtures, and was converted into an interphase linear recession rate. Crack growth in pure argon indicated that fiber creep was causing time-dependent crack bridging to occur, while crack growth in argon-oxygen mixtures indicated that time-dependent C-interphase recession was also causing time-dependent bridging with different kinetics. A model of time-dependent bridging was used to compute crack growth rates in argon and in argon-oxygen mixtures and gave an estimate of useable life of about 230 days at 1073K in a He + 1.01 Pa O_2 (10 ppm) environment.

PROGRESS AND STATUS

Introduction

Continuous fiber ceramic matrix composites (CFCCs) with a chemically-vapor infiltrated (CVI) SiC matrix and polymer-derived SiC fibers, so-called SiC/SiC materials, are being developed and evaluated for utilization in a wide variety of high-temperature applications. These applications can be divided into two categories: 1) high-temperature (>1273K) in oxidizing environments and 2) moderate temperatures (1073-1273K), relatively inert chemical environments, and neutron environments. The second category includes advanced fusion energy systems and fission reactors. The primary environmental concern for category 1 is the high-temperature, oxidizing environment, while for category 2 the primary challenge is the radiation environment. High-temperature, oxidizing environments present a challenge to SiC/SiC CFCCs because of the chemical reaction between the fiber/matrix interphase material and oxygen. The fusion environment poses different problems in contrast to rapid oxidation of the interphase material; however, the results are similar. The response of SiC/SiC CFCCs to neutron irradiation was reported [1] and a loss of strength from fiber shrinkage and the accompanying loss of fiber/matrix bonding was observed. A summary of the issues associated with the application of SiC/SiC CFCCs for fusion energy systems has been presented by Jones et al. [2-4]. Since newer, more stable fibers are being developed and will eventually be incorporated into these SiC/SiC composites the effects of neutrons on fiber dimensional stability are expected to be mitigated. However, current and future interphase technology suggests that even "high-purity" inert

* Pacific Northwest National Laboratory is operated for the U. S. Department of Energy by Battelle Memorial Institute under Contract DE-AC06-76RLO 1830.

chemical environments need to be evaluated because of the high reactivity of C-interphases with oxygen.

A model for crack growth in oxygen-containing environments has been formulated [5, 6] and is used to make an estimate of useable life for a fusion first wall made of C-interphase SiC/SiC. Temperature and oxygen effects are incorporated into a single model for lifetime prediction calculations. For this model, the rate of C-interphase removal was determined from experiments and related to a time-dependent bridging-fiber relaxation process as indicated. Calculations using this approach can be used to estimate composite lifetimes in environments and at temperatures where thermal creep of fibers is insignificant, such as the fusion energy environment. Of course, other effects, as yet to be determined, such as irradiation-induced creep, may play a role in this severe environment. These calculations are useful in determining the relative merits of pursuing material modifications for the fusion environment, which can be a very expensive proposition. A useful outcome of this effort is to define the performance limitations for these materials as a function of temperature and oxygen.

Experimental Technique

SiC/SiC CFCC materials fabricated by Refractory Composites Inc. with Nicalon-CG and C-interphase (CG-C) and by DuPont with Hi-Nicalon fibers and a C-interphase (Hi-C) were evaluated by thermal gravimetric analysis (TGA) and high-temperature mechanical testing. A summary of the material characteristics is given in Table 1 where the fracture toughness values are for 1373 K for the CG-C and CG-BN material and 1473 K for the Hi-C material. All material was made with eight plies of 0/90 fiber cloth and the composite plates were 4 mm thick.

Table 1. Summary of SiC/SiC CFCC material characteristics.

Composite Type:	CG-C	Hi-C
Fiber Type	"Ceramic grade"	"Hi-Nicalon"
Fiber Coating	1.0 ± 0.1 μm carbon	1.0 ± 0.5 μm carbon
Fibers/Tow	420	321
Fiber Diameter	14.0 ± 0.5 μm	14 ± 2.3 μm
Fiber Vol. Fraction	30	30
Composite Coating	CVD Silicon Carbide	CVD Silicon Carbide
Porosity	20 ± 5%	6 ± 1.4%
Modulus*	98 ± 6.6 GPa	150 ± 4 GPa
Fracture Toughness	17.5 MPa·$m^{1/2}$	23 ± 1.5 MPa·$m^{1/2}$

*The modulus is calculated from the specimen compliance measured from the linear portion of loading during flexural testing of SENB specimens at elevated temperature.

Samples with dimensions of about 4 mm x 4 mm x 8 mm were tested at 1373K using thermal gravimetric analysis (TGA). One face of the 4 mm x 8 mm of the samples was cut so that it was free of the SiC coating applied to the surface of the material during the last phase of fabrication. All other faces of the samples had a thin, approximately 5 μm-thick, SiC coating. All rates were normalized with respect to the cut, uncoated surface. Mixtures of O_2 with Ar were used in these experiments and the gas flow was maintained at about 1 SCFH through the instrument furnace and composition was controlled using a multi-gas controller and an oxygen meter. In each test, a sample was placed in an alumina cup in the analyzer furnace, the furnace was sealed, gas flow was adjusted, and the balance was allowed to equilibrate for about 2 h before heat up.

The SCG studies were performed using constant load tests for times up to 1 x 10^5 s, giving long-term crack velocity data, and using stepped load tests with load holding times of 1000 s carried out at

1100°C in Ar and Ar plus varying O_2 levels. Single-edge-notched bend bar (SENB) specimens with dimensions of 4 mm x 5.5 mm x 50 mm were tested. The SENB specimens were tested in 4-point bending using a fully articulated SiC bend fixture [5]. The specimens were typically loaded at an applied stress intensity of 7 to 8 MPa$\sqrt{m}$ to begin the test. The test continued until a load drop was observed. Specimens that were tested in Ar plus O_2 were brought up to temperature in pure Ar. The displacement-time curves were fit to polynomial functions and differentiated to give $\partial\delta/\partial t$. This quantity was then converted into a crack velocity [5].

Results and Discussion

Mass losses from C-interface oxidation measured by TGA were generally linear as a function of time for the composite materials between 3.1 x 10^2 Pa to 2.5 x 10^3 Pa O_2 and between 1073K and 1373K [6]. Microscopic examination of the C-interfaces in cross-sectioned SiC/SiC samples that had been exposed to oxidizing conditions revealed a remarkable uniformity in the recession distance from the unsealed surfaces exposed to O_2 [7, 8]. Recession rates calculated from these measured recession depths were compared to those calculated from TGA data assuming all the mass losses were due to C oxidation. The recession rates calculated from the two approaches were in acceptable agreement considering the experimental uncertainties. The measured optical recession rates are shown in Figure 1 as a function of pO_2 for the CG-C materials.

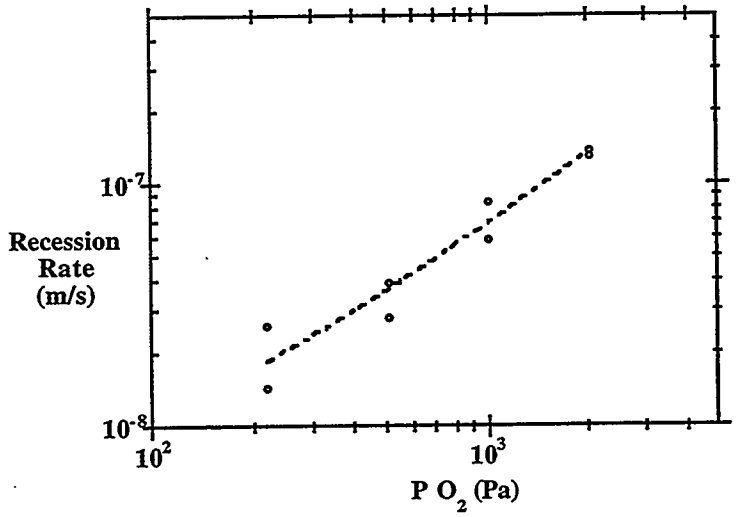

Figure 1. Measured (optical microscopy) C-interphase recession rates at 1373K as function of indicated pO_2. This recession data was used in the time-dependent bridging model.

Slow crack growth data were also obtained for these same SiC/SiC composites in mixtures of Ar and oxygen (O_2) [6-8]. Slow crack growth rates were measured as a function of pO_2 (Figure 2) and temperature in Ar + O_2 using a unique environmentally-controlled, high-temperature test apparatus at PNNL. Representative data plots are shown below in Figure 2 for C-interphase composites with Nicalon CG fibers for three different oxygen partial pressures. The addition of oxygen to the 1373K Ar environment increases the crack velocity in stage-II and shifts the stage-II-to-III transition to lower *K*-values, Figure 2. This leftward shift is consistent with a reduction in the closure forces imparted on the crack faces by the bridging fibers. Scanning electron micrographs of polished cross-sections of cracked specimens exposed to O_2 plus Ar revealed that oxidation at 1373K partially removed the

C-interphase where the crack intersects the bridging fibers [7, 8]. The removal of this interphase material reduces the extent to which the matrix can transfer load to the fibers, and, in turn, reduces the bridging-zone effectiveness. Therefore, in addition to relaxation of bridging zone stresses caused by fiber thermal creep, the strength of the fiber-matrix mechanical coupling will fall in time-dependent fashion as the interphase is removed.

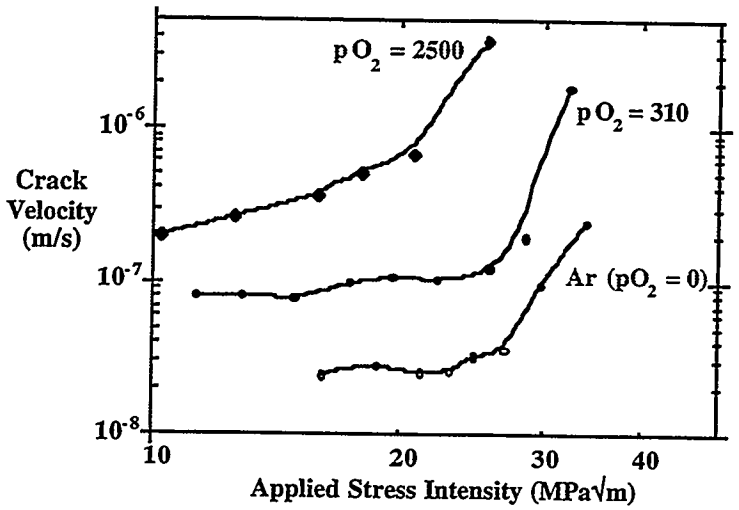

Figure 2. Crack velocity as function of oxygen partial pressure in pascals (Pa) at 1373K. Total system pressure was 1.01 x 10^5 Pa (1 atm.) with the balance Ar. Materials with easily oxidizable interphases, such as C, are vulnerable to oxidation and lifetimes are greatly decreased.

The temperature data was used to calculate activation energies for cracking in both pure Ar and in Ar + O_2 [8]. Data from the TGA experiments and crack growth experiments of C-interphase materials at 1373 K indicate that the activation energies for both weight loss as a function of time and crack growth rate are about 50 kJ/mol [9-11]. Based on these results, the rate controlling step for crack growth in oxygen-containing environments is carbon oxidation which results in mechanical de-coupling of the fiber from the matrix due to fiber/matrix interphase removal. The process envisioned for de-coupling the bridging-fibers from the matrix is shown schematically in Figure 3. The time-dependence of the fiber-bridging stress can be related to the rate of interphase removal by oxidation [6] through the implied time-dependence of the debonded region, λ, and fiber-matrix shear strength, τ.

A model for the effects of oxygen was developed by considering the time-dependent debonding of fibers from the matrix as suggested by Figure 3. For this model, the rate of C-interphase removal was determined from experiments (Figure 1) and related to a time-dependent bridging-fiber relaxation process [6]. Calculations using this approach can be used to estimate composite lifetimes in environments other than Ar and at temperatures where thermal creep of fibers is insignificant, such as the fusion energy environment. Sample calculations for this are shown in Figure 4 using Ar + 1.01 Pa O_2 at 1073K. Fiber thermal creep is considered to be negligible at this temperature [12] and only C-interphase oxidation is considered. Note that the time for an initially bridged crack to grow 0.5 mm is only about 200 days in this environment, suggesting that the C-interphase is not suitable for this environment. Of course, other effects, as yet to be determined, such as irradiation-induced creep, may play a role in this severe environment.

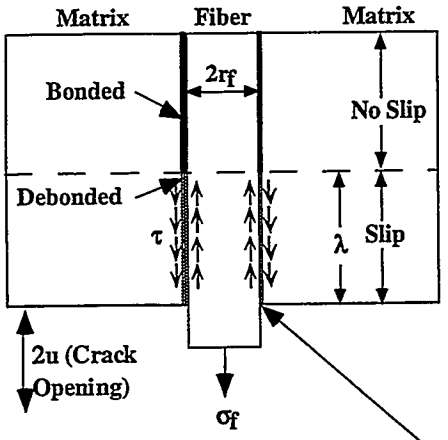

Figure 3. A schematic drawing of the time-dependent debonding mechanism envisioned for mechanically decoupling the Nicalon fiber from the SiC-matrix due to fiber-matrix interphase removal. A time-dependent debonded region implies that λ and τ are time-dependent, which suggests an approach for modeling such behavior.

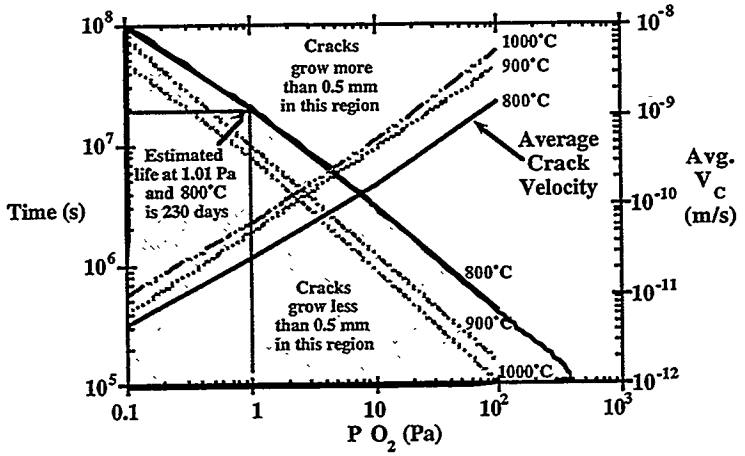

Figure 4. Calculated lifetime based on the time for a bridged crack to grow 5 x 10^{-4} m (0.5 mm) for a C-interface SiC/SiC composite as a function of pO_2 at three different temperatures, such as would be encountered in proposed helium-coolant, fusion energy environment. The lifetime for He + 1.01 Pa O_2 (10 ppm) at 800°C would be an estimate for a typical fusion energy environment if other mechanisms were negligible. This calculation is independent of fiber type.

Summary

It was shown that C-interphase removal accelerates the crack growth rates through time-dependent debonding and that a simple time-dependent bridging model can be used to estimate useful component life based on measured activation energies and recession rates. The results

suggest that improved environmental resistance is required for even a high-purity fusion energy environment. This improvement could result from more stable fiber/matrix interphase materials such as porous SiC, use of glass formers in the matrix to seal the matrix microcracks and use of coatings. The use of porous SiC interphase material is the most appealing because additions of glass formers to the matrix affects composite properties while high-temperature, oxidation resistant coatings will crack as a result of thermal cycling and creep of the composite.

References

1. G. W. Hollenberg, C. H. Henager, Jr., G. E. Youngblood, D. J. Trimble, S. A. Simonson, Newsome and E. Lewis, "The Effect of Irradiation on the Stability and Properties of Monolithic Silicon Carbide and SiC/SiC Composites up to 25 dpa," *J. Nucl. Mater.*, **219** (1995) 70-86.

2. R. H. Jones, C. H. Henager, Jr., and G. W. Hollenberg, "Composite Materials For Fusion Applications," *J. Nucl. Mater.*, **191-194** (1992) 75.

3. R. H. Jones and C. H. Henager, Jr., "Fusion Reactor Application Issues for Low Activation SiC/SiC Composites," *J. Nucl. Mater.*, **219** (1995) 55.

4. R. H. Jones and C. H. Henager, Jr. "High Temperature Properties of SiC/SiC for Fusion Applications," *J. Nucl. Mater.*, **212-215** (1994) 830-834.

5. C. H. Henager, Jr., and R. H. Jones, "Subcritical Crack Growth in CVI Silicon Carbide Reinforced with Nicalon Fibers: Experiment and Model," *J. Am. Ceram. Soc.*, **77** [9] (1994) 2381-94.

6. R. H. Jones, C. H. Henager, Jr., and C. F. Windisch, Jr., "High Temperature Corrosion and Crack Growth of SiC-SiC at Variable Oxygen Partial Pressures," *Mat. Sci. & Eng.*, **A198** (1995) 103-112.

7. C. H. Henager, Jr. and R. H. Jones, "Subcritical Crack Growth in Continuous-Fiber Reinforced Ceramic Composites," in Ceramics Transactions, Vol. 38: Advances in Ceramic-Matrix Composites, N. P. Bansal, (ed.), The American Ceramics Society, Westerville, OH, 1993, pp.317-328.

8. C. H. Henager, Jr., R. H. Jones, C. F. Windisch, Jr., M. M. Stackpoole, and R. Bordia, "Time-Dependent, Environmentally-Assisted Crack Growth in Nicalon-Fiber-Reinforced SiC Composites," *Metall. et. Mater. Trans. A*, **27A** (1995) 839-849.

9. J. M. Thomas, Chemistry and Physics of Carbon, Vol. 1, P. L. Walker Jr., ed., *Marcel-Dekker*, New York, 1965, pp.135-68.

10. A. J. Eckel, J. D. Cawley and T. A. Parthasarathy, "Oxidation Kinetics of a Continuous Carbon Phase in a Nonreactive Matrix," *J. Am. Ceram. Soc.*, **78** [4] (1995)972-80.

11. K. L. Luthra, "Oxidation of Carbon/Carbon Composites - A Theoretical Analysis," *Carbon*, **26** [2] (1988) 217-24.

12. J. A. DiCarlo, "Creep Limitations of Current Polycrystalline Ceramic Fibers," *Compos. Sci. and Technol.*, **51** (1994) 213-222.

THE CYCLIC FATIGUE BEHAVIOR OF A NICALON/SiC COMPOSITE — N. Miriyala, P. K. Liaw, and C. J. McHargue (University of Tennessee), and L. L. Snead (Oak Ridge National Laboratory).

OBJECTIVE

To develop an understanding of the fabric orientation effects on the monotonic and cyclic fatigue behavior of continuous fiber-reinforced ceramic-matrix composites (CFCCs).

SUMMARY

Cyclic fatigue tests were performed at ambient temperature on a Nicalon/SiC composite to study the effects of fabric orientation on the mechanical behavior. Four-point bend specimens were loaded either parallel or normal to the braided fabric plies. The maximum stresses chosen during the fatigue tests were 60, 70, and 80% of the monotonic strengths, respectively, in both orientations. Specimen failure did not occur in any case even after one million loading cycles. However, it was observed that much of the decrease in the composite modulus occurred in the first few (<10) cycles, and the fabric orientation did not significantly affect the effective modulus or midspan deflection trends.

PROGRESS AND STATUS

Introduction

The interest in continuous fiber-reinforced ceramic-matrix composites (CFCCs) is mainly due to the fact that they fail in a "graceful" manner, unlike the monolithic ceramics. The ability to fail in a non-catastrophic manner is primarily promoted by the large work of fracture required to pull broken fibers out of the matrix against a frictional sliding resistance between the fiber and the matrix, and crack deflection at weak interfaces oriented transversely to the main crack propagation direction [1, 2]. Unidirectional composites exhibit good strength and toughness when the load is applied parallel to the fiber orientation. However, they perform poorly when the load is applied normal to the fibers. Hence, in applications where multi-axial stresses may be encountered, two dimensional (2-D) or three dimensional (3-D) reinforcement is commonly used. One of the common approaches used in the manufacture of 2-D reinforced CFCCs is to make a woven or braided fabric preform and then infiltrate the preform with the matrix. Since the 2-D composites generally suffer from poor interlaminar shear strength, it might be expected that the load bearing capacity of CFCCs, under monotonic and fatigue loadings, may be affected by the orientation of the fabric plies to the loading direction. Previous studies under the current program [3-5] have indicated that the fabric orientation contributed to significant differences in the monotonic and fatigue behavior of Nicalon/alumina composite, while the effects were insignificant for the Nicalon/silicon carbide (SiC) composite. In view of the contrasting role played by the fabric orientation on the mechanical behavior of the two CFCCs investigated, it was decided to perform additional testing and characterization to understand the reasons for the differences observed. Towards this objective, the results from the recently performed cyclic fatigue tests on the Nicalon/SiC composite are presented in this report.

Experimental Details

Material

The Nicalon/SiC composite used in the present study was donated by AlliedSignal Engines. The as-received material was in the form of two plates, approximately 200 × 150 × 2.4 mm, manufactured by DuPont Corporation. A 2-D braided Nicalon fabric was used as the preform, which was first given an interfacial coating of carbon (approximately 0.4 to 0.5 μm) by a chemical vapor deposition (CVD) process, prior to the infiltration of SiC matrix. The SiC matrix was infiltrated by the decomposition of methyltrichlorosilane, in the presence of hydrogen, at 1100 to 1200°C. The nominal fiber volume content in the composite was approximately 40 %.

Flexure testing

Flexure bars were machined from the composite plates using diamond tooling. The ASTM Standard C 1161 configuration requires the specimens to be 50 mm long, 4 mm wide and 3 mm thick. However, in order to objectively study the effects of fabric orientation on the mechanical behavior of the two composites, flexural bars of square cross-section were fabricated. Accordingly. the flexural bars of the Nicalon/SiC composite used in the present investigation were $50 \times 2 \times 2$ mm. Ambient-temperature fatigue tests were performed on a MTS servohydraulic system, equipped with a graphite heating element furnace, that can be used to conduct elevated-temperature tests, up to 2000°C in vacuum or argon.

The cyclic fatigue tests were conducted under load control using a sinusoidal waveform. The loading frequency was 0.5 Hz up to 1000 cycles and then gradually raised to 5 Hz in a multi-ramp mode and maintained at that frequency till the completion of tests. The R-ratio (minimum load/maximum load) used was 0.1, and the fatigue run-out was set at one million cycles, which corresponded to approximately 56 hours of testing. The load and midspan deflection values were recorded at several stages of the fatigue tests to monitor the effective modulus and midspan deflection trends.

During the cyclic fatigue tests, loads were applied to the specimens either parallel or normal to the fabric plies. Accordingly, the specimen configurations were referred to as edge-on and transverse, depending on whether the load was parallel or perpendicular to the fabric plies, respectively (Figure 1).

Results and Discussion

In our previous study on the mechanical behavior of Nicalon/SiC composite [3, 4], it was observed that there was a significant scatter in ultimate strength values in both edge-on and transverse orientations. The flexural strength in the edge-on orientation was 234 ± 27 MPa, while the strength was 241 ± 23 MPa in the transverse orientation. The large scatter in the strength values was attributed to the variation in the porosity content (10 to 20%) and its distribution [5]. Although the average flexural strength was about 7 MPa higher in the transverse orientation than in the edge-on orientation, it may be noted that this difference is insignificant, considering the scatter in the strength values and the porosity content. On cyclic fatigue loading, specimen failure was not observed even when the maximum stress during the tests was greater than 80 % of the monotonic strength, in both orientations. However, it was observed that the effective modulus values decreased upon fatigue loading in all the cases. In the above studies, the load and midspan deflection values were recorded after 1000 loading cycles and beyond and, consequently, there was no understanding of how the load bearing capacity of the composite was affected in the first few loading cycles.

In the present study, flexural specimens, of comparable porosity content (10 to 12%), were subjected to a maximum stress of 140, 165 or 190 MPa, during cyclic fatigue loading, which corresponded to approximately 60, 70 and 80 %, respectively, of the monotonic strength values. The load and midspan deflection values were continuously recorded for the first ten cycles and then at periodic intervals during the

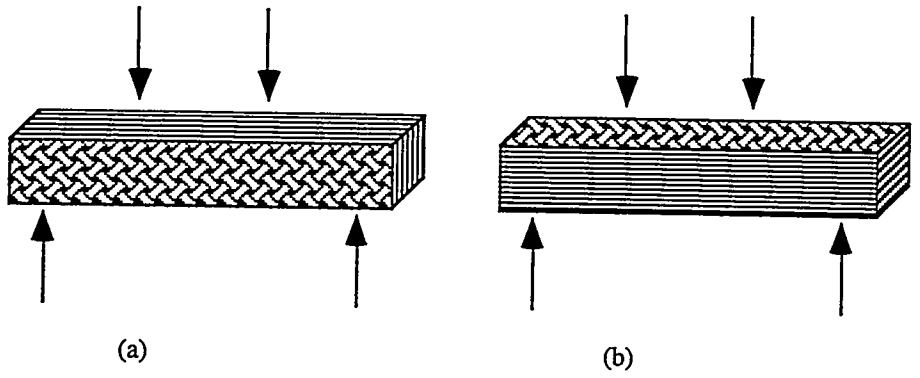

Figure 1. Geometries for testing fiber fabric composites: (a) edge-on and (b) transverse.

remaining part of the test. At least three sets of data were recorded during each log decade of cyclic loading. The slope at a particular point during the fatigue test was normalized with respect to the slope for the first cycle to calculate the "effective modulus" [3,4]. The effective modulus trends in the Nicalon/SiC composite in the edge-on and transverse orientations are presented in Figures 2 and 3, respectively. The increment in midspan deflection (Δd) values are plotted against the number of loading cycles in Figures 4 and 5, respectively, for the edge-on and transverse orientations. From the effective modulus and midspan deflection trends, it appears that the orientation effects are insignificant in the Nicalon/SiC composite.

It can be seen from Figures 2 and 3 that the slope of the load versus midspan deflection values decreased after the first loading cycle in all the samples. Also, the drop in modulus values after the first cycle was higher, as the maximum stress during the fatigue tests was increased, for both orientations. After a relatively steep drop of up to 10% in the first ten cycles, the decrease in effective modulus was less precipitous as the loading continued. At a given fatigue cycle, increasing the maximum stress decreases the effective modulus, which means that the material becomes more compliant, leading to an increase in the specimen deflection (Figures 4 and 5). From Figures 4 and 5 it can also be seen that the midspan deflection values increased steeply in the first ten cycles and more gradually thereafter. Thus, it appears that much of the damage in the composite material occurs in the first ten cycles. According to the current literature, the fatigue in CFCCs occurs due to one or more of the following mechanisms [6]; (i) the interfacial sliding resistance changes as fatigue loading proceeds, as a result of interfacial debonding and sliding, (ii) the strength of the fibers may degrade either due to sliding along the interface by means of an abrasion mechanism, which introduces flaws in the fibers and (iii) fatigue crack growth may occur in the matrix itself in accordance with a Paris law. To understand the progression of damage responsible for the effective modulus trends observed in the present study, metallographically polished flexural specimens were subjected to a maximum stress of 190 MPa and unloaded after 10^1, 10^2, 10^3, 10^4 and 10^5 cycles. It is hoped that the examination of these specimens under a scanning electron microscope, which will be performed shortly, will provide an insight into the damage progression in the material.

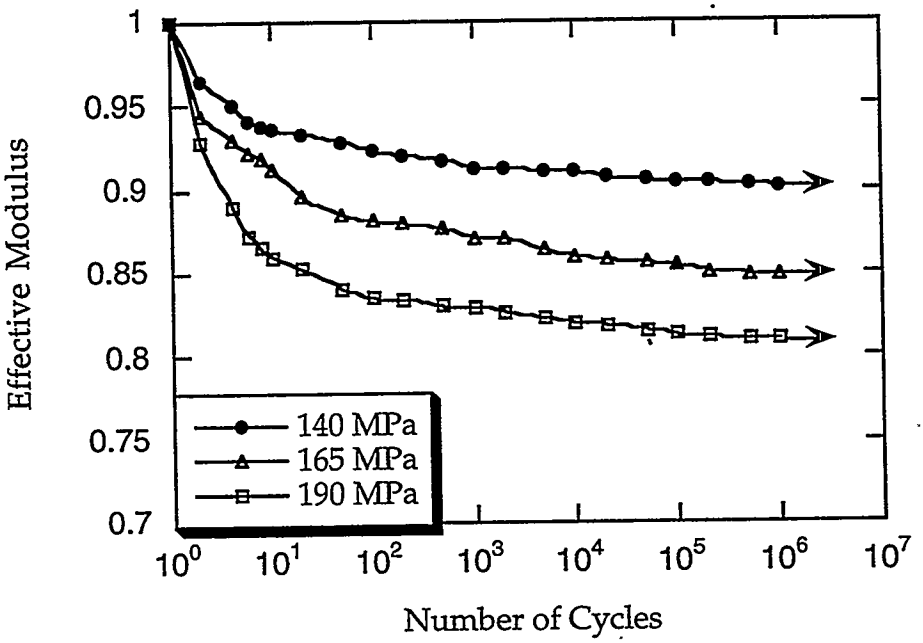

Figure 2. The reduction in effective modulus due to fatigue in the edge-on orientation of the Nicalon/SiC composite.

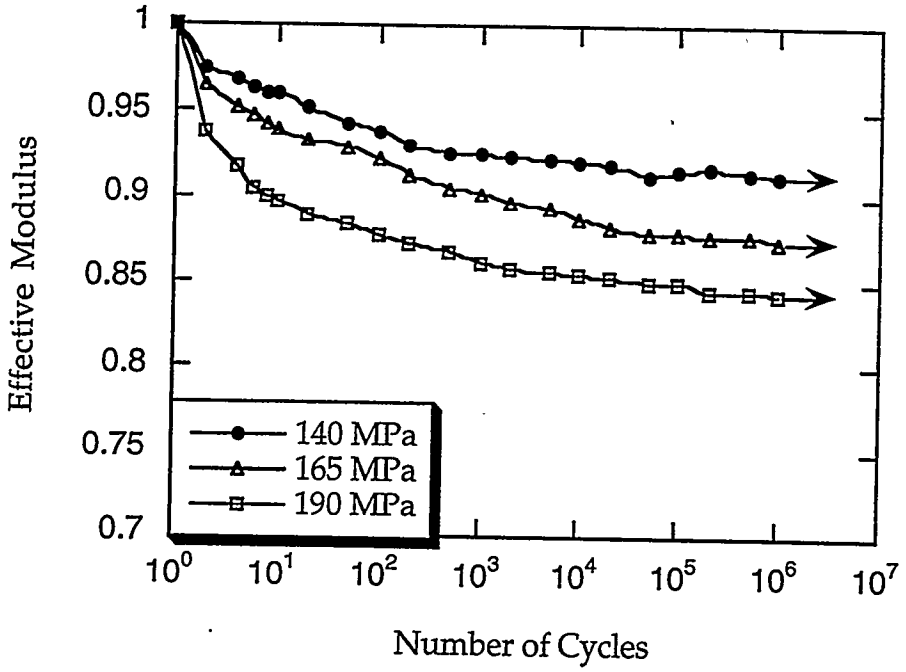

Figure 3. The reduction in effective modulus due to fatigue in the transverse orientation of the Nicalon/SiC composite.

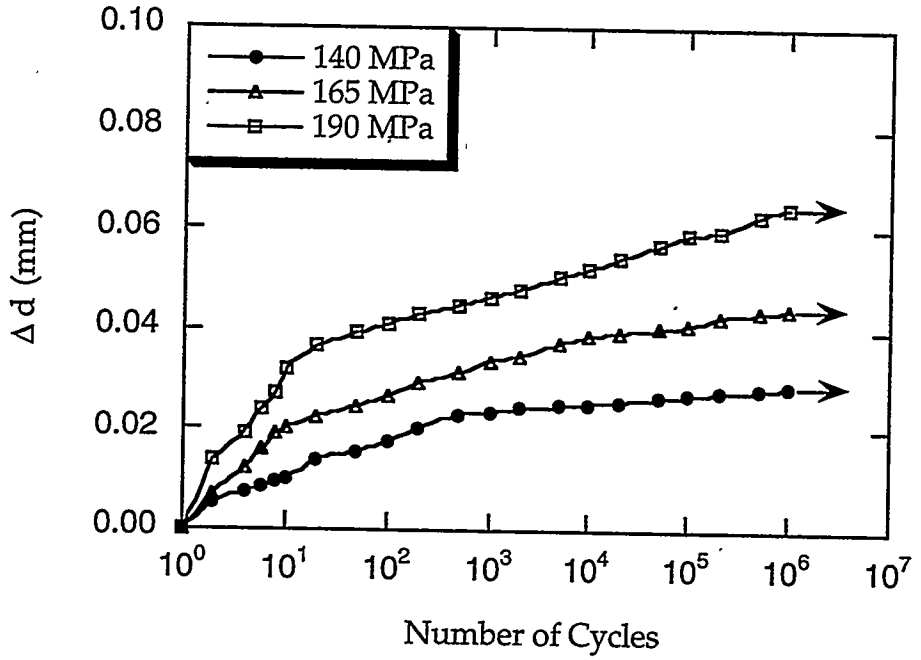

Figure 4. The increase in midspan deflection (Δd) values due to fatigue in the edge-on orientation of the Nicalon/SiC composite.

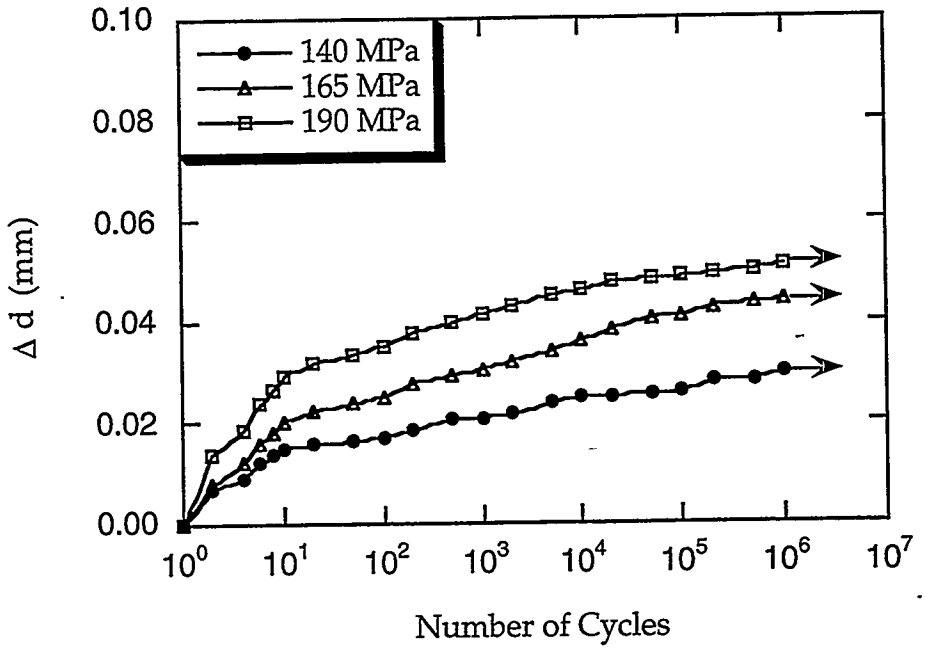

Figure 5. The increase in midspan deflection (Δd) values due to fatigue in the transverse orientation of the Nicalon/SiC composite.

CONCLUSIONS

The monotonic and fatigue behavior of the Nicalon/SiC composite appears to be unaffected by the orientation of fabric plies to the applied loads. The effective modulus of the composite decreased after the first loading cycle in both orientations. After a relatively steep decrease in the modulus values in the first ten cycles, the modulus values decreased more gradually upon further cycling. Consistent with the effective modulus decrease trends, the midspan deflection values increased rapidly in the first ten cycles and then more slowly upon further cycling. It appears that most of the damage in the composite occurs in the first few loading cycles.

FUTURE WORK

The specimens subjected to fatigue loading up to 10^5 cycles will be examined under a scanning electron microscope to gain an understanding of damage progression in the material subjected to cyclic loading. The elevated-temperature monotonic and fatigue behavior of the Nicalon/alumina and Nicalon/SiC composites will be investigated next. Finally, theoretical and numerical modeling will be attempted to help explain the fabric orientation effects on the monotonic and fatigue behavior of CFCCs.

ACKNOWLEDGMENTS

This work is supported by the Department of Energy under contract No. Lockheed Martin 11X-SV483V to the University of Tennessee. We are grateful to Dr. Arthur Rowcliffe and Dr. Everett Bloom of ORNL for their continued support and understanding. Thanks are due to Dr. Jeff Armstrong of AlliedSignal Engines for providing the composite material used in the present study. Acknowledgments are also due to Ted Long, Greg Jones, Doug Fielden, and Mike Ensor for their help in setting up the flexure test system and fabrication of the composite specimens.

REFERENCES

1. A. G. Evans, Mater. Sci. Eng. **A107** (1989) 227.

2. A. G. Evans, J. Am. Ceram. Soc. **73** (1990) 187.

3. N. Miriyala, P. K. Liaw, C. J. McHargue and L. L. Snead, Fusion Materials: Semiannual Progress Report for Period Ending December 31, 1995, DOE/ER-0313/19, p 115.

4. N. Miriyala, P. K. Liaw, C. J. McHargue, L. L. Snead and A. S. Fareed, "Effect of Fabric Orientation on the Monotonic and Fatigue Behavior of a Nicalon/Alumina Composite," Ceramic Transactions, 1996, in press.

5. N. Miriyala, "Fabric Orientation Effects on the Monotonic and Fatigue Behavior of CFCCs, " Doctoral Dissertation Proposal, The University of Tennessee, 1995.

6. A. G. Evans, F. W. Zok and R. M. McMeeking, Acta Metall. Mater. **43** (1995) 859.

NEUTRON IRRADIATION EFFECTS ON HIGH NICALON SILICON CARBIDE FIBERS - M. C. Osborne and D. Steiner (Rensselaer Polytechnic Institute), and L. L. Snead (Oak Ridge National Laboratory)

Summary

The effects of neutron irradiation on the mechanical properties and microstructure of SiC and SiC-based fibers is a current focal point for the development of radiation damage resistant SiC/SiC composites. This report discusses the radiation effects on the Nippon Carbon Hi-Nicalon™ fiber system as also discusses an erratum in earlier results published by the authors on this material. The radiation matrix currently under study is also summarized.

Introduction

Due to the intrinsically low activation of silicon carbide and the relatively high toughness of SiC/SiC composites, these materials have become an attractive alternative to conventional structural materials for future fusion devices. However, it has been demonstrated that the "off-the-shelf" SiC/SiC composites undergo significant degradation at fluences as low as 1 dpa [1]. This degradation has been attributed to the densification of the Nicalon™ fiber, which has been the standard fiber used in the study and development of SiC/SiC composites. The primary emphasis in the fusion community is toward a more stoichiometric SiC fiber, which should not undergo the large densification seen in regular Nicalon™, and hopefully exhibit the modest swelling typical of stoichiometric SiC. The Nippon Carbon Hi-Nicalon™ fiber (Table 1) in particular has received significant attention from the fusion community owing to its very low oxygen content, typically less than a few tenths of a percent.

Table 1. Properties and Composition of SiC Fibers

	Nicalon	Hi-Nicalon	Hi-Nicalon Type S (Stoichiometric)	Dow Corning Stoichiometric	CVD SiC
Diameter (mm)	14	14	12	10	
Strength (GPa)	2.8	2.8	2.6	2.8	
Modulus (GPa)	220	270	420	400	450
Failure Strain	0.014	0.010	0.006	0.007	
Density (g/cc)	2.55	2.74	3.1	>3.1	3.21
Si (wt %)	56.6	62.4	68.9	67.7	70.0
C (wt %)	31.7	37.1	30.9	28.6	30.0
O (wt %)	11.7	0.5	0.2	0.9	
B (wt %)				2.4	
N (wt %)				0.4	

Discussion

Data from earlier work by the authors [2] shows the effects of atomic displacements on the tensile strength and tensile modulus of Hi-Nicalon^{TM} fiber. Since this report, the fiber diameter measurement was found to be in error. In the original report, the fiber diameter was determined by optically imaging the fiber following tensile testing. The measurement problem arose from the cleaning treatment prior to imaging. Specifically, before the tensile testing the fiber was coated with silicon vacuum grease to minimize the spread of contamination and to aid in recovery of the fiber after it was broken. The fiber remnants were then collected and cleaned ultrasonically in a ethyl alcohol solution and imaged optically. These diameters were used to reduce the data shown in Fig. 1.

SEM imaging was later used on fibers which were cleaned in a similar fashion. It became apparent that not all of the silicon vacuum grease was removed during the cleaning process, thus leaving a residue and yielding inaccurate (high) diameter data. The inaccurate data as measured optically yielded a diameter of 15.3 μm, while that measured via SEM was 13.7 μm. As further confirmation some higher dose irradiated fibers (2.56×10^{25} n/m^2) have recently become available for tensile measurement and using the SEM for fiber diameter measurement. These fibers did not have vacuum grease residue and gave an average diameter of 13.4 μm.

To correct the data referred to above, it is noted that the density did not vary significantly up to 0.32 dpa and the density increased by about 4% at 2.56 dpa. Therefore, the diameters of the fibers for the previously reported data can be taken as the unirradiated average value and the strengths and moduli can be reconstructed as shown in Fig. 2. From this figure, the strength increases sharply at low damage levels and then shows a moderate increase. This is somewhat different than the behavior presented in the previous report and Fig. 1. The modulus of the fibers of Fig. 2 exhibit a decrease followed by an increase but the effect is not as drastic as previously reported (about 5% decrease rather than about a 10% decrease). Since these are only estimates of the low level irradiation conditions, the 0.1 and 0.32 dpa conditions are being repeated.

A slightly different representation of the data is given in Fig. 3. The strength, strain, and elastic strain energy density are plotted against dpa. Strain energy density is calculated as one half times the stress times the strain [3]. The strain shown in Fig. 3 is the average strain calculated using laser micrometer measurements of the gage length and displacement, no diameter measurements are involved in its calculation. The figure presents the data in a more intuitive manner by showing that as the fibers strengthen with irradiation, there is more elongation and more energy (on average) is needed to fracture the fibers. The reasons for this are still under investigation and will be discussed in a later semiannual.

HFIR Experiments In Progress

The fibers currently under evaluation (under irradiation or irradiated) are listed in Table 1. This table gives unirradiated fibers mechanical properties and nominal composition, as provided by the manufacturers [4, 5].

Table 2 summarizes the fiber irradiation program in the HFIR hydraulic rabbits positions HT-2, HT-7, or HT-3. The times in each position are varied to get the appropriate fluence for E>0.1 MeV. The fiber temperature is achieved through defining a gas gap between the fiber holder and the rabbit internal wall. Each rabbit includes a silicon carbide temperature monitor. The conditions for the irradiations are shown in Table 2. It is expected that the irradiations will be complete by November 1996, with the evaluation of tensile properties completed by years end.

Table 2. Irradiation Conditions of SiC Fibers

	0.1 dpa	0.5 dpa	2.0 dpa	5.0 dpa
100°C	completed	completed	completed	completed
500°C	completed	completed	completed	in progress
800°C	in progress	in progress	in progress	in progress

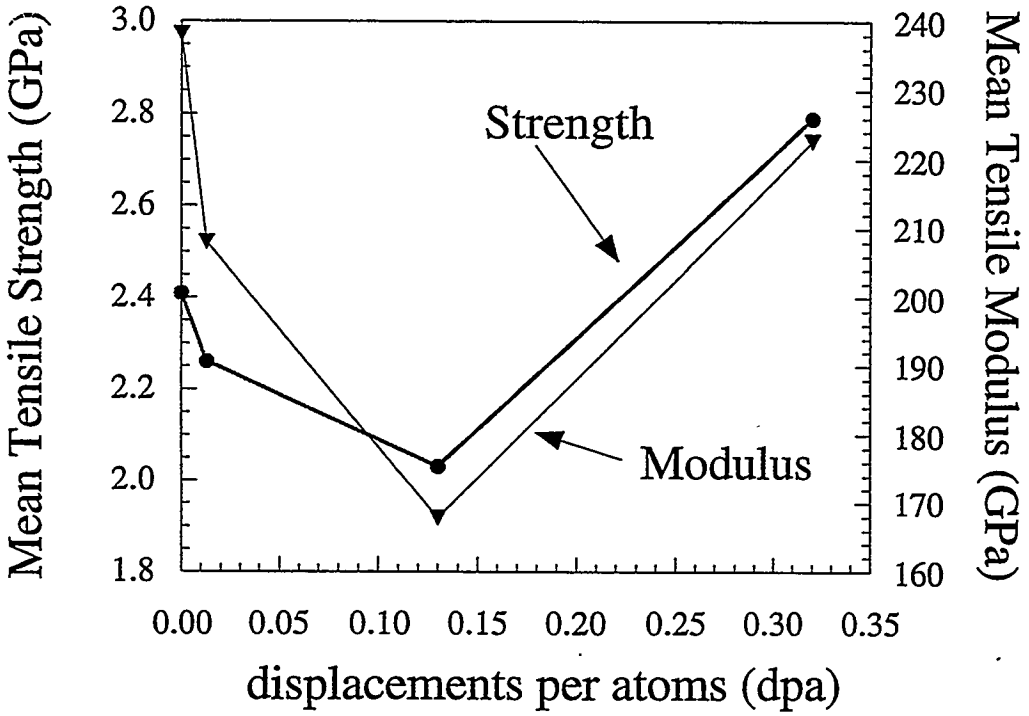

Fig. 1. Mean strength and modulus vs damage level as originally reported in [1].

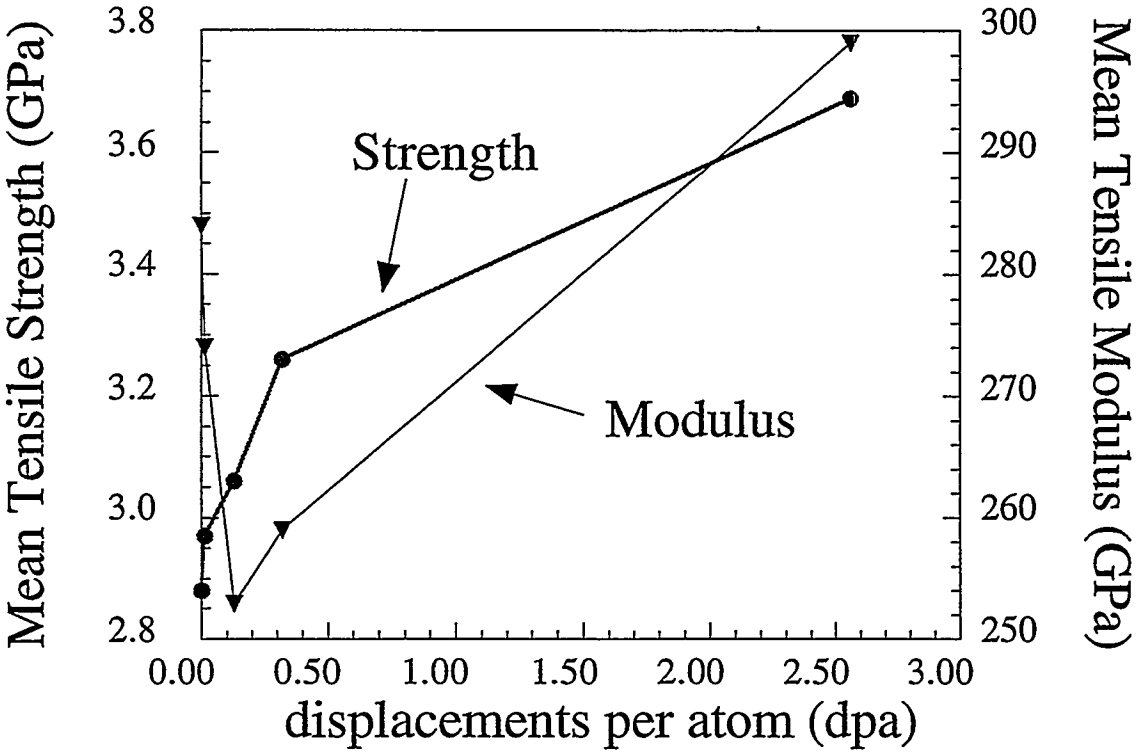

Fig. 2. Corrected strength and failure strain vs damage.

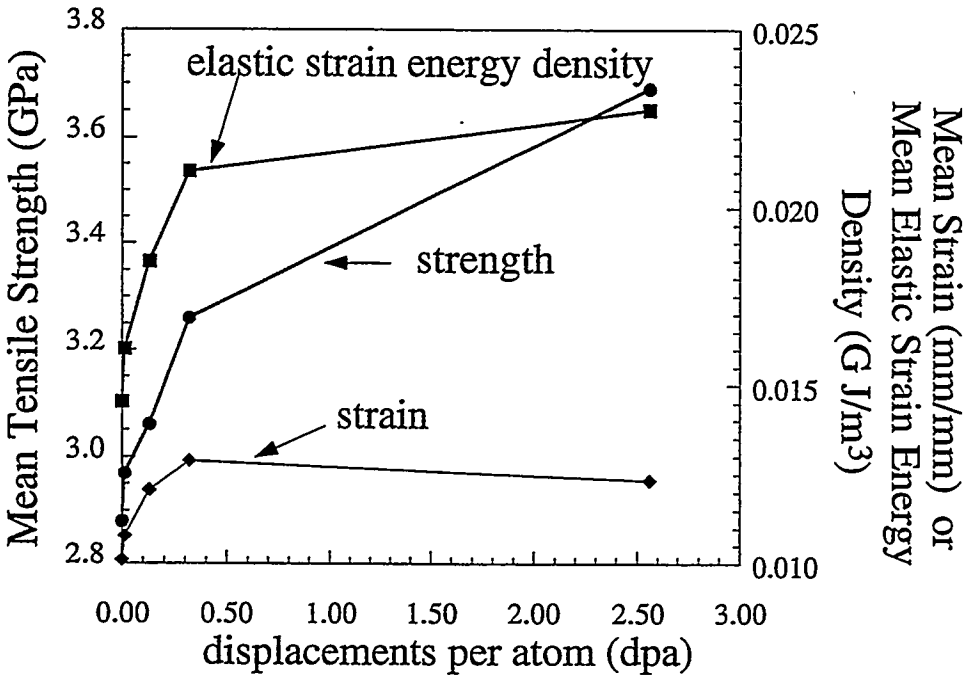

Fig. 3. Mean strength, mean strain, and mean elastic strain energy density vs damage.

References:

[1] L. L. Snead, S. J. Zinkle and D. Steiner, "Measurement of the Effect of Radiation Damage to Ceramic Composite Interfacial Strength," Journal of Nuclear Materials [191-194] 1992, pp. 566-570.

[2] M. C. Osborne, L. L. Snead, and D. Steiner, Journal of Nuclear Materials **219** (1995), 63.

[3] G. E. Dieter, *Mechanical Metallurgy*. 3rd ed., 1986, New York: McGraw-Hill Publishing Co.

[4] J. Lipowitz, *et al.*, Ceramic Engineering and Science Proceedings, **16** (1995) 55.

[5] M. Takeda, *et al.*, Ceramic Engineering and Science Proceedings, **16** (1995) 37.

SPECIMEN SIZE EFFECT CONSIDERATIONS FOR IRRADIATION STUDIES OF SiC/SiC G. E. Youngblood, C. H. Henager, Jr., and R. H. Jones (Pacific Northwest National Laboratories)*

OBJECTIVE

The objective of this work is to examine current practice for comparing the mechanical and thermal properties of irradiated, continuous SiC fiber/SiC matrix composites (SiC/SiC) and to recommend test methodologies within the constraints of limited reactor test volumes.

SUMMARY

For characterization of the irradiation performance of SiC/SiC, limited available irradiation volume generally dictates that tests be conducted on a small number of relatively small specimens. Flexure testing of two groups of bars with different sizes cut from the same SiC/SiC plate suggested the following lower limits for flexure specimen number and size: Six samples at a minimum for each condition and a minimum bar size of 30 x 6.0 x 2.0 mm^3.

PROGRESS AND STATUS

Introduction

Continuous fiber ceramic composites (CFCC's) are currently under development for advanced aerospace or heat engine components. These applications for CFCC's will require optimum material behavior and a reliable means for physical and mechanical property characterization. For this reason, the ASTM Subcommittee C28.07 recently has set some standard methods for analyzing and testing CFCC's, i.e., tensile and shear strength as of December 1995.[1] Other test methods currently are being considered, i.e., flexural and compressive strength, tension-tension cyclic fatigue, creep and creep rupture under tensile loading, fracture toughness, tube strength and interfacial and thermal property testing.

A SiC fiber-reinforced/SiC matrix composite (SiC/SiC) is a CFCC that is particularly attractive for structural applications in fusion energy systems.[2] Unfortunately, there is a very limited amount of reactor test space available with high neutron fluences in which to conduct irradiation studies of SiC/SiC. Furthermore, smaller test volumes usually involve larger flux gradients and perhaps temperature gradients, each of which are additional incentives to use small specimen sizes. Within these constraints, the effect of specimen number and size reduction on the validity of the experimental measurements for irradiation studies of SiC/SiC is an important consideration.[3]

Mechanical property testing of irradiated SiC/SiC to date has emphasized the flexural method primarily because it uses a simple sample geometry that is compatible with SiC/SiC fabrication procedures.[4-5] Reactor space and ease of testing will likely make this geometry useful for fusion purposes. Therefore, this report will focus on the influence of the specimen number and size on the mechanical property values when determined by the flexural method.

---

*Pacific Northwest National Laboratory is operated for the U. S. Department of Energy by Battelle Memorial Institute under Contract DE-AC06-76RLO 1830.

SiC/SiC Background

Figure 1 depicts a common SiC/SiC architecture, where the composite is made up of two-dimensional (2D), 0-90° plain weave cloth layers (plies) with a surrounding matrix of polycrystalline SiC deposited by chemical vapor infiltration (CVI). In this balanced 2D structure, the fibers make up about 40% of the volume with 20% in each principal direction. Obviously for this SiC/SiC architecture, care must be taken to prepare samples compatible with the principal directions, with the understanding that properties in other directions can be filled in with appropriate composite models.

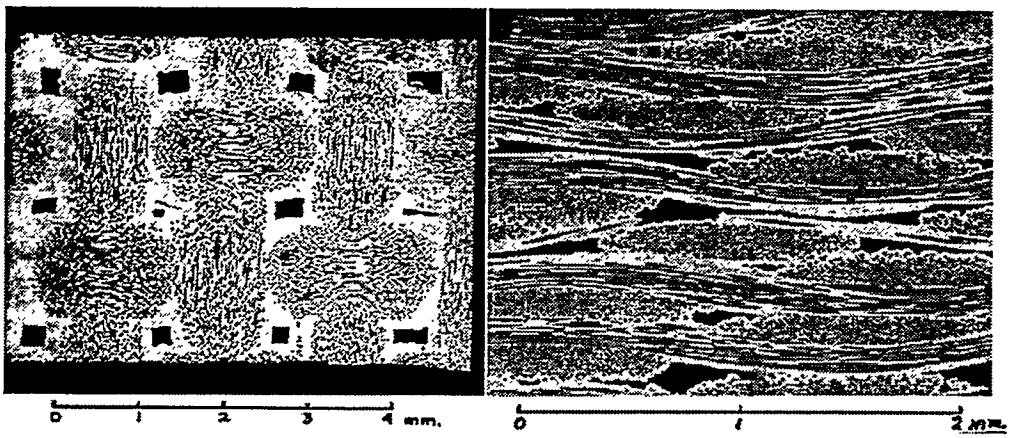

Figure 1. SiC/SiC 2D, 0-90° balanced weave architecture and macrostructural features.

The cloth layers are woven from untwisted yarns (tows) which contain 500 to 1000 individual SiC fibers with diameters of about 12 microns. The composite cell structure has a nominal repeat distance of 1-2 mm in the weave plane and about 0.3 mm ply-to-ply. The anisotropic interlayer macroscopic porosity appears correlated to the repeat cell structure. These macroscopic structural features will influence the mechanical properties, especially the interlaminar shear strength of SiC/SiC. Other physical properties, such as thermal conductivity, also will be particularly affected by the bundle geometry and the macroporosity. The shape and distribution of these macroscopic features suggest that a minimum number of repeat cells will set a practical lower limit on the specimen test size needed to be representative of this type of woven material.

In a SiC/SiC composite, the high strength fibers (~2 GPa) reinforce the matrix and can considerably improve the composite toughness and ultimate fracture strength over that of monolithic SiC. As stress levels increase, the matrix microcracks and debonds from the fibers, and the load is gradually transferred from the matrix to the stronger fibers. The mechanical properties now will be primarily determined by the nature of the matrix microcracking and by individual fiber cracking and pull-out. Due to the complex fiber-matrix interaction, these composites exhibit non-linear stress-strain behavior. The ultimate composite tensile strength is determined by gross fracture of the fiber bundles.

In Table 1, the room temperature ultimate strength and strain values and initial modulus values (% Std. Dev. in parenthesis), determined by three different test methods for a reference SiC/SiC, are compared.[6] The number of specimens and specimen dimensions used for each method also are listed. ASTM recommends that at least 10 specimens be tested for each condition to achieve statistically reliable average values.[7] To obtain a valid flexural strength, the composite must break or fail by tension or compression in the outer fibers, rather than by shear failure. Therefore, they also recommend a support span-to-depth ratio (S/d) of at least 32/1 and 16/1 for the 4-Pt and 3-Pt flexural methods, respectively. A high S/d ratio maintains the shear stresses low relative to the tensile or compressive stresses during flexural testing. Composite 2D SiC/SiC material can be relatively weak

in interlaminar shear. The specimen dimensions listed in Table 1 meet ASTM specifications, but for the flexure tests the numbers of specimens are below the recommended level.

Table 1. Comparison of Tensile and Flexural Properties (at 23%C) of a Reference SiC/SiC*

Property	Tensile	4-Pt Flex	3-Pt Flex
Number	246	6	4
Dimensions, LxWxD (mm)	150x6x2	100x6x3	52x6x3
Ultimate Strength (MPa)	192 (9)	278 (7)	338 (6)
Initial Modulus (GPa)	228 (14)	180 (14)	140 (15)
Ultimate Strain (%)	0.22 (18)	0.22 (9)	0.30 (10)

*2D 0-90° balanced weave, Nicalon-CG fibers, 150 nm PyC-interphase, fabricated by Dupont Lanxide Composites, Inc., Newark, DE.

It is apparent from the data listed in Table 1 that measured property values depend upon the test method employed. The ultimate tensile strength and strain values are lower and the initial modulus is higher for the tensile test relative to either bend test, while a similar trend is observed going from the 4-Pt to the 3-Pt bend test. A lower strength from a tensile test relative to a bend test, and correspondingly from a 4-Pt to a 3-Pt bend test, reflects the differing stress distributions and volumes exposed to the maximum stresses within the specimens as well as non-linear flexure behavior of SiC/SiC.[8] These effects influence the initial modulus and elongation values as well.

The flexural test method should only be used for material development, quality control and component design flexural specifications. In this method, the flexural stress is computed from elastic beam theory with the simplifying assumptions that the composite is homogeneous and linearly elastic, which can be approximately valid for composites with the principal fiber direction coincident/transverse with the axis of the beam. Even though methods exist to determine tensile or compressive composite strengths from flexural data,[9] the methods can be expected to result in ambiguity where the composite structures are as anisotropic and inhomogeneous as the one illustrated in Figure 1. For this reason, the statistical uncertainties (listed in parenthesis in Table 1) probably reflect sample to sample variations in the macroscopic structural features (interlayer porosity, bundle weave pattern, etc.) rather than differences in microscopic flaw distributions.

With the Table 1 data as a baseline, flexural tests were performed on a set of SiC/SiC bend bars with smaller than ASTM recommended dimensions for comparison. The dimensions were selected based on the dual practical consideration of a limited irradiation test space and a desire to retain a representative number of complete fiber bundle repeat cells in a test specimen. Currently, a second set of bars is being irradiated in the HFIR reactor as part of the U.S. DOE-Monbusho/Jupiter fusion materials program and will be evaluated later. The effect of using smaller and fewer samples for flexural measurements of unirradiated SiC/SiC will be evaluated in this progress report.

Experimental Procedure

The tested 2D 0-90° SiC/SiC composites were fabricated by CVI as before, but the fiber was Hi-Nicalon, an advanced SiC fiber. Hi-Nicalon has a much reduced oxygen content (<0.5 wt% O) and an improved thermal stability (to about 1300°C) compared to Nicalon-CG (~12 wt% O and 1100°C, respectively). In addition, the Hi-Nicalon fiber diameter uniformity is much improved over that of Nicalon-CG (about a 50% reduction in diameter variability). It is anticipated that SiC/SiC made with Hi-Nicalon will exhibit improved mechanical properties as well as improved irradiation performance. Improved mechanical properties is expected because the post-CVI fiber strength should be higher and improved irradiation performance is anticipated because the fiber is more crystalline.

Two size groups of flexural test bars (38.4 x 6.6 x 3.5 and 25.1 x 4.0 x 2.0 mm^3) were cut and machined from a 20 cm square by 3.5 mm thick plate. Although the overall dimensions differed, the S/d ratios were kept about the same for the two size groups. The bars had geometric densities in the range 2.52 ± 0.05 g/cm^3. For this size effect study, flexure tests were performed at 500°C in argon (7 bars per size group) to also provide a baseline for the later Jupiter irradiation tests.

The 4-Pt bend test procedures and fixtures generally were the same as used in previous studies.[5] The outer/inner pin spacings were 30/15 and 20/10 (mm) for the larger and smaller bars, respectively. For the 20/10 bars, the surface in compression had been machined to attain the 2 mm bar thickness. For both bar sizes, the tension surfaces were the as-received CVI-coated surfaces. The Instron cross-head speed was adjusted to maintain the outer surface strain rate at 1.1×10^{-3} s^{-1} to within 10% for each bar size, as recommended by ASTM.[7]

Results and Discussion

All of the seven bar samples in the 38 mm group appeared to fracture initially in tension between the inner load pins as required for valid flexural testing. Two of the bars in the 25 mm group appeared to fracture initially by shear directly under an inner load pin, and their data was invalidated. The other five bars in the 25 mm group appeared to fail in tension initially as required. The stress-strain curves appear slightly separated for the two size groups as shown in Figure 2. The valid average ultimate strength and strain values and the initial modulus values for the two groups are presented in Table 2 with standard deviations in percent given in parenthesis. The flexural strength and strain values measured for the Hi-Nicalon/SiC are considerably improved over the Table 1 baseline values for Nicalon-CG/SiC. The initial modulus determined for Hi-Nicalon/SiC is somewhat lower than determined for Nicalon-CG/SiC and may be due to the thicker carbon interphase used in the Hi-Nicalon composite.

Within experimental uncertainty, the initial modulus is the same for each size group, but above the matrix cracking stress of about 150-200 MPa, the 25 mm group exhibits a somewhat softer modulus than the 38 mm group. Since the S/d ratios were the same for both groups, and therefore the stress distributions based on LEFM were the same, the observed modulus difference above the matrix cracking stress likely was due to the difference in bar widths. The 38 mm and 25 mm groups contained about six and four fiber bundles across their widths, respectively. The bars containing more complete fiber bundles should statistically exhibit higher overall strength and more representative values. The somewhat larger uncertainties exhibited by the 25 mm group probably reflect the larger statistical variation in macroscopic structural features which would have a greater influence in the testing of smaller specimen volumes.

Table 2. Flexural Properties of SiC/SiC Calculated from Figure 2 Data (7 and 5 bars, respectively)*

Property	38 mm Group	25 mm Group
Ultimate Strength (MPa)	567 (3)	513 (10)
Initial Modulus (GPa)	107 (15)	108 (9)
Ultimate Strain(%)	0.83 (3)	0.86 (6)

* Fabricated by Dupont Lanxide, 2D 0-90° plain weave, Hi-Nicalon fiber, 1.2 μm C-interphase.

Although the measured differences in mechanical property values weren't large between the two groups, the 38 x 6.6 x 3.5 mm^3 bar size data appears to be more representative and reproducible than the 25 x 4 x 2 mm^3 bar size data. If reactor test volume restricts flexure bar sizes below the 38 mm group size, based on this work a recommended lower limit bar size would be 30 x 6.0 x 2.0 mm^3, which maintains the 2/1 flexure pin spacing with S/d = 10. During a flexure test, the maximum shear stress (τ) that builds up along the neutral plane is given by $\tau = 0.75P/bd$ where P is the load and b

and d are the bar width and depth, respectively. To prevent premature failure by shear rather than failure by tension, the shear stress can be reduced by increasing the bar width which compensates for decreasing the bar depth to 2.0 mm. Also, a 6.0 mm bar width would contain at least five full fiber

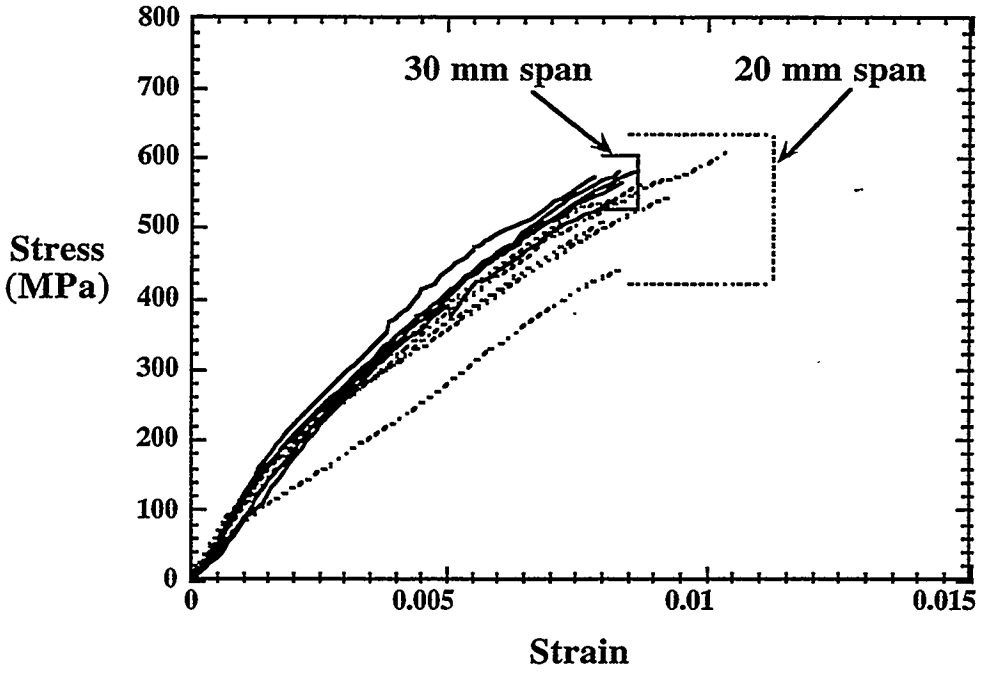

Figure 2. Stress-Strain Curves from 4-Pt Flexure Tests for Two Bar Sizes of 2D 0-90° SiC/SiC.

bundles across its width, given the current 2D 0/90° composite architecture and therefore is more representative of the composite material than a narrower bar. If bar depths are reduced, they should only be reduced from one surface and that surface should be the compression surface. A slight increase in length from 25 to 30 mm would allow a 5 mm outer pin overhang, which is recommended by ASTM specifications.[7] Finally, at a minimum, at least six samples for each condition should be tested to achieve statistically representative (± 10%) flexure property values.

CONCLUSIONS

1. The flexural ultimate strength and strain values measured for a Hi-Nicalon/SiC composite were considerably higher than baseline values representative of a Nicalon-CG/SiC reference composite.

2. For reliable and reproducible flexure testing of typical 2D 0-90° SiC/SiC, the following recommendations are proposed:

- minimum sample dimension of 30 x 6.0 x 2.0 mm^3.
- span to depth ratio of 10.
- 2/1 flex pin spacing.
- minimum width of 6 mm.
- test a minimum of 6 samples.
- reduce thickness from one side only - compressive surface.

FUTURE WORK

The size effect analysis for flexure bars will be repeated for a set of bars currently being irradiated in the HFIR reactor as part of the Jupiter fusion energy materials test program.

REFERENCES

1. M G. Jenkins and George D. Quinn, "ASTM Standards for Monolithic and Composite Advanced Ceramics: Industrial, Governmental and Academic Cooperation," ASME - IGTI 96, Birmingham U. K., 10-13 June 1996.

2. R. H. Jones, C. H. Henager, Jr. and G. W. Hollenberg, "Composite Materials for Fusion Applications," *J. Nucl. Mater.*, 191-194, 75-83 (1992).

3. R. H. Jones, G. D. Springer, G. E. Youngblood and M. L. Hamilton, "Review of Specimen Size Effects for Ceramic Matrix Composites,"

4. G. W. Hollenberg, C. H. Henager, Jr., G. E. Youngblood, D. J. Trimble, S. A. Simonson, G. A. Newsome and E. Lewis, "The Effect of Irradiation on the Stability and Properties of Monolithic Silicon Carbide and SiC_f/SiC Composites up to 25 dpa," *J. Nucl. Mater.*, 219, 70-86 (1995).

5. G. E. Youngblood, C. H. Henager, Jr., D. J. Senor and G. W. Hollenberg, "Effects of Neutron Irradiation on Dimensional Stability and on Mechanical Properties of SiC/SiC Composites," Fusion Materials Semiannual Progress Report for Period Ending September 30, 1994. DOE/ER-0313/17

6. M. H. Headinger, D. H. Roach, H. D. Driver, M. M. Gentile and R. J. Carter, "Comparison of Flex and Tensile Properties for SiC Matrix Composites Reinforced with Nicalon and T-300 Fibers," Presented at the 16th Ann. Conf. on Composites, Materials and Structures, Cocoa Beach, FL (1992).

7. "Standard Test Method for Flexural Properties of Continuous Fiber-Reinforced Advanced Ceramics Composites - ASTM Draft 1.7," 24 February 1996.

8. K. Buesing and T. Barnett, "Nonlinear Flexure Behavior of High Temperature Composites," in High Performance Composites for the 1990's, S. K. Das, C. P. Ballard and F. Marikar, eds., The Minerals, Metals and Materials Society, Warrendale, PA, pp. 283-293 (1991).

9. P. S. Steif and A. Trojnacki, "Bend Strength Versus Tensile Strength of Fiber-Reinforced Ceramics," *J. Am. Ceram. Soc.*, 77[1] 221-29 (1994).

TECHNIQUE FOR MEASURING IRRADIATION CREEP IN POLYCRYSTALLINE SiC FIBERS - G. E. Youngblood, M. L. Hamilton and R. H. Jones (Pacific Northwest National Laboratory)*

OBJECTIVE

The objective of this work is to examine irradiation enhanced creep behavior in polycrystalline SiC fibers. This data will be used in conjunction with results from irradiation creep of SiC/SiC composites to help develop a predictive creep equation for composite materials.

SUMMARY

A bend stress relaxation (BSR) test has been designed to examine irradiation enhanced creep in polycrystalline SiC fibers being considered for fiber reinforcement in SiC/SiC composite. Thermal creep results on Nicalon-CG and Hi-Nicalon were shown to be consistent with previously published data with Hi-Nicalon showing about a 100°C improvement in creep resistance. Preliminary data was also obtained on Nicalon-S that demonstrated that its creep resistance is greater than that of Hi-Nicalon.

PROGRESS AND STATUS

Introduction

A previous review examined experimental work carried out by General Atomics in the 1970's on irradiation creep in monolithic SiC.[1,2] In this work a higher rate of creep compared to thermal creep was observed, and surprisingly, the creep in this high temperature ceramic exhibited some similarity to irradiation-enhanced creep in metals. Based on this review, a systematic examination of the creep behavior of SiC/SiC composite and SiC fibers has been initiated. In particular, creep behavior of SiC/SiC composite and SiC fiber will be examined for fusion energy relevant temperatures, times and irradiation doses.

To examine creep behavior in SiC composite, a pressurized thin-walled metallic bladder will impose a constant hoop stress to a surrounding SiC/SiC tube. By a laser interference technique the circumferential strain in the SiC/SiC tube will be determined as a function of applied stress, temperature and dose. The SiC/SiC tubes will be made with different fiber types and matrix structures. Since composite creep is expected to be dominated by fiber creep, a simple bend stress relaxation (BSR) test to examine fiber creep behavior alone will be carried out in parallel to the composite creep tube test. This report presents some preliminary results for thermal control BSR tests and describes some conditions for the planned irradiated fiber BSR test.

Experimental Procedure

Theoretical and experimental details of the BSR test, developed and presented by researchers at NASA Lewis[3-7], will be closely followed. In Fig. 1, a schematic representation of a BSR test, modified to also examine the influence of irradiation, is depicted. An initial elastic bend strain (e_o) is imposed on a fiber by wrapping several coiled loops within a slightly recessed region along a SiC mandrel. The loops are captured by a split SiC jig with a known inside radius R_o. The split jig itself

*Pacific Northwest National Laboratory is operated for the U. S. Department of Energy by Battelle Memorial Institute under Contract DE-AC06-76RLO 1830.

is held together within a surrounding protective SiC sleeve (not shown in the figure). The split jig and sleeve are designed to hold the fiber loop configurations during the handling necessary for the irradiation treatment within the core of a reactor. The fiber loops are then subjected to a specific time (t), temperature (T), and irradiation dose (Φ), i.e., a high temperature (HTtΦ) treatment. To separate thermal creep effects, the test also is carried out without irradiation for equivalent times and temperatures, i.e., a high temperature (HTt) treatment.

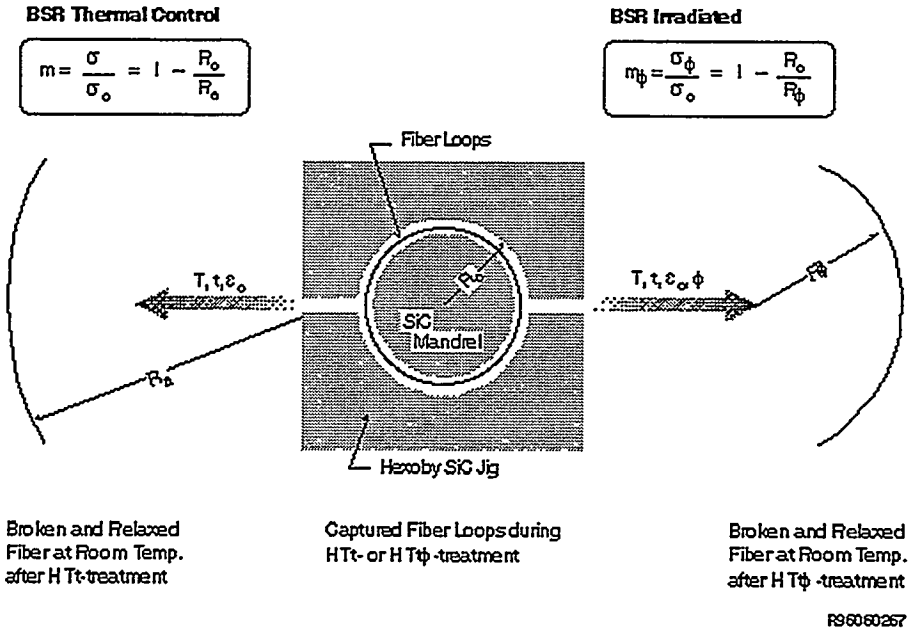

Figure 1. Schematic representation of a BSR fiber test to examine irradiation creep.

A BSR parameter "m", defined by Morscher and DiCarlo as the ratio of final to initial stress[3], quantifies the stress relaxation that occurs during either treatment:

$$m = \sigma(T,t,\Phi)/\sigma(T,0,0) = 1/[1 + (e_c/e_o)] \quad (1)$$

In Eq. (1), e_c and e_o are the total treatment-induced creep strain and the local initial elastic strain, respectively. Subject to several assumptions, m can be experimentally determined by the relations:

$$m = 1 - R_o/R_a \quad \text{(BSR thermal control)} \quad (2)$$

$$m = 1 - R_o/R_\Phi \quad \text{(BSR Irradiated)} \quad (3)$$

where R_a and R_Φ are the arc radii of the broken and relaxed fiber segments at room temperature after the HTtΦ or the HTt treatments, respectively. Values of m range from 1 to 0. If m = 1, the fiber behaved elastically or did not relax (creep) for the given time/temperature treatment. If m = 0, the fiber completely relaxed and retained the curvature subjected by the BSR jig. If $1 > m > 0$, the fiber partially relaxed during the treatment.

The assumptions necessary to arrive at the simple geometric relations given by Eqs. (2) and (3) have been critically examined by Morscher and DiCarlo.[3,4,6] They found that e_c generally was linearly dependent on stress, as expected for polycrystalline materials with stress relaxation (creep) due to grain boundary sliding mechanisms. This means that creep at each local position within the bent fiber follows the same time-temperature dependence. In pure bending, the local applied strains (held constant during treatment) increase linearly from the fiber neutral central plane to reach a maximum ($e_o = r_f/R_b$ where r_f is the fiber radius) at the fiber outer surface. Morscher and DiCarlo also observed that m generally was independent of most initial values of e_o, i.e., initial values of R_b. Finally, in an analysis of creep in polycrystalline -SiC fibers, Morscher et al[6] determined that creep determined by the BSR method was a consistent factor of two lower than that determined by a conventional tensile method. However, creep determined by either method exhibited the same time and temperature dependence. Hence fiber tensile creep, if desired, can be estimated from results for the much easier to perform BSR test.

Thermal BSR tests were performed initially on four different polymer-derived SiC fiber types. Relevant properties are given in Table 1 for the tested fiber types, which are listed in order of increasing creep resistance.

Table 1. Fiber Specimens and Properties

Type	Diameter (um)	Primary Phases	Elastic Modulus (GPa)
Tyranno S#	6.9±0.5	β-SiC, Si-O-C-Ti + C	190
Nicalon-CG^	11.4±2.5	β-SiC, Si-O-C + C	190
Hi-Nicalon^	12.0±1.6	β-SiC + C	270
Nicalon-S^	11.3±1.1	β-SiC	420

#UBE Industries, Tokyo, Japan; ^Nippon Carbon Co., Tokyo, Japan.

Except for the developmental fiber Nicalon-S, NASA Lewis has published background thermal BSR creep data for these fibers. Because the irradiation performance of monolithic SiC is quite attractive for fusion energy applications and because the Nicalon-S composition is near stoichiometric SiC, the irradiation performance of Nicalon-S fiber also is expected to be attractive. Thus, the detailed examination of the irradiation performance of Nicalon-S fiber in comparison to other SiC fibers is of current high interest. The primary goal of these initial thermal BSR tests was to assess the reliability of the modified jig and experimental procedure for use later in reactor tests. In these initial tests, several loops of a single fiber type were coiled at constant tension (≈ 7 MPa) around an alumina mandrel. The ends of the coil were temporarily held in place with a drop of Duco cement. An alumina sleeve with a 4.89 mm inside diameter, which set the applied strain at 0.24% for each case, was slipped over the fiber-wound mandrel to permanently hold the fiber loops in place during their thermal treatments. The initial maximum bend stresses, which depend on the fiber elastic modulus, ranged from 446 to 970 MPa. The alumina jigs containing the fibers to be treated were rapidly heated (5°C/min) inside a temperature controlled tube furnace and held for either one or twenty hours at 1000 or 1100°C. The BSR testing all took place in flowing argon (≈0.5 scfh) at approximately atmospheric pressure.

At the conclusion of the BSR test, the fiber coils either naturally broke up or were cut into several arc segments. Two sets of typical relaxed segments are shown in Fig. 2. The radii of the individual arc segments were determined with ruler and compass from x13 images.

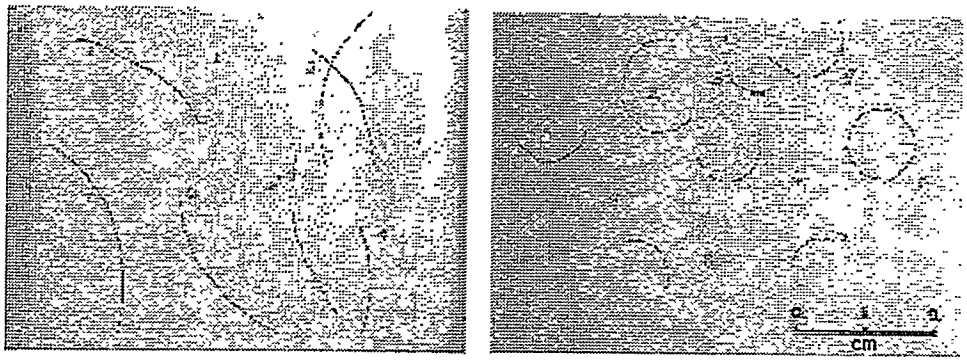

a) Nicalon-S b) Hi-Nicalon

Figure 2. Fiber segments of Nicalon-S and Hi-Nicalon after thermal BSR testing for 20 h at 1100°C in argon. Segment radius of curvature is related to creep resistance and m-value through Eqs. 1-3.

Results and Discussion

Qualitatively from Fig. 2, it is easy to ascertain that Hi-Nicalon fibers exhibit significantly more relaxation (creep) than Nicalon-S fibers for the BSR treatment conditions: 1100°C, 20 hours, argon and $e_o = 0.24\%$.

In Fig. 3, m values determined for our BSR tests on Nicalon-S, Hi-Nicalon and Nicalon-CG fibers are compared to NASA Lewis BSR data for Hi-Nicalon and Nicalon-CG. In our initial test, only two Nicalon-CG segments were recovered for measurements, thus the error bars were quite large (± 0.09). To reduce chances for accidental loss of experimental information, an important consideration for the planned reactor experiments, in later tests two separate coils of each fiber type were wrapped around the same mandrel. By determining the average relaxed radii of curvature for 8-10 segments, the typical error bars were reduced to less than ± 0.04 standard deviation. For the Nicalon-S fiber test, one of the coils inadvertently unraveled. The error bars for the average m value determined for the remaining three segments were somewhat larger (± 0.05). In this figure, the m values for the three 20 hour PNNL BSR tests fall between the data for the 1 and 100 hour NASA Lewis BSR tests, as expected. The m value shown for the PNNL 1 hour Nicalon-CG test coincides with the NASA Lewis data for that fiber. One hour BSR test results for the Tyranno S fiber at 1000 and 1100°C (data not shown) also agreed with NASA Lewis BSR results. It is obvious that the BSR test provides a convenient and reproducible method for evaluating fiber creep resistance.

The transition temperature range, where the m values appear to change from 1 to 0 over a rather narrow $\approx$ 200°C range, is an important concept. DiCarlo has shown that tensile strength data for most polycrystalline fibers exhibit a decrease at test temperatures where the rapid stress relaxation transition occurs.[3] The treatment conditions that lead to an m value of ≈ 0.5 might then be used as a practical indication of a fiber use temperature limit. Thus, for a 100 hour exposure, Nicalon-CG and Hi-Nicalon fibers would have an upper use temperature of about 1000 and 1120°C, respectively. Unfortunately, as yet BSR tests have not been completed to high enough temperature to define this transition for the Nicalon-S fiber.

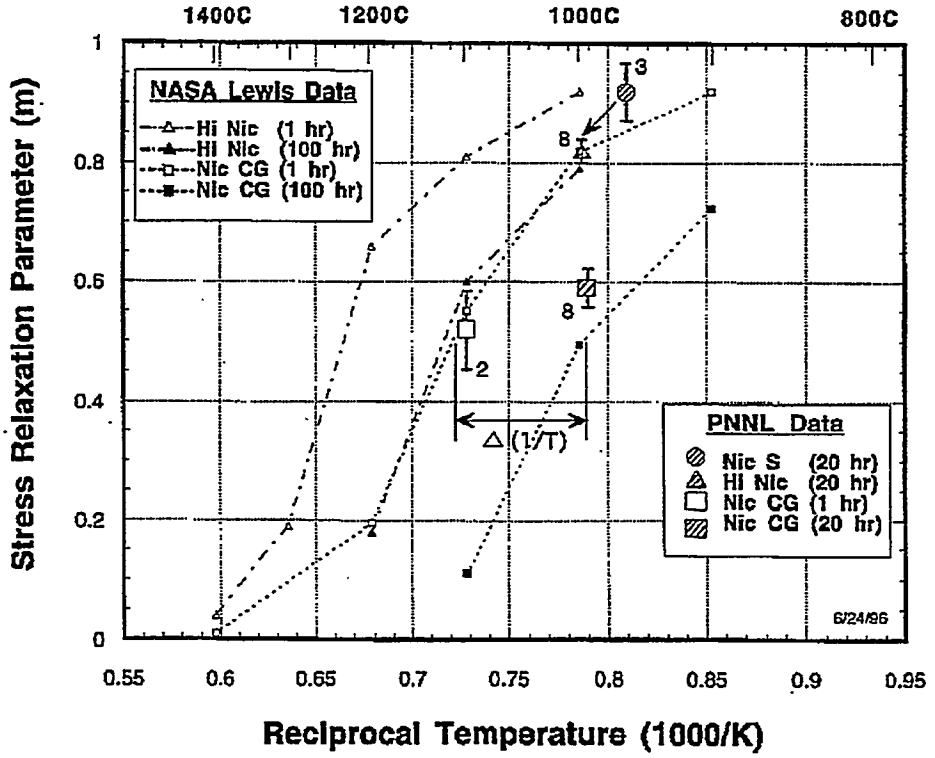

Figure 3. Comparison of PNNL BSR data with NASA Lewis BSR data for SiC type fibers.

From Fig. 3 it is apparent that the 100 hour BSR curves uniformly shift to a lower temperature range when compared to the 1 hour BSR curves. Morscher et al.[6] used the cross-cut method to provide an effective activation energy from such BSR data. They demonstrated reasonable agreement with an activation energy obtained from conventional fiber tensile tests for Nicalon-CG fiber. In this method, for one order of treatment time change the effective activation energy Q is given by:

$$Q = 2.303R/\Delta(1/T) \tag{4}$$

where R is the gas constant (8.314 J/mole). In Fig. 3, $\Delta(1/T)$ is indicated for two orders of time change, so the numerical factor in Eq. (4) must be changed to 4.606. For example, for Nicalon-CG and Hi-Nicalon fibers, Q = 555 or 722 J/mole, respectively.

CONCLUSIONS

1. The BSR test provides a convenient and reproducible method for evaluating fiber creep resistance and should be adaptable for assessing the influence of irradiation enhanced creep in SiC fibers.

2. Preliminary stress-relaxation data suggests that Nicalon-S is more creep resistant than Hi-Nicalon. This is the first creep data for this fiber.

FUTURE WORK

1. Continue thermal control BSR tests of SiC fibers at temperatures in the 1100 to 1300°C range. These tests will be carried out in a prototype SiC irradiation jig to avoid interactions between the fibers and the jig.

2. Initiate irradiation BSR tests in either the ATR reactor (Idaho Falls) or the HFBR reactor (Brookhaven).

REFERENCES

1. F. A. Garner, G. E. Youngblood and M. L. Hamilton, "Review of Data on Irradiation Creep of Monolithic SiC," Fusion Materials Semiannual Report for Period Ending December 31, 1995.

2. T. D. Gulden and C. F. Driscoll, "Creep of Chemically Vapor-deposited β-SiC with an Analysis of Creep in Bending," GA-10366, General Atomics Co. (1971).

3. G. N. Morscher and J. A. DiCarlo, "A Simple Test for Thermomechanical Evaluation of Ceramic Fibers," *J. Amer. Ceram. Soc.,75(1),136-40 (1992).*

4. J. A. DiCarlo, "Creep Limitations of Current Polycrystalline Ceramic Fibers," *Composites Science and Technology 51, 213-222 (1994).*

5. G. N. Morscher and J. A. DiCarlo, "Creep and Stress Relaxation Properties in Relation to Microstructure for SiC Fibers," *HITEMP Review Vol. III, Oct. 25-27, 1993. NASA CP19117.*

6. G. N. Morscher, H.-M. Yun and J. C. Goldsby, "Viscoelastic Analysis of Bend Stress Relaxation and Tensile Primary Creep of a Polycrystalline α-SiC Fiber," to be published in *Plastic Deformation of Ceramics III (1996).*

7. H.-M. Yun, J. C. Goldsby and J. A. DiCarlo, "Effects of Thermal treatment on Tensile Creep and Stress-Rupture Behavior of Hi-Nicalon SiC Fibers," *Ceram. Eng. Sci. Proc. (1995).*

PROGRESS IN THE DEVELOPMENT OF A SiC_f/SiC CREEP TEST- M. L. Hamilton, C. A. Lewinsohn, R. H. Jones, G. E. Youngblood, F. A. Garner (Pacific Northwest National Laboratory)[a], and S. L. Hecht (Westinghouse Hanford Company)

OBJECTIVE

The objective of this work is to determine the irradiation creep behavior of SiC_f/SiC composite materials. This requires the development of an appropriate creep specimen since pre-existing creep specimen geometries are not adequate.

SUMMARY

An effort is now underway to design an experiment that will allow the irradiation creep behavior of SiC_f/SiC composites to be quantified. Numerous difficulties must be overcome to achieve this goal, including determining an appropriate specimen geometry that will fit in the irradiation volumes available and developing a fabrication procedure for such a specimen. A specimen design has been selected, and development of fabrication methods is proceeding. Thermal and stress analyses are being performed to evaluate the viability of the specimen and to assist with determining the design parameters. A possible alternate type of creep test is also being considered. Progress in each of these areas is described in this report.

INTRODUCTION

An earlier report demonstrated that monolithic SiC exhibited irradiation creep at 800-1000°C that was very similar to that observed in metals,[1] indicating that there is a need to understand both the mechanism and the technical implications of irradiation creep in SiC. It is anticipated that a creep strain of 0.1% will result in a composite component after only three years of operation at a stress of 100 MPa; this is a significant strain for a composite such as SiC_f/SiC. Lower creep rates are possible with lower stresses but this would be a severe performance limitation for SiC_f/SiC.

It is therefore considered necessary to quantify the irradiation creep behavior of SiC_f/SiC composites in this temperature regime. The pressurized tube geometry that has come to be considered standard for irradiation creep studies of metallic specimens is not appropriate for composites since the material is not fully dense and since welded closure of the tube is impossible. Thus development of an appropriate specimen is a necessary prerequisite for determining irradiation creep in composites. The majority of the effort to date has been in this direction.

The difference in the relative creep rates of monolithic SiC and SiC fibers suggests that creep of the composite will be dominated by creep of the fibers, so a parallel effort has also been initiated to determine the irradiation creep properties of SiC fibers. The results of the latter effort are also documented elsewhere in this progress report and will not be discussed further here.[2] Because obtaining irradiation creep data on SiC_f/SiC requires development of a novel test specimen to utilize the available irradiation facilities in the U.S., a parallel effort has been initiated to determine whether such data might be generated using another irradiation facility. Progress in this area is also described below.

---

a Operated for the U.S. Department of Energy by Battelle Memorial Institute under Contract DE-AC06-76RLO 1830.

PROGRESS

Specimen Development

After considering various possible specimen geometries, a geometry similar to that of the standard pressurized tube was selected for development. The geometry that was selected comprises an open-ended SiC_f/SiC tube with a pressurized metallic bladder placed inside the tube (see Figure 1). A stress state that is nominally biaxial (but which has yet to be fully analyzed) is produced in the tube when the assembly is heated and intimate contact is obtained between the outer composite sleeve and the inner pressurized bladder. A hoop stress is produced in the sleeve via the pressurized bladder, while an axial stress is expected from the friction between the two. The ratio between the hoop and axial stresses, however, is expected to be higher than the 2:1 ratio found in a standard pressurized tube specimen, and therefore the effective stress will be even closer to the hoop stress than in a standard specimen, where the effective stress is $0.866\sigma_\theta$.

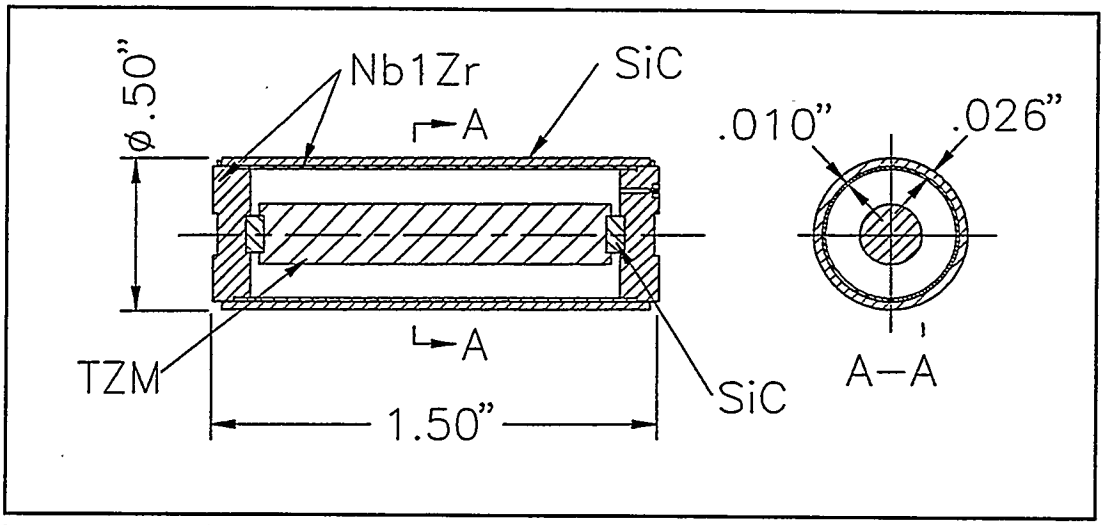

Figure 1. Schematic of the composite creep specimen design.

A number of significant fabrication and irradiation issues surfaced as development of such a specimen proceeded. Specimen volume is constrained by the space available in the proposed irradiation facility, HFIR. The choice of materials from which the bladder can be constructed is constrained by the likely effect of transmutations anticipated in HFIR, by the paucity of irradiation creep data in the temperature range of interest, and by the possible chemical interactions between the composite tube and the bladder. Additionally, fabrication of the composite in a tubular geometry is not trivial, although it has recently been demonstrated that such tubes can probably be made successfully.[3]

The material selected for the bladder is Nb-1Zr. Irradiation creep data were generated for this alloy in FFTF at temperatures ranging from about 1000-1200°C. Regressions were fit to these data, which were extrapolated to the temperatures of interest to allow the thermal and stress analyses described below to be performed for the proposed irradiations. Thermodynamic calculations indicated that the likelihood of chemical interaction between the sleeve and the bladder was high at the temperatures of interest. Some experimental effort has therefore been devoted to determining the magnitude of this interaction and to developing a coating for the bladder to prevent it. Performance predictions were made to determine the structural behavior of the proposed creep specimen to determine if the concept of using an internal bladder to drive creep of the surrounding specimen was viable. When the feasibility of this type of test had been demonstrated, parametric studies were performed to improve the design and to assess sensitivities. These issues are discussed in more detail in the following paragraphs.

Investigation of reactivity between β-SiC and Nb-1Zr

Data on the chemical compatibility between Nb-1Zr and SiC are not available in the literature. The reactivity between Nb-1Zr and SiC was therefore investigated using a computer program (CHEMSAGE) capable of calculating the Gibbs free energy of formation and rate of reaction for all compounds within the program database that can exist for a given thermodynamic state (pressure, temperature, number of moles). The actual reaction that will occur, however, will be limited by the kinetics of the transport mechanisms and the chemical reactions. After initial calculations indicated that the likelihood of reaction was high, a series of diffusion couple experiments was initiated to gather information on the kinetic aspects of the reactivity between Nb-1Zr and SiC.

Initially, the thermodynamic stability of Nb-1Zr and β-SiC (the phase present in the matrix of the chemical vapor infiltrated composites) was calculated at the lower end of the range of temperature of interest: at 800°C, with 1.01 bar total pressure, in pure helium. At this temperature, a niobium carbide (Nb_8C_7) and a niobium silicide ($NbSi_2$) had a negative Gibbs free energy of formation, as did zirconium carbide (ZrC_4), indicating that a reaction that produces these phases is energetically favorable. This does not imply that the reaction will proceed, however, since kinetic limitations must also be considered. Note that the thermodynamic calculations do not indicate metastable, or intermediate, phases that may also form.

Results of the initial thermodynamic calculation indicate that a diffusion barrier coating must be placed between the Nb-1Zr and the β-SiC to prevent a detrimental reaction from occurring during the creep experiments. Additional thermodynamic calculations were therefore performed to identify a candidate coating material. A survey of in-house coating specialists and commercial coating vendors was conducted to identify materials and fabrication methods that would be suitable for the experiment of interest. Zirconia (ZrO_2), alumina (Al_2O_3), and a proprietary aluminide coating (aluminum oxide-based with minor amounts of chromium, iron, and titanium) were selected as candidate materials. The additional calculations indicate that the most suitable coating material appears to be alumina (Al_2O_3). Alumina is stable with respect to both β-SiC and Nb up to 1000°C in pure helium (1.01 bar total pressure), but it will react with Zr at 800°C in pure helium (1.01 bar total pressure) to form zirconia (ZrO_2). Nevertheless, an alumina coating offers the best balance between ease and availability of fabrication, chemical compatibility, and ability to obtain the small coating thickness needed to minimize disruption of stress transfer from the bladder to the composite sample.

An experimental approach is being used to determine the kinetic stability of an alumina coating with Nb-1Zr and β-SiC. Since the Zr is in solid solution with the Nb, the reaction rate is expected to be slow. Fixture design and analytical methods have been verified for these experiments. Samples of Nb-1Zr and β-SiC (fabricated by chemical vapor deposition by Morton Advanced Materials, Woburn, MA), were placed in a U-shaped Mo fixture and held in flowing, gettered argon (<0.1 ppm O_2) at 1000°C for 50 hours. The fixture was designed so that the Nb-1Zr and β-SiC specimens were held together by thermal expansion at pressures comparable to those anticipated in a creep test. Although the pieces were not bonded after cooling to room temperature, energy dispersive x-ray analysis of a reaction layer on the Nb piece, performed with an analytical electron microprobe, indicated the presence of Si as much as 3 μm from the surface. These experimental results confirm the initial thermodynamic calculations and emphasize the need for a coating material.

Based on the results of the thermodynamic calculations and experiments described above, additional experiments will be performed to investigate the suitability of using alumina as a diffusion barrier coating. Alumina coatings will be deposited onto Nb-1Zr samples via sputter deposition at PNNL. These samples will be tested in the fixtures described above and analyzed by optical microscopy, scanning electron microscopy, and an analytical electron microprobe. The minimum thickness required to prevent reaction between Nb-1Zr and β-SiC will be determined. If alumina does not prevent Nb-1Zr and β-SiC from reacting, then the proprietary aluminide coating will be evaluated further.

Performance Predictions

Finite element analysis of the proposed experiment design modeled the pressurized Nb-1Zr thin-walled bladder, the composite specimen tube, and the interaction between the two tubes. A two-dimensional axisymmetric model using axisymmetric shell elements for the tubes and gap elements for the interaction were employed. The model considered internal pressure loading on the bladder tube, thermal expansion of both tubes, irradiation creep of both tubes, and irradiation swelling of the Nb-1Zr tube. Because irradiation creep and swelling correlations did not exist for the Nb-1Zr material at the temperatures of interest, regression equations were developed from data given in the space power program literature.

Analysis cases were run for variations in Nb-1Zr tube thickness, irradiation creep and swelling to account for uncertainties. Both 800°C and 1000°C full power temperatures were analyzed for all variations in other parameters. Neutron fluxes were assumed to be those for the HFIR reactor RB* location. Results showed that the experiment is indeed feasible and that the hoop stress in the composite tube varied less than 5% over a period of 300 effective full power days in the HFIR reactor. For the specimen geometries that were assumed, the calculated permanent diametral change in the specimen at the end of the test was on the order of 5 μm, a value large enough to be measurable using existing equipment. Uncertainties in the Nb-1Zr material properties did not have a significant effect on the experiment parameters.

Test Capsule Design and Thermal Analyses

Two locations in the HFIR reactor are being considered for the composite creep test, the RB* and the PTP locations. Each test location has a distinct capsule design. A scoping, finite element thermal analysis was made for each design. These analyses were 2-dimensional and axisymmetric, and considered internal heat generation due to gamma heating, conduction within the specimen/bladder assembly and capsule, thermal radiation across gas gaps, and convection to the reactor coolant.

For the RB* location, a configuration using two subcapsules, an inner and an outer one, was envisioned. The inner subcapsule would contain three creep specimens as well as other composite specimens such as bend bars and fibers. It is desired that the contents of the subcapsule be at approximately the same test temperature; analyses were run for irradiation temperatures of 500, 800 or 1000°C. The subcapsule was assumed to be filled with helium for maximum heat transfer and uniformity in temperature. The subcapsule wall (either stainless steel or TZM depending on the temperature) would provide much of the gamma heating to the subcapsule contents. The inner subcapsule would also provide structural axial constraint to the creep tube so that the Nb-1Zr pressurized bladder would not fail from creep rupture in the axial direction. The outer subcapsule would isolate the heated inner subcapsule from the reactor coolant. An annular gas gap between the two (to be filled with an argon-helium mixture) will be used for temperature control. At this time both passive (fixed gas mixture) and active (variable gas mixture) temperature control systems are being evaluated.

The initial thermal analysis focused on the passive design. The results of the analysis showed that by varying the thickness of the subcapsule wall, the annular gas gap and the gas mixture, the desired temperatures within the inner subcapsule could be obtained. It is assumed for analytical purposes that if a passive temperature control system is successful, an active system would also be successful and would provide the additional control needed to compensate for uncertainties in quantities such as gamma heating rates and emissivities.

The PTP capsule design comprises a single creep tube specimen in a subcapsule at each axial location. Most of the internal heat to the specimen would be provided by a TZM ballast located within the pressurized Nb-1Zr bladder. The outer subcapsule, which is to be in contact with reactor coolant water, will provide structural axial constraint for the Nb-1Zr tube. Argon gas is used as an insulator between the specimen system and the outer subcapsule.

Thermal analysis for the PTP test capsule showed that acceptable temperatures could be obtained in the specimens, although an axial gradient would exist. It was also demonstrated that the desired temperature could be obtained by varying the ballast size.

Alternate Irradiation Facility

One of the difficulties involved in designing irradiation creep experiments on SiC_f/SiC composites arises from the high gamma heating levels associated with the mixed spectra reactors currently available in the U.S. Most importantly, such high heating rates severely limit the allowable size and geometry of the creep specimen, in addition to imposing the constraint of symmetry. The much lower heating rates available in fast reactors allow larger specimens, larger deformations and non-symmetrical geometries. Unfortunately, fast reactors in the U.S. have been shut down. The possibility of using a reactor like the BR-10 fast reactor located at the Institute of Physics and Power Engineering in Obninsk, Russia, is therefore being considered and appears to hold promise.

The staff are eager for the work and are quite competent to perform tests on specimens similar to those currently used in the U.S. to generate thermal creep data on composites. Creep experiments in which measurements are made in-situ have been conducted for many years in BR-10 at temperatures as high as 600°C for extended periods on stainless steels and on a V-Cr-Ti alloy. An irradiation temperature of 800°C can be reached with supplementary electrical heating, which would require a small amount of modification to existing facilities. An on-site visit and review of the specimen design, available creep data, required strain rates and other considerations led to the conclusion that in-situ tests could be easily conducted on composite materials in BR-10.

Two types of creep tests can be performed in this facility. The most convenient test is torsion loaded, but this test mode is not representative of anticipated service conditions for SiC_f/SiC. In a torsion test mode, the noise arising from minor thermal fluctuations is much smaller than in tension, and the specimens are best configured as tubes to provide a relatively constant stress state throughout the specimen. Tension tests may be more suitable for SiC_f/SiC, but extra precautions are required to reduce transient noise arising from thermal fluctuations. Either flat or round tensile specimens are acceptable for such tests.

CONCLUSIONS

A specimen geometry has been selected for an irradiation creep test on composite materials, and model calculations and initial experiments confirmed the feasibility of the specimen design as well as the experimental design. An alternate creep test is also being considered in the Russian BR-10 reactor.

FUTURE WORK

Development of the creep specimen will continue and thermal control tests will be run on prototype control specimens to demonstrate the specimen viability. Design of the irradiation test will also continue.

REFERENCES

1. F. A. Garner, G. E. Youngblood and M. L. Hamilton, "Review of Data on Irradiation Creep of Monolithic SiC, Fusion Materials Semiannual Progress Report for Period Ending December 31, 1995, DOE/ER-0313/19, U.S. Department of Energy, p. 98.

2. G. E. Youngblood and R. H. Jones, "Irradiation Creep in Polycrystalline SiC Fibers," Fusion Materials Semiannual Progress Report for Period Ending June 30, 1996, DOE/ER-0313/20, U.S. Department of Energy.

3. H. Streckert and K. Norton, "Fabrication of Prototype Silicon Carbide Hermetic Tubes for Fusion Reactor Applications," GA-C22163, August 29, 1995.

3.0 FERRITIC/MARTENSITIC STEELS

TENSILE AND CHARPY IMPACT PROPERTIES OF IRRADIATED REDUCED-ACTIVATION FERRITIC STEELS -- R. L. Klueh and D. J. Alexander (Oak Ridge National Laboratory)

OBJECTIVE

The goal of this work is the development of reduced-activation ferritic steels.

SUMMARY

Tensile tests were conducted on eight reduced-activation Cr-W steels after irradiation to 15-17 and 26-29 dpa, and Charpy impact tests were conducted on the steels irradiated to 26-29 dpa. Irradiation was in the Fast Flux Test Facility at 365°C on steels containing 2.25-12% Cr, varying amounts of W, V, and Ta, and 0.1%C. Previously, tensile specimens were irradiated to 6-8 dpa and Charpy specimens to 6-8, 15-17, and 20-24 dpa. Tensile and Charpy specimens were also thermally aged to 20000 h at 365°C. Thermal aging had little effect on the tensile behavior or the ductile-brittle transition temperature (DBTT), but several steels showed a slight increase in the upper-shelf energy (USE). After ≈7 dpa, the strength of the steels increased and then remained relatively unchanged through 26-29 dpa (i.e., the strength saturated with fluence). Post-irradiation Charpy impact tests after 26-29 dpa showed that the loss of impact toughness, as measured by an increase in DBTT and a decrease in the USE, remained relatively unchanged from the values after 20-24 dpa, which had been relatively unchanged from the earlier irradiations. As before, the two 9Cr steels were the most irradiation resistant.

PROGRESS AND STATUS

Introduction

The work discussed in this report is the continuation of work on developing reduced-activation ferritic steels. Eight experimental Cr-W steels were produced based on compositions of conventional Cr-Mo steels with molybdenum replaced by tungsten and niobium replaced by tantalum [1-3]. Nominal compositions are given in Table 1, along with the designation for each steel.

TABLE 1--Nominal compositions for reduced-activation steels

Alloy	Nominal Chemical Composition[a] (wt %)				
	Cr	W	V	Ta	C
2.25CrV	2.25		0.25		0.1
2.25Cr-1WV	2.25	1.0	0.25		0.1
2.25Cr-2W	2.25	2.0			0.1
2.25Cr-2WV	2.25	2.0	0.25		0.1
5Cr-2WV	5.0	2.0	0.25		0.1
9Cr-2WV	9.0	2.0	0.25		0.1
9Cr-2WVTa	9.0	2.0	0.25	0.12	0.1
12Cr-2WV	12.0	2.0	0.25		0.1

[a] Balance iron.

Information on microstructure [1], tempering and tensile behavior [2], and Charpy impact behavior [3] of the eight steels in the unirradiated condition has been reported. Results were also published on the tensile properties after

irradiation to 6-8 dpa [4] and the Charpy properties after irradiation at 365°C to 6-8 [4], 15-17 [5], and 23-24 dpa [6] in the Fast Flux Test Facility (FFTF). Charpy specimens have now been irradiated to 26-29 dpa and tensile specimens have been irradiated to 15-17 and 26-29 dpa at 365°C in the FFTF. In this report, these data will be presented and combined with the previous data to analyze the effect of irradiation on the properties. Observations on impact behavior are extremely useful because neutron irradiation causes an increase in the ductile-brittle transition temperature (DBTT) and a decrease in upper-shelf energy (USE) of ferritic steels; those effects generally reflect a degradation in fracture toughness. Developing steels with minimal changes in these parameters is crucial if ferritic steels are to be useful structural materials for fusion.

Experimental Procedure

The eight steels (Table 1) were used in previous studies, and melt compositions have been published [1]. The steels were normalized and tempered prior to aging and irradiation. The 2 1/4Cr-2W steel was austenitized 1 h at 900°C and air cooled. The other seven heats contained vanadium and were austenitized 1 h at 1050°C and air cooled; the higher normalizing temperature assured that any vanadium carbide dissolved during austenitization. The 2 1/4CrV, 2 1/4Cr-1WV, and 2 1/4Cr-2W steels were tempered 1 h at 700°C; the other five heats were tempered 1 h at 750°C. Tensile and Charpy specimens were aged for 5000, 10000, and 20000 h at 365°C, and these specimens along with the unaged specimens (data previously reported) were tested as controls. All tensile tests were at 365°C. Details on the tensile and Charpy testing has been published [4-7].

For each irradiation condition, six Charpy specimens and two tensile specimens from each heat were irradiated in the Materials Open Test Assembly (MOTA) of FFTF in the below-core specimen canister, a sodium "weeper" operating at ≈365°C. Fluence was determined from flux monitors in the irradiation canisters; there was some variation for different specimens, depending on their position in the canister. Specimens were irradiated to 1.7-2.1x10^{26}, 4.2-4.5x10^{26}, 5.9-6.3x10^{26}, and 5.5-6.3 x10^{26} n/m^2 (E>0.1 MeV), which produced 6-8, 15-17, 23-24, and 26-29 dpa, respectively. Helium concentrations were calculated to be less than 1 appm.

Results

Tensile and Charpy results will be presented separately. The new results will be presented within the context of the results previously obtained [4-6], so that the effects of irradiation fluence on mechanical properties behavior can be analyzed.

Properties Before and After Thermal Aging

Tensile Behavior--Thermal aging for 5000, 10000, and 20000 h at 365°C had relatively little effect on yield stress [Fig. 1(a)], ultimate tensile strength [Fig. 1 (b)], uniform elongation [Fig. 1(c)], and total elongation [Fig. 1(d)]. Several of the steels showed a slight increase in strength (2 1/4CrV, 9Cr-2WV, 9Cr-2WVTa, and 12Cr-2WV), with most of the increase occurring in the first 5000 h. Despite this hardening in the first 5000h, there was often an increase in ductility after the 5000 h age, although the elongations displayed considerable scatter. The 2 1/4CrV and 2 1/4Cr-1WV were the strongest steels, and the 2 1/4Cr-2W was the weakest (these three steels were tempered at 700°C). Of the five steels tempered at 750°C, the 2 1/4Cr-2WV was the strongest, and the 5Cr-2WV the weakest. The strengths of the 9Cr-2WV and 9Cr-2WVTa were essentially the same before and after aging.

Charpy Behavior--Charpy impact properties showed relatively little change after aging for 0, 5000, 10000, and 20000 h at 365°C. The DBTT values [Fig. 2(a)] for several of the the steels showed a slight change, usually in the initial 5000 h. The 9Cr-2WVTa had the lowest DBTT, and the four 2 1/4 Cr steels and the 12Cr-2WV steel had the highest values. The USE [Fig. 2(b)] of most of the steels showed an increase with aging time with the largest change usually occurring within the first 5000 h. The 9Cr-2WVTa steel had the highest USE after 10000 h, but then decreased at 20000 h to a value similar to values for the other steels.

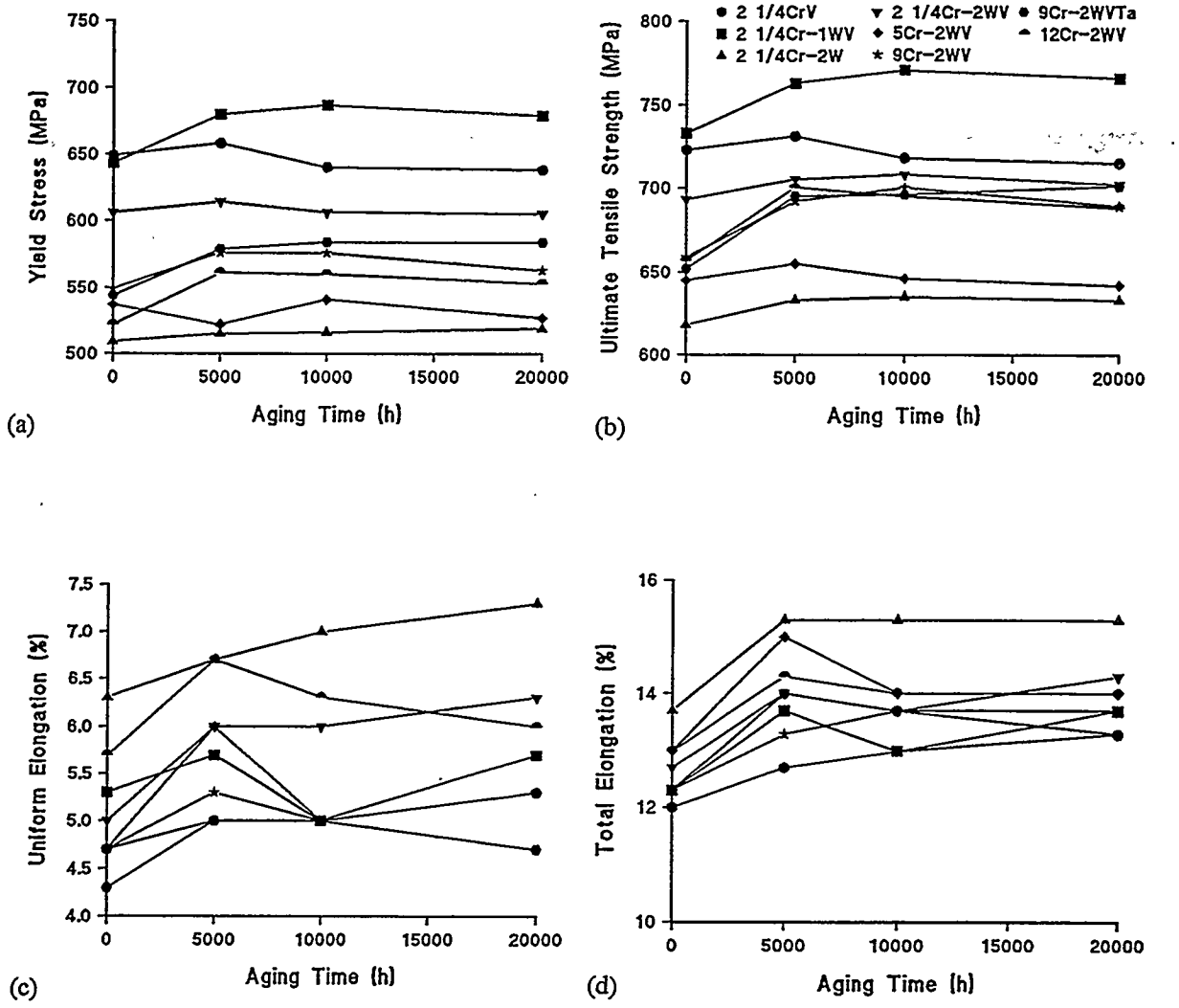

Fig. 1--The (a) yield stress, (b) ultimate tensile strength, (c) uniform elongation, and total elongation as a function of aging time at 365°C for the eight reduced-activation steels.

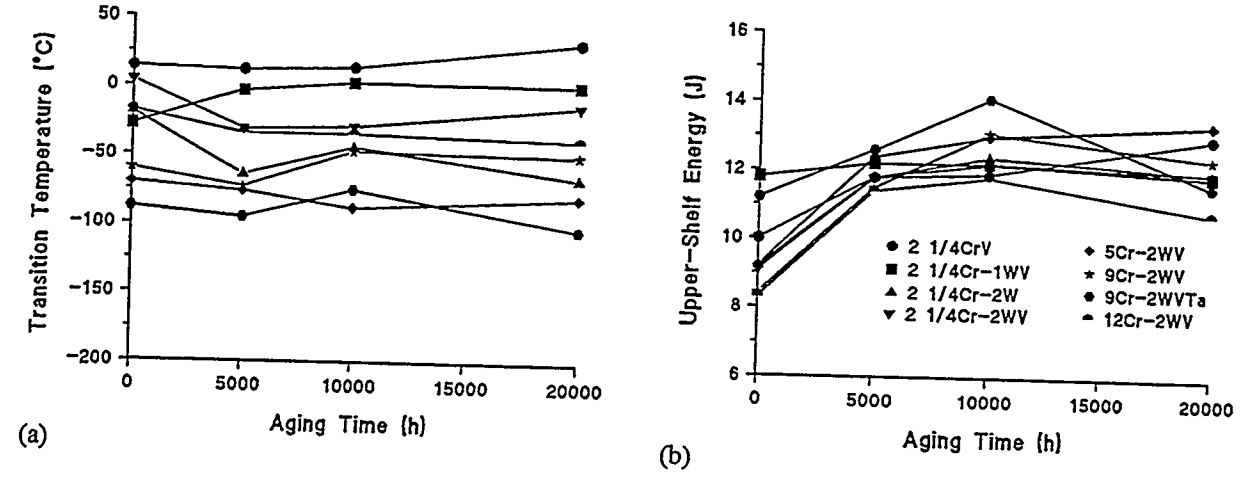

Fig. 2--The (a) ductile-brittle transition temperature and (b) upper-shelf energy as a function of aging time at 365°C for the eight reduced-activation steels.

Properties After Irradiation

Tensile behavior--Irradiation hardened the steels, as measured by yield stress [Fig. 3(a)] and ultimate tensile strength [Fig. 3(b)]. Hardening appeared to saturate with fluence, although the curve for the 2 1/4CrV appeared to go through a maximum. The curves for strength after irradiation fell into two groups: the 2 1/4Cr-2W, 5Cr-2WV, 9Cr-2WV, and 9Cr-2WVTa fell into a group showing the lowest strength and the 2 1/4CrV, 2 1/4Cr-1WV, 2 1/4Cr-2WV, and 12Cr-2WV fell in a group showing a considerably higher strength. The two 9Cr steels had the lowest strength after irradiation.

Uniform [Fig. 3(c)] and total elongation [Fig. 3(d)] decreased with fluence. As opposed to the separation into two groups observed for the strength, the ductility appeared to fall into three groups. The 9Cr-2WV and 9Cr-2WVTa steels had the highest ductility after irradiation, followed by the 2 1/4Cr-2W and 5Cr-2WV, and then the third group containing the 2 1/4CrV, 2 1/4Cr-1WV, 2 1/4Cr-2WV, and 12Cr-2WV.

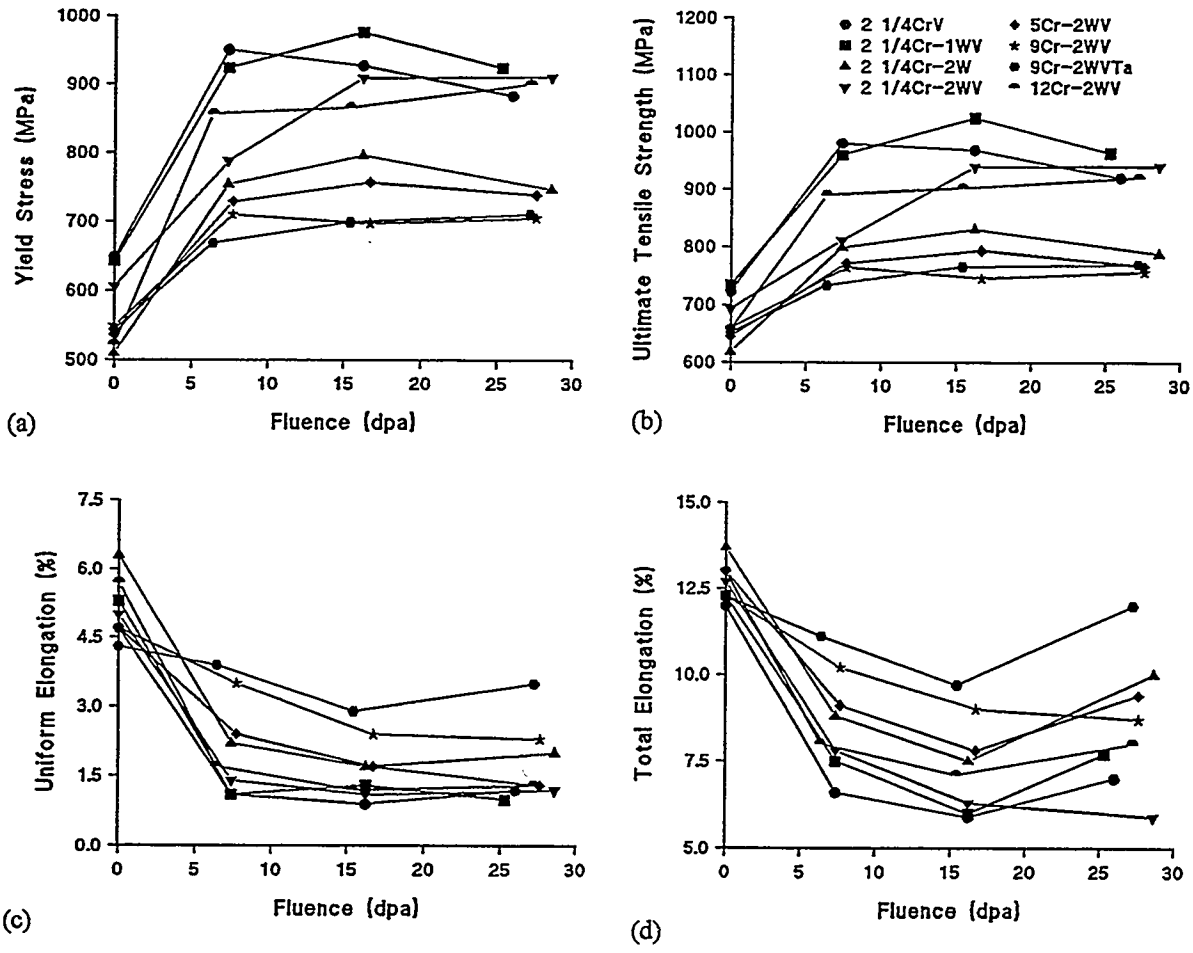

Fig. 3--The (a) yield stress, (b) ultimate tensile strength, (c) uniform elongation, and (d) total elongation as a function of fluence for the eight reduced-activation steels irradiated in FFTF at 365°C.

Charpy Behavior--The Charpy data for irradiations up to 26-29 dpa continued the trends noted for the previous irradiations [4-6]. After an initial increase in DBTT with fluence [Fig. 4(a)], the change in DBTT of most of the steels appeared to level off with increasing fluence, indicating a saturation in the shift in DBTT (ΔDBTT). The only exception was the 9Cr-2WVTa, which showed a increase in DBTT over the entire fluence range, although the increase was slight. Despite the increase, the 9Cr-2WVTa showed superior behavior at all fluences. The 9Cr-2WV and the 5Cr-2WV steels showed the next best behavior.

The USE [Fig. 4(b)] decreased with fluence and leveled off (saturated), although for several steels it decreased slightly between the third and fourth irradiations. By far the best steel was the 9Cr-2WVTa, with the 9Cr-2WV and 5Cr-2WV the second best. Comparison of Charpy curves for the two most irradiation-resistant steels indicates the superiority of the 9Cr-2WVTa steel by showing that the curves for the 9Cr-2WVTa [Fig. 5(a)] after irradiation approach the curve for the unirradiated 9Cr-2WV steel [Fig. 5(b)].

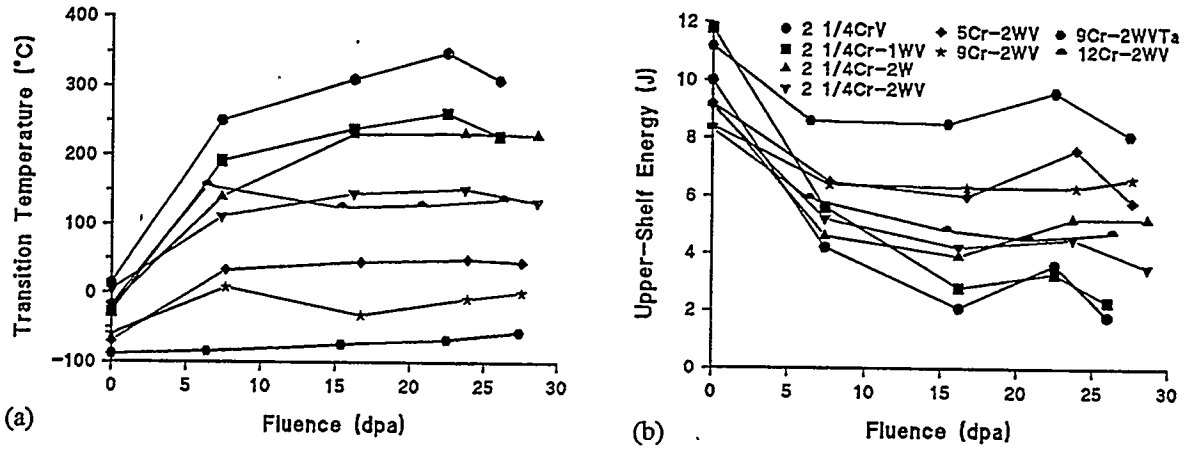

Fig. 4--The (a) ductile-brittle transition temperature and (b) upper-shelf energy as a function of fluence for the eight reduced-activation steels irradiated in FFTF at 365°C.

Large increases in DBTT and large decreases in USE (ΔUSE) were observed for the four low-chromium steels and the 12Cr-2WV. The behavior of the 2 1/4Cr-2WV and 12Cr-2WV were comparable and displayed the smallest change in DBTT of these five steels. The 2 1/4CrV had the largest ΔDBTT and ΔUSE, followed by the 2 1/4Cr-1WV and the 2 1/4Cr-2W, although the USE of the latter steel at the highest fluences was comparable to that of the 2 1/4Cr-2WV and 12Cr-2WV. The difference between the best and worst of the steels can be seen by comparing the curves for 2 1/4CrV [Fig. 5(c)] with those for 9Cr-2WV [Fig. 5(a)] and 9Cr-2WVTa in [Fig. 5(b)].

DISCUSSION

Properties Before and After Thermal Aging

The microstructures of the normalized-and-tempered 0.76-mm sheets and 15.9-mm plates from which tensile and Charpy specimens were taken, respectively, have been examined [1]. There was a difference in microstructure of the 2 1/4 Cr steels in the two geometries. All of these low-chromium steels were ≈100% bainite when heat treated as 0.76-mm sheet. When heat treated as 15.9-mm plate, all but the 2 1/4Cr-2W steel contained a duplex microstructure of tempered bainite and polygonal ferrite: 2 1/4CrV contained ≈30% tempered bainite, 70% ferrite;

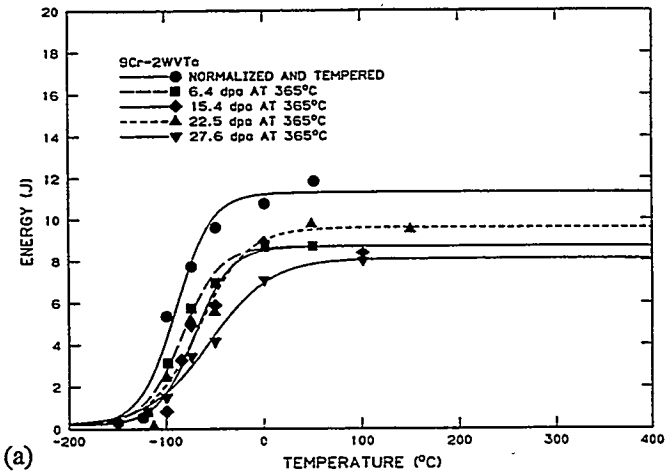

(a)

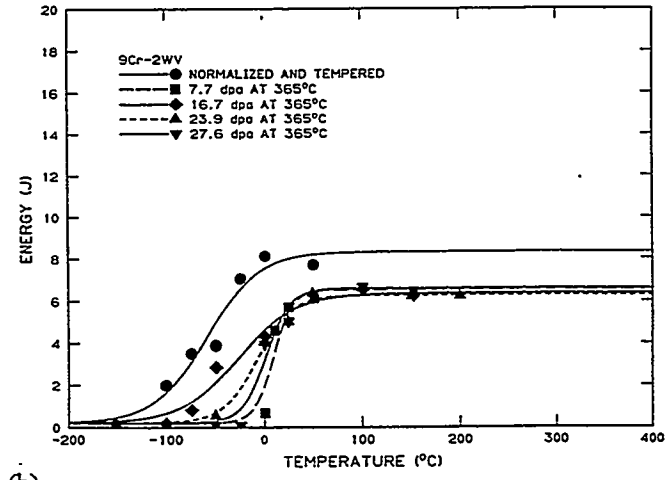

(b)

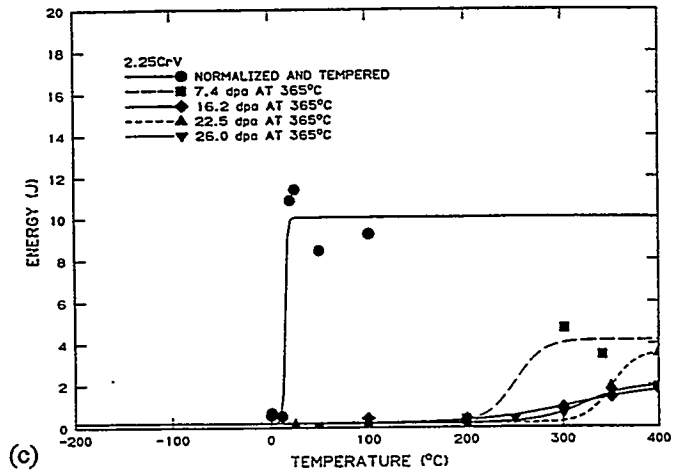

(c)

Fig. 5--Charpy curves for the normalized-and-tempered and irradiated (a) 9Cr-2WVTa, (b) 9Cr-2WV steels, and (c) 2 1/4CrV.

2 1/4Cr-1WV contained ≈55% tempered bainite, 45% ferrite; and 2 1/4Cr-2WV was ≈80% tempered bainite, 20% ferrite. The 2 1/4Cr-2W steel was 100% tempered bainite. Microstructures were the same for the high-chromium steels in both geometries: the 5Cr-2WV 9Cr-2WV and 9Cr-2WVTa steels were 100% tempered martensite, and the 12Cr-2WV steel was tempered martensite with ≈25% δ-ferrite [1].

Before irradiation, the precipitates in the three 2 1/4Cr steels with vanadium were M_7C_3, M_3C, and MC [1]. The 2 1/4Cr-2W contained M_7C_3, M_3C, $M_{23}C_6$, and M X. The 9Cr-2WV, 9Cr-2WVTa, and 12Cr-2WV contained primarily $M_{23}C_6$ and small amounts of vanadium-rich MC; some of the MC in the 9Cr-2WVTa contained tantalum, although most was vanadium rich. The major difference in the 9Cr-2WVTa and the 9Cr-2WV was that the 9Cr-2WVTa had a smaller prior austenite grain size [3]. The 5Cr-2WV contained mainly M_7C_3, with small amounts of $M_{23}C_6$ and MC, thus bridging the gap between the chromium-rich M_7C_3 found in the steels with 2 1/4% Cr and the chromium-rich $M_{23}C_6$ found in the steels with 9% Cr [1].

The relative strengths of the steels before aging or irradiation [Figs. 1(a) and 1(b)] were the result of the heat treatment given the steels. The 2 1/4CrV and 2 1/4Cr-1WV were stronger than the other steels because these steels were tempered at 700°C, as was the 2 1/4Cr-2W. All other steels were tempered at 750°C. The 2 1/4Cr-2W was the weakest, despite being tempered at 700°C, because it did not contain the strong carbide-forming element vanadium, and thus, it was not strengthened by MC. Of the steels that contained vanadium and were tempered at 750°C, the 2 1/4Cr-2WV was the strongest, followed by 9Cr-2WVTa, 9Cr-2WV,.12Cr-2WV, and the 5Cr-2WV steels. There was essentially no difference in the strength of the 9Cr-2WV and the 9Cr-2WVTa in the unirradiated condition. In the unirradiated condition, all of the steels had adequate ductility [Figs. 1(b) and 1(c)]. Aging at 365°C to 20000 h had little effect on strength and ductility of any of the steels; properties remained similar or slightly improved compared to the unaged steel.

Thermal aging had little effect on the DBTT of the steels [Fig. 2(a)]. The DBTT behavior of the unirradiated steels reflected the different microstructures. Steels with a 100% tempered martensite and a 100% tempered bainite microstructure--the 5Cr-2WV, 9Cr-2WV, 9Cr-2WVTa and 2 1/4Cr-2W--had the lowest DBTT values. The other four steels had duplex microstructures, each containing some polygonal or delta ferrite. The DBTT values increased with increasing amounts of ferrite, from the 12Cr-2WV and 2 1/4Cr-2WV, with 20-25%, to the 2 1/4Cr-1WV, with ≈45%, and the 2 1/4CrV, with ≈70% ferrite.

The USE of most of the steels increased slightly during aging, especially during the initial 5000 h period. The reason for this is not known, although a slight supersaturation of carbon may have been present from the tempering treatment, which is relieved by the low-temperature aging treatment. Little diffusion of any substitutional elements would be expected at 365°C.

Properties After Irradiation

Irradiation hardening saturated with fluence with the amount of hardening depending on microstructure [Fig. 3(a) and (b)]. By comparing the relative increase in yield stress, $\Delta\sigma_y$, for the different steels, it was found that the steels with 100% tempered martensite (5Cr-2WV, 9Cr-2WV, and 9Cr-2WVTa) hardened the least. The $\Delta\sigma_y$ of the two 9Cr steels was the lowest (≈30% increase), with that for the 5Cr steel slightly higher (35-40%). The four 2 1/4Cr steels, which had 100% bainite microstructures in the tensile specimens, hardened about the same amount (40-50%), even though they had different strengths before irradiation. Therefore, it appears that tempered bainite hardens more than tempered martensite. The 12Cr-2WV steel contained ≈75% tempered martensite, and it hardened the most (60-70%), suggesting that the difference between this steel and the 100% tempered martensitic steels must have been the 25% δ-ferrite present in the microstructure. The effect of fluence on ductility was inverse to the hardening in that an increase in hardening was accompanied by a decrease in ductility [Fig. 3(c) and 3(d)].

Despite the difference in microstructure of the 2 1/4 Cr steels used for the tensile and Charpy specimens, the effect of fluence on Charpy impact behavior was generally similar to the effect on strength. With the exception of the 9Cr-

2WVTa, which appeared to show a slight increase with fluence (this will be discussed below), the effect of irradiation on the DBTT and USE saturated with fluence. Irradiation had the least effect on the DBTT and USE of the three 100% martensitic steels. Of these, the 9Cr-2WVTa was superior to the other steels, followed by 9Cr-2WV and 5Cr-2WV, in agreement with the previous results [4-6]. The steels with the next best irradiation resistance were the 2 1/4Cr-2WV and the 12Cr-2WV steels, which contained 20-25% polygonal and delta ferrite, respectively. These steels saturated at a similar DBTT and USE, although the 2 1/4Cr-2WV had the lowest ΔDBTT. It is also hardened somewhat less than the 12Cr-2WVsteel.

For the three 2 1/4Cr steels containing vanadium that had a duplex bainite-polygonal ferrite microstructure, it appeared that the the ΔDBTT increased with the amount of ferrite in the microstructure. The 2 1/4CrV steel, which contained the most ferrite (≈70%), showed the largest ΔDBTT, followed by the the 2 1/4Cr-1WV and the 2 1/4Cr-2WV, the steels with ≈45 and 25% ferrite, respectively. Because of the difference in microstructures in the 2 1/4Cr steel specimens used in the tensile and Charpy experiments, the relationship between the increase in strength and ΔDBTT must be interpolated. By comparing tensile results for the 12Cr-2WV and the other martensitic steels, it appears that hardening was influenced substantially by the amount of ferrite in the microstructure. The similarity of the DBTT for the 12Cr-2WV and 2 1/4Cr-2WV steels, which both contain similar amounts of ferrite, appears to support that conclusion [Fig. 4(a]. This bolsters the conclusion that the relative behavior of the ΔDBTT of the 2 1/4CrV, 2 1/4Cr-1WV, and 2 1/4Cr-2WV is determined by the amount of polygonal ferrite present in the microstructure.

Anderko et al. [8] showed that for 12Cr steels containing a duplex structure of martensite and δ-ferrite, it is $M_{23}C_6$ on martensite/δ-ferrite boundaries rather than the δ-ferrite itself that causes a deterioration of the Charpy properties. Considerable $M_{23}C_6$ forms on the interfaces in the 12Cr-2WV in the unirradiated condition [1], which means that $M_{23}C_6$ could control fracture. Precipitates (mainly M_7C_3) may also control the behavior of the 2 1/4Cr-2WV [1]. This implies that reducing the size of the precipitates at ferrite/martensite or ferrite/bainite boundaries would be the most likely way to minimize ΔDBTT. In the 2 1/4Cr-2WV, the polygonal ferrite can be eliminated by heat treating. It has been demonstrated that heat treating to produce 100% bainite significantly lowered the DBTT of unirradiated 2 1/4Cr-2WV [9].

The results on the 5Cr-2WV, 9Cr-2WV, and 9Cr-2WVTa indicate that tempered martensite is more irradiation resistant than tempered bainite. More information on the irradiation resistance of tempered bainite will become known after Charpy specimens of 2 1/4Cr-2WV steel in the fully bainitic condtion have been irradiated.

The properties of the 2 1/4Cr-2W appeared anomalous with the other 2 1/4Cr steels because this steel was 100% tempered bainite but had a much higher DBTT and ΔDBTT than the 2 1/4Cr-2WV, which was 25% ferrite. The DBTT values of the irradiated 2 1/4Cr-2W were similar to those of the 2 1/4Cr-1WV, which contained 45% ferrite. A major difference between the 2 1/4Cr-2WV and 2 1/4Cr-2W is that the 2 1/4Cr-2W does not contain vanadium. During irradiation the vanadium-containing carbides are more stable than the M_7C_3 and M_3C that dominate in the 2 1/4Cr-2W [1]. The larger precipitates in the 2 1/4Cr-2W after irradiation could enhance its susceptibility to fracture relative to the steels with a more stable precipitate structure (e.g., 2 1/4Cr-2WV).

Similar explanations for the low-chromium steels have previously been used to conclude that for maximum irradiation resistance, these steels containing the combination of tungsten and vanadium must be irradiated in the entirely bainitic condition [9]. It has also been pointed out that the type of bainite formed could play a role in the irradiation resistance.

The two 9Cr steels show the least hardening and have the best impact properties after irradiation. The properties of the 9Cr-2WVTa were exceptional after the previous three irradiations, showing only a small ΔDBTT (21 °C after 22.5 dpa) [4-6]; similar behavior was observed in the present experiment. Not only does it show a very small ΔDBTT (32C°) after over 27 dpa, but because it has such a low DBTT in the unirradiated condition, the DBTT after irradiation remains substantially below that for the other steels. It was pointed out previously that the ΔDBTT data for the previous three irradiations for 9Cr-2WVTa indicated that there was a gradual increase in the post-

irradiation DBTT with increasing fluence [6]. That trend continued in the present experiment [Fig. 4(a)]. However, even after the 27.4 dpa, the DBTT of -56°C for the 9Cr-2WVTa is still comparable to the DBTT of the 9Cr-2WV before irradiation (the 9Cr-2WV had the second lowest DBTT before irradiation). A similar conclusion applies to 9Cr-1MoVNb (modified 9Cr-1Mo, Grade 91), which has one of the lowest ΔDBTT values (≈50°C) of the conventional steels considered for fusion applications [5].

One of the interesting aspects in comparing the 9Cr-2WV and 9Cr-1MoVNb steels with the 9Cr-2WVTa steel is that the difference in Charpy properties of these steels before and after irradiation occurs despite there being little difference in the strength of the 9Cr-2WVTa and the other two steels before and after irradiation. This can be seen in the similar irradiation hardening that occurred for the 9Cr-2WV and 9Cr-2WVTa steels (Fig. 3).

Transmission electron microscopy examination of the normalized-and-tempered 9Cr-2WV and 9Cr-2WVTa revealed only minor differences prior to irradiation [1,10]. Likewise, there was no marked difference in microstructure after irradiation, with similar numbers of dislocation loops formed in both steels during irradiation [10]. Thus, the similarity of strength of the two steels before and after irradiation is not unexpected. However, without any gross differences in the microstructure of the two steels, the only other major difference to account for the difference in Charpy properties is the tantalum in solid solution. Based on the amount of tantalum that appeared to be present in the MC carbides of the 9Cr-2WVTa, it was estimated that most of the tantalum remained in solid solution (or was incorporated in the $M_{23}C_6$ precipitate) [10]. An atom probe analysis of the unirradiated 9Cr-2WVTa steel indicated that ≈90% of the tantalum remained in solution in the normalized-and-tempered condition [11].

Tantalum in solution in the 9Cr-2WVTa can probably account for the smaller prior-austenite grain size in that steel than in the 9Cr-2WV; a smaller lath (subgrain) size might also be expected but was not observed. This smaller grain size was originally used to explain the difference between the 9Cr-2WV and 9Cr-2WVTa steels [4]. A smaller grain size can lead to a lower DBTT in the normalized-and-tempered condition. However, this explanation was subsequently questioned because in the normalized-and-tempered condition, the two steels had similar yield stresses, and they also had a similar yield stress as the 9Cr-1MoVNb, which had the smallest grain size of the three steels [5]. After ≈20 dpa, the ΔDBTT of the 9Cr-2WV and 9Cr-1MoVNb were similar, but above the value for the 9Cr-2WVTa [6]. This occurred even though there were differences in the microstructural changes that occurred in the 9Cr-2WV and 9Cr-1MoVNb during irradiation, while the microstructural changes in the 9Cr-2WV and 9Cr-2WVTa were similar [10].

These observations lead to the conclusion that microstructure (grain size, precipitate type, etc.) does not provide the sole explanation for the observations on mechanical property changes. It appears that tantalum in solution must cause a higher fracture stress for 9Cr-2WVTa than 9Cr-2WV, and the combination of tungsten and tantalum in the 9Cr-2WVTa leads to a higher fracture stress than produced by molybdenum and niobium in 9Cr-1MoVNb.

The observation that the ΔDBTT of the 9Cr-2WVTa appeared to increase slightly with fluence appears to be in agreement with such an explanation. This increase would follow if tantalum is being removed from solution during irradiation and being incorporated in the existing or new precipitates. If this were the case, the ΔDBTT of the 9Cr-2WVTa would be expected to increase with fluence as tantalum is removed from solution. Eventually, it might be expected to approach the ΔDBTT for the 9Cr-2WV. Even if that were to happen, however, the 9Cr-2WVTa should still have the lowest DBTT after irradiation because of the lower DBTT before irradiation.

SUMMARY AND CONCLUSIONS

Tensile and Charpy impact properties of eight reduced-activation Cr-W ferritic steels have been determined after irradiation in FFTF at 365°C. Tensile specimens were irradiated to 6-8 , 15-17, and 26-29 dpa and Charpy specimens to ≈ 6-8, 15-17, 20-24, and 26-29 dpa (results for all but the tensile irradiations to 15-17 and 26-29 dpa and the Charpy irradiations to 26-29 dpa were presented previously). Chromium concentrations in the eight steels

ranged from 2.25 to 12wt% (all steels contained 0.1%C). The 2.25Cr steels contained variations of tungsten and vanadium (2 1/4CrV, 2 1/4Cr-1WV, 2 1/4Cr-2W) and steels with 2.25, 5, 9, and 12% Cr contained a combination of 2% W and 0.25% V (2 1/4Cr-2WV, 5Cr-2WV, 9Cr-2WV, and 12Cr-2WV). A 9Cr steel with 2% W, 0.25% V, and 0.07% Ta (9Cr-2WVTa) was also irradiated. The microstructures of the 2 1/4Cr steels were bainite with various amounts of polygonal ferrite, while the two 9Cr steels and the 5Cr steel were 100% martensite. The 12Cr-2WV steel was martensite with ≈25% δ-ferrite. The properties of the steels with 100% martensite were superior to those with the duplex structures of bainite and ferrite or martensite and ferrite.

Irradiation caused an increase in strength during the first irradiation period (6-8 dpa), but there was little further hardening for the subsequent irradiations, indicating that the hardening saturated with fluence. The DBTT increased with irradiation, and the USE decreased, but indications were that saturation occurred for most of the steels after the initial 6-8 dpa irradiation. The 2 1/4Cr-2WV steel had the most irradiation resistance of the four 2 1/4 Cr steels, and it was concluded that this resistance would be improved if it were 100% bainite (it contained ≈25% polygonal ferrite). The 9Cr steels were least affected by irradiation, with the 9Cr-2WVTa showing only a 32°C increase in DBTT after 27.4 dpa. This was the only steel that showed a slight increase in the shift with increasing fluence, with the 32°C shift being an increase from shifts of 4, 14, and 21°C in the previous irradiations to ≈6.4, 15.4, and 22.5 dpa, respectively. Despite the slight increase, 32°C is one of the lowest shifts in DBTT ever observed for this type of steel irradiated to these conditions, and it compares with a 61°C shift for the 9Cr-2WV, which had the second lowest shift. The advantage for the 9Cr-2WVTa over the 9Cr-2WV is further enhanced by the much lower DBTT of the 9Cr-2WVTa before irradiation. The advantage of the 9Cr-2WVTa was attributed to the tantalum in solution, and the increase in DBTT with irradiation was thought to be caused by a loss of the tantalum from solution.

REFERENCES

[1] R. L. Klueh and P. J. Maziasz, Metallurgical Transactions, Vol. 20A, 1989, pp. 373-382.
[2] R. L. Klueh, Metallurgical Transactions, Vol. 20A, 1989, pp. 463-470.
[3] R. L. Klueh and W. R. Corwin, Journal of Materials Engineering, Vol. 11, 1989, pp. 169-175.
[4] R. L. Klueh, D. J. Alexander, and P. J Maziasz, Journal of Nuclear Materials, Vol. 186, 1992, pp. 185-195.
[5] R. L. Klueh and D. J. Alexander, Journal of Nuclear Materials, Vol. 212-215,1994, pp. 736-740.
[6] R. L. Klueh and D. J. Alexander, Journal of Nuclear Materials, to be published.
[7] Alexander, D. J., Nanstad, R. K., Corwin, W. R., and Hutton, J. T., "A Semiautomated Computer-Interactive Dynamic Impact Testing System," Applications of Automation Technology to Fatigue and Fracture Testing, ASTM STP 1092, Braun, A. A., Ashbaugh, N. E., and Smith, F. M., Eds., American Society for Testing and Materials, Philadelphia, 1990, pp. 83-94.
[8] K. Anderko, L. Schafer, and E. Materna-Morris, Journal of Nuclear Materials, Vol. 179-181, 1991, pp. 492-495.
[9] R. L. Klueh, P. J. Maziasz, and D. J. Alexander, Journal of Nuclear Materials, Vol. 179-181, 1991, pp. 679-683.
[10] J. J. Kai and R. L. Klueh, Journal of Nuclear Materials, to be published
[11] R. Jayaram and R. L. Klueh, to be published.

CHARPY IMPACT TEST RESULTS OF FOUR LOW ACTIVATION FERRITIC ALLOYS IRRADIATED AT 370°C TO 15 DPA - L. E. Schubert, M. L. Hamilton, and D. S. Gelles (Pacific Northwest National Laboratory)[a]

OBJECTIVE

The objective of this work is to evaluate the effects of neutron irradiation in low activation ferritic alloys, primarily by examining the shift of the ductile to brittle transition temperature (DBTT) and the reduction of the upper shelf energy (USE) in miniature Charpy V-notch (CVN) specimens.

SUMMARY

Miniature CVN specimens of four low activation ferritic alloys have been impact tested following irradiation at 370°C to 15 dpa. Comparison of the results with those of control specimens indicates that degradation in the impact behavior occurs in each of these four alloys. The 9Cr-2W alloy referred to as GA3X and the similar alloy F82H with 7.8Cr-2W appear most promising for further consideration as candidate structural materials in fusion energy system applications. These two alloys exhibit a small DBTT shift to higher temperatures but show increased absorbed energy on the upper shelf.

PROGRESS AND STATUS

Introduction

Previous reports[1,2] described results of CVN tests on six low activation ferritic alloys which had been irradiated in the FFTF MOTA 1C through 1E experiments below core at 370°C to approximately 10 dpa and 30 dpa. This document reports results of CVN impact tests on identical specimens irradiated in FFTF in the MOTA 2A and 2B experiments, also below core, to ~15 dpa at a temperature of 370°C. The alloys under investigation are F82H (7.8Cr-2W), GA3X (9Cr-2W), GA4X (11Cr-2W), and HT9 (12Cr-1Mo-0.5W). Each alloy also contains 0.2-0.3V. Note that while GA3X was designed to be a 9Cr alloy, and that the current work reports results of tests conducted on a 9Cr heat of GA3X, the results reported in reference 2 were obtained from specimens of an experimental heat obtained from General Atomics which had only 7.5Cr.

The HT9 alloy was included in this study for reference purposes since there are substantial data available on the alloy. However the HT9 alloy contains molybdenum and does not meet the criteria established for a low activation material, and it is not a candidate for fusion applications.

Experimental Procedure

The specimens utilized were about one third the size of the ASTM standard CVN specimen.[3] The specimens of three of the alloys were fatigue precracked before irradiation. The GA4X was expected to exhibit a duplex microstructure; therefore precracking of the specimens of this alloy was not conducted. The impact tests were conducted inside a hot cell using a remotely operated vertical drop tower. The fracture energy was calculated from the load versus time record of each impact. The method of calculation and data analysis as well as the details of the system have been described previously.[4,5]

---

[a]Operated for the U.S. Department of Energy by Battelle Memorial Institute under Contract DE-AC06-76RLO 1830.

was not conducted. The impact tests were conducted inside a hot cell using a remotely operated vertical drop tower. The fracture energy was calculated from the load versus time record of each impact. The method of calculation and data analysis as well as the details of the system have been described previously.[2, 4, 5]

Specimen temperature control was accomplished in a ceramic enclosure adjacent to the anvils.[6] A pneumatic ram moved the specimen from the temperature chamber to the test position. Elevated temperatures were achieved by passing low voltage electric current (AC) through the specimen. Temperatures below ambient were achieved by flowing nitrogen gas chilled to about -196°C over the specimen. The flow rate was adjusted to obtain different specimen temperatures. Specimens typically reach the test temperature in 10-20 minutes and are allowed to stabilize at temperature for three minutes prior to test initiation. Two seconds is the approximate time interval between the specimen exit from the chamber and impact. If positioning is not completed properly, or if the time interval exceeds three seconds, the impact test is not performed, the specimen is returned to the temperature chamber, and the heating/cooling cycle is repeated. The highest temperature at which tests were performed was 300°C due to limitations of the test system.

Results

Tests were conducted on each alloy over a range of temperatures in order to establish full DBTT curves. The data are plotted in Figures 1-4 with the control data. Of these four alloys, the two higher chromium alloys, HT9 and GA4X, exhibited large increases in the DBTT and a significant drop in the USE. The two alloys with lower chromium content, GA3X and F82H, retained DBTTs below room temperature with only a 20-30°C DBTT increase. Both also exhibited higher USE values after irradiation. Thus only the GA3X and F82H alloys appear to warrant continued interest on the basis of DBTT, although the DBTT values obtained on these one-third size specimens can be expected to be lower than those that would be obtained on standard full size specimens.

Discussion

The GA3X and GA4X alloys have the same composition except for chromium content. The higher chromium in GA4X results in a two-phase microstructure. Since the GA4X specimens were not precracked, direct comparisons of the USE and DBTT values of the alloy to the corresponding values for the GA3X alloy are not valid. However, since the DBTT curves of precracked and notch-only specimens are qualitatively the same, the magnitude of the shift in the DBTT and the relative change in the USE of the two alloys can be compared. Given that a large shift in the DBTT is unacceptable and that reduction of the USE indicates loss of toughness, the 9Cr alloy, GA3X, is superior to the 11Cr alloy, GA4X.

In reference 2, the particular heat of GA3X investigated had only 7.5% chromium, which is approximately the same as was in the F82H alloy investigated here. In Figure 5, the reference 2 data on GA3X are reproduced with the data generated on the GA3X and F82H alloys of the current study. The DBTT curve of the irradiated F82H is approximately the same as the DBTT curves of the 7.5Cr GA3X irradiated to 10 and to 30 dpa. The DBTT value obtained is approximately the same for each of the three data sets, but the USE value for the F82H is ~15% greater. The DBTT curve of the irradiated 9Cr GA3X heat exhibits a DBTT value that is ~40°C lower than both the 7.5Cr GA3X heat and the F82H alloy. For the irradiated materials, the USE value of the 9Cr GA3X heat is about the same as that of the F82H alloy and, likewise, ~15% greater than the value obtained for the 7.5Cr GA3X heat. These results tend to indicate an advantage for a 9% chromium content in comparison to a 7.5% composition.

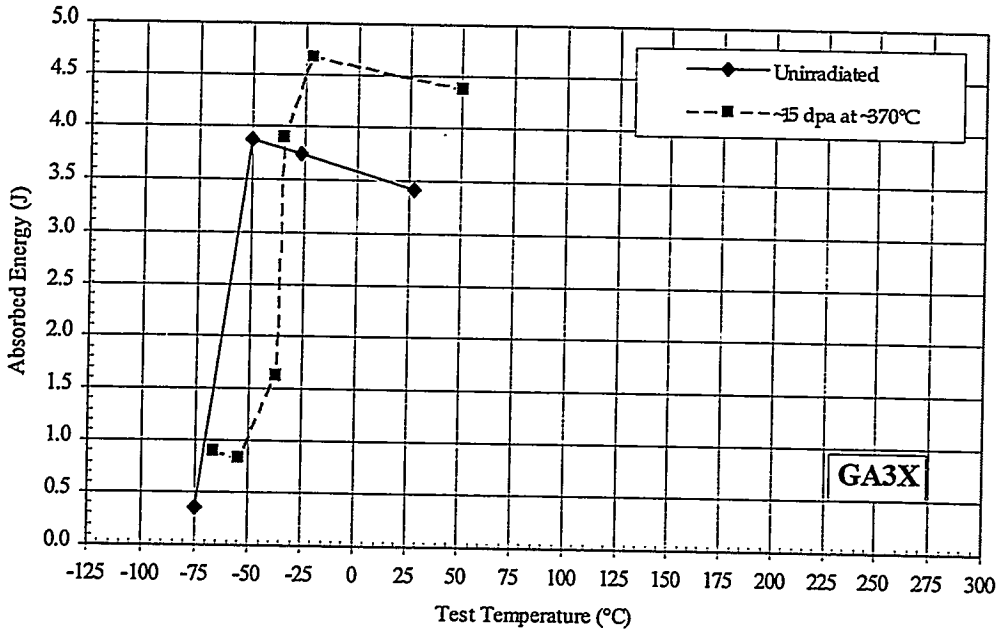

Figure 1. Test results of impact tests of precracked, miniature CVN specimens of alloy GA3X, Fe-0.15C-9.0Cr-2.0W-0.3V (no Mn).

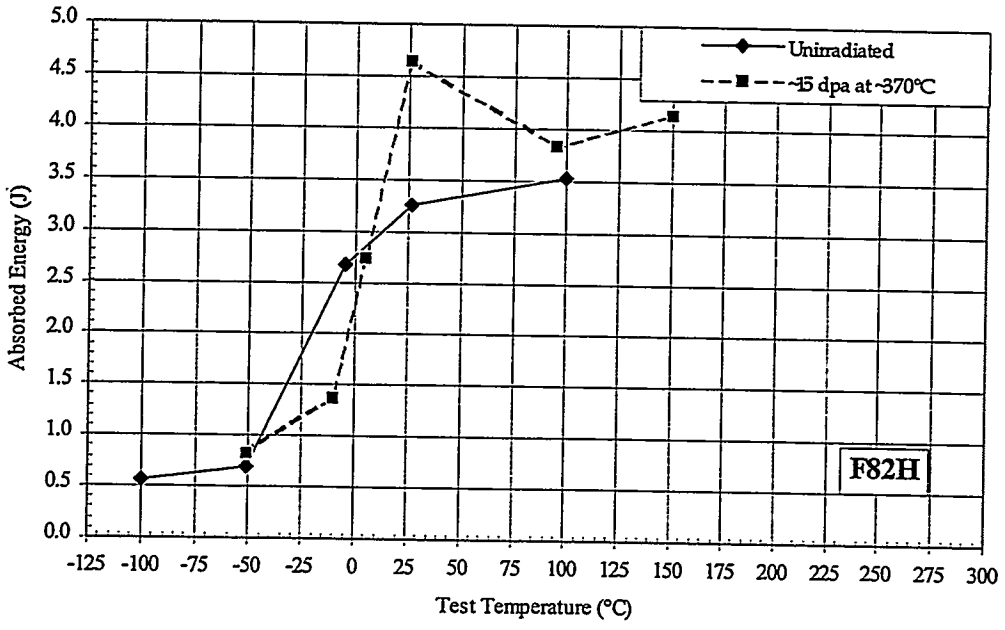

Figure 2. Test results of impact tests of precracked, miniature CVN specimens of alloy F82H, Fe-0.10C-7.8Cr-2.0W-0.5Mn-0.2V.

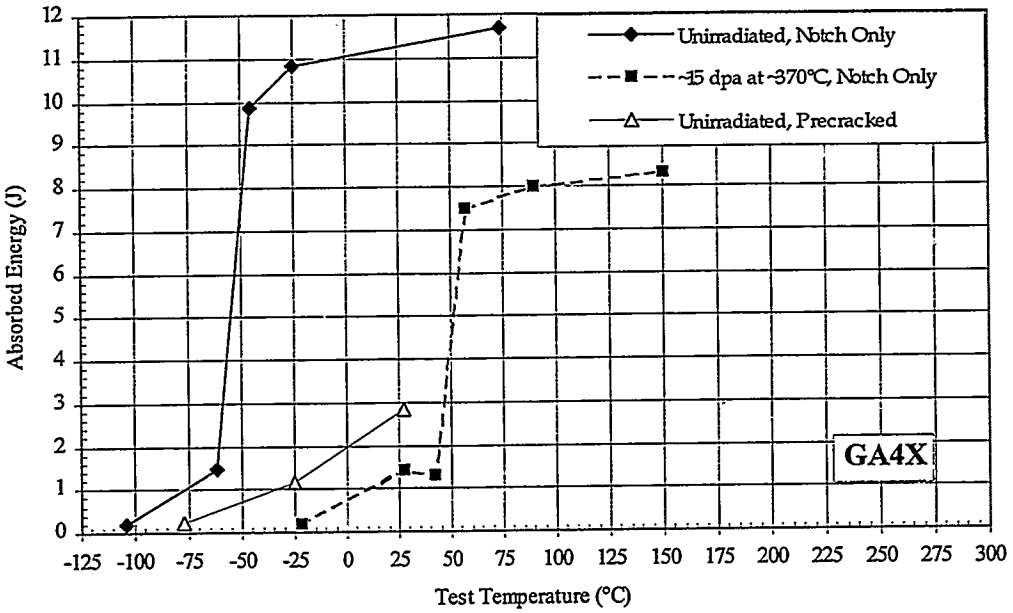

Figure 3. Test results of impact tests of miniature CVN specimens of alloy GA4X, Fe-0.14C-11.0Cr-2.0W-0.3V (no Mn).

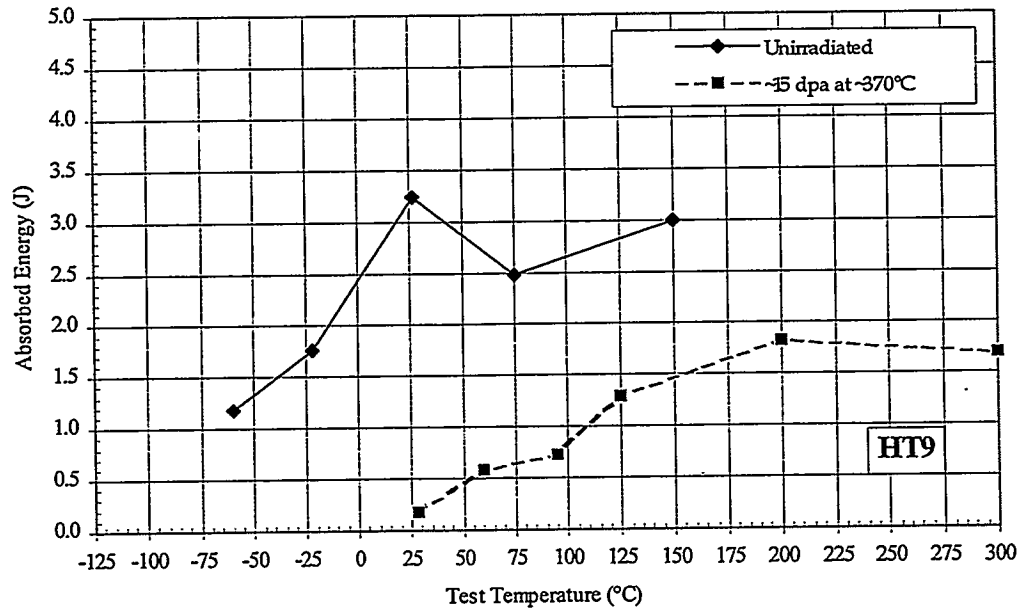

Figure 4. Test results of impact tests of precracked, miniature CVN specimens of alloy HT9, Fe-0.20C-12.1Cr-1.0Mo-0.6Mn-0.5Ni-0.5W-0.3V.

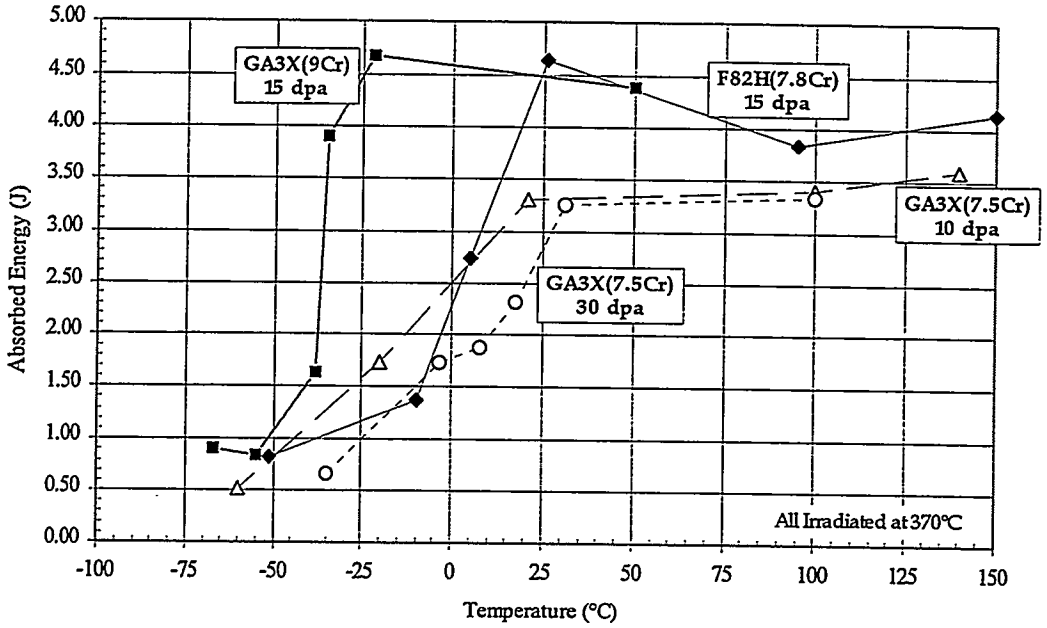

Figure 5. The DBTT curve for 9Cr GA3X in comparison with those of the 7.5Cr GA3X heat and the 7.8Cr F82H alloy. Specimens were irradiated below core in FFTF MOTA at 370°C.

CONCLUSION

Impact tests were performed on four ferritic alloys irradiated at 370°C to 15 dpa in order to determine behavior in reduced activation alloys. The impact behavior of the GA3X and F82H alloys is clearly superior to that of the GA4X and HT9 alloys. On the basis of the impact data, both the GA3X and F82H alloys appear to warrant further consideration as potential structural materials in fusion reactors, and chromium content of about 9% appears to be optimum for Fe-Cr-W/V ferritic alloys.

FUTURE WORK

Scanning electron microscopy will be performed on fracture surfaces from the specimens tested in this work to determine the fracture mode. Additional impact testing will be performed on similar one-third size specimens irradiated in core in FFTF MOTA at ~430°C to ~67 dpa.

1. N. S. Cannon, W. L. Hu, and D. S. Gelles, "Charpy Impact Test Results for Low Activation Ferritic Alloys," p. 119 in Fusion Reactor Materials Semiannual Progress Report for the Period Ending March 31, 1987, DOE/ER-0313/2, U.S. DOE, Office of Fusion Energy.

2. L. E. Schubert, M. L. Hamilton, D. S. Gelles, "Charpy Impact Test Results for Low Activation Ferritic Alloys Irradiated to 30 dpa," p. 133 in Fusion Reactor Materials Semiannual Progress Report for the Period Ending December 31, 1995, DOE/ER-0313/19, U.S. DOE, Office of Fusion Energy.

3. "Standard Test Method for Notched Bar Impact Testing of Metallic Materials," Designation: E 23, The American Society for Testing and Materials.

4. W. L. Hu and N. F. Panayotou, "Miniature Charpy Specimen Test Device Development and Impact Test Results for the Ferritic Alloy HT9," p. 235 in Alloy Development for Irradiation Performance Semiannual Progress Report for the Period Ending September 30, 1981, DOE/ER-0045/7, U.S. DOE, Office of Fusion Energy.

5. L. E. Schubert, "Effects of Specimen Size Reduction on the Transition Curve of the Charpy V-Notch Impact Test," Master of Science Thesis, Nuclear Engineering, A. S. Kumar--Advisor, University of Missouri-Rolla, May 1995

6. W. L. Hu, "Miniature Charpy Impact Test Results for Irradiated Ferritic Alloys," p. 255 in Alloy Development for Irradiation Performance Semiannual Progress Report for the Period Ending September 30, 1982, DOE/ER-0045/9, U.S. DOE, Office of Fusion Energy.

FRACTOGRAPHIC EXAMINATION OF REDUCED ACTIVATION FERRITIC/MARTENSITIC STEEL CHARPY SPECIMENS IRRADIATED TO 30 DPA AT 370°C

D. S. Gelles and M. L. Hamilton (Pacific Northwest National Laboratory)[a] and L. E. Schubert (University of Missouri, Rolla)

OBJECTIVE

The objective of this research is to assess irradiation embrittlement in reduced activation ferritic/Martensitic steels for first wall applications in a fusion energy system.

SUMMARY

Fractographic examinations are reported for a series of reduced activation ferritic/Martensitic steel Charpy impact specimens tested following irradiation to 30 dpa at 370°C in FFTF. One-third size specimens of six low activation steels developed for potential application as structural materials in fusion reactors were examined. A shift in brittle fracture appearance from cleavage to grain boundary failure was noted with increasing manganese content. The results are interpreted in light of transmutation induced composition changes in a fusion environment.

PROGRESS AND STATUS

Introduction

Charpy impact test results have been recently reported for a series of reduced activation ferritic/Martensitic alloys irradiated in the FFTF at 370°C to 30 dpa.[1] The same alloys had been tested earlier following irradiation to 10 dpa,[2] and fractography previously reported for the earlier test specimens.[3] The purpose of the present work is to extend the interpretation of the most recent impact tests by determination of changes in fracture appearance.

Six alloys were under consideration in this series of tests, one containing 2.5% Cr, three containing 7 to 9% Cr and two containing 12% Cr, all strengthened with V and/or W, and several using Mn additions to control austenite phase stability. The recent impact test results showed that degradation in the impact behavior appears to have saturated by 10 dpa in at least four of the six alloys. The most promising of the alloys, a 7.5Cr-2W alloy referred to as GA3X, exhibited the best impact properties, with no decrease in ductile to brittle transition temperature (DBTT) or upper shelf energy (USE) between 10 and 30 dpa.

Experimental Procedure

Details concerning specimen fabrication, irradiation and testing have been previously reported.[3] Fractographic examination followed procedures developed previously.[2] However, due to space limitations, stereo pairs of fracture surfaces will not be shown, but can be obtained by request from the authors. Specimens selected for examination represent behavior at the ductile to brittle transition temperature (DBTT).

---

[a]Operated for the U.S. Department of Energy by Battelle Memorial Institute under Contract DE-AC06-76RLO 1830.

Results

Fractographs of tested specimens are provided in Figures 1 through 6. Each figure shows the entire fracture surface at low magnification in part (a) and the central portion immediately adjacent to the fatigue precrack at higher magnification in part (b). Figure 1 shows the fracture appearance for specimen L317 of Fe-2.5Cr-1.5V-0.3Mn irradiated at 370°C to 30 dpa and tested at 300°C. The area of Figure 1b can be found in the lower center part of Figure 1a. Fracture is found to be by brittle cleavage adjacent to the fatigue precrack, but by dimple rupture in the final third of the fracture surface. This specimen can be seen to have a very large grain size, as large as 500 μm, and cleaved surfaces containing river pattern features that extend across many of the grains. The cleavage facets are unusually steeply inclined to the plane of the fracture surface. The stretch zone between the fatigue precrack and the cleaved grains is difficult to identify, indicating a very small stretch zone and corresponding crack opening displacement, but cleavage initiates somewhat below the fatigue surface in the area shown in Figure 1b.

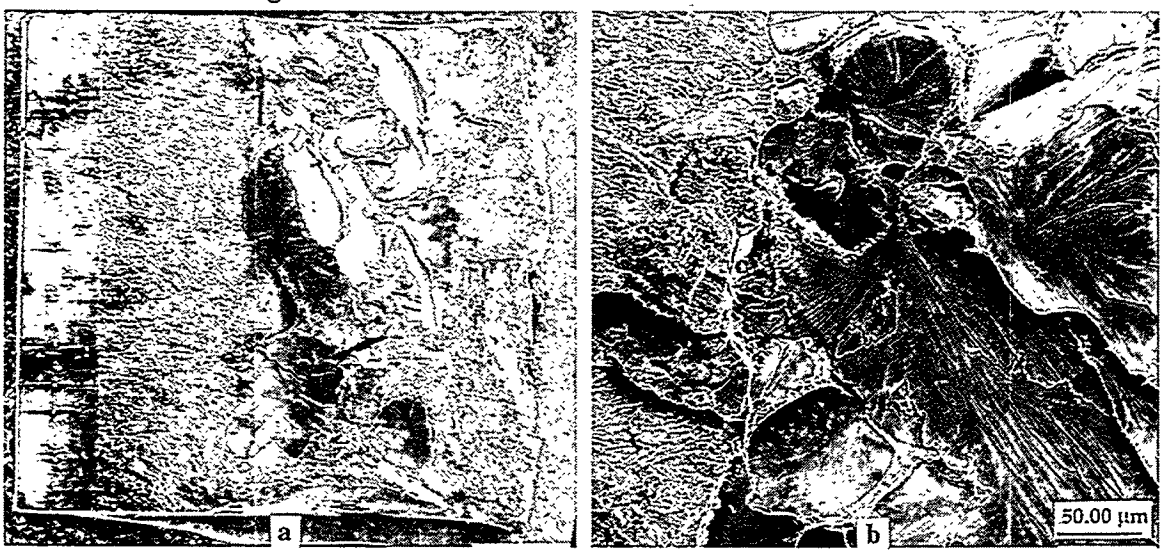

Figure 1 Low and higher magnification fractographs of specimen L317 of Fe-2Cr-1.5V irradiated at 370°C to 30 dpa and tested at 300°C.

Figure 2 shows the fracture appearance for specimen L010 of Fe-7.5Cr-2W irradiated at 370°C to 30 dpa and tested at 8°C. Fracture is again found to be by brittle cleavage adjacent to the fatigue precrack but by dimple rupture for the remaining half of the fracture surface. The grain size is much finer, on the order of 100 μm, and a well defined stretch zone, on the order of 25 μm can be identified.

Figure 3 shows the fracture appearance for specimen L508 of Fe-9Cr-1.3V-1.1Mn irradiated at 370°C to 30 dpa and tested at -39°C. Fracture is found to be by a mixture of cleavage fracture and grain boundary decohesion in the brittle region and by dimple rupture in the remaining quarter of the specimen. The grain size is about 100 μm, and grain boundary decohesion occurs with very little surface dimpling. The ratio of grain boundary decohesion to brittle cleavage is about 50% in the area of Figure 3b and deep grain boundary wedge cracking can be seen. Stretch zone formation is probably less than 1 μm.

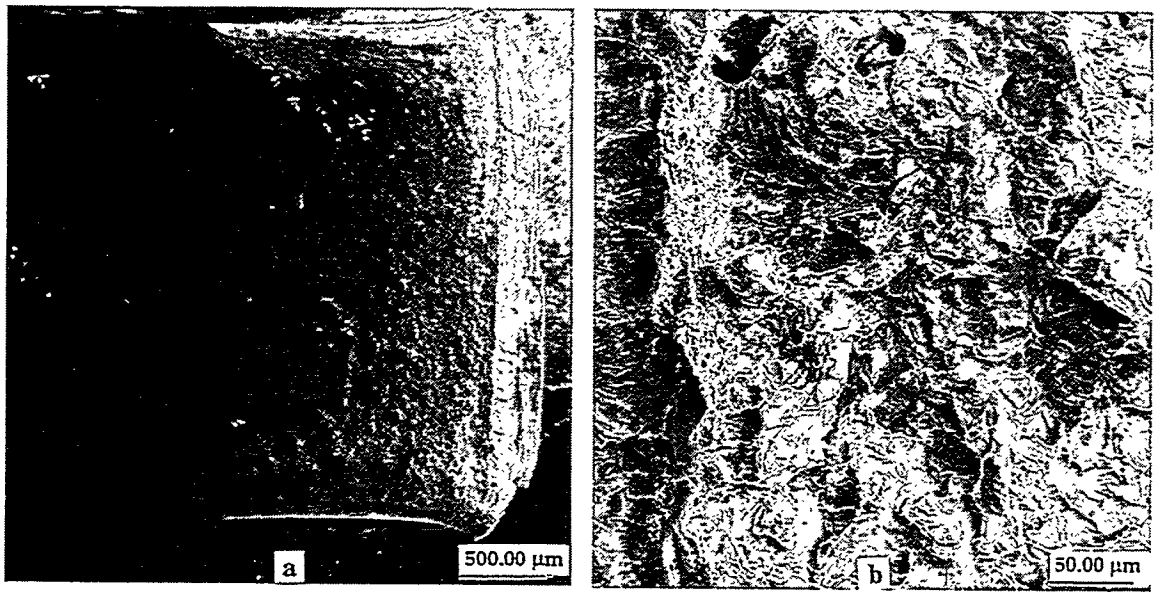

Figure 2 Low and higher magnification fractographs of specimen L010 of Fe-7.5Cr-2W irradiated at 370°C to 30 dpa and tested at 8°C.

Figure 3 Low and higher magnification fractographs of specimen L508 of Fe-9Cr-1V-1Mn irradiated at 370°C to 30 dpa and tested at -39°C.

Figure 4 shows the fracture appearance for specimen L806 of Fe-9Cr-2.4Mn-1W-0.3V irradiated at 370°C to 30 dpa and tested at 65°C. Fracture is found to be predominantly by grain boundary decohesion in the brittle region and by dimple rupture in the remaining third of the specimen. The grain size is about 100 μm, and grain boundary decohesion occurs with very little surface dimpling. The ratio of grain boundary decohesion to brittle cleavage is about 90% in the area of Figure 4b and deep grain boundary wedge cracking can be seen. The stretch zone is again very narrow, with one example of grain boundary decohesion extending 30 μm back into the fatigue region, in the upper left of Figure 4b.

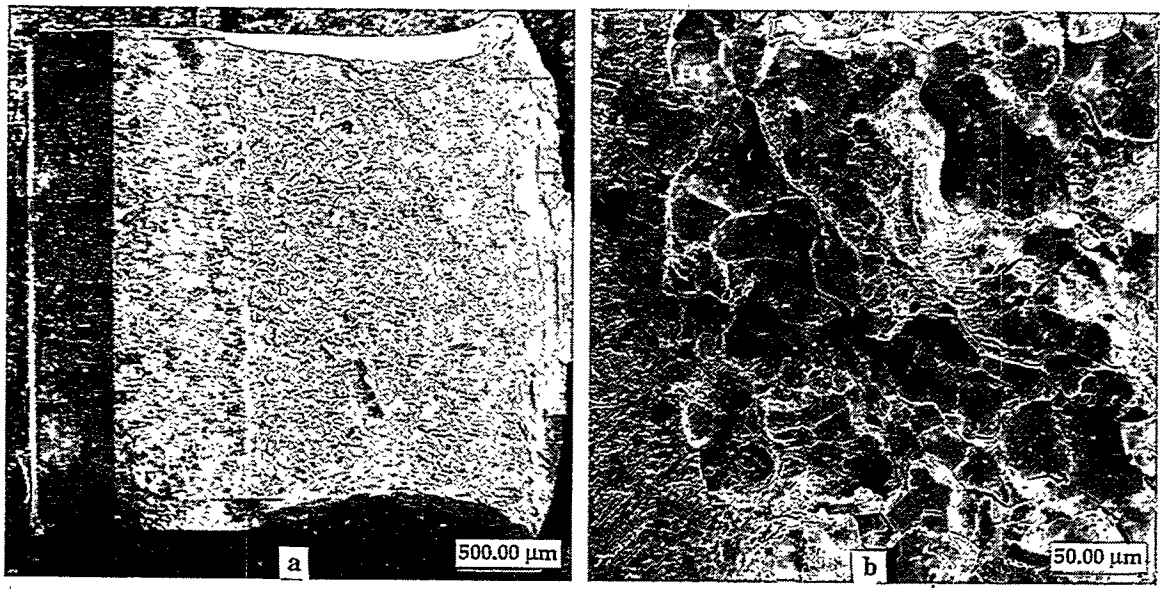

Figure 4 Low and higher magnification fractographs of specimen L806 of Fe-9Cr-1W-2Mn irradiated at 370°C to 30 dpa and tested at 65°C.

Figure 5 shows the fracture appearance for specimen L710 of Fe-12Cr-6.5Mn-1V irradiated at 370°C to 30 dpa and tested at 225°C. Fracture is found to be predominantly by grain boundary decohesion in the brittle region and by dimple rupture over half the specimen, distributed in three regions, two in small regions in the middle of the brittle region. Therefore, in this sample, fracture probably began by grain boundary decohesion, but two central regions actually failed by dimple rupture, possible before brittle fracture continued by grain boundary decohesion, followed by final ligament failure by dimple rupture. Grain boundary decohesion occurs with a fair amount of surface dimpling. The ratio of grain boundary decohesion to brittle cleavage is very high in the area of Figure 5b and deep grain boundary wedge cracking can be seen. The stretch zone is about 20 μm wide.

Figure 6 shows the fracture appearance for specimen L910 of Fe-12Cr-6.5Mn-1W-0.3V irradiated at 370°C to 30 dpa and tested at 200°C. Fracture is found to be predominantly by grain boundary decohesion in the brittle region and by dimple rupture over half the specimen, distributed in two regions, one in a band in the middle of the brittle region. Therefore, fracture probably began by grain boundary decohesion, but a central region actually failed by dimple rupture, possible before a second region failed by grain boundary decohesion. Grain boundary decohesion occurs with surface dimpling. The ratio of grain boundary decohesion to brittle cleavage is very high in the area of Figure 6b and deep grain boundary wedge cracking can be seen. The stretch zone is about 20 μm wide.

Discussion

Comparing the present fractographic results with previous results from specimens irradiated to 10 dpa[2] shows little change in response. The major difference appears to be that for the Fe-9Cr-1.3V-1.1Mn alloy L5, fracture appearance shifts from predominantly grain boundary decohesion at 10 dpa, to about 50% cleavage at 30 dpa. Thus, the reduction in DBTT of about 30°C upon irradiation from 10 to 30 dpa that was observed in this alloy may arise due to a return to cleavage fracture, probably from an overaging process. Also, specimens of Fe-12Cr-6.5Mn-1V alloy L7 and Fe-12Cr-6.5Mn-1W-0.3V alloy L9 developed regions of dimple rupture within regions that failed by brittle grain boundary decohesion following irradiation to 30 dpa that were not found after 10 dpa. However, these last

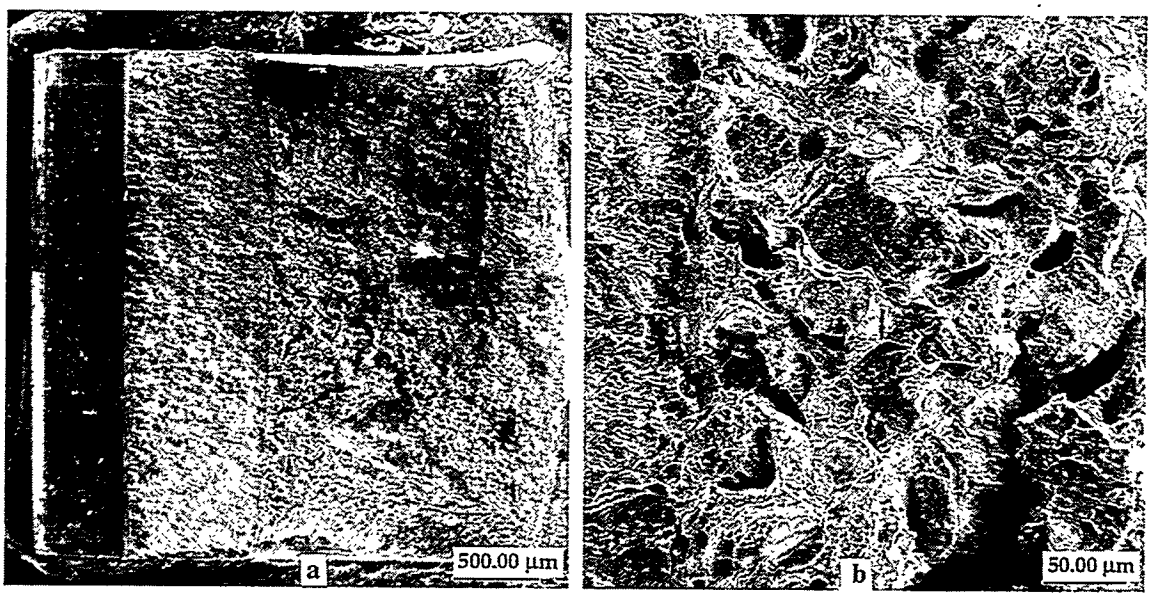

Figure 5 Low and higher magnification fractographs of specimen L710 of Fe-12Cr-6Mn-1V irradiated at 370°C to 30 dpa and tested at 225°C.

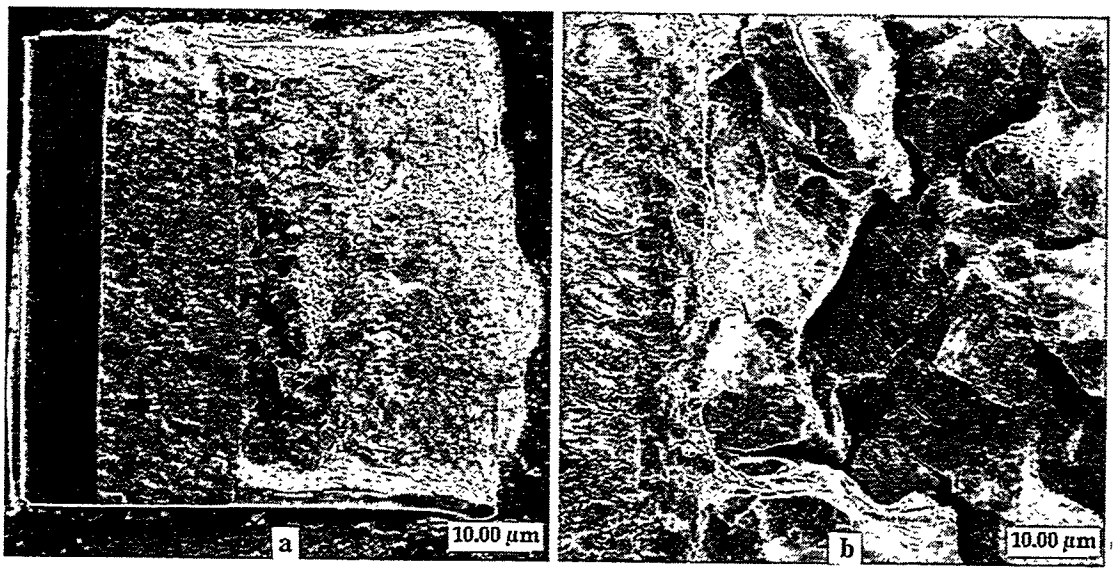

Figure 6 Low and higher magnification fractographs of specimen L910 of Fe-12Cr-6Mn-1W irradiated at 370°C to 30 dpa and tested at 200°C.

observations may arise from specimen to specimen variation and are common observations in welded samples were microstructural variation can occur on a coarse scale.

It is possible to relate change in DBTT due to irradiation in these steels with manganese content. Such a relation is anticipated based on the observation of Fe-Cr-Mn chi phase reported following irradiation.[4] Figure 7 shows shift in DBTT as a function of Mn content for all the higher chromium (7-12%) alloys. From this figure it is apparent that shifts in DBTT of about 100°C can be expected when Mn levels reach about 2% and saturation may be occurring when Mn levels exceed 5%.

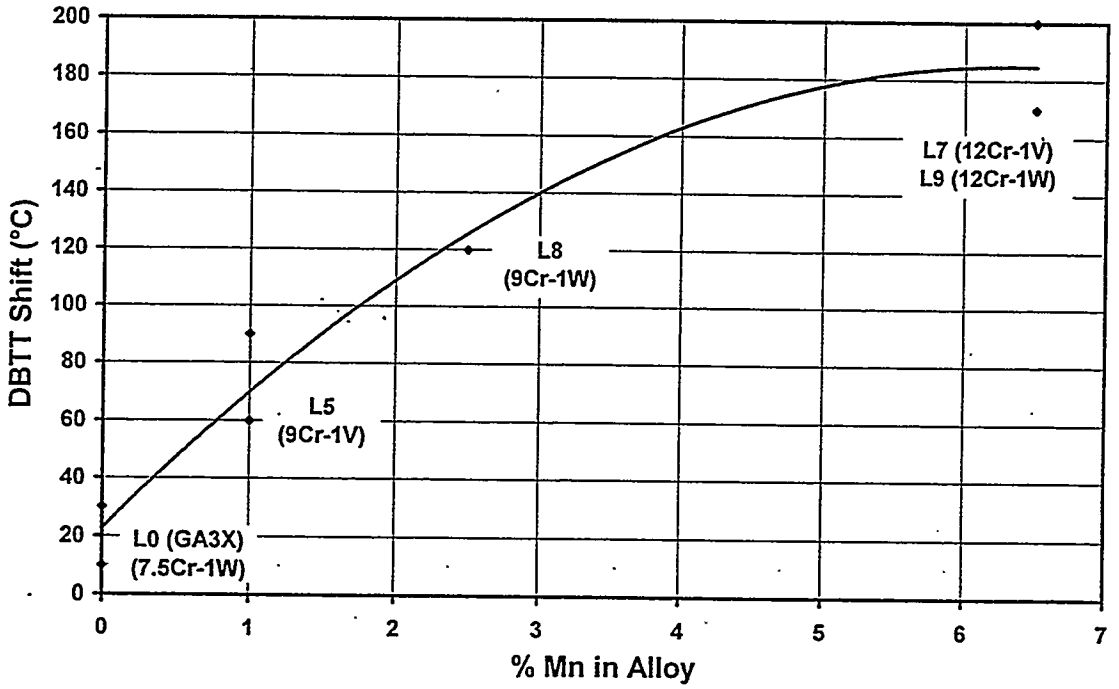

Figure 7 Shift in DBTT following irradiation at 370°C to 10-30 dpa for 7-12Cr alloys as a function of Mn content.

However, it has been predicted that Mn levels will only increase to about 1% Mn by transmutation in a ferritic alloy following irradiation in a fusion device to about 200 dpa.[5] Figure 7 predicts that the consequence will be only a 50°C increase in DBTT.

CONCLUSIONS

Fractographic examination has been performed on charpy specimens of six reduced activation alloys irradiated in the FFTF at 370°C to 30 dpa. Only minor differences were observed in comparison with a similar study following irradiation to 10 dpa, and confirm that radiation-induced embrittlement at 370°C saturates in this alloy class at low dose. Analysis of charpy results also provides a correlation between shift in DBTT and increasing Mn content. Based on this correlation, it is predicted that manganese buildup of 1% following irradiation to 200 dpa in a fusion machine will cause a DBTT shift of only 50°C.

Future work

This work is completed.

REFERENCES

1 L. E. Schubert, M. L. Hamilton, and D. S. Gelles, in DOE/ER-0313/19 (1996) 133.
2 N. S. Cannon, and D. S. Gelles, in DOE/ER-0313/2 (1987) 119.
3 D. S. Gelles and N. S. Cannon, in DOE/ER-0313/4 (1988) 95.
4 D. S. Gelles and W. L. Hu, in DOE/ER-0313/1 (1986) 251.
5 F. M. Mann, "Transmutation of Alloys in MFE Facilities as Calculated by REAC," HEDL-TME 81-37, August 1982.

LOW-CHROMIUM REDUCED-ACTIVATION CHROMIUM-TUNGSTEN STEELS – R. L. Klueh, D. J. Alexander, and P. J. Maziasz (Oak Ridge National Laboratory)

OBJECTIVE

The goal of this work is the development of reduced-activation ferritic steels.

SUMMARY

Bainitic microstructures formed during continuous cooling can differ from classical upper and lower bainite formed during isothermal transformation. Two types of non-classical bainite were observed depending on the cooling rate: carbide-free acicular bainite at rapid cooling rates and granular bainite at slower cooling rates. The Charpy impact toughness of the acicular ferrite was found to be considerably better than for the granular bainite. It was postulated that alloying to improve the hardenability of the steel would promote the formation of acicular bainite, just as increasing the cooling rate does. To test this, chromium and tungsten were added to the 2 1/4Cr-2W and 2 1/4Cr-2WV steel compositions to increase their hardenability, and the microstructures and mechanical properties were examined.

PROGRESS AND STATUS

Introduction

Most of the work on reduced-activation steels has been concentrated on high-chromium steels [1]. The ORNL alloy development program studied eight steels with chromium contents ranging from 2.25 to 12%[2-4]. An Fe-2.25Cr-2W-0.25V-0.1C (2 1/4Cr-2WV) steel had the highest strength of the eight steels examined [2], but the Charpy impact properties were inferior to an Fe-9Cr-2W-0.25V-0.07Ta-0.1C (9Cr-2WVTa) steel. Despite the excellent behavior of the 9Cr-2WVTa, there are advantages for low-chromium bainitic steels [5]. Because bainitic steels often have excellent strength and toughness in the as-quenched or as-normalized condition, it might be possible to use such steels without a post-weld heat treatment, which is not possible for any of the martensitic 9Cr steels. This could be a very important consideration for the construction of a complicated structure such as a fusion power plant.

Work on an Fe-3Cr-1.5Mo-0.1V-0.1C (3Cr-1.5MoV) steel demonstrated that the Charpy properties depended on the type of bainite microstructure that developed during heat treatment [6]. This information was factored into the earlier work on developing improved low-chromium reduced-activation steels [7], and an extension of that work is discussed in this report.

Bainite forms when a steel transforms from austenite in the critical temperature range between the temperature where ferrite and pearlite form (high temperatures) and the temperature where martensite forms (low temperatures). Bainite was originally described as consisting of only two distinguishable microstructures: upper and lower bainite, which are defined according to their temperature of formation [8,9]. Habraken [10] demonstrated that there are microstructural variations of the classical bainite that formed in the bainite transformation temperature regime. Such "nonclassical" bainite formed more readily during continuous cooling than during isothermal transformation , where upper and lower bainite formed. Habraken and Economopoulos [10] contrasted classical and nonclassical bainite using the isothermal transformation (IT) and continuous-cooling transformation (CCT) diagrams. The bainite transformation region of an IT diagram can be divided into two temperature regimes by a horizontal line. Transformation above the temperature represented by this line produces upper bainite, and transformation below it produces lower bainite. Upper bainite consists of laths with carbides at the lath boundaries. Lower bainite consists of plates or laths containing parallel arrays of carbides that form at ≈60° to the plate axis [8,9]. For nonclassical bainite, Habraken and Economopoulos [11] found that a CCT diagram could be divided into three vertical regimes. Different microstructures form for cooling rates that pass through these different zones. For the fastest cooling rate (Zone I), a "carbide-free acicular" structure was formed, which consisted of side-by-side plates or laths of ferrite containing a high dislocation density [10]. At an intermediate cooling rate (Zone II), a carbide-free

"massive" or "granular" structure resulted, which was designated granular bainite and was described as consisting of equiaxed subgrains of low-carbon ferrite with a high dislocation density coexisting with dark "islands" [11], which were enriched in carbon during the bainite transformation. The islands were shown to be retained austenite with a high carbon concentration, part of which often transformed to martensite when cooled below the M_s temperature. These high-carbon regions are referred to as "martensite-austenite (M-A) islands" [11]. Microstructures developed by still slower cooling rates (Zone III) were not observed in this study and will not be discussed.

To demonstrate that the microstructure of the 2 1/4Cr-2W and 2 1/4Cr-2WV was determined by cooling rate, 10-mm- and a 3-mm-square bars of the steels were austenitized in a helium atmosphere in a tube furnace and then cooled in static or flowing helium, respectively. Granular bainite formed in the slowly cooled 10-mm bar, and acicular bainite formed in the 3-mm bar rapidly cooled in the flowing helium [6].

It was proposed previously that formation of carbide-free acicular bainite could be promoted by improving the hardenability [6]. Hardenability is defined as the relative ability of a steel to avoid forming ferrite when cooled from the austenitizing temperature. Increasing hardenability should have the same relative effect as increasing cooling rate: the transformation of austenite to ferrite is delayed so the steel can be cooled more slowly and still obtain a martensitic or bainitic microstructure (depending on the cooling rate). It was reasoned that increased hardenability should also widen the zone for acicular-bainite formation to longer times and allow it to form at a slower cooling rate [6]. Hardenability can be altered by changing composition. As a first attempt to vary hardenability, more chromium and small amounts of boron were added to the 2 1/4Cr-2WV composition [6]. Boron was chosen because small amounts are known to increase hardenability [12,13]. The chromium concentration was increased to 2.6%, and ≈0.005 B was used. Tantalum additions were also made, because tantalum in 9Cr-2WVTa appeared to improve the properties of that steel compared to a steel without tantalum [6]. The addition of the Cr and B resulted in a marked improvement in the Charpy properties. However, there were still indications of granular bainite in the microstructure of an Fe-2.6Cr-0.25V-0.004B-0.1C (2.6Cr-2WVB) steel. Therefore, it was decided to add still more chromium (to a total of 3%) and also to add additional tungsten (up to 3%). These 3Cr-W and 3Cr-WV steels are the subject of the work presented here.

Experimental Procedure

Small 450-g vacuum arc-melted button heats of nominal composition Fe-2Cr-2W-0.1C (3Cr-2W), and Fe-3Cr-3W-0.1C (3Cr-3W), Fe-3Cr-2W-0.25V-0.1C (3Cr-2W), and Fe-3Cr-3W-0.25V-0.1C (3Cr-3WV) steels were made using the 2 1/4Cr-2W and 2 1/4Cr-2WV from the original eight heats of reduced-activation steel [3] as starting material. Data on these latter two heats and the 9Cr-2WVTa from the original heats were used for comparison [2-4]. Half of each 12.7 x 25.4 x 127 mm ingot was hot rolled to 6.4 mm and half to 0.76 mm. Tests were made on normalized-and-tempered SS-1 tensile specimens taken from the 0.76-mm sheet. In the normalization treatment, the steels without vanadium were austenitized at 900°C and those with vanadium were austenitized at 1050°C. Steels were tested after tempering at 700 and 750°C. The steels were examined by transmission electron microscopy (TEM) after normalization to determine the type of bainite formed.

Results and Discussion

Microstructure

The addition of ≈0.75% Cr to the 2 1/4Cr-2W composition to produce 3Cr-2W resulted in an acicular bainite microstructure after normalization, as expected for a steel with increased hardenability [Fig. 1(a)]. However, the microstructure of 3Cr-3W produced by the addition of 0.75% Cr and 1% W contained a significant amount of coarse precipitate, and the laths were not well defined [Fig 1(b)]. It is not known whether the additional tungsten induces the formation of this precipitate or whether the 900°C austenitization temperature was too low to dissolve all the carbides for a steel with this much tungsten. When vanadium was added to produce 3Cr-2WV and 3Cr-3WV steels, this coarse precipitate did not form during austenitization at 1050°C.

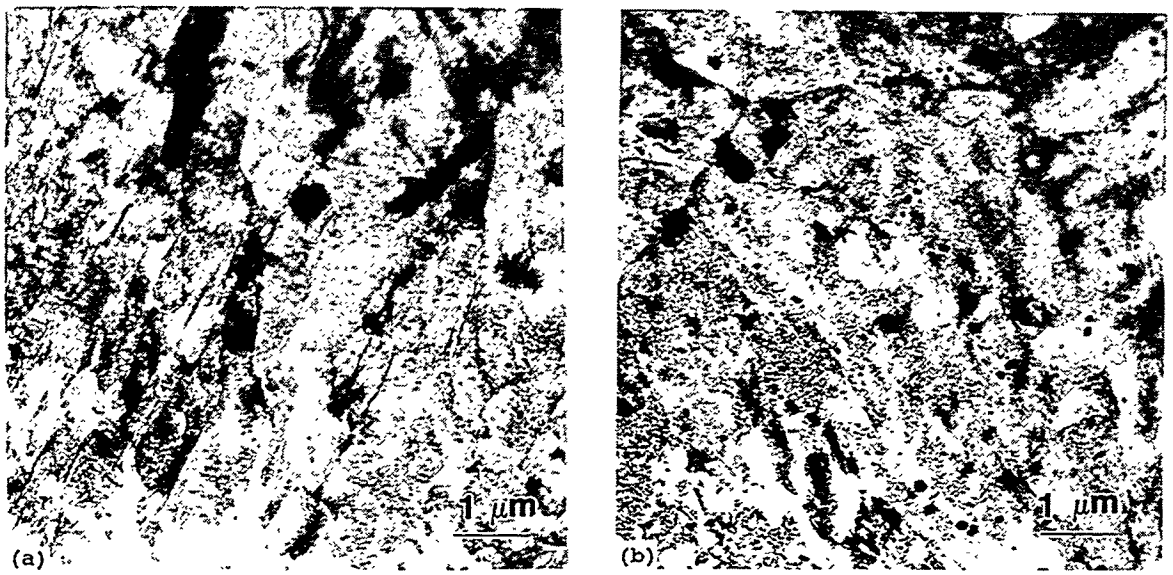

Figure 1. Transmission electron micrographs of normalized (a) 3Cr-2W and (b) 3Cr-3W steels.

TEM indicated that both the normalized 3Cr-2WV [Fig. 2(a)] and 3Cr-3WV [Fig. 2 (b)] steels contained carbide-free acicular microstructures, with the lath size decreasing with increasing tungsten. Thus, the combination of additional chromium and tungsten produces the preferred acicular bainite structure when normalized.

The microstructures of the the 3Cr-2WV and 3Cr-3WV contrasted with those of the 2 1/4Cr-2WV, which had a granular bainite structure when heat treated in the 3-mm-bar geometry used for the Charpy specimens [6]. Thus, the additional chromium and tungsten improved the hardenability and promoted the desired microstructure.

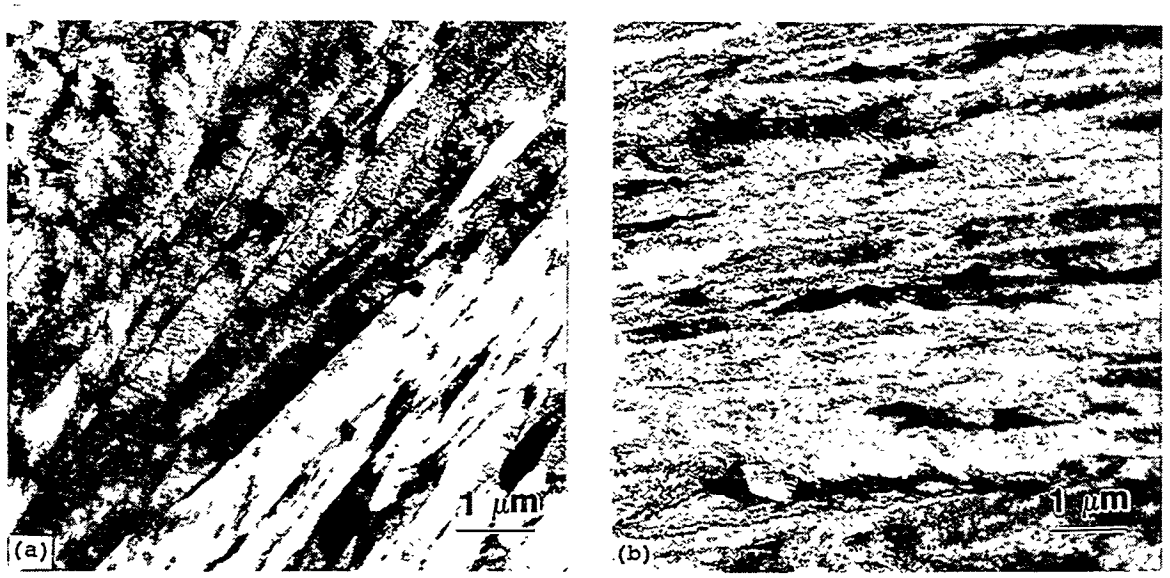

Figure 2. Transmission electron micrographs of normalized (a) 3Cr-2WV and (b) 3Cr-3WV steels.

Tensile Properties

After tempering at 700°C, the yield stress [Fig. 3(a)] between room temperature and 600°C of the new steels and those used for comparison fell into two regimes, depending on whether or not the steels contained vanadium. There was little difference in the yield stress of the 2 1/4Cr-2W, 3Cr-2W, and 3Cr-3W steels—steels without vanadium. For the steels containing vanadium, the 3Cr-3WV was slightly weaker than 2 1/4Cr-2WV at all temperatures but 600°C, but it was stronger than 9Cr-2WVTa, which was stronger than the 3Cr-2WV, indicating that the tungsten content had an effect on the 3Cr-WV steels that was not apparent in the 3Cr-W steels without vanadium. Note, however, that the strength of the 3Cr-2WV approached that of the 9Cr-2WVTa at 500 and 600°C. The relative behavior of the ultimate tensile strength was similar to the yield stress.

The ductility (uniform and total elongations) after tempering at 700°C also fell into two regimes and, with one exception, the steels could again be separated on the basis of vanadium content. The three steels without vanadium, which were the weakest, had the highest total elongation [Fig. 3(b)], with the 2 1/4Cr-2W having the highest elongation at the highest temperatures. The 2 1/4Cr-2WV, 3Cr-2WV, and 3Cr-3WV steels all had similar total elongations, slightly above those for 9Cr-2WVTa. The uniform elongation showed a similar behavior, except that the 2 1/4Cr-2WV steel had a uniform elongation that approached those of the steels without vanadium below 600°C, and then became less than those steels at 600°C.

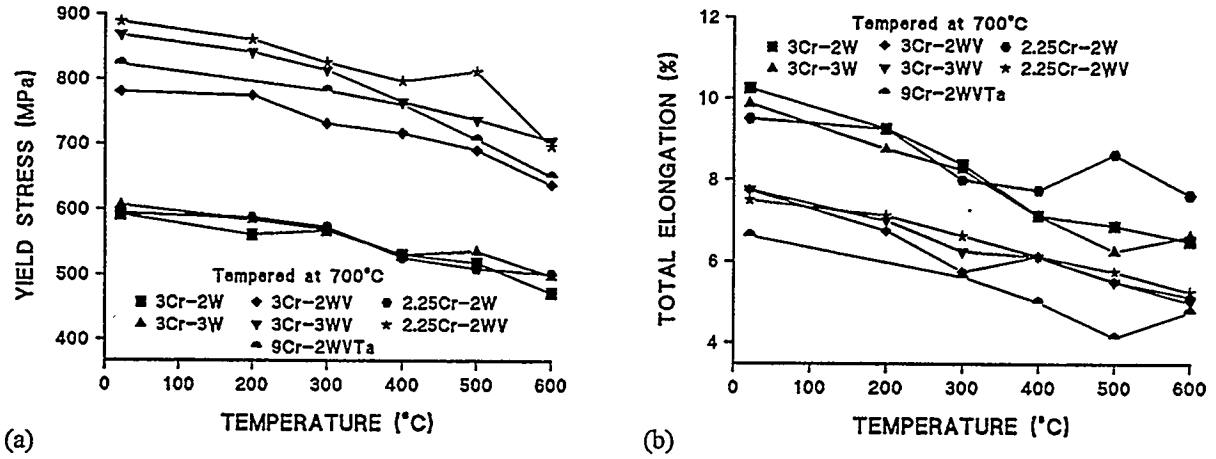

Figure 3. (a) Yield stress and (b) total elongation vs. test temperature for the 3Cr-2W, 3Cr-3W, 3Cr-2WV, 3Cr-3WV, 2 1/4Cr-2W, 2 1/4Cr-2WV, and 9Cr-2WVTa steels after normalizing and tempering 1 h at 700°C.

There was more variation in the tensile properties after tempering at 750°C. The steels without vanadium were again the weakest, with little difference between the yield strengths of the 3Cr-2W and 3Cr-3W [Fig. 4(a)]. Although 2 1/4Cr-2W was stronger than these two steels below 400°C, it became weaker at 500 and 600°C. For the vanadium-containing steels, the 2 1/4Cr-2WV was strongest over the entire temperature range; the 9Cr-2WVTa was slightly stronger than the 3Cr-3WV at the lower temperatures, becoming similar at 500 and 600°C. The 3Cr-2WV was the weakest of the vanadium-containing steels except at 600°C, where it approached the strength of the 3Cr-3WV and 9Cr-2WVTa. The ultimate tensile strength behave similar to the yield strength, except there was less difference between the strongest and weakest steels. Also, for the vanadium-containing steels, the 2 1/4Cr-2WV and 9Cr-2WVTa showed less difference than for the yield stress, although at 600°C, the 9Cr-2WVTa had the lowest strength of the vanadium-containing steels, with the value for the 3Cr-2WV and 3Cr-3WV approaching that of the 2 1/4Cr-2WV. Ductility after tempering at 750°C [Fig. 4(b)] again fell into two categories, with the steels without vanadium having the highest ductility (uniform and total elongation). The 9Cr-2WVTa had the lowest ductility.

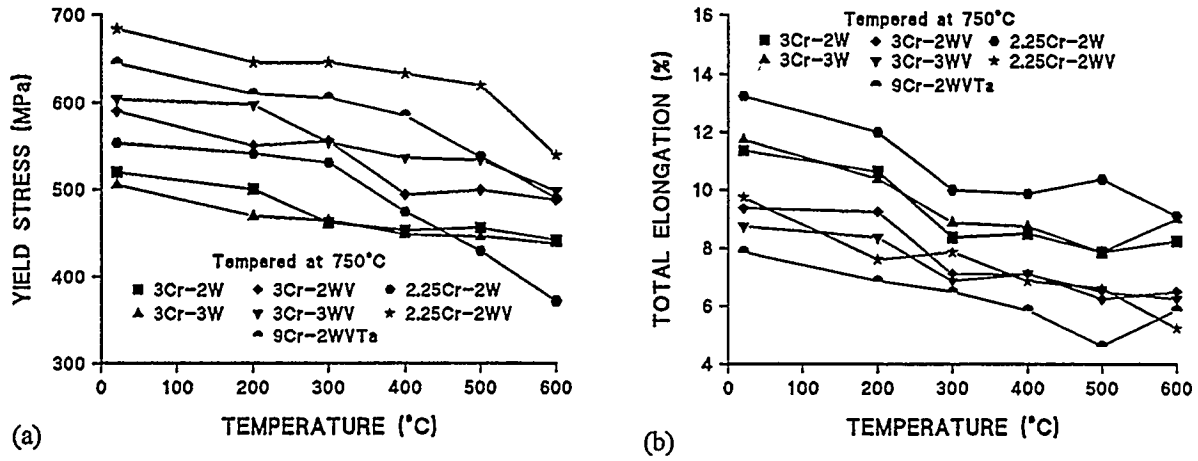

Figure 4. (a) Yield stress and (b) total elongation vs. test temperature for the 3Cr-2W, 3Cr-3W, 3Cr-2WV, 3Cr-3WV, 2 1/4Cr-2W, 2 1/4Cr-2WV, and 9Cr-2WVTa steels after normalizing and tempering 1 h at 750°C.

The results indicated that the 3Cr-3WV steel had strength and ductility generally as good as or better than that of 9Cr-2WVTa and approached the strength of the 2 1/4Cr-2WV, which was the strongest steel of the original eight heats of reduced-activation steel [3].

SUMMARY

It was proposed that increasing the hardenability of a steel that forms granular bainite under a given cooling rate could promote the formation of acicular bainite, just as an increased cooling rate does. Hardenability of a 2 1/4Cr-2WV reduced-activation steel was increased by adding chromium and tungsten to obtain 3Cr-2W, 3Cr-3W, 3Cr-2WV, and 3Cr-3WV. These steel had a 100% acicular bainitic microstructure in the normalized condition. The tensile properties of one of the new steels in the normalized-and-tempered condition was as good or better than those of the 9Cr-2WVTa steel, which was the best of the steels of the original reduced activation steels studied.

FUTURE WORK

The Charpy properties of the new steels will be presented in the next report, and the mechanical properties results for the new steels will be compared with those for the conventional steels and the earlier reduced-activation steels.

REFERENCES

1. R. L. Klueh, K. Ehrlich, and F. Abe., *J. Nucl. Mater.* 1992, vol. 191-194, pp. 116-24.
2. R.L. Klueh and P.J. Maziasz, *Met. Trans.* 1989, vol. 20A, pp. 373-82.
3. R.L. Klueh, *Met. Trans.*, 1989, vol. 20A, pp. 463-470.
4. R.L. Klueh and W.R. Corwin, *J. Eng. Mater.*, 1989, vol. 11, 169-75.
5. R.L. Klueh and A.M. Nasreldin, *Met. Trans. A*, 1987, vol. 18A, pp. 1279-90.
6. R.L. Klueh and D.J. Alexander, *J. Nucl. Mater.*, 1995, vol. 227, pp. 11-23.
7. R.L. Klueh, *Nucl. Eng. Design*, 1982, vol. 72, 329-44.
8. R.W.K. Honeycomb, *Steels: Microstructure and Properties*, Edward Arnold, London, 1981, pp. 106-19.

9. H.K.D.H. Bhadeshia, *Bainite in Steels*, The Institute of Materials, London, 1992, pp. 283-85.
10. L.J. Habraken, *Proc. 4th Int. Conf. Electron Microscopy, Vol. 1*, Springer-Verlag, Berlin, 1960, pp. 621-28.
11. L.J. Habraken and M. Economopoulos, *Transformation and Hardenability in Steels*, Climax-Molybdenum Company, Ann Arbor, MI, 1967, pp. 69-108.
12. F.B. Pickering, *Physical Metallurgy and the Design of Steels*, Applied Science Publishers, London, 1978, pp. 103-105.
13. W.C. Leslie, *The Physical Metallurgy of Steels*, McGraw-Hill Book Company, New York, 1981, pp. 269-81.

HEAT-TO-HEAT VARIABILITY OF IRRADIATION CREEP AND SWELLING OF HT9 IRRADIATED TO HIGH NEUTRON FLUENCE AT 400-600°C -

M.B. Toloczko and F.A. Garner (Pacific Northwest National Laboratory)[1]

To be published in the Proceedings, 18th ASTM International Symposium on Effects of Radiation on Materials, Hyannis, MA, June 1996.

EXTENDED ABSTRACT

Irradiation creep data on ferritic/martensitic steels are difficult and expensive to obtain, and are not available for fusion-relevant neutron spectra and displacement rates. Therefore, an extensive creep data rescue and analysis effort is in progress to characterize irradiation creep of ferritic/martensitic alloys in other reactors and to develop a methodology for applying it to fusion applications.

In the current study, four tube sets constructed from three nominally similar heats of HT9 subjected to one of two heat treatments were constructed as helium-pressurized creep tubes and irradiated in FFTF-MOTA at four temperatures between 400 and 600°C. Each of the four heats exhibited a different stress-free swelling behavior at 400°C, with the creep rate following the swelling according to the familiar $B_o + D\dot{S}$ creep law. No stress-free swelling was observed at the other three irradiation temperatures.

Using a stress exponent of $n = 1.0$ as the defining criterion, "classic" irradiation creep was found at all temperatures, but, only over limited stress ranges that decreased with increasing temperature. The creep coefficient B_o is a little lower (~50%) than that observed for austenitic steel, but the swelling-creep coupling coefficient D is comparable to that of austenitic steels. Primary transient creep behavior was also observed at all temperatures except 400°C, and thermal creep behavior was found to dominate the deformation at high stress levels at 550 and 600°C.

[1]Operated for the US Department of Energy by Battelle Memorial Institute under Contract DE-AC06-76RLO 1830

PRELIMINARY RESULTS OF THE ROUND-ROBIN TESTING OF F82H --- K. Shiba, N. Yamanouchi [Japan Atomic Energy Research Institute (JAERI)] and A. Tohyama [Nippon Kohkan Co. (NKK)]

OBJECTIVE

The IEA round-robin tests for the accumulation of the basic properties of the low activation ferritic steels are in progress under the international corporation. Preliminary results of a reduced activation martensitic steel F82H IEA obtained in this round-robin tests are reviewed in this report.

SUMMARY

Preliminary results of metallurgical, physical and mechanical properties of low activation ferritic steel F82H (IEA heat) were obtained in the round-robin test in Japan.

The properties of IEA heat F82H were almost the same as the original F82H.

PROGRESS AND STATUS

The basic property tests of a low activation martensitic steel F82H is in progress by IEA international corporation now. The irradiation experiment of this steel is included in the Japan/US collaborative program on the fusion reactor materials, either. Some data obtained from the Japanese round-robin test program are reported in this report.

EXPERIMENTAL PROCEDURE

The alloy investigated was a low activation martensitic steel F82H (8Cr-2WVTa) This steel was prepared for the reference material for the IEA international collaborative research on the low activation ferritic/martensitic steels, hereafter, this alloy is called as F82H IEA heat to distinguish from the original F82H. The plates used for the tests are listed in Table 1 and the chemical composition of these plates are shown in table 2. These alloys were normalized at 1040°C for 1 h, then tempered at 720°C.

Table 1 The plate IDs

Alloy ID	Plate IDs	Thickness (mm)
RB801-5	5-3, 5-14, 5-16	7.5
KG819-2	2w-10, 2w-23	15
KG820-2	42w-18	25

Table 2 Chemical composition of F82H materials (IEA heat)

Alloy ID	Elements (mass%)[1)]								
	C	Si	Mn	P	S	Cu	Ni	Cr	Mo
RB801-1	0.09	0.11	0.16	0.002	0.002	0.01	0.02	7.70	0.003
KG819-2	0.09	0.07	0.1	0.003	0.001	0.01	0.02	7.87	0.003
KG820-2	0.09	0.07	0.1	0.003	0.001	0.01	0.02	7.84	0.003

Alloy ID	Elements (mass%)[1)]								
	V	Nb	B	T.N	Sol. Al	Co	Ti	Ta	W
RB801-1	0.16	0.0001	0.0002	0.006	0.003	0.005	0.01	0.02	1.94
KG819-2	0.19	0.0002	0.0002	0.006	0.001	0.003	0.004	0.04	1.98
KG820-2	0.19	0.0002	0.0002	0.007	0.001	0.003	0.004	0.04	1.98

1) Ladle analysis results

Metallurgical Tests

The specimens (50 x 30 x t mm) were fabricated from the 7.5, 15, 25 mm plates (5-14, 2w-23, 42w-18) were polished and etched (Ethanol 100 : Hydrochloric acid 5 : Picric acid 1). Non-metallic inclusions were tested according to the ASTM E45-87 "Standard Practice for Determining the Inclusion contest of Steel". The hardness of the micro structure specimens were also tested with Vickers' hardness test machine. The test load was 10 kgf (98 N).

Physical properties Measurements

Specific heat

Specific heat of the specimen (ϕ14 x 30L mm) fabricated from a 15 mm plate (2w-10) were measured in the temperatures between room temperature and 800°C by the isothermal continuous measurement. The time (Δt) for the temperature increment ($\Delta\theta$) was measured in the isothermal condition.

Thermal expansion

Rod specimen (4 x 4 x 12 mm) machined from the 15 mm plate (2w-10) were used for the thermal expansion measurement in the temperatures between room temperature and 1000°C. The expansion of specimen was measured by the contacting rod. The expansion during the heating and cooling pass was obtained. The rates for heating and cooling were both 0.4°C/min.

Thermal conductivity

Disk specimens (ϕ10 x 2 mm) fabricated from the 15 mm plate (2w-10) were used for the thermal conductivity measurement in the temperatures between room temperature and 800°C by the laser flash method. The temperature of a specimen surface rises by the uniform heating of the another side. Thermal diffusion coefficient (α) is calculated with the following equation by the measured half-time (t) for the temperature saturation and the thermal conductivity is the product of α, specific heat (measured in this paper) and density (7.89 g/cm^2);

$$\alpha = 1.37\frac{L^2}{\pi^2 t} \qquad (1)$$

, where L is the specimen thickness

Young's modulus, modulus of rigidity and Poisson ratio

Young's modulus and modulus of rigidity were measured in the temperature ranging room temperature to 800°C using density measurement specimens (2w-10; ϕ16 x 10L mm) by ultrasonic method. The sound speed in the specimen was calculated from the interval of the multiple reflected echo of the signal emitted by the oscillator contacted to a specimen surface (parallel with the another surface) and specimen thickness. Young's modulus (E), modulus of rigidity (G) and Poisson ratio (ν) were calculated by the following equations;

$$E = \rho\frac{V_s^2(3V_c^2 - 4V_s^2)}{V_c^2 - V_s^2},\quad G = \rho V_s^2,\quad \nu = \left(\frac{E}{2G}\right) - 1 \qquad (2)$$

, where

ρ: Density (7.89 g/cm^2)

Vc: Velocity of longitudinal wave (m/s)

Vs: Velocity of transverse wave (m/s)

Magnetic property

Disk Specimens (ϕ7 x 0.5t mm) were fabricated from 7.5 mm plate (5-3). Magnetic property measurements were carried out at temperatures of room temperature, 200, 300 and 400°C in air. Magnetic moment was measured by AC voltage produced by the cyclic movement of magnetized specimen in the secondary coil.

Mechanical Property Tests

The specimens machined from the 15 mm plate (2w-10) in parallel with the rolling direction were used for the high temperature tensile tests at temperatures ranging between room temperature and 700°C. Round bar tensile specimen (ϕ6 x 30 mm in gauge section) were tested with the strain rate of $1x10^{-4}$ s^{-1}.

The specimens fabricated from the 15 mm plate (2w-10) were used for the Charpy impact tests. Full size V-notched Charpy specimens (10 x 10 x 55 mm, V-notch: 45° x 2 (depth) x 0.25 (root radius) mm) were machined in parallel (L) and perpendicular (T) with the plate rolling direction. The specimens were tested at temperatures ranging between -100 and -20°C to obtain the ductile-brittle transition behavior.

RESULTS

Metallurgical Tests

The inclusion test results of each plates by ASTM method are listed in Table 3. The amount of the non-metallic inclusions are small and this steel can be said clean. The hardness of each plate were almost the same each other (Table 3) and the average hardness was about HV218. This value of the hardness is in the range of the same heat material measured by the several institutes in EU homogeneity test.

Physical properties

The specific heat, thermal expansion and thermal conductivity are shown in Figs. 1 and 2 as a function of test temperature with the data of the original F82H [1]. The immersion density measured at 20°C (7.87 g/cm^3) was used to calculate the thermal conductivity. These properties of the IEA heat material are almost the same as those of the original F82H previously measured. These properties changed discontinuously above 800°C. These phenomenon were due to the re-austenization (A_{C1}). Ehrlich, et.al. estimated A_{C1b} and A_{C1e} of F82H IEA heat were about 820°C and 910°C, respectively [2].

Young's modulus, modulus of rigidity and Poisson ratio are shown in Fig. 3. Both Young's modulus and modulus of rigidity decreased linearly with the test temperature from room temperature to 450°C, then decreased linearly with steeper slope at higher temperatures. Poisson ratio was constant to 500°C, then increased with temperature over the temperature corresponding the change in Young's modulus and modulus of rigidity. This temperature dependence was caused by the annealing of the martensite structure. The same temperature dependence was obtained by the hardness measurement at high temperature.

Table 3 Non-metallic inclusions in F82H IEA heat

Alloy ID	Plate ID	Thickness (mm)	Inclusion Types (ASTM)							
			A type		B type		C type		D type	
			T	H	T	H	T	H	T	H
RB801-5	5-14	7.5	1.0	0	1.5	0.5	0	0	1.0	0.5
KG819-2	2w-23	15	0	0	1.0	1.0	0	0	1.5	0.5
KG820-2	42w-18	25	0	0	1.5	0	0	0	1.0	0.5

Table 4 Vickers' hardness of F82H IEA heat

Alloy ID	Plate ID	Thickness (mm)	HV10			
			1	2	3	Average
RB801-5	5-14	7.5	216	222	220	219
KG819-2	2w-23	15	219	215	219	218
KG820-2	42w-18	25	213	218	214	215

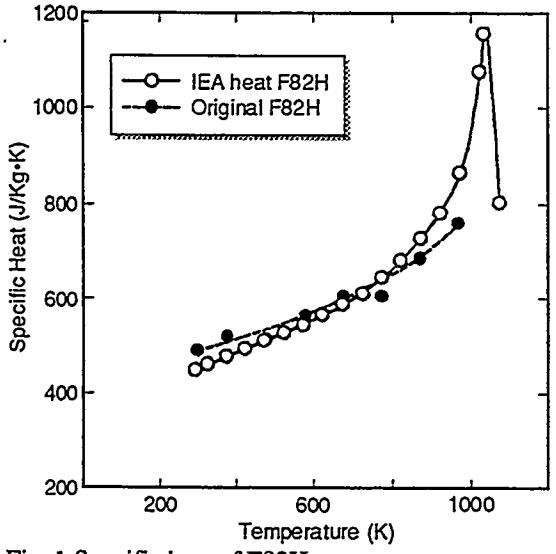

Fig. 1 Specific heat of F82H

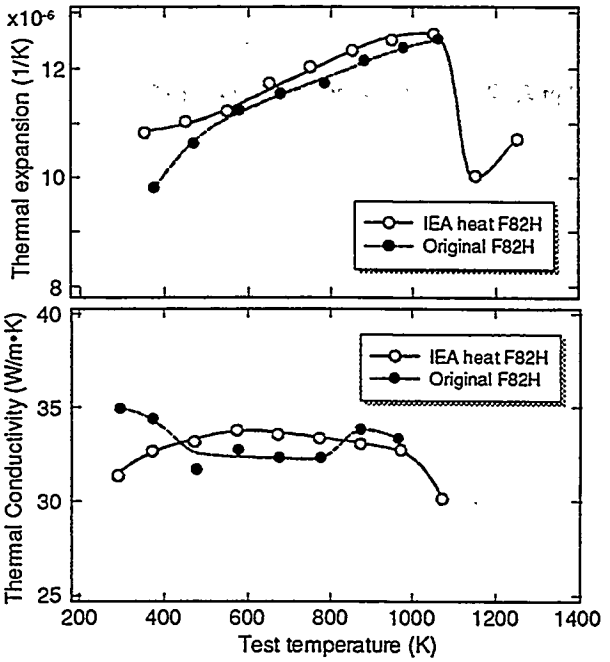

Fig. 2 Thermal expansion and Thermal conductivity of F82H

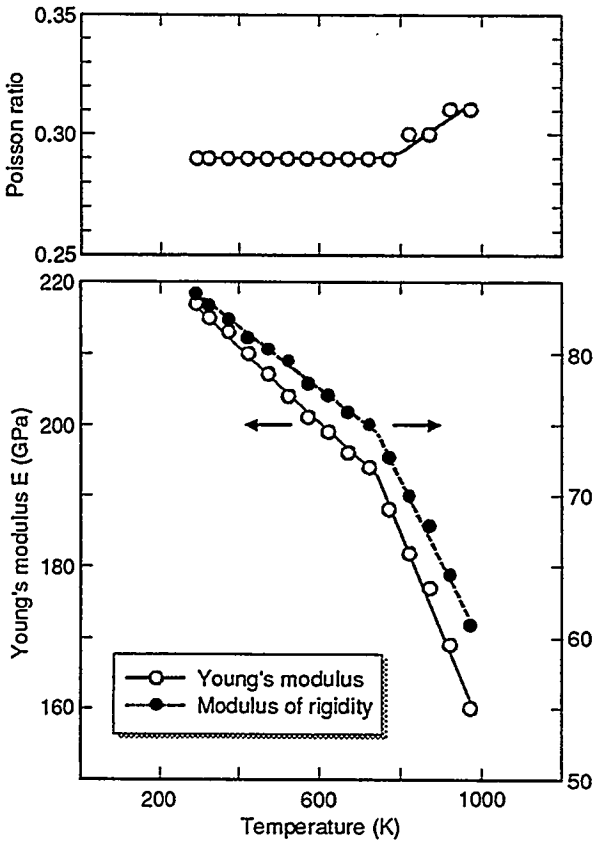

Fig. 3 Young's modulus, modulus of rigidity and Poisson ratio of F82H

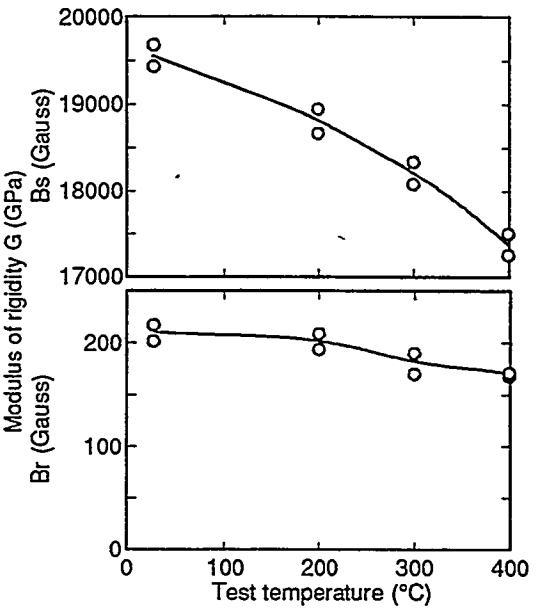

Fig. 4 Saturation and residual magnetization of F82H

Magnetic hysteresis loops were measured in the temperature ranging between room temperature and 400°C. The temperature dependence of the saturation and residual magnetization were plotted in Fig. 4. Saturation and residual magnetization were about 19500 and 200 Gauss at room temperature and both of them decreased with temperature increase.

Mechanical properties

The results of round bar tensile test are shown in Fig. 5. The hatched regions indicate the data band of the original F82H in this figure. The strength decreased with temperature increase and the ductility increased above 550°C.

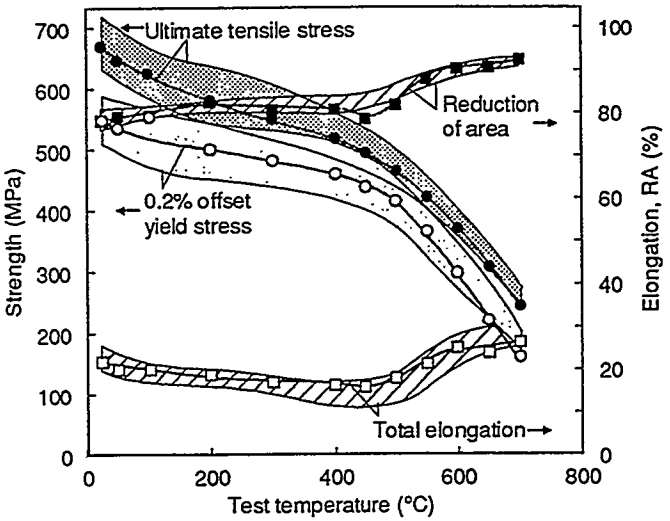

Fig. 5 Tensile properties of F82H IEA heat

The results of Charpy impact test are plotted in Fig. 6. The specimens were machined along the rolling direction (L-direction) and perpendicular with the rolling direction (C-direction). The curves in the figure were fit by hyperbolic arc tangent and the ductile-brittle transition temperatures (DBTT) were obtained from this fitting curve. The DBTT in the absorbed energy and the fracture surface area were -48°C and -44°C in L-direction, respectively. C-direction exhibited slightly higher DBTT than L-direction, but the difference in both direction was small (5 - 10°C).

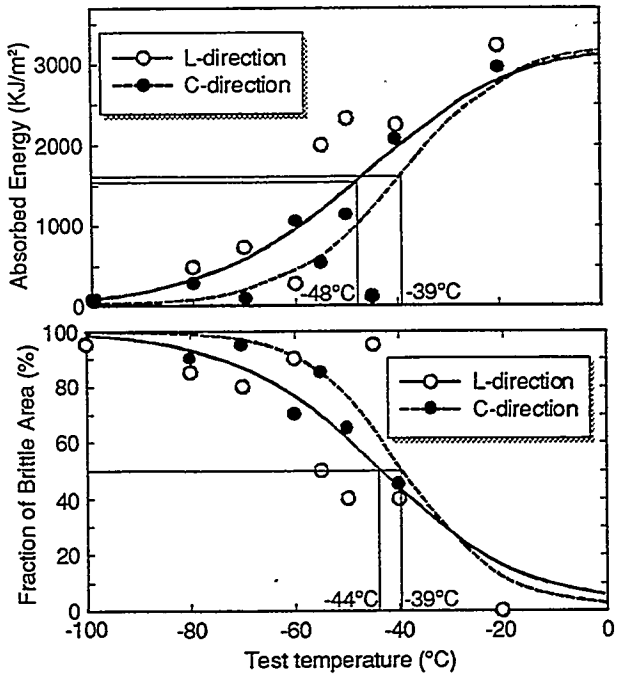

Fig. 6 Charpy impact test results of F82H IEA heat

FUTURE WORK

The testing of some other properties, such as fatigue and creep properties are in progress. The aging of base metal to 3000 and 5000 h in the temperature ranging 450 to 650°C have been completed and the testing are going on. The fabrication of the welded joints (TIG and EB welding) have been completed. The properties of welded joints will be available soon.

REFERENCE

[1] N. Yamanouchi, M. Tamura, H. Hayakawa, A. Hishinuma and T. Kondo, J. Nucl. Mater. 191-194 (1992) 822.

[2] R.L. Klueh, "Proceedings of the IEA Working Group Meeting on Ferritic/Martensitic Steels", ORNL/M-4939 (1995).

MECHANICAL PROPERTIES AND MICROSTRUCTURE OF F-82H WELDED JOINTS USING CO_2 LASER BEAM --- N. Yamanouchi, K. Shiba [Japan Atomic Energy Research Institute (JAERI)]

OBJECTIVE

On going work is being conducted to characterize the mechanical properties of welded joints of F-82H. The joints were prepared with CO_2 laser beam to make a small specimens for the irradiation experiments.

SUMMARY

The laser welding of F-82H was successfully conducted. The heat affected zone of the welding was about 2 mm width. It was quite adequate to make small specimens, such as SS-3 type sheet tensile specimen.

INTRODUCTION

As the reduced-activation material for the first wall of fusion reactor, we have developed a 0.1C-8Cr-2W-0.2V-0.04Ta steel (referred to as F-82H hereafter) [1,2].

EXPERIMENTAL DETAILS

The ingot of F-82H was made from high purity commercial raw materials using with a vacuum induction furnace. The ingot was heated at 1523 K and rolled into a slab. The slab was rolled to 15 mm thickness plate. The plate was heat-treated as follows: normalized for 1.8 ks at 1313 K followed by tempering for 3.6 ks at 1013 K. The chemical composition of the steel are given in Table 1. The thin plates (2 mm thickness) of F-82H were machined from 15 mm thickness plate which was a factory product. The thin plate cut into 50 mm length along the rolling direction and 300 mm width.

Two plates were contacted each other without gap to make a 100 mm length and 300 mm width plate. The plates were welded by 3 kW CO_2 gas laser beam radiation moving along the seam line at 33 mm/s in Ar gas shield of which flow rate was 3.3×10^{-5} m^3/s.

After welding, stress relieving heat treatment on the weldment was conducted at 993 K for 3.6 ks. This temperature was 20 K lower than the tempering temperature of the base metal. The Vickers hardness of the cross section of the weld joint was measured with 50 g load for the as weld and the stress relieving heat treated specimens. The measured positions are shown in Fig. 1.

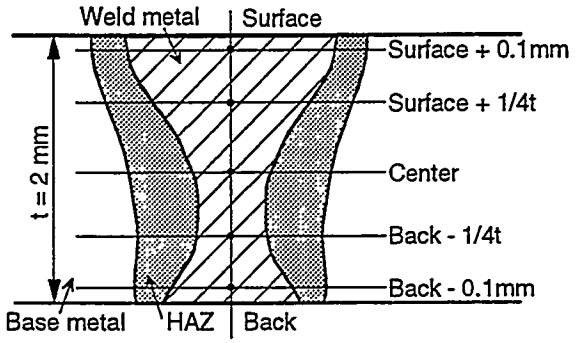

Fig. 1 The locations of the hardness measurement of the laser weld joint

Table 1 Chemical composition of F-82H

Elements (mass%)								
C	Si	Mn	P	S	Cu	Ni	Cr	Mo
0.097	0.09	0.07	0.002	0.003	-	0.030	7.46	<0.001
V	Nb	B	N	Al	Co	Ti	Ta	W
0.18	0.00007	0.0004	0.004	0.014	0.005	0.01	0.030	2.1

RESULTS

The view of the seam and the cross section of the weld joint are shown in Fig. 2 and Fig. 3, respectively. The hardness of the weld joint are plotted on Fig. 4. The maximum hardness of the weld joint were improved from Hv 473 to Hv 315 by the stress relieving heat treatment. The size of the heat affected zone was about 2 mm width. Small tensile specimens (SS-3 type sheet tensile specimen; gauge section: 7.62^{L} x 1.52^{W} x 0.76^{t} mm) were machined from the weld joint. Fig. 5 shows the cross section of the tensile specimen indicating the location of the welding.

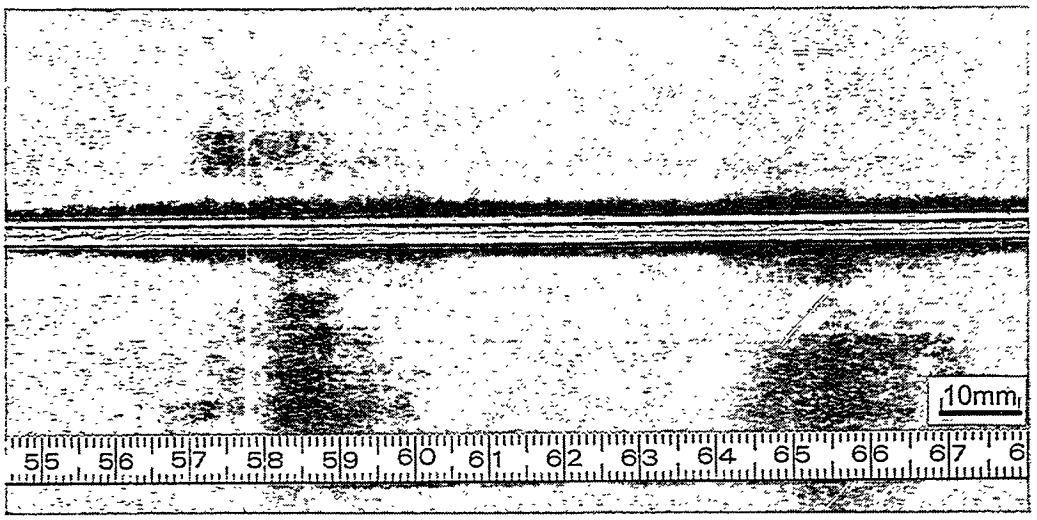

Fig. 2 The view of the seam of the weld joint

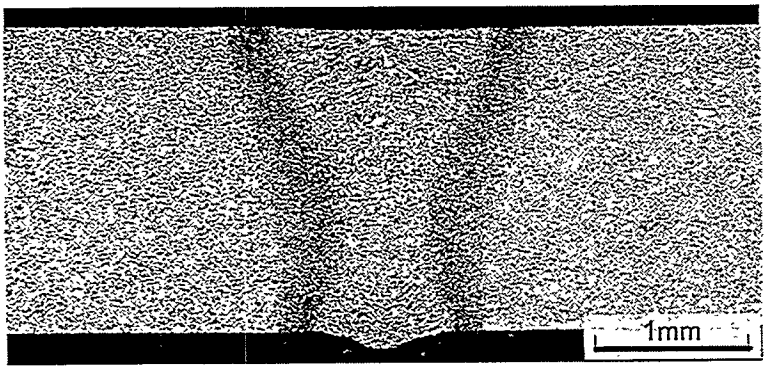

Fig. 3 The view of the cross section of the weld joint

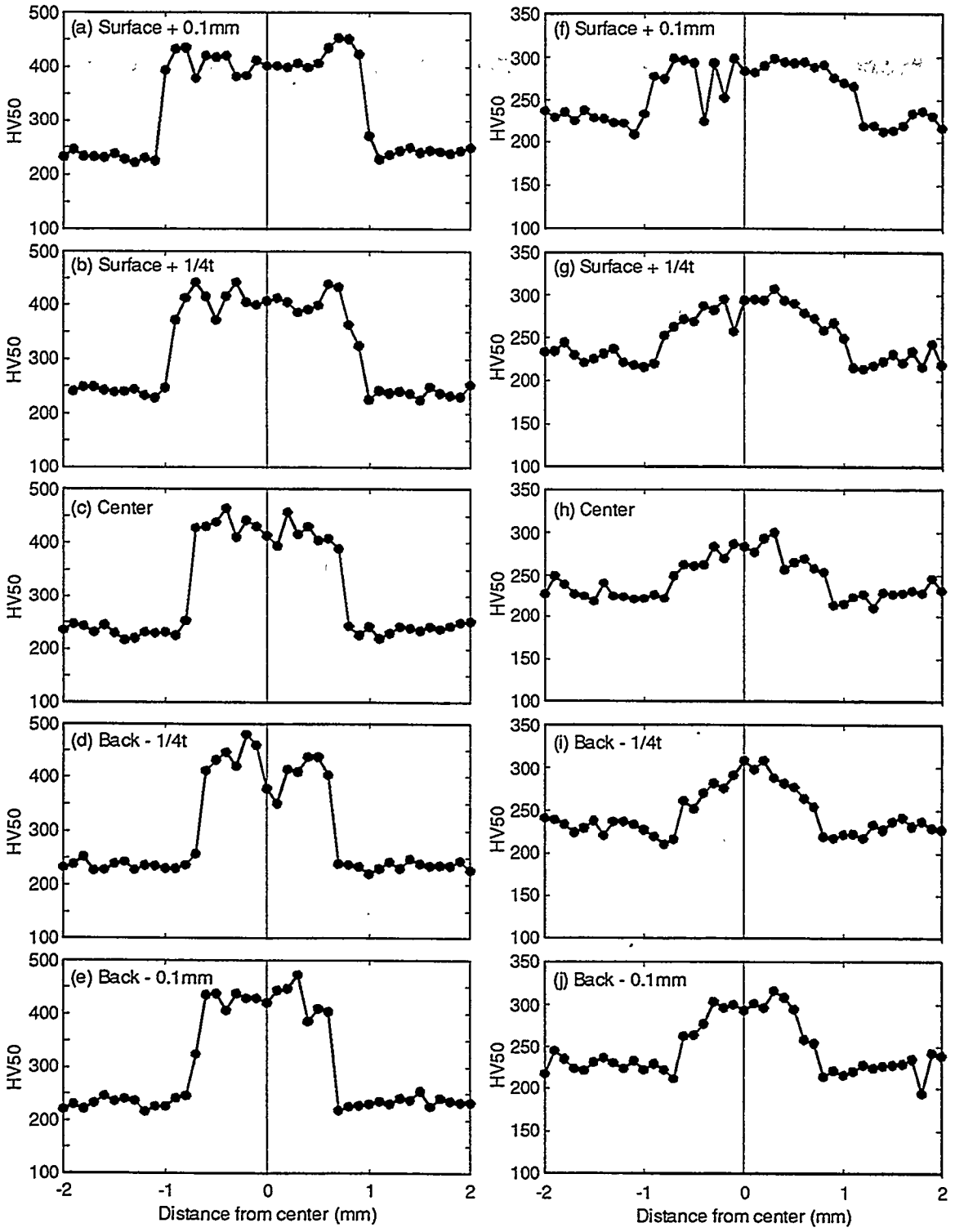

Fig. 4 Vickers hardness of the laser welded joints; (a) - (e): as weld, (f) - (j): stress relieving heat treated

CONCLUSIONS

The laser welding of F-82H was successfully conducted. The heat affected zone of welding was about 2 mm width. It was quite adequate to make small specimens.

FUTURE WORK

The measurement of the tensile properties of the weld joint using the small specimens are in progress. Ductility of the weld joints must be measured to compare with that of after irradiation using small specimens. These results will be compared with the TIG welded joints irradiated in the same conditions.

REFERENCE

[1] M. Tamura, H. Hayakawa, M. Tanimura, A. Hishinuma and T. Kondo, J. Nucl. Mater. 141-143 (1986) 1067.

[2] M. Tamura, H. Hayakawa, A. Yoshitake, A. Hishinuma and T. Kondo, J. Nucl. Mater. 155-157 (1988) 620.

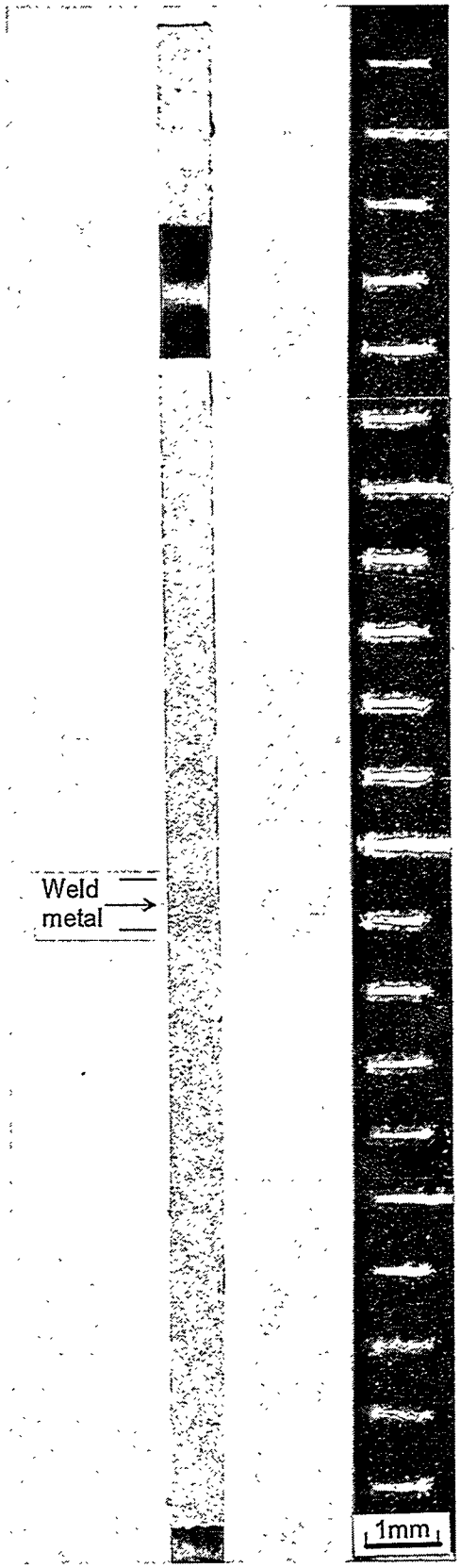

Fig.5 Cross section of the SS-3 specimen

THE CONSEQUENCES OF HELIUM PRODUCTION ON MICROSTRUCTURAL DEVELOPMENT IN ISOTOPICALLY TAILORED FERRITIC ALLOYS - D. S. Gelles (Pacific Northwest Laboratory)[a]

OBJECTIVE

The objective of this research is to assess the effect of fusion relevant He/dpa levels on microstructural development in martensitic steels for first wall applications in a fusion energy system.

SUMMARY

A series of alloys have been made adding various isotopes of nickel in order to vary the production of helium during irradiation by a two step nuclear reaction in a mixed spectrum reactor. The alloys use a base composition of Fe-12Cr with an addition of 1.5% nickel, either in the form of ^{60}Ni which produces no helium, ^{59}Ni which produces helium at a rate of about 10 appm He/dpa, or natural nickel (^{Nat}Ni) which provides an intermediate level of helium due to delayed development of^{9} Ni. Specimens were irradiated in the HFIR at Oak Ridge, TN to ≈7 dpa at 300 and 400°C. Microstructural examinations indicated that nickel additions promote precipitation in all alloys, but the effect appears to be much stronger at 400°C than at 300°C. There is sufficient dose by 7 dpa (and with 2 appm He) to initiate void swelling in ferritic/martensitic alloys. Little difference was found between response from ^{59}Ni and ^{Nat}Ni. Also, helium bubble development for high helium generation conditions appeared to be very different at 300 and 400°C. At 300°C, it appeared that high densities of bubbles formed whereas at 400°C, bubbles could not be identified, possibly because of the complexity of the microstructure, but more likely because helium accumulated at precipitate interfaces.

PROGRESS AND STATUS

Introduction

In order to better understand the effects of helium on embrittlement in ferritic/martensitic steels, an isotopic tailoring[1,2] approach has been taken, similar to that used to study this behavior in austenitic steels[3-5] but requiring irradiation in the HFIR. A series of alloys has been made adding various isotopes of nickel in order to vary the production of helium during irradiation by the two step nuclear reaction. The alloys use a base composition of Fe-12Cr with an addition of 1.5% nickel, either in the form of ^{60}Ni which produces no helium,^{59} Ni which produces helium at a rate of about 10 appm He/dpa, or natural nickel which provides an intermediate level of helium due to delayed development of ^{59}Ni. Although the experiment was first envisioned over ten years ago, specimens have only now been successfully irradiated in the HFIR at Oak Ridge, TN to 10 dpa at 300 and 400°C for examination. This paper reports on microstructural differences found between these specimens irradiated under identical conditions but with the different nickel isotopes.

Experimental Procedure

Experimental details will be published elsewhere.[6] Specimens were irradiated in HFIR-MFE-JP23.[7] The resulting fluences, taking into account specimen positions in reactor are 3.93×10^{22} and 3.14×10^{22} n/cm^2 for the 400 and 300°C conditions, respectively.[8] Table 1 includes estimates of dose and helium

---

[a]Operated for the U.S. Department of Energy by Battelle Memorial Institute under Contract DE-AC06-76RLO 1830.

accumulation based on reference 8. Note that significantly more helium is accumulated in specimens containing ^{59}Ni, less for ^{Nat}Ni and negligible amounts for ^{60}Ni and no nickel, whereas only slight further increases in dose arise in ^{59}Ni and ^{Nat}Ni containing conditions, which is not the case in alloys with higher nickel content.

Table 1. Alloy Details with Irradiation Conditions Including Irradiation Temperature, Dose in dpa and Helium Production in appm, and Compositions in Weight Percent. All Other Impurities are ≤0.01 w/o.

Codes	Heat #	Nominal	Cr	Ni	C	Other	Irradiation conditions
6A5M 6A5N	E62	Fe-12Cr	11.6	na	.002	.026O_2	300°C/6.5dpa/2He 400°C/7.3dpa/2He
715M 715N	R168	Fe-12Cr -1.5^{60}Ni	11.7	1.32	.004	.02Si .02Mn	300°C/6.4dpa/2He 400°C/7.2dpa/2He
735M 735N	R169	Fe-12Cr -1.5^{59}Ni	na	na	na	na	300°C/6.6dpa/71He 400°C/7.5dpa/77He
745M 745N	R170	Fe-12Cr 1.5^{Nat}Ni	11.5	1.54	.004	.02Si .02Mn	300°C/6.5dpa/41He 400°C/7.4dpa/46He

na: not available

Results

Microstructural damage resulting from irradiation in HFIR was only on a fine scale. Figure 1 shows low magnification examples of damage at 300 and 400°C respectively for each of the four alloys. The scale of the damage is seen as a fine background mottle. However, the mottling in specimens irradiated at 400°C is coarser than that from 300°C, and the alloy without nickel at 400°C contains mottling that is equiaxed whereas the mottling in the alloys containing nickel is non-equiaxed. Larger particles, for example those in specimen 6A5N are probably carbides, believed to have been present prior to irradiation.

As the damage is more easily understood following irradiation at the higher temperature, the microstructures formed at 400°C will first be described in greater detail. The microstructure of specimen 6A5N, Fe-12Cr, following irradiation to 7.3 dpa at 400°C and 2 appm He was found to be typical of irradiated Fe-12Cr, and contained dislocation loops, voids and precipitation typical of α', a chromium rich body centered cubic phase often formed by phase separation. An example is provided in Figure 2, comparing the same area of a specimen in $\vec{g}$=[110] contrast (a), $\vec{g}$=[002] contrast (b) and void contrast (c) for a foil near a (110) orientation. In dislocation contrast (Figures 2a and b), straight dislocations can be identified at the upper left and diagonally across the center from lower left to upper right. Also, many small black spot features can be identified representing small loops in the range 5 to 15 nm in diameter. Comparison of the two dislocation images indicates that more are present under [110] contrast, indicating the loops are generally of Burgers vector a<200>. In Figure 2c, a number of cavities can be identified, as large as 16 nm, but many as small as 3 nm. Of particular note is the row of three voids of intermediate size in the center that are connected to dislocations by comparison with the micrographs in dislocation contrast. Areas could be found without such dislocations, where only voids on the order of 3 nm were present. Also, in Figure 2c, a background mottling can be identified from α' precipitation. This microstructural response to irradiation in HFIR was similar to that found following irradiation in fast reactors at a higher dose but the scale is finer.

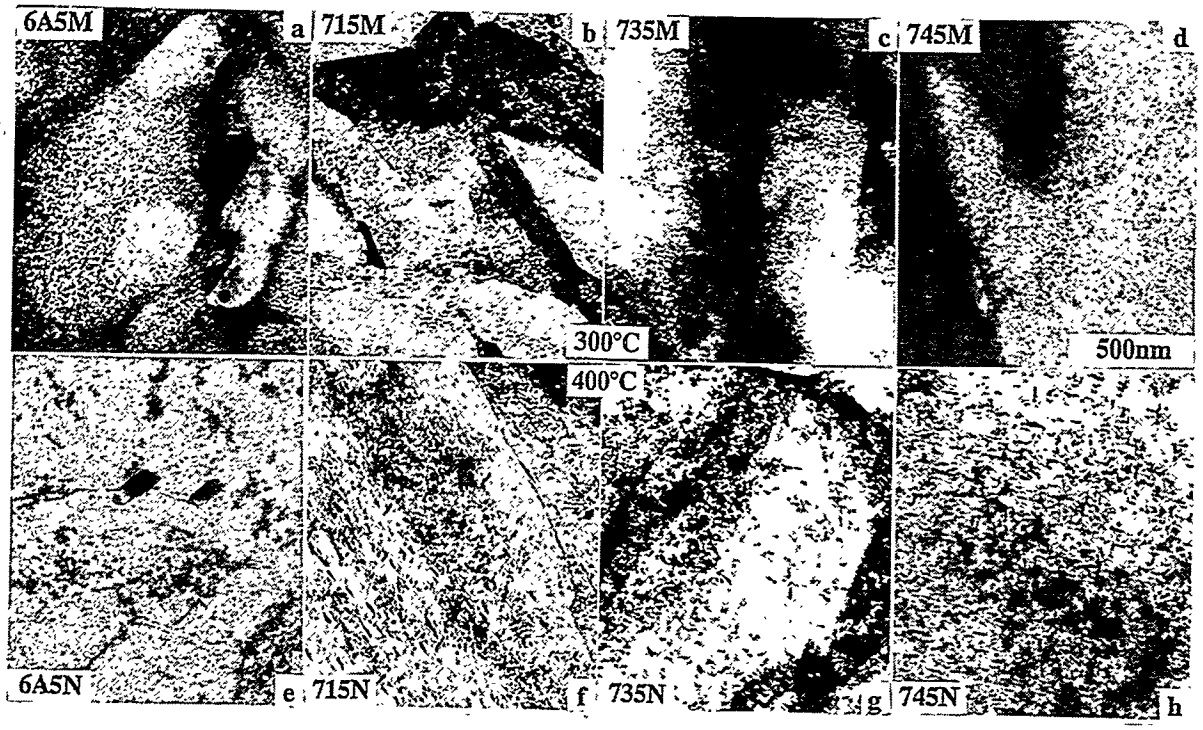

Figure 1. Microstructures in Isotopically Tailored Fe-12Cr Alloys irradiated at 300 and 400°C to 7 dpa.

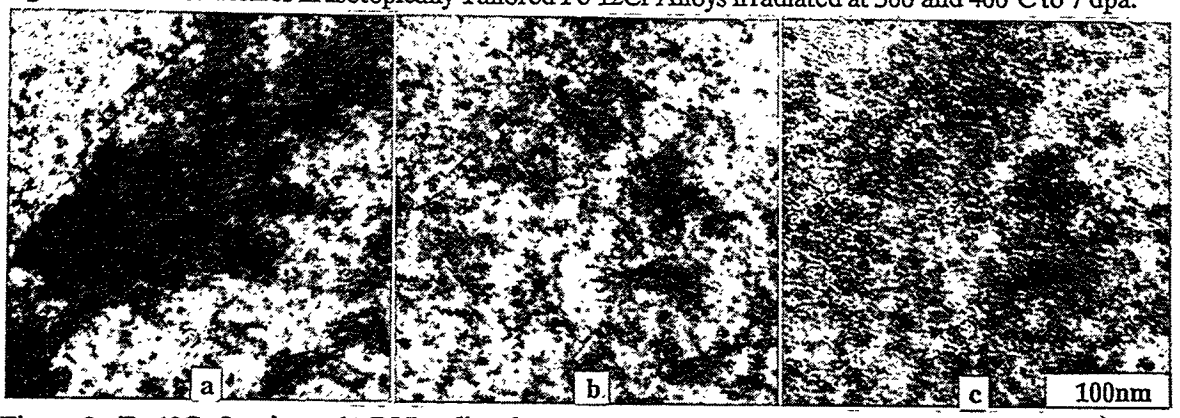

Figure 2. Fe-12Cr Specimen 6A5N Irradiated at 400°C to 7.3 dpa and 2 appm He Imaged using $\vec{g}$ = [110] ↑ in a), $\vec{g}$ = [002] → in b) and Void Contrast in c) for a Foil near ($\bar{1}$10) Orientation.

The microstructure of specimen 715N, Fe-12Cr-1.5^{60}Ni, following irradiation to 7.2 dpa at 400°C and 2 appm He was found to be similar in some ways to irradiated Fe-12Cr, and contained dislocation loops, voids and precipitation typical of α', but loop development was significantly further advanced, examples of larger voids were not found, and a rod-shaped precipitate had developed. Examples are found in Figure 3. Again, the same area of a specimen can be compared in $\vec{g}$=[110] contrast (a), $\vec{g}$=[002] contrast (b) and void contrast (c) for a foil near a ($\bar{1}$10) orientation. Many examples of loops as large as 300 nm are seen in dislocation contrast. More loops are found under [002] contrast, but several examples can be found only under [110] contrast, indicating that both a<100> and $\frac{a}{2}$<111> Burgers vectors are present. Again straight dislocation line segments are easily identified, believed to have been present prior to irradiation. Voids can be identified in Figure 3c, ranging in size from 3 to 7 nm, but none were found as large as those in specimen 6A5N. Precipitation, similar to the equiaxed phase found in 6A5N can be found but several examples of a rod shaped phase 7 nm wide and 24 nm long can be identified. Therefore major differences arising from the addition of ^{60}Ni are larger loops, smaller maximum void diameters and the presence of a rod shaped precipitate phase.

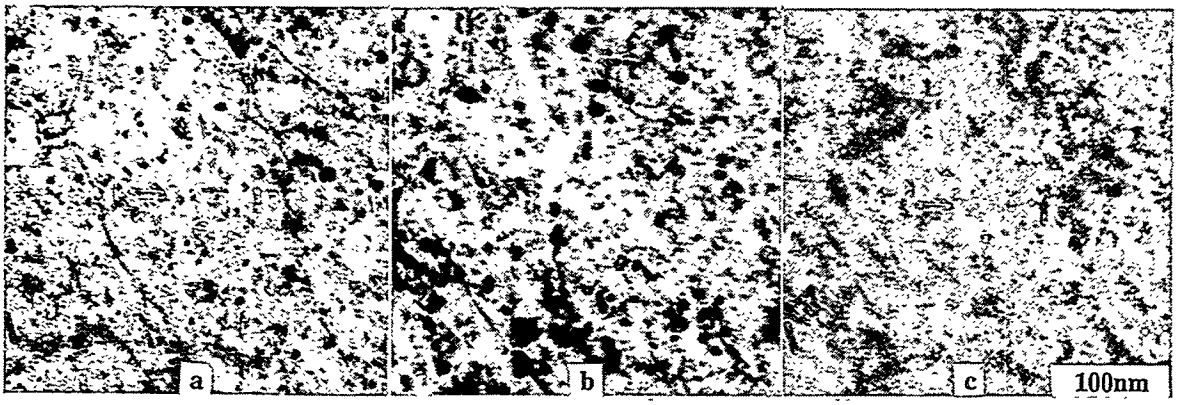

Figure 3. Fe-12Cr-1.5^{60}Ni Specimen 715N Irradiated at 400°C to 7.2 dpa and 2 appm He Imaged using $\vec{g}$ = [110] ↑ in a), $\vec{g}$ = [002] → in b) and Void Contrast in c) for a Foil near ($\bar{1}$10) Orientation.

The microstructure of specimen 735N, Fe-12Cr-1.5^{59}Ni, following irradiation to 7.5 dpa at 400°C and 77 appm He was again found to contain differences in comparison with specimens described above. The dislocation structure was similar but precipitation appeared to be more advanced and cavitation could not be identified, suggesting that it was on a much finer scale but could not been resolved. Examples are provided in Figure 4. An area is shown in $\vec{g}$=[110] contrast (a), $\vec{g}$=[002] contrast (b) and void contrast (c) for a foil near a ($\bar{1}$10) orientation. Loops 130 nm in diameter can be identified, and several short line segments are found which may be remnants of even larger loops. However, the dominant microstructural features are precipitates, in the form of rod shaped features as large as 20 nm wide and 60 nm long. The microstructure is so complex that it is difficult to see cavities, but if cavities are present, Figure 4c indicates that they must be less than 2 nm in diameter. Therefore, it appears that additions of helium to levels on the order of 80 appm result in enhanced accumulation of interstitials to dislocation loops, enhanced precipitation kinetics, and most probably a much finer distribution of helium bubbles.

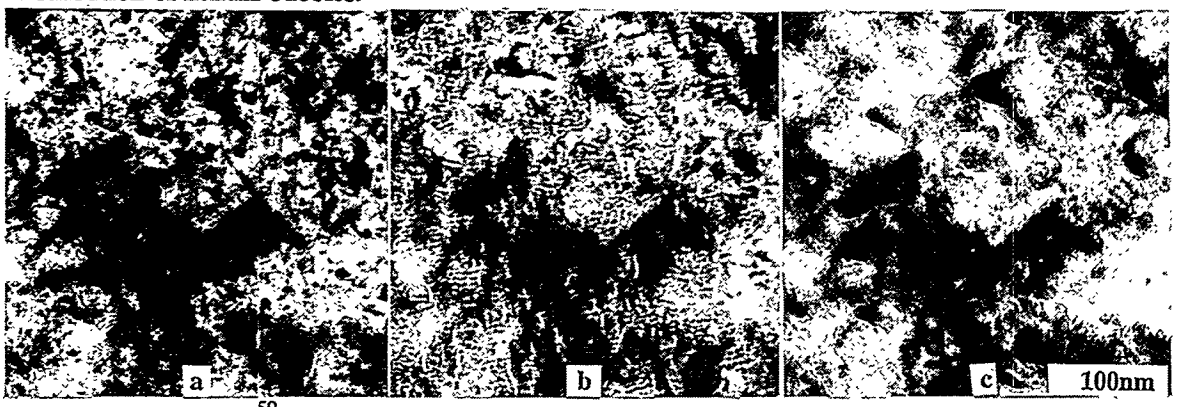

Figure 4. Fe-12Cr-1.5^{59}Ni Specimen 735N Irradiated at 400°C to 7.5 dpa and 77 appm He Imaged using $\vec{g}$ = [110] ↑ in a), $\vec{g}$ = [002] → in b) and Void Contrast in c) for a Foil near ($\bar{1}$10) Orientation.

The microstructure of specimen 745N, Fe-12Cr-1.5^{Nat}Ni, following irradiation to 7.4 dpa at 400°C and 46 appm He was found to be similar, confirming conclusions obtained based on specimen 735N. Examples of the irradiated microstructure are in Figure 5. Again, an area is shown in $\vec{g}$=[110] contrast (a), $\vec{g}$=[002] contrast (b) and void contrast (c) for a foil near a ($\bar{1}$10) orientation. Loops 200 nm in diameter can be identified, and several short line segments are found which may be remnants of larger loops. The dominant microstructural features are again precipitates, in the form of rod

shaped features as large as 15 nm wide and 50 nm long. This microstructure is also so complex that it is difficult to see cavities, but if cavities are present, they are <3 nm in diameter.

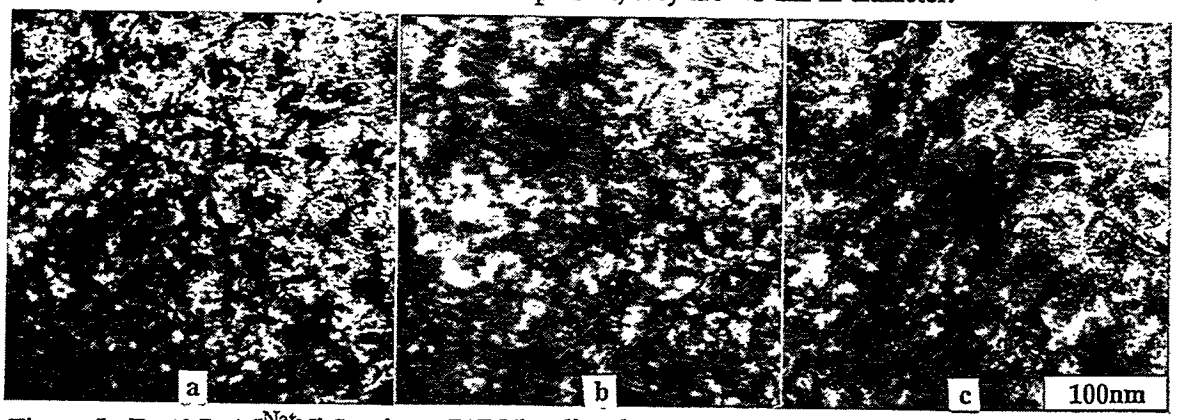

Figure 5. Fe-12Cr-1.5^{Nat}Ni Specimen 745N Irradiated at 400°C to 7.4 dpa and 46 appm He Imaged using $\vec{g}$ = [110] ↑ in a), $\vec{g}$ = [002] → in b) and Void Contrast in c) for a Foil near ($\bar{1}$10) Orientation.

In order to further emphasize that nickel additions lead to precipitation Figure 6 has been prepared showing precipitate dark field images in specimens 715N and 735N. In both cases, the precipitate dark field image was taken for an orientation near ($\bar{2}$10) for $\vec{g}\approx\frac{2}{3}$(420) and the bright field image was without further tilt. The areas chosen include larger precipitate particles located on subgrain boundaries, to emphasize that particle growth was accelerated at boundaries. Although particle sizes for these two conditions are similar based on the dark field images, the bright field images emphasize the greater complexity that appears to arise from the added helium. Certainly, it must be concluded that nickel additions to Fe-12Cr develop complex microstructures due to precipitation.

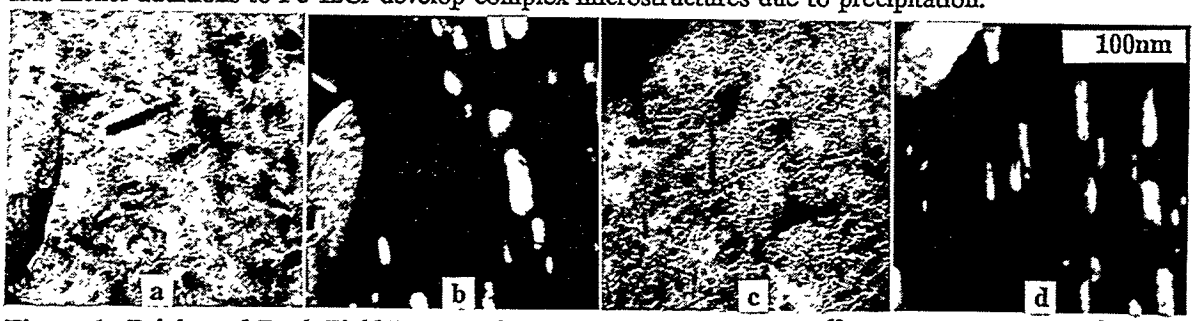

Figure 6. Bright and Dark Field Images of Precipitation in Fe-12Cr-1.5^{60}Ni specimen 715N, a) and b), and Fe-12Cr-1.5^{59}Ni specimen 735N, c) and d), irradiated at 400°C to ≈7 dpa.

The conclusions drawn based on specimens irradiated at 400°C are much more difficult to prove from specimens irradiated at 300°C. The scale of the irradiation induced microstructure was finer and precipitation due to the presence of nickel appeared to be significantly reduced. Of particular note was the fact that voids could be seen in specimens 735M and 745M, indicating voids as large as 3 nm, but at much higher density than at 400°C. Therefore, irradiation at 300°C appears to promote less precipitation than at 400°C, so that helium bubble formation can be observed in the high helium generating conditions.

Discussion

These results indicate that the addition of nickel isotopes to ferritic/martensitic steels in order to provide understanding of helium effects add the complicating factor of precipitate formation, particularly for irradiation at 400°C, in interpretation of response. If precipitation is curtailed as for irradiation at 300°C, then helium bubbles develop at very high densities. But if precipitation is

extensive as for irradiation at 400°C, bubble development appears to be restricted. Therefore, effects of helium generation on ferritic/martensitic steels can better be studied with irradiation experiments at 300°C than at 400°C when helium production is from nickel transmutation.

CONCLUSIONS

Isotopic tailoring by additions of 1.5% nickel of ^{60}Ni, ^{59}Ni, and ^{Nat}Ni to a base alloy Fe-12Cr have provided ferritic/martensitic alloys with very different helium levels following irradiation in the HFIR to ≈7 dpa at 300 and 400°C. Microstructural examinations revealed: 1) Nickel additions promote precipitation in all alloys, but the effect appears to be much stronger at 400°C than at 300°C. 2) There is sufficient dose by 7 dpa (and with 2 appm He) to initiate void swelling in ferritic/martensitic alloys. 3) Little difference was found between response from ^{59}Ni and ^{Nat}Ni. 4) Helium bubble development for high helium generation conditions appeared to be very different at 300 and 400°C. At 300°C, it appeared that high densities of bubbles formed whereas at 400°C, bubbles could not be identified, possibly because of the complexity of the microstructure, but more likely because helium accumulated at precipitate interfaces.

Future work

The present experiment was limited by the small quantities of material available for experiments, and by the limited irradiation space available in HFIR. To provide further understanding of the effect of helium generation on deformation processes, shear punch tests will be performed on available unpolished disks. Extraction replicas are also available for each irradiated condition.

Acknowledgements

Many have played a role allowing this experiment to reach fruition: to R. L. Simon, who first proposed the idea, with encouragement from G. R. Odette; to F. A. Garner who made the ^{59}Ni available for this project and encouraged in many other ways, to P. J. Maziasz who made the ^{60}Ni available and built the first HFIR irradiation experiments, to R. M. Ermi who melted the alloys, to E. M. Dieffenbacher who prepared specimens, to A. E. Ermi who organized the JP23 experiment, to J. E. Pawels, who built the JP23 experiment and distributed specimens, to A. F. Rowcliffe who fathered this experiment during its inception and to its completion, to E. M. Dieffenbacher and B. A. Walker who thinned the specimens for examinations, and finally to L. R. Greenwood who provided further understanding of the transmutation response.

REFERENCES

1 R. L. Simon, in Damage Analysis and Fundamental Studies Quarterly Progress Report October-December 1982, DOE/ER-0046/12, p. 37, 1983.
2 G. R. Odette, J. Nucl. Matl. 141-3 (1986) 1011.
3 F. A. Garner, M. L. Hamilton, R. L. Simon, and M. K. Maxon, J. Nucl. Matl. 179-81 (1991) 554.
4 M. L. Hamilton and F. A. Garner, J. Nucl. Matl. 191-4 (1992) 1239.
5 M. L. Hamilton, F. A. Garner, and D. J. Edwards, J. Nucl. Matl. 212-5 (1994) 325.
6 D. S. Gelles, submitted for publication in 18th ASTM International Symposium on Effects of Radiation on Materials.
7 A. M. Ermi and D. S. Gelles, in Fusion Materials Semiannual Progress Report for the Period Ending September 30, 1994, DOE/ER-0313/17, 35.
8 L. R. Greenwood and R. T. Ratner, to be published in Fusion Materials Semiannual Progress Report for the Period Ending June 30, 1996, DOE/ER-0313/20.

4.0 COPPER ALLOYS AND HIGH HEAT FLUX MATERIALS

TENSILE AND ELECTRICAL PROPERTIES OF UNIRRADIATED AND IRRADIATED HYCON 3HP™ CuNiBe - S.J. Zinkle and W.S. Eatherly (Oak Ridge National Laboratory)

OBJECTIVE

The objective of this report is to summarize recent tensile and electrical resistivity measurements on a commercial high-strength, high-conductivity CuNiBe alloy that is being considered for the divertor structure in ITER.

SUMMARY

The unirradiated tensile properties of two different heats of Hycon 3HP™ CuNiBe (HT Temper) have been measured over the temperature range of 20-500°C for longitudinal and long transverse orientations. The room temperature electrical conductivity has also been measured for both heats. Both heats exhibited a very good combination of strength and conductivity at room temperature. The strength remained relatively high at all test temperatures, with a yield strength of 420-520 MPa at 500°C. However, low levels of ductility (<5% uniform elongation) were observed at test temperatures above 200-250°C, due to flow localization adjacent to grain boundaries. Fission neutron irradiation to a dose of ~0.7 dpa at temperatures between 100 and 240°C produced a slight increase in strength and a significant decrease in ductility. The measured tensile elongation increased with increasing irradiation temperature, with a uniform elongation of ~3.3% observed at 240°C. The electrical conductivity decreased slightly following irradiation, due to the presence of defect clusters and Ni, Zn, Co transmutation products. The data indicate that CuNiBe alloys have irradiated tensile and electrical properties comparable or superior to CuCrZr and oxide dispersion strengthened copper at temperatures <250°C, and may be suitable for certain fusion energy structural applications.

PROGRESS AND STATUS

Introduction

High-strength, high-conductivity copper alloys are being considered for first wall heat sink and divertor structural applications in fusion energy systems such as the proposed International Thermonuclear Experimental Reactor (ITER) [1,2]. The divertor structure poses a particularly challenging operating environment, where good mechanical properties (strength, fatigue, etc.) and high thermal conductivity are required. The proposed operating temperatures for the divertor structure are ~100 to 350°C. The main radiation effects which occur in copper alloys in this temperature regime are radiation hardening (with accompanying embrittlement) and void swelling. Due to the low anticipated damage levels in the ITER divertor structure (<1 dpa), void swelling is not considered to be a design-limiting factor. However, radiation hardening becomes significant in copper alloys at damage levels as low as 0.01 dpa in this temperature range. The uniform elongation of irradiated CuCrZr and alumina-dispersion-strengthened copper (GlidCop) alloys has been found to be <0.5% after neutron irradiation to damage levels of 0.01 to 0.1 dpa at temperatures below 200°C [1-5]. The irradiated tensile elongations of these alloys generally increases above 1% for irradiation temperatures >200°C. However, the strength of these alloys decreases steadily with increasing test temperature and is typically only ~250-300 MPa at a test temperature of 300°C.

Hycon 3HP™ CuNiBe has a superior unirradiated room temperature strength and thermal stress figure of merit compared to other candidate copper alloys [1,6,7]. The room temperature yield strength and electrical conductivity of large (600-1900 kg) heats of Hycon CuNiBe has been measured to be 630-725 MPa and 68-74% IACS [6]. However, there is no known information on the elevated temperature (>200°C) properties of this alloy [1,7] and also relatively little information is available regarding the effects of neutron irradiation on the mechanical and physical properties [1,2]. Recent unpublished work by Singh and coworkers [8] on a European heat of CuNiBe suggested that the irradiated ductility was slightly better than CuCrZr and GlidCop at an irradiation temperature of ~47°C, but significantly worse than these alloys at 250-350°C.

Table 1. Chemical composition (wt.%) of the two heats of Hycon 3HP™ CuNiBe (balance copper).

Heat No.	Ni	Be	Fe	Co	Si	Al	Zn	Sn	Cr	Pb
33667	2.04	0.340	0.020	0.010	0.010	<0.010	<0.010	<0.005	<0.005	<0.003
46546	1.92	0.350	<0.010	<0.010	<0.010	<0.010	<0.010	<0.005	<0.005	<0.003

Experimental Procedure

Plates of dimensions ~15 x 15 x 2.5 cm were cut from larger plates of two different Hycon 3HP™ CuNiBe heats by Brush-Wellman and shipped to ORNL. Table 1 summarizes the chemical analysis certified by the manufacturer for these two alloy heats. Both heats were received in HT temper (cold-worked and aged) conditions. The general thermomechanical processing steps are summarized elsewhere [9,10]. Heat #46546 was aged to maximize the conductivity. The room temperature yield strength and electrical conductivity quoted by Brush-Wellman ranged from σ_y=723 MPa and σ_e=68% IACS for heat #33667 to σ_y=633 MPa and σ_e=74% IACS for heat #46546. Miniature SS-3 sheet tensile specimens with nominal gage dimensions 0.76 mm x 1.5 mm x 7.6 mm were electro-discharge machined in the longitudinal and long transverse orientations from both heats.

The tensile properties of the SS-3 sheet tensile specimens were determined at 20,100,200,300,400 and 500°C at a crosshead speed of 0.0085 mm/s, which corresponds to an initial strain rate of 1.1×10^{-3}/s in the gage region. The room temperature tests were performed in air, and the elevated temperature tests were performed in vacuum (10^{-6} to 10^{-5} torr). The specimens were held at the test temperature for 0.5 h prior to the start of each tensile test. One or two specimens were typically tested for each experimental condition. The tensile tests on the neutron irradiated samples were performed on one specimen at each of three irradiation temperatures.

The fracture surfaces of the unirradiated broken tensile specimens were examined using a Hitachi 4100 scanning electron microscope (SEM) equipped with a field emission gun. The detailed microstructure of the unirradiated alloys was examined using a Philips CM12 transmission electron microscope (TEM) operating at 120 kV. TEM specimens cut from as-supplied material and deformed gage regions of selected broken tensile specimens were prepared in a Tenupol jetpolishing apparatus with a solution of 90% orthophosphoric acid in water, cooled to ~0°C.

Four-point probe electrical resistivity measurements were performed following the general recommendations summarized in ASTM Standard Method of Test for Resistivity of Electrical Conductor Materials, ASTM B193-87 (reapproved 1992). Measurements were made on SS-3 sheet tensile specimens at room temperature prior to tensile testing, with a distance between the spring-loaded voltage contacts of 7.10 mm. The temperature was recorded for each measurement and the resistivity data were corrected to a reference temperature of 20°C using the copper temperature coefficient for resistivity of $d\rho/dT = 6.7 \times 10^{-11}$ Ω-m/K. The typical measured resistance drop was ΔR~150 μΩ (ASTM B193-87 recommends ΔR>10 μΩ). The 100 mA current was supplied by a Keithley 237 Source Measure Unit, and the voltage drop was measured with a Keithley 182 Sensitive Digital Voltmeter equipped with a low thermal connector cable (resolution limit of 1 nV). Thermal emf offset potentials were subtracted using the "relative reading" offset function on the Keithley 182. Ohmic behavior was verified on several specimens by varying the applied current between 10 and 100 mA and measuring the corresponding voltage drop. The typical scatter in the data due to thermal drift was ± 40 nV. The main source of experimental error was associated with uncertainties in the cross-sectional area of the specimen. The specimen thickness and width were measured to a nominal accuracy of ± 1 μm in two different gage locations with a Mitotoyo precision digital micrometer in order to convert the resistance measurements to resistivity values. Nonuniformities in the width and thickness in the specimen gage region caused the typical experimental uncertainty of individual resistivity measurements to be ±0.5%. A minimum of two different unirradiated specimens were tested for each experimental condition, whereas only one specimen was available for each of the three irradiation temperatures.

Three longitudinal SS-3 tensile specimens machined from heat #46546 were irradiated for 545 h in a core thimble position of the High Flux Beam Reactor (HFBR) at Brookhaven National Laboratory as part of the V1 and V2 irradiation capsules [11]. The irradiation produced to a fast (E>0.1 MeV) neutron fluence of $8.3x10^{24}$ n/m^2, which corresponds to a damage level of ~0.7 dpa in copper. The thermal neutron fluence was ~$3x10^{24}$ n/m^2, which is calculated to produce ~0.06 at% Ni and Zn from transmutation reactions with the copper matrix (ignoring additional solute production from resonance and fast neutron reactions). The specimens were contained in three gas-gapped subcapsules which operated at irradiation temperatures of 110, 205 and 240°C. The irradiation temperature was continuously monitored by thermocouples in each subcapsule. Further details regarding the irradiation conditions are given elsewhere [11]. Following irradiation, room temperature Vickers microhardness measurements were performed in the grip region of the specimens and the room temperature electrical resistivity was measured. The specimens were then tensile tested at the irradiation temperature.

Results

The room temperature (20°C) electrical resistivity of Hycon 3HP™ heat #33667 was measured to be 26.27 ±0.11 nΩ-m (65.6% IACS). The corresponding resistivity of heat #46546 was 24.05 ±0.06 nΩ-m (71.7% IACS). No significant orientation dependence was observed for the transverse and longitudinal directions in either heat. The measured conductivities were slightly lower than the values reported by Brush-Wellman of 68% IACS for heat #33667 and 74% IACS for heat #46546.

Figures 1 and 2 summarize the temperature-dependent tensile properties measured for the longitudinal and transverse orientations of both heats of Hycon 3HP™ CuNiBe. The measured yield strengths at room temperature were in good agreement with the values obtained by Brush-Wellman for both heats. The transverse and longitudinal tensile properties were identical for the lower-strength heat (#46546). On the other hand, the yield and ultimate strengths were typically about 40 MPa higher in the longitudinal orientation compared to the long transverse orientation at temperatures above room temperature for heat #33667. Both heats showed very good retention of their strength up to a test temperature of 500°C. For example, the yield strength of heat 33667 in the longitudinal orientation was ~710 MPa at 200°C, ~590 MPa at 400°C and ~510 MPa at 500°C. These strengths are much higher than that obtainable with as-wrought GlidCop Al25 oxide dispersion strengthened copper (335 MPa at 200°C and 256 MPa at 400°C) [1].

The ductility of both Hycon 3HP™ heats decreased rapidly with increasing test temperature. The ductility at room temperature was good (e_u~6 to 9%, e_{tot}~10 to 14%), but the total elongation of both heats dropped to ~4 to 5% at 300°C. The uniform elongation of both heats was only about 1% at 400°C, and was only about 0.5% at 500°C. The total elongation decreased to similar values at both of these temperatures. All of the specimens at 400 and 500°C failed at the maximum load, without any macroscopic necking (although there was some work hardening prior to failure). The shape of the elevated temperature stress-strain curves suggested that the poor ductility may be associated with flow localization (similar to the tensile behavior of copper alloys irradiated at low temperatures).

The fracture surfaces of several specimens were examined with scanning electron microscopy in order to investigate the cause of the poor ductility at elevated temperatures. Figure 3 compares the fracture surfaces of specimens tensile tested at room temperature and 500°C. The room temperature failure mode was ductile transgranular fracture, whereas the failure mode at 400 and 500°C was ductile intergranular fracture. The fracture surface of a specimen tensile tested at 300°C exhibited predominantly dimpled transgranular fracture, with ~25% of the fracture surface showing ductile intergranular fracture. As evident in Fig. 3, the fracture surfaces at 500°C and room temperature appeared identical at high magnification (typical dimple size of a few microns), even though the deformation mode changes from intergranular to transgranular. This suggests that the loss of macroscopic ductility at elevated temperatures is due to localized deformation at the grain boundaries, due to their relatively weak strength compared to the grain interior.

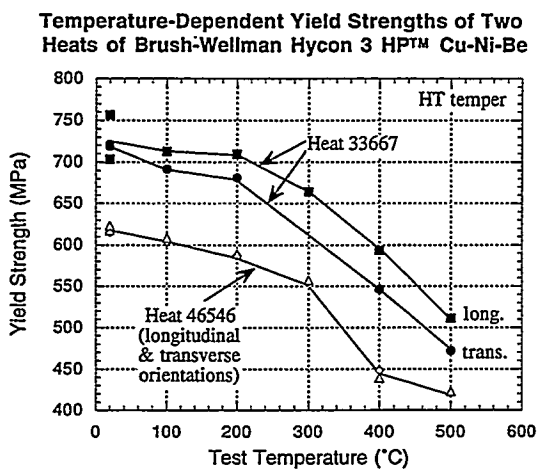

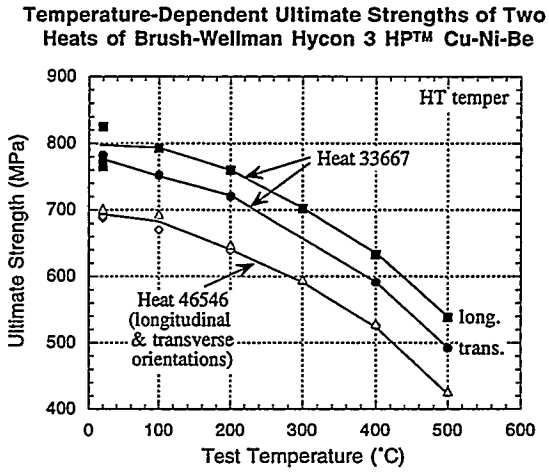

Fig. 1. Summary of the temperature-dependent yield and ultimate strengths of two different heats of Hycon 3HP™ CuNiBe (HT temper).

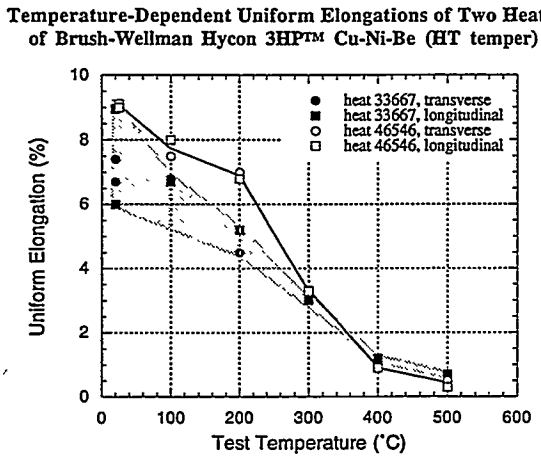

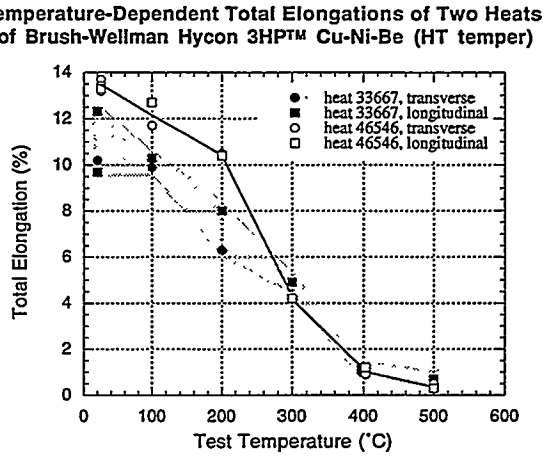

Fig. 2. Summary of the temperature-dependent uniform and total elongations of two different heats of Hycon 3HP™ CuNiBe (HT temper).

ORNL-PHOTO 4119-96

FRACTURE SURFACES OF HYCON 3HP™ CuNiBe
FOLLOWING TENSILE TESTING AT 20 AND 500°C

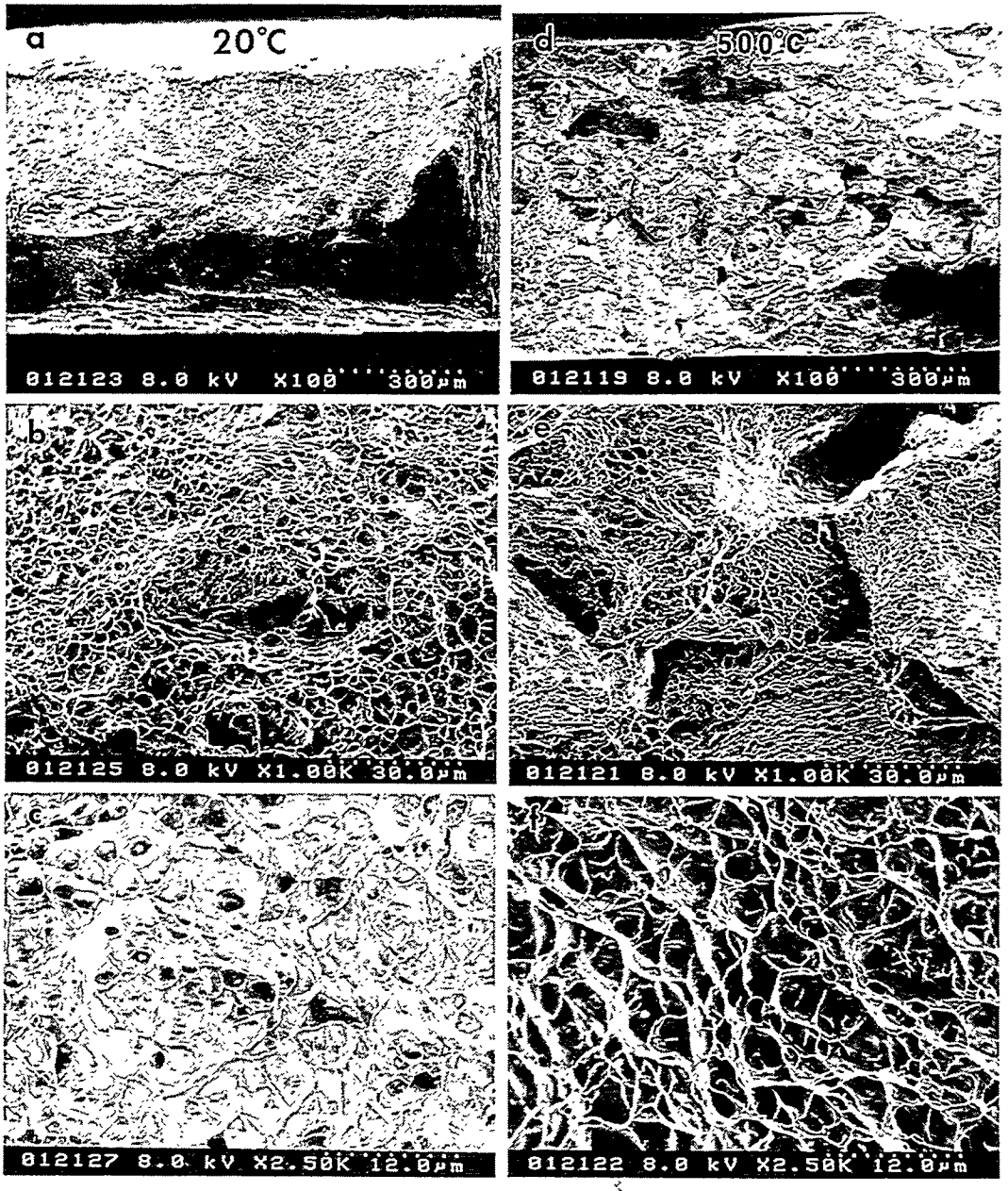

Fig. 3. Fracture surfaces of unirradiated Hycon 3HP™ CuNiBe heat #46546 (longitudinal orientation) following tensile testing at room temperature (a-c) and 500°C (d-f).

A preliminary analysis of the Hycon 3HP™ CuNiBe microstructure by transmission electron microscopy revealed the presence of three types of precipitates. As shown in Fig. 4, a low density (~1 to 5 x $10^{17}/m^3$) of large precipitates with a typical diameter of 1 to 5 μm were visible at low magnifications. These large particles were present in both nondeformed and tensile-tested specimens, and are likely sites for microvoid initiation during the tensile testing. Previous work by Guha [12] identified these large particles as an intermetallic beryllide with a cubic B2 structure and a lattice parameter of 0.279 nm. The second type of precipitate was located along grain boundaries, and had a typical size of ~50 nm. Several of these grain boundary precipitates are arrowed in Fig. 5. These precipitates were reported to be Ni-rich by Spitznagel et al. [13]. The third type of precipitate occurred uniformly throughout the matrix (Figs. 5 and 6), and is responsible for the high strength of this alloy. Initial measurements indicate that these semicoherent precipitates have a typical diameter of 15-20 nm and a number density of nearly $1x10^{24}/m^3$. Previous studies on CuNiBe alloys have identified these semicoherent precipitates as either GP zones [13] or a mixture of GP zones and γ″ phase [12]. In the present study, electron diffraction patterns showed streaks along <001> directions which were bunched into intensity maxima at ±2/3(002) positions. According to the Cu-Be precipitation sequence reviewed by Rioja and Laughlin [14], this indicates that these matrix precipitates are predominantly γ″ phase.

A small (~20 nm width) precipitate-free zone was observed near the grain boundaries in nondeformed and tensile-tested specimens. The width of the precipitate-free zone did not increase following tensile testing at 500°C, where low macroscopic ductility was observed in the tensile tests. Figure 7 shows an example of the microstructure of the deformed gage region of a tensile specimens tested at 500°C. A twin boundary is imaged in this micrograph, and the zone axis is near [110] in both grains.

Tables 2 and 3 summarize the electrical resistivity, Vickers microhardness, and tensile data obtained on the three SS3 tensile specimens of CuNiBe heat #46546 (longitudinal orientation) following HFBR neutron irradiation to ~0.7 dpa. The Vickers microhardness measurements were performed at room temperature at a load of 1 kg and had a standard error of ±1 VHN. The tensile measurements were obtained at a test temperature close to the irradiation temperature. Irradiation at 110°C produced a modest (~5%) increase in the Vickers hardness and ultimate tensile strength of the alloy. The corresponding increase in yield strength and electrical resistivity was ~15%. A pronounced reduction in uniform elongation occurred for this irradiation temperature. The increment of radiation hardening decreased with increasing irradiation temperature, and amounted to only about a 1% increase in hardness and ultimate tensile strength at 240°C. This produced a corresponding increase in the tensile ductility with increasing irradiation temperature. Figure 8 shows the tensile load-elongation curves for specimens irradiated at 110 and 240°C.

The observed increase in electrical resistivity of the 3 specimens following neutron irradiation is in accordance with the expected changes associated with solute transmutation (predominantly Ni, Zn and Co) and defect cluster formation [1,2,4]. The defect cluster density decreases with increasing irradiation temperature above ~150°C, due to thermal annealing of the vacancy clusters produced in the displacement cascades [1,2]. This factor along with increased solute segregation at the higher irradiation temperatures are likely explanations for the observed decrease in electrical resistivity with increasing irradiation temperature. Similar temperature-dependent effects have been observed in neutron-irradiated CuCrZr and GlidCop AL25 alloys 1,2,4].

ORNL-PHOTO 4121-96

LARGE PRECIPITATES IN HYCON 3HP™ CuNiBe

Fig. 4. Low magnification microstructure of Hycon 3HP™ CuNiBe heat #46546 showing large precipitates in the matrix.

ORNL-PHOTO 4122-96

PRECIPITATE FORMATION ADJACENT TO A GRAIN BOUNDARY IN HYCON 3HP™ CuNiBe

Fig. 5. Matrix and grain boundary precipitates in CuNiBe heat #46546.

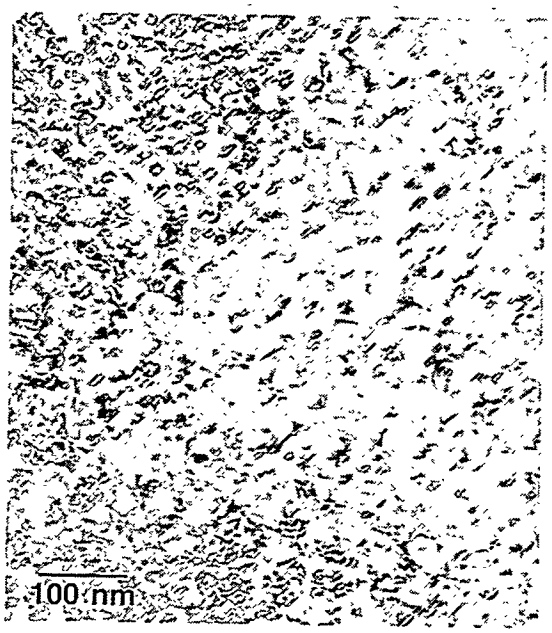

Fig. 6. Semicoherent γ″ matrix precipitates in CuNiBe heat #46546.

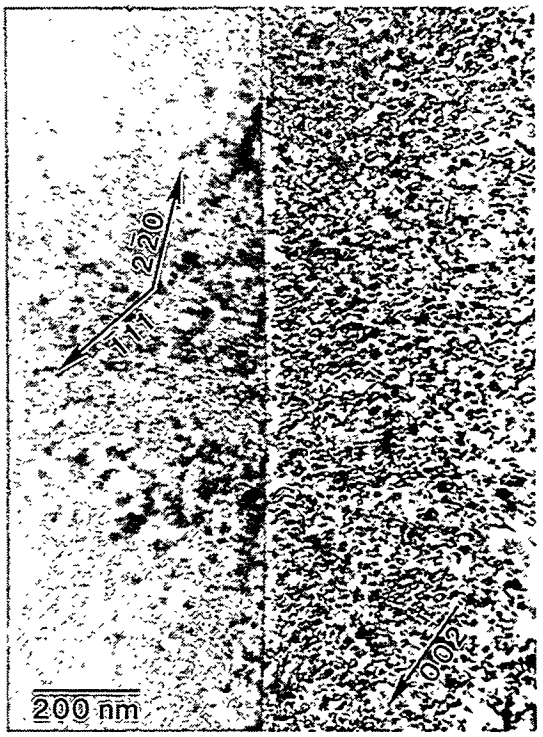

Fig. 7. Microstructure of the deformed gage region of CuNiBe heat #46546 (longitudinal orientation) following tensile testing at 500°C.

Table 2. Summary of electrical resistivity measurements on CuNiBe Hycon 3HP™ heat number 46546, longitudinal orientation.

Sample	Condition	$\rho_{20°C}$ (nΩ-m)	$\Delta\rho$ (nΩ-m)	% IACS*	$\Delta\rho/\rho_0$ (%)
CV31,34,18	unirradiated	24.05	—	71.7	—
CV03	110°C, 0.7 dpa	27.71	3.66	62.2	15
CV01	207°C, 0.7 dpa	26.61	2.56	64.8	11
CV02	237°C, 0.7 dpa	25.48	1.43	67.7	6

*100% IACS = 17.241 nΩ-m

Table 3. Summary of Vickers hardness and tensile measurements on CuNiBe heat #46546, longitudinal orientation.

Irr. Temp.	Vickers hardness	σ_Y (MPa)	σ_{UTS} (MPa)	ε_u (%)	ε_{tot} (%)
unirr.	218.5	see Fig. 1	see Fig. 1	see Fig. 2	see Fig. 2
110°C	233.0	700	712	0.67	6.5
207°C	229.0	645	668	0.90	6.7
237°C	219.9	595	633	3.3	6.1

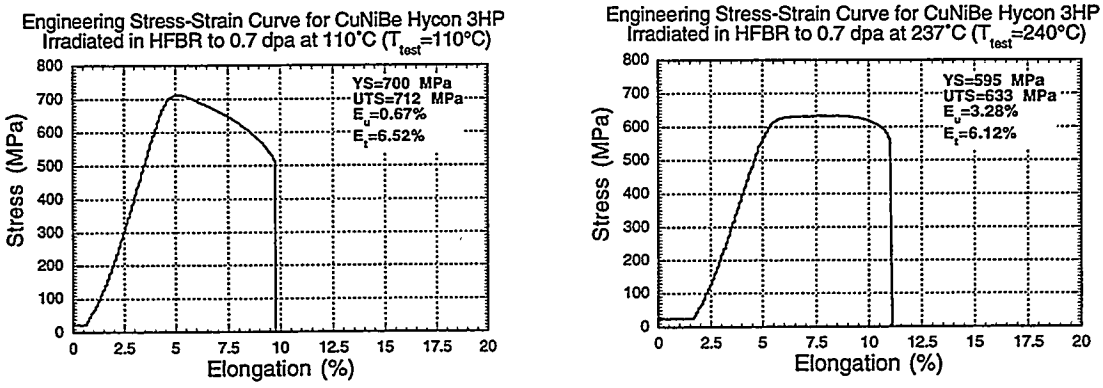

Fig. 8. Load-elongation curves for CuNiBe (heat #46546) longitudinal tensile specimens irradiated at 110 and 240°C.

Discussion

One useful parameter for evaluating the suitability of a material for high-heat flux structural applications is the thermal stress figure of merit, $M=\sigma_y k_{th}(1-\nu)/\alpha E$. This parameter can be calculated for the two Hycon 3HP™ CuNiBe heats from the present data by assuming that the temperature-dependent pure copper values [1] for Young's modulus (E), Poisson's ratio (ν) and the coefficient of thermal expansion (α) are also valid for the alloy, and by utilizing the Wiedemann-Franz relation to convert the electrical conductivity measurements to thermal conductivity (k_{th}). The calculated values at room temperature are M=60 and 57 kW/m for heats 33667 and 46546 (longitudinal orientations), respectively. These values are significantly higher than the thermal stress figure of merit of other high-strength, high-conductivity copper alloys. For example, the calculated room temperature values for as-wrought GlidCop AL25 dispersion strengthened copper and cast & aged CuCrZr are M=39 and 37, respectively. The calculated thermal stress figure of merit decreases with increasing temperature for all of the copper alloys, mainly due to the decrease in yield strength (and also minor decreases in thermal conductivity and an increase in the Poisson's ratio which are partially balanced by a decrease in Young's modulus). The values at 500°C are M=36 and 34 kW/m for CuNiBe heat #s 33667 and 46546, respectively. These values are about a factor of two larger than the calculated values at 500°C for GlidCop Al25 and CuCrZr of M=14 and 18 kW/m, respectively.

The main disadvantage associated with CuNiBe alloys is poor ductility at elevated temperatures. The observed change in deformation mode from transgranular to intergranular failure with increasing test temperature is a common feature in FCC metals [15]. However, the physical mechanism responsible for the dramatic decrease in uniform elongation with increasing test temperature up to 500°C is not readily apparent from the TEM studies performed to date. Further work is needed to identify the cause of the low ductility in these two alloy heats at test temperatures above ~300°C. It is worth noting that higher elongations (e.g., 5% at 500°C) have been obtained in an AT temper of this alloy [16].

The observed radiation hardening and decrease in tensile elongation in the three CuNiBe specimens irradiated at 110-240°C is qualitatively similar to the behavior observed in other high-strength, high-conductivity copper alloys [1-5,8]. It is worth noting that the reported uniform elongations of GlidCop Al25 and CuCrZr specimens irradiated in this temperature range are generally lower than the CuNiBe values. Figure 9 compiles the unirradiated and irradiated tensile data on Hycon 3HP™ CuNiBe (heat #46546) obtained at Risø [8] and ORNL. The data indicate that the radiation hardening component decreases with increasing irradiation temperature, and becomes negligible at temperatures above 250-300°C. The elongation data indicate that radiation hardening at ~100°C induces severe embrittlement (ε_u<1%), and that the tensile elongation increases rapidly between irradiation temperatures of 200 and ~250°C. The irradiation datum obtained at 350°C suggests that the low ductility observed in CuNiBe at high temperatures prior to irradiation is maintained (or perhaps slightly more pronounced) following high temperature irradiation.

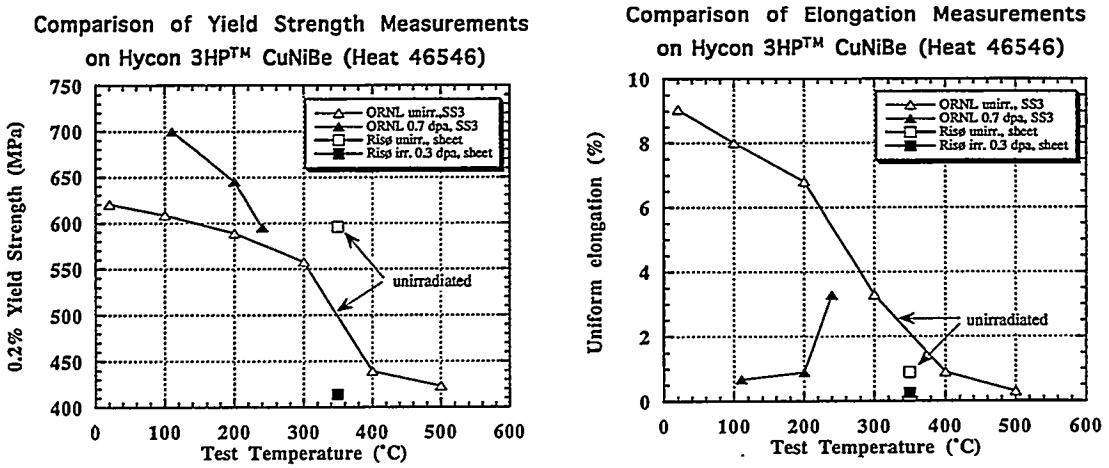

Fig. 9. Yield strength and elongation vs. temperature for unirradiated and irradiated Hycon 3HP™ CuNiBe.

Acknowledgements

The two Hycon 3HP™ alloy heats for this study were supplied by David Krus, Brush-Wellman Inc. The authors thank L.L. Snead for experimental assistance with the HFBR neutron irradiation, and J.E. Pawel-Robertson for assistance with the irradiated tensile data acquisition.

References

1. S.J. Zinkle and S.A. Fabritsiev, Nuclear Fusion (Atomic and Plasma-Material Interaction Data for Fusion supplement) 5 (1994) 163-192; also Fusion Materials Semiann. Prog. Report for period ending March 31, 1994, DOE/ER-0313/16, pp. 314-341.

2. S.A. Fabritsiev, S.J. Zinkle and B.N. Singh, "Evaluation of Copper Alloys for Fusion Reactor Divertor and First Wall Components," 7th Intern. Conf. on Fusion Reactor Materials, Obninsk, Russia, Sept. 1995, proceedings to be published in J. Nucl. Mater.

3. S.A. Fabritsiev, A.S. Pokrovsky, S.J. Zinkle and D.J. Edwards, "Low Temperature Embrittlement of Copper Alloys," 7th Intern. Conf. on Fusion Reactor Materials, Obninsk, Russia, proceedings to be published in J. Nucl. Mater.

4. S.A. Fabritsiev, A.S. Pokrovsky, S.J. Zinkle, A.F. Rowcliffe, D.J. Edwards, F.A. Garner, V.A. Sandakov, B.N. Singh and V.R. Barabash, "The Effect of Neutron Spectrum on The Mechanical and Physical Properties of Pure Copper and Copper Alloys," 7th Intern. Conf. on Fusion Reactor Materials, Obninsk, Russia, proceedings to be published in J. Nucl. Mater.

5. B.N. Singh, D.J. Edwards, A. Horsewell and P. Toft, Risø-R-839 (EN) Sept. 1995.

6. H.A. Murray, I.J. Zatz and J.O. Ratka, in Cyclic Deformation, Fracture, and Nondestructive Evaluation of Advanced Materials, 2nd Vol., ASTM STP 1184, M.R. Mitchell and O. Buck, eds. (ASTM, Philadelphia, 1994) pp. 109-133.

7. J.O. Ratka and W.D. Spiegelberg, IEEE Trans. Mag. 30, No. 4 (July 1994) 1859.

8. B.N. Singh, Risø National Laboratory, viewgraphs presented at ITER Working Group Meetings on Irradiation Testing of In-Vessel Structural Materials and Components (Gatlinburg, Tennessee, Nov. 5-10,1995) and Materials and Joints for In-Vessel Components (Garching, Germany, May 13-16, 1996).

9. H. Murray, I.D. Harris and J.O. Ratka, Proc. 14th IEEE/NPSS Symp. on Fusion Engineering (1991) p. 272; H. Murray, ibid. p. 280.

10. J.C. Harkness, W.D. Spiegelberg and W.R. Cribb, Metals Handbook, 10th Ed., Vol. 2 (ASM International, 1990) p. 403.

11. D.J. Alexander, L.L. Snead, S.J. Zinkle, A.N. Gubbi, A.F. Rowcliffe and E.E. Bloom, "Effects of Irradiation at Low Temperature on V-4Cr-4Ti," in Fusion Materials Semiann. Prog. Report for period ending June 30, 1996, DOE/ER-0313/20, this report.

12. A. Guha, in High Conductivity Copper and Aluminum Alloys, eds. E. Ling and P.W. Taubenblat (TMS/AIME, Warrendale, PA, 1984) p. 133.

13. J.A. Spitznagel et al., Nucl. Instr. Meth. B 16 (1986) 279.

14. R.J. Rioja and D.E. Laughlin, Acta Metall. 28 (1980) 1301.

15. H.W. Hayden, W.G. Moffatt and J. Wulff, The Structure and Properties of Materials, Vol. III: Mechanical Behavior (Wiley & Sons, New York, 1965), p. 122.

FRACTURE TOUGHNESS OF OXIDE-DISPERSION STRENGTHENED COPPER -
D. J. Alexander, Oak Ridge National Laboratory

OBJECTIVE

The fracture toughness of an oxide-dispersion strengthened copper alloy was examined to determine the suitability of such alloys as candidate materials for first wall and divertor structural applications for ITER.

SUMMARY

The fracture toughness of an oxide-dispersion strengthened copper alloy AL-15 has been examined at room temperature and 250°C, in air and in vacuum (< 10^{-6} torr). Increasing test temperature causes a significant decrease in the fracture toughness of this material, in either air or vacuum environments. In addition, specimens oriented in the T-L orientation (crack growth parallel to the extrusion direction) show significantly lower toughness than those in the L-T orientation (crack growth perpendicular to the extrusion direction).

PROGRESS AND STATUS

Introduction

High-strength copper alloys with high thermal conductivity are attractive candidates for some structural applications in ITER. One type of copper alloys are dispersion-strengthened by internal oxidation. An early version of this alloy, called GLIDCOP AL-15, contains 0.15 wt % Al that has been internally oxidized to produce small Al_2O_3 particles in a copper matrix. Testing of unirradiated material was conducted to determine the fracture toughness as a function of test temperature and specimen orientation. Preliminary testing [1] had shown that the toughness of the AL-15 material decreased significantly as the test temperature increased from 22 to 250°C, although the tensile properties showed only a slight change over the same temperature range [2]. This suggested that an environmental effect might be responsible for the decrease in toughness at higher temperatures. Therefore, tests were carried out in vacuum to determine whether this could mitigate the decrease in toughness observed at higher temperatures.

Experimental Procedure

Specimens of the AL-15 material were fabricated from an as-wrought plate measuring 165 mm wide by 12.7 mm thick by approximately 3 m long that was produced by SCM Metals for the ORNL Fusion Energy Division in 1987 [3]. This plate had been warm worked during the consolidation of the -20 mesh powder. The plate was then extruded at about 820°C with an extrusion ratio of 25:1. Specimens were oriented in the T-L orientation so that crack growth was in the extrusion direction, or in the L-T orientation for crack growth perpendicular to the extrusion direction.

Small disk compact specimens 12.5 mm in diameter by 4.62 mm thick (0.492 by 0.182 in.) [designated 0.18 T DC(T) specimens] were fabricated from the middle of the plate thickness. All specimens were fatigue precracked at room temperature and then side grooved 10% of their thickness on each side prior to testing. Testing was conducted on an 89-kN (20-kip) capacity servohydraulic test machine in

laboratory air, or on a 223-kN (50-kip) servohydraulic machine equipped with a vacuum chamber. The vacuum tests were conducted with a vacuum of better than 10^{-6} torr. A thermocouple was spotwelded to the specimen to monitor the temperature during each test. Testing was conducted in general accordance with ASTM E 813-89, Standard Test Method for J_{Ic}, A Measure of Fracture Toughness, and ASTM E 1152-87, Standard Test Method for Determining J-R Curves, using a computer-controlled data acquisition and analysis system operating in strain control. The J-integral equations from E 1152-87 were used for the calculations. Tensile properties used in the analyses were taken from the literature [2].

Crack growth was monitored by the unloading compliance technique for all tests. An outboard clip gage was used that seated in grooves machined on the outer diameter of the disk, above and below the loading holes. The experimental techniques developed for testing the small DC(T) specimens have been described elsewhere [4].

To mark the extent of crack growth for some of the preliminary testing the specimens were heat tinted by placing them on a hot plate and heating them until a noticeable color change had occurred. The specimens were cooled to room temperature and then broken open to allow the initial and final crack lengths to be measured. Later tests used fatigue crack extension at room temperature after the tests were completed to mark the final crack front. The crack lengths were measured from the fracture surfaces with a measuring microscope.

Results and Discussion

The results of the fracture toughness testing are shown in Fig. 1 and are summarized in Table 1. The fracture toughness decreased markedly as the test temperature increased, as Fig. 1 shows. The toughness was also quite different depending on the specimen orientation, with specimens from the L-T orientation being much tougher than the T-L specimens. The toughness was only slightly improved by testing in vacuum, and the increase in test temperature from 25 to 250°C caused a significant decrease in the fracture toughness in either air or vacuum.

The significant decrease in the toughness as the test temperature increases is a surprising response, as there is no indication of a significant change in the tensile properties over this same range of temperatures [2]. These results are similar to data for the AL-25 alloy [5], a more recent variant of oxide-dispersion strengthened copper which has 0.25 wt % Al. Interestingly, impact tests of notched specimens of AL-25 [5] do not show a decrease in absorbed energy over a similar range of test temperatures. The fact that the toughness is degraded in the quasistatic fracture toughness test but not under dynamic conditions suggests that an environmental effect such as oxygen embrittlement of grain boundaries may be responsible for the drop in toughness at higher temperature. It was thought that the fracture toughness may not be so impaired in a vacuum environment. However, although there is a slight improvement in the toughness at 250°C under vacuum conditions as compared to air, the toughness is still much lower than one would expect on the basis of the small changes in the tensile properties over the same temperature range.

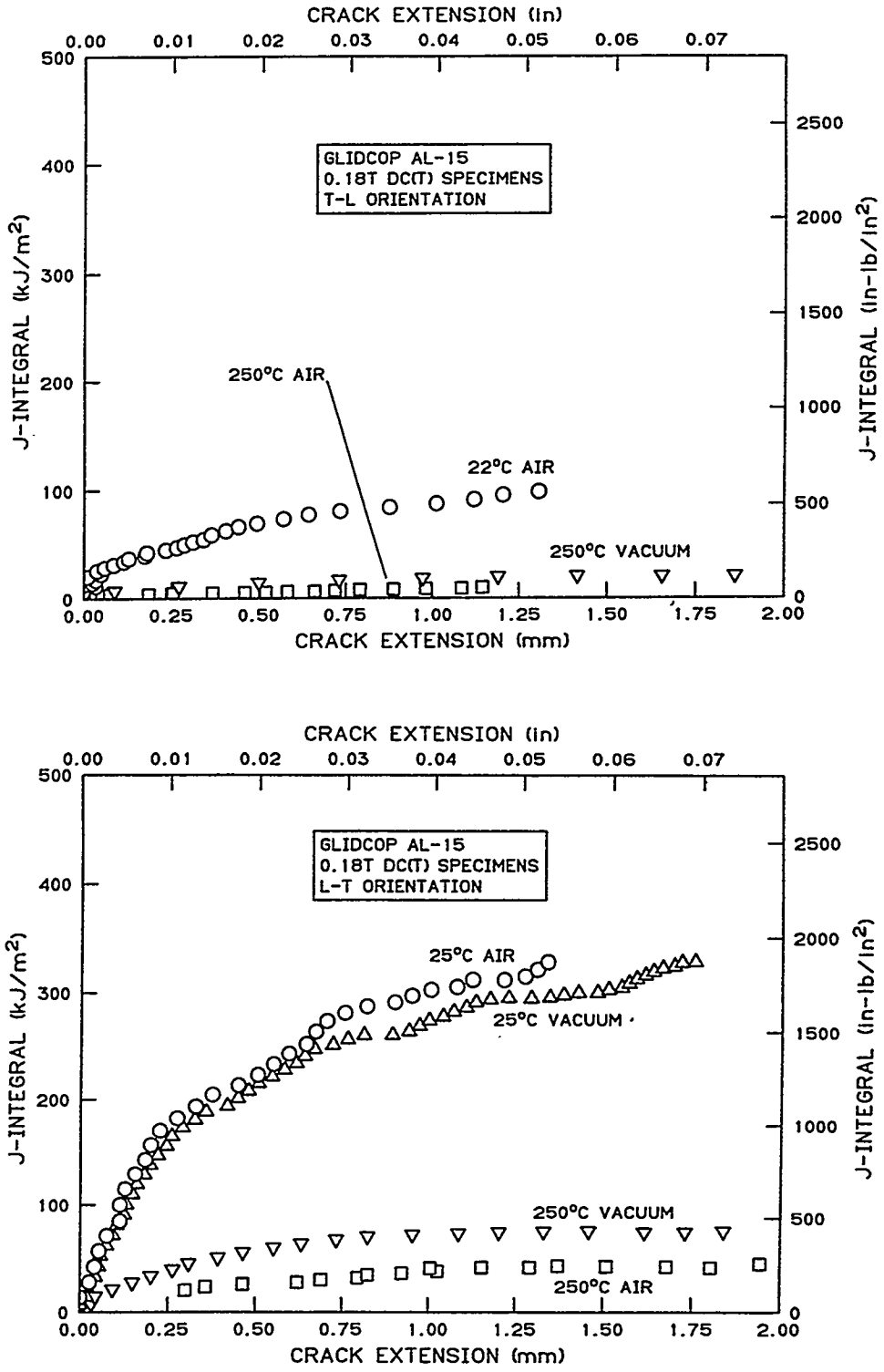

Fig. 1. J-integral resistance curves for AL-15 oxide-dispersion strengthened copper. Top: T-L orientation; bottom: L-T orientation. The L-T specimens have much higher toughness than the T-L specimens.

Table 1. Fracture toughness values of GLIDCOP AL-15

Orientation	Specimen	Temperature (°C)	Environment	J_Q (kJ/m^2)	K_{JQ} (MPa$\sqrt{m}$)	T
T-L	FJ4	22	air	51	78	42
	FJ1	250	air	3	20	9
	GC1	250	vacuum	11	34	13
L-T	GC5	25	air	241	168	87
	GC11	25	vacuum	220	161	75
	GC6	250	air	19	46	30
	GC7	250	vacuum	48	72	37

The results show that the toughness of L-T specimens is much greater than that of T-L specimens. The processing used in the fabrication of this material results in the alignment of particles and the creation of an aligned grain structure parallel to the rolling or extrusion direction. Specimens in the T-L orientation will have crack extension parallel to this microstructure. This will result in a greatly reduced resistance to crack extension by providing a path that favors crack growth, whether by a ductile fracture mechanism, as will occur at room temperature, or by an intergranular mechanism, as may be occurring at high temperature. Preliminary fractography indicates this change in fracture mode occurs for the T-L specimens tested in air. Additional examination of the specimens tested in vacuum and in the L-T orientation is needed.

REFERENCES

1. D. J. Alexander and B. G. Gieseke, "Fracture Toughness and Fatigue Crack Growth of Oxide-Dispersion Strengthened Copper," in Fusion Materials Semiannual Progress Report for Period ending December 31, 1995, DOE/ER-0313/19, 1996, pp. 189-94.

2. T. J. Miller, S. J. Zinkle, and B. A. Chin, "Strength and Fatigue of Dispersion-Strengthened Copper," J. Nuc. Mat., 1991, Vol. 179-181, pp. 263-66.

3. S. J. Zinkle, Oak Ridge National Laboratory, personal communication, 1995.

4. D. J. Alexander, "Fracture Toughness Measurements with Subsize Disk Compact Specimens," in Small Specimen Test Techniques Applied to Nuclear Vessel Thermal Annealing and Plant Life Extension, ASTM STP 1204, W. R. Corwin, F. M. Haggag, and W. L. Server, Eds., American Society for Testing and Materials, Philadelphia, 1993, pp. 130-42, also published in Fusion Reactor Materials Semiannual Progress Report for Period Ending March 31, 1992, DOE/ER-0313/12, pp. 35-45.

5. R. R. Solomon, A. V. Nadkarni, and J. D. Troxell, SCM Metal Products, Inc., unpublished information presented at ITER Workshop, Gatlinburg, Tenn., November 7, 1995

EFFECTS OF BONDING BAKEOUT THERMAL CYCLES ON PRE- AND POST IRRADIATION MICROSTRUCTURES, PHYSICAL, AND MECHANICAL PROPERTIES OF COPPER ALLOYS - B. N. Singh, M. Eldrup, P. Toft (Risø National Laboratory) and D. J. Edwards (Pacific Northwest National Laboratory)

To be submitted for publication in the Journal of Nuclear Materials.

Extended Abstract

At present, dispersion strengthened (DS) copper is being considered as the primary candidate material for the ITER first wall and divertor components. Recently, it was agreed among the ITER parties that a backup alloy should be selected from the two well known precipitation hardened copper alloys, CuCrZr and CuNiBe. It was therefore decided to carry out screening experiments to simulate the effect of bonding and bakeout thermal cycles on microstructure, mechanical properties, and electrical resistivity of CuCrZr and CuNiBe alloys. On the basis of the results of these experiments, one of the two alloys will be selected as a backup material.

Tensile specimens of CuCrZr and CuNiBe alloys were given various heat treatments corresponding to solution anneal, prime ageing, and bonding thermal cycle followed by reageing and the reactor bakeout treatment at 623K for 100 hours. Tensile specimens of the DS copper were also given the heat treatment corresponding to the bonding thermal cycle. A number of these heat treated specimens of CuCrZr, CuNiBe, and DS copper were neutron irradiated at 523K to a dose level of ~0.3 dpa (NRT) in the DR-3 reactor at Risø. Both unirradiated and irradiated specimens with the various heat treatments were tensile tested at 532K. The dislocation, precipitate and void microstructures and electrical resistivity of these specimens were also determined. Results of these investigations will be reported and discussed in terms of thermal and irradiation stability of precipitates and irradiation-induced precipitation and recovery of dislocation microstructure. Results show that the bonding and bakeout thermal cycles are not likely to have any serious deleterious effects on the performance of these alloys. The CuNiBe alloys were found to be susceptible to radiation-induced embrittlement, however, the exact mechanism is not yet known. It is thought that radiation-induced precipitation and segregation of the beryllium may be responsible. The CuCrZr specimens were much more resistant to these effects, presumably due the sluggish precipitation kinetics of the slowly diffusing chromium.

INFLUENCE OF NICKEL AND BERYLLIUM CONTENT ON SWELLING BEHAVIOR OF COPPER IRRADIATED WITH FAST NEUTRONS - B. N. Singh (Risø National Laboratory), F. A. Garner and D. J. Edwards (Pacific Northwest National Laboratory) and J. H. Evans (University of London)

To be submitted for publication in the Journal of Nuclear Materials.

Extended Abstract

In the 1970's, the effects of nickel content on the evolution of dislocation microstructures and the formation and growth of voids in Cu-Ni alloys were studied using 1 MeV electrons in a high voltage electron microscope. The swelling rate was found to decrease rapidly with increasing nickel content. The decrease in the swelling rate was associated with a decreasing void growth rate with increasing nickel content at irradiation temperatures up to 450°C. At 500°C, both void size and swelling rate were found to peak at 1 and 2% Ni, respectively, and then to decrease rapidly with increasing nickel content. However, recent work has demonstrated that the swelling behavior of Cu-5%Ni irradiated with fission neutrons is very similar for that of pure copper. The present experiments were designed to investigate this apparent discrepancy.

Five Cu-x%Ni alloys, where x = 0.17, 1.0, 2.0, 5.0, and 10 weight percent, were irradiated in Cobra-1A irradiation experiment in the EBR-II reactor at about 390°C and 500°C to a dose level of ~11.3 dpa (NRT). These copper alloys were from the same stock which was used for the 1 MeV electron irradiations. Specimens of Cu-0.5 wt% Be were also included in the irradiation experiment. Transmission electron microscopy was used to determine the effect of irradiation on dislocation microstructure and void swelling.

Results show that both the void size and swelling first increase between 0 and 1%Ni and then decrease rather rapidly with increasing nickel content. This behavior is very similar to that observed under 1 MeV electron irradiation at 500°C. Furthermore, the decrease in swelling in the present experiments occurs via a decrease in the void size as was observed in the earlier 1 MeV electron irradiations. This temperature shift can be understood in terms of a very large difference in the damage rate between the 1 MeV electron and fission neutron irradiations. The fact that at high doses the swelling rate in pure copper and Cu-5%Ni is very similar during neutron irradiation may be due to the loss of nickel from the matrix to void surfaces and grain boundaries via radiation-induced segregation. The reduced concentration of nickel in the matrix and the low damage rate during neutron irradiation would reduce the dynamic concentration of metastable clusters/precipitates in Cu-Ni alloys. Hence, a decrease in the swelling resistance occurs since these metastable clusters/precipitates act as recombination centers.

5.0 AUSTENITIC STAINLESS STEELS

TEMPERATURE DEPENDENCE OF THE DEFORMATION BEHAVIOR OF 316 STAINLESS STEEL AFTER LOW TEMPERATURE NEUTRON IRRADIATION —
J. E. Pawel-Robertson (Oak Ridge National Laboratory), I. Ioka (Japan Atomic Energy Research Institute), A. F. Rowcliffe, M. L. Grossbeck (Oak Ridge National Laboratory), and S. Jitsukawa (Japan Atomic Energy Research Institute)

Presented at the 18th Symposium on the Effects of Radiation on Materials, and to be published in Effects of Radiation on Materials: 18th International Symposium, ASTM STP 1325, R. K. Nanstad, M. L. Hamilton, F. A. Garner, and A. S. Kumar, Eds., American Society for Testing and Materials, Philadelphia, 1997.

OBJECTIVE

The objective of this work is to determine the effects of neutron irradiation on the mechanical properties of austenitic stainless steel alloys. In this experiment, the spectrum has been tailored to reduce the thermal neutron flux and achieve a He/dpa level near that expected in a fusion reactor.

SUMMARY

The effects of low temperature neutron irradiation on the tensile behavior of 316 stainless steel have been investigated. A single heat of solution annealed 316 was irradiated to 7 and 18 dpa at 60, 200, 330, and 400°C. The tensile properties as a function of dose and as a function of temperature were examined. Large changes in yield strength, deformation mode, strain to necking, and strain hardening capacity were seen in this irradiation experiment. The magnitudes of the changes are dependent on both irradiation temperature and neutron dose. Irradiation can more than triple the yield strength over the unirradiated value and decrease the strain to necking (STN) to less than 0.5% under certain conditions. A maximum increase in yield strength and a minimum in the STN occur after irradiation at 330°C but the failure mode remains ductile.

PROGRESS AND STATUS

Introduction

Austenitic stainless steels will be used in first wall/shield (FW/S) structures for near term fusion machines such as the International Thermonuclear Experimental Reactor (ITER). These steels have favorable strength, toughness, and fabrication properties, and there is an enormous reservoir of experience in fabricating and operating code qualified austenitic stainless steel components in nuclear systems. The proposed dose/temperature operating conditions for ITER are below the regimes for void swelling (400-600°C) and for grain boundary embrittlement (500-700°C), however, mechanical properties such as yield strength, ductility, and strain hardening capacity change rapidly with dose at these low temperatures [1-3]. These changes in mechanical properties are also dependent on irradiation temperature. In the vicinity of 300°C, neutron-irradiated austenitic steels undergo a transition in microstructure from a low temperature regime dominated by black dots to a high temperature regime dominated by Frank loops and small cavities [4,5]. This transition as a function of temperature is apparent in the tensile response of specimens irradiated in this low temperature regime.

A reactor irradiation experiment has been conducted in the Oak Ridge Research Reactor and the High Flux Isotope Reactor to quantify the effects of neutron irradiation on the tensile behavior of austenitic stainless steels irradiated to doses up to 18 dpa at temperatures from 60 to 400°C. In each reactor, the thermal to fast neutron flux ratio was tailored using thermal neutron shields such that the helium generation rate in 316 stainless steel was within the range expected for a fusion first wall and shield, about 10-20 appm He/dpa. For this report, the tensile data from a single heat of 316 solution annealed material have been examined and both the dose dependence and the temperature dependence of the changes in tensile properties are discussed. Some insights into the dose-temperature regime in which the tensile properties are most severely affected by neutron irradiation and the microstructural features of this regime are presented.

Experimental Procedures

The composition of the solution annealed (SA) J316 material irradiated in this experiment is given in Table 1. The specimens were in the form of SS-1 flat tensile specimens with an overall length of 44.45 mm. The gage section of this type of specimen is 20.32 mm long by 1.52 mm wide by 0.76 mm thick.

The irradiation experiment was conducted in two stages. In the first stage, the tensile specimens were irradiated in the Oak Ridge Research Reactor (ORR) at temperatures of 60, 200, 330, and 400°C to a peak damage level of about 7 dpa (9.2×10^{21} n/cm^2, E>0.1 MeV) [6-9]. The dual-temperature irradiation capsules used for this stage were designated ORR-MFE-6J (which operated at 60 and 200°C) and ORR-MFE-7J (which operated at 330 and 400°C). The 60°C capsule region was cooled directly with reactor cooling water. The 200°C temperature was maintained by conduction of heat through aluminum holders. The temperatures of the higher temperature regions, 330 and 400°C, were monitored and controlled during irradiation by modifying the composition of the thermal conduction gas surrounding the specimens. The details of this irradiation are described in Table 2 and elsewhere [6-8].

Some of these specimens were then re-encapsulated into irradiation capsules designed to operate in the removable beryllium (RB) positions of the High Flux Isotope Reactor (HFIR). The capsules were designed such that the test specimens continued to operate at the same temperature as in the first stage of the irradiation. The capsules were designated HFIR-MFE-RB-60J-1, 200J-1, 330J-1 and 400J-1. A 4.2 mm thick hafnium shield surrounded the capsules in the HFIR in order to reduce the thermal neutron flux and maintain a He/dpa level near that expected in a fusion reactor for the combined two stage experiment. The 60J-1 and 330J-1 capsules accumulated a peak dose of approximately 11 dpa (1.94×10^{22} n/cm^2, E > 0.1 MeV) [10] in the HFIR (in addition to 7 dpa in the ORR). The 200J-1 and 400J-1 capsules accumulated a peak dose of approximately 10 dpa in the HFIR (the dosimetry for the 200J-1 and 400J–1 capsules is still in progress). Details of the irradiation can be found in Table 2 and elsewhere [10-12]. For the purposes of this report, the lower dose level will be referred to as 7 dpa and the higher dose level as 18 dpa.

TABLE 1--Alloy composition of J316.

	Composition (wt %)									
Alloy	Fe	Ni	Cr	Ti	Mo	Mn	Si	C	P	S
J316	Bal	13.52	16.75	0.005	2.46	1.80	0.61	0.058	0.028	0.003

TABLE 2--Maximum neutron fluence values accumulated in each capsule.

	Experiment					
Neutron Fluence, ¥ 10^{21} n/cm2	ORR -MFE -6J (60 and 200°C)	ORR -MFE -7J (330 and 400°C)	HFIR -MFE -60J-1 (60°C)	HFIR -MFE -200J-1* (200°C)	HFIR -MFE -330J-1 (330°C)	HFIR -MFE -400J-1* (400°C)
Total	24.0	27.0	39.5	33.3	39.5	33.3
Thermal (<0.5 eV)	6.71	8.07	4.71	3.97	4.71	3.97
0.5 eV- 0.1 MeV	8.55	9.46	15.4	13.0	15.4	13.0
>0.1 MeV	8.76	9.47	19.4	16.4	19.4	16.4
>1 MeV	4.84	5.14	7.04	5.93	7.04	5.93

*Estimated from reactor power data

The transmutation of Ni-58 to Ni-59 and then to Fe-55 and helium can be calculated from the dosimetry results. The irradiation in the ORR produced approximately 75-100 appm He in the steel, giving a He/dpa ratio of about 11 appm/dpa. Continued irradiation in the HFIR produced approximately 188 appm He in 60J-1 and 225 appm He in 330J-1 [10], total. The helium content calculation was confirmed by isotope-dilution gas mass spectrometry [10]. This HFIR irradiation, combined with the ORR irradiation, resulted in a helium to displacement ratio of 10.2 appm He/dpa in 60J-1 and 11.8 appm He/dpa in 330J-1. It is estimated that the combined 6J/200J-1 and the 7J/400J-1 experiments resulted in about 9.9 and 11.7 appm He/dpa, respectively. These data are summarized in Table 3.

The operating temperature of the HFIR-MFE-RB-60J-1 capsule was 60°C, with the specimens in direct contact with the reactor cooling water. The HFIR-MFE-RB-200J-1, 330J-1, and 400J-1 capsules operated at 200, 330, and 400°C, respectively, with the temperature actively controlled as before by changing the gas mixture around the specimen holder in response to 21 thermocouples located inside the holder. Thermocouple data and detailed discussions of the capsule operations are given in the references [12,13].

An Instron universal testing machine was used for the tensile testing. The specimens irradiated at 60°C (from the 60J-1 capsule) were tested at room temperature (25°C) in air. The specimens irradiated at 200, 330, and 400°C (from 200J-1, 330J-1, and 400J-1, respectively) were tested at the irradiation temperature under vacuum. In each case, the strain rate was 0.0004/s. The 0.2% offset yield strength (YS), ultimate tensile strength (UTS), uniform elongation (E_u), and total elongation (E_t) were calculated from the engineering load-elongation curves. At least two specimens were tested for each experimental condition.

The appropriateness of the conventional methods of determining uniform strain in irradiated materials is a subject of current debate [14-16]. The standard approach to determining the extent of uniform elongation utilizes the point of maximum stress in the engineering stress-strain curve. For unirradiated material, the maximum engineering stress defines the point at which the strain hardening capacity is exhausted and the next local area contraction, which raises the true stress, is no longer balanced by an increase in materials strength. Additional plastic deformation is localized in the necked region. Irradiation and testing at temperatures below about 350°C results in an engineering stress-strain curve in which a load drop occurs just after yielding. As the test continues, the load increases again, sometimes only slightly, and the material continues to deform at a low work-hardening rate. Thus, the observed local maximum load that occurs just after yielding should not be used as the point for measurement of uniform elongation [3,17]. Horsten and de Vries [16,18-20] have studied this situation by repeatedly loading and unloading a specimen

TABLE 3--Maximum damage and accumulated helium† for 316* stainless steel.

Experiment	dpa	appm He
ORR-MFE-6J	6.9	75
ORR-MFE-7J	7.4	102
HFIR-MFE-60J-1	11.6	113
HFIR-MFE-200J-1	9.9‡	92‡
HFIR-MFE-330J-1	11.6	123
HFIR-MFE-400J-1	9.9‡	101‡
6J + 60J-1	18.5	188
6J + 200J-1	16.8‡	167‡
7J + 330J-1	19.0	225
7J + 400J-1	17.3‡	203‡

†HFIR data assume the previous exposure in the ORR; this is important for the accurate calculation of the Ni-59 burn-in

*316 stainless steel: Fe (0.645), Ni (0.13), Cr (0.18), Mn (0.019), Mo (0.026) wt%

‡Estimated from reactor power data

and measuring the dimensions of the gage section. They were able to show that, following the initial load drop after yielding, deformation occurs uniformly up to the point where the engineering stress-strain curve undergoes a rapid downturn prior to fracture, the so-called strain to necking (STN) [16,18,19]. The strain to necking is also tabulated in this report.

Results

The tensile data for the J316 solution annealed specimens are given in Table 4. Typical engineering stress-strain curves for the solution annealed material are shown in Figs. 1-4. Zero strain in these figures is set where the modulus line extrapolates to the x-axis; however, this is not a true modulus line since it includes machine load train deflection.

TABLE 4--Tensile data from solution annealed J316 irradiated in the ORR and HFIR spectrally tailored experiment.

Specimen number	dose, dpa	irradiation temp., °C	test temp., °C	YS, MPa	UTS, MPa	STN, %	Eu, %	Et, %	He level, appm	appm He/dpa	Reactor
EL61	0.0	...	25	327	602	50.4	50.4	56.5	...	...	...
EL26	0.0	...	25	283	552	49.5	49.5	54.0	...	...	...
EL30	0.0	...	200	254	492	31.9	31.9	36.2	...	...	...
EL62	0.0	...	200	263	503	31.3	31.3	34.6	...	...	...
EL31	0.0	...	330	230	484	28.8	28.8	31.3	...	...	...
EL63	0.0	...	330	262	508	28.4	28.4	34.6	...	...	...
EL32	0.0	...	400	252	476	26.1	26.1	28.4	...	...	...
EL64	0.0	...	400	222	476	33.0	33.0	35.1	...	...	...
EL33	6.9	60	25	703	752	26.1	24.5	29.9	100	14.5	ORR
EL34	6.9	60	25	690	745	29.9	27.6	32.5	100	14.5	ORR
EL44	6.9	200	200	758	765	13.6	0.2	15.9	100	14.5	ORR
EL46	6.9	200	200	733	737	12.0	11.5	14.5	100	14.5	ORR
EL1	7.4	330	330	848	855	0.3	0.3	3.1	100	13.5	ORR
EL2	7.4	330	330	869	869	0.3	0.3	2.9	100	13.5	ORR
EL14	7.4	400	400	595	677	5.1	4.6	7.0	100	13.5	ORR
EL15	7.4	400	400	650	717	4.9	4.3	6.8	100	13.5	ORR
EL36	18.5	60	25	716	743	22.2	20.4	24.6	188	10.2	ORR+HFIR
EL37	18.5	60	25	747	765	23.3	20.4	25.6	188	10.2	ORR+HFIR
EL48	17.0	200	200	745	752	3.4	0.2	5.7	197	11.6	ORR+HFIR
EL49	17.0	200	200	740	740	7.2	0.2	9.8	197	11.6	ORR+HFIR
EL04	19.0	330	330	903	913	0.4	0.4	3.1	224	11.8	ORR+HFIR
EL05	19.0	330	330	909	921	0.4	0.4	3.1	224	11.8	ORR+HFIR
EL17	17.0	400	400	663	720	2.4	2.4	4.3	197	11.6	ORR+HFIR
EL20	17.0	400	400	634	716	5.8	5.8	8.1	197	11.6	ORR+HFIR

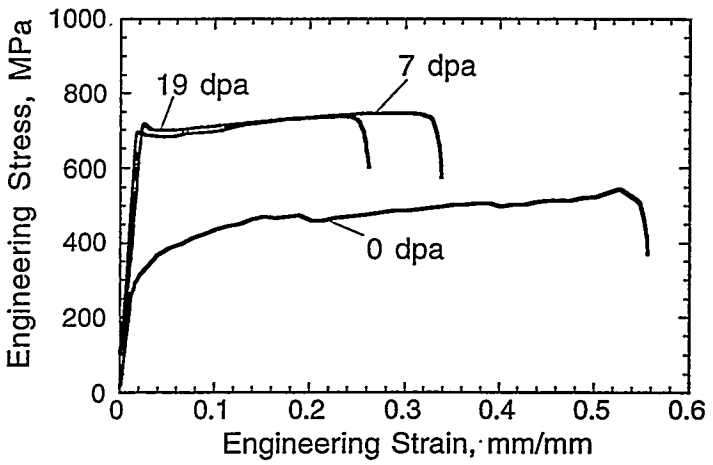

FIG. 1--Typical engineering stress-strain curves for SA J316 irradiated at 60°C and tested at 25°C.

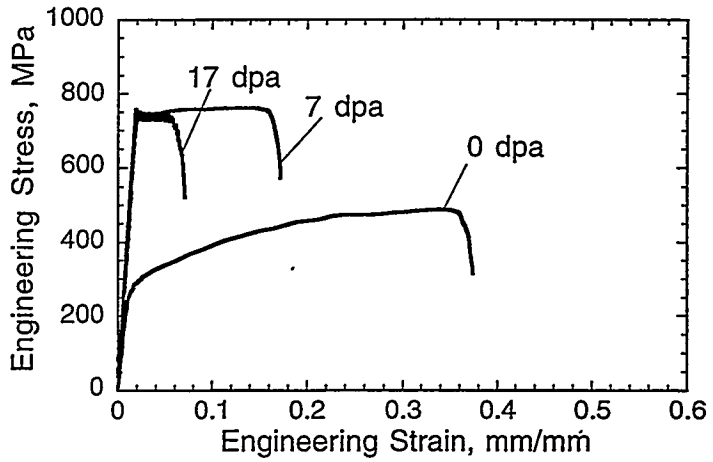

FIG. 2--Typical engineering stress-strain curves for SA J316 irradiated and tested at 200°C.

Irradiation at 60°C (Fig. 1) results in a greater than twofold increase in yield stress. The smooth yielding behavior of the unirradiated material is replaced by the appearance of a small yield drop. Following the yield drop, the irradiated material work hardens at a much lower rate than in the unirradiated condition but still elongates more than 20% before necking and failure occur. At both 7 and 18 dpa, the UTS is less than 10% higher than the YS. While there is no significant yield strength increase from 7 to 18 dpa, the strain to necking and the total elongation are both reduced with this dose increment.

After irradiation and testing at 200°C (Fig. 2), the yield stress is almost three times higher than the unirradiated value. The material work hardens only slightly, with the maximum in the engineering stress-strain curve sometimes occurring at the upper yield point. The yield strength is the same (745 MPa) after irradiation to both 7 and 18 dpa. However, the STN and the total elongation continue to decrease with the dose increment from 7 to 18 dpa. The strain to necking is 8-14% after 7 dpa but drops to only 3-7% after 18 dpa. Total elongation remains high at 15 to 20% after 7 dpa but is only 6-10% after 18 dpa.

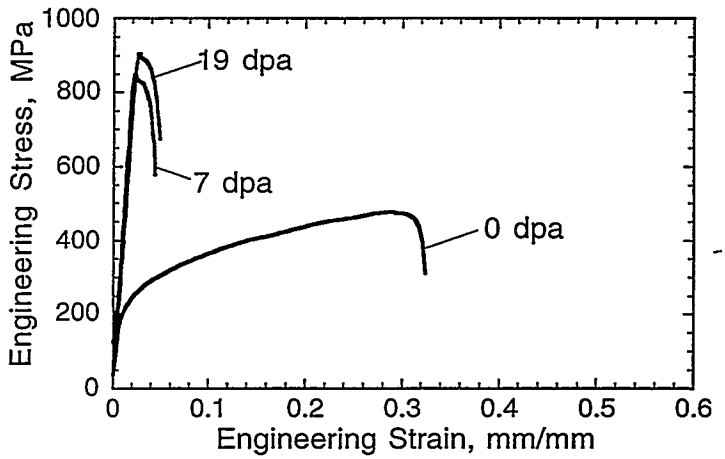

FIG. 3--Typical engineering stress-strain curves for SA J316 irradiated and tested at 330°C.

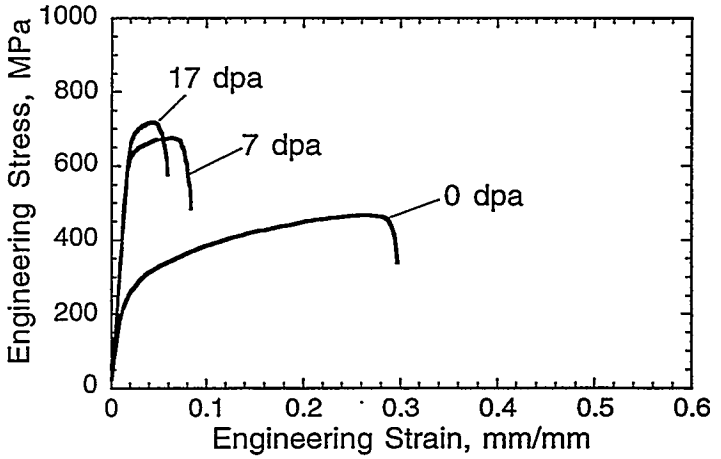

FIG. 4--Typical engineering stress-strain curves for SA J316 irradiated and tested at 400°C.

After irradiation and testing at 330°C (Fig. 3), the deformation behavior is significantly different. The yield strength increases from the unirradiated value of about 250 MPa to more than 850 MPa at 7 dpa, an increase of 250%. The increase in yield stress is greater than the increase seen at 60°C by about 150 MPa. The yield stress only increases about 5% from 7 to 18 dpa. After yielding, the characteristic yield drop is apparent, but the material does not exhibit any work hardening capability. The applied load falls rapidly and failure occurs after only about 3% total elongation. The strain to necking is less than 0.5% in each case. The failure mode, however, is ductile [3].

Irradiation and testing at 400°C shows another regime as a function of temperature (Fig. 4), and results in the least amount of hardening (increase in yield strength) of the four temperature sets and more work hardening than at 200 or 330°C. There is no evidence of the yield drop seen after irradiation at lower temperatures. The yield strength increases from 237 MPa to 623 MPa at 7 dpa, and then increases an additional 4% at 18 dpa. The strain to necking is much greater than that at 330°C, but is still less than 6%.

The 0.2% offset yield strengths as a function of neutron dose are plotted for each temperature in Fig. 5. For all four irradiation temperatures, irradiation to about 7 dpa resulted in a yield strength increase over the unirradiated value of 130-250%. Additional irradiation to 18 dpa caused further increases in the yield strength of less than 5%. For the 200°C irradiation, there was no increase in yield strength beyond 7 dpa. Under these conditions for this alloy, the yield strength has essentially saturated with dose by 7 dpa. These data are consistent with data taken from the literature for a variety of austenitic stainless steels irradiated at low (less than 250°C) temperatures. Prior to irradiation, type 316 steels have room temperature yield strengths in the range of 225-350 MPa and the YS decreases slightly with increasing temperature. After even modest irradiation levels of about 1 dpa at low temperatures, the yield strength increases by several hundred MPa. For example, Tavassoli [21] reports significant increases in yield and ultimate tensile strengths at fluences less than 1 dpa and saturation of these strengths at approximately 3 dpa for 316LN irradiated at temperatures less than 400°C. Kallstrom et al. [22] irradiated 316LN to only 0.3 dpa at 35°C and report a yield strength of 552 MPa after testing at 75°C. Heinisch [23] also reports significant increases in the yield strength of 316 as the result of very low dose irradiations (<0.01 dpa). These data are shown in Fig. 6 along with other data from the literature. The rate of yield strength increase slows with increasing neutron dose and a saturation value is approached in the range of 1 to 3 dpa. This observation is generally consistent with microstructural data, which indicate that the doses necessary to approach the saturation of the black dot and loop densities, although somewhat dependent on irradiation temperature, are about 0.1 and ≥1 dpa, respectively [4].

Before irradiation, the ultimate tensile strengths are 240-270 MPa (84-114%) higher than the corresponding yield strengths. The ultimate tensile strengths after irradiation at temperatures less than or equal to 330°C are only slightly higher (<8%) than the corresponding yield strengths and follow the same trends as yield strength with dose. Literature data also reveal that the YS approaches the UTS for irradiations ≤ 350°C or so [14,24,33,34], indicative of the loss of strain hardening capacity. After irradiation at 400°C, the UTS are 8-14% higher than the yield strength.

The strain to necking values are shown as a function of dpa and temperature in Fig. 7. At 25°C, the unirradiated values are very high, about 50%. At the higher test temperatures, the unirradiated values are about 30%. The STN drops off quickly with dose at each temperature, with the decline most severe for the 330°C case. After irradiation to both 7 and 18 dpa at 60°C, the STN remains high, greater than 25%. Irradiation at 200°C results in STN of more than 12% at 7 dpa, but only 3-7% after 18 dpa. Irradiation at 330°C results in STN less than 1% at each dose, with total elongations of only 3%. Elongations increase slightly at 400°C over those at 330°C. The STN continues to drop with increasing dose from 7 to 18 dpa for the 60°C irradiation and even the 200°C irradiation, which showed saturation of the hardening by 7 dpa.

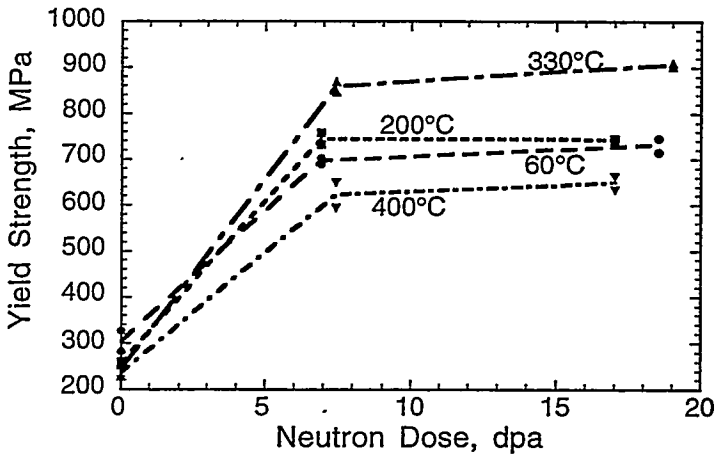

FIG. 5--Yield strength as a function of neutron dose. The irradiation and test temperature are shown in the figure.

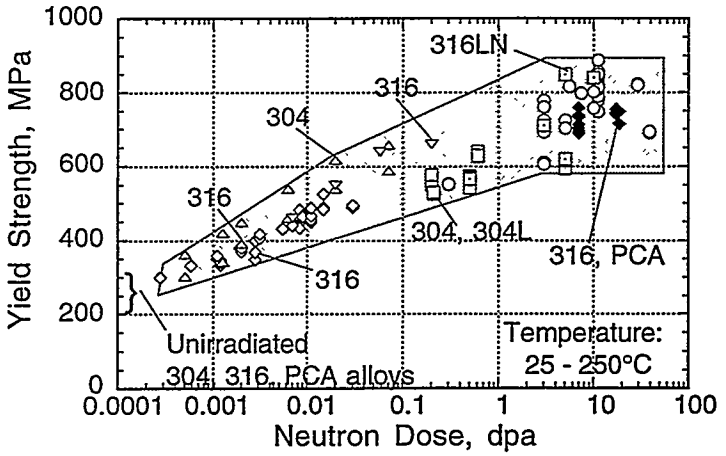

FIG. 6--Yield strength as a function of neutron dose for 304, 316, and PCA type austenitic stainless steels irradiated in a variety of experiments. In each case, the test temperature equals the irradiation temperature and is in the range of 25-250°C [1,2,15,16,18,19,21-32].

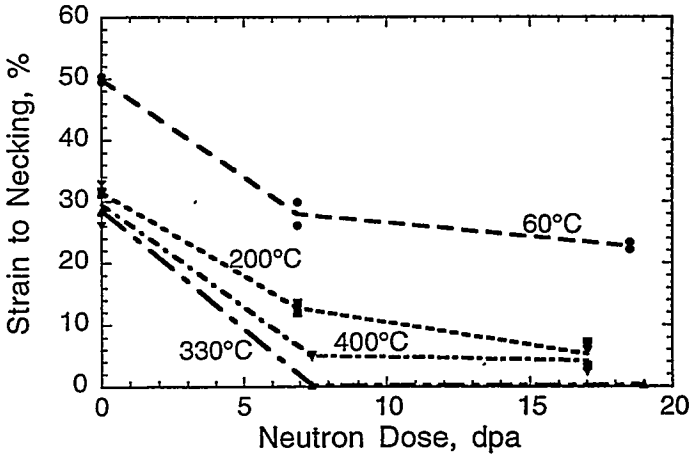

FIG. 7--Strain to necking as a function of neutron dose. The irradiation and test temperature are shown in the figure.

The STN change has essentially saturated with dose by 7 dpa for the 330 and 400°C irradiations. In general, for irradiation and test temperatures up to about 250°C, the strain to necking values are high, even after irradiation to about 10 dpa. In the 250-350°C regime, however, the strain to necking values appear to fall off quickly after irradiation to doses higher than 3 dpa [1,2,15,16,18,19,22,24-28,30,35].

One of the unique features of this experiment was the irradiation of the same heat of J316 in capsules under the same reactor conditions with precise temperature control. The changes in tensile properties as a function of temperature may influence the ITER desired operating regime and it is useful to reiterate the data in the form of property versus temperature plots in which the trends with irradiation temperature are more clearly seen. Figure 8 shows typical engineering stress-strain curves for the J316 solution annealed material irradiated in the ORR to 7 dpa at each temperature. The high yield stress, the loss of work hardening, and the rapid failure after 330°C irradiation are particularly evident.

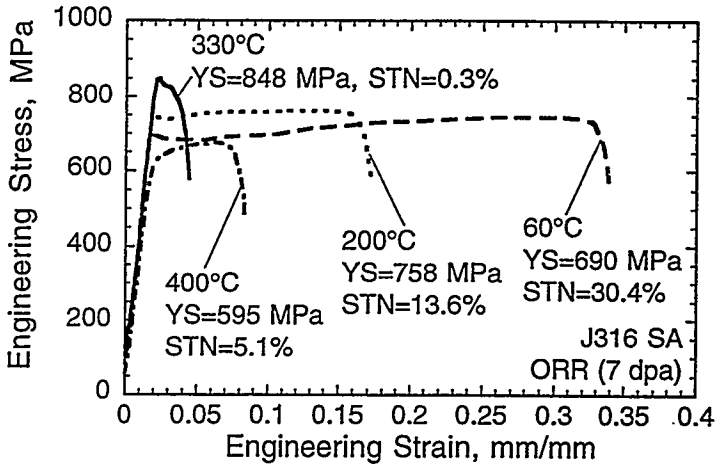

FIG. 8--Typical engineering stress-strain curves for SA J316 irradiated to 7 dpa at 60, 200, 330, and 400°C. The 0.2% offset YS and the STN are given in the figure for each curve.

The solution annealed J316 material irradiated to 7 dpa showed a peak in the yield strength as a function of temperature at 330°C (Fig. 9). The 18 dpa data superimposed on this figure for comparison follow the same trend. Composite plots of yield strength as a function of irradiation temperature for solution annealed austenitic stainless steel variants have been generated from literature data [e.g., 36]. For specimens irradiated up to 20 dpa in a variety of reactors, these combined data also reveal a maximum in yield strength around 300°C in spite of the many different experimental variables.

The STN measured in the experiment reported here have been combined with other data from the literature [1,2,16,18,22,24,25,27,37, 38] in the form of a damage-temperature map (Fig. 10). Three regimes of STN have been designated based on the discussion by Majumdar [39] on design rules for ITER components. For STN values greater than 5%, the material is considered to be sufficiently ductile for ASME Code rules to be applicable. For the semi-brittle (1% < STN <5%) and brittle (STN <1%) regimes, a different set of design rules to protect against failure by plastic collapse in regions of high stress concentration need to be adopted. STN values less than 1% are represented by closed circles in Fig. 10. In this regime, the yield stress is increased by more than a factor of three above the unirradiated value, the material has zero strain hardening capacity, and following the initial load drop, strain is intensely localized (e.g., Fig. 3). Although this type of behavior, with less than 1% STN, is frequently classified as "brittle" for design code purposes, failure actually occurs in a ductile tearing mode [3] as opposed to the brittle cleavage type of failure observed in body-centered-cubic materials. Significant post-necking ductility is still retained even in the regime where the material undergoes plastic instability immediately after yielding. For example, other experiments have shown that the reduction in area (RA), which is used to measure the true strain at failure, of 316LN decreases from an unirradiated value of about 70% to about 60% after irradiation to 11 dpa at 250°C [25]. The low STN is a consequence of severe flow localization [36] and is the subject of continuing investigation.

Discussion

The macroscopic changes in mechanical properties such as yield strength and ductility are determined by the microstructure and microcomposition resulting from the irradiation [40,41]. The damage microstructure in austenitic stainless irradiated at temperatures up to about 250°C consists of a very high density of small black dot defect clusters, about 2 nm diameter [4]. The density of these black dots is independent of temperature from 50°C up to about 250°C; at higher irradiation temperatures the black dot density decreases sharply. The density of observable faulted Frank loops, 10 to 20 nm in diameter, increases continuously up

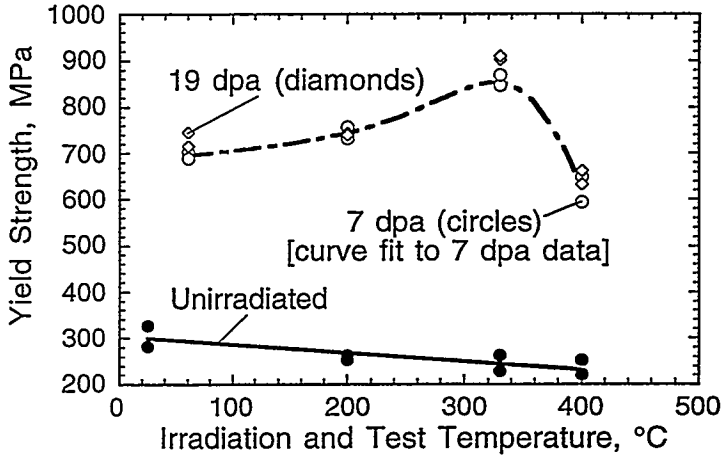

FIG. 9--Yield strength as function of temperature (the irradiation temperature equals the test temperature) for both the 7 and 19 dpa dose levels.

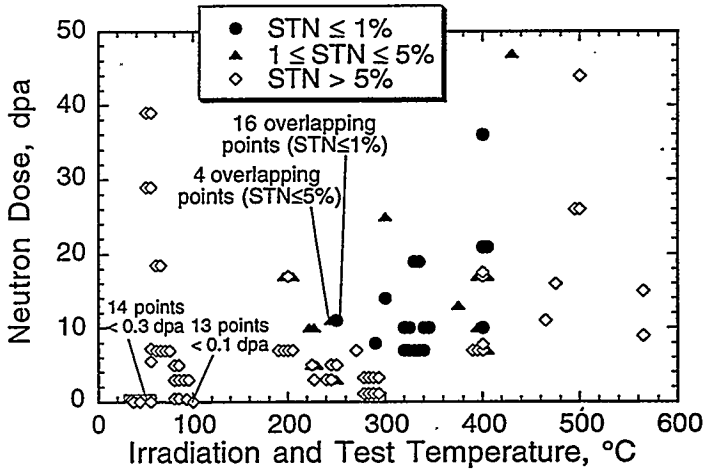

FIG. 10--Strain to necking as a function of neutron dose and temperature for solution annealed austenitic stainless steels [1,2,16,18,22,24,25, 27,37,38]. Several sets of overlapping data are noted on the figure. Horizontal sets of data represent the same nominal irradiation temperature: the distribution is used to distinguish otherwise overlapping points.

to about 300-350°C before decreasing rapidly [4,42,43]. These loops dominate the microstructure at temperatures from about 250 to 400°C. Above irradiation temperatures of about 400°C, the microstructure is dominated by cavities, precipitates, and network dislocations. Small cavities may also be present at temperatures as low as 200°C [44,45].

The changes in yield strength after neutron irradiation can be correlated with the observed changes in microstructure using simple hardening models [5,41,46-50]. Cavities (both bubbles and voids), Frank loops, black dot defect clusters, network dislocations, and precipitates all contribute to the hardening either as short range or long range obstacles. The qualitative agreement between the models and several sets of data is reasonably good [e.g., 47]. In general, the irradiation defect structure provides a very effective barrier

to dislocation motion and raises the yield stress to very high levels. At some critical stress level, dislocations break free, producing a burst of deformation that is sufficient to cause the initial load drop that is seen in Figs. 1-3. This load drop may be due to the onset of a very localized deformation in the form of a Luders-like band associated with dislocation channeling [36]. The subsequent low work hardening rates may also be related to dislocation channeling [41,46,51-55]. Yield stress increases with irradiation temperature until a point is reached where yielding is followed by mechanical instability (Fig. 3). A local reduction in area of the specimen cannot be compensated for by work hardening and deformation concentrates in this region until failure occurs. At 400°C, the barriers to gliding dislocations continue to produce strengthening but, because the spacing of the defects is larger here than in the lower temperature regime, the strengthening is less [4,52,56,57].

The changes in flow properties with irradiation temperature are related to the nature of the defect structure [46]. The dominant microstructural features of each irradiation temperature are superimposed on the dose-temperature map in Fig. 11. In the regime where STN values are less than 1%, the microstructure is dominated by faulted Frank loops and small cavities. Conversely, the STN remains high (greater than 5%) up to at least 40 dpa at temperatures where the microstructure is dominated by black dots (below 200°C) or by large cavities, precipitates and network dislocations (above 400°C). The relationships between the nature and density of radiation defects and deformation and fracture processes are very complex with many unresolved issues [51,58]. For example, the deformation behavior is also dependent on the test temperature and the strain rate [19,24,59]. Additional microscopy and off-temperature tensile tests may help to separate the contributions of the different microstructural features and lead to better modeling techniques.

Conclusions

A single heat of solution annealed 316 was irradiated to 7 and 18 dpa at 60, 200, 330, and 400°C. The tensile properties as a function of dose and as a function of temperature have been investigated. Large changes in yield strength, deformation mode, strain to necking, and strain hardening capacity were seen in this irradiation experiment. The magnitudes of the changes are dependent on both irradiation temperature and neutron dose. Irradiation can more than triple the yield strength over the unirradiated value and decrease the strain to necking to less than 0.5% under certain conditions. A maximum increase in yield strength and a minimum in the STN occur after irradiation at 330°C but the failure mode remains ductile. The macroscopic changes in mechanical properties are determined by the microstructure resulting from irradiation. The radiation-induced defect structure provides effective barriers to dislocation motion and raises yield strength to high levels. In the regime where the yield strength is maximum and STN is minimum, the microstructure is dominated by Frank loops and small cavities. Additional microscopy and off-

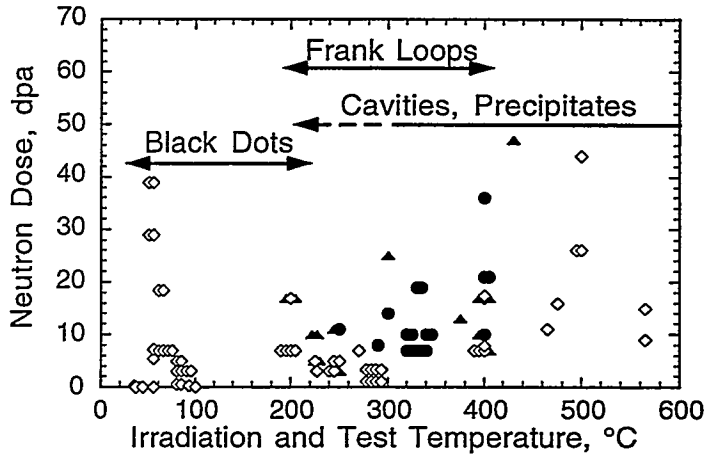

FIG. 11--Dose-temperature map of Fig. 10 with the temperature regions of the dominant microstructural features superimposed.

temperature tensile tests may help to separate the contributions of the different microstructural features and lead to better modeling techniques.

Acknowledgments

Research sponsored by the Office of Fusion Energy Sciences, U.S. Department of Energy, under contract DE-AC05-96OR22464 with Lockheed Martin Energy Research Corporation, and the Japan Atomic Energy Research Institute. The tensile testing was performed by R. L. Martin, L. T. Gibson, and W. S. Eatherly. The authors are grateful to Ms. G. L. Burn for preparation of the manuscript.

References

[1] M. L. Grossbeck, T. Sawai, S. Jitsukawa, and L. T. Gibson, Fusion Reactor Materials Semiannual Progress Report for Period Ending March 31, 1989, Office of Fusion Energy, DOE/ER-0313/6, 1989, p. 259.

[2] M. L. Grossbeck, Fusion Reactor Materials Semiannual Progress Report for Period Ending March 31, 1989, Office of Fusion Energy, DOE/ER-0313/6, 1989, p. 243.

[3] S. Jitsukawa, P. J. Maziasz, T. Ishiyama, L. T. Gibson, and A. Hishinuma, Journal of Nuclear Materials, Vols. 191-194, 1992, p. 771.

[4] S. J. Zinkle, P. J. Maziasz, and R. E. Stoller, Journal of Nuclear Materials, Vol. 206, 1993, p. 266.

[5] P. J. Maziasz, Journal of Nuclear Materials, Vols. 191-194, 1992, p. 701.

[6] I. I. Siman-Tov, Fusion Reactor Materials Semiannual Progress Report for Period Ending September 30, 1987, Office of Fusion Energy, DOE/ER-0313/3, 1988, p. 7.

[7] L. R. Greenwood, Fusion Reactor Materials Semiannual Progress Report for Period Ending March 31, 1989, Office of Fusion Energy, DOE/ER-0313/6, 1989, p. 23.

[8] L. R. Greenwood and D. V. Steidl, Fusion Reactor Materials Semiannual Progress Report for Period Ending March 31, 1990, Office of Fusion Energy, DOE/ER-0313/8, 1990, p. 34.

[9] L. R. Greenwood, Alloy Development for Irradiation Performance Semiannual Progress Report for Period Ending March 31, 1986, Office of Fusion Energy, DOE/ER-0045/16, 1986, p. 17.

[10] L. R. Greenwood, C. A. Baldwin and B. M. Oliver, Fusion Materials Semiannual Progress Report for Period Ending September 30, 1994, Office of Fusion Energy, DOE/ER-0313/17, 1995, p. 28.

[11] A. W. Longest, J. E. Pawel, D. W. Heatherly, R. G. Sitterson and R. L. Wallace, Fusion Reactor Materials Semiannual Progress Report for Period Ending March 31, 1993, Office of Fusion Energy, DOE/ER-0313/14, 1993, p. 14.

[12] A. W. Longest, D. W. Heatherly, E. D. Clemmer and J. E. Corum, Fusion Reactor Materials Semiannual Progress Report for Period Ending September 30, 1991, Office of Fusion Energy, DOE/ER-0313/11, 1992, p. 17.

[13] A. W. Longest, J. E. Pawel, D. W. Heatherly, R. G. Sitterson and R. L. Wallace, Fusion Reactor Materials Semiannual Progress Report for Period Ending September 30, 1993, Office of Fusion Energy, DOE/ER-0313/15, p. 23.

[14] G. E. Lucas, M. Billone, J. E. Pawel, and M. L. Hamilton, presented at the 7th International Conference on Fusion Reactor Materials, Obninsk, Russia, September 25-29, 1995, and to be published in Journal of Nuclear Materials.

[15] J. E. Pawel, A. F. Rowcliffe, D. J. Alexander, M. L. Grossbeck, and K. Shiba, presented at the 7th International Conference on Fusion Reactor Materials, Obninsk, Russia, September 25-29, 1995, and to be published in Journal of Nuclear Materials.

[16] M. G. Horsten and M. I. de Vries, Effects of Radiation on Materials: 17th International Symposium, ASTM STP 1270, D. S. Gelles, R. K. Nanstad, A. S. Kumar, and E. A. Little, Eds., American Society for Testing and Materials, Philadelphia, 1996, in press.

[17] J. D. Elen and P. Fenici, Journal of Nuclear Materials, Vols. 191-194, 1992, p. 766.

[18] M. G. Horsten and M. I. de Vries, Journal of Nuclear Materials, Vols. 212-215, 1994, p. 514.

[19] M. G. Horsten, J. van Hoepen and M. I. de Vries, Tensile Tests on Plate and Electron-Beam Welded Type 316L(N) Material, Netherlands Energy Research Foundation ECN, ECN-CX--93-112, 1993.

[20] M. I. de Vries, Private Communication.

[21] A. A. Tavassoli, Assessment of Austenitic Stainless Steels, ITER Task BL-URD3, N.T. SRMA 94-2061, Revision June 1994.

[22] R. Kallstrom, B. Josefsson and Y. Haag, Results From Tensile Testing of 316L Plate and Weld Material, Studsvik Material AB, Sweden, STUDSVIK/M-93/45, PSM 1-1, 1993.

[23] H. L. Heinisch, Journal of Nuclear Materials, Vols. 155-157, 1988, p. 121.

[24] J. E. Pawel, M. L. Grossbeck, A. F. Rowcliffe and K. Shiba, Fusion Materials Semiannual Progress Report for Period Ending September 30, 1994, Office of Fusion Energy, DOE/ER-0313/17, 1994, p. 125.

[25] B. Van der Schaaf, M. Grossbeck, and H. Scheurer, Oak Ridge Test Matrix No. 5B and 5C HFR and HFIR Irradiations and Post-Irradiation Tensile Tests in Support of Fusion Reactor First Wall Material Development, Nuclear Science and Technology, Commission of the European Communities, Luxembourg, EUR 10659 EN, 1986.

[26] F. W. Wiffen and P. J. Maziasz, Journal of Nuclear Materials, Vols. 103&104, 1981, p. 821.

[27] H. R. Higgy and F. H. Hammad, Journal of Nuclear Materials, Vol. 55, 1975, p. 177.

[28] E. E. Bloom, W. R. Martin, J. O. Stiegler, and J. R. Weir, Journal of Nuclear Materials, Vol. 22, 1967, p. 68.

[29] W. R. Martin and J. R. Weir, in Flow and Fracture of Metals and Alloys in Nuclear Environments, ASTM STP 380, American Society for Testing and Materials, Philadelphia, 1965, p. 251.

[30] H. L. Heinisch, M. L. Hamilton, W. F. Sommer, and P. D. Ferguson, Journal of Nuclear Materials, Vols. 191-194, 1992, p. 1177.

[31] R. L. Klueh, Alloy Development for Irradiation Performance Semiannual Progress Report for Period Ending March 31, 1984, Office of Fusion Energy, DOE/ER-0045/12, 1984, p. 45.

[32] M. J. Makin, in Radiation Effects, Metallurgical Society Conferences, Vol. 37, W. F. Sheely, Ed., Gordon and Breach, Science Publishers, Inc., New York, 1967, p. 629.

[33] M. L. Grossbeck, Journal of Nuclear Materials, Vols. 179-181, 1991, p. 568.

[34] G. R. Odette and G. E. Lucas, Journal of Nuclear Materials, Vols. 179-181, 1991, p. 572.

[35] A. J. Jacobs, G. P. Wozadlo, K. Nakata, T. Yoshida, and I. Masaoka, Environmental Degradation of Materials in Nuclear Power Systems--Water Reactors, G. J. Theus and J. R. Weeks, Eds., The Metallurgical Society, Inc., Warrendale, PA, 1988, p. 673.

[36] J. E. Pawel, A. F. Rowcliffe, G. E. Lucas, and S. J. Zinkle, presented at the 117th Meeting of the Japan Institute of Metals: International Symposia on Advanced Materials and Technology for the 21st Century, Honolulu, Hawaii, December 12-15, 1995, and to be published in Journal of Nuclear Materials.

[37] M. L. Grossbeck and P. J. Maziasz, Journal of Nuclear Materials, Vols. 85&86, 1979, p. 883.

[38] K. Shiba, S. Jitsukawa, J. E. Pawel and A. F. Rowcliffe, Fusion Reactor Materials Semiannual Progress Report for Period Ending September 30, 1993, Office of Fusion Energy, DOE/ER-0313/15, 1994, p. 181.

[39] S. Majumdar, Fusion Engineering and Design 29, 1994, p. 158.

[40] L. K. Mansur, Kinetics of Nonhomogeneous Processes, G. R. Freeman, Ed., John Wiley & Sons, Inc., New York, 1987 p. 377.

[41] G. E. Lucas, Journal of Nuclear Materials, Vol. 206, 1993, p. 287.

[42] P. J. Maziasz, Journal of Nuclear Materials, Vol. 205, 1993, p. 118.

[43] P. J. Maziasz and D. N. Braski, Journal of Nuclear Materials, Vols. 122 & 123, 1984, p. 311.

[44] S. J. Zinkle and R. L. Sindelar, Journal of Nuclear Materials, 155-157, 1988, p. 1196.

[45] S. J. Zinkle, private communication, 1996.

[46] G. R. Odette and D. Frey, Journal of Nuclear Materials, Vols. 85 & 86, 1979, p. 817.

[47] M. L. Grossbeck, P. J. Maziasz and A. F. Rowcliffe, Journal of Nuclear Materials, Vols. 191-194, 1992, p. 808.

[48] H. R. Brager, L. D. Blackburn and D. L. Greenslade, Journal of Nuclear Materials, Vols. 122 & 123, 1984, p. 332.

[49] F. A. Garner, M. L. Hamilton, N. F. Panayotou, and G. D. Johnson, Journal of Nuclear Materials, Vols. 103 & 104, 1981, p. 803.

[50] R. L. Simons and L. A. Hulbert, Effects of Radiation on Materials: 12th International Symposium, ASTM STP 870, F. A. Garner and J. S. Perrin, Eds., American Society for Testing and Materials, Philadelphia, 1985, p. 820.

[51] M. S. Wechsler, The Inhomogeneity of Plastic Deformation, R. E. Reed-Hill, Ed., American Society for Metals, Metals Park, Ohio, 1973, p. 19.

[52] M. L. Grossbeck, J. O. Stiegler and J. J. Holmes, Radiation Effects in Breeder Reactor Structural Materials, M. L. Bleiberg and J. W. Bennett, Eds., The Metallurgical Society of AIME, New York, 1977, p. 95.

[53] L. K. Mansur and M. L. Grossbeck, Journal of Nuclear Materials, Vols. 155-157, 1988, p. 130.

[54] R. L. Fish, J. L. Straalsund, C. W. Hunter and J. J. Holmes, Effects of Radiation on Substructure and Mechanical Properties of Metals and Alloys, ASTM STP 529, J. Moteff, Ed., American Society for Testing and Materials, Philadelphia, 1973, p. 149.

[55] M. S. Wechsler, Fundamental Aspects of Radiation Damage in Metals, M. T Robinson and F. W. Young, Jr., Eds., U. S. Energy Research and Development Administration, CONF-751006, Gatlinburg, Tennessee, 1975, p. 991.

[56] E. E. Bloom, Radiation Damage in Metals, N. L. Peterson and S. D. Harkness, Eds., American Society of Metals, Metals Park, OH, 1976, p. 295.

[57] D. R. Harries, Journal of Nuclear Materials, Vols. 82, 1979, p. 2.

[58] R. D. Carter, M. Atzmon, G. S. Was, and S. M. Bruemmer, Microstructure of Irradiated Materials, Materials Research Society Symposium Proceedings, Vol. 373, I. M. Robertson, L. E. Rehn, S. J. Zinkle, and W. J. Phythian, Eds., Materials Research Society, Pittsburgh, 1995, p. 171.

[59] J. L. Brimhall, J. I. Cole, J. S. Vetrano, and S. M. Bruemmer, Microstructure of Irradiated Materials, Materials Research Society Symposium Proceedings, Vol. 373, I. M. Robertson, L. E. Rehn, S. J. Zinkle, and W. J. Phythian, Eds., Materials Research Society, Pittsburgh, 1995, p. 177.

TENSILE PROPERTIES OF A TITANIUM MODIFIED AUSTENITIC STAINLESS STEEL AND THE WELD JOINTS AFTER NEUTRON IRRADIATION --- K. Shiba, I. Ioka, S. Jitsukawa, S. Hamada, A. Hishinuma [Japan Atomic Energy Research Institute (JAERI)] and J. Pawel Robertson [Oak Ridge National Laboratory (ORNL)]

OBJECTIVE

To investigate the irradiation behavior on the tensile properties of a titanium-modified austenitic stainless steels (JPCA) and its weldments by the HFIR target and the spectrally tailored irradiation.

SUMMARY

Tensile specimens of a titanium modified austenitic stainless steel and its weldments fabricated with Tungsten Inert Gas (TIG) and Electron Beam (EB) welding techniques were irradiated to a peak dose of 19 dpa and a peak helium level of 250 appm in the temperature range between 200 and 400°C in spectrally tailored capsules in the Oak Ridge Research Reactor (ORR) and the High Flux Isotope Reactor (HFIR). The He/dpa ratio of about 13 appm/dpa is similar to the typical helium/dpa ratio of a fusion reactor environment. The tensile tests were carried out at the irradiation temperature in vacuum. The irradiation caused an increase in yield stress to levels between 670 and 800 MPa depending on the irradiation temperature. Total elongation was reduced to less than 10%, however the specimens failed in an ductile manner. The results were compared with those of the specimens irradiated using irradiation capsules producing larger amount of He. Although the He/dpa ratio affected the microstructural change, the impact on the post irradiation tensile behavior was rather small for not only base metal specimens but also for the weld joint and the weld metal specimens.

INTRODUCTION

Fe-Cr-Ni austenitic alloys are recognized to be the candidate alloys for the structural materials of the first walls of the blankets (FWB) for the fusion experimental reactors. The austenitic alloys will be used at temperatures below 400°C in the International Thermonuclear Experimental Reactor (ITER). The accumulated damage level to the end of life at the FWB position will be 1 to 30 displacements per atom (dpa) depending on the project. For instance, the maximum damage level is proposed to be 30 dpa for ITER Extended Performance Phase [1].

Microstructural evolution in the austenitic alloys is strongly affected by the helium due to nuclear transmutation reaction during neutron irradiation [2,3]. The ratio between the helium level and the displacement damage level (He/dpa) by fusion neutrons will be about 14 appmHe/dpa for Fe-Cr-Ni austenitic alloys. Fission neutron irradiation in the spectral tailoring capsules of the Oak Ridge Research Reactor (ORR) and the High Flux Isotope Reactor (HFIR) at Oak Ridge National Laboratory (ORNL) is capable to achieve the He/dpa ratio relevant to fusion neutrons by adjusting thermal and fast neutron flux ratio. The spectral tailored irradiation was planned to evaluate the effects of the He/dpa ratio and to estimate the irradiation induced property changes of austenitic alloys in a fusion reactor, and conducted in the Japan-US collaborative program for the fusion reactor materials development.

Since welding will be used for the fabrication of FWB, it is important to evaluate the irradiation response of the weldments. It has been reported that the helium embrittlement strongly depends on thesegregation of helium at grain boundaries [4]. Because welding often causes to the coarsening of grains, He embrittlement is one of the interesting subjects for the weldment of austenitic alloys after irradiation.

TABLE 1--Chemical compositions of alloys

	Fe	C	Si	Mn	P	S
JPCA	bal.	0.052	0.51	1.78	0.28	0.005
TIG wire	bal.	0.057	0.35	1.77	0.008	0.002

	Cr	Ni	Mo	Ti	N
JPCA	14.3	15.5	2.3	0.24	0.004
TIG wire	14.4	16.1	2.4	0.23	0.0095

TABLE 2--TIG welding condition

Voltage	Beam Current	Welding Speed	Wire Feed	Cover Gas
11 V	200 A (DC-SP)	8-10 cm/min	8-10 gram/min	Ar (20-25 l)

TABLE 3--EB welding condition

Accelerating Voltage	Beam Current	Welding Speed	Working Distance	Focal Length
60 kV	300 mA	500 mm/min	400 mm	370 mm

In this paper, the tensile properties of the base metal specimens irradiated in the spectrally tailored capsules compared with those irradiated at the target position producing large amount of helium, and the effect of He is evaluated. Also, tensile properties of the weld metal and the weld joint are examined to evaluate the irradiation performance of the weldments including the susceptibility to the He embrittlement.

EXPERIMENTAL PROCEDURES

Tungsten Inert Gas (TIG) and Electron Beam (EB) welded joints made of titanium modified austenitic stainless steel (JPCA) were investigated in this study. The chemical composition of JPCA is listed in TABLE 1. JPCA was used in the solution annealed (SA) condition (1120°C) for both welding and irradiation. The welding conditions of each type of welding are listed in TABLE 2 and TABLE 3. TIG welding was performed with the TIG wire of chemical composition listed in TABLE 1, and EB welded joints were fabricated without filler metal. No post-welding heat treatments (PWHT) were performed on either type of weldments.

Base metal (BM), weld metal (WM) and weld-joint (WJ) type specimens were prepared to investigate the irradiation behavior of welded joints. These types of specimens were machined from different locations of the welded joints as shown in FIG. 1. Weld metal type specimens were made of all weld metal and the tensile specimens were machined in parallel with the weld direction. Weld joint type specimens contain base metal, heat affected zones (HAZ) and weld metal in each specimen. Two types of sheet tensile specimens, SS-1 and SS-3 type, were employed in this experiment. The dimensions of each type of specimen are shown in FIG. 2 with the location of each part in a WJ type specimen; i.e. a fusion line is located at the center of an SS-3 and one half of the specimen is the weld metal in both TIG and EB weldments, while weld metal is located at the center of an SS-1 specimen and the fusion lines are an both sides of the weld metal. The length of the weld metal part of EB WJ specimens is about 3-5 mm, while that of TIG WJ specimens is about 5-10 mm in both types of specimens.

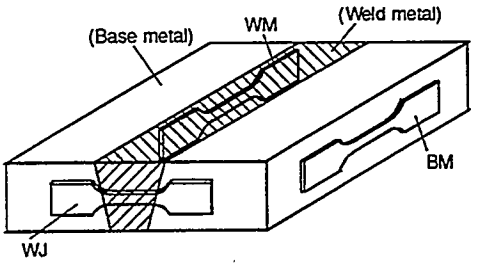

FIG. 1--The sampling location of specimens

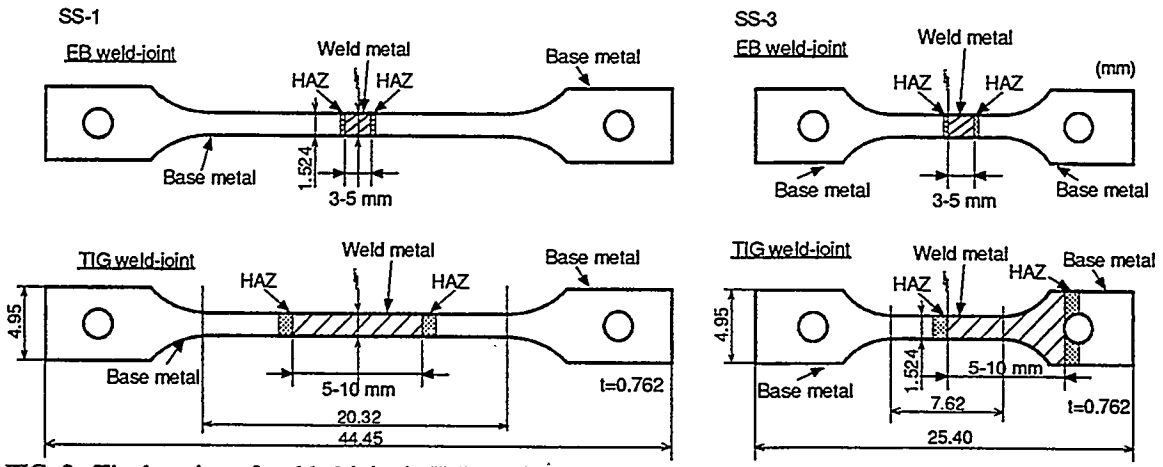

FIG. 2--The location of welded joint in WJ specimens

TABLE 4--Summary of Irradiation conditions (at capsule mid plane)

Capsules	Neutron Fluence (n/cm^2)			Dose	He	Irradiation Temperature
	Total	Thermal	Fast (E>0.1MeV)	(dpa)	(appm)	(°C)
JP-10,11,13,16	7.9×10^{22}	3.1×10^{22}	2.1×10^{22}	17.5	1 080	300, 400, 500, 600
JP-14*	1.5×10^{23}	6.0×10^{22}	4.1×10^{22}	33.9	2 400	400, 500
JP-17	1.3×10^{22}	4.8×10^{21}	3.7×10^{21}	3.0	50	250
JP-20*	3.7×10^{22}	4.5×10^{22}	1.0×10^{22}	8.2	350	400
6J	2.4×10^{22}	6.7×10^{21}	6.8×10^{21}	6.9	90	60, 200
7J	2.7×10^{22}	8.1×10^{21}	9.5×10^{21}	7.4	120	330, 400
60J-1	4.0×10^{22}	4.7×10^{21}	1.9×10^{22}	11.6	130	60
330J-1	4.0×10^{22}	4.7×10^{21}	1.9×10^{22}	11.6	130	330
200J-1*	3.3×10^{22}	4.0×10^{21}	1.6×10^{22}	9.8	100	200
400J-1*	3.3×10^{22}	4.0×10^{21}	1.6×10^{22}	9.8	100	400
6J+60J-1	6.4×10^{22}	1.1×10^{22}	2.8×10^{22}	17.5	240	60
6J+200J-1*	5.7×10^{22}	8.7×10^{21}	2.3×10^{22}	16.7	190	200
7J+330J-1	6.7×10^{22}	1.3×10^{22}	2.9×10^{22}	19.0	250	330
7J+400J-1*	6.0×10^{22}	1.2×10^{22}	2.6×10^{22}	17.2	220	400

*Estimated from reactor power data.

Base metal, weld metal and weld joint specimens were irradiated at target and Removable Beryllium (RB) positions in the High Flux Isotope Reactor (HFIR). The spectral tailoring applied in this HFIR RB experiment is based on the 2-step nuclear reaction of ^{58}Ni, ^{58}Ni(n, γ)^{59}Ni(n, α)^{56}Fe in which the thermal neutron flux is controlled by using a thermal neutron shield. On the other hand, the HFIR target capsules are exposed to a much higher thermal flux generating much more helium in the specimens during the irradiation. The HFIR target capsules, HFIR-MFE-JP-10, 11, 13, 14, 16, 17 and 20 (JP10-20, hereafter)were irradiated up to 34 dpa at temperatures ranging from 250 to 600°C. Spectral tailoring was applied to the RB capsules, HFIR-MFE-200J-1, 330J-1 and 400J-1 at temperatures of 200, 330 and 400°C up to the dose of 12 dpa. The similar spectrally tailoring irradiation (ORR-MFE-6J, -7J) to about 7 dpa were carried out in ORR. Some of the ORR irradiated specimens were re-encapsuled in RB capsules. Therefore, the total dose level of the spectrally tailored irradiation was up to 19 dpa. Hereafter, the spectrally tailoring irradiation (ORR+RB irradiation) is called as "ORR/RB" in this paper. The detailed irradiation conditions of each capsule are summarized in TABLE 4 and further information of each irradiation capsule can be found in other reports [5-10]. The neutron fluence listed in TABLE 4 is the

typical neutron fluence at the mid plane of each capsule. Some data in TABLE 4 were estimated from the reactor power data and the Greenwood's equations [11]. Since neutron flux has a distribution along the axial direction, the neutron fluence of each specimen varies according to its distance from the reactor mid plane. The damage and generated helium of each specimen were calculated using its position in the capsule. The dose level of each specimen is in the range of 2-34 dpa with 35-2380 appm He (He/dpa ~16-71) for JP10-20 and 7-19 dpa with 86-220 appm He (He/dpa ~11-16) for ORR/RB irradiation.

Tensile testing of irradiated specimens was carried out with an universal tensile machine in the hot laboratory at ORNL. The strain rates were 4×10^{-4} /s for SS-1 and 1×10^{-3} /s or 6×10^{-4} /s for SS-3 type specimens. Tensile testing was carried out at the nominal irradiation temperature of each irradiated specimen in vacuum. The 0.2% offset yield stress (YS), ultimate tensile stress (UTS), uniform elongation (Eu) and total elongation (Et) were obtained from the load-displacement curve of each specimen. The load drop just after yielding was neglected in the measurement of the uniform elongation. The fracture surface area of some specimens were measured with an optical microscope in order to calculate reduction of area (RA) and the fracture stress.

RESULTS AND DISCUSSION

Irradiation behavior of base metal

The irradiation in the spectrally tailored capsules

The SS-1 tensile specimens of JPCA SA were irradiated to 7 and 18 dpa in the temperature range between 200 to 400°C. The 0.2% offset yield stress levels of base metal (BM) specimens are plotted in FIG. 3.

It has been reported that the yield stress level saturates with the dose to a level depending on the temperature [1,12]. The yield stress levels exhibited almost no change between 7 and 18 dpa at 200°C. The yield stress level at 18 dpa seems to be close to the saturation level at 400°C. The yield strength increases rapidly with the first dose increment to 7 dpa, and both the total elongation and the uniform elongation decrease rapidly (see FIG.4 (e) and (g)) and the next dose increment between 7 and 18 dpa increased the yield stress only about 50% of that from 7 dpa. Evidence from related work indicates that the yield strength of 316 irradiated under similar conditions at 200-400°C has essentially saturated with dose by about 7 dpa [13].

The irradiation at 250°C with He/dpa ratios relevant to the fusion neutrons also conducted in the High Flux Reactor (HFR) at Petten and R2 reactor at Mol, and the results for JPCA SA are also plotted in FIG. 3 [14,15]. The yield stress level attained 655 MPa to 3 dpa, this was followed by an increase by only 150 MPa to 11 dpa. The tensile tests for the specimens irradiated at 330°C have been carried out for the specimens irradiated to one damage level of 7 dpa. Therefore, it is rather difficult to evaluate the saturation level. The yield stress levels of about 800 MPa at 330°C is, however, close to the saturation level at 250°C.

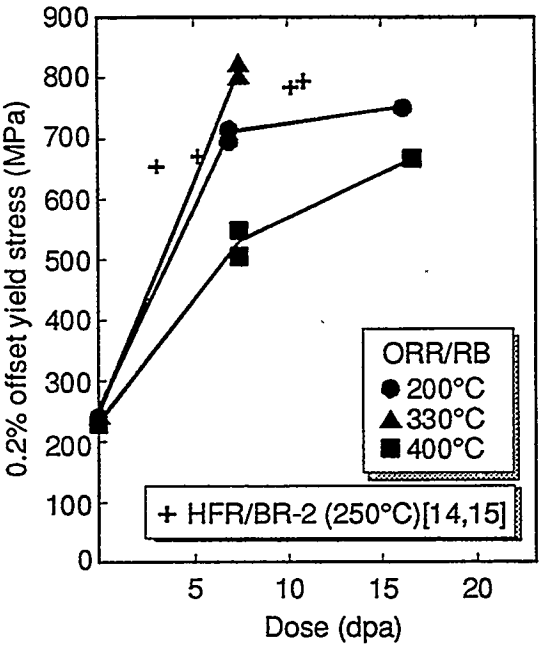

FIG. 3--Comparison of yield stress of PCA/JPCA irradiated in the different irradiation environments.[14,15]

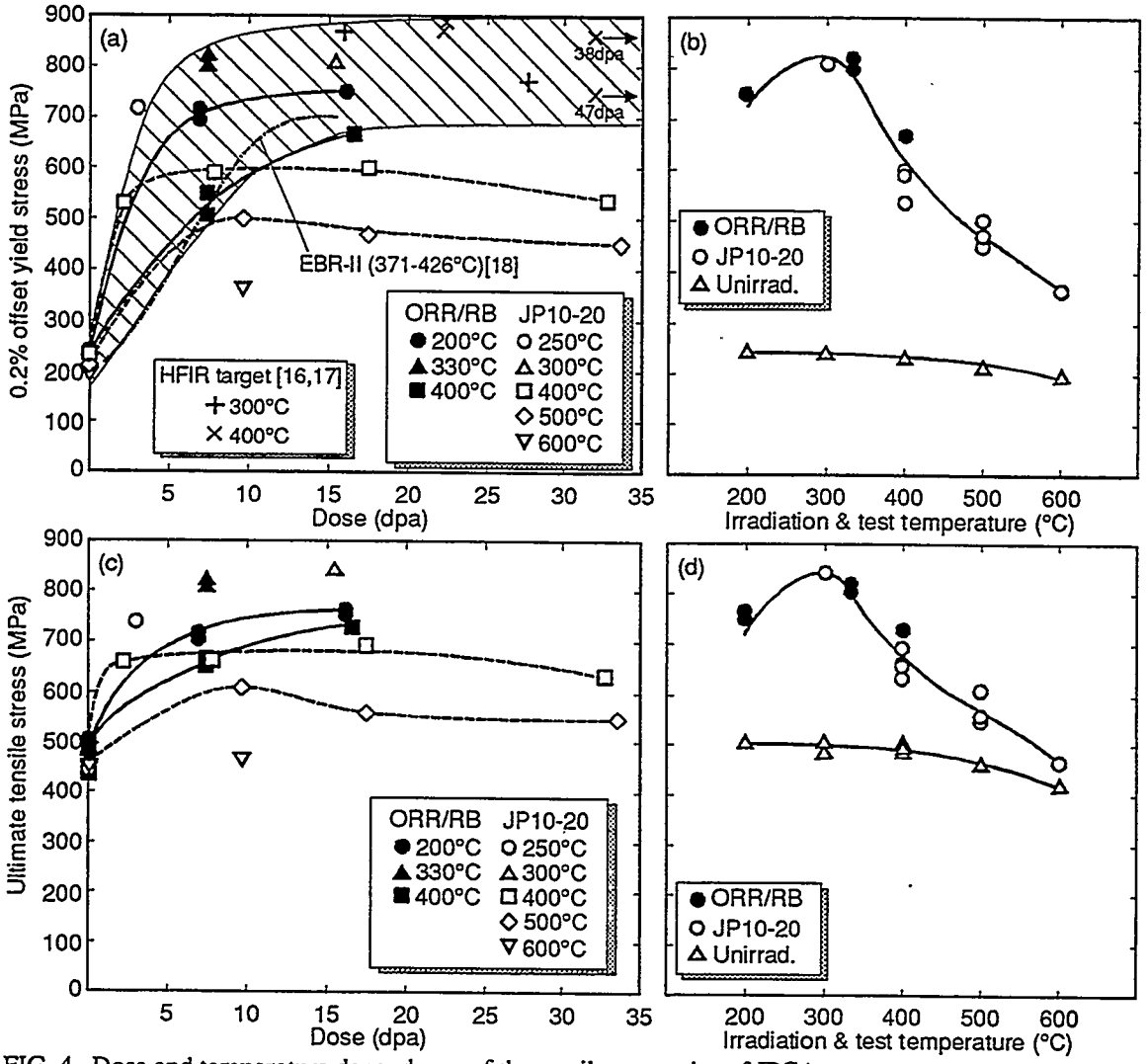

FIG. 4--Dose and temperature dependence of the tensile properties of JPCA irradiated in HFIR target capsules and spectrally tailored capsules. [16-18]

The irradiation at the target position in the HFIR

The SS-3 tensile specimens of JPCA SA were irradiated in JP10-20 to the dose levels ranging between 3 to 34 dpa at the temperatures ranging between 250 to 600°C. The He level is calculated to be 2400 appm for the specimens irradiated to 34 dpa. FIG. 4 (a) shows the yield stress levels of the JPCA SA before and after the irradiation (open symbols). The yield stress at 400°C increased by 300 MPa during the irradiation to only 2 dpa. This was followed by an increase by less than 100 MPa during the irradiation to 34 dpa. The saturation level at 400°C seems to be 550 MPa.

The tensile properties of JPCA SA irradiated at the HFIR target position have been reported previously [16,17]. The dose levels were ranged from 16 to 47 dpa. The yield stress of the previous experiments using round bar tensile specimen with the gauge section of 20.3 mm-long and 2.03 mm-diameter are also plotted in FIG. 4 (a). They are distributed in the hatched region, and indicating that the yield stress level saturated to dose levels between 10 and 20 dpa.

Plots for the spectral tailoring experiments (close symbols) also distributed in the hatched region, indicating that the helium effect on the yield stress level is rather small.

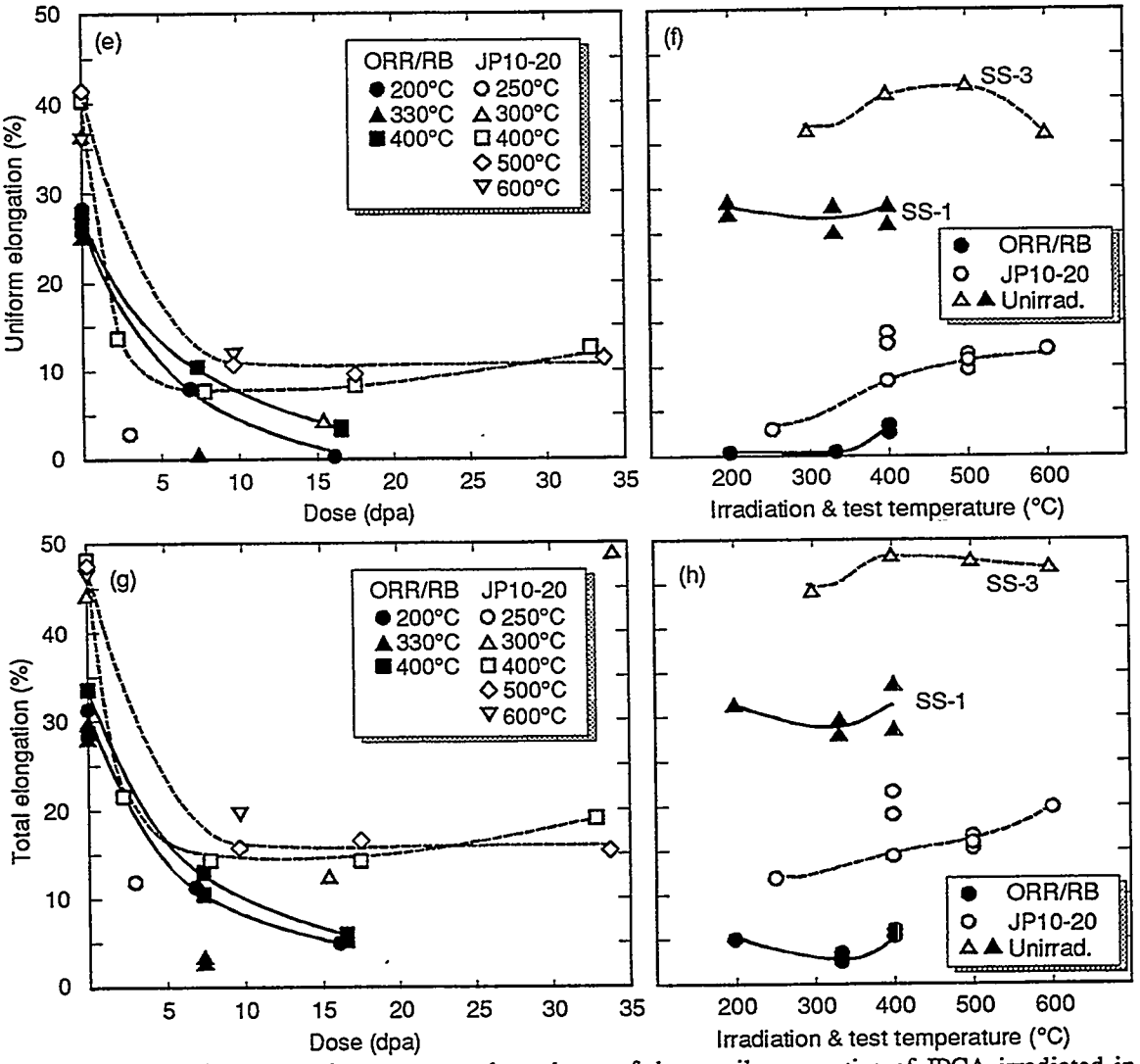

FIG. 4 (continued)--Dose and temperature dependence of the tensile properties of JPCA irradiated in HFIR target capsules and spectrally tailoring capsules.

The saturation level of the present results of HFIR target irradiation at 400°C is smaller than the previous results by more than 100 MPa. The temperature dependence at and above 400°C is rather large. The smaller saturation level may be resulted from that the irradiation temperature was higher than the expected temperature. Post-assembly inspection of capsules by X-ray radiograph technique, however, revealed that there was no disagreement between the measured and the designed gas gap dimensions.

Ultimate tensile strength, uniform elongation and total elongation are also plotted as functions of damage level and temperature in FIG. 4(c)-(h). The results with the damage levels higher than 7 dpa are plotted in the figures for the temperature dependence. Irradiation caused to increase UTS, as well as the yield stress. Total and uniform elongation decreased by irradiation. Higher yield stress accompanied with lower uniform elongation. The yield stress level decreased with temperature, while the uniform elongation increased.

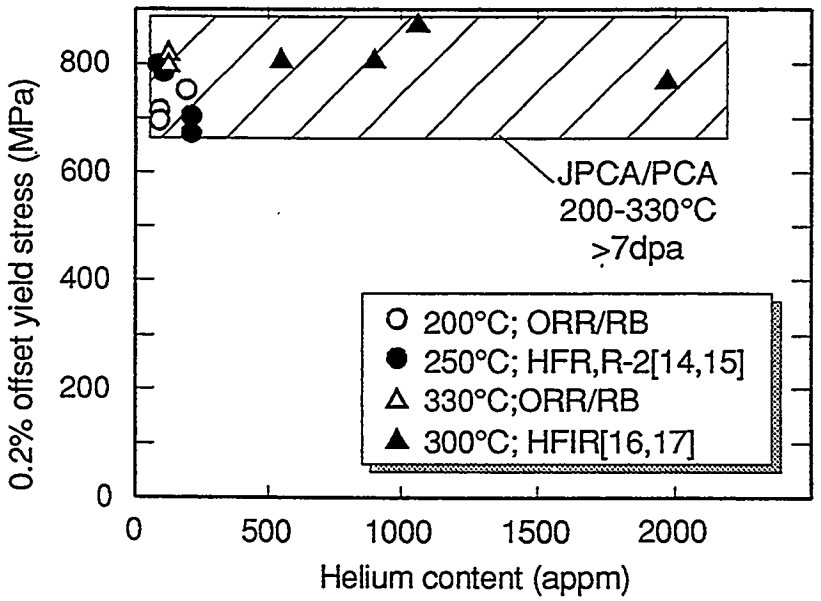

FIG. 5--Yield stress of PCA/JPCA irradiated in the different irradiation environments as a function of helium level.[14-17]

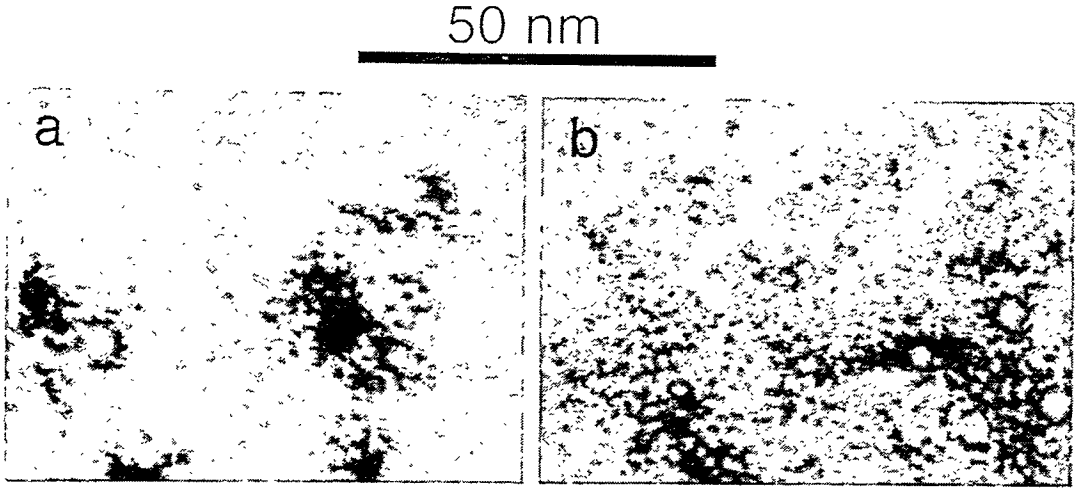

FIG. 6---Microstructure of JPCA irradiated at 400°C in (a) ORR 6J/7J (7 dpa) and (b) HFIR target capsules (17 dpa). [19,20]

TABLE 5--Cavities and dislocation loops in HFIR target and ORR irradiations

	Irradiation temperature	Cavities		Dislocation loops	
		Number density ($10^{23}/m^3$)	Average diameter (nm)	Number density ($10^{23}/m^3$)	Average diameter (nm)
HFIR 17 dpa (1100 appmHe)	400°C	6.9	2.5	0.4	36
ORR 7 dpa (130 appmHe)	400°C	0.3	2.6	2.2	27

Helium Effect on Tensile Properties

There is no significant difference between the levels of the yield stress after the irradiation in JP10-20 and those in ORR/RB. This is also true for UTS. On the other hand, the elongation for the specimens irradiated in ORR/RB are systematically smaller than those irradiated in JP10-20. The tensile specimen of SS-1 was irradiated in ORR/RB, while SS-3 was used for the JP10-20 irradiation. The sizes of SS-1 and SS-3 specimens are identical, except for the gauge length. Gauge length of SS-1 is 20.3 mm, which is 2.7 times longer than that of SS-3. The absolute value of elongation due to neck development is the same in both types of specimen, which correspond to 3% and 7.8% in total elongation for SS-1 and SS-3, respectively. The uniform elongation of these specimens also has some deference, as shown in FIG. 4 (f). One of the reason of this is the deformation occurred at the outside of the gauge section. Therefore, the elongation obtained from the different types of the specimens is not suitable to compare the ductility. As another index of ductility, reduction of area (RA) is applicable. The measurement of RA is in progress to compare the ductility of the specimens irradiated in each irradiation environments.

The yield stress data at or close to the saturation level are plotted against the helium levels in FIG. 5. No strong effect of helium on the yield stress level is seen.

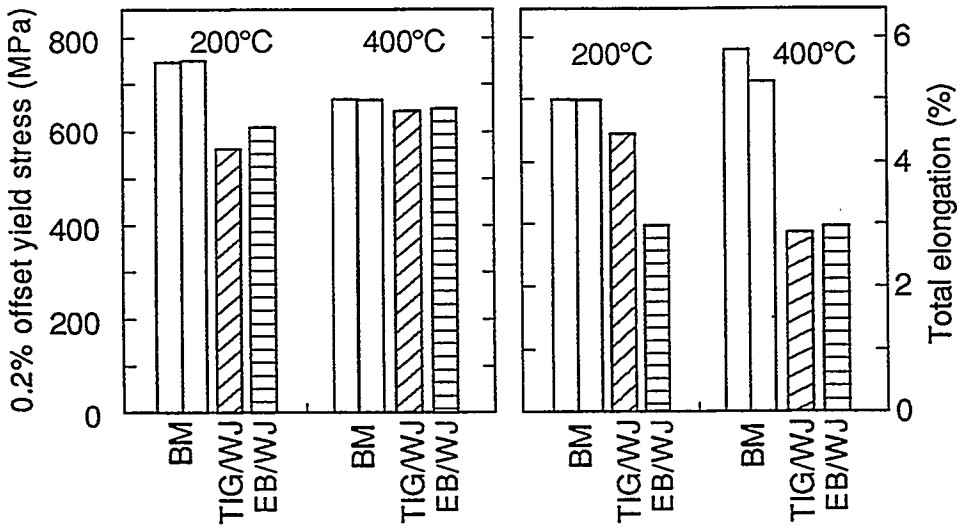

FIG. 7--The tensile properties of TIG and EB weld-joint specimens irradiated in spectrally tailoring capsules to 17 dpa.

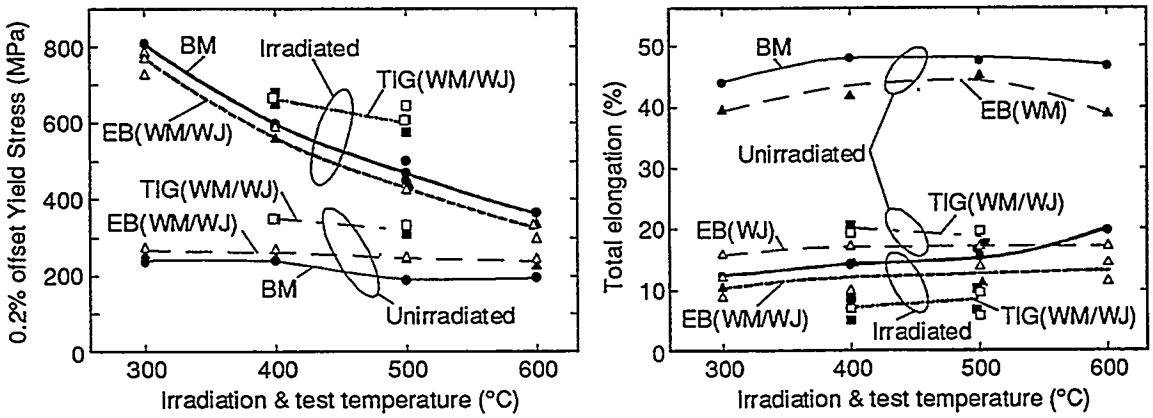

FIG. 8--Tensile properties of TIG and EB welded joints before and after irradiation to 8-34 dpa in HFIR target capsules.

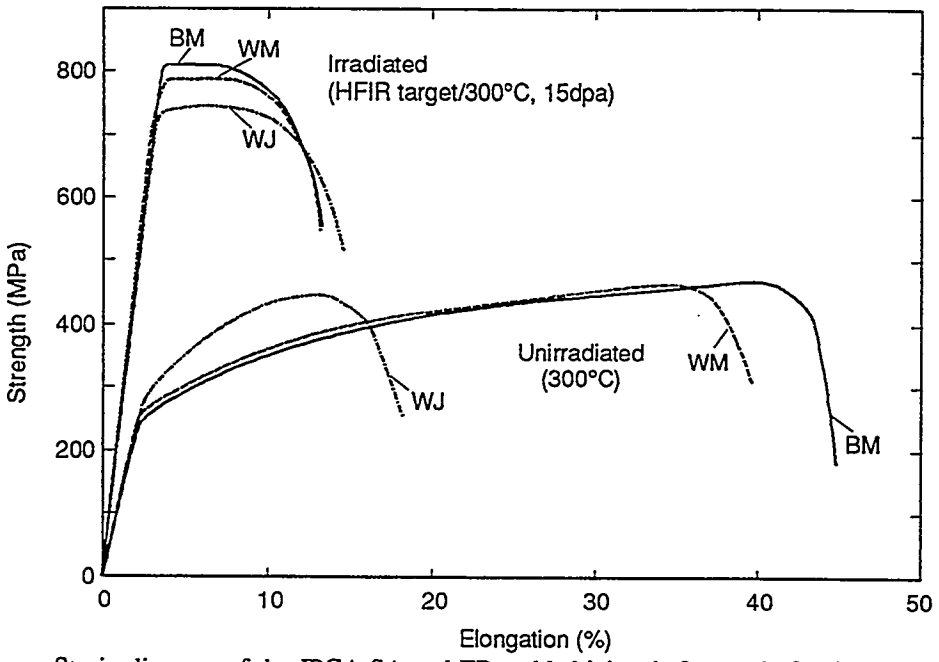

FIG. 9--Stress-Strain diagram of the JPCA SA and EB welded joints before and after irradiation in HFIR target capsules.

Microsructural observations on the specimens irradiated to 7 dpa in ORR/RB and those irradiated to 17 dpa in JP10-20 have been carried out. The tensile specimens irradiated in ORR/RB to 7 dpa and in JP10-20 to 17 dpa exhibited similar levels ranged from 500 to 550 MPa at 400°C. FIG. 6 shows TEM images in the kinematical condition [19,20]. The number densities and the diameters of the dislocation loops and the cavities observed in the specimens irradiated at 400°C in JP10-20 and ORR/RB are summarized in Table 5. The number density of cavities after the irradiation in JP10-20 is about twenty times higher than that of in ORR irradiation. In addition, more dislocation loops developed in the spectrally tailored irradiation. These differences in the microstructure suggest the hardening observed in both HIFR target and ORR/RB irradiation might be caused by the different mechanism; i. e. the irradiation hardening was strongly affected by cavities in JP10-20 irradiation, while it was caused by the frank loops mainly in ORR/RB irradiation, in spite of their similar yield stress levels.

The performance of the weld metal and the weld joint

FIG. 7 shows the yield stress and the total elongation of weld joint specimens of JPCA SA irradiated to 18 dpa in ORR/RB at 200 and 400°C. The results of JPCA SA base metal specimens are also plotted with those of the weld joint specimens of TIG and EB in the figure. The TIG WJ and EB WJ specimens exhibited slightly lower yield stress levels than that of base metal. This is similar to the result for the WJ specimens of 316 stainless steel irradiated to 7 dpa in MFE6/7J [21].

The total elongation of the JPCA TIG WJ and the EB WJ specimens are about 3%. This values are also close to those of the 316 TIG WJ and EB WJ.

The tensile properties of weldments irradiated in JP10-20 at temperatures ranging between 300 and 600°C to a damage level of about 17 dpa are plotted in FIG. 8. The yield stress levels and the total elongation of the weldments of JPCA with TIG and EB welding techniques are plotted with JPCA SA base metal. Results for the unirradiated specimens are also plotted in the figure. The yield stress levels of the TIG WM and WJ specimens were higher than base metal before and after the irradiation. The position of fracture

has not been examined yet, however the lower yield stress levels for the EB welded specimens indicates that plastic deformation had mainly occurred in the weld metal region.

As indicated in FIG. 9, the elongation values of the WJ specimens before irradiation were often significantly smaller than those of the base metal specimens. The smaller elongation value for the WJ may be caused by the localized deformation in the weld metal region comparing with those of the heat affected zone and the base metal region. The deformation behaviors of the weld metal, the heat affected zone and the base metal regions in the WJ specimens are different. Therefore, the significance of the elongation values of the WJ specimens are not quite clear. On the other hand, the value of the reduction of area (RA) indicates the ductility level where fracture occurred.

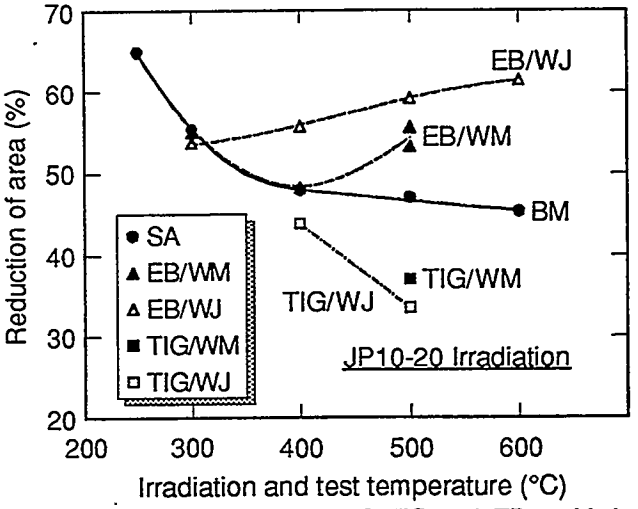

FIG. 10--Reduction of area of TIG and EB welded joints of JPCA SA irradiated to 3-18 dpa in HFIR target capsules.

The reduction of area can also be used as an indication of the ductility of the welded specimens. The RA values after the irradiation in JP10-20 are shown in FIG. 10. Note that while the irradiated RA values of the EB WM and WJ specimens are equal to or higher than the RA values of the base metal, the total elongation (FIG. 8) of the EB WM and WJ specimens were slightly less than the base metal. All the RA values are rather large suggesting the residual ductility level after irradiation is high enough for the application to fusion reactor components.

The welding often causes to form coarse grains at the heat affected zone and in the weld metal region. Because the He embrittlement is accompanied with the grain boundary separation, the welding may increase susceptibility to He embrittlement. The RA for EB/WJ specimens irradiated to 17 dpa with a helium levels of 1080 appm are revealed to be large and are higher than those of JPCA SA even at the highest temperature of 600°C.

CONCLUSION

The tensile properties of the base metal and TIG and EB welded joints of JPCA irradiated in HFIR target capsules and spectrally tailored capsules were studied.

1. The post irradiation strengths and the elongation values tend to saturate with the displacement damage at the temperatures below 400°C. No large effect of helium on the saturation levels is obtained.
2. The tensile properties of welded joints were very similar to those of the base metal. The weld metal and the weld joint specimens exhibited the same temperature and dose dependence as the base metal after irradiation.
3. Reduction of area observed in welded joints suggests weldments still retain enough ductility after irradiation.

ACKNOWLEDGMENTS

The authors appreciate the ORNL hot laboratory staff for the testing of irradiated specimens. We also thank to technicians of M&C division for their great assistance to the completion of this research.

This research was sponsored by the Japan Atomic Energy Research Institute and the Office of Fusion Energy Sciences, U.S. Department of Energy, under contract DE-AC05-96OR22464 with Lockheed Martin Energy Research Corporation.

REFERENCES

[1] Tavassoli, A.A., "Assessment of austenitic stainless steels", Fusion Engineering and Design 29 (1995), 371-390.

[2] Stoller, R.E. and Odette, G.R., "The effect of helium on swelling in stainless steel: influence of cavity density annd morphology", Effects of Radiation on Materials: 11th International Symposium, ASTM STP 782, F.R. Brager, and J.S. Perrin, Eds., American Society For Testing and Materials, Philadelphia, (1982) 275-294.

[3] Rowcliffe, A.F., Hishinuma, A., Grossbeck, M.L. and Jitsukawa, S, "Radiation effects at fusion reactor He:dpa ratios", J. Nucl. Mater. 179-181 (1991) 125-129.

[4] Kesternich, W. and Nandedkar, R.V., "On the role of helium in high temperature embrittlement of irradiated austenitic steels", Effects of Radiation on Materials: 14th International Symposium, ASTM STP 1046, N.H. Packan, R.E. Stoller and A.S. Kumar, Eds., American Society For Testing and Materials, Philadelphia, (1990) 284-294.

[5] Greenwood, L.R. and Ratner, R.T., "Neutron dosimetry and calculation for the JP-10, 11, 13 and 16 experiments in HFIR" Fusion Reactor Material Semiannual Progress Report, DOE/ER-0313/19, Office of Fusion Energy (1995) 281-283.

[6] Greenwood, L.R. and Baldwin, C.A., "Neutron dosimetry and calculation for the JP-17, 18 and 19 experiments in HFIR", Fusion Reactor Material Semiannual Progress Report, DOE/ER-0313/19, Office of Fusion Energy (1995) 286-290.

[7] Greenwood, L.R. Baldwin, C.A. and Oliver, B.M., "Neutron dosimetry, damage calculations and helium measurements for the HFIR-MFE-60J-1 and MFE-330J-1 spectral tailoring experiments", Fusion Reactor Material Semiannual Progress Report, DOE/ER-0313/17, Office of Fusion Energy (1994) 28-34.

[8] Pawel, J.E., Lenox, K.E. and Ioka, I., "Status of DOE/JAERI collaborative program Phase II and Phase III capsules" Fusion Reactor Material Semiannual Progress Report, DOE/ER-0313/19, Office of Fusion Energy (1995) 312-313.

[9] Greenwood, L.R., "Neutron Dosimetry and Damage Calculations for the ORR-MFE 7J Experiment" Fusion Reactor Material Semiannual Progress Report, DOE/ER-0313/6, Office of Fusion Energy (1989) 23-25.

[10] Greenwood, L.R., "Neutron Dosimetry and Damage Calculations for the ORR-MFE 6J Experiment" Fusion Reactor Material Semiannual Progress Report, DOE/ER-0313/8, Office of Fusion Energy (1990) 34-42.

[11] Greenwood, L.R., "A new calculation of thermal neutron damage and helium production in nickel", J. Nucl. Mater. 115 (1983) 137-142.

[12] Horsten, M.G. and de Vries, M.I, "Irradiation hardening and loss of ductility of type 316L(N) stainless steel plate material due to neutron-irradiation", Effects of Radiation on Materials: 17th International Symposium, ASTM STP 1270, D.S. Gelles, R.K. Nanstad, A.S. Kumar, and E.A. Little, Eds., American Society for Testing and Materials, 1995. (in press)

[13] Pawel, J.E., Ioka, I., Rowcliffe, A.F., Grossbeck, M.L. and Jitsukawa, S., "Temperature Dependence of the Deformation Behavior of 316 Stainless Steel after Low Temperature Neutron

Irradiation", Effects of Radiation on Materials: 18th International Symposium, ASTM STP 1325, R.K. Nanstad, M.L. Hamilton, F.A. Garner and A.S. Kumar, Eds., American Society for Testing and Materials, 1997. (these proceedings)

[14] Elen, J.D. and Fenici, P., "Fast neutron irradiation hardening of austenitic stainless at 250°C", J. Nucl. Mater. 191-194 (1992) 766-770.

[15] Jitsukawa, S., Grossbeck, M.L. and Hishinuma, A., "Stress-strain relations of irradiated stainless steels below 673K", J. Nucl. Mater. 191-194 (1992) 790-794.

[16] Tanaka, M.P., Hishinuma, A., Hamada, S. and Grossbeck, M.L., "Post irradiation tensile and fatigue behavior of austenitic PCA stainless steels irradiated in HFIR", J. Nucl. Mater. 155-157 (1988) 957-962.

[17] Hishinuma, A. and Jitsukawa, S., "Radiation damage of HFIR-irradiated candidate stainless steels for fusion applications", J. Nucl. Mater. 169 (1989) 241-248.

[18] Brager, H.R., Blackburn, l.D. and Garner, F.A., "The dependence on disolacement rate of radiation-induced changes in microstructure and tensile properties of ANSI 304 and 316", J. Nucl. Mater. 122-123 (1984) 332-337.

[19] Sawai, T., Shiba, K. and Hishinuma, A., "Microstructural Observation on HFIR-irradiated Austenitic Stainless Steels Including Welds from JP9-16" Fusion Reactor Material Semiannual Progress Report, DOE/ER-0313/19, Office of Fusion Energy (1995) 217-222.

[20] Sawai, T., Maziasz, P.J., Kanazawa, H. and Hishinuma, A., "Microstructural evolution of austenitic stainless steels irradiated in spectrally tailored experiment in ORR at 400°C", J. Nucl. Mater. 191-194 (1992) 712-716.

[21] Jitsukawa, S., Maziasz, P.J., Ishiyama, T., Gibson, L.T. and Hishinuma, A., "Tenisile properties of austenitic stainless Steels and their weld joints after irradiation by the ORR-spectrally-tailoring experiment", J. Nucl. Mater. 191-194 (1992) 771-775.

IRRADIATION CREEP AND SWELLING OF VARIOUS AUSTENITIC ALLOYS IRRADIATED IN PFR AND FFTF - F.A. Garner and M.B. Toloczko (Pacific Northwest National Laboratory)[1] - B. Munro and S. Adaway (AEA Technology), J. Standring (UKAEA, retired).

To be published in the Proceedings, 18th ASTM International Symposium on Effects of Radiation on Materials, Hyannis, MA, June 1996.

EXTENDED ABSTRACT

In order to use data from surrogate neutron spectra for fusion applications, it is necessary to analyze the impact of environmental differences on property development. This is of particular importance in the study of irradiation creep and its interactions with void swelling, especially with respect to the difficulty of separation of creep strains from various non-creep strains.

As part of an on-going creep data rescue and analysis effort, the current study focuses on comparative irradiations conducted on identical gas-pressurized tubes produced and constructed in the United States from austenitic steels (20% CW 316 and 20% CW D9), but irradiated in either the Prototype Fast Reactor (PFR) in the United Kingdom or the Fast Flux Test Facility in the United States. In PFR, Demountable Subassemblies (DMSA) serving as heat pipes were used without active temperature control. In FFTF the specimens were irradiated with active (±°5C) temperature control. Whereas the FFTF irradiations involved a series of successive side-by-side irradiation, measurement and reinsertion of the same series of tubes, the PFR experiment utilized simultaneous irradiation at two axial positions in the heat pipe to achieve different fluences at different flux levels. The smaller size of the DMSA also necessitated a separation of the tubes at a given flux level into two groups (low-stress and high-stress) at slightly different axial positions, where the flux between the two groups varied ≤ 10%. Of particular interest in this study was the potential impact of the two types of separation on the derivation of creep coefficients.

It was shown that when the axial separations in PFR were relatively small, there was no impact on the derived creep coefficients. Thus, for the low-stress and high-stress separations, the impact was negligible. For separations involving more significant flux-ratio separations (0.67 and 0.83) the impact was larger and necessitated treating the low-flux and high-flux sets as separate data sets. The influence of flux differences were expressed in the non-creep strains, specifically the carbide-related densification and the void swelling. The creep coefficients themselves were not affected, however. Thus the variations in behavior in PFR were only a reflection of the well-known history effect on void swelling. When comparing the results between PFR and FFTF, the non-creep strains again showed a sensitivity to the different temperature/stress/flux history of each reactor, but the creep coefficients were again found to be relatively insensitive. The results of both experiments validated the use of the Bo +DṠ creep model employed in all earlier studies.

[1]Operated for the US Department of Energy by Battelle Memorial Institute under Contract DE-AC06-76RLO 1830

RADIATION-INDUCED INSTABILITY OF MnS PRECIPITATES AND ITS POSSIBLE CONSEQUENCES ON IASCC OF AUSTENITIC STAINLESS STEELS - HM Chung (Argonne National Laboratory), FA Garner (Pacific Northwest National Laboratory)

To be published in the Proceedings, 18th ASTM International Symposium on Effects of Radiation on Materials, Hyannis, MA, June 1996.

EXTENDED ABSTRACT

Irradiation assisted stress corrosion cracking (IASCC) continues to be a significant materials issue for the light water reactor industry and may also pose a problem for fusion power devices that employ water cooling. Although a number of potential mechanisms have been proposed to participate in this phenomenon, at this time it is not clear that any of these candidate mechanisms are sufficient to rationalize the observed failures.

A new mechanism is proposed in this paper that involves the radiation-induced release into solution of elements not usually thought to participate in IASCC. It is shown in this paper that MnS precipitates, which contain most of the sulphur in stainless steels, are probably unstable under irradiation. First, the Mn transmutes very strongly to Fe in highly thermalized neutron spectra. Second, the combination of cascade-induced disordering and the inverse-Kirkendall effect operating at the incoherent interfaces of MnS precipitates will probably act as a pump to export Mn from the precipitate surface into the alloy matrix. Both of these processes will most likely allow some of the sulphur to re-enter the alloy matrix. Sulphur is known to exert a deleterious influence on grain boundary cracking. MnS precipitates are also thought to be a reservoir of other deleterious impurities such as fluorine which could be also released due to radiation-induced instability of the precipitates.

This possibility has been confirmed by Auger electron spectroscopy on Types 304, 316 and 348 stainless steel specimens sectioned from several BWR components irradiated up to 3.5×10^{21} n cm^2 ($E > 1$ MeV). Prior to irradiation, the composition of the various analyzed precipitates was found to be nearly stoichiometric MnS. As the irradiation proceeds, however, the Mn was progressively replaced by Fe, Cr, Ni and smaller amounts of many impurities of relatively low solubility. The loss of Mn from the precipitate in favor of Fe, Ni and Cr is consistent with the strong operation of the Inverse Kirkendall effect. In order to further validate the feasibility of the MnS instability proposal, additional examination using scanning electron microscopy and electron-dispersive x-ray analysis is required. Planning for such activities is now in progress.

TENSILE BEHAVIOR OF IRRADIATED MANGANESE-STABILIZED STAINLESS STEEL - R. L. Klueh (Oak Ridge National Laboratory)

Journal of Nuclear Materials

Publication Expected: Fall, 1996

EXTENDED ABSTRACT

Tensile tests were conducted on seven experimental, high-manganese austenitic stainless steels after irradiation up to 44 dpa in the FFTF. An Fe-20Mn-12Cr-0.25C base composition was used, to which various combinations of Ti, W, V, B, and P were added to improve strength. Nominal amounts added were 0.1% Ti, 1% W, 0.1% V, 0.005% B, and 0.03% P. Irradiation was carried out at 420, 520, and 600°C on the steels in the solution-annealed and 20% cold-worked conditions. Tensile tests were conducted at the irradiation temperature. Results were compared with type 316 SS.

Neutron irradiation hardened all of the solution-annealed steels at 420, 520, and 600°C, as measured by the increase in yield stress and ultimate tensile strength. The steel to which all five elements were added to the base composition showed the least amount of hardening. It also showed a smaller loss of ductility (uniform and total elongation) than the other steels. The total and uniform elongations of this steel after irradiation at 420°C was over four times that of the other manganese-stabilized steels and 316 SS. There was much less difference in strength and ductility at the two higher irradiation temperatures, where there was considerably less hardening, and thus, less loss of ductility.

In the cold-worked condition, hardening occurred only after irradiation at 420°C, and there was much less difference in the properties of the steels after irradiation. At the 420°C irradiation temperature, most of the manganese-stabilized steels maintained more ductility than the 316 SS. After irradiation at 420°C, the temperature of maximum hardening, the steel to which all five of the elements were added had the best uniform elongation.

6.0 INSULATING CERAMICS AND OPTICAL MATERIALS

IN-SITU MEASUREMENT OF THE ELECTRICAL CONDUCTIVITY OF ALUMINUM OXIDE IN HFIR - S.J. Zinkle, D.P. White, L.L. Snead, W.S. Eatherly, A.L. Qualls, D.W. Heatherly, R.G. Sitterson, R.L. Wallace, D.G. Raby and M.T. Hurst (Oak Ridge National Laboratory), E.H. Farnum and K. Scarborough (Los Alamos National Laboratory), T. Shikama and M. Narui (Tohoku University), and K. Shiiyama (Kyushu University)

OBJECTIVE

The objective of this work is to determine the existence or absence of bulk radiation induced electrical degradation (RIED) in neutron-irradiated Al_2O_3.

SUMMARY

A collaborative DOE/Monbusho irradiation experiment has been completed which measured the in-situ electrical resistivity of 12 different grades of aluminum oxide during HFIR neutron irradiation at 450°C. No evidence for bulk RIED was observed following irradiation to a maximum dose of 3 dpa with an applied dc electric field of 200 V/mm.

PROGRESS AND STATUS

Introduction

Ceramic insulators are required for the heating, control and diagnostic measurement of magnetically confined plasmas [1]. A potentially serious degradation of the electrical resistance of ceramic insulators, known as radiation induced electrical degradation (RIED), has raised concern about the suitability of ceramic insulators in intense radiation fields [1-5]. Since the original reported observation of RIED by Hodgson in 1989 [4], numerous studies have been performed with conflicting results (see ref. 3 for a recent summary). Previous studies indicate that RIED is most pronounced at temperatures between 300 and 600°C and at applied voltages >100 V/mm, with an apparent maximum degradation rate occurring near 450°C. Therefore, the present HFIR experiment was chosen to be performed at 450°C with an applied potential of 200 V/mm. The experiments were performed in the Temperature-Regulated In-Situ Test (TRIST) facility located in a Removable Beryllium position of the High Flux Isotope Reactor (HFIR) at Oak Ridge National Laboratory (ORNL). A total of 15 specimens were irradiated in the in-situ electrical conductivity capsule. The specimen matrix included 12 different grades of polycrystal and single crystal alumina (Table 1) in order to confirm published studies which suggested that the threshold dose for initiation of RIED depends on specimen purity [5,6].

Experimental Procedure

The Al_2O_3 specimens were machined into disks that were 8.5 mm diameter by 0.75 mm thick. The specimens were vacuum brazed at 870°C to alumina pedestals using a Ticusil braze foil. This braze material covered the entire bottom surface of the sample and the top of a nickel pin which served as the rear electrode. The alumina pedestal was simultaneously vacuum brazed to a vanadium heat sink using Ticusil braze foil. InCuSil braze pads were applied to the center and guard electrode regions on the top surface of the alumina specimens. Nickel wires were subsequently laser welded to the braze pads to provide a secure electrical connection. Metallic electrodes were then sputtered onto the specimens in a guard ring configuration with a 4 mm central electrode diameter and a 1.0 mm gap between the central electrode and the guard ring. The electrodes were deposited as a thin layer (<0.1 μm) of titanium followed by ~1 μm Pt layer using a two-gun vacuum deposition system. Ohmic behavior of the Ti + Pt electrodes (in the absence of irradiation) was verified for a Wesgo AL995 and sapphire specimen. All of the subcapsules were sealed to minimize the amount of surface contamination buildup during irradiation.

Table 1: Specimen list for the HFIR TRIST-ER1 in-situ electrical conductivity capsule.

HFIR position	Material	Appl. Voltage	Vendor and grade
1	Al_2O_3, single crystal	150 V	Crystal Systems (Hemex UV grade) a-axis
2	Al_2O_3, single crystal	150 V	Crystal Systems (Hemex UV grade) c-axis
3	Al_2O_3, single crystal	150 V	Crystal Systems (Hemex regular) c-axis
4	Al_2O_3, single crystal	150 V	Crystal Systems (Hemex regular) a-axis
5	Al_2O_3, polycrystalline	150 V	Vitox (99.9% purity, Morgan Matroc, Anderman Div.)
6	Al_2O_3, polycrystalline	150 V	Kyocera A-480 (99.9% purity)
7	Al_2O_3, polycrystalline	150 V	Wesgo AL300 (97.0% purity)
8	Al_2O_3, polycrystalline	150 V	Kyocera A-479 (99.0% purity)
9	Al_2O_3, polycrystalline	150 V	Coors AD998 (99.8% purity)
10	Al_2O_3, polycrystalline	150 V	Wesgo AL995 (99.5% purity)
11	Al_2O_3, polycrystalline	0 V	Wesgo AL995 (99.5% purity)
12	Al_2O_3, single crystal	0 V	Crystal Systems (Hemex regular) c-axis
13	Al_2O_3+Cr, single crystal	150 V	Union Carbide (UV grade), 60° from c axis
14	Al_2O_3, single crystal	150 V	Kyocera SA100 ($1\bar{1}02$ orientation)
15	Al_2O_3, single crystal	0 V	Kyocera SA100 ($1\bar{1}02$ orientation)

A total of 60 stainless steel sheathed, mineral insulated (MI) cables were used to instrument the samples contained in the subcapsules. A 1.1 mm OD triaxial MI cable with a copper center wire and a braided copper sheath was used as the low-side data lead from each subcapsule. A 1.6 mm OD coaxial MI cable with a copper center conductor was used as the power lead. The leads for the coax and triax cables were torch-brazed to the appropriate Ni wires from each subcapsule. The line resistances of the MI coaxial and triaxial cables were all ~1 Ω. The specimen temperatures were continuously monitored by two chromel/alumel (type K) thermocouples embedded in each subcapsule. Further details about the capsule design and assembly are given elsewhere [7].

The capsule was cooled with 49°C reactor coolant water flowing downward at a flow rate of 0.9 l/s, with a water temperature rise of 5°C over the length of the capsule. The sample temperatures were controlled by adjusting the composition of a flowing mixture of helium and neon in the control gas gap between the subcapsules and the holder sleeve [7,8]. The gas gap on the outside of each vanadium subcapsule body was sized, based on a thermal analysis and the known HFIR nuclear heating axial profile, to maintain an irradiation temperature of ~450°C during irradiation. The output of the 30 thermocouples was fed into a PC-based μDCS Plus control system. Operating temperatures, pressures, and flow rates were monitored continuously and trended at a rate of approximately once per 5 to 10 seconds. The measured irradiation temperatures for the 15 subcapsules ranged from ~440 to 500°C, depending on the subcapsule position. Details of the irradiation temperature history are described elsewhere [8].

The in-situ electrical measurements were performed in full accordance with the guidelines outlined in ASTM Standard Test Method for DC Resistance or Conductance of Insulating Materials (ASTM D257-91), and also followed the IEA guidelines established at a ceramics fusion energy workshop in Stresa, Italy [9]. In particular, the measurements utilized a guard ring configuration with secure, low resistance electrical connections and the dimensions of the electrodes met ASTM recommendations. Data acquisition and control was performed using a National Instruments Labview III program running on a Macintosh computer. A Keithley 7002 matrix switch system (containing Keithley 7169A switch cards on the high side and 7058 switch cards on the low side) was used to switch the specimen leads to the appropriate electrical instruments. A dc potential of 150 V was continuously supplied to the brazed base surface of 12 of the specimens (except for brief periods when electrical measurements were taken) by two HP 6035A power supplies, producing an electric field of 200 V/mm in the specimens.

Several different types of electrical measurements were performed on the specimens in order to differentiate between bulk conductivities and surface conductances. First, the specimen current through the guard and center electrode leads with an applied potential of 100 V was periodically measured in order to monitor the qualitative electrical conductivity of the specimens. A Keithley 237 Source Measure Unit was used to supply the specimen voltage and measured the corresponding current through the coax cable, and two Keithley 6517 high-resistance electrometers were used to measure the guard and center electrode currents for each specimen. A Keithley 617 electrometer was used to independently measure the potential supplied by the 237 power supply. These measurements were performed with a frequency of about twice per hour during the first five days of the irradiation, and about twice per day thereafter. In addition, measurements were taken more frequently (about 20 times per hour) during reactor startup and shutdown. Second, the ohmic nature of these electrical measurements was determined with the same set of electrical equipment over a typical potential range of +100 V to -100V with 20 V increments. These measurements were typically performed about once per day (more frequently during reactor startup and shutdown). A limited set of ohmic check measurements were also performed from +10 V to -10 V and from +150 V to -150 V on selected specimens in order to further study the electrical behavior. Third, a series of four types of diagnostic measurements were performed approximately twice per month which allowed the surface resistance and cable insulation conductivities to be measured. The first diagnostic test measured the leakage current from the center lead of each coax cable at voltages from +100 V to -100 V while the triax cable was floating. The other three diagnostic tests applied voltages from +2 V to -2 V in 0.5 V increments to the center and/or guard sheath of each triax cable. This allowed the center-guard and guard-ground resistances to be measured for each subcapsule/triax cable pair, and allowed the possible presence of gaseous conduction current paths to be detected. Finally, the ac impedance was measured over a frequency of 100 Hz to 10 MHz using an HP4194A Impedance/ Gain-Phase Analyzer. Further details regarding the electrical equipment, cabling, and Labview program capabilities are described elsewhere [10-13].

For each electrical measurement, a settling time of 20 to 30 seconds was typically used from the time the specimen was switched to the power supply until the electrical currents were measured in order to eliminate signal noise associated with the cable and specimen capacitance. Due to the long cable length (~20 m), the specimen capacitance was negligible (3 orders of magnitude smaller) compared to the cable capacitance. Similarly, the circuit resistance was mainly determined by the coax cable resistance, since the specimen and cable resistances were in parallel and the specimen resistance was typically 3 orders of magnitude larger than the cable resistance during irradiation. Using a calculated cable capacitance of ~10 pF and a typical cable resistance of 100 kΩ during irradiation, the calculated circuit RC time constant is ~1 ms, which is negligible compared to the settling times used for the data collection. During the reactor startup and shutdown, a settling time of 5 to 10 seconds was typically used in order to obtain data more rapidly. Experimental tests at applied potentials between +100 V and -100 V on several specimens during full-power HFIR irradiation demonstrated that the measured electrical currents were similar for settling times between 5 seconds and 180 seconds.

During the first five days of the irradiation, all of the biased specimens which were not undergoing an electrical measurement were left connected to the 150 V dc bias from the HP power supplies. This was performed in order to minimize the amount of time that the "biased" samples were exposed to irradiation with the electric field turned off. However, this arrangement had a disadvantage of producing current spikes in the coax cables during the switching operations, particularly when specimens were switched from an ohmic check measurement at -100 V back into the bias circuit at +150 V. Large transient electrical currents were observed on the power supply current meter during these switching operations, some of which blew the 0.5 A fuses installed on the individual coax cable leads. Larger fuses (1 A) were installed in an attempt to eliminate blown fuses. However, several of the electrical cables failed (electrical short) over a period of several days due to the high transient currents. The Labview program was modified after five days of irradiation to shut off the 150 V bias during electrical measurements, and to slowly ramp the power supply from 0 to 150 V when the bias was reapplied following completion of a set of electrical measurements. The frequency of electrical measurements was reduced to ~ two per day when this change was implemented in order to minimize the amount of time that specimens were irradiated without the 150 V bias. The 150 V potential was applied to the biased specimens ~98% of the total irradiation time.

The irradiation was accomplished over a time period of about three and one half months, and involved three irradiation cycles (each ~26 days) of the HFIR reactor operating at 85 MW. The electrical conductivity of the specimens was measured before, during and following each of the three HFIR irradiation cycles. Due to the relatively low levels of nuclear heating when the reactor was not at full power, the specimen temperatures could not be maintained at 450°C when the reactor was off or at 10% power. The capsule was initially installed in the HFIR pool on Feb. 23, 1996 during the refueling outage between reactor cycles 343 and 344, and a series of preirradiation electrical measurements were performed for two weeks prior to the start of the irradiation. The capsule was installed in the HFIR core on March 4, 1996, and reactor startup occurred on March 8, 1996. The irradiation capsule reached its target centerline fluence of ~$3x10^{25}$ n/m^2 (E>0.1 MeV) on June 20, 1996, which corresponds to a damage level of ~ 3 dpa in alumina. The irradiation temperature was maintained at 440 to 500°C for all 15 specimens during the irradiation. The full-power reactor ionizing dose rate [8] was 10 to 16 kGy/s and the average displacement damage rate was ~2.4 to 4.3 $x10^{-7}$ dpa/s, with the lowest dose rates obtained for subcapsules 1 and 15 and the highest dose rate for subcapsule 8 (Table 2). The ionizing dose rate in the core with the reactor turned off (spent fuel removed) was dominated by the EuO_2 control plates, and the dose rate at the capsule location was estimated by HFIR staff to be ~10 Gy/s. Further analysis is underway to verify the quantitative accuracy of this reactor-off ionizing dose rate. 12 of the 15 specimens were irradiated with a dc bias of 150 V (electric field of 200 V/mm), with the remaining three specimens irradiated without dc bias (Table 1). The experimental matrix included 7 high purity single crystal alumina (sapphire) specimens (2 of which were irradiated without dc bias), including UV grade and normal grade sapphire with 3 different crystallographic orientations. A Cr-doped sapphire specimens was also irradiated under dc bias, and the remaining 7 specimens were different grades of polycrystalline alumina obtained from 4 different vendors (Wesgo AL300, Wesgo AL995--with and without dc bias, Coors AD998, Kyocera A-479, Kyocera A-480, Vitox).

Results and Discussion

The specimens exhibited a typical resistivity >$2x10^{10}$ Ω-m (the maximum resistivity measurable with our system due to the ~1 TΩ resistance in the scanner cards) at 40°C prior to insertion in the reactor. The measured in-core resistivities of the 15 specimens are summarized in Table 2. The measured RIC was independent of crystallographic orientation, but was strongly dependent on specimen purity at low ionizing dose rates. The preirradiation in-reactor resistivities at a temperature of ~50°C (with ~10 Gy/s ionizing dose rate) ranged from ~0.3 to 10 GΩ-m for the different specimens. The lowest resistivities were obtained for the high-purity sapphire specimens, and the highest resistivities were observed for the polycrystalline specimens. The resistivities were obtained from the slope of the current vs. voltage (ohmic check) plots. The high-purity sapphire specimens generally exhibited approximately ohmic behavior at 10 Gy/s, whereas the polycrystalline specimens and the Cr-doped sapphire specimen exhibited moderate nonohmic behavior.

Figure 1 shows examples of the ohmic check data for four different specimens (samples 1,3,9 and 10) obtained from about 20 series of measurements performed over a period of 4 days prior to reactor startup. It can be seen that the ohmic check data for a given sample were generally very reproducible. The typical standard error in resistivity determined from the slope of an ohmic check curve was less than ±50%. Significant nonohmic behavior was observed in all 15 of the specimens in two nonsequential series of measurements, as demonstrated by the dashed curves in Fig. 1. The main controllable experimental parameters such as RC settling time (20 s) were held constant during these measurements, and the cause of the nonohmic behavior is uncertain. The nonohmic behavior occurred mainly in the positive quadrant of the current vs. voltage plot and consisted of a positive offset current of a few nA. All of the resistivities quoted in this report were obtained from the slope in the negative quadrant of the ohmic check curves. Further data analysis is planned to find a possible cause of this nonohmic behavior.

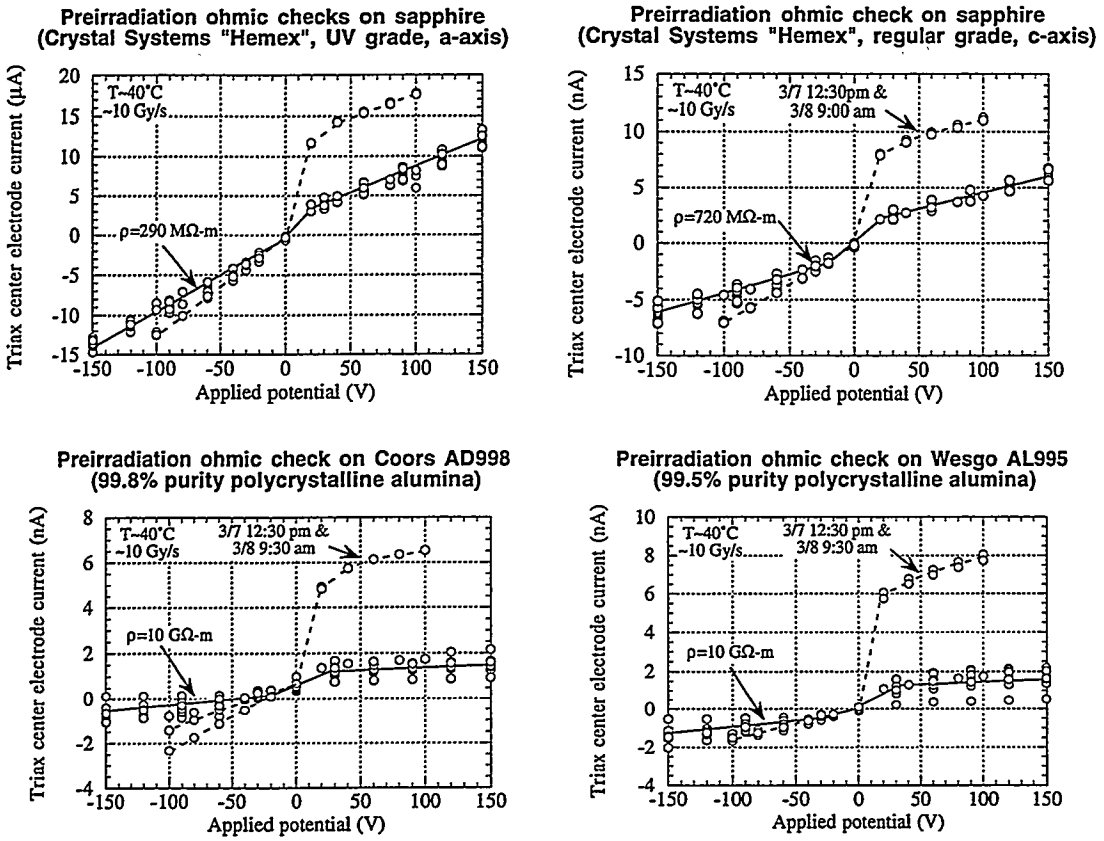

Fig. 1. Comparison of the preirradiation electrical behavior of four different grades of alumina (samples 1,3,9 and 10). The dashed curves represent atypical behavior that was observed on two separate (nonsequential) occasions during the last two days prior to reactor startup.

Table 2. Summary of measured in-core resistivities (MΩ-m) at the start of the irradiation (from the negative quadrant of the ohmic check plots). The data marked with an asterisk denote values that are a lower limit to the bulk resistivity due to low (<100 kΩ) surface leakage resistances.

HFIR position	Material	Preirradiation (10 Gy/s,50°C)	10% power, 0 dpa (1-1.6 kGy/s, 170°C)	full power, 0 dpa (10-16 kGy/s, 440-500°C)
1	UV sapphire, a-axis	300	28	7.7
2	UV sapphire, c-axis	300	16	3.0
3	regular sapphire, c-axis	700	20	5.6
4	regular sapphire, a-axis	700	12	3.0
5	Vitox	(>20)*	(>2.5)*	(>2)*
6	Kyocera A-480	10000	11	1.0
7	Wesgo AL300	7000	6	1.7
8	Kyocera A-479	10000	15	3.9
9	Coors AD998	10000	26	erratic
10	Wesgo AL995	10000	19	(>1.5)*
11	Wesgo AL995	10000	22	5.2
12	regular sapphire, c-axis	500	16	5.0
13	Cr-doped sapphire	5000	15	5.5
14	SA100 sapphire $(1\bar{1}02)$	400	14	5.4
15	SA100 sapphire $(1\bar{1}02)$	(>10)*	(>0.8)*	(>0.3)*

Figure 2 shows the electric currents measured at 100 V in two of the specimens during the initial stages of the first irradiation cycle. A nonconventional startup was used for this irradiation cycle (#344) in order to perform reactor operating training and to allow a full set of in-situ conductivity data to be obtained at an intermediate power level. For the first irradiation cycle, the reactor was brought to 10% power within 10 minutes and held at this power level for ~1.5 h. The reactor was then scrammed, and a conventional ascension to full power operation (~1 h from 0 to 100% power) was then followed. The specimen temperatures during the 10% power operation for this cycle were ~180°C, achieved by flowing Ar gas in the gas gap region outside of the subcapsules. The gas mixture was changed to He and Ne prior to ascension to full power.

The radiation induced conductivity (RIC) behavior was tested at 10% and full reactor power (~1-1.6 and 10-16 kGy/s, respectively), and was found to be sublinear for all of the specimens (Table 2). The material dependence of the RIC was small at 10% and full reactor power, in contrast to the strong material dependence observed at 10 Gy/s. It is interesting to note that the polycrystalline specimens generally had slightly lower resistivities than high-purity sapphire at 10% and full reactor power, which is opposite to the RIC behavior observed at 10 Gy/s. This change in material dependence of the RIC behavior may be partially due to temperature differences at the three dose rates. Further work is needed to determine role of irradiation temperature and dose rate on the RIC of these different grades of alumina. The typical resistivity at full reactor power (~15 kGy/s) was 3 to 5 MΩ-m for all of the specimens, which agrees well with previous RIC studies on alumina [2].

Approximately half of the high voltage coaxial cables failed (electrical short) during the course of the 3-month irradiation. The first five cable failures (in sequential order, subcapsules 6,10,14,5 and 1) occurred during the first five days of full power irradiation, where specimens were switched between the 150 V circuit and the electrical measurement circuit with the 150 V power supply turned on. Three additional cables (#12,7,8) failed after the Labview program was modified to turn off the power supply during electrical measurement and switching operations. One of these cable failures occurred after 16 days of irradiation in a "control" subcapsule (#12) which was not exposed to 150 V bias during the irradiation. The failure in two of the coax cables (#7,10) occurred near the end of an ohmic check measurement as the voltage was ramped from -80 V to -100 V. Figure 3 shows an example of the electrical current measured in the Wesgo AL300 specimen for the first two irradiation cycles. The specimen current at reactor full power decreased by about a factor of two as displacement damage was accumulated during the first irradiation cycle, and the measured conductivity during the subsequent HFIR shutdown at the end of the first cycle was comparable to the preirradiation conductivity. The coaxial cable for this specimen shorted approximately two days after the reactor was restarted for the second irradiation cycle. The failure occurred as an ohmic check measurement was being performed at -100 V. The data obtained at +100 V to -80 V immediately prior to the cable failure did not indicate any unusual behavior.

The cause of the coax cable failures is mostly likely due to dielectric breakdown in the glass seals used for the coaxial cable terminations; the maximum electric field in the glass seal at an applied potential of 150 V was ~1 MV/m, and the calculated operating temperature of the glass seals in the HFIR capsule was ~200°C. This temperature is close to the softening temperature of the Ferro 7556 lead borosilicate glass used to seal the HFIR MI cables (330°C). The typical dielectric breakdown strength (DBS) of glass is 10-100 MV/m at 20°C, and the DBS of glass decreases rapidly with increasing temperature above 20°C [14]. The DBS of the Ferro 7556 glass used in the HFIR irradiations will be experimentally measured in the near future. Simple diagnostic tests performed on the specimens with shorted coaxial cables demonstrated that the specimen bulk resistance was comparable to that of all of the other alumina specimens; therefore, the cable failure was not associated with RIED in the alumina specimens. These tests included measurement of the resistance between the coax cable and triax lead, and measurement of the surface resistances. A higher temperature grade of glass (EG3606 Zn borosilicate) that was successfully used in a previous RIED experiment at the HFBR reactor [13] was not utilized for the HFIR cables due to problems with impurity pickup that could not be resolved within the short amount of time available prior to the deadline for inserting the capsule into HFIR.

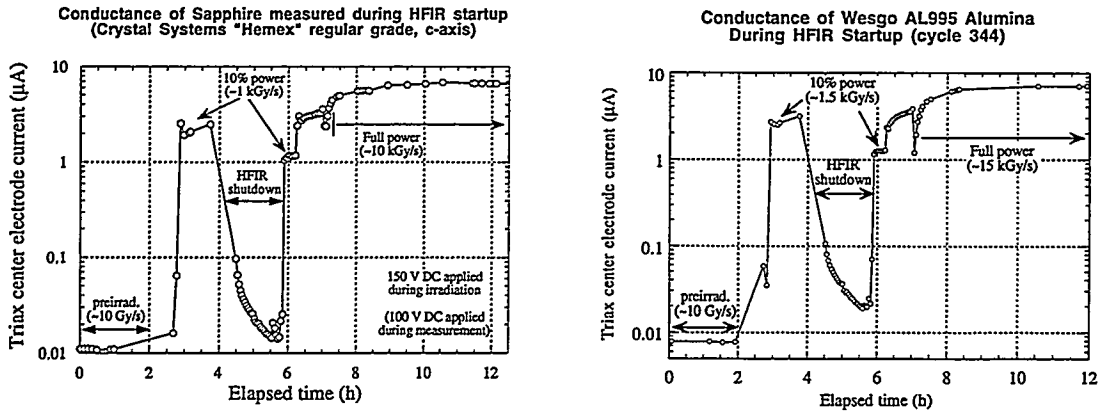

Fig. 2. Electrical currents measured in samples 3 and 10 during the first 12 hours of the irradiation.

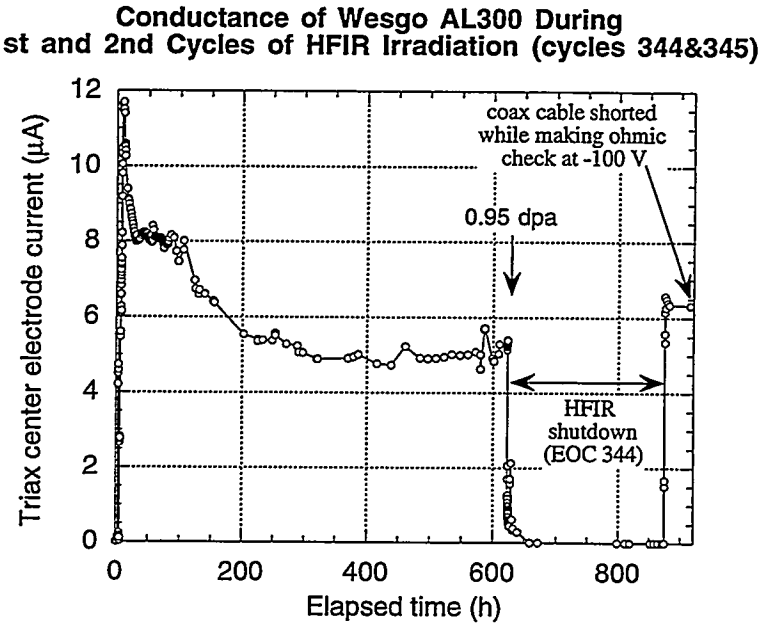

Fig. 3. Measured current at 100 V in Wesgo AL300 during the first two cycles of irradiation.

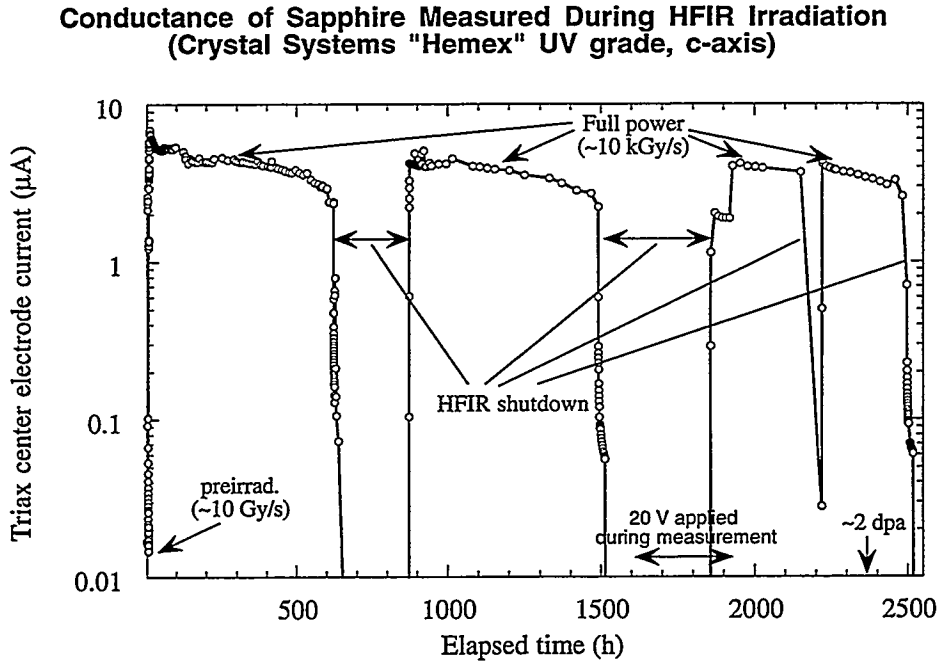

Fig. 4. Measured current at 100 V in UV grade sapphire (sample 2) during the three cycles of HFIR irradiation. The measurement voltage was 20 V for a brief period during the 3rd cycle, as indicated.

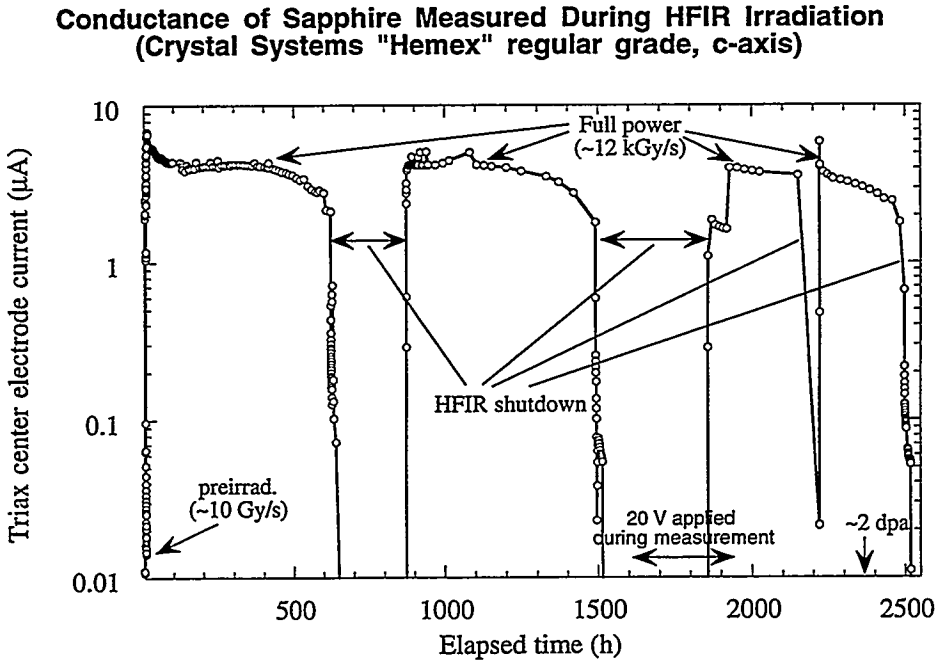

Fig. 5. Measured current at 100 V in regular grade sapphire (sample 3) during the three cycles of HFIR irradiation. The measurement voltage was 20 V for a brief period during the 3rd cycle.

No evidence for radiation induced electrical degradation (RIED) above the RIC level was observed during irradiation to 3 dpa at 450 to 500°C with a continuously applied dc electric field of 200 V/mm. It is particularly noteworthy that RIED was not observed in the sapphire specimens, which were found to have an incubation dose of <0.001 dpa for catastrophic RIED in electron irradiation studies [4,6]. Figures 4 and 5 show the electrical currents measured at 100 V in two sapphire specimens over the 3 HFIR irradiation cycles. The measured current decreased over the course of each irradiation cycle, due in part to changes in the ionizing radiation dose rate as the control rods were repositioned. Except for an initial ~50% decrease in current during the first 2 days of irradiation, the shape of the curves was similar for the 3 irradiation cycles. Two comments should be made regarding the third irradiation cycle. First, as evident from Figs. 4 and 5, a reactor scram occurred during the third irradiation cycle, and the reactor was restarted two days later. Second, the measurement voltage was inadvertently left at 20 V following some diagnostic tests performed prior to the third irradiation cycle, and was not changed back to 100 V until several days after the restart of the reactor. This produced a lower measured current for these data points. The bias voltage was maintained at 150 V on these specimens during this time period (except for brief interruptions to perform the electrical measurements).

The measured resistivity increased rapidly following reactor shutdown for each of the 3 irradiation cycles, and was typically ~5 to 10 GΩ-m at ~20°C in the irradiated sapphire specimens after removal from the HFIR core. These resistivities are slightly lower than that measured in pre-irradiation tests outside of the reactor (typically >20 GΩ-m), which is attributed to slight increases in surface leakage currents in the irradiation capsule. Most of the increased surface leakage occurred during the first irradiation cycle.

Figure 6 compares ohmic check measurements at ~0 and ~1 dpa in sapphire (sample 2) at two ionizing dose rates. The ohmic check data were obtained at the start of the first and second reactor cycles. A pronounced increase in resistivity (compared to the preirradiation value) was observed for all specimens at 10 Gy/s following irradiation to ~1 dpa. On the other hand, the resistivity increase between 0 and ~1 dpa was relatively small at 10% and full reactor power levels. This improvement in the electrical resistivity (which is opposite to the reported RIED effect) may be attributable to increased electron-hole trapping at radiation-produced defects, and is in agreement with previous studies performed on alumina where an electric field was not applied during the irradiation [1,2]. The resistivities measured at all three ionizing dose rates (10 Gy/s, ~1 kGy/s and ~10 kGy/s) showed no evidence of bulk RIED for doses up to 3 dpa. These results indicate that bulk RIED should not be a problem for good-quality alumina insulators in ITER and other fusion energy devices for doses up to at least several dpa. Additional postirradiation measurements at the irradiation temperature are planned to determine if any slight underlying amount of RIED has occurred.

FUTURE WORK

Dielectric breakdown strength measurements will be performed in the next reporting period on the glass seals of several control MI coax cables from the HFIR experiment. The TRIST-ER1 capsule will be stored in the HFIR pool until about November 1996, and will then be taken to a hot cell for disassembly and post-irradiation examination (PIE) of the samples. Planned measurements include inspection and electrical tests of the failed coaxial cables and electrical conductivity as a function of test temperature for the irradiated specimens. Optical absorption, fluorescence and scattering, thermal conductivity, and transmission electron microscopy examination of the specimens may also be performed.

REFERENCES

1 S.J. Zinkle and E.R. Hodgson, J. Nucl. Mater. 191-194 (1992) 58.

2. L.W. Hobbs, F.W. Clinard, Jr., S.J. Zinkle and R.C. Ewing, J. Nucl. Mater. 216 (1994) 291.

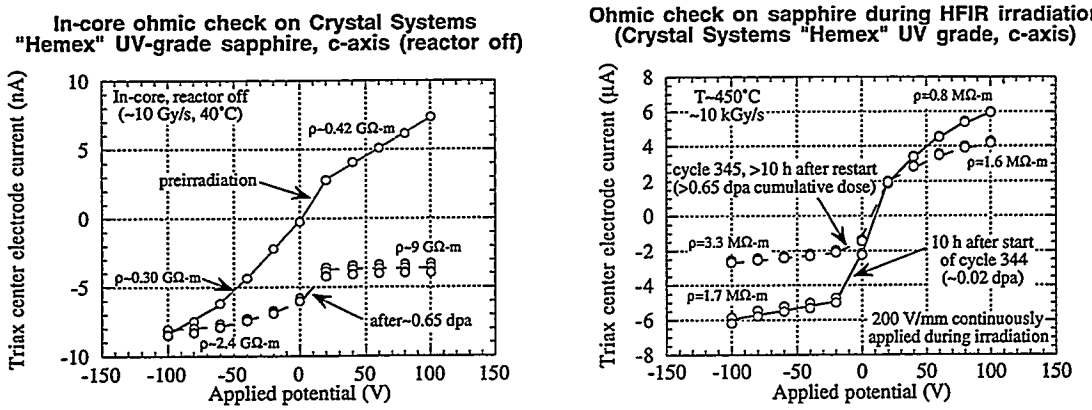

Fig. 6. Comparison of the electrical behavior of UV grade sapphire (sample 2) at 10 Gy/s and 10 kGy/s at the start of the first and second irradiation cycles.

3. S.J. Zinkle and C. Kinoshita, in Fusion Materials Semiannual Progress Report for the Period Ending Dec. 31, 1995, DOE/ER-0313/19, p. 229; also C. Kinoshita and S.J. Zinkle, proc. 7th Int. Conf. on Fusion Reactor Materials, Obninsk, Russia, J. Nucl. Mater. (in press).

4. E.R. Hodgson, Cryst. Latt. Def. Amorph. Mater. 18 (1989) 169.

5. A. Möslang, E. Daum and R. Lindau, proc. 18th Symp. of Fusion Technology, Karlsruhe, Germany, August 1994, p. 1313.

6. E.R. Hodgson, J. Nucl. Mater. 212-215 (1994) 1123.

7. W.S. Eatherly et al., in Fusion Materials Semiannual Progress Report for the Period Ending Dec. 31, 1995, DOE/ER-0313/19, p. 241.

8. A.L. Qualls, W.S. Eatherly, D.W. Heatherly, M.T. Hurst, D.G. Raby, R.G. Sitterson, L.L. Snead, K.R. Thoms, R.L. Wallace, and S.J. Zinkle, in Fusion Materials Semiann. Prog. Report for the period ending June 30, 1996, DOE/ER-0313/20, this report.

9. S.J. Zinkle, G.P. Pells and F.W. Clinard, Jr., in Fusion Reactor Materials Semiannual Progress Report for the Period Ending Sept. 30, 1993, DOE/ER-0313/15, p. 417.

10. D.P. White, in Fusion Materials Semiannual Progress Report for the Period Ending Sept. 30, 1994, DOE/ER-0313/17, p. 346.

11. E.H. Farnum, T. Shikama, M. Narui, T. Sagawa and K. Scarborough, J. Nucl. Mater. 228 (1996) 117.

12. L.L. Snead, D.P. White and S.J. Zinkle, in Fusion Materials Semiannual Progress Report for the Period Ending March 31, 1995, DOE/ER-0313/18, pp. 385-396; also J. Nucl. Mater. 226 (1995) 58.

13. L.L. Snead, D.P. White, W.S. Eatherly and S.J. Zinkle, in Fusion Materials Semiannual Progress Report for the Period Ending Dec. 31, 1995, DOE/ER-0313/19, p. 249.

14. J.J. O'Dwyer, The Theory of Dielectric Breakdown of Solids (Oxford Univ. Press, London, 1964).

SUMMARY OF THE IRRADIATION HISTORY OF THE TRIST-ER1 CAPSULE.

A. L. Qualls, W. S. Eatherly, D. W. Heatherly, M. T. Hurst, D. G. Raby, R. G. Sitterson, L. L. Snead, K. R. Thoms, R. L. Wallace, S. J. Zinkle (Oak Ridge National Laboratory).

OBJECTIVE

The objective of this work is to determine the existence or absence of radiation induced electrical degradation (REID) in Al_2O_3 with and without voltage applied to the sample.

SUMMARY

The TRIST-ER1 capsule was assembled and irradiated in a large Removable Beryllium (RB☆) position of the High Flux Isotope Reactor (HFIR) during this reporting period. Irradiation began on March 8, 1996, was completed on June 20, 1996, during operating cycles 344, 345, and 346. This report describes the thermal operation of the capsule.

PROGRESS AND STATUS

Background

The TRIST-ER1 capsule was designed to irradiate 15 alumina specimens at 450°C. The specimens were 8.5-mm O.D. disks 0.75-mm thick. Three electrodes were connected to the specimens so they could be electrically biased during irradiation and the electrical resistance could periodically be measured. The specimens were housed in sealed subcapsules which were contained in a holder sleeve and separated into three temperature zones to form the experimental region of the capsule. The subcapsules and capsule are described in Reference 1.

The total amount of heat generated in a subcapsule during reactor operation is dependent upon its location in the experimental region. The neutron and gamma fluxes responsible for the heating are reduced from their peak values near the reactor mid-plane by approximately 40% towards the ends of the experimental region. The size of the gas gap between the subcapsule enclosures and the holder were decreased for subcapsules located closer to the reactor mid-plane to compensate for increased heating in those regions. A heat transfer model was developed to determine the required operating gas gap thickness for each of the 15 subcapsules. Each subcapsule was essentially identical, except for its axial location in the experimental region and every other subcapsule was inverted (which makes almost no difference in the result). The design gas gap dimensions were determined by assuming a thermal conductivity equal to the average value of neon and helium in the gas gaps and a heat generation rate across the experimental region equal to the average of the measured value[2] near the beginning and end of an operating cycle. After the operating gas gap dimensions were set, the fabrication dimensions of the enclosure were determined by calculating the expected thermal expansion of the holder sleeve and the subcapsules from ambient to operating temperatures. Due to the evolution of the heating profile in the RB☆ facilities, the relative amount of neon required to maintain temperatures was expected to be greater than that of helium at the beginning of a reactor cycle, and the neon flow would be reduced over the course of the reactor cycle to compensate for the increased heat generated in the subcapsules.

Vanadium was chosen for the enclosure material because its low thermal expansion permitted the alumina pedestal to be brazed to the enclosure. Vanadium has a low thermal conductivity however, which decreased the heat loss characteristics of the subcapsules. This was compensated for by reducing the temperature control gas gap dimension. The operating gas gap dimensions for those subcapsules located near the reactor mid-plane were approximately .0025 cm. Small errors in gas gap dimensions of this size (due to fabrication errors or mis-

calculations) can result in large deviations in the actual specimen temperature. For subcapsules 7, 8, and 9, the expected temperature change for a deviation of .00025 cm was approximately 6 °C. It was anticipated that the specimens could be controlled to within +/- 20°C of the design temperature of 450°C. The expansion of the subcapsules with increasing temperature reduces the gas gap dimension and increases the heat loss from the component. Because the thermal expansion of subcapsules 7, 8, and 9 were predicted to be significant compared to the operating gas gap dimension, the available temperature adjustment was expected to be reduced. It was anticipated that a large degree of temperature adjustment would not be possible for those subcapsules.

Operation

The capsule was irradiated during HFIR cycles 344, 345, and 346 in an unshielded RB☆ position and was rotated 180° with respect to the reactor center-line for successive cycles. Cycles 344 and 345 were fairly typical, however the reactor scrammed 13 days into Cycle 346 and was down for approximately 2 days. Cycle 346 also terminated approximately 24 hours before the scheduled end-of-cycle due to equipment failure. The subcapsule temperatures were inadvertently increased above the desired temperature range during cycle 344 due to an improperly performed instrumentation test. The central specimen temperatures were increased approximately 100°C above their normal operating temperatures for approximately 6 minutes. (This is not observed in the presented data due to the short duration of the event.) The temperature of other specimens were increased less severely. The subcapsules were designed to withstand these temperatures and based on a comparison of temperature readings and electrical resistance measurements taken before and after the event, no damage was incurred in any of the subcapsules. Other than this event, the operation of the capsule was very consistent.

The specimen and enclosure temperature soon after the initial startup is shown in Figure 1. The specimen thermocouple of subcapsule 12 was not fully inserted into the specimen pedestal and was not indicative of the specimen temperature.

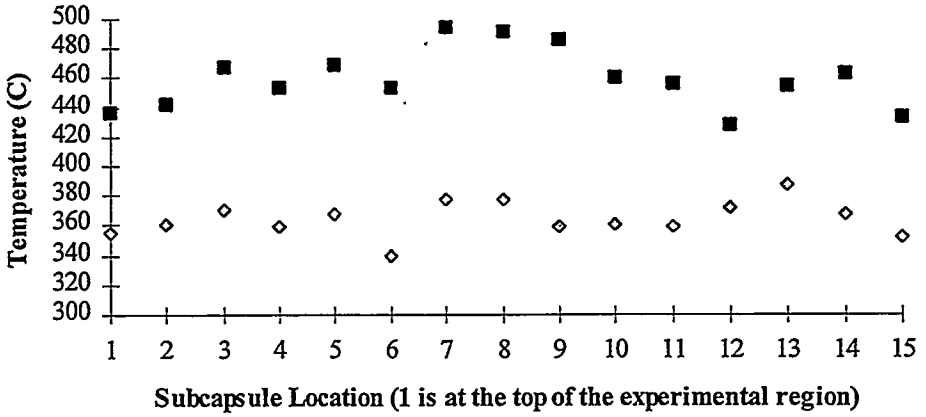

Figure 1: Temperature of the specimens (squares) and the base of the enclosures after the reactor reached full power for the first time. The temperature of the end zones (1- 4 and 12 -15) was being controlled.

The average temperature of the specimens was approximately 459°C, and the average deviation of the specimen temperatures from the design temperature of 450°C was approximately 17°C at the time of the initial start-up. The temperature of the specimens located closest to the reactor mid-plane (7, 8 and 9) averaged

approximately 40°C above the design temperature. The temperature of the specimens in the upper zone (1-4) and lower zone (12-15) operated within a controllable range, however the required neon flow rate was lower than anticipated. The subcapsules tended to operate at lower inherent temperatures as the experiment progressed, which resulted in an increased ability to control specimen temperatures. The difference is most notable in the central temperature zone, where by the third irradiation cycle the specimen temperatures were actively controlled by introducing neon into the gas mixture. It is not yet known if the reduction in operating temperature was due to cycle-to-cycle variations in the operation of the reactor or if the heat transfer characteristics of the subcapsules were actually changing.

A plot of the average specimen temperature in the three temperature zones over the course of the three cycles is shown in Figure 2. The lower temperature zone operated at a higher inherent temperature than the upper zone and it was not possible to maintain the temperature in the lower zone at 450°C during the final week of a cycle. It is suspected that the temperature difference in the end zones is due to differences in the heat loss from the subcapsule holder sleeve to the capsule housing at those locations. The outer surface of the holder sleeve housed axial grooves to provide paths for the thermocouples, gas tubing and electrical leads used to monitor the subcapsules and control the temperatures. At the base of the experimental region these grooves were occupied by fewer leads, and the void areas of the grooves were greater than at the top of the experimental region, where the grooves were filled to capacity. It is possible that the heat loss from the holder sleeve to the housing was reduced in the lower end, resulting in a higher housing temperature and ultimately higher specimen temperatures.

The fact that all of the subcapsules operated at slightly higher than predicted temperatures suggests that either the heat transfer calculations or the predictions of subcapsule thermal expansion used to determine the fabrication dimensions of the subcapsule enclosure were incorrect. For the central subcapsules (7, 8 and 9), little could have been done about the high temperatures. The minimum operating temperature of subcapsules with vanadium enclosures was essentially reached at this location for this combination of subcapsule and capsule design. The gap between the central subcapsules and the holder sleeve was approximately .00015 cm at ambient temperature. The enclosures could not have been made much larger and still fit into the holder sleeve. If similar experiments at colder temperatures are desired, then the enclosure material must be changed or the subcapsule and capsule redesigned.

It is difficult to infer anything from the temperature data without a more detailed analysis, however based on preliminary examination some general conclusions can be made.

Expected change in thermal conductivity of alumina

It was expected that the thermal conductivity of alumina would begin to decrease upon the initial irradiation and stabilize after approximately .1 dpa (after about 2 to 3 days). The value of the thermal conductivity of the alumina used in the thermal analysis of the subcapsules was 1/3 the value given in the literature for un-irradiated alumina. Because the primary heat conduction path between the two thermocouples was through the alumina pedestal, the difference between the thermocouple readings was expected to increase as the thermal conductivity of the alumina decreased. However, the actual difference in the specimen and enclosure temperature at the time of the initial startup was very close to the value predicted by the thermal analysis and while the temperature difference did increase over the first week of irradiation, the increase was only on the order of 2 - 3%, which was smaller than anticipated. The data will need to be examined in greater detail and the heat transfer analysis revisited to determine if and to what extent the thermal conductivity actually changed.

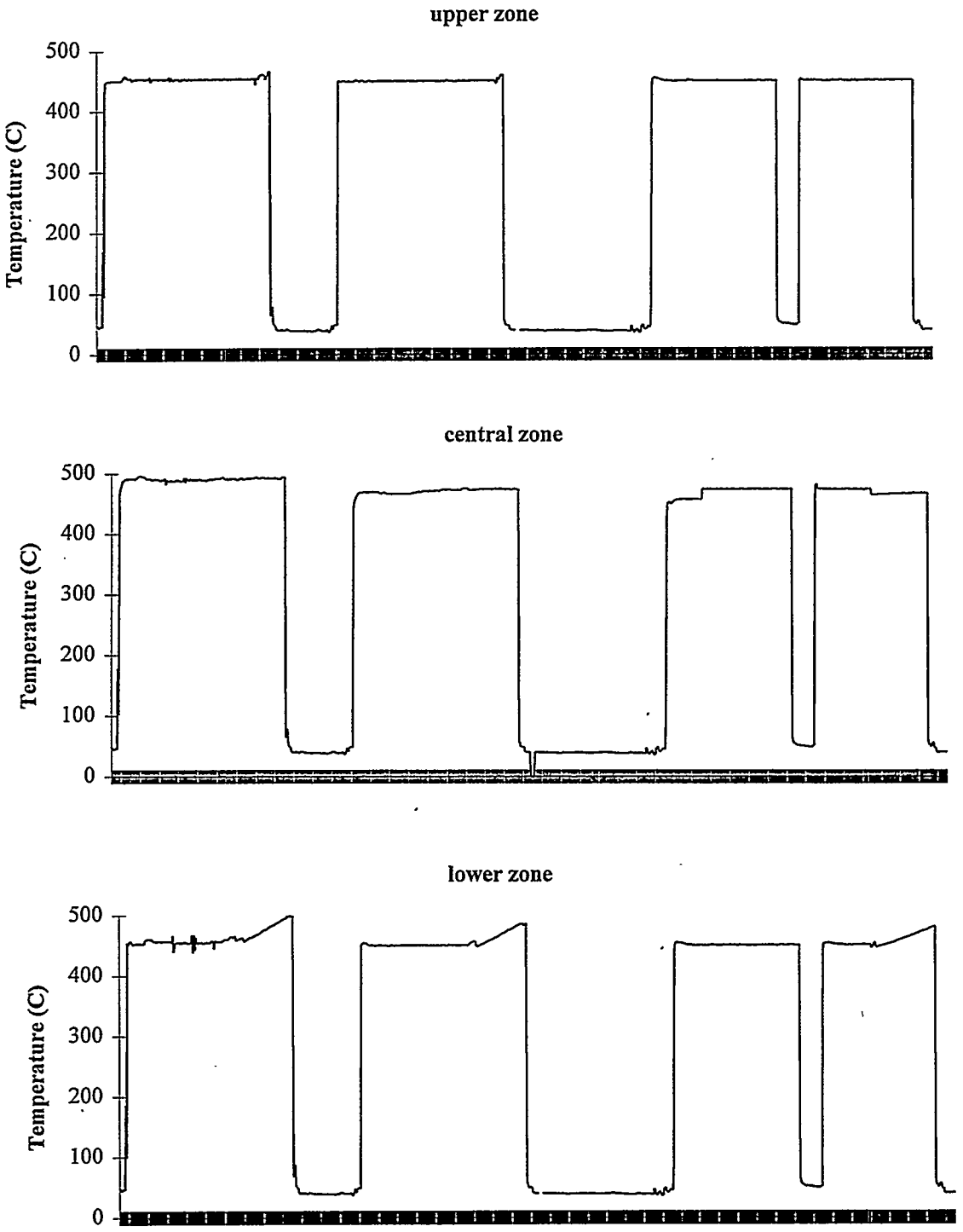

Figure 2: Average temperature of the three temperature zones over the course of the irradiation. The third irradiation cycle was interrupted for approximately 2 days.

Evolution of the heating profile during a reactor cycle

One area in which the data suggests the need for further examination is the evolution of the nuclear heating profile in the RB☆ facility during a reactor cycle. The difference in the specimen and enclosure temperatures increases with increased heat generation within the subcapsule. A plot of the percentage change in the temperature difference between the specimen and enclosure thermocouples from the beginning to the end of the cycles (averaged over the three cycles) is shown in Figure 3. The subcapsules located towards the end of the experimental region show an increasing temperature difference as the reactor cycle progresses. This is indicative of the increased heating in that region and is consistent with the gradual reduction in the flow of neon to those regions required to maintain specimen temperature. For subcapsules 6 through 11, the temperature difference decreased as the reactor cycle progressed, which implies that the heating rate in this region decreases during a cycle. Data used in the design of the capsule does not reflect such a reduction. The magnitude of the change for subcapsules 1 and 15 does not follow the pattern of the other subcapsules. These subcapsules may be located in a portion of the experimental region in which the fluxes behave differently than in the portion of experimental region bounded by subcapsules 2 and 14.

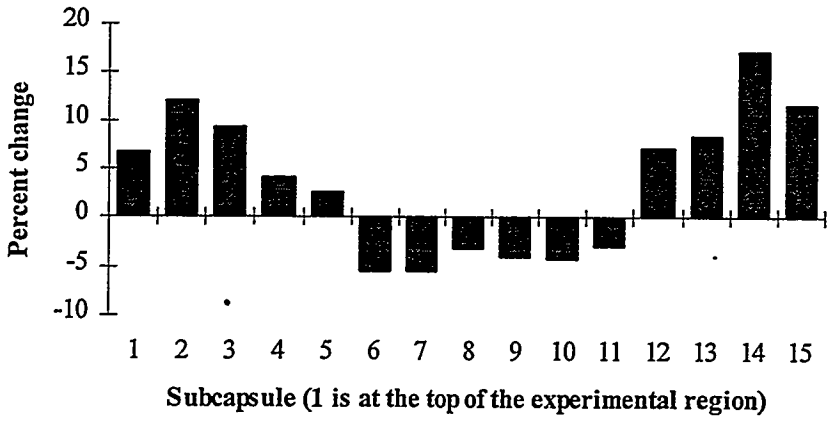

Figure 3: Plot of the percentage change in the temperature difference across the subcapsules over the course of a reactor cycle. The temperature difference is indicative of the heat generation within a subcapsule.

FUTURE WORK

In order to effectively address the issues raised concerning the operation of the TRIST-ER1 capsule, additional analysis must be undertaken. These investigations may be helpful in answering questions concerning the heat generation profile in the RB☆ position in order to assist in the design of future capsules.

REFERENCES

1. W.S. Eatherly et. al., in Fusion Materials Semiannual Progress Report for the Period Ending December 31, 1995, DOE/ER-0313/19, PP. 241-248.

2. Senn and Mixon, Nuclear Technology, 12, 1971, p235.

SUMMARY OF ROUND ROBIN MEASUREMENTS OF RADIATION INDUCED CONDUCTIVITY IN WESGO AL995 ALUMINA — S. J. Zinkle (Oak Ridge National Laboratory)

OBJECTIVE

The objective of this report is to summarize recent measurements of the radiation induced conductivity of Wesgo AL995 polycrystalline alumina.

SUMMARY

This existing data on radiation induced conductivity (RIC) measurements performed on the same heat of the IEA reference ceramic insulator are summarized. Six different sets of RIC measurements have been performed on Wesgo AL995 at dose rates between 10 Gy/s and 1 MGy/s. In general, good agreement was obtained between the different groups of researchers. The data indicate that the RIC at a test temperature of 400-500°C is approximately linear with ionizing dose rate up to ~1000 Gy/s, and exhibits an approximately square root dependence on dose rate between 1 kGy/s and 1 MGy/s.

PROGRESS AND STATUS

Introduction

In order to obtain a better understanding of the radiation induced electrical degradation (RIED) process in ceramic insulators, an international round-robin RIED experiment was recently performed on the IEA reference ceramic insulator, Wesgo AL995 [1]. This well-known grade of polycrystalline alumina has been produced for over 30 years, and has good dielectric properties [2] and mechanical strength. As summarized elsewhere, significant levels of electrical degradation were not observed by any of the research groups involved in the round-robin RIED experiment [1]. In conjunction with this round-robin experiment, measurements of the radiation-induced conductivity were obtained over a wide range of ionizing dose rates. The purpose of the present report is to compile the RIC data obtained on this single heat of material. Recent RIC data obtained on the same heat of Wesgo AL995 in the HFIR TRIST-ER1 reactor irradiation experiment [3,4] are also included in this compilation.

Summary of Round-robin RIC Measurements on Wesgo AL995 Alumina

All of the specimens for the round robin tests on Wesgo AL995 alumina were machined from a single bar of material (IEA reference heat) that was obtained by Roger Stoller at ORNL [5]. A total of 6 different research groups participated in the round-robin experiment [4,6-10]. The irradiation sources for the in-situ radiation induced conductivity measurements included 1.8 MeV electrons [9], 28 MeV He ions [6], 104 MeV He ions [8], Lasref spallation neutrons [7], and the HFBR [10] and HFIR [4] fission reactors. All of the measurements except ref. [8] employed a guard ring electrode configuration to make the measurements. Most of the experiments [4,7,10] utilized a low-side electrical measurement technique in order to minimize leakage current artifacts (i.e., the high voltage was applied on the base electrode and the electrical signal from the guarded center electrode was measured on the low side of the electrical circuit). The electron [9] and 28 MeV ion irradiation [6] experiments utilized a high side measurement technique in order to avoid electrical current contributions from the irradiating beam. All of the RIC measurements were made at temperatures between 400 and 500°C, with the exception of the 10 Gy/s and 1.5 kGy/s dose rate measurements in the HFIR TRIST-ER1 experiment, which were performed at ~50°C and 170°C, respectively [4]. Further experimental details are contained in the original references [4,6-10].

The results of the six RIC studies on Wesgo AL995 alumina are summarized in Fig. 1 [4,6-10]. Two different specimens were measured for the HFIR irradiations. The HFIR data plotted at an ionizing dose rate of 10 Gy/s were obtained with the capsule inserted in the core prior to reactor startup [4]. This ionizing dose rate is based on rough calculations, and further analysis is underway to determine the accuracy of the quoted 10 Gy/s ionizing dose rate. The HFIR data plotted at 1500 Gy/s were obtained with the reactor operating at 10% power. Due to the nonohmic response of Wesgo AL995 observed in the HFIR TRIST-ER1 experiment [4], the electrical conductivities obtained from slope of the current vs. voltage curve for both positive and negative applied voltages are shown. The RIC data obtained from the negative quadrant are considered to be the most accurate representation of the bulk conductivity in HFIR [4]. Excluding the HFBR data, the results suggest that the RIC is roughly proportional to the ionizing dose rate between 10 Gy/s and ~1000 Gy/s, and that the RIC is nearly proportional to the square root of the dose rate between 1500 Gy/s and 1 MGy/s. The measured RIC value from the HFBR experiment [10] is approximately one order of magnitude lower than the HFIR data [4] at comparable dose rates. One possible contributing factor is that the HFBR conductivity data were obtained after a displacement damage level of 0.1 dpa had been reached. All of the other RIC data plotted in Fig. 1 were obtained for damage levels <0.01 dpa. Several studies have shown that the RIC in high-purity grades of alumina is decreased by irradiation damage, due to increased electron-hole trapping at the radiation-produced defects [11-15]. A decrease in the RIC value with increasing damage level was also observed for Wesgo AL995 in the HFIR experiment [4]. For example, the RIC measured at 15 kGy/s (450°C) decreased by about a factor of five in Wesgo AL995 after 1 dpa. An additional possible explanation for the low reported RIC value in the HFBR experiment is the possibility that some of the Pt electrode may have delaminated during the irradiation [10].

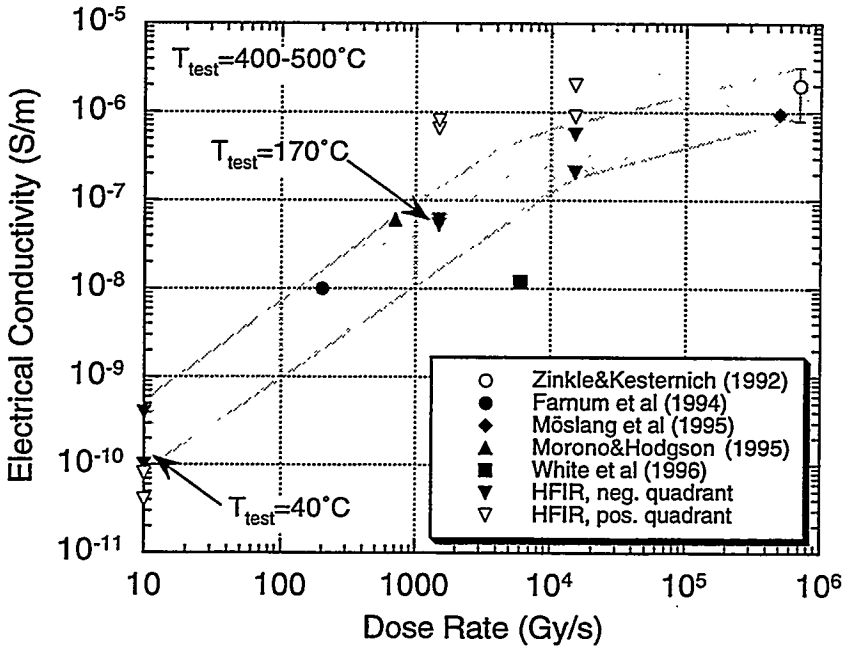

Figure 1. Summary of the round-robin RIC measurements on Wesgo AL995 alumina [4,6-10].

The temperature dependence of the RIC in Wesgo AL995 alumina is unknown. Previous RIC studies on other grades of alumina have shown that either a slight increase or decrease in RIC with increasing temperature is possible, depending on the details of the irradiation source and residual impurities in the insulator [11,16]. An initial RIC of ~$3x10^{-7}$ S/m was reported in ref. [17] for Wesgo AL995 irradiated in the HFBR reactor at 350°C, 6000 Gy/s. The Wesgo AL995 results summarized in Fig. 1 are somewhat higher than previously reported room temperature RIC values for Vitox (99.9% purity) polycrystalline alumina [18], and somewhat lower than reported room temperature RIC values for high-purity sapphire [16,19] and Wesgo AL998 (99.8% purity) and AL300 (97% purity) grades [19] of polycrystalline alumina.

References

1. S.J. Zinkle, in Fusion Materials Semiann. Prog. Report for period ending Dec. 31, 1995, DOE/ER-0313/19, p. 258.
2. S.J. Zinkle and R.H. Goulding, in Fusion Materials Semiann. Prog. Report for period ending Dec. 31, 1995, DOE/ER-0313/19, p. 231.
3. W.S. Eatherly, D.W. Heatherly, M.T. Hurst, A.L. Qualls, D.G. Raby, R.G. Sitterson, L.L. Snead, K.R. Thoms, R.L. Wallace, D.P. White and S.J. Zinkle, in Fusion Materials Semiann. Prog. Report for period ending Dec. 31, 1995, DOE/ER-0313/19, p. 241.
4. S.J. Zinkle, D.P. White, L.L. Snead, W.S. Eatherly, A.L. Qualls, D.W. Heatherly, R.G. Sitterson, R.L. Wallace, D.G. Raby, M.T. Hurst, E.H. Farnum, K. Scarborough, T. Shikama, M. Narui, and K. Shiiyama in Fusion Materials Semiann. Prog. Report for period ending June 30, 1996, DOE/ER-0313/20, this report.
5. R.E. Stoller, in Fusion Reactor Materials Semiann. Prog. Report for period ending Mar. 31, 1990, DOE/ER-0313/8, p. 299.
6. W. Kesternich, F. Scheuermann and S.J. Zinkle, J. Nucl. Mater. 219 (1995) 190. The RIC measurements on Wesgo AL995 alumina were described by S.J. Zinkle and W. Kesternich in Fusion Reactor Materials Semiann. Prog. Report for period ending Mar. 31, 1993, DOE/ER-0313/14, p. 437.
7. E.H. Farnum and F.W. Clinard, Jr., J. Nucl. Mater. 219 (1995) 161.
8. A. Möslang, E. Daum and R. Lindau, Proc. 18th Symp. on Fusion Technology, Karlsruhe, Germany, Aug. 1994, p. 1313.
9. A. Morono and E.R. Hodgson, 7th Intern. Conf. on Fusion Reactor Materials, Obninsk, Russia, J. Nucl. Mater, in press (Sept. 1996).
10. D.P. White, L.L. Snead, W.S. Eatherly and S.J. Zinkle, to be submitted to J. Appl. Phys.; also L.L. Snead, D.P. White, W.S. Eatherly and S.J. Zinkle, in Fusion Materials Semiann. Prog. Report for period ending Dec. 31, 1995, DOE/ER-0313/19, p. 249.
11. L.W. Hobbs, F.W. Clinard, Jr., S.J. Zinkle and R.C. Ewing, J. Nucl. Mater. 216 (1994) 291.
12. R.W. Klaffky, in Special Purpose Materials Ann. Prog. Report, DOE/ER-0048/1 (1980) 19.
13. E.R. Hodgson, J. Nucl. Mater. 179-181 (1991) 383.
14. G.P. Pells, J. Nucl. Mater. 184 (1991) 177.
15. E.H. Farnum et al., J. Nucl. Mater. 191-194 (1992) 548.
16. R.W. Klaffky et al., Phys. Rev. B 21 (1980) 3610.
17. L.L. Snead, D.P. White and S.J. Zinkle, J. Nucl. Mater. 226 (1995) 58.
18. G.P. Pells, Rad. Eff. 97 (1986) 199.
19. R.H. Goulding, S.J. Zinkle, D.A. Rasmussen and R.E. Stoller, J. Appl. Phys. 79 (1996) 2920.

OPTICAL ABSORPTION OF NEUTRON-IRRADIATED SILICA FIBERS -- D. W. Cooke, E. H. Farnum and B. L. Bennett (Los Alamos National Laboratory)

SUMMARY

Induced-loss spectra of silica-based optical fibers exposed to high (10^{23} n-m^{-2}) and low (10^{21} n-m^{-2}) fluences of neutrons at the Los Alamos Spallation Radiation Effects Facility (LASREF) have been measured. Two types of fibers consisting of a pure fused silica core with fluorine-doped (~ 4 mole %) cladding were obtained from Fiberguide Industries and used in the as-received condition. Anhydroguide™ and superguide™ fibers contained less than 1 ppm, and 600 to 800 ppm of OH, respectively. The data suggest that presently available silica fibers can be used in plasma diagnostics, but the choice and suitability depends upon the spectral region of interest. Low-OH content fibers can be used for diagnostic purposes in the interval ~ 800 to 1400 nm if the exposure is to high-fluence neutrons. For low-fluence neutron exposures, the low-OH content fibers are best suited for use in the interval ~ 800 to 2000 nm, and the high-OH content fibers are the choice for the interval ~ 400 to 800 nm.

PROGRESS AND STATUS

The fibers were irradiated at LASREF over a two and one-half month period and subjected to either a low or high fluence environment. We have previously reported optical absorption in the spectral region 190 to 800 nm from high fluence-exposed fibers[1]. The low fluence region is characterized by neutrons with 97.8% having energy less than 0.1 MeV; there is only minimal gamma component in this region due to shielding. We now report optical absorption of silica fibers exposed to the low fluence neutron environment. The previous work was done in the interval 200 - 800 nm; we now extend the range to cover 200 - 2000 nm and measure the radiation-induced optical attenuation for fibers exposed to both low and high fluence environments.

Figure 1 shows the optical absorption spectrum of anhydroguide silica fibers exposed to high and low fluence neutron environments and compares it with absorption of an unirradiated sample. In the visible part of the spectrum we measure less than 50 dB/km attenuation in the virgin sample. Prior to the onset of band-edge absorption, there is a peak near 300 nm, which may be due to the fiber drawing process[2] or to the presence of chlorine.[3] Of interest is the significant radiation-induced absorption for both low and high fluence-exposed fibers. Although not shown, we measured attenuation up to 10^4 dB/km in the high fluence fiber for wavelengths below about 800 nm. The low fluence fiber exhibits a peak near 630 nm, which is attributed to the well-known radiation-induced nonbridging oxygen hole center.[4] Near 400 nm the attenuation has increased to 10^4 dB/km. We also observe an attenuation peak near 1400 nm for both low and high fluence-exposed fibers and attribute it to an overtone vibration mode of the 2750 and 2830 OH fundamental band.

Shown in Fig. 2 are the attenuation spectra for superguide silica fibers exposed to both low and fluence environments. For comparative purposes we also show the attenuation for a virgin specimen. Again, the pristine sample exhibits a weak peak near 300 nm with less than 50 dB/km attenuation in the region 400 to 800 nm. However, there is significant attenuation for all fibers above 800 nm. Three peaks near 950, 1250 and 1400 nm are all due to combination and overtone bands of the OH fundamental mode.[2] This is expected because of the high OH content (600 to 800 ppm) of the superguide fiber compared to the low OH content (< 1 ppm) of the anhydroguide specimen. This assignment of the combination and overtone modes is further substantiated by the fact that the intensities of these three peaks are not affected by radiation. This is not the case however for a peak observed near 1900 nm. As shown in Fig. 2, this particular peak grows with radiation exposure and its origin is presently unknown.

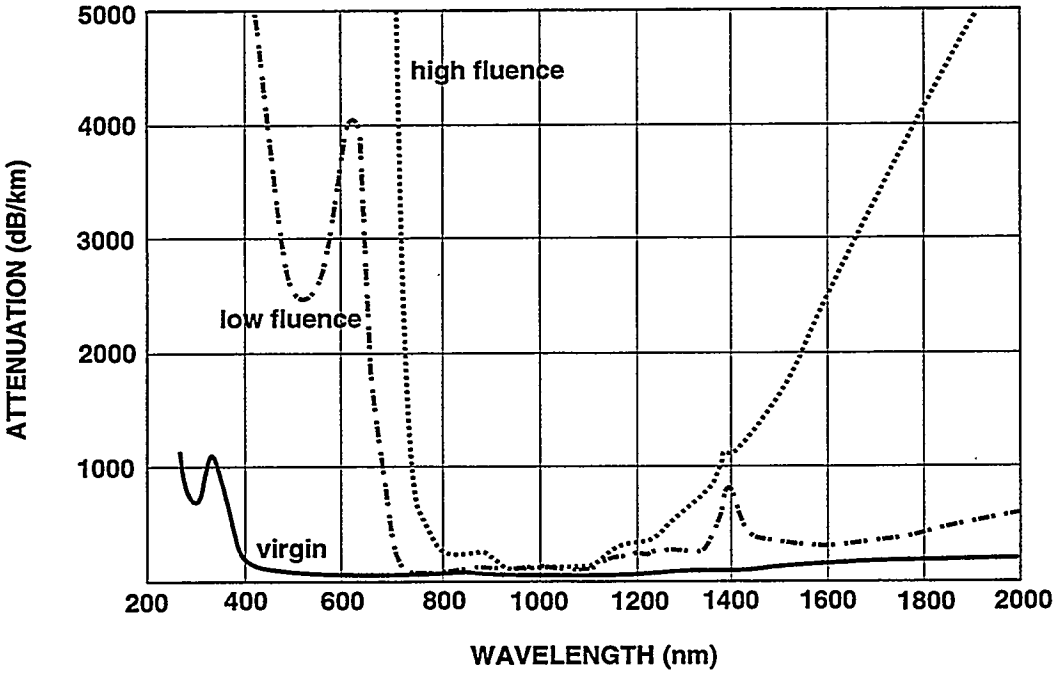

Fig 1. Optical attenuation of anhydroguide™ fibers exposed to low and high fluence neutron environments. The attenuation of a virgin specimen is shown for comparative purposes.

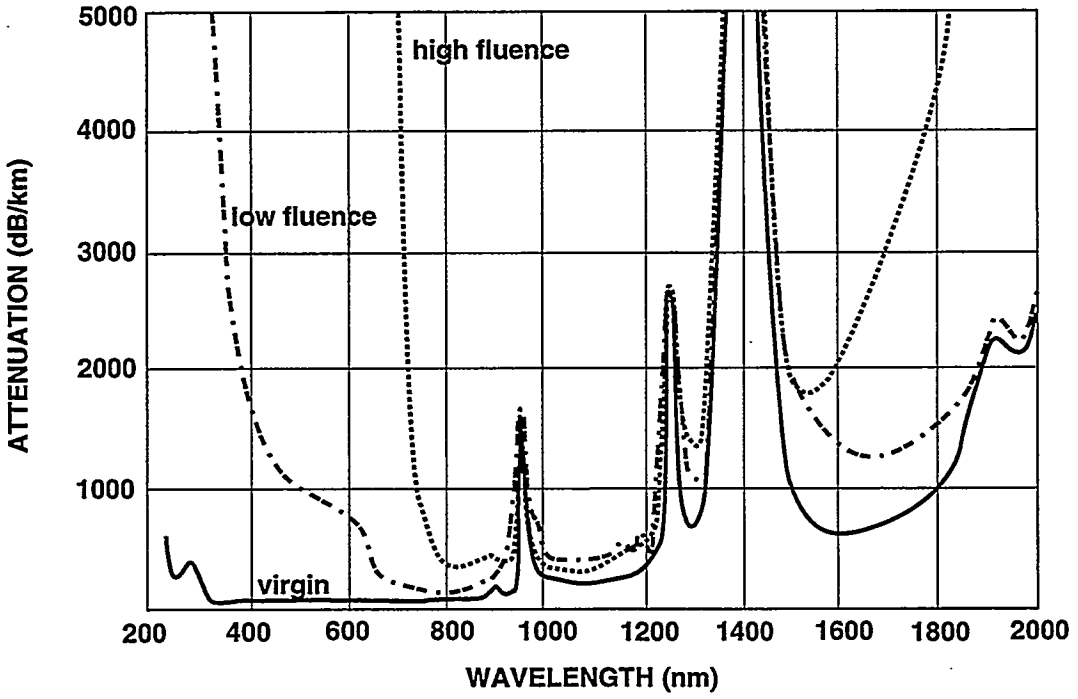

Fig. 2. Optical attenuation of superguide™ fibers exposed to low and high fluence neutron environments. The attenuation of a virgin specimen is shown for comparative purposes.

Figure 2 also shows the relative growth of non-bridging oxygen hole and short wavelength (< 400 nm) centers (usually attributed to E'-type defects). For the low fluence exposure it is easy to discern the non-bridging oxygen hole center peak near 630 nm as it grows with exposure. However, for high fluence exposures the attenuation is so large as to preclude observation of individual peaks below about 700 nm.

From a comparison of the attenuation data obtained on superguide™ and anhydroguide™ fibers exposed to high and low fluence neutron environments, we see that the low-OH anhydroguide™ fibers are more radiation resistant and, therefore, are the current material of choice for ITER applications. However, it is also evident that low OH fibers are susceptible to radiation damage in the visible portion of the spectrum even when subjected to low fluence neutron environments. This will obviously limit their usefulness in ITER diagnostic applications.

Although not exposed to neutrons, we show for comparative purposes in Fig. 3 the optical attenuation of two pristine Russian fibers possessing both low and high OH content. These were obtained from the Fiber Optics Research Center of the Russian Academy of Sciences through D. L. Griscom. The low-OH specimen is comprised of a KS-4V silica core and contains < 200 ppb OH and < 20 ppm chloride. The fiber labeled high OH in Fig. 3 has a KU silica core and contains 800 - 900 ppm OH.

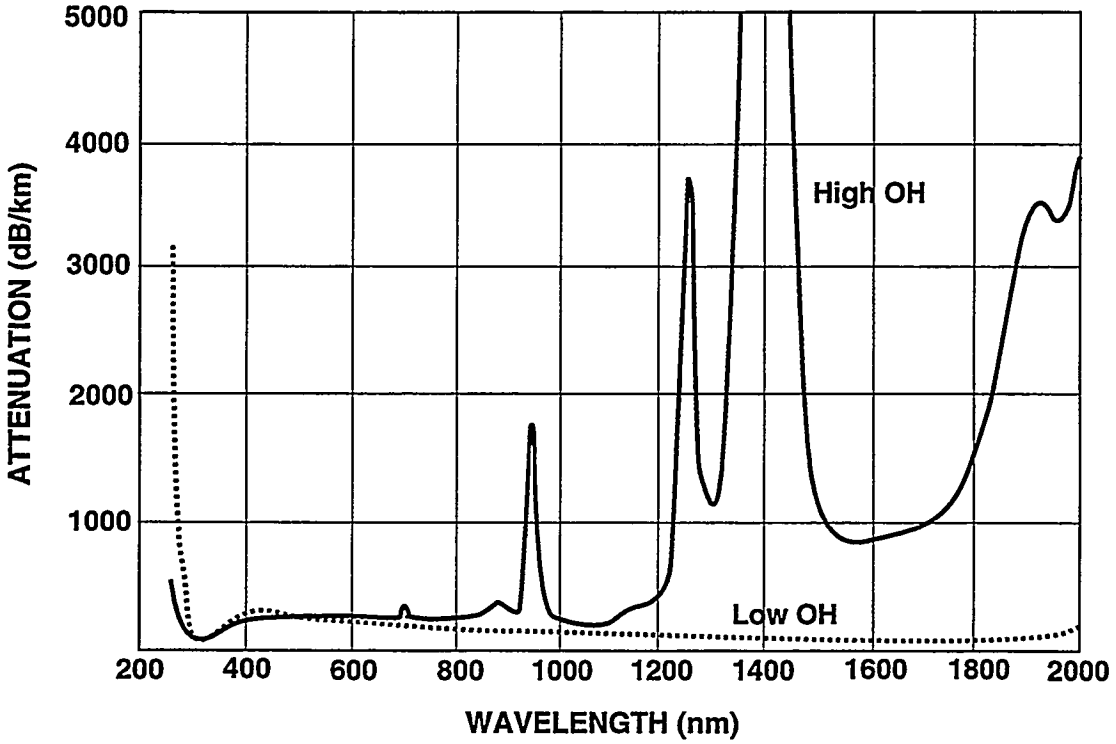

Fig. 3. Optical attenuation of unirradiated low- and high-OH content silica fibers obtained from Russia.

Consistent with the stated low OH content, there is no measurable attenuation due to OH stretching modes of this fiber. There is, however, a peak of unknown origin near 400 nm. The radiation resistance of this

fiber to neutrons has not been examined; however, D. L. Griscom has measured the gamma-induced attenuation and found significant sensitivity in the visible spectrum.[5]

Finally, we attempted radioluminescence measurements on low-fluence-exposed fibers, but were unsuccessful because of the extreme brittleness of the nylon jackets. In a typical experiment we prepare a bundle of 4 - 5 fibers with polished ends for the measurement. Because of the radiation-induced brittleness of the nylon jackets on each fiber, we were unable to polish the ends, which precluded any radioluminescence measurement. The nylon jackets apparently are very radiation sensitive and become darkened upon exposure even to a low fluence neutron environment; this may limit their use in ITER diagnostic applications.

CONCLUSIONS

We have measured the optical attenuation of pristine and neutron-irradiated, low- and high-OH content silica fibers in the wavelength interval 250 to 2000 nm. The low-OH content fibers are devoid of the intrinsic absorption associated with combination and overtone modes of the OH molecule and exhibit minimal attenuation over the entire region investigated. Exposure to high fluence neutrons induces strong absorption of the well-known defects (E' type, peroxy radical and nonbridging oxygen hole center), in addition to band-like absorption above ~ 1400 nm. Overall, the useful optical window is ~ 800 to 1400 nm and exists only in the low-OH specimen, making these fibers not particularly well suited for diagnostic use near the fusion plasma, and certainly not useable in the visible region.

Fibers exposed to low-fluence neutrons suffer radiation-induced attenuation similar to that observed from high fluence exposure, but with the attenuation reduced in magnitude. For diagnostic use in the visible portion of the spectrum, the high-OH content fibers exhibit less attenuation than the low content counterpart and are preferred. Their intrinsic OH absorption at longer wavelengths, however, makes them less attractive for diagnostic use above ~ 800 nm than the low-OH fibers.

The data suggest that presently available silica fibers can be used in plasma diagnostics, but the choice and suitability depends upon the spectral region of interest. Low-OH content fibers can be used for diagnostic purposes in the interval ~ 800 to 1400 nm if the exposure is to high fluence neutrons. For low fluence neutron exposures, the low-OH content fibers are best suited for use in the interval ~ 800 to 2000 nm, and the high-OH content fibers are the choice for the interval ~ 400 to 800 nm. Strong absorption of all fibers below ~ 400 nm will likely preclude their use in this spectral region unless other mechanisms (heating during irradiation, thermal or optical quenching, etc.) can be found to mitigate the radiation-induced damage.

REFERENCES

1. D. W. Cooke, E. H. Farnum, F. W. Clinard, Jr., B. L. Bennett, B. Sundlof and W. P. Unruh, Fusion Reactor Materials Semiannual Progress Report, DOE/ER-0313/17, Oak Ridge National Laboratory, Oak Ridge, TN. September, 1994.
2. E. J. Friebele, D. L. Griscom and J. J. Marrone, *J. Non-Cryst. Solids* **71**, 133 (1985).
3. K. Awazu and H. Kawazoe, *J. Non-Cryst. Solids* **179**, 214 (1994).
4. D. L. Griscom, *J. Ceram. Soc. Jpn.* **99**, 923 (1991).
5. D. L. Griscom. Personal Communication.

7.0 SOLID BREEDING MATERIALS

No contributions.

8.0 RADIATION EFFECTS, MECHANISTIC STUDIES, AND EXPERIMENTAL METHODS

AN INTEGRATED APPROACH TO ASSESSING THE FRACTURE SAFE MARGINS OF FUSION REACTOR STRUCTURES

G. R. Odette (Department of Mechanical Engineering and Department of Materials, University of California, Santa Barbara)

SUMMARY

Design and operation of fusion reactor structures will require an appropriate data base closely coupled to a reliable failure analysis method to safely manage irradiation embrittlement. However, ongoing irradiation programs will not provide the information on embrittlement necessary to accomplish these objectives. A new engineering approach is proposed based on the concept of a master toughness-temperature curve indexed on an absolute temperature scale using shifts to account for variables such as size scales, crack geometry and loading rates as well as embrittlement. While providing a simple practical engineering expedient, the proposed method can also be greatly enhanced by fundamental mechanism based models of fracture and embrittlement. Indeed, such understanding is required for the effective use of small specimen test methods, which is a integral element in developing the necessary data base.

INTRODUCTION

Design and operation of fusion reactors will require quantitative predictions of in-service degradation of a wide range of mechanical properties. For defect tolerant structural designs, the maximum allowable stresses and strains will often be dictated by the sizes and configurations of cracks that develop (or are presumed to develop) in service and the effective fracture toughness of the structural material. In this context, the effective fracture toughness (K_e) is defined as an engineering parameter that can be used in a structural mechanics analysis to determine the stresses (loads) and strains (load point displacements) resulting in unstable extension of a plane strain Mode I fatigue (sharp) crack of specified size and geometry. Since it may increase the probability of such rapid failures, irradiation induced degradation of fracture toughness, or embrittlement, has been identified as one of the most severe challenges to the use of martensitic steels and vanadium alloys in fusion structures. Therefore, reliable methods must be developed to predict toughness as a function of temperature (T) throughout service. Methods of measuring $K_e(T)$ must also be closely coupled to the analytical procedures used to specify safe operating limits. Developing a $K_e(T)$ data base will, in large part, rely on small specimen testing.

A particular, albeit not unique, challenge of using body centered cubic (bcc), tempered martensitic steels and vanadium alloys is related to the fact that their $K_e(T)$ increases from a lower shelf to a (quasi-) upper shelf over a temperature range defining a brittle-to-ductile transition. Except in very restricted cases, $K_e(T)$ is not a fundamental, unique material property. In particular, $K_e(T)$ depends on size scales, geometry and loading rates, as well as the alloy microstructure, which is modified by irradiation and other characteristics of the service environment.

Figure 1 illustrates the general features of a prototypical $K_e(T)$ curve and the associated stress (σ) displacement (Δ) curve. In the lower shelf and knee region, fracture occurs by a brittle cleavage (or intergranular) mechanism. Up to toughness levels of about 60 MPa$\sqrt{m}$ the macroscopic fracture is linear elastic; that is, the fracture stress (σ_f) is less than or close to the general yield stress of the specimen or structure (σ_{gy}), which is geometrically related to the uniaxial yield stress (σ_y) of the alloy. In restricted cases, $K_e(T)$ can be specified as a material property; namely, the linear elastic fracture toughness (K_{Ic}). However, operating safety-sensitive components in a brittle regime is sometimes not acceptable. Fracture also occurs by cleavage initiation in the transition region between about 60 and 175 MPa$\sqrt{m}$. However, macroscopically this takes place after general yielding at a finite plastic displacement (Δ_f). Again in restricted cases, $K_e(T)$ can be specified in terms of an elastic-plastic material property, $K_{Jc} = \sqrt{E'J_{Ic}}$, where E' is the plane strain elastic modulus and J_{Ic} is the critical crack tip energy release rate. For cleavage

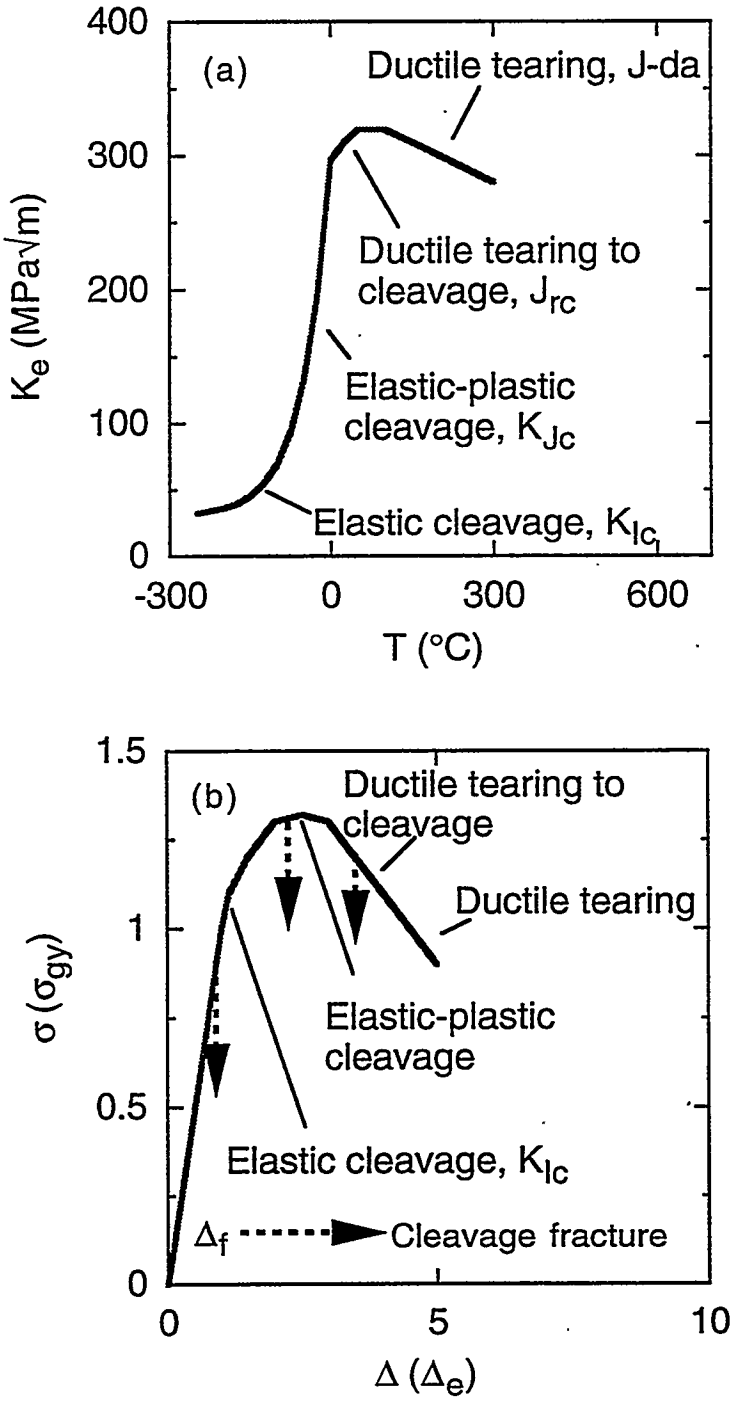

Figure 1 Schematic illustration of a) a $K_e(T)$ curve showing various fracture regimes; and b) the corresponding macroscopic applied stress-deflection (or strain) curve for a test specimen or structure.

initiation, J_{Ic} is the area under the stress-displacement curve. It is notable that in this regime, while the microscopic fracture mechanism is by propagation of brittle cleavage cracks, the structure possesses the key engineering property of ductility; and that the major benefit of plastic fracture is the capacity to "bend-before-breaking" rather than a significantly increased load bearing capacity. At still higher temperatures in the transition regime, fracture may occur by ductile tearing preceding a transition to cleavage; and in the quasi-upper shelf regime, fracture occurs by instability of ductile tearing cracks. In this work the focus will be on cleavage initiation, since for most fusion applications ductile tearing can be considered a safe, high ductility regime.

Thus the key question is how to obtain appropriate measures of $K_e(T)$ for cleavage initiation that can be applied to predict σ_f and Δ_f in actual structures. Since irradiation has profound and complex effect on $K_e(T)$, such measurements will inevitably require the use of small specimens. Further, most fusion structures themselves will not have typical heavy section (pressure vessel) configurations, with potentially deep cracks that can make direct use of traditional measures of toughness (i.e., K_{Ic}, K_{Jc}) In the past, advanced methods have been proposed based on the concept of local fracture mechanics, which will be described briefly below[1-8].

However, a much simpler master curve (MC)-temperature shift (ΔT) method is developed here that not only directly links to specifying engineering design and operation limits, but also is compatible with a more fundamental mechanism-based approach. Note, the MC-ΔT method is conceptually similar to the K_{Ir} reference curve indexed by Charpy/drop weight nil-ductility transition temperature currently used to regulate nuclear reactor pressure vessels (RPV)[9]. However, the MC-ΔT procedure proposed here is much more physically meaningful, and is specifically pertinent to fusion applications. A variety of F82H data are used to test the feasibility of the method. Note, corollary approaches are under development for RPV applications[10,11].

The specific objectives are to:

1) Evaluate the effect of specimen width (W), crack length (a) to W ratio (a/W) and loading rate on $K_e(T)$ in unirradiated F82H to assess the possibility of establishing a MC characterized by a specified reference shape that is positioned (indexed) on an absolute temperature scale by a reference temperature (T_o) plus temperature shifts (ΔT) to account for the variables noted above.

2) Interpret the fundamental basis for the observed behavior using physically-based micromechanical models and concepts.

3) Extend the results to the effects of irradiation induced shifts in miniaturized Charpy V-notch energy (E)-temperature (T) curves for F82H and similar 8 Cr martensitic alloys.

4) Illustrate how the method can be applied.

5) Identify unresolved issues.

$K_e(T)$ CURVES FOR F82H

A significant body of data on low alloy RPV steels suggest that their $K_{Ic}/J_{Ic}(T)$ curve has a relatively constant shape[10,11]. Thus unirradiated alloys can be placed on an absolute scale by measuring the temperature (T_o) at a reference mean toughness level. For RPV steels, the reference K_{Jc} is typically 100 MPa$\sqrt{m}$. Further, it has been argued that the effects of irradiation can also be treated as temperature shifts (ΔT_i) measured at the reference toughness level. This so-called master curve (MC) approach also accounts for the inherent large scatter in the transition region using Weibull statistics to set lower bound confidence

limits. This statistical interpretation also leads to size corrections, where K_{Jc} varies with the length of the crack front (B) as $B^{-1/4}$.

Figure 2 plots absolute $K_e(T)$ for F82H which has been presented previously[4,5]. Two limiting cases are shown: a) a dynamically loaded, deeply pre-cracked (a/W ≈ 0.5) Charpy specimen (DPCC); and b) a statically loaded shallow pre-cracked (a/W ≈ 0.2) minicharpy (1/3 sized) specimen (SPCMC). The SPCMC is shifted significantly downward in temperature relative to the DPCC data. However, an "eyeball" examination suggests that the two data sets can be superimposed in the lower shelf and transition regions by a ΔT of about 140°C, suggesting the possibility of a MC for F82H.

To further test this hypothesis, Figure 3 plots K_e on an adjusted temperature scale (T') for a variety of specimen configurations and dynamic versus static loading rates. The T' = T - ΔT is adjusted by the shifts (ΔT) estimated at a reference K_e of 60 MPa√m relative to the curve for deeply pre-cracked Charpy (PCC) test with T_o = -115°C. A value 60 MPa√m was chosen for referencing, since it is close to the maximum temperature of elastic fracture in PCC and deeply pre-cracked minicharpy (PCMC) tests; hence, the data are believed to be approximately "valid" even for the small "atypical" specimens used in this study. The ΔT are given in Table 1.

Table 1 -- Values of ΔT at 60 MPa√m for Tests on F82H With Various Specimen Configurations and Loading Rates

Specimen/loading rate		ΔT(°C)
Shallow pre-cracked minicharpy	(SPCMC)	-60
Shallow pre-cracked Charpy	(SPCC)	-55
Deeply pre-cracked minicharpy	(PCMC)	-20
Deeply pre-cracked Charpy	(PCC)	0 (reference)
0.6T bend bar (about 3x Charpy size)	(0.6TBB)	+10
Dynamic deeply pre-cracked minicharpy	(DPCMC)	+50
Dynamic deeply pre-cracked Charpy	(DPCC)	+80

Figure 3 also shows the recommended MC for RPV steels with a 60 MPa√m reference T_o of -115°C. The RPV MC is given by

$$Ke(T') = 30 + 30\exp[A(T'-T_o)] \text{ (MPa}\sqrt{\text{m}}\text{)} \quad (1)$$

where A = 0.019. Note, the data for the all the PCMC specimens and the SPCC are grossly invalid (K_e is not a material property like K_{Ic} or K_{Jc}) from a standard fracture mechanics perspective at levels above about 100 MPa√m. The data for PCC are reasonably valid up to about 175 MPa√m. In spite of these specimen limitations and differences in the steels, however, the RPV MC reasonably represents the F82H $K_e(T)$ trends. Adding a +30°C margin, shown as the dashed line, approximately bounds the entire data set.

However, closer examination of the data shows that the transition is somewhat steeper for F82H than predicted by the RPV MC, particularly for the specimens that are: very small; and/or have shallow cracks; and/or are dynamically loaded. This is illustrated in Figure 4 where data for these 'atypical' specimens/ tests are shown as circles, while the squares represent more "standard" PCC and 0.6TBB tests. The latter

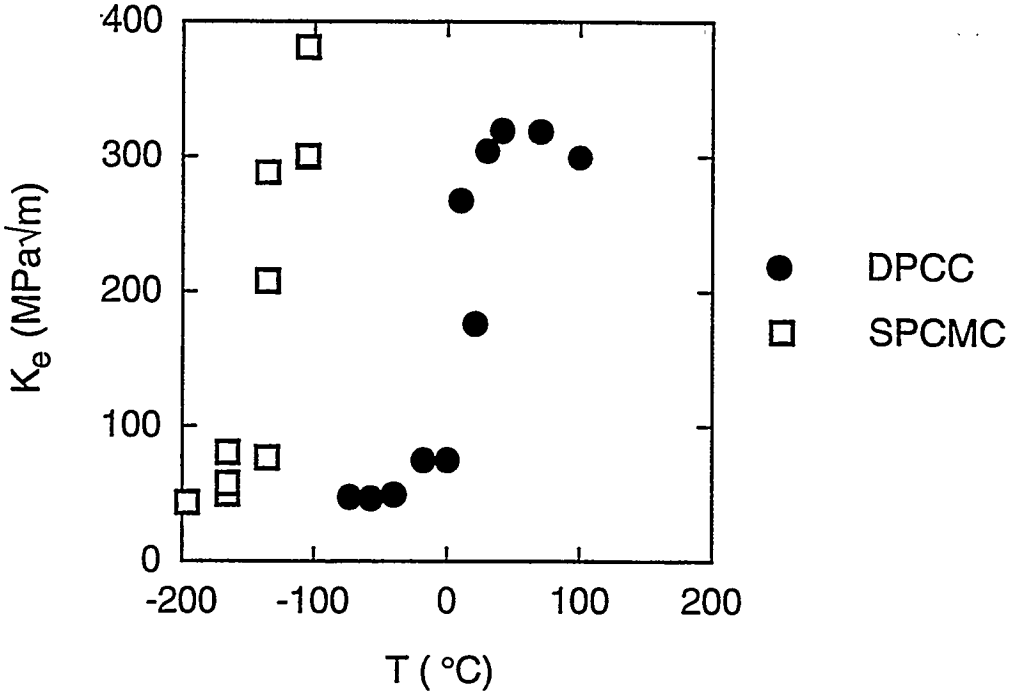

Figure 2 Comparison of the $K_e(T)$ curves for the SPCMC (squares) and DPCC (circles) tests.

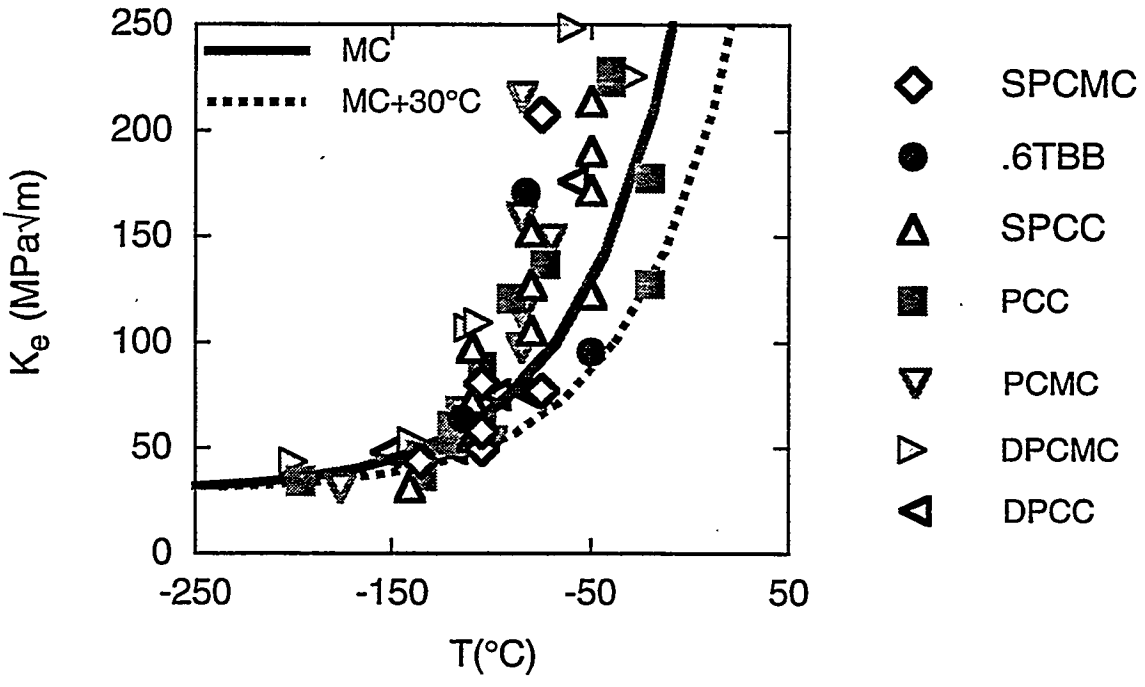

Figure 3 The adjusted $K_e(T')$ curves compared to the RPV MC and MC + 30°C bound.

data tend to follow the RPV MC, although the transition may be a little steeper even in this case. The dashed curve shows a crude fit to the data for the atypical specimens/tests, where the exponential coefficient in Equation 1 has been increased to $A = 0.038$.

Both the shape differences and the shifts shown in Table 1 can be qualitatively understood in terms of the underlying micromechanics of cleavage and the brittle-to-ductile transition. Further, these concepts can be used to model the effects of irradiation and other in-service degradation processes.

LOCAL FRACTURE MECHANICS, CRACK BLUNTING AND MCIROMECHANICS MADE SIMPLE

The underlying assumption of traditional fracture mechanics is that the crack tip fields that cause fracture are the same in a specimen as a structure, and can be fully characterized by a single macroscopic loading parameter (K or J)[12]. Further, cleavage fracture and the brittle-to-ductile transition in body centered cubic alloys can be explained as follows: a) fracture is caused by the concentrated stress and/or strain fields that develop in the vicinity of an initially sharp fatigue crack as it blunts to a tip opening (δ) in response to externally applied loads; b) fracture occurs at a critical opening (δ_{Ic}); c) δ can be related to the external loading conditions, hence, the applied J or K (and δ_{Ic} to K_{Ic} or K_{Jc}); d) the relationship between K, J and δ depends on the alloy stress-strain or constitutive properties (e.g., $\delta/J \approx 0.5\sigma_y$) and the specimen/structure-crack geometry; e) in limited cases for deep-through (versus surface) cracks in sufficiently large specimens (all dimensions more than about $100\delta_{Ic}$), local tip small scale yielding (SSY) stress and strain fields are totally dominated by the nearby crack and are self-similar (e.g., the amplitudes of the stress and strain distributions do not change with δ and the spatial extent of these fields is normalized by δ); f) cleavage requires very high local stresses normal to the fracture plane (σ_n) operating over a microstructurally relevant region ahead of the crack tip (note, it is this stressed area/volume requirement that establishes the physical size scaling in cleavage fracture processes); g) high σ_n requires a combination of a large tensile flow stress which is further elevated by the multiaxial constraint near the crack tip ($\sigma_{nmax} \geq M\sigma_y$, where σ_y is the yield stress and M is a strain hardened constraint factor ≥ 3); h) in bcc alloys large σ_y (used here as a surrogate for flow stress) increases with decreasing T and increasing strain rate ($\dot{\varepsilon}$); i) hence, cleavage is promoted by low T and high $\dot{\varepsilon}$; j) if the required σ_n-stressed regions condition is not achieved, ductile fracture occurs by strain-controlled, stress-mediated nucleation, growth and coalescence of microvoids that form on hard particles.

While more complex descriptions have been proposed, these ideas can be further quantified by a simple model which postulates that cleavage occurs when the σ_n exceeds a critical local stress (σ^*) over a critical area (A^*) in front of the crack tip, where the σ^*/A^* properties are approximately independent of temperature, strain rate and irradiation. The stressed area (A) can most simply be defined by the isostress contour of σ_n. Under SSY conditions A is proportional to the square of the applied J or δ. The σ^*/A^* condition occurs when the $J/K/\delta$ reach critical values $J_{Ic}/K_{Jc}/\delta_{Ic}$.

These ideas directly explain the ductile-to-brittle transition. At very low temperatures σ_y is high and A^*/σ^* is achieved at a small δ_{Ic}. On the lower shelf K(T) is roughly constant due to the fact that there is an approximately equal trade-off between the increased magnitude of σ_n and a decreased size of the stress field with higher σ_y (lower T). However, as σ_y continues to decrease with increasing T, the δ_{Ic} required to produce σ^*/A^* begins to increase rapidly. At even higher T, σ_{nmax} is less than σ^*, thus cleavage fracture cannot occur. The effects of loading rate on the position the $K_e(T)$ curve can be simply understood based on the increase of σ_y with $\dot{\varepsilon}$. The sharper transition in the dynamic loading tests can also be partly explained on the basis of adiabatic heating in the plastic zone which locally decreases σ_y.

Unique, self-similar relations between σ^*/A^* and δ_{Ic} occur only for SSY conditions, which are not maintained in small or shallow cracked specimens. In small specimens σ_n decreases due to a loss of

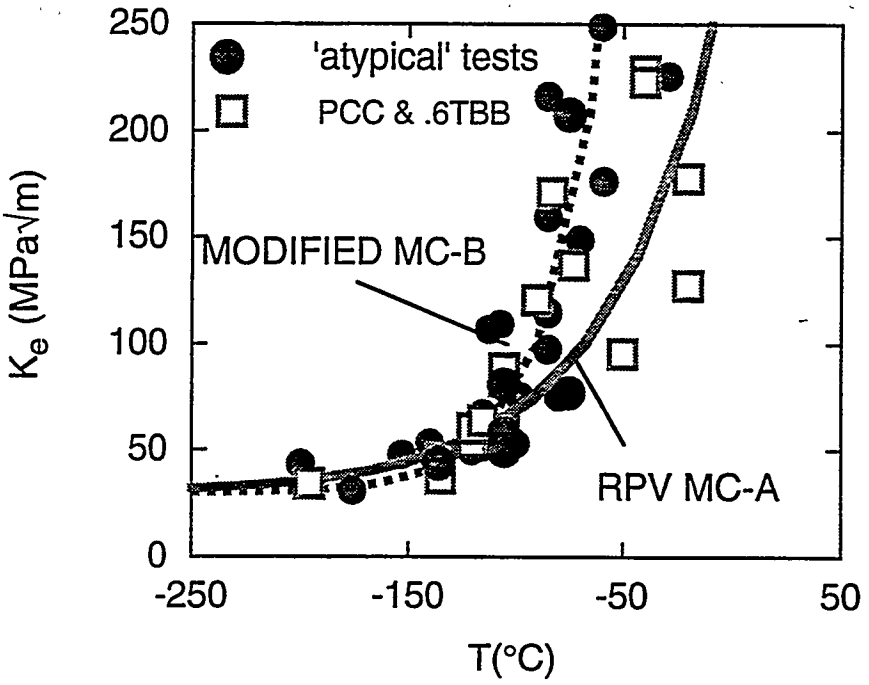

Figure 4 The $K_e(T)$ data for atypical tests (circles) versus PCC and 0.6TBB data (squares) along with the RPV MC (A) and modified MC (B).

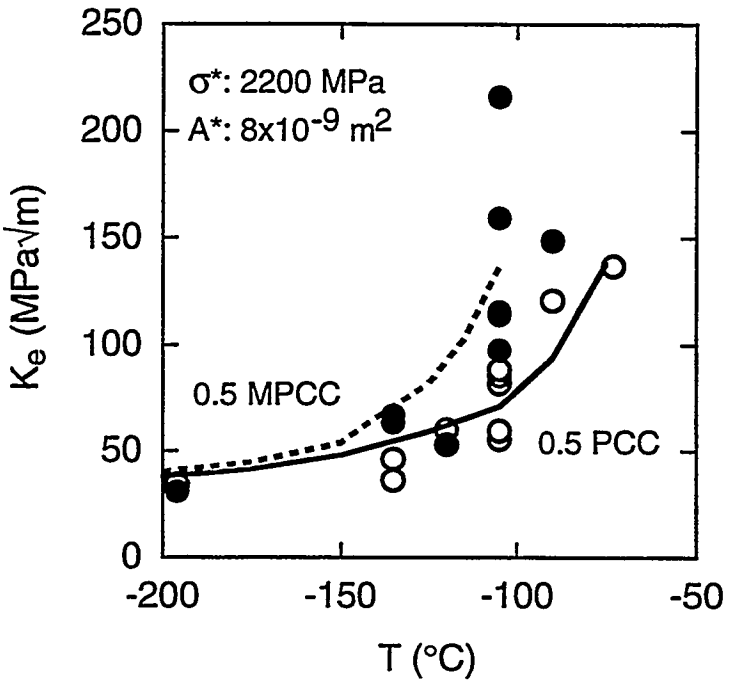

Figure 5 $K_e(T)$ curves predicted by the σ^*/A^* model compared to data for PCMC and PCC specimens.

constraint (lower M) when plastic deformation reaches free surfaces. Likewise for shallow cracks, σ_n decreases due to a constraint reduction caused by secondary non-singular compressive stress fields (so-called T-stresses) in the direction of the specimen width. In both cases, a larger δ_{Ic} is needed to achieve the A^*/σ^* cleavage condition. Thus for small and/or shallow cracked specimens the $K_e(T)$ curves are shifted to lower temperature, where the higher σ_y offsets the effects of lower constraint. The somewhat steeper transition in these cases can be explained by a combination of three effects: a) $d\sigma_y/dT$ is higher at lower temperature; b) $\delta(A^*/\sigma^*)$ increases with δ, viz., an initial loss of constraint leads to even more loss of constraint before fracture; and c) loss of lateral plane strain conditions at larger deformation.

Constraint loss retards microvoid nucleation and growth, hence, also increases the ductile fracture toughness. Ultimately small specimens lose the capacity to fracture at all and simply respond to applied loads by massive deformation and crack blunting. Thus great caution must be used in interpreting small specimen data. Small specimens can not only lack the ability to provide "valid" intrinsic properties, but may also fail to detect real physical phenomena such as cleavage or even any type of fracture.

MODELS OF TEMPERATURE SHIFTS DUE TO SIZE, GEOMETRY, LOADING RATE AND IRRADIATION

It has been previously shown that the qualitative concepts described in the previous section can be used to qualitatively model the effects of size, geometry, loading rate and irradiation on both $K_e(T)$ data (only up to a point) as well as Charpy V-notch (CVN) energy-temperature (E-T) curves for both RPV steels and a 12 Cr martensitic stainless steel (HT9)[1-8].

Application of an A^*/σ^* model to predict size effects in F82H is shown in Figure 5. Here, crack tip stress fields, represented in terms of $A(\sigma_n)$ versus K_J, were computed with the finite element method (FEM) code ABAQUS using an experimentally derived constitutive law. Figure 5 shows the predicted $K_e(T)$ curves for the deeply cracked PCC and PCMC are consistent with the data trends for fixed A^* and σ^* values of $8x10^{-9}$ m^2 and 2200 MPa, respectively. The predicted ΔT at 60 MPa$\sqrt{m}$ of about 25°C is in good agreement with the estimated shift of about 20°C. The same model also correctly predicts that the $K_e(T)$ for specimens with shallow cracks are shifted to lower temperatures, have steeper slopes in the transition region and manifest smaller SPCMC to SPCC shifts than the corresponding curves for the deeply cracked specimens. However, using the same A^*/σ^* of $8x10^{-9}$ m^2/2200 MPa does not yield good quantitative agreement between the model and the shallow crack $K_e(T)$ data. Thus a simple local fracture toughness model (fixed A^*/σ^*) appears sufficient to treat the gross effect of size, but not crack depth. More detailed micromechanical models are needed to resolve this issue.

The effects of loading (strain) rate ($\dot{\varepsilon}$) and radiation hardening ($\Delta\sigma_i$) can be treated even more simply based on the assumption that the maximum temperature of elastic fracture (T_o at 60 MPa$\sqrt{m}$ for static and dynamic toughness) occurs at a specified σ_y. Assumptions of this simple equivalent yield stress (EYSM) model include: a) the overall stress-strain curve is the same at the same σ_y, independent of $\dot{\varepsilon}$ and $\Delta\sigma_i$; b) the local fracture conditions (A^*/σ^*) are independent of T, $\dot{\varepsilon}$ and irradiation; c) $\Delta\sigma_i$ is independent of T and $\dot{\varepsilon}$; and d) T_o is at about 10J for standard and 0.5J for miniaturized Charpy tests.

First consider shift due between dynamic (d) and static (s) loading rates (ΔT_d). The EYSM states that $\Delta T_d = T_d - T_s$ where $\sigma_{yd}(T_d) = \sigma_{ys}(T_s)$. The effect of $\dot{\varepsilon}$ on σ_y can be treated in terms of a strain rate compensated temperature ($T_{s/d}$) as

$$\sigma_y (T_{s/d}, \dot{\varepsilon}_{s/d}) = \sigma_y (T_r, \dot{\varepsilon}_r) \qquad (2a)$$

where,

$$T_r = T_{s/d}[1+C\ln(\dot{\varepsilon}_r/\dot{\varepsilon})] \quad (2b)$$

Here T_r and $\dot{\varepsilon}_r$ are the reference temperature (°K) and strain rate; for F82H, $\dot{\varepsilon}_r$ was taken as 3.33×10^{-3}/s and $C \approx 0.028$[8]. Thus ΔT_d is simply given by

$$\Delta T_d = T_{os}\{[1+0.028\ln(\dot{\varepsilon}_r/\dot{\varepsilon}_s)]/[1+0.028\ln(\dot{\varepsilon}_r/\dot{\varepsilon}_d] - 1\} \quad (3)$$

where T_{os} is the 60 MPa$\sqrt{m}$ reference temperature for the static tests. The estimated static strain rates for PCC and PCMC are about 7.7 and 23.1×10^{-3}/s, respectively. The ratio of the dynamic to static time to fracture is typically about 1.67×10^{-4}. The predicted (ΔT_{dp}) versus measured (ΔT_{dm}) shifts for the PCC and PCMC specimens are shown in Table 2.

Table 2 - Predicted vs. Measured Static to Dynamic ΔT_d

Specimen	T_{os} (°C)	ΔT_{dp}(°C)	ΔT_{dm}(°C)
PCC	-115	75	80
PCMC	-135	65	70

The EYSM can also be applied to the shifts (ΔT_i) due to irradiation hardening ($\Delta\sigma_i$). In this case the shift ΔT_i in the irradiated (T_{oi}) versus unirradiated (T_{ou}) reference temperature is simply given by the condition that $\sigma_y(T_{oi}) = \sigma_y(T_{ou}) + \Delta\sigma_i$. Unfortunately, there is no irradiated $K_e(T)$ data available for F82H. However, the model can be applied to RPV steels as illustrated in Figure 6. Here tests were on PCMC specimens of a A533B reference steel plate (HSST-02) irradiated at 288°C to about 0.04 displacements-per-atom (dpa), producing a $\Delta\sigma_i \approx 155$ MPa. The model predicts a reasonable ΔT_i of about 90°C. However, the predicted decrease in the $K_e(T)$ slope in the transition region is not observed. Further, the EYSM predicts that the $\Delta T_i/\Delta\sigma_i$ ratio (S) increases with increasing $\Delta\sigma_i$ and T_{ou}. Indeed, at very high $\Delta\sigma_i/T_{ou}$ combinations, the model suggests that S increases rapidly above "normal" values in the range of 0.7±0.4°C/MPa. However, large reductions in slope and S values much greater than 1 have not been observed in RPV steels. Hence, as in the case of shallow cracks, more detailed micromechanical models are needed to resolve this apparent limitation of the EYSM.

The EYSM has been successful in using $\Delta\sigma_i$ to predict ΔT_i measured in standard Charpy V-notch tests[1]. Application to data reported by Klueh on miniature Charpy V-notch (MCVN) tests on two 9Cr based alloys, similar to F82H, irradiated at 375°C to 7 dpa[13] is shown in Table 3. The static $\sigma_y(T)$ data is represented by a polynomial given elsewhere[8]. The $\dot{\varepsilon}$ for the MCVN tests is taken at 275/s. While the predictions of ΔT_i for the 9Cr-2VWTa alloy are somewhat greater than observed values, the results support the very low embrittlement sensitivity of these alloys, and suggest that this is in part due to the very low T_{ou}.

Figure 7 shows the EYSM applied to some recent data for irradiation of F82H MCVN specimens to 0.8 dpa at 250°C reported by Rieth and co-workers[14]. The 0.5J reference T_{ou} was estimated as -90°C, based on MCVN data for F82H[5]. The $\Delta\sigma_i$ are values for dynamic yield stress changes at 100°C. The measured ΔT_i were taken at the reported shifts referenced at 50% of the upper shelf energy, rather than at 0.5J. Good agreement between the measured and predicted ΔT_i is observed.

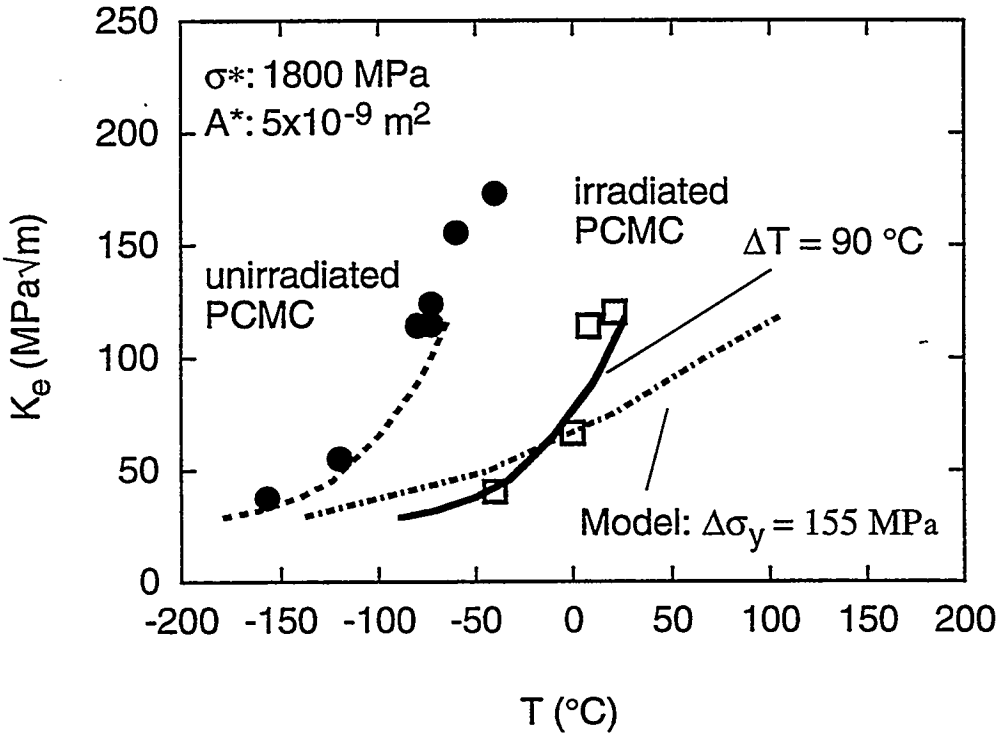

Figure 6 Predicted versus measured shifts in the PCMC $K_e(T)$ curve for an A533B RPV steel due to irradiation resulting in $\Delta\sigma_i$ of 155 MPa.

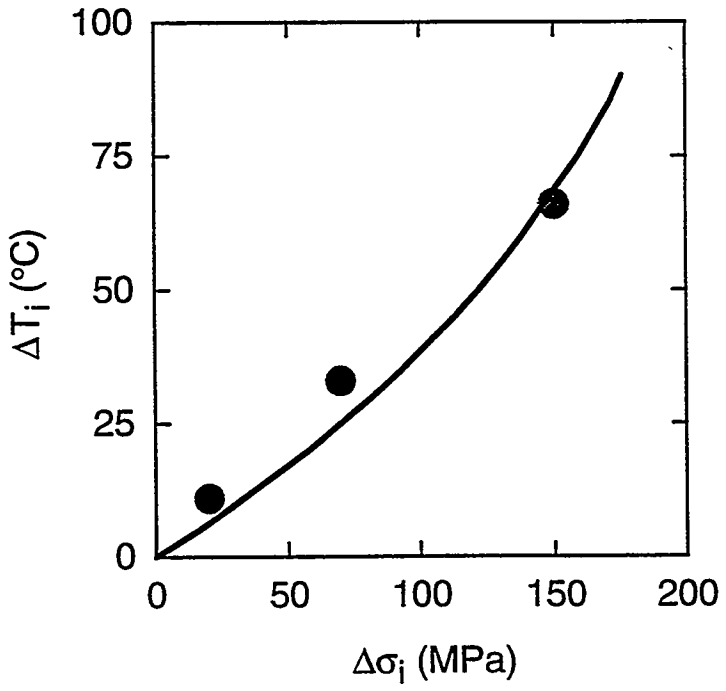

Figure 7 EYSM prediction of ΔT_i as a function of $\Delta\sigma_i$ compared to MCVN data on F82H.

Table 3 - Predicted vs. Measured ΔT_i for MCVN Tests on 9 Cr Steels

Spec./Prop.	T_{ou}(°C)	$\Delta\sigma_i$ (MPa)	$\Delta T_{i\,p}$(°C)	$\Delta T_{i\,m}$(°C)
9Cr-2VW	-120	161	68	68
9Cr-2VWTa	-150	125	36	11

Overall, the results described in this section demonstrate that application of the simple micromechanical models to F82H qualitatively, and in some cases quantitatively, rationalize the effects of size, geometry and strain rate on $K_e(T)$ curves; and also reasonably predict ΔT_i measured in MCVN tests. In addition, as noted previously, elaboration of the simple models can be used to predict statistical confidence limits and the effects of size scales on the statistics. For example, the slope of 4 assumed (and often observed) in Weibull rank probability versus K log-log plots[10,11] is consistent with the σ^*/A^* model where the stressed area (A) varies as K^4 under SSY conditions; the scaling of A with K^4 under SSY, also rationalizes the $B^{-1/4}$ dependence on the crack front length, assuming cleavage fracture actually depends on a net stressed volume, rather than area.

The most notable deficiencies in these models are inadequate treatment of shallow versus deep cracks and possible conservative predictions of the effects of irradiation on shifts and shape changes in $K_e(T)$ curves. Predictions of the EYSM are also very sensitive to the value of T_o which may be difficult to accurately define, particularly for CVN and MCVN tests. However, these limitations can be addressed by additional fundamental research. Finally, it is important to emphasize that rigorous micromechanical models have importance far beyond analyzing and applying fracture data. In particular, such models would be of immense benefit in linking microstructure to mechanical properties and in helping to guide the rational design of higher performance alloys.

ENGINEERING APPLICATION OF THE MC-ΔT METHOD FOR SETTING STRESS , STRAIN AND OPERATING LIMITS ON FUSION STRUCTURES

It is axiomatic that fusion structures will operate under a wide range of conditions of temperature, loading and flaw configurations. Thus design procedures and the supporting data base must be sufficiently general and quantitative to reliably specify safe stress and strain limits for a variety of circumstances, including abnormal events, such as plasma disruptions.

Since fusion reactors will undoubtedly go though many cycles of startups and shutdowns, as well as sustained operation, an analogy to the so called operating-curves for RPVs may be warranted. The RPV operating-curve specifies the combination of pressures (P) and T (P-T) that insure against fracture of the vessel. At low T the allowed P is low since the toughness is low. However, as long as the actual P-T combination is held below the prescribed P-T curve, the vessel is considered safe, even at low K_{Ic}. As the T and K_{Ic}/J_{Ic} increases, the safe operating P also increases. Thus the vessel can be brought from cold-shutdown to hot-operation as long as the primary cooling system can provide enough heat (by pumps in pressurized water reactors) to remain below the P-T curve. However, irradiation-induced shifts in toughness shift the P-T curve up in T, and a very large ΔT may even close the operating window. Other RPV analogies that may be pertinent to fusion structures are treatment of transient events such as pressurized thermal shock.

It is possible to determine the stress-strain limits for fusion structures by appropriate mechanics analysis if the $K_e(T)$ and the basic constitutive properties of a structural alloy are known. In addition to use of

advanced FEM methods, sophisticated non-destructive examination methods will certainly play a key role in assuring the reliability of fusion structures. However, in the following discussion the use of the MC-ΔT method is demonstrated with a very simple example, for purposes of illustration only.

First it is assumed that the two basic shapes shown in Figure 3 can be used as provisional MC [$K_{mc}(T')$] for two classes of application: MC-A for static loads with fracture in or near the SSY regime for sufficiently large dimensions and deep cracks, with A = 0.019; and MC-B for high loading rates, shallow cracks and applications involving small dimensions when cleavage fracture occurs well beyond the SSY, with A = 0.038.

Figure 8 shows estimates of various stresses for a shallow surface crack (a/W = 0.3) in a relatively thin (W = 1.0 cm) plate with a surface length (2c) three times the crack depth (2c/a = 3) subject to a rapid disruption stress peaking in about 1 ms (typical of dynamic tests). Hence, MC-B is used in the form

$$K_e(T) = 30 + 30\exp[0.038(T - \Delta T_t - T_o)] \quad (MPa\sqrt{m}) \tag{4}$$

where ΔT_t is the total shift accounting for size (ΔT_s), loading rate (ΔT_d), crack depth ($\Delta T_{a/W}$), irradiation (ΔT_i) and a safety margin (ΔT_m). The values used in this example are shown in Table 4.

Table 4 - ΔT Values Used in the MC-ΔT Application Example

Adjustment	Temperature/Shift(°C)
T_o	-115
ΔT_s	+ 10
ΔT_d	+ 80
$\Delta T_{a/W}$	- 20
ΔT_i	+100, 200, 300
ΔT_m	+ 60

The solid curves are the estimates of the stresses at cleavage initiation based on a elastic stress intensity factor and ΔT_i of 100, 200 and 300°C (indicated respectively by the increasing line thickness). The dashed curves are the unirradiated static and dynamic σ_y (σ_{ysu}, σ_{ydu}) and σ_{ysi} is simply the σ_{ysu} increased by an arbitrary $\Delta\sigma_i$ = 300 MPa. The results show that for ΔT_i = 300°C the structure is brittle at operating temperatures below about 260°C and must be operated at a value well below σ_{ysu}. At higher operating temperatures, the stress limits may increase slightly above σ_{ysu} (e.g., ≈ 20%); however, since the stress capacity of the structure is ultimately limited by deformation controlled collapse (rather than fracture), higher temperatures are significant primarily in increasing the structures ductility. Sufficient ductility is very important since it reduces the effects of secondary (self-relieving) stresses, and also enables the stress reductions provided by typical structural compliance. Of course, what constitutes sufficient ductility depends on the specific design. The minimum temperature of the ductile regime varies directly with ΔT_i .

Figure 8 can also be viewed as an example of an operating curve. Consider the following set of scenarios (again, as examples only). At startup in the brittle regime the primary stresses (σ_p) and thermal (or residual) stresses (σ_{th}) might be limited to

$$\sigma_p + \sigma_{th} < 0.33\,\sigma_{max} \tag{5a}$$

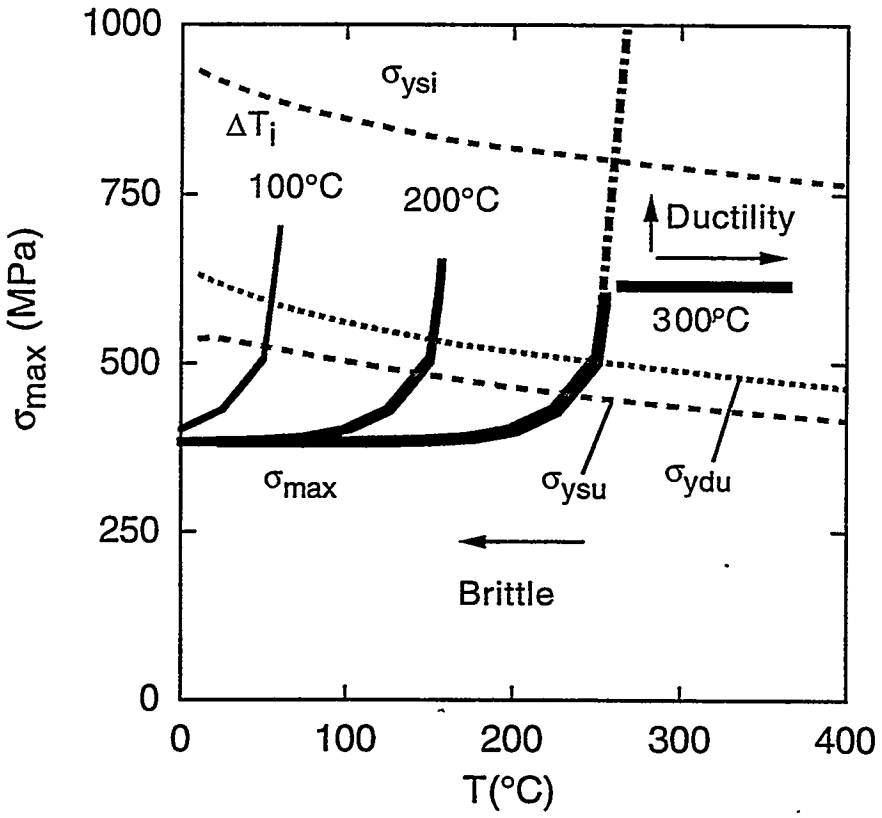

Figure 8 A schematic illustration of how the MC-ΔT method could be used to establish maximum operation stress-temperature limits in a fusion reactor structural component. At low temperatures in the brittle regime the stresses would be limited to a small fraction of the σ_{syu}. At higher temperatures above the transition, the stress limits could be increased, depending on the structural ductility requirement. In the ductile regime the maximum stresses would be limited to the σ_{syu} unless credit were taken for the $\Delta\sigma_i$.

giving a safety factor of 3. This might be managed by controlling the heating rate and the coolant pressure. At higher operating temperatures, in the ductile regime, the allowed stress limits might be increased to something like,

$$2\sigma_p + \sigma_{th} < 0.9\sigma_{ysu} \tag{5b}$$

giving a safety factor of 2 for primary stresses and 1 for thermal stresses. Finally, during a rare transient the safety margins might be further relaxed to

$$\sigma_p + \sigma_{th} < 0.9\,\sigma_{ysu} \tag{5c}$$

While these results are not numerically significant, they illuminate a key point. That is, unless an appropriate data base and closely coupled fracture mechanics method are available, it will not be possible to design a fusion reactor structure that can be licensed and operated in a safe, efficient and reliable manner. Clearly, a key element of this is an appropriate data base on irradiation embrittlement. Hence, it is particularly unfortunate that previous, ongoing and most planned irradiation programs will collectively provide only very limited information necessary to accomplish this objective.

USE AND MISUSE OF SMALL SPECIMEN TESTS

The technical conclusions of this work point to the need for a significant modification of current approaches to irradiation experiments in particular, and methods of dealing with embrittlement in general. Hence, while the author does not intend that the following statements be viewed as being too harsh or overly critical, given the costs, time and often one-of-a-kind nature of irradiation experiments, a wake up call is clearly needed. First, small specimen test methods can and will play a critical role in developing an appropriate embrittlement data base. However, this will be effective if, and only if:

- the small specimen tests are specifically designed to provide a comprehensive range of data including information on size, geometry, loading rate (as well as irradiation effects) on $K_e(T)$ and the basic alloy constitutive properties;
- the small specimen test data are analyzed, interpreted and applied with a sufficient level of understanding of the fundamental micro- and macro-mechanics of fracture;
- the data base is closely coupled to an analytical method to determine the safe stress and displacement (or strain) limits of actual fusion structures.

While these points seem obvious, they have not been generally reflected in the past, current and most planned irradiation experiments. For example, MCVN tests are typically used as the main measure of embrittlement. However, no method has been presented, or proposed, as to how to use this data base to predict the performance of fusion structures. Indeed, it has been argued that the MCVN tests are good "screening tools" that can rank the relative performance of different alloys; however, even this assumption has been shown to be incorrect[5] (as well as being a limited and dated objective). It is further noted that efforts to relate MCVN to full sized Charpy test results are not useful in this regard. Perhaps an even more egregious shortcoming of these simple-minded approaches is the persistent failure to include sufficient numbers of tensile specimens in key irradiation experiments.

CONCLUSIONS

A practical engineering method for managing the problem of irradiation embrittlement fusion reactor structures based on a master curve-reference temperature shift (MC-ΔT) method has been proposed. A preliminary evaluation of existing data shows the approach to be very promising. In particular, the MC-ΔT method is, on one hand, compatible with quantitative evaluation of stress and strain limits in actual structures while also capable of being interpreted and supplemented by a fundamental understanding of the micromechanics of fracture and embrittlement. The latter is absolutely necessary if small specimen test methods are to be used to develop the necessary embrittlement data base. However, significant research is needed to implement the MC-ΔT method or any other viable alternative. For example, the understanding of fracture due to shallow cracks and the effect of irradiation on the shape of the toughness-temperature curve are currently inadequate. However, the most critical need is to carry out irradiation experiments that will actually be useful in developing a data base for an integrated method of assessing the fracture safe margins of fusion structures.

ACKNOWLEDGMENTS

The contributions of G. Lucas, K. Edsinger, W. Sheckherd and B. Wirth to the research supporting the approach developed in this work are greatly appreciated. The research was supported by the US Department of Energy, Office of Fusion Energy Grant # DE-FG03-87ER-52143.

REFERENCES

1. G. R. Odette, P.M. Lombrozo, P.M., R. A. Wullaert, "The Relationship Between Irradiation Hardening and Embrittlement of Pressure Vessel Steels", Effects of Irradiation on Materials, 13, ASTM-STP-870, ASTM (1985) 841.

2. G. R. Odette, "On the Ductile to Brittle Transition in Martensitic Stainless Steels", J. Nucl. Mater., 212-215 (1994) 45.

3. G. R. Odette, B. L. Chao, G. E. Lucas, "On Size and Geometry Effects on the Brittle Fracture of Ferritic and Tempered Martensitic Steels", J. Nucl. Mater., 191-194 (1992) 827.

4. K. Edsinger, G. R. Odette, G. E. Lucas, J. W. Sheckherd, "The Effect of Size, Crack Depth and Strain Rate on the Fracture Toughness-Temperature Curves of a Low Activation Martensitic Stainless Steel", J. Nucl. Mater. (in press).

5. G. E. Lucas, G. R. Odette, J. W. Sheckherd, K., Edsinger and B. Wirth, B., "On the Role of Strain Rate, Size and Notch Acuity on Toughness: A Comparison of Two Martensitic Stainless Steels", Effects of Radiation on Materials, 17, ASTM STP 1270, ASTM (in press).

6. K. Edsinger, G. R. Odette, G. E. Lucas, B. Wirth, "The Effect of Constraint on Toughness of a Pressure Vessel Steel", ibid 5.

7. B. Wirth, K. Edsinger, G. R. Odette and G. E. Lucas, "Evaluation of Embrittlement in a Pressure Vessel Steel by Fracture Reconstruction", ibid 5.

8. K. Edsinger, "Fracture Reconstruction and Advanced Micromechanical Modeling of Structural Steels", PhD Thesis - Department of Chemical and Nuclear Engineering, University of California, Santa Barbara (1995)

9. United States Nuclear Regulatory Commission, Regulatory Guide 1.99: Radiation Embrittlement to Reactor Vessel Materials, U.S. Government Printing Office, Washington, D.C. (1988).

10. K. Wallin. , "The Scatter in KIc Results", Engineering Fracture Mechanics, 19-6 (1984) 1085

11. D. McCabe, J. G. Merkle and R. Nanstad, "A Perspective on Transition Temperature and KIc Data Characterization", Fracture Mechanics, 24, ASTM STP 1207, ASTM (1994) 215

12. D. Broek, Elementary Engineering Fracture Mechanics, Kluwer Academic Publishers (1991)

13. R. Klueh and D. Alexander, "Impact Toughness of Irradiated Reduced Activation Ferritic Steels", Fusion Reactor Materials Semiannual Progress Report 9/30/93 DOE/ER-0313/15 (1994) 148

14. M. Reith, B. Dafferner, H.D. Rohrig, "Charpy Impact Properties of Low Activation Alloys for Fusion Applications After Neutron Irradiation", J. Nucl. Mat. (in press)

DEFECT INTERACTIONS WITHIN A GROUP OF SUBCASCADES - H. L. Heinisch (Pacific Northwest National Laboratory[1])

OBJECTIVE

The objective of this work is to determine the energy and temperature dependence of defect production and microstructure evolution for the development of fission-fusion correlations.

SUMMARY

The evolution of the defect distributions within high energy cascades that contain multiple subcascades is studied as a function of temperature for cascades in copper. Low energy cascades generated with molecular dynamics are placed in close proximity to simulate the arrangement of subcascades within a high energy event, then the ALSOME code follows the evolution of the cascade damage during short term annealing. The intersubcascade defect interactions during the annealing stage are found to be minimal. However, no conclusions regarding effects of subcascades on defect production should be drawn until intersubcascade defect interactions during the quenching stage are examined.

PROGRESS AND STATUS

Molecular dynamics (MD) studies of cascade-producing radiation damage are limited in the size of cascade that can be simulated and the length of time the simulation can be followed at the atomic scale. MD simulations of cascades at energies capable of producing well defined subcascades (E > 50 keV in Cu) are not possible, and simulated cascade evolution times greater than about 100 ps are not practical. To obtain a quantitative understanding of defect production and evolution under fusion irradiation conditions, it is necessary to go beyond the practical size and time restrictions of MD using models that realistically describe the important characteristics of the defects and their interactions.

To go beyond MD in time, stochastic annealing simulations have been used to follow the evolution of cascade damage at an atomic scale[1]. Annealing simulations have demonstrated a differential in the number of mobile vacancies and SIAs escaping the cascade that has a strong temperature dependence and is the basis for the "production bias" that promotes void swelling. This phenomenon is shown to be the result of the production of vacancy and self-interstitial atom (SIA) clusters directly in the collision cascade, the stability of SIA clusters relative to the stability of vacancy clusters, the existence of small, highly mobile SIA loops, and the relative spatial separation of the vacancy and SIA defects. All of these features are modeled explicitly in the ALSOME stochastic annealing code.

To go beyond MD limitations on recoil energy, binary collision approximation (BCA) models have been considered. A BCA model is capable of dealing with the highest energy recoils, but one cannot follow the cascade beyond the collisional stage. Calibrations of BCA to MD results at lower energies have been attempted with limited success[2]. The total numbers of vacancies and SIAs remaining after the quenching stage can be acceptably modeled in the calibration, but the cluster size distributions, which have been found to be extremely important during the subsequent annealing stage[1], are not sufficiently similar by the calibrated BCA and MD models.

---

[1]*Pacific Northwest National Laboratory is operated for the U.S. Department of Energy by Battelle Memorial Institute under Contract DE-AC06-76RLO 1830.*

Defect Interactions Among Subcascades. To gain some insight into the effects of defects produced in subcascades interacting with defects within other subcascades, high energy cascades were "constructed" from MD cascades of lower energies. Two 25 keV cascades generated with MD[3] were placed within the same ALSOME annealing volume, separated by a fixed distance, and annealed as a single cascade. Results for three different center-to-center cascade separations R are displayed in each plot here: R=35a (lattice parameters), which is just greater than edge to edge separation of the defect distributions; R=5a , which is near total overlap of the cascades; and R=infinite, which is the sum of the results when the two cascades were annealed separately. Each data point is for the annealing of 100 configurations of randomly-chosen, constant-separation translations of one cascade relative to the other.

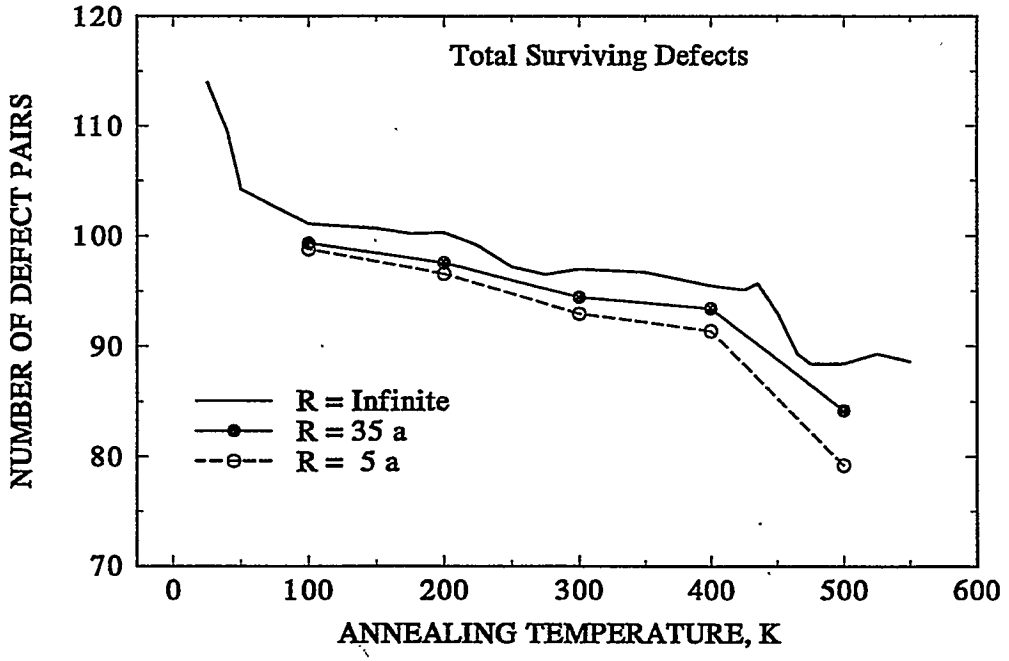

Figure 1. The total number of surviving defect pairs as a function of annealing temperature for subcascade separations of 35a, 5a, and infinite separation.

Figure 1 is for the total number of surviving defect pairs, i.e., the initial (post-quench) number minus the annihilations. The accounting is done in terms of single point defects (a cluster of 6 point defects counts as 6). At any temperature, a fraction of the surviving defects is mobile, and most of the mobile defects leave the cascade region during annealing. The remainder are immobile clusters remaining in the vicinity of the cascade. The longer solid line is the sum of surviving defect pairs for the two individual cascades (R=infinite), which was simulated at about 20 different temperatures. The solid line with filled circles is for R=35a and was done for only 5 temperatures. The lines are to aid the eye in grouping the data for a particular condition. The actual shape of the annealing curve would be similar to the R=infinite curve. The dashed line with open circles is for R=5a. Note the small differences in total defect pair survival as a function of separation. The trend of these small differences is that fewer defects survive as the subcascade separation decreases and that the differences due to subcascade separation are greater with increasing

temperature. These trends are also in the data for escaping SIAs and vacancies in Fig. 2 and Fig. 3, respectively.

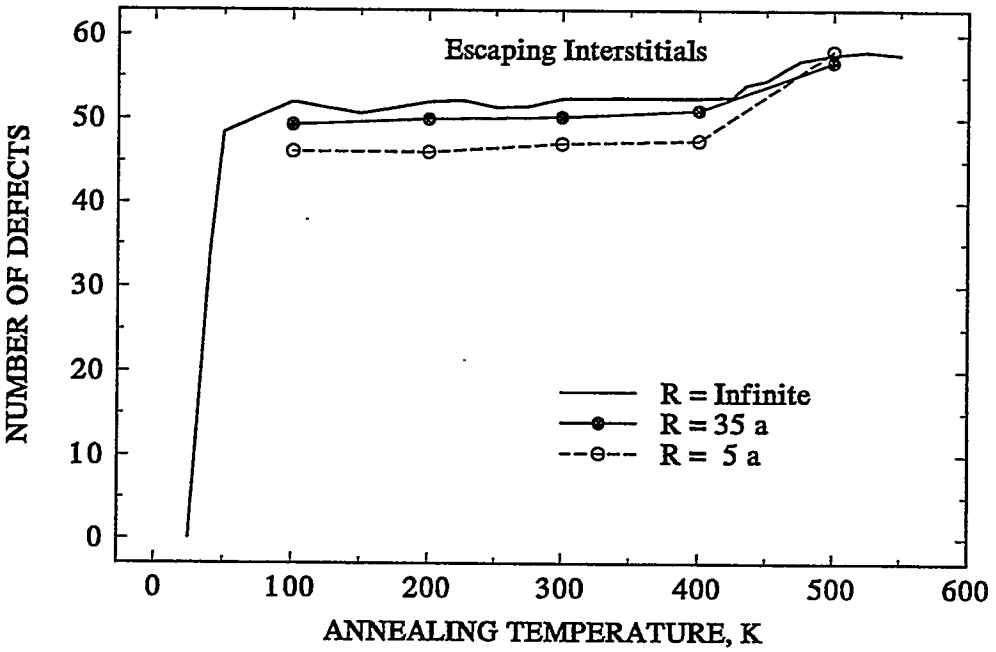

Figure 2. The number of SIAs escaping the cascade as a function of annealing temperature for subcascade separations of 35a, 5a, and infinite separation.

The results of this simulation indicate that during the annealing stage of cascade evolution there is little interaction of defects with other defects in an adjacent subcascade. This is due to the spatial separation of the vacancy and SIA distributions in a single subcascade and the difference in mobilities of vacancy and SIA defects. The SIAs are spread around the periphery of each subcascade and move much more quickly than the vacancies, which are concentrated near the center of each subcascade. When entering the region of another subcascade, the mobile SIAs are more likely to encounter the surrounding SIAs than the vacancies in the center. In this simulation at R=35a there is about 20% recombination within each subcascade, and about 5% additional recombination involving defects from different subcascades. Above about 400 K, where vacancy clusters become unstable, the vacancies stream out from the centers of the subcascades, but only after the mobile SIAs have already escaped the cascade. Some additional recombination occurs as a few vacancies find the remaining larger immobile SIA clusters. The simulation at R=5a is unphysical because two separate subcascades could not form in the same place without affecting each other significantly during the quenching stage. It was simply included to see if additional defect interactions would occur if the two sets of defects were in even closer proximity. There is only slightly more interaction.

This simulation investigated the defect interactions occurring only during the annealing stage, which takes place by thermally activated diffusion of defects after the thermal spikes of each subcascade have quenched.

The effects of the thermal spikes of adjacent subcascades quenching simultaneously have not been considered here, but it is an important issue that needs to be understood before conclusions are drawn.

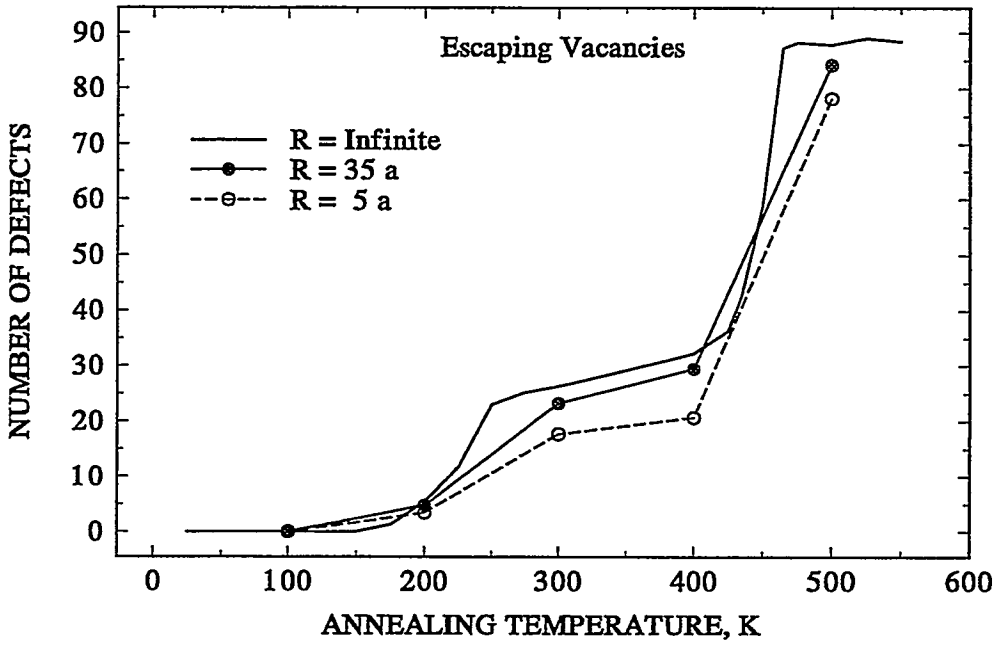

Figure 3. The number of vacancies escaping the cascade as a function of annealing temperature for subcascade separations of 35a, 5a, and infinite separation.

FUTURE WORK

The results here will be part of a presentation at the workshop on Defect Production, Accumulation and Materials Performance in Irradiation Environment, Davos, Switzerland, October 2-8, 1996. Proceedings will be published in the Journal of Nuclear Materials. New methods are being investigated for calibrating the output of the BCA cascade model to MD results to give more realistic cluster size distributions after quenching. MD simulations to determine the characteristics of subcascade interactions during the quenching stage are being considered. The sensitivity of ALSOME annealing results to the characteristics of small glissile loops, which are a key element in the defect evolution, is being tested.

REFERENCES

1. H. L. Heinisch and B. N. Singh, "Stochastic Annealing Simulation of Differential Defect Production in High Energy Cascades," J. Nucl. Mater., in press.

2. H.L. Heinisch, B. N. Singh and T. Diaz de la Rubia, "Calibrating a Multi-model Approach to Defect Production in High Energy Collision Cascades," J. Nucl. Mater. 212-215 (1994) 198.

3. T. Diaz de la Rubia and M.W. Guinan, Mater. Res. Forum 97-99 (1992) 23.

9.0 DOSIMETRY, DAMAGE PARAMETERS, AND ACTIVATION CALCULATIONS

NEUTRON DOSIMETRY AND DAMAGE CALCULATIONS FOR THE HFIR-JP-23 IRRADIATIONS

L. R. Greenwood and R. T. Ratner (Pacific Northwest National Laboratory)

OBJECTIVE

To provide dosimetry and damage analysis for fusion materials irradiation experiments.

SUMMARY

Neutron fluence measurements and radiation damage calculations are reported for the joint U.S.- Japanese experiment JP-23, which was conducted in target position G6 of the High Flux Isotope Reactor (HFIR) at Oak Ridge National Laboratory (ORNL). The maximum neutron fluence at midplane was 4.4E+22 n/cm^2 resulting in about 9.0 dpa in type 316 stainless steel.

PROGRESS AND STATUS

The JP-23 experiments were irradiated in the G6 target position of HFIR during cycles 322 through 326, starting December 16, 1993, and ending June 3, 1994, for a net exposure of 110.2 effective full power days at 85 MW. The experiment was a collaborative effort co-sponsored by the U. S. Neutron Interactive Materials Program at PNNL and the Japanese Monbusho Program. The goal of the experiment was to irradiate TEM specimens at four temperatures of 300, 400, 500, and 600°C. A complete description of the specimen matrix and irradiation assembly has been published previously.[1]

Neutron dosimetry capsules were inserted in the bottom cavities of each TEM specimen holder, each of which measured 4.17 cm in length. The dosimetry capsules consisted of small, welded aluminum tubes measuring about 1.3 mm in diameter and 6.4 mm in length. Each tube contained small monitor wires of Fe, Ni, Ti, Nb, and 0.1% Co-Al alloy. Six capsules were irradiated with the JP-23 specimens; however, only five were recovered during disassembly. Each capsule was opened in a hot cell at PNNL and each individual monitor wire was gamma counted to determine the residual activation.

The measured activities were converted to activation rates as listed in Table 1 by correcting for nuclear burnup, gamma self-absorption, decay during and after irradiation, isotopic abundance, and atomic weight. Burnup corrections are based on an iterative procedure for the thermal/epithermal monitor reactions. The resultant estimates of the thermal/epithermal neutron fluences were then used to calculate burnup corrections for the threshold fast neutron monitor reactions. Burnup corrections averaged 20-30% for the thermal/epithermal reactions and 5-15% for the threshold reaction rates. The activation rates listed in Table 1 are normalized to full reactor power of 85 MW and have a net absolute uncertainty of about 5%.

The activation rates in Table 1 were fit to a polynomial function of form $f(x) = f(0) [1 + a x^2]$, where x is the vertical height from reactor centerline in cm. All of the data are reasonably well fit by the average polynomial (coefficient $a = -1.139 \times 10^{-3}$). Midplane activation rates were then used in the STAY'SL computer code to adjust the neutron flux spectrum determined in previous spectral measurements in the target position in HFIR.[3] STAY'SL performs a generalized least-squares adjustment of all measured and calculated values including the measured activities, calculated spectra, and neutron cross sections. Neutron cross sections and their uncertainties were generally taken from the ENDF/B-V[4] evaluation. The resultant neutron fluence values are listed in Table 2. The activation rates and the derived neutron spectra and fluences are in excellent agreement with previous measurements in the target position of HFIR.[3]

Neutron damage calculations were performed using the SPECTER computer code[5] at the midplane position of HFIR. Midplane dpa and helium (appm) values are also listed in Table 2. The fluence and

damage values at other experimental positions can be calculated by the gradient equation given above. Damage parameters for other elements or compounds have been calculated and are readily available on request.

Helium production in nickel and nickel alloys requires a more complicated non-linear calculation.[6] Helium production in stainless steel is detailed in Table 3.

FUTURE WORK

Additional experiments still in progress in HFIR include MFE-200J-1 and MFE-400-J1 as well as JP9-16 and JP20-22. Activation data from the MFE-60J and -330J irradiations in HFIR and neutron flux monitors from the COBRA irradiation in EBR-II are currently being analyzed at PNNL.

REFERENCES

1. A. M. Ermi and D. S. Gelles, Preliminary Report on the Irradiation Conditions of the HFIR JP-23 Experiment, Fusion Reactor Materials Semiannual Progress Report, DOE/ER-0313/17, pp. 35-49 (1995).

2. F. G. Perey, Least Squares Dosimetry Unfolding: The Program STAY'SL, ORNL/TM-6062 (1977).

3. L. R. Greenwood, Alloy Development for Irradiation Performance Semiannual Report, DOE/ER-0045/11, pp. 30-37 (1983).

4. Evaluated Nuclear Data File, Part B, Version V, National Nuclear Data Center, Brookhaven National Laboratory.

5. L. R. Greenwood and R. K. Smither, SPECTER: Neutron Damage Calculations for Materials Irradiations, ANL/FPP-TM-197, January 1985.

6. L. R. Greenwood, A New Calculation of Thermal Neutron Damage and Helium Production in Nickel, Journal of Nuclear Materials 116, pp. 137-142 (1983).

TABLE 1 - ACTIVATION RATES (AT/AT-S) - HFIR JP-23

$^{46}Ti(n,p)^{46}Sc$ (E-12)	$^{55}Mn(n,2n)^{54}Mn$ (E-14)	$^{59}Co(n,\gamma)^{60}Co$ (E-9)	$^{93}Nb(n,\gamma)^{94}Nb$ (E-10)
1.18	2.70	3.44	3.06
1.49	3.39	3.85	3.84
1.59	3.60	4.26	4.25
1.72	3.82	3.94	4.33
1.74	4.01	4.02	4.37
1.65	3.82	4.38	4.29
1.57	3.65	3.58	3.92
1.24	2.95	a	3.09

[a] Wire not recovered in hot cell.

TABLE 2 - Midplane Fluence and Damage Values for MFE-60J/330J

Neutron Fluence, n/cm2-s		Element	dpa	He, appm
Total	3.95E+22	C	14.1	13.9
Thermal (<,5eV)	4.71E+21	Al	22.5	5.4
0.5 eV - 0.1 MeV		V	14.6	0.18
>0.1 MeV	1.94E+22	Cr	12.4	1.3
>1 MeV	7.04E+21	Fe	11.1	2.4

Ni Fast	12.3	34.2
59-Ni	0.5	276.0
Total	12.8	310.2
Cu	14.7	2.0

TABLE 3 - DPA and He Values for 316 SS in MFE-60J/330J
(Includes ^{59}Ni effect)

Ht (cm)	dpa	He (appm)
0	11.5	42.0
3	11.4	41.3
6	11.0	38.9
9	10.4	35.0
12	9.5	29.9
15	8.4	23.8
18	7.0	17.2

316SS = Fe(0.645), Ni(0.13), Cr(0.18), Mn(0.019), Mo(0.026) wt%

TABLE 4 - Maximum DPA and Helium Production in ORR/HFIR Irradiations
(Calculations for 316 Stainless Steel)

	dpa	He (appm)		dpa	He (appm)
ORR-6J	6.9	75.3	ORR-7J	7.4	102.0
HFIR-60J-1	11.6	112.5	HFIR-330J-1	11.6	122.5
Total	18.5	187.8	Total	19.0	224.5

A REVALUATION OF HELIUM/DPA RATIOS FOR FAST REACTOR AND THERMAL REACTOR DATA IN FISSION-FUSION CORRELATIONS - FA Garner and LR Greenwood (Pacific Northwest National Laboratory), BM Oliver (Rockwell International Corporation)

To be published in the Proceedings, 18th ASTM International Symposium on Effects of Radiation on Materials, Hyannis, MA, June 1996.

EXTENDED ABSTRACT

For many years it has been accepted that significant differences exist in the helium/dpa ratios produced in fast reactors and various proposed fusion energy devices. In general, the differences arise from the much larger rate of (n,α) threshold reactions occurring in fusion devices, reactions which occur for energies $\geq$ 6 MeV. It now appears, however, that for nickel-containing alloys in fast reactors the difference may not have been as large as was originally anticipated. In stainless steels that have a very long incubation period for swelling, for instance, the average helium concentration over the duration of the transient regime have been demonstrated in an earlier paper to be much larger in the FFTF out-of-core regions than first calculated.

The helium/dpa ratios in some experiments conducted near the core edge or just outside of the FFTF core actually increase strongly throughout the irradiation, as ^{59}Ni slowly forms by transmutation of ^{58}Ni. This highly exothermic ^{59}Ni(n,α) reaction occurs in all fast reactors, but is stronger in the softer spectra of oxide-fueled cores such as FFTF and weaker in the harder spectra of metal-fueled cores such as EBR-II. The formation of ^{59}Ni also increases strongly in out-of-core unfueled regions where the reactor spectra softens with distance from the core.

In this paper measurements of helium concentrations are presented for a variety of Fe-15Cr-XNi ternary alloys irradiated in EBR-II to in-core doses ranging from 76 to 131 dpa. Within the core the measured helium levels are consistent with nickel being the dominant contributor and are also consistent with the operation only of the (n,α) high energy threshold reactions. The ^{59}Ni contribution is only important far from the EBR-II core. While significant amounts of fusion-relevant data were generated out-of-core in FFTF, very little useful data for fusion purposes was generated outside the EBR-II core.

In addition, there has been a tendency to overlook the concurrent generation of hydrogen by the ^{59}Ni(n,p) reaction which is also highly exothermic. Estimates have been made of the hydrogen arising from various neutron spectra. The impact of this (n,p) reaction on calculation of displacement damage and the development of fission-fusion correlations is also discussed.

---

*Operated for the US Department of Energy by Battelle Memorial Institute under Contract DE-AC06-76RLO 1830

10.0 MATERIALS ENGINEERING AND DESIGN REQUIREMENTS

No contributions.

11.0 IRRADIATION FACILITIES, TEST MATRICES, AND EXPERIMENTAL METHODS

STATUS OF ATR-A1 IRRADIATION EXPERIMENT ON VANADIUM ALLOYS AND LOW-ACTIVATION STEELS*

H. Tsai, R. V. Strain, I. Gomes, and D. L. Smith (Argonne National Laboratory), and H. Matsui (Tohoku University, Japan)

SUMMARY

The ATR-A1 irradiation experiment was a collaborative U.S./Japan effort to study at low temperature the effects of neutron damage on vanadium alloys. The experiment also contained a limited quantity of low-activation ferritic steel specimens from Japan as part of the collaboration agreement. The irradiation started in the Advanced Test Reactor (ATR) on November 30, 1995, and ended as planned on May 5, 1996. Total exposure was 132.9 effective full power days (EFPDs) and estimated neutron damage in the vanadium was 4.7 dpa. The vehicle has been discharged from the ATR core and is scheduled to be disassembled in the next reporting period.

OBJECTIVE

The principal objective of the ATR-A1 irradiation experiment was to obtain mechanical property data, including in-reactor creep, on vanadium alloys irradiated at two low temperatures (≈200 and 300°C). Such data, important for fusion first-wall/blanket applications, are presently lacking.

SUMMARY DESCRIPTION OF EXPERIMENT

The irradiation vehicle was a drop-in capsule consisting of four gas-filled segments. The test specimens were contained in 15 lithium-bonded subcapsules and placed in the capsule as shown in Fig. 1. With a few exceptions, the capsule segments were constructed according to the ASME Boiler & Pressure Vessel Code, Section III. The materials for both the capsule and subcapsule components were Type 304 stainless steel. The size of the gap between the capsule and subcapsules and the selection of the fill gas in the gap established the temperature for the test specimens in the subcapsules. The fill gas was pressurized to 130 psig at room temperature to partially counterbalance the ATR system pressure of ≈335 psig.

A total of 154 tensile, 144 Charpy, 19 compact tension, 10 creep, and 610 transmission-electron-microscope disk specimens (combined vanadium alloys and ferritic steels) were used in the experiment. All subcapsules but two (AS4 and AS16), which contained only ferritic steel specimens, contained only vanadium alloy specimens. A gadolinium filter set, consisting of a tube, a top end disk, and a bottom end disk, was used in each subcapsule to reduce thermal flux and mitigate vanadium-to-chromium transmutation. Flux dosimeters and melt-wire temperature monitors were incorporated in selected subcapsules.

U.S. Vanadium Alloy Test Matrix

The key variables of the U.S. test matrix were

- Material (Heats 832665, T87, T89, T90, T91, T92, BL-47, and boron-doped BL-70).
- Heat treatment conditions (final vacuum annealing at 1000°C for 1.0 or 2.0 h).
- Weldment (EB, laser, and resistance).
- Irradiation temperatures (≈200 and 300°C).

The test specimen types were Charpy (MCVN, PCVN), tensile (SS-3 and Matron-size), compact tension (DCT), transmission-electron-microscope (TEM) disks, and biaxial creep (pressurized tubes). A summary of the test matrix is presented in Table 1.

*Work supported by U.S. Department of Energy, Office of Fusion Energy Research, under Contract W-31-109-Eng-38.

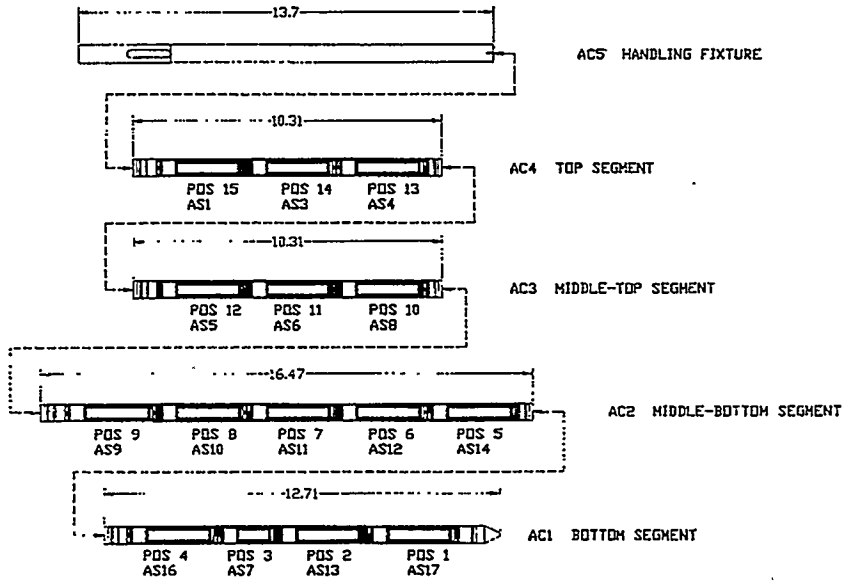

Fig. 1 Schematic Drawing of ATR-A1 Showing Capsule Segments and Subcapsule Locations

Table 1. U.S. Vanadium Alloy Test Matrix

T (°C)	Material[1]	MCVN	PCVN	SS-3	Matron	DCT	Creep	TEM
	832665 (Prim. Anneal)	4	3	3	2	3	4	16
	832665 (Sec. Anneal)	4		2		3		10
	832665, EB Weld			2				
	832665 Lz, TIG Weld	2		1				1
	BL-47	4		2		2		10
	BL-47 TIG Weld	4[2]						
300	T89							10
	T87			2	2	2		16
	T91			2	2			16
	BL-70							10
	T92			2				16
	T90							10
	Total	18	3	16	6	10	4	115
	832665 (Prim. Anneal)	5		3	2	3	4	16
	832665 (Sec. Anneal)	4		2		2		10
	832665, EB Weld							
	832665 Lz, TIG Weld	2		2				1
	BL-47	4		2		2		10
200	T89							10
	T87			2	2	2		16
	T91			2	2			16
	BL-70							10
	T92			2				16
	T90							10
	Total	15	0	15	6	9	4	115

[1]Primary Anneal: 1000°C for 1.0 h.
Secondary Anneal: 1000°C for 2.0 h.
[2]1.5 CVN size specimens.

Japanese Vanadium Alloy Test Matrix

The main variables of the Japanese vanadium test matrix were materials and temperature. The major JP vanadium alloys were V-4Cr-4Ti-0.1Si, V-3Fe-4Ti-0.1Si, and V-5Cr-5Ti-1YSiAl. A small number of

specimens were made from the U.S. V-4Cr-4Ti (Heat 832665) for comparison to check the effects of specimen geometry on measured data. The test specimen types were Charpy, tensile, compact tension, transmission-electron-microscope disks, and biaxial creep tubes. A summary of the test matrix is shown in Table 2.

Table 2. JP Vanadium Alloy Test Matrix

T (°C)	Material	CVN	TS	DCT	Creep	TEM
300	V-4Cr-4Ti-0.1Si	7	9		1	6
	V-3Fe-4Ti-0.1Si	5	8	3		3
	V-5Cr-5Ti-1YiSiAl	14	18			25
	V-4Cr-4Ti (832665)	4				0
	Other V Alloys					30
	Total	30	35	3	1	64
200	V-4Cr-4Ti-0.1Si	10	9		1	6
	V-3Fe-4Ti-0.1Si	5	8	3		3
	V-5Cr-5Ti-1YiSiAl	10	17			25
	V-4Cr-4Ti (832665)	5				0
	Other V Alloys					30
	Total	30	34	3	1	64

Irradiation History

The experiment was irradiated in three ATR cycles (108A, 108B, and 109A), for a total of 132.9 EFPDs as follows:

- 108A: 11/30/95 -- 1/14/96, 25.0 MW SE lobe power, for 42.8 EFPDs.
- 108B: 1/20/96 -- 3/3/96, 27.0 MW SE lobe power, for 43.3 EFPDs.
- 109A: 3/17/96 -- 5/5/96, 25.0 MW SE lobe power for 46.8 EFPDs.

The peak damage (at near the axial midplane) was ≈4.7 dpa. Because of the increased reactor lobe power in Cycle 108B, the specimen temperatures were modestly higher than in the other two cycles. The calculated specimen temperatures and dpa values are summarized in Table 3.

Table 3. Calculated Temperature and DPA in ATR-A1 Subcapsules

Position	Subcapule Number	Test Mat'l	Gas Gap (mils)	Gas Composition	Target Temp. (°C)	Specimen Temp. (°C)[1]	dpa
15 (top)	AS1	V	8	He-15%Ar	200	139/144	0.7
14	AS3	V	8	He-15%Ar	200	186/194	1.5
13	AS4	FS	8	He-15%Ar	low	263/277	2.2
12	AS5	V	5	He	200	198/212	3.0
11	AS6	V	5	He	200	223/234	3.5
10	AS8	V	5	He	200	246/259	3.9
9	AS9	V	5	He	300	273/286	4.3
8	AS10	V	5	He	300	288/302	4.6
7	AS11	V	5	He	300	285/300	4.7
6	AS12	V	5	He	300	281/295	4.5
5	AS14	V	6	He	300	284/300	4.1
4	AS16	FS	8	He-5%Ar	high	337/355	3.8
3	AS7	V	8	He-5%Ar	300	287/303	3.0
2	AS13	V	8	He-5%Ar	300	245/258	2.3
1	AS17	V	8	He-5%Ar	200	204/213	1.5

[1]Averaged specimen temperatures in subcapsules, some with two tiers of specimens. First value is for Cycles 108A and 109A (25 MW lobe power), and second value is for Cycle 108B (27 MW lobe power).

FUTURE ACTIVITIES

The four segments of the capsule will be separated by underwater cutting in the ATR canal. This step is necessary because of the size limitation on the shipping cask. The work plan for this cutting activity has been generated and forwarded to the ATR. The separated segments will be shipped to ANL for disassembly. A suitable cask for this shipment has been identified and the contract for the cask rental is being prepared. Opening of the subcapsules to retrieve the test specimens at ANL is expected to be a routine operation that uses previously established procedures. The cleaned specimens will be disseminated to participating U.S. and Japanese laboratories for postirradiation examination and testing. The gadolinium filters will be removed and analyzed to determine their effectiveness, i.e., extent of burnout. This information may be useful in planning future experiments in the ATR. The flux and thermal monitors will be analyzed to determine actual irradiation conditions.

FEASIBILITY OF CONDUCTING A DYNAMIC HELIUM CHARGING EXPERIMENT FOR VANADIUM ALLOYS IN THE ADVANCED TEST REACTOR*

H. Tsai, I. Gomes, R. V. Strain, and D. L. Smith (Argonne National Laboratory), and
H. Matsui (Tohoku University, Japan)

SUMMARY

The feasibility of conducting a dynamic helium charging experiment (DHCE) for vanadium alloys in the water-cooled Advanced Test Reactor (ATR) is being investigated as part of the U.S./Monbusho collaboration. Preliminary findings suggest that such an experiment is feasible, with certain constraints. Creating a suitable irradiation position in the ATR, designing an effective thermal neutron filter, incorporating thermocouples for limited specimen temperature monitoring, and handling of tritium during various phases of the assembly and reactor operation all appear to be feasible. An issue that would require special attention, however, is tritium permeation loss through the capsule wall at the higher design temperatures (>≈600°C). If permeation is excessive, the reduced amount of tritium entering the test specimens would limit the helium generation rates in them. At the lower design temperatures (<≈425°C), sodium, instead of lithium, may have to be used as the bond material to overcome the tritium solubility limitation.

OBJECTIVE

The objective of this task is to determine the feasibility of conducting a dynamic helium charging experiment in the water-cooled ATR for the recently procured large heats of vanadium alloys. This test would be a follow-up to the previous DHCE that was conducted in the MOTA-2B experiment in the Fast Flux Test Facility (FFTF).

General Design Considerations of the ATR-DHCE Experiment

The purpose of a DHCE is to study the effects of concurrent helium generation and neutron damage in vanadium alloys that may be used to construct first-wall/blanket structures in a fusion device. Target temperature range for the proposed ATR-DHCE experiment, denoted ATR-A2, is ≈350 to 650°C. The goal fluence is ≈10 dpa and the desired helium generation rate is ≈4-5 appm/dpa.

The concept of conducting a DHCE in the ATR would be similar to that of the MOTA-2B in the FFTF. During the experiment assembly, tritium that had been predissolved in a mother alloy would be added to the lithium-bonded subcapsules containing the vanadium test specimens. During irradiation, diffusion of the tritium into the test specimens would occur and some of the diffused-in tritium would decay ($T_{1/2}$ = 12.3 yr) in-situ, forming ^{3}He. In this manner, helium generation from the (n,a) reactions in a fusion device would be simulated in the vanadium alloy material.

The major difference between the ATR and the FFTF is the neutron spectrum. Because of the thermal flux in the water-cooled ATR, the proposed A2 experiment would require effective thermal neutron filtering to mitigate two undesirable, thermal-flux dominated events: (1) vanadium-to-chromium transmutation and (2) annihilation of ^{3}He already generated in the vanadium alloy. The latter becomes more significant at higher dpa levels when the concentrations of accumulated ^{3}He in the specimens are high. Material compatibility and burnout concerns dictate that the filter be placed outside the capsule where it can be replaced, if necessary.

Permeation loss through the subcapsule wall would reduce the tritium partial pressure, and hence the helium generation rate in vanadium, with time. TZM, a molybdenum-based alloy with better permeation resistance than that of stainless steel, would be used for the subcapsule. Still, premenation loss could be significant at

*Work supported by U.S. Department of Energy, Office of Fusion Energy Research, under Contract W-31-109-Eng-38.

higher temperatures. To compensate, natural lithium (7.5% ^{6}Li) or enriched lithium could be used as the bond material to generate additional tritium from the ^{6}Li(n,T)^{4}He reactions. The drawback of tritium breeding is the cogeneration of ^{4}He, which would cause capsule pressurization.

The rate of helium generation in vanadium specimens depends on the concentration of tritium in V, i.e., the partial pressure of tritium in the subcapsule. The distribution of tritium between vanadium and lithium is temperature-dependent and varies with vanadium alloy composition. Within the solubility limit, the partial pressure of tritium is proportional to the concentration of tritium in lithium. At the low design temperatures, the low solubility limit of tritium in lithium may prevent the required tritium partial pressure from being attained for the desired He generation. An alternative would be to use sodium, instead of lithium, as the bond. The favorable distribution of tritium in a V/Na system is such that the required tritium content would be much lower than in a V/Li system.

Preliminary Findings

Reactor-Related Feasibility Issues

A study conducted by ATR staff indicated that a new irradiation channel with desirable attributes (high fast flux, low thermal flux, adequate test volume, etc.) could be created in the East Flux Trap. An aluminum flux trap insert would have to be built. Preliminary calculations indicated that the flux spectrum in the new channel would be comparable to that in the A-10 channel, where the first fusion structural material experiment, ATR-A1, was conducted. Approximately 11 dpa per calendar year in vanadium is projected based on a 30 MW lobe power in the East Flux Trap and an 80% ATR duty factor.

ATR concluded that lithium could be used as the bond material, as it was in the ATR-A1 experiment. Incorporation of sodium as the low-temperature subcapsule bond is possible but would require additional safety evaluation. The magnitude of permeation of tritium from the ATR-A2 experiment would not be a concern because the facility is capable of handling significantly greater quantities of tritium from other sources in reactor.

Vehicle-Related Feasibility Issues

The diameter of the new irradiation channel would be 26.2 mm, sufficient to accommodate a reasonably-sized capsule with an external thermal neutron filter. The cross section of a conceptual capsule design is shown in Fig. 1. The capsule would have several axial segments, each containing several subcapsules in an arrangement similar to that of the ATR-A1. The gas gaps between the capsule and subcapsules would determine the specimen temperatures. Specimens would be bonded with lithium (or sodium) in the subcapsules. The top segment of the capsule would have annular subcapsules, allowing thermocouples to penetrate along the centerline. These thermocouples would provide the needed data to corroborate the temperatures predicted by modeling. Handling and routing the thermocouples out of the reactor vessel for measurement appears to be feasible from the standpoint of reactor operation.

The external filter assembly would be a cylindrical shell made as an integral part of the basket holding the capsule during irradiation. It would contain thermal-flux-absorbing material jacketed in stainless steel sheets. Several filtering materials have been considered, and Eu_2O_3 appears to be the best choice in terms of blackness and lifetime. Simulated Eu_2O_3 packing tests with a mockup assembly have been conducted and the results show that Eu_2O_3 powders can be packed to the desired ≈50% theoretical density.

The subcapsules would be constructed with a TZM alloy (0.5%Ti, 0.07%Zr, balance Mo) that has a superior tritium-retention capability compared to that of other construction materials. Preliminary welding tests showed the TZM can be satisfactorily welded with the electron-beam welder available at the ANL assembly laboratory. The capsule would be constructed of 304 stainless steel and will meet the ASME Pressure Vessel and Boiler Code, Section III, as required by ATR.

The total test specimen volume in the experiment would be ≈10-25% greater than that in ATR-A1, depending on the detailed design.

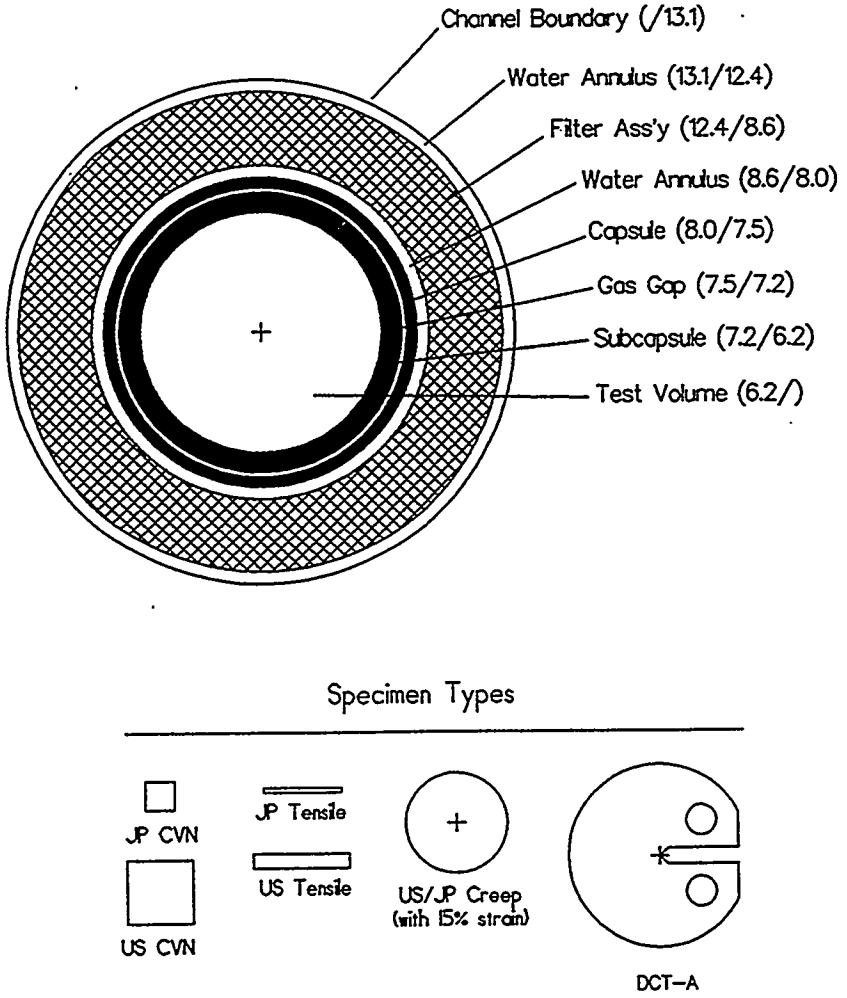

Fig. 1. Cross section of a conceptual ATR-A2 capsule design. Numbers in parentheses are inside and outside radii, respectively, in mm. Sizes of all components are to proportion.

Issues Related to Helium Generation

Physics scoping calculations are being conducted to evaluate the effects of the following intertwining parameters on He/dpa ratios: temperature, tritium distribution coefficient, filtering material and thickness, fluence, initial tritium charge, ^{6}Li enrichment, and subcapsule wall thickness (which affects tritium permeation). To address the uncertainties in the distribution coefficients (C_V/C_{Li}), which directly affect the rates of helium generation in vanadium, a range of 0.002-0.02 (by weight) was used in the present study. These values are ≈5 times smaller than those used in the design of MOTA-2B to correct the deficiencies found in the helium generation rates in the MOTA-2B specimens. It is imperative that before the construction of ATR-A2, the distribution coefficients for all major vanadium alloys are experimentally determined to remove these uncertainties.

At 400°C, the ^3T saturation partial pressure in a Li/H system is low and probably would limit the achievable He appm/dpa ratio in vanadium to ≈1.3. The lowest temperature where the target ratio of 5 is attainable is ≈425-450°C. If temperatures lower than ≈425-450°C are desired in the ATR-A2 experiment, an alternative, such as a Na/H system, would be necessary. (In the 300-400°C range, the ^3T saturation pressure in a Na/H system is approximately 10^3 higher than in a Li/H system.) Preliminary results indicated that Na-bonded subcapsules can be fabricated and would produce the desired He appm/dpa ratio of ≈5. Impurity uptake by vanadium alloy specimens in sodium is not expected to be a problem at these low temperatures. Tritium leakage loss likewise would also be low.

At 500°C, DHCE appears to be feasible for lithium-bonded subcapsules for a wide range of possible distribution coefficients. Tritium leakage loss would be modest, ≈10% of the initial charge, at a nominal TZM wall thickness of 1 mm.

At temperatures >≈600°C, tritium leakage through the TZM subcapsule becomes significant as the permeability constant increases rapidly with temperature. Because as much as ≈60% of the initial tritium loading may be lost at the end of the 10 dpa irradiation (with 1-mm nominal TZM wall), achieving a steady He appm/dpa ratio during irradiation would require bonding with enriched lithium. Preliminary calculations indicate that the achievable He appm/dpa ratio at 600°C would be ≈3.3-4.3, depending on the distribution coefficient. While increasing the wall thickness would reduce the tritium loss, it would have adverse effects on specimen volume and temperature. The more desirable solution would be to use innovative materials for construction to reduce the permeation, such as more permeation-resistant material (e.g., tungsten-based alloys) or an external permeation-inhibiting coating for the subcapsules. Alternatively, it may be possible to construct the outer capsule of aluminum, a material with low permeation coefficient, to form a secondary barrier for tritium.

FUTURE ACTIVITIES

Refined flux spectrum data for the East flux trap channel will be obtained from ATR. Further parametric studies on the helium generation rates will be conducted. The feasibility of using sodium as the bond material for the low-temperature subcapsules will be studied in greater detail. Alternative materials of construction will be examined to address the high-temperature tritium permeation issue.

SCHEDULE AND STATUS OF IRRADIATION EXPERIMENTS – A. F. Rowcliffe and M. L. Grossbeck (Oak Ridge National Laboratory)

OBJECTIVE

To provide an updated summary of the status of irradiation experiments for the neutron-interactive materials program.

SUMMARY

The current status of reactor irradiation experiments is presented in tables summarizing the experimental objectives, conditions, and schedule.

PROGRESS AND STATUS

In the following table, the status of each experiment is shown in the last column with the following legend:

Irradiation complete 

Irradiation in progress 

Irradiation planned

Currently, the program has two irradiation experiments in reactor; and 10 experiments in the planning or design stages.

Summary of Reactor Irradiation Experiments

Experiment	Lead Lab	Collaborators	Responsible Person	Major Objectives	Materials	Temperature °C	Dose (dpa) or fluence	Irrad. Start	Irrad. Finish	Status
EBR-II, Reactor, ANL, Idaho Falls, ID										
COBRA 1A1	PNL	ORNL, ANL, MONBUSHO	M.L. Hamilton	Tensile and fatigue prop., Charpy impact, fracture toughness, TEM	Austenitic and ferritic steels, Fe-alloys, V, Be, low act. materials, Cu alloys, Ti-Al, SiC, C-C comp.	370, 500, 600	9	Nov-92	Apr-93	
COBRA 1A2	PNL	ORNL, ANL, MONBUSHO	M.L. Hamilton	Tensile and fatigue prop., Charpy impact, fracture toughness, TEM	Austenitic and ferritic steels, Fe-alloys, V, Be, low act. materials, Cu alloys, Ti-Al, SiC, C-C comp.	370, 400, 800	33	Nov-92	Sep-94	
X530	ANL		H. Tsai, H.M. Chung	He-effects, swelling, Charpy impact, fracture toughness, tensile prop.	V alloys	370	5	Aug-94	Sep-94	
High Flux Isotope Reactor, ORNL, Oak Ridge, TN										
HFIR-CTR-60	ORNL		S.J. Zinkle	Flexure bars, TEM, indentation disks	Isotopically tailored ceramics	100-600	2.4E+26 n/m2	Dec-94	Aug-95	
HFIR-CTR-61	ORNL		S.J. Zinkle	Similar to HFIR-CTR-60			7.20E+26	Dec-94	Aug-97	
HFIR-JP-9	ORNL	JAERI	P.J. Maziasz/ J.E. Pawel	He effects by isotopic tailoring, tensile prop., TEM	Austenitic and ferritic steels	300-600	57	Jul-90	Apr-94	
HFIR-JP-10	ORNL	JAERI	P.J. Maziasz/ J.E. Pawel	He effects by isotopic tailoring, tensile prop., TEM	Austenitic and ferritic steels	300-600	18	Jul-90	Sep-91	
HFIR-JP-11	ORNL	JAERI	P.J. Maziasz/ J.E. Pawel	Similar to HFIR-JP-10			18	Jul-90	Sep-91	
HFIR-JP-12	ORNL	JAERI	P.J. Maziasz/ J.E. Pawel	Similar to HFIR-JP-9			57	Jul-90	Apr-94	
HFIR-JP-13	ORNL	JAERI	P.J. Maziasz/ J.E. Pawel	Similar to HFIR-JP-10			18	Jul-90	Sep-91	
HFIR-JP-14	ORNL	JAERI	P.J. Maziasz/ J.E. Pawel	He effects by isotopic tailoring, tensile prop., TEM	Austenitic and ferritic steels	300-600	34	Jul-90	Sep-92	

Summary of Reactor Irradiation Experiments

Experiment	Lead Lab	Collaborators	Responsible Person	Major Objectives	Materials	Temperature °C	Dose (dpa) or fluence	Irrad. Start	Irrad. Finish	Status
HFIR-JP-15	ORNL	JAERI	P.J. Maziasz/ J.E. Pawel	Similar to HFIR-JP-9			57	Jul-90	Apr-94	
HFIR-JP-16	ORNL	JAERI	P.J. Maziasz/ J.E. Pawel	Similar to HFIR-JP-10			18	Jul-90	Sep-91	
HFIR-JP-17	ORNL	JAERI	M.L. Grossbeck/ J.E. Pawel	Fracture toughness, tensile prop. TEM	Austenitic and ferritic steels	250-300	3	Dec-91	Feb-92	
HFIR-JP-18	ORNL	JAERI	M.L. Grossbeck/ J.E. Pawel	Fracture toughness, tensile prop. TEM	Austenitic and ferritic steels	60-125	3	Aug-91	Oct-91	
HFIR-JP-19	ORNL	JAERI	M.L. Grossbeck/ J.E. Pawel	Similar to HFIR-JP-18		60-125	3	Aug-91	Oct-91	
HFIR-JP-20	ORNL	JAERI	J.E. Pawel	Tensile Prop., TEM, He effects by isotopic tailoring	Austenitic and ferritic steels	300-600	8	Dec-93	Jun-94	
HFIR-JP-21	ORNL	JAERI	J.E. Pawel	Similar to HFIR-JP-20			18	Dec-93	Apr-95	
HFIR-JP-22	ORNL	JAERI	J.E. Pawel	Similar to HFIR -JP-20			34	Dec-93	Jan-96	
HFIR-JP-23	PNL	MONBUSHO	D.S. Gelles	TEM	Austenitic and ferritic steels, Cu, Mo, V alloys, TiAl	300-600	8	Dec-93	Jun-94	
HFIR-MFE-60J	ORNL	JAERI	J.L. Scott/ M.L. Grossbeck	Spectrally tailored for fusion He prod. Began in ORR as ORR-MFE-6J (6.9 dpa). TEM, Charpy, Irrad. creep, tensile and crack growth prop.	Austenitic and ferritic steels, and Ni alloys	60	18 (total)	Jul-90	Nov-92	
HFIR-MFE-330J	ORNL	JAERI	J.L. Scott/ M.L. Grossbeck	Similar to HFIR-MFE-60J. Began in ORR as ORR-MFE-7J (7.4 dpa)		330	18 (total)	Jul-90	Nov-92	
HFIR-MFE-200J	ORNL	JAERI	M.L. Grossbeck/ J.E. Pawel	Similar to HFIR-MFE-60J. Began in ORR as ORR-MFE-6J (6.9 dpa)		200	18 (total)	Nov-92	Jan-95	
HFIR-MFE-400J	ORNL	JAERI	M.L. Grossbeck/ J.E. Pawel	Similar to HFIR-MFE-60J. Began as ORR-MFE-7J (7.4 dpa)		400	18 (total)	Nov-92	Jan-95	
HFIR-HT-S1, -S7	ORNL		L.L. Snead	Thermal conductivity	Various insulators	80-350	0.01-1.0	Jun-95	Aug-95	
HFIR-HT-F Series	ORNL		L. L. Snead	Fiber tensile	SiC	80-800	0.001-1.0	Jan-95	Mar-96	

Summary of Reactor Irradiation Experiments

Experiment	Lead Lab	Collaborators	Responsible Person	Major Objectives	Materials	Temperature °C	Dose (dpa) or fluence	Irrad. Start	Irrad. Finish	Status
HFIR-TRIST-ER1	ORNL	MONBUSHO/ JAERI	S.J. Zinkle	In-situ electrical conductivity	Al2O3	450	3E+25 n/m2	Apr-96	Jun-96	
HFIR-MFE-RB-10J	ORNL	JAERI	J.E. Pawel	Tensile, fracture	316LN-1G, J316	200, 300	4	Jan-97	Aug-97	
HFIR-MFE-RB-11J	ORNL	MONBUSHO/ JAERI	M. L. Grossbeck	Tensile, fracture, TEM	Low activation ferritics, V alloys, SiC	300	5	Oct-96	May-97	
HFIR-MFE-RB-12J	ORNL	MONBUSHO/ JAERI	M. L. Grossbeck	Tensile, fracture, TEM	Low activation ferritics, V alloys, SiC	500	5	Oct-96	May-97	
HFIR-CTR-62	ORNL	JAERI	R.L. Klueh	Charpy impact and He effects	Reduced act. and conventional ferritic steels	300, 400	10	Feb-95	Dec-95	
HFIR-CTR-63	ORNL	JAERI	R.L. Klueh	Charpy impact and tensile, TEM, He effects	Reduced act. and conventional ferritic steels	300, 400	10	Feb-95	Dec-95	
HFIR-JP25	ORNL	JAERI	R.L. Klueh	Tensile, fracture, TEM	Low activation ferritics	300, 400, 500	20	Jun-97	Sep-98	
HFIR-JP27	ORNL	JAERI	L.L. Snead	Fracture, TEM	Intermetallics, SiC	500-800	10	Oct-97	Jan-98	
HFIR-JP28	ORNL	JAERI	L.L. Snead	Fracture, TEM	SiC	500-800	10	Sep-97	Mar-98	
HFIR-P3-6	ORNL	MONBUSHO	K. R. Thoms	Varying Temperature	TBD	400-600	5	May-97	Apr-98	
High Flux Beam Reactor, Brookhaven National Laboratory										
HFBR-ISEC-3	ORNL		L.L. Snead	In-situ electrical	WESGO Al2O3	450	1.5	Jul-95	Sep-95	
HFBR-V1	ORNL		L.L. Snead	Tensile, fracture	V-4Cr-4Ti	75, 150, 225	0.5	May-95	Jun-95	
HFBR-V2	ORNL		L.L. Snead	Tensile, fracture	V-4Cr-4Ti	75, 225, 300, 375	0.5	Jul-95	Aug-95	
HFBR-V3	ORNL		L.L. Snead	Tensile, fracture	V-4Cr-4Ti	275, 330, 400	0.5	Sep-96	Oct-96	
HFBR-V4	ORNL		L.L. Snead	Tensile, fracture	V-4Cr-4Ti	110, 205, 275, 330, 400	0.1	Sep-96	Oct-96	
Advanced Test Reactor, Idaho Falls										
ATR-A1	ANL	MONBUSHO	D.L. Smith	Tensile, fracture toughness, TEM, creep	Vanadium alloys	200, 300	5	Dec-95	May-96	

Summary of Reactor Irradiation Experiments

Experiment	Lead Lab	Collaborators	Responsible Person	Major Objectives	Materials	Temperature °C	Dose (dpa) or fluence	Irrad. Start	Irrad. Finish	Status
BOR-60 Reactor, RIAR, Dimitrovgrad, Russia										
BOR-60-Fusion-1	ORNL, ANL	RDIPE, RIAR	A.F. Rowcliffe, D.L. Smith	Mechanical and microstructural properties	V alloys	350-380	10	Jul-95	Mar-96	
SM-2 Reactor, RIAR, Dimitrovgrad, Russia										
SM-2.1	ORNL, PNL	RIAR	S.J. Zinkle	Tensile, electrical, microstructural, and creep properties	Cu alloys	100, 200, 330	1, 5	Dec-93	Feb-94	
SM-2.2	PNL	SRIAR	D.J. Edwards	Mechanical behavior of bonded materials	Cu alloys/SS, Cu/Be	120, 300	0.2	Jan-96	Mar-96	
SM-2.3	PNL	SRIAR	D.J. Edwards	Mechanical behavior of bonded materials	Cu alloys/SS, Cu/Be	100, 250	0.2	Sep-96	Nov-96	

Irradiation complete

Irradiation in progress

Irradiation planned

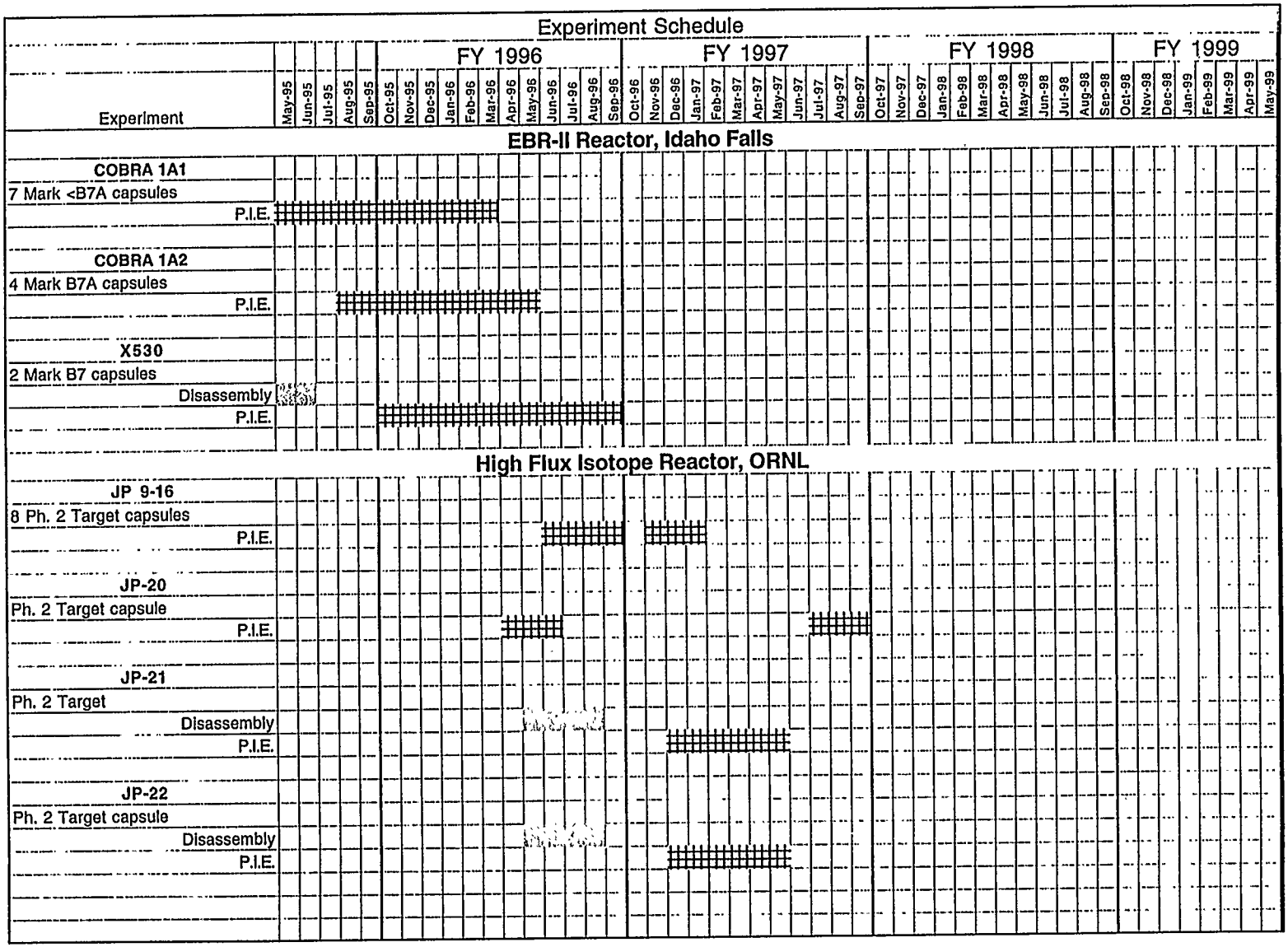
Experiment Schedule
FY 1996
FY 1997
FY 1998
FY 1999
Experiment
May-95 Jun-95 Jul-95 Aug-95 Sep-95 Oct-95 Nov-95 Dec-95 Jan-96 Feb-96 Mar-96 Apr-96 May-96 Jun-96 Jul-96 Aug-96 Sep-96 Oct-96 Nov-96 Dec-96 Jan-97 Feb-97 Mar-97 Apr-97 May-97 Jun-97 Jul-97 Aug-97 Sep-97 Oct-97 Nov-97 Dec-97 Jan-98 Feb-98 Mar-98 Apr-98 May-98 Jun-98 Jul-98 Aug-98 Sep-98 Oct-98 Nov-98 Dec-98 Jan-99 Feb-99 Mar-99 Apr-99 May-99
EBR-II Reactor, Idaho Falls
COBRA 1A1
7 Mark <B7A capsules
P.I.E.
COBRA 1A2
4 Mark B7A capsules
P.I.E.
X530
2 Mark B7 capsules
Disassembly
P.I.E.
High Flux Isotope Reactor, ORNL
JP 9-16
8 Ph. 2 Target capsules
P.I.E.
JP-20
Ph. 2 Target capsule
P.I.E.
JP-21
Ph. 2 Target
Disassembly
P.I.E.
JP-22
Ph. 2 Target capsule
Disassembly
P.I.E.

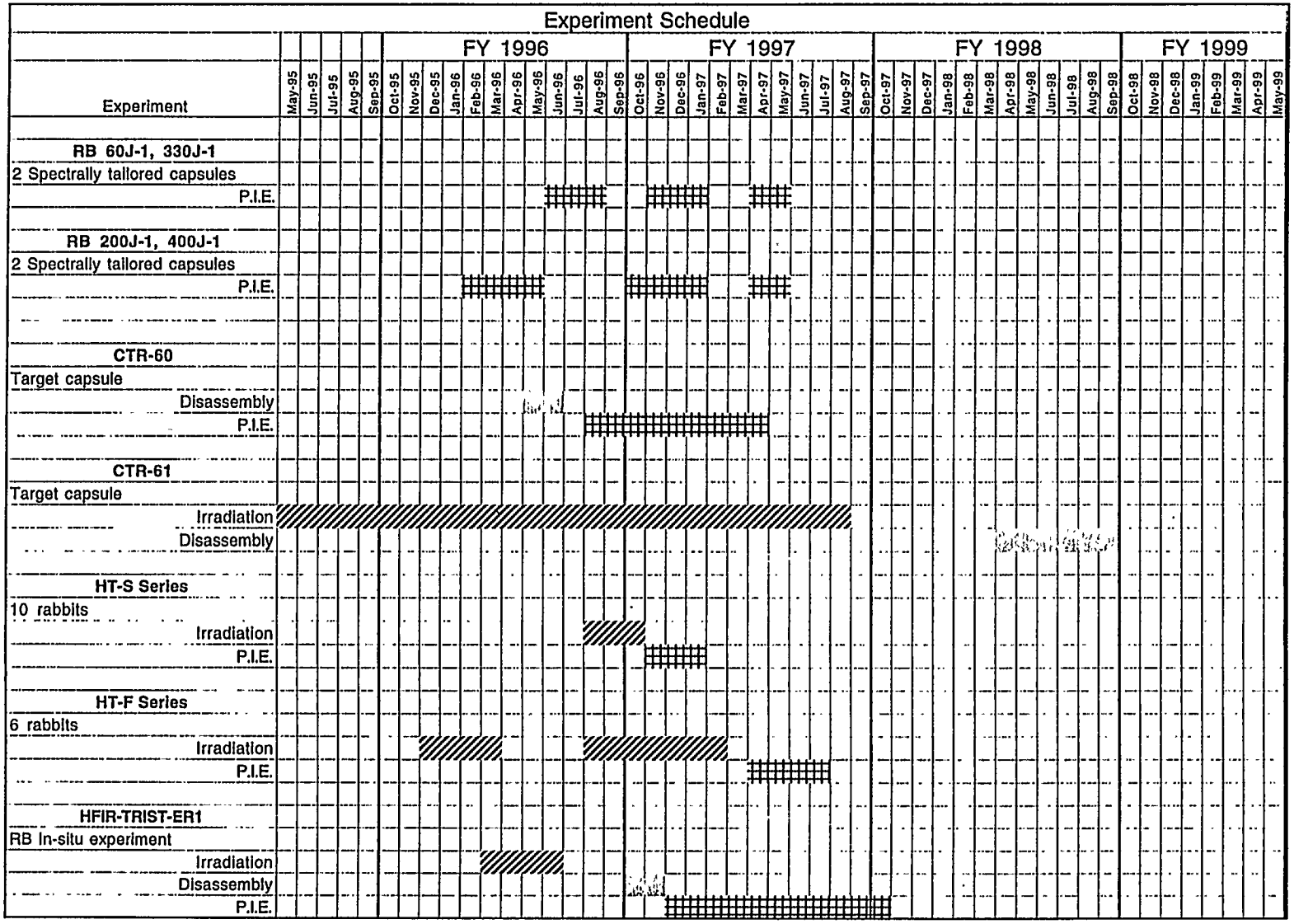
Experiment Schedule
FY 1996
FY 1997
FY 1998
FY 1999
Experiment
May-95
Jun-95
Jul-95
Aug-95
Sep-95
Oct-95
Nov-95
Dec-95
Jan-96
Feb-96
Mar-96
Apr-96
May-96
Jun-96
Jul-96
Aug-96
Sep-96
Oct-96
Nov-96
Dec-96
Jan-97
Feb-97
Mar-97
Apr-97
May-97
Jun-97
Jul-97
Aug-97
Sep-97
Oct-97
Nov-97
Dec-97
Jan-98
Feb-98
Mar-98
Apr-98
May-98
Jun-98
Jul-98
Aug-98
Sep-98
Oct-98
Nov-98
Dec-98
Jan-99
Feb-99
Mar-99
Apr-99
May-99
RB 60J-1, 330J-1
2 Spectrally tailored capsules
P.I.E.
RB 200J-1, 400J-1
2 Spectrally tailored capsules
P.I.E.
CTR-60
Target capsule
Disassembly
P.I.E.
CTR-61
Target capsule
Irradiation
Disassembly
HT-S Series
10 rabbits
Irradiation
P.I.E.
HT-F Series
6 rabbits
Irradiation
P.I.E.
HFIR-TRIST-ER1
RB In-situ experiment
Irradiation
Disassembly
P.I.E.

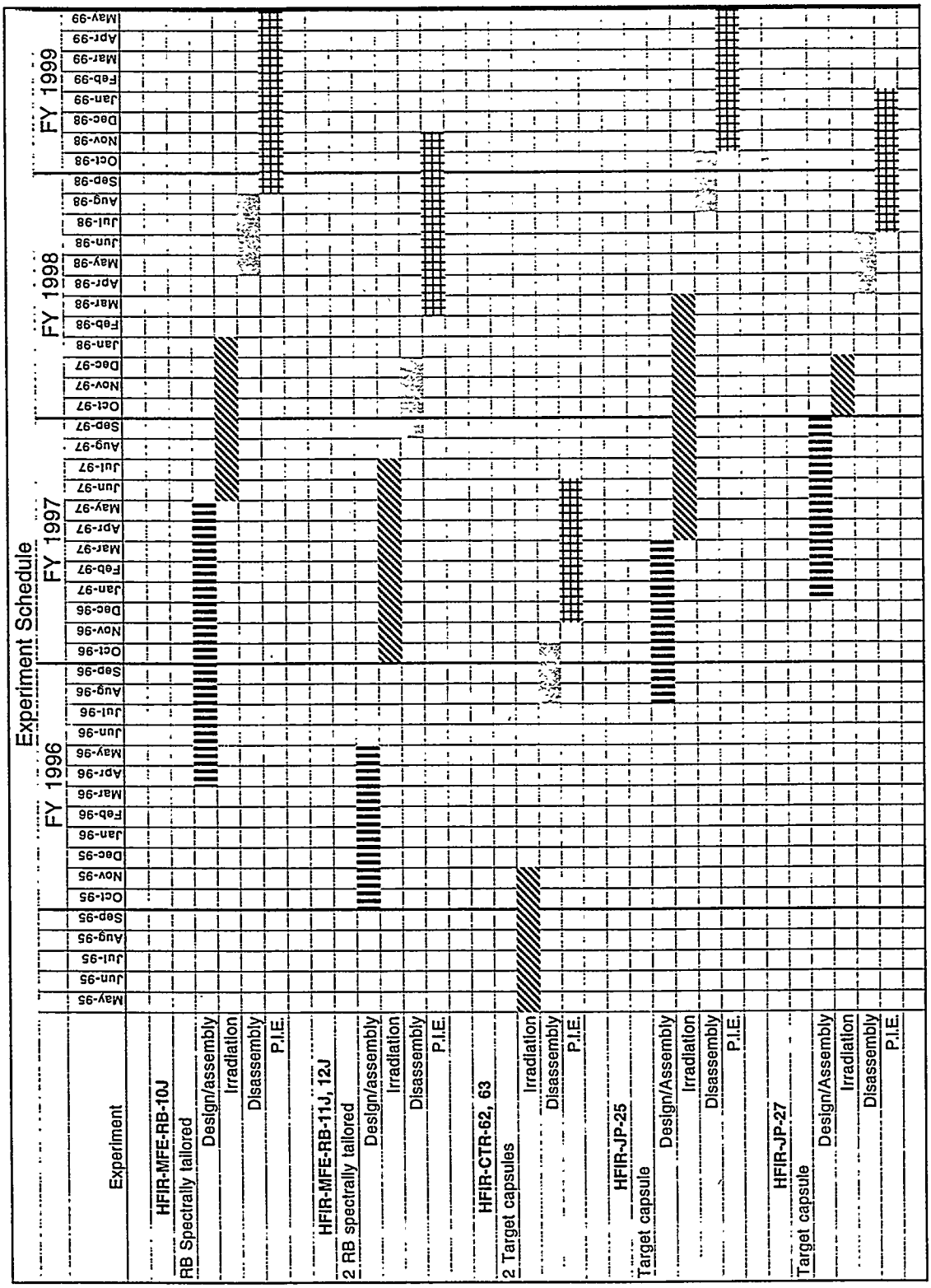
Experiment Schedule
FY 1996
FY 1997
FY 1998
FY 1999
Experiment
HFIR-MFE-RB-10J
RB Spectrally tailored
Design/assembly
Irradiation
Disassembly
P.I.E.
HFIR-MFE-RB-11J, 12J
2 RB spectrally tailored
Design/assembly
Irradiation
Disassembly
P.I.E.
HFIR-CTR-62, 63
2 Target capsules
Irradiation
Disassembly
P.I.E.
HFIR-JP-25
Target capsule
Design/Assembly
Irradiation
Disassembly
P.I.E.
HFIR-JP-27
Target capsule
Design/Assembly
Irradiation
Disassembly
P.I.E.
May-95
Jun-95
Jul-95
Aug-95
Sep-95
Oct-95
Nov-95
Dec-95
Jan-96
Feb-96
Mar-96
Apr-96
May-96
Jun-96
Jul-96
Aug-96
Sep-96
Oct-96
Nov-96
Dec-96
Jan-97
Feb-97
Mar-97
Apr-97
May-97
Jun-97
Jul-97
Aug-97
Sep-97
Oct-97
Nov-97
Dec-97
Jan-98
Feb-98
Mar-98
Apr-98
May-98
Jun-98
Jul-98
Aug-98
Sep-98
Oct-98
Nov-98
Dec-98
Jan-99
Feb-99
Mar-99
Apr-99
May-99

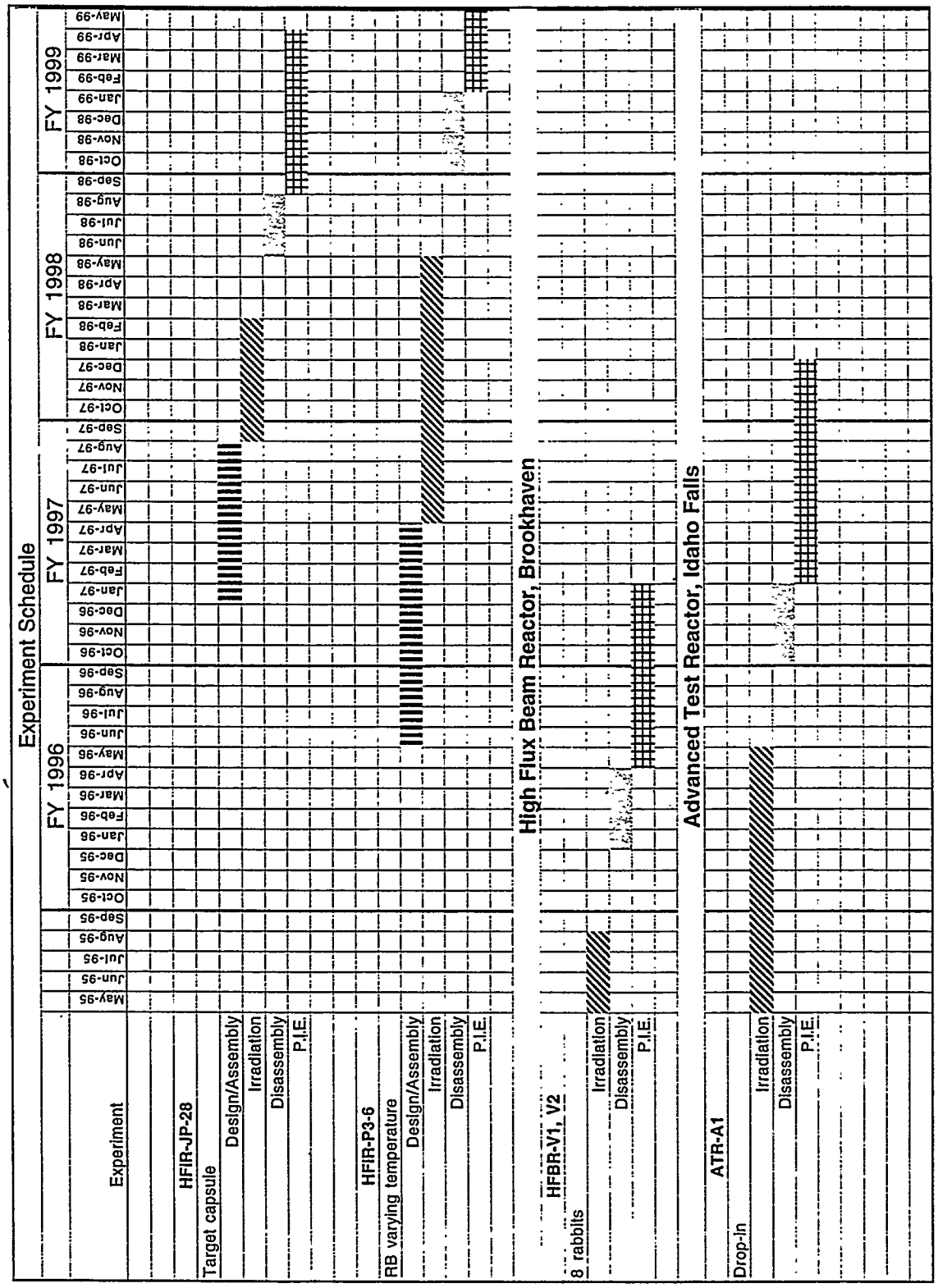
Experiment Schedule
FY 1996
FY 1997
FY 1998
FY 1999
May-95
Jun-95
Jul-95
Aug-95
Sep-95
Oct-95
Nov-95
Dec-95
Jan-96
Feb-96
Mar-96
Apr-96
May-96
Jun-96
Jul-96
Aug-96
Sep-96
Oct-96
Nov-96
Dec-96
Jan-97
Feb-97
Mar-97
Apr-97
May-97
Jun-97
Jul-97
Aug-97
Sep-97
Oct-97
Nov-97
Dec-97
Jan-98
Feb-98
Mar-98
Apr-98
May-98
Jun-98
Jul-98
Aug-98
Sep-98
Oct-98
Nov-98
Dec-98
Jan-99
Feb-99
Mar-99
Apr-99
May-99
Experiment
HFIR-JP-28
Target capsule
Design/Assembly
Irradiation
Disassembly
P.I.E.
HFIR-P3-6
RB varying temperature
Design/Assembly
Irradiation
Disassembly
P.I.E.
High Flux Beam Reactor, Brookhaven
HFBR-V1, V2
8 rabbits
Irradiation
Disassembly
P.I.E.
Advanced Test Reactor, Idaho Falls
ATR-A1
Drop-In
Irradiation
Disassembly
P.I.E.

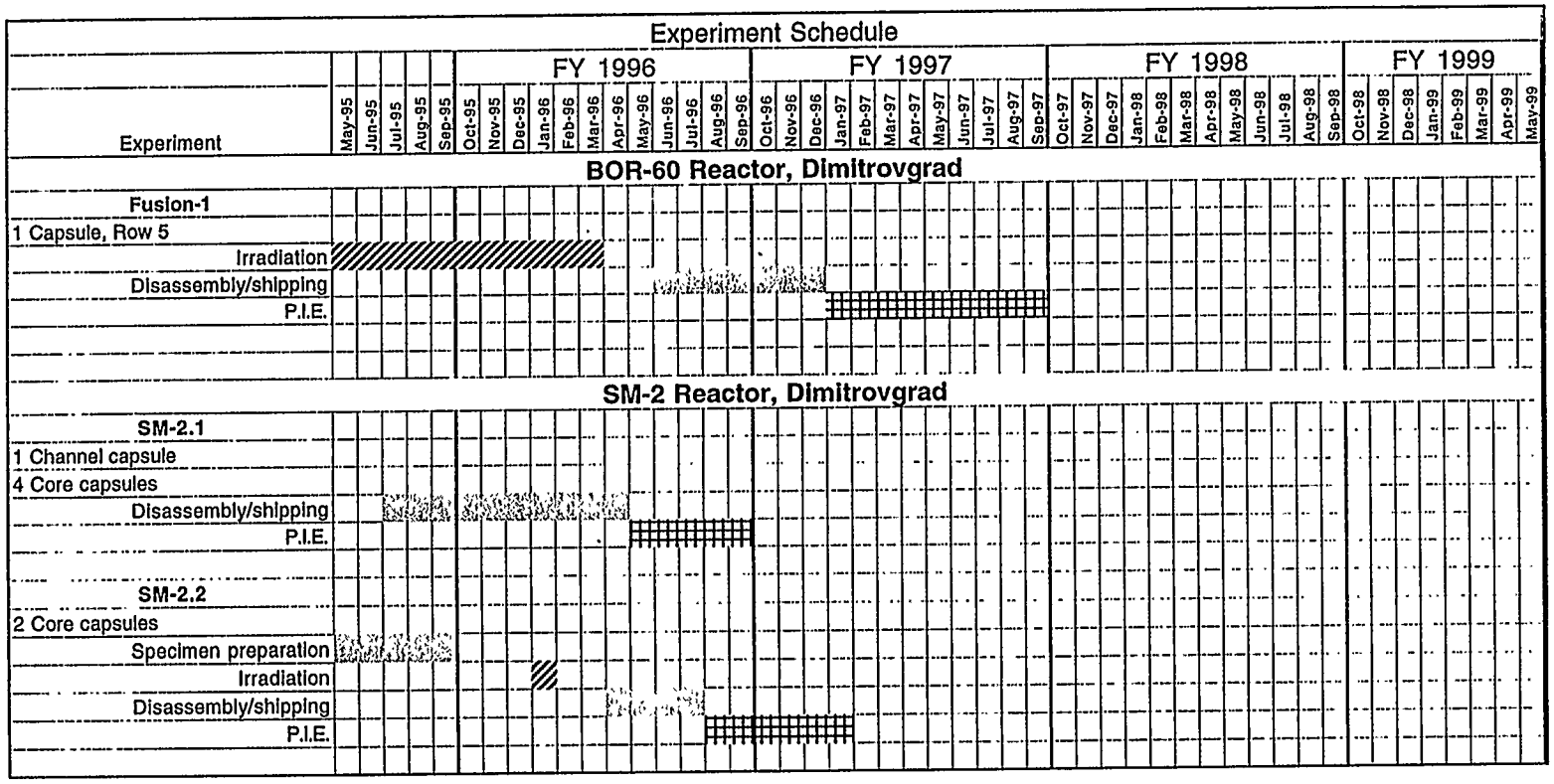
Experiment Schedule
FY 1996
FY 1997
FY 1998
FY 1999
Experiment
May-95 Jun-95 Jul-95 Aug-95 Sep-95 Oct-95 Nov-95 Dec-95 Jan-96 Feb-96 Mar-96 Apr-96 May-96 Jun-96 Jul-96 Aug-96 Sep-96 Oct-96 Nov-96 Dec-96 Jan-97 Feb-97 Mar-97 Apr-97 May-97 Jun-97 Jul-97 Aug-97 Sep-97 Oct-97 Nov-97 Dec-97 Jan-98 Feb-98 Mar-98 Apr-98 May-98 Jun-98 Jul-98 Aug-98 Sep-98 Oct-98 Nov-98 Dec-98 Jan-99 Feb-99 Mar-99 Apr-99 May-99
BOR-60 Reactor, Dimitrovgrad
Fusion-1
1 Capsule, Row 5
Irradiation
Disassembly/shipping
P.I.E.
SM-2 Reactor, Dimitrovgrad
SM-2.1
1 Channel capsule
4 Core capsules
Disassembly/shipping
P.I.E.
SM-2.2
2 Core capsules
Specimen preparation
Irradiation
Disassembly/shipping
P.I.E.

Distribution

1-16. Argonne National Laboratory, 9700 South Cass Avenue, Argonne, IL 60439

M. C. Billone	C. E. Johnson	L. A. Niemark
O. K. Chopra	F. Kassner	J. H. Park
H. M. Chung	J. P. Kopasz	D. L. Smith
D. R. Diercks	R. F. Mattas	W. Tam
J. Gazda	K. Nateson	H. C. Tsai
A. B. Hull		

17-18. Argonne National Laboratory, EBR-II Division, P.O. Box 2528, Idaho Falls, ID 83403-2528
H. P. Planchon D. L. Porter

19. Auburn University, Department of Mechanical Engineering, 201 Ross Hall, Auburn, AL 36849
B. A. Chin

20-34. Pacific Northwest National Laboratory, P.O. Box 999, Richland, WA 99352

J. L. Ethridge	M. L. Hamilton	W. W. Laity
F. A. Garner (5)	H. L. Heinisch	O. D. Slagle
D. S. Gelles	G. W. Hollenberg	J. Youngblood
L. R. Greenwood	R. H. Jones	

35. Carnegie Institute of Technology, Carnegie-Mellon University, Schenley Park, Pittsburgh, PA 15213
W. M. Garrison, Jr.

36. Commissariat à l'Energie Atomique, Direction des Technologies Advancées, M2R1/DECM Cen-Saclay, Gif Sur Yvette, Cedex, France
F. Tavassoli

37-39. General Atomics, P.O. Box 85608, San Diego, CA 92138
W. R. Johnson K. R. Schultz C. Wong

40. General Dynamics Convair Division, 3302 Pacific Hwy, San Diego, CA 92101-1137
T. L. Cookson

41. Georgia Institute of Technology, Fusion Research Center, 0225, Atlanta, GA 30332
W. M. Stacey

42. Grand Canyon University, Department of Natural Science, 3300 W. Camelback Rd., Phoenix, AZ 85017
W. A. Coghlan

43-45. Idaho National Engineering Laboratory, Fusion Safety Program, P.O. Box 1625, Idaho Falls, ID 83415-3523
G. Longhurst K. McCarthy D. Petti

46. Knolls Atomic Power Laboratory, P.O. Box 1072, Schenectady, NY 12301
G. Newsome

47-48. Lawrence Livermore National Laboratory, P.O. Box 808, Livermore, CA 94550
E.C.N. Dalder J. Perkins

49-55. Los Alamos National Laboratory, P.O. Box 1663, Los Alamos, NM 87545

J. L. Anderson	H. M. Frost	W. F. Sommer
D. W. Cooke	R. E. Siemon	K. E. Sickafus
E. H. Farnum		

56. Manlabs, Inc., 231 Erie Street, Cambridge, MA 02139
D. Tognarelli

57-59. Massachusetts Institute of Technology, Department of Metallurgy and Materials Science, Cambridge, MA 02139
L. W. Hobbs N. J. Grant K. C. Russell

60-61. Massachusette Institute of Technology, Plasma Fusion Center Headquarters, Cambridge, MA 02139
H. D. Becker D. B. Montgomery

62-63. McDonnell-Douglas Corporation, Mail Code 106 7211, McDonnell Blvd., Dock 106, Berkeley, MO 63134
J. W. Davis G. W. Wille

64. Merrimack College, Dept. of Physics, 315 Turnpike Street, North Andover, MA 01845
D. P. White

65. M. J. Schiff & Associates, 1291 N. Indian Hill Blvd., Claremont, CA 91711-3897
G.E.C. Bell

66-68. National Institute of Standards and Technology, Boulder, CO 80302
F. R. Fickett H. I. McHenry R. P. Reed

69-70. Naval Research Laboratory, Code 6506, Washington, DC 20375
D. L. Gibson J. A. Sprague

71-112. Oak Ridge National Laboratory, P.O. Box 2008, Oak Ridge, TN 37831

Central Research Library	M. L. Grossbeck	T. C. Reuther
Document Reference Section	A. N. Gubbi	A. F. Rowcliffe (10)
Laboratory Records Department (2)	J. F. King	M. J. Saltmarsh
Laboratory Records-RC	E. A. Kenik	J. Sheffield
Patent Section	R. L. Klueh	L. L. Snead
D. J. Alexander	E. H. Lee	R. E. Stoller
J. Bentley	L. K. Mansur	K. R. Thoms
E. E. Bloom	P. J. Maziasz	P. F. Tortorelli
T. D. Burchell	M. C. Osborne	R. L. Wallace
G. M. Goodwin	P. M. Rice	S. J. Zinkle
R. H. Goulding	J. P. Robertson	

113. Oregon Graduate Institute, Dept. of Materials Science & Engineering, 19600 N.W. Von Neumann Drive, Beaverton, OR 97006
J. M. McCarthy

114-116. Princeton University, Princeton Plasma Physics Laboratory, P.O. Box 451, Princeton, NJ 08540
R. C. Davidson Long-Poe Ku D. M. Meade

117-119. Rensselaer Polytechnic Institute, Troy, NY 12181
S. D. Connery D. Duquette D. Steiner

120. Rockwell International Corporation, NA02, Rocketdyne Division, 6633 Canoga Avenue, Canoga Park, CA 91304
D. W. Kneff

121-123. Sandia National Laboratories, Fusion Technology Dept., Dept. No 6531, P.O. Box 5800, Albuquerque, NM 87185-5800
M. J. Davis M. Ulrickson R. D. Watson

124-126. Sandia National Laboratories, Livermore Division 8316, Livermore, CA 94550
W. Bauer K. Wilson W. G. Wolfer

127. San Diego State University, Mechanical Engineering Dept., San Diego, CA 92182-0191
L. D. Thompson

128. Texas A&M University, Box 397, Prairie View, TX 77446
D. Baker

129. TSI Research, 225 Stevens Ave., #110, Solana Beach, CA 92075
E. T. Cheng

130. Westinghouse Hanford, P.O. Box 1970, Richland, WA 99352
A. M. Ermi (L6-37)

131-132. University of California at San Diego, U.S. ITER Project Office, 9500 Gilman Drive, Bldg. 302, La Jolla, CA 92093-0035
C. C. Baker T. R. James

133-134. University of California, Dept. of Mechanical and Environmental Engineering, Engineering II, Room 2355, Santa Barbara, CA 93106-5070
G. E. Lucas G. R. Odette

135-137. University of California, Dept. of Chemical, Nuclear, and Thermal Engineering, Los Angeles, CA 90024
M. A. Abdou N. M. Ghoniem S. Sharafat

138. University of Michigan, Dept. of Nuclear Engineering, Ann Arbor, MI 48109
T. Kammash

139. University of Missouri, Department of Nuclear Engineering, Rolla, MO 65401
A. Kumar

140. University of Tennessee, Dept. of Materials Science and Engineering, 427-B Dougherty Bldg., Knoxville, TN 37996-2200
P. K. Liaw

141-142. University of Wisconsin, Nuclear Engineering Dept., 1500 Johnson Drive, Madison, WI 53706
J. B. Blanchard G. L. Kulcinski

143-145. Hokkaido University, Faculty of Engineering, Kita 13, Nishi 8, Kita-ku, Sapporo 060, Japan
Heischichiro Takahashi Somei Ohnuki Akira Okada

146-147. Japan Atomic Energy Research Institute, Tokai Research Establishment, Tokai-mura, Naka-gun, Ibaraki-ken 319-11, Japan
Akimichi Hishinuma K. Noda

148. Kyoto University, Institute of Atomic Energy, Gokasho, Uji, Kyoto 611, Japan
Akira Kohyama

149. Kyushu University, Dept. of Nuclear Engineering, Faculty of Engineering, Kyushu University 36, Hakozaki, Fukuoka 812, Japan
C. Kinoshita

150. Kyushu University, Research Institute for Applied Mechanics, Kasuga, Fukuoka 816, Japan
Naoaki Yoshida

151-152. Muroran Institute of Technology, Dept. of Metallurgical Engineering, 27-1 Mizumoto-cho, Mororan 050, Japan
Toshihei Misawa Akihiko Kimura

153-154. Nagoya University, Dept. of Nuclear Engineering, Furo-Cho, Chikusa-ku, Nagoya 464-01, Japan
Michio Kiritani Tetuo Tanabe

155-159. National Institute for Fusion Science, Furo-cho, Chikusa-ku, Nagoya 464-01, Japan
Yutai Katoh Chusei Namba
Osamu Motojima Nobuaki Noda
Takeo Muroga

160-163. National Research Institute for Metals, Tsukuba Branch, Sengen, Tsukuba-shi, Ibaraki-ken, 305, Japan
Fujio Abe Tetsuji Noda
Josei Nagakawa Haruki Shiraishi

164. PNC Oarai, 4002 Narita, Oarai, Ibaraki 311-13, Japan
Itaru Shibahari

165. Science University of Tokyo, Dept. of Materials Science & Technology, 2641 Yamazaki Noda City, Chiba Prefecture 278, Japan
Naohira Igata

166. Teikyo University, Otsuka, Hachioji, Tokyo 192-03, Japan
Akira Miyahara

167-169. Tohoku University, Institute for Materials Research, Katahira 2-2-1, Sendai 980-77, Japan
Akihiko Kimura Hideki Matsui

170-172. Tohoku University, Institute for Materials Research, Oarai Branch, Oarai, Ibaraki 311-13, Japan
Hideo Kayono Tamaki Shibayama
Hiroaki Kurishita Tatsuo Shikama

173-174. Tohoku University, Dept. of Nuclear Engineering, Aoba, Aramaki, Sendai 980-77, Japan
Katsunori Abe Akira Hasegawa

175. Tohoku University, Dept. of Machine Intelligence and Systems Engineering, Aramaki, Aoba-ku, Sendai 980-77, Japan
Tatsuo Kondo

176. Tokai University, Dept. of Nuclear Engineering, 1117 Kitakaname, Hiratsuka-shi, Kanagawa-ken 259-12, Japan
Shiori Ishino

177. University of Tokyo, Dept. of Nuclear Engineering, 3-1, Hongo 7-Chome, Bunkyo-Ku, Tokyo 113, Japan
Naoto Sekimura

178. University of Tokyo, Dept. of Materials Science, 3-1, Hongo 7-Chome, Bunkyo-ku, Tokyo 113, Japan
Yutaka Kohno

179. Commission of European Communities, Directorate-General for Research Science and Education, Fusion Programme RUE De La Loi 200, B-1049 Brussels, Belgium
J. Darvas

180-181. Chalk River Nuclear Laboratories, Atomic Energy of Canada, Ltd., Chalk River, Ontario KOJ 1J0, Canada
I. J. Hastings D. P. Jackson

182. Southwestern Institute of Physics, P.O. Box 432, Chenedu 610041, Sichuan, P.R. China
J. P. Qian

183. Institute of Atomic Energy, Academia Sinica, P.O. Box 275-51, Beijing, P.R. China
J. Yu

184. Riso National Laboratory, Materials Dept., P.O. Box 49, DK-4000, Roskilde, Denmark
B. N. Singh

185. Centre d'Etudes Nucleaires, Saclay, DLPC/SMCM, Commissariat a l'Energie Atomique, 91191 Gif-Sur-Yvette, Cedex, France
N. Roux

186. Commission for European Communities, Joint Research Centre, I.A.M. Ispra Establishment 21020 Ispra (Varese), Italy
P. Fenici

187. EURATOM/CIEMAT Fusion Association, Avenida Complutense 22, 28040, Madrid, Spain
E. R. Hodgson

188. Paul Scherrer Institute, CH-5232 Villigen, Wuerenlingen PSI, Switzerland
M. Victoria

189. Harwell Laboratory, B393, Radiation Damage Dept., Oxfordshire, OX11 ORA, United Kingdom
C. A. English

190. Metallurgical and Nuclear Consultant, 9A Cumnor Rise Road, Cumnor Hill, Oxford OX2 9HD, United Kingdom
D. R. Harries

191. Hahn-Mietner-Institut fur Kernforschung Berlin, Postfach 390128, Glienicker Str. 100, D-14109, Germany
H. Wollenberger

192. Institut fur Festkorperforschung Forschungszentrum Jülich, Postfach 1913, D-52425 Jülich, Germany
H. Ullmaier

193-196. ITER Garching Joint Work Site, Max-Planck-Institute für Plasmaphysik, Boltzmannstrasse 2, D-85748 Garching bei München, Germany
B. Barabash G. Kalinin
Y. Gohar R. Parker

197-198. ITER Naka Joint Work Site, 801-1 Mukouyama, Naka-machi, Naka-gun, Ibaraki-Ken, 311-01, Japan
M. Huguet (2)

199-202. ITER San Diego Joint Work Site, 11025 N. Torrey Pines Road, La Jolla, CA 92037
V. Chuyanov F. Puhn
S. J. Piet P. Smith

203-204. Kernforschungszentrum Karlsruhe, Postfach 3640, 75 Karlsruhe 1, Germany
M. Dalle-Donne (INR) K. Ehrlich (IMF-II)

205. Max-Planck-Institut für Plasmaphysik, Boltzmannstrasse 2, D-85748 Garching bei München, Germany
Patrick Lorenzetto

206. A. A. Baikov Institute of Metallurgy, USSR Academy of Sciences, Leninsky Prospect 49, Moscow, Russia
L. I. Ivanov

207. CRISM "Prometey," Naberezhnava r. Monastyrick 1, 193167, St. Petersburg, Russia
V. V. Rybin

208. D. V. Efremov Institute of Electro-Physical Apparatus, 189631, St. Petersburg, Russia
S. A. Fabritsiev

209. Kharkov Institute of Physics & Technology, Radiation Damage and Materials Dept., Akademicheskaya 1, 310108 Kharkov, Ukraine
I. M. Neckludov

210-212. V. I. Lenin Research Institute of Atomic Reactors, 433510 Dimitrovgrad-10, Ulyanovsk Region, Russia
V. Kazakov A. S. Pokrovsky V. K. Shamardin

213. Korea Advanced Institute of Science and Technology, Department of Nuclear Engineering, DaeDukDanji, Taejon, 305-701, Korea
I-S. Kim

214. Korean Atomic Energy Research Institute, P.O. Box 105, Yusung, Taejon, 305-600, Korea
Jun Hwa Hong

215. Seoul National University, Dept. of Nuclear Engineering, 56-1 Shinrim-Dong, Kwanak-Ku Seoul, 151-742, Korea
K. H. Chung

216. Sung Kyun Kwan University, Dept. of Metallurgical Engineering, 300 Chun Chun-dong, Jang An-Ku, Swon, 440-746, Korea
J. G. Han

217. Department of Energy, DOE Oak Ridge Field Office, P.O. Box 2008, Oak Ridge, TN 37831-6269
Assistant Manager for Energy Research and Development

218. Department of Energy, DOE Oak Ridge Field Office, P.O. Box 2008, Oak Ridge, TN 37831-6269
S. D. Frey

219. Department of Energy, Office of Basic Energy Sciences, Washington, D.C. 20585
R. J. Gottschall

220-227. Department of Energy, Office of Fusion Energy, Germantown, MD 20874

S. E. Berk	W. F. Dove	R. E. Price
M. M. Cohen	R. McKnight	F. W. Wiffen
N. A. Davies	W. Marton	

228. Department of Energy, Richland Operations Office, P.O. Box 550, MS-K850, Richland, WA 99352
J. Turner

229-230. Department of Energy, Office of Scientific and Technical Information, Office of Information Services, P.O. Box 62, Oak Ridge, TN 37831
For distribution by microfiche as shown in DOE/OSTI-4500-R75, Distribution Categories UC-423 (Magnetic Fusion Reactor Materials) and UC-424 (Magnetic Fusion Energy Systems)